

UNCLASSIFIED

AD NUMBER

AD904090

NEW LIMITATION CHANGE

TO

**Approved for public release, distribution
unlimited**

FROM

**Distribution authorized to U.S. Gov't.
agencies only; Test and Evaluation; 12
Jun 1972. Other requests shall be referred
to Air Force Flight Dynamics laboratory,
Wright-Patterson AFB, OH 45433.**

AUTHORITY

AFFDL ltr, 21 Oct 1974

THIS PAGE IS UNCLASSIFIED

AD 904090

AFFDL-TR-72-46

BUFFET DYNAMIC LOADS DURING TRANSONIC MANEUVERS

R. E. MULLANS, C. E. LEMLEY

MCDONNELL AIRCRAFT COMPANY

TECHNICAL REPORT AFFDL-TR-72-46

SEPTEMBER 1972

D D C
REF ID: A65146
OCT 18 1972
REGULUS B

Distribution limited to U.S. Government agencies only, test and evaluation; statement applied 12 June 1972. Other requests for this document must be referred to AF Flight Dynamics Laboratory, (FY), Wright Patterson AFB, Ohio 45433.

AIR FORCE FLIGHT DYNAMICS LABORATORY
AIR FORCE SYSTEMS COMMAND
WRIGHT-PATTERSON AIR FORCE BASE, OHIO

NOTICE

When Government drawings, specifications, or other data are used for any purpose other than in connection with a definitely related Government procurement operation, the United States Government thereby incurs no responsibility nor any obligation whatsoever; and the fact that the government may have formulated, furnished, or in any way supplied the said drawings, specifications, or other data, is not to be regarded by implication or otherwise as in any manner licensing the holder or any other person or corporation, or conveying any rights or permission to manufacture, use, or sell any patented invention that may in any way be related thereto.

Copies of this report should not be returned unless return is required by security considerations, contractual obligations, or notice on a specific document.

AIR FORCE/56780/2 October 1972 - 100

BUFFET DYNAMIC LOADS DURING TRANSONIC MANEUVERS

R. E. MULLANS, C. E. LEMLEY

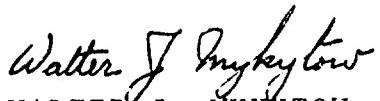
Distribution limited to U.S. Government agencies only; test and evaluation, statement applied 12 June 1972. Other requests for this document must be referred to AF Flight Dynamics Laboratory, (FY), Wright-Patterson AFB, Ohio 45433.

FOREWORD

This report was prepared by the McDonnell Aircraft Company, (MCAIR), a Division of the McDonnell Douglas Corporation, St. Louis, Missouri for the Aerospace Dynamics Branch, Vehicle Dynamics Division, Air Force Flight Dynamics Laboratory, Wright-Patterson Air Force Base, Ohio under Contract AF 33615-70-C-1272, Project No. 1370, "Dynamic Problems in Military Flight Vehicles", Task No. 137008, "Prediction of Dynamic Loads in Military Aircraft." Mr. Verner J. Johnson was the Project Engineer at the Air Force Flight Dynamics Laboratory.

This program represents efforts by MCAIR personnel of the Engineering Technology and Laboratory Flight Test Divisions, as well as by Dr. John Houbolt, Consultant. The major portion of the technical effort was provided by Mr. Robert E. Mullans, Senior Structural Dynamics Engineer, under the direction of Dr. Clark Lemley, Project Dynamics Engineer. Dr. Norman Zimmerman provided overall program management. The authors wish to acknowledge the participation of Dr. Houbolt who made significant contributions to Sections 5 and 6 of this Final Report. The manuscript was released by the authors for publication in March 1972.

This technical report has been reviewed and is approved.



WALTER J. MYKYTOW
Asst. for Research and Technology
Vehicle Dynamics Division
AF Flight Dynamics Laboratory

ABSTRACT

This report describes an empirical/theoretical study program to develop a first generation method for predicting the buffet dynamic loads and fighter aircraft responses that occur during transonic maneuvers. The prediction method applies to wing upper surface loads acting on the airplane and the induced aircraft dynamic responses. Wind tunnel tests of a 10% scale model of the YF-4E aircraft were used to enhance understanding of the buffet mechanism for lifting surfaces and to obtain data needed to deduce the surface load formulas. A first test phase (Series I) gave oil flow and tuft information regarding flow on the upper wing surfaces. A second test phase (Series II) was used to acquire both steady and fluctuating pressure and strain data as well as acceleration response.

The fluctuating pressure data were converted to power and cross-power spectra and a mathematical model was formulated to describe the amplitude and the spatial and spectral distributions of the pressures on the wing.

The mathematical pressure distribution was then used as the forcing function in a dynamic response computer program to assess the structural response. Model pressure data and the predicted airplane responses were in reasonable agreement with flight test data.

In the process of developing the method for buffet loads prediction, a great deal of valuable information was collected pertaining to the nature of the buffeting flow over a lifting surface and the resulting structural responses. This data together with its interpretation are included in this report and supplementary reports that are referenced herein.

PRECEDING PAGE BLANK-NOT FILMED.

TABLE OF CONTENTS

<u>Section</u>	<u>Page</u>
1. INTRODUCTION	1
1.1 History	1
1.1.1 Earlier Studies	1
1.1.2 Recent Studies	1
1.2 Buffet Prediction Method	2
1.2.1 Technical Approach	2
2. TEST PROGRAM	4
2.1 Model Design	4
2.2 Flow Visualization Tests	4
2.3 Dynamic Instrumentation on Model	5
2.3.1 Sensor Description	5
2.3.2 Microphone Grid	7
2.4 Vibration Tests	9
2.5 Buffet Data Acquisition Tests	10
3. DATA ACQUISITION AND REDUCTION	12
3.1 On-Line Data Acquisition and Reduction System at AEDC	12
3.2 Data Reduction at MCAIR	12
3.2.1 Oscillograph Traces	13
3.2.2 Broad Band FM Recording	13
3.3 Mathematical Functions, Spectral Analysis	13
3.3.1 Correlation Functions	13
3.3.2 Power and Cross Power Spectral Density Functions	15
3.4 Accuracy of Data	19
4. DATA ANALYSIS	21
4.1 Flow Analysis	21
4.1.1 Turbulence	21
4.1.2 Oil Flow	21
4.1.3 Flow Characteristics	22
4.2 Analysis of rms Data	22

TABLE OF CONTENTS (Continued)

<u>Section</u>		<u>Page</u>
4.2.1	Noise in Wind Tunnel	22
4.2.2	Pressure rms Measurements	22
4.2.3	Bending Moment Measurements	23
4.3	Analysis of Spectral Data	24
4.3.1	Noise Power Spectral Densities	24
4.3.2	Buffet Power Spectral Densities	25
4.3.3	Ratio of Peak to Low Frequency Spectral Levels	27
4.3.4	Buffet Cross Power Spectral Densities	28
4.3.5	Tail Buffet	30
4.4	Comparison of Wind Tunnel and Flight Data	30
4.4.1	Overall rms	31
4.4.2	Frequency Distribution	32
5.	PREDICTION METHOD FOR FLUCTUATING PRESSURES	35
5.1	General	35
5.2	Nature of Pressure Function	36
5.2.1	rms levels	36
5.2.2	Spectral Shape	38
5.2.3	Fitting Data to the Model	39
5.2.4	Preliminary Design Data	41
5.2.5	Experimental Values of n	42
5.3	Spatial Correlation Effects	43
5.4	Procedure for Applying Prediction Method	46
5.4.1	Spectral shape	46
5.4.2	Overall rms level	48
6.	PREDICTION METHOD FOR BUFFET DYNAMIC RESPONSE	49
6.1	Outline of Response Prediction Method	49
6.2	Wing Area Partition	50
6.3	Overview of Mathematical Development	50
6.3.1	Monoshape Averaging	52
6.3.2	Real Representation of Response Spectrum	52
6.3.3	Simplifying Assumption	54
7.	PREDICTION OF AIRCRAFT RESPONSE AND COMPARISON WITH MEASURED FLIGHT DATA	58
7.1	Response Equations	58
7.2	Wing Identification	58
7.3	Structural Representation of F-4 Wing	58

TABLE OF CONTENTS (Continued)

<u>Section</u>	<u>Page</u>
7.4 Flight Conditions	63
7.5 Predicted Fluctuating Pressures	65
7.6 Results	65
7.6.1 Effect of Damping	65
7.6.2 Variations in Measured Response Data	65
7.6.3 Comparison of Predicted and Measured Response Data	68
7.6.4 Summary of Comparison with Measured Response Data	70
8. CONCLUDING REMARKS	72
9. RECOMMENDATIONS	74
APPENDIX A - Flow Analyses	237
REFERENCES	267

LIST OF ILLUSTRATIONS

<u>Figure</u>		<u>Page</u>
1	Buffet Loads Prediction Method	77
2	General Arrangement of F-4E 10% Model	78
3	Tufts and Oil Flow on 10% F-4 Model	79
4	Model Instrumentation	80
5	Wing Instrumentation Locations	81
6	Vibration Test Setup at MCAIR	82
7	Vibration Test Setup at Wind Tunnel	83
8	Fluctuating Pressure Oscillograph Traces for Configuration 1, Mach 0.7, Wing Angle of Attack 12°	84
9	Bending, Torsion, and Acceleration Oscillograph Traces for Configuration 1, Mach 0.7, Wing Angle of Attack 12°	85
10	Fluctuating Pressure Oscillograph Traces for Configuration 1, Mach 0.9, Wing Angle of Attack 12°	86
11	Bending, Torsion, and Acceleration Oscillograph Traces for Configuration 1, Mach 0.9, Wing Angle of Attack 12°	87
12	Flow Diagram of Spectral Data Reduction at MCAIR	88
13	Tufts and Oil Flow (Photograph)	89
14	Root Mean Square Pressure Coefficient vs. Percent Chord (Configuration 1, Mach 0.7, Wing Angle of Attack -0.8°)	90
15	Root Mean Square Pressure Coefficient vs. Percent Chord (Configuration 1, Mach 0.7, Wing Angle of Attack 12°)	91
16	Root Mean Square Pressure Coefficient vs. Percent Chord (Configuration 1, Mach 0.9, Wing Angle of Attack -0.8°)	92
17	Root Mean Square Pressure Coefficient vs Percent Chord (Configuration 1, Mach 0.9, Wing Angle of Attack 8°)	92
18	Root Mean Square Pressure Coefficient vs Percent Chord (Configuration 1, Mach 0.9, Wing Angle of Attack 12°)	93
19	Root Mean Square Pressure Coefficient vs Percent Chord (Configuration 1, Mach 0.9, Wing Angle of Attack 14°)	94
20	Root Mean Square Pressure Coefficient vs Percent Chord (Configuration 1, Mach 1.0, Wing Angle of Attack 0°)	95
21	Root Mean Square Pressure Coefficient vs Percent Chord (Configuration 1, Mach 1.0, Wing Angle of Attack 12°)	95
22	Root Mean Square Pressure Coefficient vs Percent Chord (Configuration 5, Mach 0.7, Wing Angle of Attack 11°)	96
23	Root Mean Square Pressure Coefficient vs Percent Chord (Configuration 5, Mach 0.9, Wing Angle of Attack 11°)	97
24	Root Mean Square Pressure Coefficient vs Percent Chord (Configuration 5, Mach 0.9, Wing Angle of Attack 14°)	98

LIST OF ILLUSTRATIONS (Continued)

<u>Figure</u>		<u>Page</u>
25	Root Mean Square Pressure Coefficient vs Percent Chord (Configuration 6, Mach 0.7, Wing Angle of Attack 11°)	99
26	Ratio of rms Inner Wing Bending Moment to Steady Bending Moment, Configuration 1, Mach 0.7	100
27	Ratio of rms Inner Wing Bending Moment to Steady Bending Moment, Configuration 1, Mach 0.8	100
28	Ratio of rms Inner Wing Bending Moment to Steady Bending Moment, Configuration 1, Mach 0.9	101
29	Fluctuating Pressure Power Spectral Density (Configuration 1, Mach 0.7, Wing Angle of Attack -1 Deg., Transducer 10)	102
30	Fluctuating Pressure Power Spectral Density (Configuration 1, Mach 0.7, Wing Angle of Attack -1 Deg., Transducer 11)	103
31	Fluctuating Pressure Power Spectral Density (Configuration 1, Mach 0.7, Wing Angle of Attack -1 Deg., Transducer 13)	104
32	Fluctuating Pressure Power Spectral Density (Configuration 1, Mach 0.7, Wing Angle of Attack -1 Deg., Transducer 14)	105
33	Fluctuating Pressure Power Spectral Density (Configuration 1, Mach 0.9, Wing Angle of Attack -1 Deg., Transducer 10)	106
34	Fluctuating Pressure Power Spectral Density (Configuration 1, Mach 0.9, Wing Angle of Attack -1 Deg., Transducer 11)	107
35	Fluctuating Pressure Power Spectral Density (Configuration 1, Mach 0.9, Wing Angle of Attack -1 Deg., Transducer 13)	108
36	Fluctuating Pressure Power Spectral Density (Configuration 1, Mach 0.9, Wing Angle of Attack -1 Deg., Transducer 14)	109
37	Fluctuating Pressure Power Spectral Density (Configuration 1, Mach 1.0, Wing Angle of Attack 0 Deg., Transducer 13)	110
38	Fluctuating Pressure Power Spectral Density (Configuration 1, Mach 1.0, Wing Angle of Attack 0 Deg., Transducer 14)	111
39	Fluctuating Pressure Power Spectral Density (Configuration 1, Mach 0.7, Wing Angle of Attack 12 Deg., Transducer 1)	112
40	Fluctuating Pressure Power Spectral Density (Configuration 1, Mach 0.7, Wing Angle of Attack 12 Deg., Transducer 2)	113
41	Fluctuating Pressure Power Spectral Density (Configuration 1, Mach 0.7, Wing Angle of Attack 12 Deg., Transducer 3)	114
42	Fluctuating Pressure Power Spectral Density (Configuration 1, Mach 0.7, Wing Angle of Attack 12 Deg., Transducer 4)	115
43	Fluctuating Pressure Power Spectral Density (Configuration 1, Mach 0.7, Wing Angle of Attack 12 Deg., Transducer 5)	116
44	Fluctuating Pressure Power Spectral Density (Configuration 1, Mach 0.7, Wing Angle of Attack 12 Deg., Transducer 6)	117

LIST OF ILLUSTRATIONS (Continued)

<u>Figure</u>		<u>Page</u>
45	Fluctuating Pressure Power Spectral Density (Configuration 1, Mach 0.7, Wing Angle of Attack 12 Deg., Transducer 7)	118
46	Fluctuating Pressure Power Spectral Density (Configuration 1, Mach 0.7, Wing Angle of Attack 12 Deg., Transducer 8)	119
47	Fluctuating Pressure Power Spectral Density (Configuration 1, Mach 0.7, Wing Angle of Attack 12 Deg., Transducer 9)	120
48	Fluctuating Pressure Power Spectral Density (Configuration 1, Mach 0.7, Wing Angle of Attack 12 Deg., Transducer 10)	121
49	Fluctuating Pressure Power Spectral Density (Configuration 1, Mach 0.7, Wing Angle of Attack 12 Deg., Transducer 11)	122
50	Fluctuating Pressure Power Spectral Density (Configuration 1, Mach 0.7, Wing Angle of Attack 12 Deg., Transducer 12)	123
51	Fluctuating Pressure Power Spectral Density (Configuration 1, Mach 0.7, Wing Angle of Attack 12 Deg., Transducer 13)	124
52	Fluctuating Pressure Power Spectral Density (Configuration 1, Mach 0.7, Wing Angle of Attack 12 Deg., Transducer 14)	125
53	Fluctuating Pressure Power Spectral Density (Configuration 1, Mach 0.7, Wing Angle of Attack 12 Deg., Transducer 15)	126
54	Fluctuating Pressure Power Spectral Density (Configuration 1, Mach 0.7, Wing Angle of Attack 12 Deg., Transducer 16)	127
55	Fluctuating Pressure Power Spectral Density (Configuration 1, Mach 0.7, Wing Angle of Attack 12 Deg., Transducer 17)	128
56	Fluctuating Pressure Power Spectral Density (Configuration 1, Mach 0.7, Wing Angle or Attack 12 Deg., Transducer 18)	129
57	Fluctuating Pressure Power Spectral Density (Configuration 1, Mach 0.7, Wing Angle or Attack 12 Deg., Transducer 19)	130
58	Fluctuating Pressure Power Spectral Density (Configuration 1, Mach 0.7, Wing Angle or Attack 12 Deg., Transducer 20)	131
59	Fluctuating Pressure Power Spectral Density (Configuration 1, Mach 0.7, Wing Angle or Attack 12 Deg., Transducer 21)	132
60	Fluctuating Pressure Power Spectral Density (Configuration 1, Mach 0.7, Wing Angle or Attack 12 Deg., Transducer 23)	133
61	Fluctuating Pressure Power Spectral Density (Configuration 1, Mach 0.7, Wing Angle or Attack 12 Deg., Transducer 24)	134
62	Wing Locations at which Peaks are Evident in Pressure Power Spectral Density Functions (Configuration 1, Mach 0.7, Wing Angle of Attack 12°)	135
63	Fluctuating Pressure Power Spectral Density (Configuration 1, Mach 0.9, Wing Angle of Attack 8 Deg., Transducer 10)	136
64	Fluctuating Pressure Power Spectral Density (Configuration 1, Mach 0.9, Wing Angle of Attack 8 Deg., Transducer 11)	137

LIST OF ILLUSTRATIONS (Continued)

<u>Figure</u>		<u>Page</u>
65	Wing Locations at which Peaks are Evident in Pressure Power Spectral Density Functions (Configuration 1, Mach 0.9, Wing Angle of Attack 8°)	138
66	Fluctuating Pressure Power Spectral Density (Configuration 1, Mach 0.9, Wing Angle of Attack 12 Deg., Transducer 10)	139
67	Fluctuating Pressure Power Spectral Density (Configuration 1, Mach 0.9, Wing Angle of Attack 12 Deg., Transducer 11)	140
68	Fluctuating Pressure Power Spectral Density (Configuration 1, Mach 0.9, Wing Angle of Attack 12 Deg., Transducer 13)	141
69	Fluctuating Pressure Power Spectral Density Configuration 1, Mach 0.9, Wing Angle of Attack 12 Deg., Transduc... 14)	142
70	Wing Locations at which Peaks are Evident in Pressure Power Spectral Density Functions (Configuration 1, Mach 0.9, Wing Angle of Attack 12°)	143
71	Fluctuating Pressure Power Spectral Density (Configuration 1, Mach 0.9, Wing Angle of Attack 14 Deg., Transducer 10)	144
72	Fluctuating Pressure Power Spectral Density (Configuration 1, Mach 0.9, Wing Angle of Attack 14 Deg., Transducer 11)	145
73	Fluctuating Pressure Power Spectral Density (Configuration 1, Mach 0.9, Wing Angle of Attack 14 Deg., Transducer 13)	146
74	Wing Locations at which Peaks are Evident in Pressure Power Spectral Density Functions (Configuration 1, Mach 0.9, Wing Angle of Attack 14°)	147
75	Fluctuating Pressure Power Spectral Density (Configuration 1, Mach 1.0, Wing Angle of Attack 12 Deg., Transducer 10)	148
76	Fluctuating Pressure Power Spectral Density (Configuration 1, Mach 1.0, Wing Angle of Attack 12 Deg., Transducer 11)	149
77	Fluctuating Pressure Power Spectral Density (Configuration 1, Mach 1.0, Wing Angle of Attack 12 Deg., Transducer 13)	150
78	Fluctuating Pressure Power Spectral Density (Configuration 1, Mach 1.0, Wing Angle of Attack 12 Deg., Transducer 14)	151
79	Fluctuating Pressure Power Spectral Density (Configuration 5, Mach 0.7, Wing Angle of Attack 11 Deg., Transducer 10)	152
80	Fluctuating Pressure Power Spectral Density (Configuration 5, Mach 0.7, Wing Angle of Attack 11 Deg., Transducer 11)	153
81	Fluctuating Pressure Power Spectral Density (Configuration 5, Mach 0.7, Wing Angle of Attack 11 Deg., Transducer 14)	154
82	Wing Locations at which Peaks are Evident in Pressure Power Spectral Density Functions (Configuration 5, Mach 0.7, Wing Angle of Attack 11°)	155
83	Fluctuating Pressure Power Spectral Density (Configuration 5, Mach 0.9, Wing Angle of Attack 11 Deg., Transducer 10)	156

LIST OF ILLUSTRATIONS (Continued)

<u>Figure</u>		<u>Page</u>
84	Fluctuating Pressure Power Spectral Density (Configuration 5, Mach 0.9, Wing Angle of Attack 11 Deg., Transducer 11)	157
85	Fluctuating Pressure Power Spectral Density (Configuration 5, Mach 0.9, Wing Angle of Attack 11 Deg., Transducer 13)	158
86	Fluctuating Pressure Power Spectral Density (Configuration 5, Mach 0.9, Wing Angle of Attack 11 Deg., Transducer 14)	159
87	Wing Locations at which Peaks are Evident in Pressure Power Spectral Density Functions, (Configuration 5, Mach 0.9, Wing Angle of Attack 11°)	160
88	Fluctuating Pressure Power Spectral Density (Configuration 5, Mach 0.9, Wing Angle of Attack 14 Deg., Transducer 10)	161
89	Fluctuating Pressure Power Spectral Density (Configuration 5, Mach 0.9, Wing Angle of Attack 14 Deg., Transducer 11)	162
90	Fluctuating Pressure Power Spectral Density (Configuration 5, Mach 0.9, Wing Angle of Attack 14 Deg., Transducer 13)	163
91	Fluctuating Pressure Power Spectral Density (Configuration 5, Mach 0.9, Wing Angle of Attack 14 Deg., Transducer 14)	164
92	Wing Locations at which Peaks are Evident in Pressure Power Spectral Density Functions, (Configuration 5, Mach 0.9, Wing Angle of Attack 14°)	165
93	Fluctuating Pressure Power Spectral Density (Configuration 6, Mach 0.7, Wing Angle of Attack 11 Deg., Transducer 10)	166
94	Fluctuating Pressure Power Spectral Density (Configuration 6, Mach 0.7, Wing Angle of Attack 11 Deg., Transducer 11)	167
95	Fluctuating Pressure Power Spectral Density (Configuration 6, Mach 0.7, Wing Angle of Attack 11 Deg., Transducer 13)	168
96	Wing Locations at which Peaks are Evident in Pressure Power Spectral Density Functions (Configuration 6, Mach 0.7, Wing Angle of Attack 11°)	169
97	Ratio of Peak to Average Low Frequency Power Spectral Density Level vs Percent Chord (Configuration 1, Mach 0.7, Wing Angle of Attack 12°)	170
98	Ratio of Peak to Average Low Frequency Power Spectral Density Level vs Percent Chord (Configuration 1, Mach 0.9, Wing Angle of Attack 8°)	171
99	Ratio of Peak to Average Low Frequency Power Spectral Density Level vs Percent Chord (Configuration 1, Mach 0.9, Wing Angle of Attack 12°)	172
100	Ratio of Peak to Average Low Frequency Power Spectral Density Level vs Percent Chord (Configuration 1, Mach 0.9, Wing Angle of Attack 14°)	173

LIST OF ILLUSTRATIONS (Continued)

<u>Figure</u>		<u>Page</u>
101	Ratio of Peak to Average Low Frequency Power Spectral Density Level vs Percent Chord (Configuration 5, Mach 0.7, Wing Angle of Attack 11°)	174
102	Ratio of Peak to Average Low Frequency Power Spectral Density Level vs Percent Chord (Configuration 5, Mach 0.9, Wing Angle of Attack 11°)	175
103	Ratio of Peak to Average Low Frequency Power Spectral Density Level vs Percent Chord (Configuration 5, Mach 0.9, Wing Angle of Attack 14°)	176
104	Ratio of Peak to Average Low Frequency Power Spectral Density Level vs Percent Chord (Configuration 6, Mach 0.7, Wing Angle of Attack 11°)	177
105	Fluctuating Pressure Normalized Cross Power Spectral Density (Magnitude) (Configuration 1, Mach 0.7, Wing Angle of Attack 12 Deg., Transducers 6 and 10)	178
106	Fluctuating Pressure Normalized Cross Power Spectral Density (Phase) (Configuration 1, Mach 0.7, Wing Angle of Attack 12 Deg., Transducers 6 and 10)	179
107	Fluctuating Pressure Normalized Cross Power Spectral Density (Magnitude) (Configuration 1, Mach 0.7, Wing Angle of Attack 12 Deg., Transducers 12 and 18)	180
108	Fluctuating Pressure Normalized Cross Power Spectral Density (Phase) (Configuration 1, Mach 0.7, Wing Angle of Attack 12 Deg., Transducers 12 and 18)	181
109	Fluctuating Pressure Normalized Cross Power Spectral Density (Magnitude) (Configuration 1, Mach 0.9, Wing Angle of Attack 8 Deg., Transducers 6 and 10)	182
110	Fluctuating Pressure Normalized Cross Power Spectral Density (Phase) (Configuration 1, Mach 0.9, Wing Angle of Attack 8 Deg., Transducers 6 and 10)	183
111	Fluctuating Pressure Normalized Cross Power Spectral Density (Magnitude), (Configuration 1, Mach 0.9, Wing Angle of Attack 8 Deg., Transducers 12 and 18)	184
112	Fluctuating Pressure Normalized Cross Power Spectral Density (Phase) (Configuration 1, Mach 0.9, Wing Angle of Attack 8 Deg., Transducers 12 and 18)	185
113	Fluctuating Pressure Normalized Cross Power Spectral Density (Magnitude) (Configuration 1, Mach 0.9, Wing Angle of Attack 12 Deg., Transducers 6 and 10)	186
114	Fluctuating Pressure Normalized Cross Power Spectral Density (Phase) (Configuration 1, Mach 0.9, Wing Angle of Attack 12 Deg., Transducers 6 and 10)	187
115	Fluctuating Pressure Normalized Cross Power Spectral Density (Magnitude) (Configuration 1, Mach 0.9, Wing angle of Attack 12 Deg., Transducers 12 and 18)	188

LIST OF ILLUSTRATIONS (Continued).

<u>Figure</u>		<u>Page</u>
116	Fluctuating Pressure Normalized Cross Power Spectral Density (Phase) (Configuration 1, Mach 0.9, Wing Angle of Attack 12 Deg., Transducers 12 and 18)	189
117	Fluctuating Pressure Normalized Cross Power Spectral Density (Magnitude) (Configuration 1, Mach 0.9, Wing Angle of Attack 14 Deg., Transducers 6 and 10)	190
118	Fluctuating Pressure Normalized Cross Power Spectral Density (Phase) (Configuration 1, Mach 0.9, Wing Angle of Attack 14 Deg., Transducers 6 and 10)	191
119	Fluctuating Pressure Normalized Cross Power Spectral Density (Magnitude) (Configuration 1, Mach 0.9, Wing Angle of Attack 14 Deg., Transducers 12 and 18)	192
120	Fluctuating Pressure Normalized Cross Power Spectral Density (Phase) (Configuration 1, Mach 0.9, Wing Angle of Attack 14 Deg., Transducers 12 and 18)	193
121	Fluctuating Pressure Normalized Cross Power Spectral Density (Magnitude) (Configuration 1, Mach 1.0, Wing Angle of Attack 12 Deg., Transducers 6 and 10)	194
122	Fluctuating Pressure Normalized Cross Power Spectral Density (Phase) (Configuration 1, Mach 1.0, Wing Angle of Attack 12 Deg., Transducers 6 and 10)	195
123	Fluctuating Pressure Normalized Cross Power Spectral Density (Magnitude) (Configuration 1, Mach 1.0, Wing Angle of Attack 12 Deg., Transducers 12 and 18)	196
124	Fluctuating Pressure Normalized Cross Power Spectral Density (Phase) (Configuration 1, Mach 1.0, Wing Angle of Attack 12 Deg., Transducers 12 and 18)	197
125	Fluctuating Pressure Power Spectral Density (Configuration 1, Mach 0.9, Wing Angle of Attack 8 Deg., Transducer 27)	198
126	Fluctuating Pressure Power Spectral Density (Configuration 1, Mach 0.9, Wing Angle of Attack 12 Deg., Transducer 27)	199
127	Fluctuating Pressure Power Spectral Density (Configuration 1, Mach 0.9, Wing Angle of Attack 14 Deg., Transducer 27)	200
128	Fluctuating Pressure Power Spectral Density (Configuration 1, Mach 0.9, Wing Angle of Attack 8 Deg., Transducer 21)	201
129	Fluctuating Pressure Power Spectral Density (Configuration 1, Mach 0.9, Wing Angle of Attack 12 Deg., Transducer 21)	202
130	Fluctuating Pressure Power Spectral Density (Configuration 1, Mach 0.9, Wing Angle of Attack 14 Deg., Transducer 21)	203
131	Fluctuating Pressure Normalized Cross Power Spectral Density (Magnitude) (Configuration 1, Mach 0.9, Wing Angle of Attack 12 Deg., Transducers 21 and 27)	204

LIST OF ILLUSTRATIONS (Continued)

<u>Figure</u>		<u>Page</u>
132	Fluctuating Pressure Normalized Cross Power Spectral Density (Phase) (Configuration 1, Mach 0.9, Wing Angle of Attack 12 Deg., Transducers 21 and 27)	205
133	Comparison of Model and Full Scale rms Pressure Coefficient Variation with Angle of Attack at Mach 0.8, 90 Percent Chord, 86 Percent Semispan	206
134	Comparison of Model and Full Scale rms Pressure Coefficient Variation with Angle of Attack at Mach 0.8, 90 Percent Chord, 78 Percent Semispan	206
135	Comparison of Model and Full Scale rms Pressure Coefficient Variation with Angle of Attack at Mach 0.8, 90 Percent Chord, 33 Percent Semispan	207
136	Comparison of Model and Full Scale rms Pressure Coefficient Variation with Angle of Attack at Mach 0.8, 95 Percent Chord, 33 Percent Semispan	207
137	Comparison of Model and Full Scale rms Pressure Coefficient Variation with Angle of Attack at Mach 0.9, 90 Percent Chord, 86 Percent Semispan	208
138	Comparison of Model and Full Scale rms Pressure Coefficient Variation with Angle of Attack at Mach 0.9, 90 Percent Chord, 78 Percent Semispan	208
139	Comparison of Model and Full Scale rms Pressure Coefficient Variation with Angle of Attack at Mach 0.9, 90 Percent Chord, 33 Percent Semispan	209
140	Comparison of Model and Full Scale rms Pressure Coefficient Variation with Angle of Attack at Mach 0.9, 95 Percent Chord, 33 Percent Semispan	209
141	Comparison of Model and Full Scale Pressure Spectral Shape for Configuration 1 (Mach 0.8, Wing Angle of Attack 12°, Transducer 17)	210
142	Comparison of Model and Full Scale Pressure Spectral Shape for Configuration 1 (Mach 0.8, Wing Angle of Attack 12°, Transducer 18)	211
143	Comparison of Model and Full Scale Pressure Spectral Shape for Configuration 1 (Mach 0.85, Wing Angle of Attack 10°, Transducer 17)	212
144	Comparison of Model and Full Scale Pressure Spectral Shape for Configuration 1 (Mach 0.85, Wing Angle of Attack 10°, Transducer 18)	213
145	Comparison of Model and Full Scale Pressure Spectral Shape for Configuration 6 (Mach 0.8, Wing Angle of Attack 9°, Transducer 17)	214

LIST OF ILLUSTRATIONS (Continued)

<u>Figure</u>		<u>Page</u>
146	Comparison of Model and Full Scale Pressure Spectral Shape for Configuration 6 (Mach 0.8, Wing Angle of Attack 9°, Transducer 18)	215
147	Model for rms Pressure Coefficient, ΔC_{Prms}	216
148	Comparison of Linear Model of rms Pressure Coefficient with Measured Data, Clean Wing	217
149	Mathematical Model for Fluctuating Pressure Nondimensional Power Spectral Density $\frac{k_o G(k)}{\sigma^2}$	218
150	Buffet Pressure Prediction Parameter λ as a Function of Parameter n	219
151	Comparison of Theoretical and Measured Power Spectral Density Spectra	220
152	Nondimensional Frequencies Associated with Leading Edge, Tip and Snag Vortices	221
153	Model for Ratio of Peak to Average Low Frequency Power Spectral Density Level (n)	224
154	Spatial Decay of Pressure Normalized Cross Power Spectral Density	226
155	Example of Division of Wing Planform into Regions and Areas	227
156	Idealization of F-4 Wing Planform for Prediction of Buffet Response	228
157	Estimated Locations of Vortices for Flight Conditions 1 and 2	229
158	Estimated Locations of Vortices for Flight Condition 3	230
159	Effect of Damping Ratio on Predicted Acceleration Response	231
160	Comparison of Measured Acceleration Response at Two Dynamic Pressures	232
161	Comparison of Predicted and Measured Acceleration Response at Flight Condition 1	233
162	Comparison of Predicted and Measured Acceleration Response at Flight Condition 2	234
163	Comparison of Predicted and Measured Acceleration Response at Flight Condition 3	235

LIST OF ILLUSTRATIONS (Continued)

APPENDIX A

<u>Figure</u>		<u>Page</u>
A-1	Schematic of Four Plausible Vortex Patterns	246
A-2	Flow Visualization (Oil and Tufts) Configuration 1, Mach 0.9, $Re = 1.25 \times 10^6/\text{ft}$, Wing Angle of Attack $(\alpha_w) = 4^\circ$	247
A-3	Flow Visualization (Oil and Tufts) Configuration 1, Mach 0.9, $Re = 1.25 \times 10^6/\text{ft}$, Wing Angle of Attack $(\alpha_w) = 8^\circ$	248
A-4	Flow Visualization (Oil and Tufts) Configuration 1, Mach 0.9, $Re = 1.25 \times 10^6/\text{ft}$, Wing Angle of Attack $(\alpha_w) = 12^\circ$	249
A-5	Flow Visualization (Oil and Tufts) Configuration 1, Mach 0.9, $Re = 1.25 \times 10^6/\text{ft}$, Wing Angle of Attack $(\alpha_w) = 16^\circ$	250
A-6	Flow Visualization (Oil and Tufts) Configuration 1, Mach 0.9, $Re = 1.25 \times 10^6/\text{ft}$, Wing Angle of Attack $(\alpha_w) = 20^\circ$	251
A-7	Flow Visualization (Oil and Tufts) Configuration 1, Mach 0.7, $Re = 1.25 \times 10^6/\text{ft}$, Wing Angle of Attack $(\alpha_w) = 12^\circ$	252
A-8	Flow Visualization (Oil and Tufts) Configuration 1, Mach 1.0, $Re = 1.25 \times 10^6/\text{ft}$, Wing Angle of Attack $(\alpha_w) = 12^\circ$	253
A-9	Flow Visualization (Oil and Tufts) Configuration 1, Mach 1.2, $Re = 1.25 \times 10^6/\text{ft}$, Wing Angle of Attack $(\alpha_w) = 12^\circ$	254
A-10	Flow Visualization (Oil and Tufts) Configuration 1, Mach 0.9, $Re = 3.75 \times 10^6/\text{ft}$, Wing Angle of Attack $(\alpha_w) = 8^\circ$	255
A-11	Flow Visualization (Oil and Tufts) Configuration 1, Mach 0.9, $Re = 3.75 \times 10^6/\text{ft}$, Wing Angle of Attack $(\alpha_w) = 12^\circ$	256
A-12	Lift Coefficient vs Wing Angle of Attack for Configuration 1, Mach 0.7	257
A-13	Lift Coefficient vs Wing Angle of Attack for Configuration 1, Mach 0.9	257
A-14	rms Inner Wing Bending Moment vs Wing Angle of Attack for Configuration 1, Mach 0.7	258
A-15	rms Inner Wing Bending Moment vs Wing Angle of Attack for Configuration 1, Mach 0.9	258
A-16	Static Pressure Coefficient vs Wing Angle of Attack, Configuration 1, Mach 0.7	259

LIST OF ILLUSTRATIONS (Continued)

<u>Figure</u>		<u>Page</u>
A-17	Static Pressure Coefficient vs Wing Angle of Attack. Configuration 1, Mach 0.9	259
A-18	Root Mean Square Pressure Coefficient vs Wing Angle of Attack. Configuration 1, Mach 0.7	260
A-19	Root Mean Square Pressure Coefficient vs Wing Angle of Attack. Configuration 1, Mach 0.9	261
A-20	Static Pressure Coefficient vs Percent Semispan. Configuration 1, Mach 0.7	262
A-21	Static Pressure Coefficient vs Percent Semispan. Configuration 1, Mach 0.9	264
A-22	Root Mean Square Pressure Coefficient vs Percent Semispan. Configuration 1, Mach 0.7	265
A-23	Root Mean Square Pressure Coefficient vs Percent Semispan. Configuration 1, Mach 0.9	266

LIST OF TABLES

<u>Table</u>		<u>Page</u>
I	Model Configuration	6
II	Test Conditions for Flow Visualization (Series I)	6
III	Functional Grouping for Fluctuating Pressure Transducers	8
IV	Model Resonant Frequencies (MCAIR Test)	11
V	Model/Sting Frequencies (Tunnel Installation)	11
VI	Parameter Variations for Buffet Data Acquisition (Series II)	11
VII	Test Conditions for Reduced Dynamic Data	14
VIII	Normalized Standard Errors	20
IX	Test Conditions for Comparison of Model and Full Scale Spectral Shapes	33
X	Comparison of Analytical and Measured F-4 Wing Vibration Frequencies, Hz	59
XI	Analytical F-4 Wing Vibration Frequencies and Corresponding Generalized Masses	60
XII	Analytical F-4 Wing Vibration Modeshapes	61
XIII	Identification of Rows in Modeshape Matrix (Table XII)	62
XIV	F-4 Wing Modal Damping Values	64
XV	Flight Conditions for Which Responses of F-4 Wing to Buffeting Pressures Were Predicted	66
XVI	Constants Defining Spectral Shapes	66
XVII	ΔC_{prms} at Centers of Areas for Flight Conditions 1, 2, and 3	67

NOMENCLATURE

Symbols

A	Surface area
a	Parameter in mathematical model for pressure autocorrelation function
b	Wing span (wing tip to wing tip)
BW	Filter bandwidth in Hz
C	Co-spectrum, real part of G defined below
c	Local wing chord
\bar{c}	Mean aerodynamic chord
C_L	Lift coefficient
C_p	Static pressure divided by freestream dynamic pressure
$\Delta C_{p\text{rms}}$	Root mean square fluctuating pressure divided by freestream dynamic pressure
D	Exponential decay function
DCF	Decay correction factor
f	Frequency in Hz
$f_1(t), f_2(t)$	Arbitrary time dependent functions 1 and 2
Δf	Filter bandwidth in Hz
G	"Physical" power spectral density function or "physical" cross power spectral density function depending upon (1) alike or unlike superscripts or (2) alike or unlike variables within parentheses (G is defined only for positive frequencies)
H_1, H_2	Functions of frequency defined in text
i	$\sqrt{-1}$
k	Nondimensional frequency
k_o	Nondimensional frequency of peak in mathematical model of power spectral density
L	Length scale value
M	Mach number
M	Bending Moment
M	Generalized mass
m	Empirical constant
P	Pressure
Q	Quad-spectrum, imaginary part of G defined above
q	Dynamic pressure
q	Normal coordinate

R	Autocorrelation function or cross-correlation function depending upon (1) alike or unlike superscripts, or (2) alike or unlike variables within parentheses
r	Distance between two points
Re	Unit Reynolds number
S	Power spectral density function or cross power spectral density function depending upon (1) alike or unlike superscripts or (2) alike or unlike variables within parentheses. (S is defined for both positive and negative frequencies.)
s	Nondimensional distance
T	One-half period of time over which spectral functions are determined, theoretically approaching infinity
t	Time
V	Free stream velocity
v_c	Convection velocity
x	Distance aft of wing leading edge
x	Chordwise wing coordinate
y	Distance outboard from aircraft centerline
y	Spanwise wing coordinate
Z	Reciprocal of complex frequency response function
z	Displacement
a	Streamwise decay coefficient
α_{BO}	Wing angle of attack at buffet onset
α_w	Wing angle of attack
β	Spanwise decay coefficient
γ	Magnitude of cross power spectral density function normalized by dividing by square root of product of two corresponding power spectral density functions. Also, square root of coherence function.
δ	Spatial decay coefficient
ζ	Ratio of damping to critical damping
η	Ratio of the peak level to the low frequency level in a power spectral density function
ϕ	Phase angle of cross power spectral density function
λ	Parameter in mathematical model for power spectral density
ρ	Streamwise distance
ν	Spanwise distance
$\rho(\tau)$	Autocorrelation function of a pressure normalized by dividing by the mean square value of the pressure

$\rho(r, \tau)$	Cross-correlation function of two pressures normalized by dividing by the product of the rms values of the pressures
σ	Root mean square value of a quantity indicated by a subscript or the context
τ	Time shift for autocorrelation or cross-correlation functions
ϕ	Modal deflection
ψ	Power spectral density function defined only for positive frequencies and normalized by dividing by the corresponding mean square value
ω	Frequency in radians per second
ω_0	Frequency parameter in mathematical model for pressure auto-correlation function

Subscripts and Superscripts

a, b	Indicate geometrical points on structure
d	Indicates modified by decay correction factor
F	Indicates filtered time function
FS	Indicates full scale
i, j	Indicate modes i and j, respectively
k, l	Indicate areas k and l, respectively
M	Indicates relationship to bending moment
M	Indicates model (as opposed to full-scale)
p	Indicates relationship to pressure
q	Indicates relationship to normal coordinate
z	Indicates relationship to displacement
1, 2	Indicate relationship to arbitrary functions 1 and 2

Matrix Notation

[]	Square matrix
[]	Row matrix
[] ^T	Transpose (of row matrix, for example)
()	Column matrix

Miscellaneous Notation

-	Denotes mean value
*	Denotes complex conjugate

Differentiation of a variable with respect to time is indicated by dots over the variable.

SECTION I
INTRODUCTION

Airplane wing buffet occurs when an aircraft is in a high angle of attack flight regime and the air flow on the upper wing surface becomes detached. Air flow in the detached regions becomes turbulent thereby giving rise to fluctuating pressures on the wing, and the possibility of induced pressures on the tail. While some loss of lift may be experienced, there is an appreciable range of angles of attack beyond the buffet boundary in which an airplane can maneuver. The upper limit is usually determined by wing rock or stall. This report describes the development of a first generation buffet load prediction method for a modern fighter aircraft in the transonic flight regime.

1.1 History

Buffet investigations that have dealt with aircraft can be divided into two distinct time periods - those that occurred prior to the intensive U.S. space effort (which dominated the late 1950's and 1960's), and those which have occurred since about 1968.

1.1.1 Earlier Studies - Impetus for the earlier studies was provided mainly by the necessity to understand the nature and severity of the buffeting loads and their potentially destructive effect on aircraft structures. While the results of buffet could be readily noted by ride quality and sometimes by aircraft damage (Reference 1), analytical attack on the problem was hampered by the transient and random nature of the airloads causing buffet. The buffet problem cannot be handled in a deterministic manner. While mathematical theory was available, it remained for the speed and capacity of modern electronic computers and signal processing equipment to open the door to a more thorough treatment of the theoretical aspects of the problem.

1.1.2 Recent Studies - Recent studies have, in a sense, been a continuation of the earlier efforts. However, the scope of needed buffet investigations has been greatly increased by the desire to utilize aircraft maneuver capabilities beyond buffet onset even well into the transonic flight regime. The Air Force (References 2, 3, and 4) and the NASA (References 5 and 6) have conducted in-depth investigations of buffet both analytically and experimentally and Reference 7 indicates some of the effort being carried on in Great Britain. Most of these studies, however, have been concerned mainly with definition of buffet onset, and with the measurement of static pressures and

loads. The use of wide band fluctuating pressure sensors to measure aircraft buffet pressures is still very limited, and most effort in this direction has been sponsored by NASA Ames and by the Air Force (as described in this contract).

Although some of the technology gained from space launch vehicle buffet studies (References 8 and 9) has been applied to aircraft, it has been found that the fluctuating buffet pressures on a highly swept airplane wing present very different characteristics. In general, the flow pattern on the upper surface of a wing ~~de~~, in buffet does not exhibit a recognizable flow pattern, and it is not at all safe to assume that convected flow occurs in the streamwise direction. (See Section 4 of this report).

1.2 Buffet Prediction Method

This report describes the development of a method to predict both the fluctuating pressures and the structural response of a modern fighter airplane in transonic flight when it penetrates and flies beyond the buffet onset boundary.

1.2.1 Technical Approach - The variety of approaches to the problem of defining the input loads (i.e., the spectral and spatial energy distribution of the fluctuating pressures) ranges from purely empirical to purely theoretical. A purely empirical approach could be conceived as a test of many wing geometries and planforms to obtain a catalog of pressure distributions that could be applied to different aircraft wings. The main disadvantage of this approach is the inordinately large amount of wind tunnel testing and data reduction that would be required to provide for the variety of wings currently in use on high performance fighters. At the other extreme, a purely theoretical treatment is not possible because the state-of-the-art in theoretical aerodynamics and fluid mechanics is not sufficiently advanced to predict the regions and levels of fluctuating pressure on a three dimensional wing. In both the above cases, verification of predicted buffet response loads would remain a problem. The approach selected for this effort uses a combination of experimental and theoretical inputs.

The calculated response, whether it be wing tip acceleration or root bending moment, requires an input excitation force (forcing function) and a structural response function. The development of the prediction method described herein is based on the interaction effects shown in Figure 1.

In this method the steps are defined as follows:

- (1) First, establish the nature of the unsteady pressures acting on the wing.
- (2) Second, determine the surfaces to which the pressures of (1) are to be applied.
- (3) Next, define the dynamic characteristics of the airplane system.
- (4) The fourth step provides for the combination of pressure - area - displacement to yield a forcing function in the form of generalized (modal) buffeting forces.
- (5) The forcing function is then applied to the elastic system and the required buffet response loads and displacements are computed.

Step (1), of course, is the key analytic ingredient which is obtained by a theoretical/experimental method. Step (2) is based on wind tunnel flow visualization studies, and step (3) may be done either analytically or through ground vibration tests. Steps (4) and (5) are computational procedures that have been obtained by modifying an existing program. The overall objective of the plan is the development of a first generation buffet prediction method for use in preliminary design. The method offers capability for predicting the nature of the unsteady pressures that cause the input buffet loads as well as the response loading in the aircraft structure. The method used to calculate structural response loading from input buffet dynamic pressures is a slight modification of the previously developed method of Reference 10.

SECTION 2

TEST PROGRAM

The experimental phase of the program was structured around two series of wind tunnel tests that were conducted on a 10% scale YF-4E airplane model in the 16T tunnel at AEDC. The purpose of the first test (Series I) was to obtain flow visualization data on the upper surface of the wings to aid in understanding the flow patterns and to aid in finalizing locations for fluctuating pressure transducers (microphones). The purpose of the second test (Series II) was to obtain measurements of the time histories of pressures, accelerations, strains and forces obtained during tunnel runs.

2.1 Model Design

The model configuration was determined by the YF-4E version of the basic F-4E airplane that was used in the flight test program described in Reference 2. A full span 10% model was selected in order to make optimum use of the AEDC 16T tunnel without introducing either blockage or reflected shock effects. A Task Mk XXI-A balance was installed between the model and the sting to measure static and dynamic components of forces and moments acting on the model. Figure 2 presents a three-view of the model showing overall dimensions. Both the inner and outer wing sections (separated by a chordwise line at the snag span location) are equipped with leading edge flaps. Trailing edge flaps are located on the inner wing adjacent to the fuselage. Rather than having adjustable flaps, however, the model was fitted with removable flaps of different angular deflection - two sets for the leading edge (0° and 8°) and three sets for the trailing edge (0° , 7.5° , and 15°). Six model configurations were defined on the basis of leading and trailing edge flap combinations as shown in Table 1. In addition, the left-hand wing was fitted with a row of oil extrusion holes 1/2 inch apart located along a line that went from about 15 percent chord at the wing root to about 30 percent chord to the wing tip. These holes were fed from a common manifold imbedded in the wing.

2.2 Flow Visualization Tests

The first phase of wind tunnel testing, designated Series I, consisted of obtaining still and moving pictures of oil flow and tuft patterns to identify flow characteristics on the wing and to aid in locating fluctuating pressure transducers. The left-hand wing was equipped with the oil orifices and had its upper surface painted white to provide contrast with

the colored oil. The upper surface of the right-hand wing was painted black to provide contrast with the white nylon tufts that were attached in a rectangular grid pattern in rows approximately one inch apart.

The flow visualization program was to be conducted at a Reynolds number $Re = 3.75 \times 10^6$ per foot over a Mach range of 0.7 to 1.2 at angles of attack α_w between -4° and 20° . However, at this Reynolds number excessive dynamic loads were experienced at α_w greater than 14° to 16° . To permit reaching the higher angles of attack much of the testing was conducted at a reduced Reynolds number $Re = 1.25 \times 10^6$ per foot. (A limited number of runs at $Re = 2.5 \times 10^6$ per foot were also made.) Table II shows the test conditions for which flow data were obtained (except that the higher angles of attack were not achieved simultaneously with the higher Reynolds numbers). A photograph showing both oil flow and tufts during tunnel flow is shown in Figure 3. Additional test details, including aerodynamic force data, are given in References 11 and 12.

2.3 Dynamic Instrumentation on Model

After the flow visualization test and prior to model vibration tests, the dynamic instruments were installed on the model. This instrumentation consisted of fluctuating pressure transducers (microphones), accelerometers and strain gages. The microphones were installed on the upper surface of the wing and tail to measure fluctuating surface pressures. Three strain gages were installed on the wing and one was installed on the horizontal tail to measure bending and torsional strains induced during buffet. In addition to an accelerometer located at the model c.g., a pair of high frequency accelerometers was located near the wing tip to measure bending and torsion acceleration response to buffet pressure. Figure 4 shows the overall model instrumentation while Figure 5 shows the detailed location of the sensors on the wing. All wing mounted transducers were recessed in the wing to preserve a smooth wing contour. Leads were routed through grooves in the wing, into the fuselage and hence into the sting.

A description of the date acquisition system used by AEDC at the 16T tunnel is given in paragraph 3.1 of the next section.

2.3.1 Sensor Description - The dynamic sensors used on the 10% YF-4E model are described as follows:

Microphones -

Disc mounted - Kulite P/N CQL-080-25

Flush mounted - Kulite P/N LQS-156-25

Table I - Model Configurations

Configuration	Leading Edge Flap Deflection (degrees)	Trailing Edge Flap Deflection (degrees)
1 (Clean)	0	0
2	8	0
3	8	7.5
4	0	7.5
5	0	15
6	8	15

Table II - Test Conditions for Flow Visualization (Series I)

Configuration	M	Range of α_w (deg)	Re/ft ($\times 10^{-6}$)
1	0.7, 0.9, 1.0, 1.2	-2, +20	1.25, 3.75
2	0.7, 0.9, 1.0, 1.1, 1.2	-2, +20	1.25, 2.5, 3.75
3	0.7, 0.9, 1.0, 1.2	-2, +20	1.25, 3.75
4	0.7, 0.9, 1.0, 1.2	-4, +20	1.25, 3.75
5	0.7, 0.9, 1.0, 1.2	-4, +20	1.25, 3.75
6	0.7, 0.85, 0.9, 1.0, 1.2	-3, +20	1.25, 3.75

See Table 1, Reference 11 for Additional Details

Accelerometers -

Endevco 2222A

Strain Gages -

Two-element rosettes (2 per Wheatstone bridge to measure torsion)

Bean BAB-06-125XS-350

Uniaxial gages (4 per Wheatstone bridge to measure bending)

Micro-Measurements EA-06-090DH-350

Micro-Measurements EA-06-090EG-350

2.3.2 Microphone Grid - A grid of twenty-eight wide band fluctuating pressure transducers was installed on the model prior to the buffet data acquisition tests. The grid was based on the following criteria:

- (1) Microphones would be densely grouped in areas of high turbulence and sparsely grouped in regions of low turbulence.
- (2) The microphones would be arranged so that key flow characteristics could be readily determined.
- (3) Some microphones would be located to provide direct comparison with flight test data.
- (4) Fluctuating pressure on the tail should be monitored.

The microphone locations shown in Figures 4 and 5 were based on these criteria and the results of flow visualization tests. The forward most locations on the inner wing panel could not extend forward of the 12% chord line because of interference with the flap, and those on the outer wing panel could not be forward of about the 30% chord line because of thinness of the wing and interference with the oil flow manifold. Also, the locations of transducers 17 and 18 could be located no further aft than the 90% chord (because of wing thinness) although it was desirable to correlate the outputs with flight test pickups located at 95% chord. However, transducers 17 and 18 do coincide with those of flight test pickups on the 90% chord. The functional groupings of the sensors are listed in Table III together with the purpose each grouping was intended to serve.

The transducers in Group 1 formed four chordwise rows. Three of these rows were about equally spaced on the outboard half of the wing. Emphasis given to the outboard half because as angle of attack is increased this region is the first to have separated airflow. The location of the inboard row consisting of 5, 14, and 21 was fixed by pressure transducers on the flight test airplane.

Table III
Functional Grouping for Fluctuating Pressure Transducers

Group	Transducers (See Figure 4)	Purpose
1	1,2,4,5,6,7,9,10, 11,13,14,16,18, 20,21	Coarse Grid for Defining Major Flow Features on Wing
2	11,15,16,17,18 21,26,27,28 21,22,23,24,25	Fine Grid for Defining Flow Features on Outer Wing Wing-Tail Correlation Close Correlation on Flap and Check of Pressure Distribution
3	2,3,4,7,8,9,11,12, 13,18,19,20	Investigate Localized Effect of Snag
4	17,18,21,24	Compare with Flight Test Data

The first grid in Group 2 was to examine the streamwise and spanwise correlation between closely spaced points on the outer wing panel. The second grid in Group 2 was for determining correlations between fluctuating pressures on the wing and tail, and between those on the two sides of the tail. The third grid was to provide a check of the mathematical model for the fluctuating pressures and contained five transducers on the trailing edge flaps. This check could not be made because a strain gage on the flap support, needed for the correlation, malfunctioned.

The purpose of the transducers in Group 3 was to investigate the localized effect of the snag.

The locations of the fluctuating pressure transducers in Group 4 were the same as those in the flight test airplane (Reference 2).

Twenty-four of the twenty-eight microphones used on the model were installed in mounting discs (see Figure 14 of Reference 13) that recessed the diaphragms and protected them from any possible direct stream impingement. Comparative frequency calibrations showed that frequency response was not affected by the mounting discs. The calibration is discussed in Reference 13. No microphones were lost due to diaphragm damage during the Series II tests.

2.4 Vibration Tests

A vibration test was made after installation of sensors, to determine the vibration modes and frequencies that might influence buffet data measured on the model. It was believed that wide-band buffet pressure excitation could excite and amplify resonant structural modes that would in turn induce pressure peaks. Such peaks should obviously not be included in mathematical modeling of the pressure. The test was done in two parts at two different locations - the first part was conducted in the MCAIR laboratories and consisted of a comprehensive evaluation of model modeshapes and frequencies. These data were obtained with the setup shown in Figure 6. The model was mounted through the model balance flexures to a rigid sting, and excitation was provided by a pair of electromagnetic shakers. By properly phasing the shaker force outputs (i.e., in-phase or 180° out-of-phase), either symmetrical or anti-symmetrical vibration modes could be excited. The test procedure consisted of (1) sweeping through a range of frequencies between 0 and 1500 Hz and recording the output of monitor accelerometers, (2) identifying the modes represented by the peaks of the swept response and (3) mapping

dominant modes. Table IV lists and identifies model resonant frequencies.

The remaining part of the vibration test was made at AEDC with the model mounted through the balance flexures to the wind tunnel sting. The vibration test setup shown in Figure 7 was used to determine the sting/model vibration characteristics. Sting/model frequencies measured in this test are listed in Table V. Details of the vibration tests are presented in Reference 14.

2.5 Buffet Data Acquisition Tests

The Series II buffet data acquisition tests consisted of a series of tunnel runs at various Mach numbers and angles of attack to gather pressure, acceleration, strain, and force and moment coefficient data related to aircraft buffet.

The test was conducted at Mach numbers between 0.7 and 1.10 and most of the data were obtained at a Reynolds number of 3.75 millions per foot. The angle-of-attack range was from -1.5 to 16 degrees at zero degrees yaw.

Data also were taken with configuration 1 (clean) through a Reynolds number range of 1.25 through 5.25 millions per foot at several angles of attack. A summary of parameter variations is presented in Table VI.

The general operating procedure was to record simultaneously 60 seconds of VIDAR analog data, and then record tunnel and model static pressure data digitally. This sequence was done at an angle corresponding to zero lift ($C_L = 0$) and at a number of angles in the region of buffet onset and beyond. At some additional angles of attack, digital data only were recorded for the purpose of better definition of overall aircraft aerodynamic curves. A complete list of the angles at which data were recorded is presented in Table 2 of Reference 13.

Table IV - Model Resonant Frequencies (MCAIR Test)

Frequency (Hz)	Mode
95.1	1st Sym. Wing Bending
108	1st Anti-Sym. Wing Bending
223	2nd Sym. Wing Bending
252	2nd Anti-Sym. Wing Bending
327-347	1st Sym. Wing Torsion
348	1st Anti-Sym. Wing Torsion

Table V Model/Sting Frequencies (Tunnel Installation)

Frequency (Hz)	Mode
11.3	Pitch
22.0	Roll

Table VI Parameter Variations for Buffet Data Acquisition (Series II)

Configuration	M	Range of α_w	$Re/ft \times 10^{-6}$
1	0.7, 0.8, 0.85, 0.9, 0.95 1.0, 1.05, 1.1	-15°, 16°	1.25, 1.75, 2.25, 2.5 2.75, 3.25, 3.75, 4.25, 4.75, 5.25
5	0.7, 0.8, 0.9, 1.0 1.1	2°, 14°	3.75
6	0.7, 0.8, 0.85	7°, 11°	3.75

*See Table II, Reference 13 for additional details.

SECTION 3

DATA ACQUISITION AND REDUCTION

This section describes the data acquisition and data reduction techniques utilized in obtaining the power spectral density plots that are employed in deriving a mathematical model of the fluctuating pressure. The raw data were obtained during the Series II wind tunnel tests conducted at the AEDC in the 16T transonic tunnel.

3.1 On-Line Data Acquisition and Reduction System at AEDC

The 16T tunnel was equipped with a readout system for obtaining and digitizing the mean and rms outputs of the strain-gage and piezoelectric type transducers installed in the model/sting balance assembly. On-line data consisted of a tabulation of the mean (static) and rms (dynamic) response values in engineering units of the transducer signals during each tunnel run performed at a specific Mach number, model angle of attack, and model configuration.

The on-line data acquisition system provided FM tape records of the raw transducer outputs for each wind tunnel run for off-line data analysis. The analog data were recorded on a multiplex tape recording system utilizing a CEC Model VR 700 wide-band tape recorder transport, Vidar multiplexing electronics, and 14 track FM magnetic tapes. A tape recording speed of 60 inches per second (ips) with discriminator center frequencies of 160, 220, 280, 340, 400, and 460 KHz provided effective bandwidths of 8 KHz. A description of the on-line data acquisition and reduction system used for the 16T tunnel is presented in Reference 15.

3.2 Data Reduction at MCAIR

Off-line analysis of the FM magnetic tape records of the dynamic data recorded during the buffet dynamic loads program was performed at MCAIR. Since the raw data tapes were recorded by a multiplex frequency modulated recorder, the tapes were played back through discriminators to separate the individual data signals. The individual signals were then stripped out on a recording oscillograph and time histories were obtained for all outputs of the acceleration, strain, and dynamic pressure transducers. The oscillograph traces were subsequently edited for data validity and thirty-five transducer pairs were chosen to be analyzed. Choice of the transducer pairs was guided by the kinds of information being sought: the spectral content, convection, and spatial decay of fluctuating pressures acting on the wing and the spectral

content of and correlation between various model responses. The data were reduced for the 16 test conditions that are outlined in Table VII. Most of these test conditions were chosen to exhibit the effect of Mach number, angle of attack, and model configuration on buffet. Other conditions were chosen to match those of flight buffet tests or to show the nature of background noise (at $C_L = 0$).

3.2.1 Oscillograph Traces - Time histories of typical dynamic pressures, accelerations, and bending moments recorded during the test are presented in Figures 8 through 11. Since the fitting of these traces by deterministic functions seems unlikely, the data were treated as random. Moreover, the data were taken to be stationary since no changes in the statistical characteristics are obvious from visual examination of the traces.

3.2.2 Broad Band FM Recording - After editing, the data selected for reduction were recorded on broad band FM tape. Since the center frequencies and effective bandwidths of the MCAIR discriminators were twice those used to record the data at AEDC, the multiplexed data were played back through the MCAIR discriminators at 120 inches per second. The signals obtained from the discriminators were recorded on broad band FM tape at 30 ips and a center frequency of 27 KHz in a 5 KHz frequency band.

The actual data reduction was performed on tape loops obtained from the 30 ips, 27 KHz FM tapes. These loops, made to minimize phase shifts and to insure coherence of the transducers in a given pair, were used for all spectral analysis at MCAIR. They were played back at 15 ips with a center frequency of 13.5 KHz. Thus, the effective frequency response of the data analysis was from 0 to 2.5 KHz.

3.3 Mathematical Functions, Spectral Analysis

As discussed in Section 3.2.1, the dynamic data studied in this program appear to be random and stationary. The analysis of such data is generally given in terms of correlation and spectral density functions, which are Fourier transforms of one another. These functions are discussed below, and further details may be found in References 16 and 17.

3.3.1 Correlation Functions - The correlation functions for random data are defined as follows:

Autocorrelation function

$$R^{11}(\tau) = \lim_{T \rightarrow \infty} \frac{1}{2T} \int_{-T}^T f_1(t) f_1(t+\tau) dt \quad (3-1)$$

Table VII
Test Conditions for Reduced Dynamic Data

Model Configuration	Mach Number	Reynolds Number (per foot)	Wing Angle-of-Attack (deg)
1	0.7	3.75×10^6	- 0.85
1	0.7	3.75×10^6	12.08
1	0.85	3.75×10^6	10.02
1	0.9	3.75×10^6	7.98
1	0.9	3.75×10^6	12.08
1	0.9	3.75×10^6	14.08
1	0.9	3.75×10^6	- 0.85
1	0.8	3.75×10^6	8.99
1	0.8	3.75×10^6	9.95
1	1.0	3.75×10^6	0
1	1.0	3.75×10^6	12.0
6	0.7	3.75×10^6	11.0
5	0.9	3.75×10^6	11.0
5	0.9	3.75×10^6	14.0
6	0.7	3.75×10^6	11.0
6	0.8	3.75×10^6	9.0

Cross-correlation function

$$R^{12}(\tau) = \lim_{T \rightarrow \infty} \frac{1}{2T} \int_{-T}^T f_1(t) f_2(t+\tau) dt \quad (3-2)$$

where

$f_1(t)$ = time function 1

$f_2(t)$ = time function 2

T = one-half of integration period

$R(\tau)$ = correlation function as function of time delay τ .

Autocorrelation and cross-correlation functions were computed using a Princeton Applied Research analyzer. The analyzer performed the following function

$$R^{12'}(\tau) = \lim_{T \rightarrow \infty} \frac{1}{2T} \int_{-T}^T f_1(t) f_2(t - \tau) dt \quad (3-3)$$

The primary difference between this function and the one expressed in Equation (3-2) is the time delay $-\tau$. A negative time delay does not affect the autocorrelation. The cross-correlation is affected as follows

$$R^{12}(\tau) = R^{12'}(-\tau) \quad (3-4)$$

The cross-correlation function can be changed to correspond to the format of Equation (3-2) by changing the sign of the abscissa.

3.3.2 Power and Cross Power Spectral Density Functions - The power spectrum of a stationary random function is the Fourier transform of the correlation function.

Power Spectral Density

$$S^{11}(f) = \int_{-\infty}^{\infty} R^{11}(\tau) e^{-i2\pi f \tau} d\tau \quad (3-5)$$

Cross Power Spectral Density

$$S^{12}(f) = \int_{-\infty}^{\infty} R^{12}(\tau) e^{-i2\pi f \tau} d\tau \quad (3-6)$$

where

$S^{11}(f)$ = power density spectrum as a function of cyclic frequency (f)
defined for $-\infty < f < \infty$ and with units (amplitude 1) 2 /Hz

$S^{12}(f)$ = cross power density spectrum as a function of (f) defined
for $-\infty < f < \infty$ and with units (amplitude 1)(amplitude 2)/Hz

The corresponding inverse transforms are

$$R^{11}(\tau) = \int_{-\infty}^{\infty} S^{11}(f) e^{i2\pi\tau f} df \quad (3-7)$$

$$R^{12}(\tau) = \int_{-\infty}^{\infty} S^{12}(f) e^{i2\pi\tau f} df \quad (3-8)$$

The mean squared value of a time function is the value of the correlation function at $\tau = 0$. This function can be expressed as the integrated power spectrum

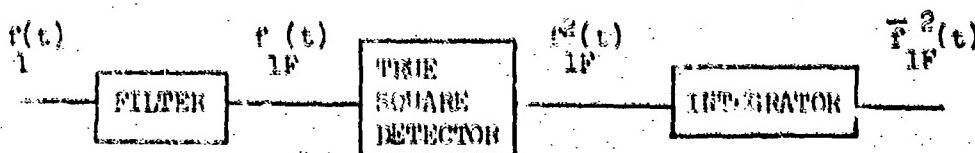
$$\begin{aligned} \sigma_{11}^2 &= R^{11}(0) = \lim_{T \rightarrow \infty} \frac{1}{2T} \int_{-T}^T r_1^2(t) dt = \int_{-\infty}^{\infty} S^{11}(f) df \\ &= 2 \int_0^{\infty} S^{11}(f) df = \int_0^{\infty} G^{11}(f) df \end{aligned} \quad (3-9)$$

where

$G^{11}(f)$ = the "physical" one-sided power spectral density defined for $0 \leq f$.

The above equation is used in the physical determination of the power spectrum and the cross power spectrum.

The analog technique used to compute power spectral density is based on the following operations: filtering, true square detection, and integration. The combination of these three functions allows the computation of power spectral density for random functions. A block diagram of the operation of the analog analyzer follows:



where

$r(t)$ = time function 1

$r_{1F}(t)$ = filtered time function 1

$r_{1F}^2(t)$ = mean squared value of $r_{1F}(t)$

If the time function is filtered and the bandwidth of the filter is small, the power spectral density within the bandwidth can be assumed to be constant. Equation (3-9) can then be rewritten as follows:

$$\sigma_{11}^2 = R^{11}(0) = \lim_{T \rightarrow \infty} \frac{1}{2T} \int_{-T}^T f_{1F}^2(t) dt = G^{11}(f) \int_{-\frac{\Delta f}{2}}^{\frac{\Delta f}{2}} df = G^{11}(f)\Delta f \quad (3-10)$$

where

$G^{11}(f)$ = power spectral density of time function 1 at frequency f

Δf = filter bandwidth, Hz

The power spectral density can now be expressed in terms of the filtered time function

$$G^{11}(f) = \lim_{\Delta f \rightarrow 0, T \rightarrow \infty} \frac{1}{2T\Delta f} \int_{-T}^T f_{1F}^2(t) dt \quad (3-11)$$

A similar relation exists for the cross power spectral density. The cross power spectrum is expressed in terms of the in-phase (real, Re) and the quadrature phase (imaginary, Im) functions. (These functions are also called the co-spectrum C and the quad-spectrum Q respectively.)

Real

$$\text{Re}[G^{12}(f)] = \lim_{\Delta f \rightarrow 0, T \rightarrow \infty} \frac{1}{2T\Delta f} \int_{-T}^T f_{1F}(t) f_{2F}(t) dt = C^{12}(f) \quad (3-12)$$

Imaginary

$$\text{Im}[G^{12}(f)] = \lim_{\Delta f \rightarrow 0, T \rightarrow \infty} \frac{1}{2T\Delta f} \int_{-T}^T f'_{1F}(t) f_{2F}(t) dt = Q^{12}(f) \quad (3-13)$$

where

$f_{1F}(t)$ = filtered time function $r_1(t)$

$f_{2F}(t)$ = filtered time function $r_2(t)$

$r'_{1F}(t)$ = filtered time function of $f_1(t)$ phase shifted 90°

$C^{12}(f)$ = the "physical" one-sided cross power spectral density defined for $0 \leq f$.

The cross power spectral density can then be expressed as the following complex quantity

$$\begin{aligned} G^{12}(f) &= \text{Re}[G^{12}(f)] + i \text{Im}[G^{12}(f)] \\ &= C^{12}(f) + i Q^{12}(f) \end{aligned} \quad (3-14)$$

or, written in terms of magnitude and phase,

$$G^{12}(f) = |G^{12}(f)| e^{-i\theta_{12}(f)} \quad (3-15)$$

where

$$|G^{12}(f)| = [[C^{12}(f)]^2 + [Q^{12}(f)]^2]^{1/2} \quad (3-16)$$

$$\theta_{12}(f) = \tan^{-1} [Q^{12}(f)/C^{12}(f)] \quad (3-17)$$

and $i = \sqrt{-1}$

Figure 12 shows the data flow and steps involved in reducing raw data to obtain PSD and CPSD plots. Power spectral density (PSD) analysis was performed on a Honeywell Model ASA9300B Automatic Spectrum Analyzer which can analyze a pair of transducers simultaneously. This analyzer consisted of a programmable tuning oscillator, a pair of filters having four possible bandwidths (2 Hz, 5 Hz, 10 Hz and 50 Hz), a true square detector, an integrator, and a logarithmic converter. The tuning oscillator of the Honeywell system was programmed to step through a spectrum from 0 to 2000 Hz utilizing bandwidths and integration times as follows:

Frequency	Filter Bandwidth	Integration Time
0 Hz - 30 Hz	2 Hz	20.0 sec.
30 Hz - 150 Hz	5 Hz	20.0 sec.
150 Hz - 800 Hz	10 Hz	10.0 sec.
800 Hz - 2000 Hz	50 Hz	3.0 sec.

The filtered data were then further processed to obtain the PSD. The programmable oscillator also provided a D.C. voltage signal proportional to the center frequency of the bandwidth being analyzed. The PSD's, along with the frequency related voltage, were recorded digitally on a DYMEC Model DY-2010H Data Acquisition System, which was compatible with an IBM 360/85 input format.

A parallel tap was made between the narrow bandpass filter and the true square detector in the Honeywell system to obtain filtered data in each stepped bandwidth for coincident and quadrature analysis. The coincident and quadrature analysis was performed using Spectral Dynamics Model SD 1012 Tracking Filter, a Model SD 1010 Carrier Generator, and a Model SD

109A Co/Quad Analyzer. The center frequency of the carrier generator was referenced to a 7.5 KHz signal used in the Honeywell system. The tracking filter (equipped with 100 Hz bandwidth filters) was used to provide compatibility between the spectrum analyzer, operating with a carrier frequency of 7.5 KHz, and the co/quad analyzer having a carrier frequency of 100 KHz. The 100 Hz filters caused no additional filtering of the data since they were twice the possible programmed bandwidth of the Honeywell system. Thus, a coincident and a quadrature value were obtained for each bandwidth "stepped off" by the Honeywell system. The values of the coincidence and the quadrature were recorded digitally utilizing the DYMEC Data Acquisition System. The DYMEC was also able to record a manual input channel which provided the recording of run number, transducer pairs, system gain factors, bandwidth, and integration times.

The IBM 360/85 computer was used to read the digital records, convert all data to engineering units, and to compute the magnitude and the phase of the cross power spectral density, the square root of the coherence function, and the cumulative root mean square values through the PSD spectrum for both transducers. The computer presented the data in two formats. The first was in the form of a computer printout for each "stepped off" bandwidth throughout the 0 Hz to 2000 Hz frequency spectrum of each parameter calculated. The second format consisted of a digital "history tape" for later use on the Model 663 Cal Comp Plotter. The history tape provided the means by which data could be saved for later recall and plotting, if necessary.

3.4 Accuracy of Data

Uncertainties in the dynamic data analyzed in this test program result from (1) the instrumentation errors associated with the hardware that was used to convert recorded raw data into power spectra and (2) statistical inaccuracy. Instrumentation accuracy is estimated to be $\pm 8\%$ of the data presented. The larger uncertainty is due to statistical inaccuracy, which is presented for the PSD and CPSD data in Tables VIII(a) and VIII(b) respectively. As indicated in this table, the standard deviation (error) introduces uncertainty in the cross power spectral data as large as 22.4%.

Table VIII
Normalized Standard Errors

(a) Power Spectral Density

Spectrum Section (Hz)	Bandwidth (Hz)	Integration Time (sec)	Statistical Degrees of Freedom*	Normalized Standard Error**
1 - 30	2	20	80	15.8%
30 - 150	5	20	200	10.0%
160 - 800	10	10	200	10.0%
800 - 2000	50	3	300	8.2%

*Degrees of Freedom = 2 (Bandwidth) (Integration Time)

**Normalized Standard Error, % = $100 / \sqrt{(\text{Bandwidth}) (\text{Integration Time})}$

(b) Cross Power Spectral Density

Spectrum Section (Hz)	Bandwidth (Hz)	Integration Time (sec)	Statistical Degrees of Freedom	Normalized Standard Error
1 - 30	2	10	40	22.4%
30 - 150	5	10	100	14.1%
160 - 800	10	5	100	14.1%
800 - 2000	50	1.5	150	11.5%

SECTION 4
DATA ANALYSIS

This section presents discussion and some results from analysis of data obtained during the flow visualization (Series I) and buffet data acquisition (Series II) wind tunnel tests. The first part of the analysis, related to aerodynamic flow, had as its principal objectives: (1) determine the nature of the flow on the upper wing as it varies with Mach number, with angle of attack, and with Reynolds number, (2) assess the effect on pressure distribution of vortices, (3) define buffet onset and (4) locate fluctuating pressure transducers. The second part (data from Series II test), dealing with rms and PSD data, had the following main objectives: (1) define the trends in ΔC_{Prms} (overall rms value of fluctuating pressure) with angle of attack and Mach number, and with position on the wing, (2) determine the distribution of fluctuating pressures with respect to frequency and position on the wing during changes in angle of attack and Mach number, and (3) make a comparison of wind tunnel and flight data.

4.1 Flow Analysis

The flow characteristics on the upper wing surfaces were monitored visually by tufts and oil flow to determine flow patterns and aid in locating transducers. Data reduction was done using color movies and black and white still photographs. A summary of the type of information obtained is presented below and details of flow analysis are given in Appendix A. Additional still photographs are given in Reference 12.

4.1.1 Tufts - Nylon tufts were attached to the upper surface of the right wing in rectangular rows 1 inch apart. For analysis, tuft motion was categorized according to degree of turbulence based upon tuft motion and direction.

4.1.2 Oil Flow - Oil flow photographs were analyzed in a similar manner although the criteria for judging degree of turbulence (and hence separation) were different. Flow where oil streaks were largely oriented streamwise and where most of the oil was rapidly swept away was judged to be attached. At the opposite extreme, highly turbulent (separated) flow is judged to occur where oil collects and appears to have a poorly defined flow direction. Separation boundaries were identified by using both tufts and oil flow.

4.1.3 Flow Characteristics - The flow on the F-4 model wing is strongly influenced by the leading edge discontinuity called the snag. Figure 13 is an oil flow photograph made at $M = 0.9$ and $\alpha_w = 12^\circ$ that shows both the tuft and oil flow patterns for a representative buffet condition. In general, flow separation began on the outer wing panel, and progressed inboard with increasing angle of attack.

4.2 Analysis of rms Data

4.2.1 Noise in Wind Tunnel - It is known that a wind tunnel produces noise. Special runs were made for the clean configuration at $C_L = 0$ to determine the nature of this background noise. In this zero lift condition the flow is attached and laminar and pressure fluctuations are attributed to perturbations in the stream flow. Noise level measurements are compared with turbulence measurements in the following paragraphs, and it is shown that in general the noise level is not high compared to the buffeting pressure level.

4.2.2 Pressure rms Measurements - In the analysis of rms pressure measurements presented in this report, emphasis was placed on configuration 1 for examining the effect of Mach number and angle of attack. At Mach 0.9 data were analyzed at $\alpha_w = 8^\circ$, 12° , and 14° to study the effect of angle of attack; at 12° wing angle of attack, data were analyzed at $M = 0.7$, 0.9 , and 1.0 to study the effect of Mach number. For configuration 5, the effects of angle of attack and Mach number were examined by analyzing data at $M = 0.7$, $\alpha_w = 11^\circ$; $M = 0.9$, $\alpha_w = 11^\circ$; and $M = 0.9$, $\alpha_w = 14^\circ$. To provide an indication of the effect of model configuration, data were analyzed for Configuration 6 at $M = 0.7$, $\alpha_w = 11^\circ$ for comparison with data at similar conditions for Configurations 1 and 5.

Figure 14 shows the variations of $\Delta C_{p_{rms}}$ with percent chord for the model at $C_L = 0$ and Mach 0.7. This value (between 0.01 and 0.02) is assumed to represent tunnel noise and will serve as a Mach 0.7 reference for the buffet data. Buffet pressures significantly higher than this will be essentially unaffected by tunnel noise. The variation of $\Delta C_{p_{rms}}$ at Mach 0.7 and $\alpha_w = 12^\circ$ is shown in Figure 15. The values are usually well above the noise level and below 0.1 except for the aft part of the 78 percent semispan, where they are above 0.2. This high level is associated with the snag vortex as discussed in Appendix A.

Figure 16 shows variation of $\Delta C_{p_{rms}}$ with percent span at $M = 0.9$ and $C_L = 0$. Except for one point, these values are below 0.02, which is taken as the tunnel noise level at Mach 0.9. Figures 17, 18, and 19 are plots of $\Delta C_{p_{rms}}$ versus percent chord at Mach 0.9 and wing angles-of-attack of 8° , 12° and 14° , respectively. Most of the $\Delta C_{p_{rms}}$ data are below 0.07. The exceptions are the 78 percent semispan and 90 percent chord at $\alpha_w = 8^\circ$ and the 78 and 93 percent semispan at $\alpha_w = 12^\circ$ and 14° . In the latter two cases, $\Delta C_{p_{rms}}$ gets as high as 0.16. These high values are thought to be associated with the snag and tip vortices as discussed in Appendix A.

The tunnel noise level at Mach 1 is shown by the plot of $\Delta C_{p_{rms}}$ versus percent chord in Figure 20 to be about 0.01. The few values above this level are thought to be due to snag and tip vortices and some flow perturbation caused by the engine inlet. Figure 21 shows that at Mach 1 and $\alpha_w = 12^\circ$, $\Delta C_{p_{rms}}$ is below 0.06 at all the measurement locations. It thus appears that the larger buffeting pressures occur below Mach 1.

Variations of $\Delta C_{p_{rms}}$ over the wing with the trailing edge flaps deflected 15 degrees are shown in Figures 22, 23, and 24. A comparison of Figures 15 and 22 shows little effect due to trailing edge flap deflection at Mach 0.7 and α_w in the neighborhood of 12° . Comparing Figures 18 and 23 shows that at Mach 0.9 and around $\alpha_w = 12^\circ$, deflecting the trailing edge flaps 15° raises $\Delta C_{p_{rms}}$ roughly 30 percent at the 78 percent semispan and inboard and lowers it slightly at the tip. At Mach 0.9 and $\alpha_w = 14^\circ$, deflecting the trailing edge flaps 15° has little effect on $\Delta C_{p_{rms}}$, as shown in Figures 19 and 24.

Some indication of the effect of deflecting the leading edge flaps 8° degrees is obtained by comparing Figures 22 and 25. The greatest effect is to raise $\Delta C_{p_{rms}}$ at the aft part of the 78 percent semispan by a factor of 2 to 3.

4.2.3 Bending Moment Measurements - Wing root bending moment data were analyzed to help assess the magnitude of the buffet dynamic loads problem. The total wing root bending moment signal was resolved into a steady component and an unsteady component. The rms of the latter signal was corrected by subtracting (on a mean square basis) tunnel background noise contributions yielding the rms bending moment due to buffet. These rms bending moments, σ_M , expressed as a fraction of the corresponding steady bending moments, M , are presented in Figures 26 through 28 for Configuration 1 - clean wing.

(Examination of uncorrected data for other Mach numbers and other configurations suggested that the data in these figures encompasses the most adverse σ_M/M ratios).

The maximum rms root bending moments are of the order of 5-7% of the steady moment, being maximum at about Mach 0.8. Preliminary unpublished information from other current dynamic buffet investigations yields pretty much the same story - maximum ratio of σ_M/M of about the same order, also being most critical around Mach 0.8. The orders of magnitude coming out of this and other recent programs suggest something about the magnitude of the buffet dynamic loads problems. Translated into operating envelopes of fighter aircraft (such as the F-4), σ_M translates roughly as 5-7% of the static design load at sea level; but under typical transonic combat maneuvering at 30,000 feet for existing aircraft, σ_M is about 2-3% of the design static load at the same time the actual static load is roughly only 1/3 to 1/2 of design static limit load. The 3 σ_M dynamic dispersion applied to the static load is then 6-9% of the static load. It begins to appear that the buffet dynamic loads problem is not of major impact on static design criteria.

4.3 Analysis of Spectral Data

Spectral data were obtained by the procedures explained in Section 3 and data are presented as plots of power spectral density and normalized cross power spectral density versus frequency. The buffet test conditions chosen for data analysis and the reasons for choosing them are as stated at the beginning of Section 4.2.2.

4.3.1 Noise Power Spectral Densities - The noise data measured at $C_L = 0$ and discussed in Paragraph 4.2 were also analyzed for spectral content. Mach 0.7 noise data at four points along the 70 percent chord line are shown in Figures 29 through 32. These and other noise data indicate a strong peak in the neighborhood of 400 Hz on all parts of the wing at $M = 0.7$. In most of the figures, the value of this peak is between 2×10^{-5} and $4 \times 10^{-5} (\text{psi})^2/\text{Hz}$. Peaks at 60, 120, 240 Hz, etc., are assumed to be due to electrical noise.

Pressure spectra for four points along the 70 percent chord line at $C_L = 0$ and $M = 0.9$ are shown in Figures 33 through 36. These and other spectra exhibit fairly broad peaks between 500 and 700 Hz at levels generally between 2×10^{-6} and $1 \times 10^{-5} (\text{psi})^2/\text{Hz}$.

Two spectral plots for $C_L = 0$ and $M = 1.0$ are shown in Figures 37 and 38. These and some other spectral data for this test condition exhibit small, broad peaks between 500 and 1000 Hz. The levels vary, but generally they are below 10^{-5} (psi) $^2/\text{Hz}$.

4.3.2 Buffet Power Spectral Densities - Figures 39 through 61 contain the power spectral density functions for the fluctuating pressures at Mach 0.7 and $\alpha_w = 12^\circ$. They show the spatial variation of the fluctuating pressure spectra over the wing planform. There are four significant characteristics evident to varying degree in these plots: a broad peak centered about 650 Hz, a broad peak centered about 1500 Hz, an extremely broad peak with a maximum at 650 Hz with delayed roll-off beyond the peak, and a negative slope from about 10 to 200 Hz. Transducers whose PSD plots exhibit any of the first three characteristics are indicated on the wing planform in Figure 62. Peaks at 650 Hz are evident for the transducers in a cone-shaped region emanating from the snag. Based on flow visualization (oil and tuft) studies and analysis of the static pressures over the wing, this general region is thought to be affected by a vortex caused by the snag. Thus the 650 Hz peaks are also thought to be caused by this vortex. The transducers along the 78 percent span line have particularly broad peaks at 650 Hz with delayed roll-off beyond the peak. The spectrums for transducers 12 and 19 along the 68 percent semispan line have no evidence of a peak at 650 Hz although the spectra to either side of them do exhibit the peak.

Transducers whose PSD's have 1500 Hz peaks are in two regions as shown in Figure 62. For one group, it is thought that the peak is due to the leading edge vortex. For the other group the peak is thought to be due to the tip vortex. The existence of these vortices is discussed in Appendix A. Estimated boundaries for the regions affected by these vortices are shown in Figure 62. The estimates are based on the positions of the transducers whose PSD's exhibit the 1500 Hz peaks.

The frequencies associated with the different vortices are thought to be related to some kind of circulation or rotation frequency of the vortices.

Negative slopes from about 10 to 200 Hz are evident in the PSD's for the transducers along the tip and leading edge. Because of the locations of these transducers, it is likely that the negative slopes are also related to the leading edge and tip vortices although in a different manner from the transducers with 1500 Hz peaks. The two phenomena do not always occur together.

The power spectral density curves in Figures 39 through 61 show no indication of the model wing resonances listed in Table III. The only model resonances which are evident in these curves are pitch and roll of the model vibrating on the balance. Many of the power spectral density curves contain small peaks at the frequencies (12 and 18 Hz) of these resonances (Table IV).

Power spectral density plots for two fluctuating pressures along the 70 percent chord line at Mach 0.9 and $\alpha_w = 8^\circ$ are shown in Figures 63 and 64. These plots are representative ones for this test condition. Most of the curves have negative slopes from about 10 Hz out to around 200 Hz. The spectral density for transducer 10 (Figure 63) contains a low peak at 1500 Hz and for transducer 11 (Figure 64) there is a medium peak around 1000 Hz. These frequencies and those exhibited by the power spectral density plots of the other pressure transducers are indicated on the wing planform in Figure 65. While the situation here is not as clear as it was at Mach 0.7 and $\alpha_w = 12^\circ$, regions affected by three vortices are evident and are indicated in Figure 65. An inner wing leading wing vortex is associated with peaks in the neighborhood of 1500 Hz at transducers 8, 12, 19, and 20. The snag vortex is associated with 1000 to 1200 Hz peaks measured by chordwise transducers along the 78 percent semispan line. Chordwise transducers along the 93 percent semispan line have peaks from 1200 to 1500 Hz. There is some question as to what vortex causes them. If the peaks were not evident for transducer 1, it would be assumed they are associated with the tip vortex. Since a peak is evident for transducer 1, it is indicated in Figure 65 that the peaks are due to an outer wing leading edge vortex. Since this is a unique case among the test conditions analyzed, this vortex is included with the tip vortex in the prediction method.

Power spectral density curves for four fluctuating pressures measured with transducers located along the 70 percent chord at Mach 0.9 and $\alpha_w = 12^\circ$ are shown in Figures 66 through 69. The curves for transducers 10 and 11 are shown in Figures 66 and 67, respectively, and exhibit strong peaks at 425 Hz. The curves for transducers 13 and 14 are shown in Figures 68 and 69. These curves have peaks at 750 Hz. A summary of the peaks in the pressure power spectral densities at this test condition is presented in Figure 70, and the areas of the wing over which the vortex frequencies are evident in the fluctuating pressures are indicated.

Figures 71 through 73 contain power spectral density curves for fluctuating pressures measured with transducers 10, 11, and 13 at Mach 0.9 and $\alpha_w = 14^\circ$. The curve for transducer 10 does not exhibit a significant high frequency peak. The curve for transducer 11 has peaks at 375 and 700 Hz. For transducer 13, there is a peak only at 700 Hz. As shown in Figure 74, the 375 Hz frequency is associated with the snag vortex, and the 700 Hz frequency is associated with the leading edge and tip vortices.

Power spectral density plots for four fluctuating pressure transducers along the 70 percent chord at Mach 1 and $\alpha_w = 12^\circ$ are shown in Figures 75 through 78. No trend is apparent in these and the other plots examined at this test condition. A possible explanation for the lack of a pattern is that the spectrums may be affected by shock waves on the wing.

The general trends discussed above for configuration 1 in different flow conditions are also apparent for configurations 5 and 6. Some PSD plots for fluctuating pressures measured along the 70 percent chord line and drawings showing how peaks in these and other plots are located on the wing are shown in Figures 79 through 96.

4.3.3 Ratio of Peak to Low Frequency Spectral Levels. - The model for the spectral shape of the fluctuating pressures developed in Section 5 has as one of its parameters a quantity η , which is the ratio of the magnitude of the peak level in the spectrum to the low frequency level. The low frequency level is assumed constant from a very low frequency out to the frequency at which the spectrum starts to increase towards the peak. Values of η have been computed for the buffeting pressure power spectral density plots which contain significant peaks associated with the vortices discussed in Section 4.3.2. These values are plotted as functions of percent chord in Figures 97 through 104. For plots containing more than one such peak, η was computed for the higher one. For plots which are not constant at the low frequencies, an average value of the power spectral density at the low frequencies was used in the denominator of η . When this average value is greater than the value of the peak, then $\eta < 1$.

There are two patterns evident in the plots of η versus percent chord in Figures 97 through 104. The first is that η is generally larger along the 78 percent semispan line than along the other constant span lines on which measurements were taken. This pattern was also evident in the plots of overall rms pressures in Figures 14 through 25. This semispan line is close

to the center of the region affected by the snag vortex. The second pattern is that η tends to increase from the leading edge to the trailing edge of the wing.

4.3.4 Buffet Cross Power Spectral Densities - Normalized cross power spectral densities were computed to determine (a) whether a convection velocity exists in the separated region (and if so its value), and (b) the value of the spatial decay. The functions were plotted as magnitude, γ , and phase, θ , versus frequency. The spatial decay parameter is determined from the value of the magnitude as a function of the distance between the transducers in the pair. If a condition of pure convection independent of frequency exists, then the phase is proportional to frequency. The normalized cross power spectral density plots in Figures 105 through 124 are samples of many which show that this is not the case for the F-4 wing as a whole in separated flow. These plots are for pressures measured with transducer pairs (6, 10) and (12, 18) and the test conditions for configuration 1 covered in Section 4.3.2 in the discussion of power spectral densities.

Figures 105 and 106 show the magnitude and phase, respectively, of the normalized cross power spectral density function for transducer pair (6, 10) at Mach 0.7 and $\alpha_w = 12^\circ$. There are large changes in γ between 700 and 1000 Hz and between 1300 and 1700 Hz. An average value for γ , taking into account the logarithmic frequency scale, is about 0.35. This and similar values are used to determine the spatial decay. The phase has varying slopes, but the trend is positive from 0 to around 900 Hz. From 900 Hz to 2000 Hz, the trend in slope is negative. Thus, the phase is definitely not proportional to frequency in this case. Figures 107 and 108 present γ and θ for pair (12, 18). Again, γ is not constant; an approximate average value is 0.35. The phase again is not proportional to frequency, although it is more nearly so than that for pair (6, 10).

Figures 109 and 110 contain the γ and θ functions for pair (6, 10) at Mach 0.9 and $\alpha_w = 8^\circ$. The relatively small variation in γ over most of the frequency band and the good approximation of θ to a linear function of frequency indicate the existence of a nearly pure (i.e., independent of frequency) time delay from transducer 10 to transducer 6. One explanation for the time delay is the existence of a local convection velocity having its fore-aft component directed forward. The time delay might also be partially caused by a difference in propagation distances from a fluctuating

pressure source above the wing. Figures 111 and 112 show γ and θ for pair (12, 18). There is a large variation in γ . The graph of phase versus frequency has three distinct average slopes. Therefore, there is no pure time delay between transducers 11 and 18 and no pure convection.

The plots of magnitude and phase of the normalized cross power spectral density for pair (6, 10) at Mach 0.9 and $\alpha_w = 12^\circ$ are shown in Figures 113 and 114 and indicate the absence of a pure time delay. The plots for pair (12, 18) are shown in Figures 115 and 116. They also indicate the absence of a pure time delay. The snag vortex frequency of 425 Hz is evident in Figure 115.

Plots of γ and θ for pairs (6, 10) and (12, 18) at Mach 0.9 and $\alpha_w = 14^\circ$ are shown in Figures 117 through 120. Figure 118 again shows that there is no pure time delay between transducers 6 and 10. The phase plot for pair (12, 18) has several regions of different average slopes.

The normalized cross power spectral densities for pairs (6, 10) and (12, 18) at Mach 1 and $\alpha_w = 12^\circ$ are shown in Figures 121 through 124. The plots of γ show that the signals in the first pair are more strongly correlated than are those in the second pair. The plot of θ for pair (6, 10) has a change in average slope at about 1000 Hz; this again shows the absence of a pure time delay between transducers 6 and 10. The plot of θ for pair (12, 18) also shows the absence of a pure time delay.

Examination of many cross power spectral density functions, of which the ones discussed above are samples, has led to the conclusion that convection is not a highly significant parameter in buffet of highly swept fighter wings and that convection effects can be neglected in the development of a first generation mathematical model for the prediction of buffet loads. The observations which led to this conclusion were the following:

- o The correlation between the fluctuating pressures at two points decays fairly rapidly with distance between the points.
- o The existence of convection is indicated when the phase of the cross power spectral density function is linear with frequency and passes through the origin. In general, the data did not follow this trend.
- o The interaction of vortices originating from the leading edge, snag, and tip is so complex that convection in a broad sense seems to be fairly random in nature. Convection appears to be highly localized.

Additional justification was provided by cursory a study made to establish the general effects of n localized but independent convection zones. The results indicated that the structural response of a simple torsion model would be reduced by a factor $\frac{1}{n}$ compared to the response for a pure convection situation. The flow visualization oil and tuft studies indicate that n is 6 or greater; hence, even if the localized convection effects were orderly, little convection influence on response would be expected.

4.3.5 Tail Buffet - For an examination of tail buffet, power spectral densities were calculated for transducer 27, located on the left horizontal tail (stabilizer) at Mach 0.9 and $\alpha_w = 8^\circ, 12^\circ$, and 14° . These curves are shown in Figures 125 through 127. The corresponding curves for transducer 21, located on the left trailing edge flap, are shown in Figures 128 through 130 for comparison. At $\alpha_w = 8^\circ$, the fluctuating pressures on the stabilizer were due to tunnel noise. At $\alpha_w = 12^\circ$, the power spectral density of the fluctuating pressures there has a peak at the snag vortex frequency, but the leading edge vortex frequency is not evident. The overall rms level on the stabilizer is lower than that at most points on the wing. Observations for $\alpha_w = 12^\circ$ apply equally well for $\alpha_w = 14^\circ$.

The normalized cross power spectral density between transducer 21 on the trailing edge flap and transducer 27 on the stabilizer at Mach 0.9 and $\alpha_w = 12^\circ$ is shown in Figures 131 and 132. This and similar functions at Mach 0.9 and $\alpha_w = 8^\circ$ and 14° show that there is little correlation between the fluctuating pressures on the wing and those on the tail. There is some coherence at the snag vortex frequency at $\alpha_w = 12^\circ$ and 14° . This indicates the existence of some kind of convection from the wing to the tail, but not one with which there is associated a clear convection velocity.

The cross power spectral density between the pressures on either side of the stabilizer at Mach 0.9 and $\alpha_w = 12^\circ$ was computed. As was expected, there is essentially no correlation between these pressures.

4.4 Comparison of Wind Tunnel and Flight Data

The comparison of wind tunnel (model) and flight (full scale) fluctuating pressures is studied in two parts: (1) the overall rms level, and (2) the spectral shapes. These parts are considered separately using commonly accepted relationships for fluctuating pressures (References 18, 19, 20). Flight data are from a YF-4E airplane flight test program which was reported in Reference 2.

4.4.1 Overall rms - The overall rms level, σ , of fluctuating pressures is generally assumed to be proportional to the freestream dynamic pressure, q . Hence, the rms pressure coefficient, $\Delta C_{p_{rms}} = \sigma/q$, is considered to be independent of scale. Comparisons of model and full scale rms pressure coefficient variations with angle of attack at Mach 0.8 and 0.9 are presented in Figures 133 through 140. Full scale data are shown for flights at 25,000 feet and 35,000 feet. The comparisons are for transducers 17 ($\frac{x}{c} = 0.9$, $\frac{2y}{b} = 0.86$), 18 ($\frac{x}{c} = 0.9$, $\frac{2y}{b} = 0.78$), 21 ($\frac{x}{c} = 0.9$, $\frac{2y}{b} = 0.33$), and 24 ($\frac{x}{c} = 0.95$, $\frac{2y}{b} = 0.33$). At Mach 0.8, the model and full scale curves for transducer 17 (Figure 133) have different curvatures and compare unfavorably. For transducer 18 (Figure 134), the curves are very similar in shape and the curve for flight data is displaced 2° to 3° to the right of that for the tunnel data. A given value of $\Delta C_{p_{rms}}$ would therefore occur at an angle of attack 2° to 3° lower in the tunnel than in flight. For transducer 21 (Figure 135) the curves for model and full scale are similar. To compare values of $\Delta C_{p_{rms}}$ at a given angle of attack, the corresponding noise values (those at low angle of attack) should be subtracted on a mean square basis. When $\Delta C_{p_{rms}}$ is large compared to its corresponding noise level, however, the effect of the noise is negligible. Thus, at the higher angles of attack shown, the model data is not only higher than the full scale data but it is also increasing faster. Transducer 24 is near transducer 21 and the data (although limited for flight) for transducer 24 (Figure 136) appear essentially the same as those for transducer 21.

At Mach 0.9, the model and full scale curves for transducer 17 (Figure 137) are similar; however, above 5° the model data are higher and above 12° they are increasing faster than are the full scale data. For transducer 18, the curves for tunnel data are much higher, particularly from $\alpha_V = 8^\circ$ through 14° . Figure 139 again shows that the flight and tunnel curves are similar. The differences are that the curve for the tunnel is higher and that from 11° to 14° the curvatures of the two curves are different. The limited amount of flight data for transducer 24 at Mach 0.9 agrees fairly well with the tunnel data for that transducer except that the tunnel data are lower. This is shown in Figure 140.

In summary, the $\Delta C_{p_{rms}}$ versus α_V curves for model and full scale, which by common assumption should coincide, are similar but are not identical. For transducers 21 and 24, located on the trailing edge flap, buffet $\Delta C_{p_{rms}}$ is higher in the tunnel than in flight. It is thought that some of the

differences between the tunnel and flight curves for transducers 17 and 18 can be explained by the strong pressure field generated by the snag vortex. If the axis of this vortex (and, hence, other parts of it) is in a slightly different position relative to these transducers in the wind tunnel than it is in flight, then ΔC_{Prms} could vary considerably between tunnel and flight. The strongest evidence for such a possibility is shown in Figure 134. A given value of ΔC_{Prms} is reached in the tunnel at a 2° to 3° lower angle of attack than in flight. If the axis of the snag vortex reaches a given position relative to transducer 18 at a 2° to 3° lower angle of attack in the tunnel than it does in flight, then Figure 134 would be explained.

Another possible explanation for some of the differences between the ΔC_{Prms} versus α_w curves for wind tunnel and flight is an error in the flight measurements of α_w due to nose boom upwash. If such an error does exist, the values of α_w (flight) shown are thought to be high by about 1 degree.

4.4.2 Frequency Distribution - The key element in comparing the spectral shapes of the fluctuating pressures in the tunnel and in flight is the commonly accepted assumption that the frequency, f , associated with a pressure phenomenon is proportional to the freestream velocity, V , and inversely proportional to a reference length, b . In other words, the non-dimensional frequency, $k = \frac{fb}{V}$, is assumed independent of scale. One problem is choosing a suitable reference length. In boundary layer studies, the reference length is often chosen as the displacement thickness or the momentum thickness. In the separated flow associated with buffet, there is no classical boundary layer as such. It will be shown that a reference length associated with the structure (wing, for example) gives good scaling results.

For the comparison of frequency distributions - i.e., of nondimensional spectral shapes rather than of actual PSD levels - flight data were scaled to model data using the following equations:

$$f_{FS} = \frac{b_M}{b_{FS}} \cdot \frac{V_{FS}}{V_M} \cdot f_M \quad (4-1)$$

$$G_M(f_M) = \frac{G_{FS}^2}{\sigma_{FS}^2} \cdot \frac{b_M}{b_{FS}} \cdot \frac{V_{FS}}{V_M} \cdot G_{FS}(f_{FS}) \quad (4-2)$$

where

G is power spectral density of fluctuating pressure, $(\text{psi})^2/\text{Hz}$

f is frequency, Hz

σ is overall rms fluctuating pressure

b is structural reference length

V is freestream velocity

M (subscript) denotes model

FS (subscript) denotes full scale

Equation (4-1) assumes that $\frac{fb}{V}$ is independent of scale. Equation (4-2) follows from equation (4-1) and the fact that $\sigma^2 = \int_0^\infty G(f) df$.

Wind tunnel and flight pressure spectral shapes are compared in Figures 141 through 146. The flight spectral shape was obtained by applying equations (4-1) and (4-2) to power spectral density data which were plotted on a linear-linear graph. A series of points near zero on the linear graph appear on the log-log graph as a straight line. The power spectral density functions for the flight data were computed digitally at 2 Hz intervals. The equivalent bandwidths and averaging times were 4 Hz and 2.5 seconds, respectively. Some points from the linear-linear plots were not plotted in Figures 141 through 146 because they were not needed to display the principal characteristics of the spectral shapes.

The six comparisons of model and full scale spectral shapes shown in Figures 141 through 146 are for transducers 17 ($\frac{x}{c} = 0.90$, $\frac{2y}{b} = 0.36$) and 18 ($\frac{x}{c} = 0.90$, $\frac{2y}{b} = 0.78$) and three test conditions. The test conditions are shown in Table IX. All six comparisons show good agreement, particularly

Table IX
Test Conditions for Comparison of Model and
Full Scale Spectral Shapes

Configuration	Mach No.	Wing Angle of Attack, Deg
1	0.8	10
1	0.85	10
6	0.8	9

in the regions of the peaks caused by vortices. Some of the flight spectral shapes contained a broad peak around 90 Hz (scaled to model frequency) that is not evident in the tunnel spectral shape. This is in the neighborhood of the (scaled) first bending frequency of the full-scale wing and, coincidentally, of the first bending frequency of the model wing also. The fact that the broad high frequency peaks for the model and scaled full scale spectral

shapes coincide indicates that the scaling relations of equations (4-1) and (4-2), for spectral shapes (not actual PSD values) are valid for the study of wing buffet.

SECTION 5

PREDICTION METHOD FOR FLUCTUATING PRESSURES

The buffet prediction method described herein requires that spatial, magnitude and spectral characteristics of random, fluctuating pressures be described on the upper wing surface, where significant flow separation occurs at the higher angles of attack in the buffet regime. This section presents a general discussion of the nature of the flow pattern over a highly swept wing in buffet, the nature of the fluctuating pressures and their distribution on the wing, and a feasible method for prediction. A mathematical model is developed and a step-by-step method is set forth for using the pressure prediction method.

5.1 General

It was shown in Section 4 and in Appendix A that the aerodynamic flow over the F-4 wing is extremely complex, and that the associated fluctuating pressures are similarly complex. Two factors have dominated the study of the nature of fluctuating pressures to be applied to an upper wing surface:

- (1) Some rms pressure levels and spectral peaks have been related to vortices (Section 4 and Appendix A) but a comprehensive pattern describing the flow on the F-4 wing has not emerged.
- (2) In the preliminary design stage of a new airplane, knowledge of wing flow characteristics in buffet is extremely limited because the available tools (lift and drag data, flow visualization data) have not been sufficiently developed to provide reliable correlations.

Therefore, a significant portion of the study effort was devoted to examining the data obtained with F-4 wing studies for the purpose of establishing generalizations that are believed to be common to all wings.

It was originally envisioned that the mathematical modeling of the input buffeting pressures could be based on spectral functions formulated in terms of rms value, spectral shape, length scale value L, and convection velocity V_c . The experimental data do not indicate an overall convection pattern on the F-4 wings; if "convective" phenomena are present, they probably occur only in highly localized regions. Attempts to extract V_c and L have little meaning, therefore, and characterization in terms of more general spectral and cross-spectral functions was adopted. It is significant

to understand that the direct use of the experimentally indicated cross-spectral functions does not exclude convection effects or imply that some important factor is being overlooked. Convective effects, if they are present, are implicit in these functions. The practical use of spectral functions always involves the ratio L/V_c ; thus in general it is only necessary to find the value of this ratio. The separation into values L and V_c is meaningful, and serves as a convenient way to describe the flow in a more detailed fashion, only when convection is clearly present.

5.2 Nature of Pressure Function

The characteristics of the buffeting fluctuating pressures that are of importance in computing structural response are the power spectra of the pressures at various locations on the wing surface, and the cross spectra between separated points. It is convenient to split the representation of each of these functions into two parts, the rms values of the pressures, and the spectral function shape. The variation of these quantities with angle of attack α_w and Mach number M forms the essence of the method.

5.2.1 rms Levels - Generally, the descriptions of the rms pressure fluctuating levels in shear flow, turbulent boundary layers, or buffeting is commonly and conveniently given in terms of a reference q . This convention has also been used here and the equation for overall rms pressure level that has been adopted is

$$\sigma_p = \Delta C_{p_{rms}} q \quad (5-1)$$

where

q is freestream dynamic pressure

and

$\Delta C_{p_{rms}}$ is the local fluctuating pressure coefficient.

Application of this equation requires that the coefficient $\Delta C_{p_{rms}}$ be known at various locations on the wing and for various values of α_w and M .

Simplified models representing the variation of $\Delta C_{p_{rms}}$ over the wing surface were derived by considering the spatial distribution of the data contained in Figures 14 through 25. Aside from this data itself, several other factors were considered in arriving at these representations, such as those listed below:

- (a) The applicability of the prediction method would be limited to the determination of the primary loads in the structure in contrast to localized loads such as on individual wing skin panels. Also the corresponding primary structure model deformations influencing these loads do not vary greatly over localized areas. Hence, detailed definition of localized fluctuating pressure variations is an unnecessary luxury.
- (b) Magnitudes of fluctuating pressures and structural loads were a fraction of the corresponding static values. Hence, any reasonable rough approximation of the fluctuating pressures is consistent with its overall structural impact.
- (c) The intent of the research program was to develop a first generation method for buffet load prediction during preliminary design. Excessive detail and complexity would be antithesis to this intent and could, in fact, discourage its use for that purpose.
- (d) In spite of the overall complexity of the flow details, a gross behavior pattern seemed to emerge. Excluding the singular snag effect, flow separation and fluctuating pressure intensities tended to increase outboard along the span and rearward along the chord.
- (e) The present state-of-the-art in predicting buffeting pressures on lifting surfaces is yet in its infancy. The limited information available is inconclusive beyond first order effects.

In light of the above considerations, it was decided to employ a linear variation of $\Delta C_{p_{rms}}$ over the wing such as those shown in Figure 147. An example comparison between the linear model of Figure 147(a) and measured data points from Figures 15, 18, and 19 (for the clean wing) is shown in Figure 148. The models in Figure 147 are for use in computational response studies and constitute the $\Delta C_{p_{rms}}$ models to be used for wings in general. For design purposes one would be justified in designing to the most adverse environment. In linearized representation, Figure 147(a) can be used to this end for clean (unflapped) configurations while Figure 147(c) can be used for deflected flap configurations, at least for the present state of knowledge in this area. These are consistent with the more intense environments encompassed in the wind tunnel test program - generally the high supersonic Mach numbers and angles of attack from about 10° to 14° . At sonic

and supersonic speeds a marked reduction in fluctuating pressures was clearly evident (compare Figure 147(b) with 147(a) for example). There was some evidence of a leveling-off trend in buffet intensity at the higher angles of attack around $10^\circ - 14^\circ$, but such data were too sparse to be really conclusive.

5.2.2 Spectral Shape - In general the power spectra of the buffeting pressures measured on the F-4 wings indicated either a flat or white noise spectral shape or a shape with a pronounced peak at some discrete frequency. These shapes, corroborated by the fact that the autocorrelation functions generally were of the decaying oscillatory wave type, suggest the adoption of the following mathematical description of the autocorrelation function:

$$R(\tau) = \sigma^2 e^{-a|\tau|} \cos \omega_0 \tau \quad (5-2)$$

This function leads to a wide latitude in spectral shapes. For $\omega_0 = 0$, a spectrum is obtained which is flat in the low frequency range; for $a = 0$, it yields a spike type spectrum at the frequency ω_0 . Various combinations of a and ω_0 yield spectral shapes with a peak.

A non-dimensional form of equation (5-2) is

$$R(s) = \sigma^2 e^{-\frac{2\pi}{m}|s|} \cos 2\pi k_0 s \quad (5-3)$$

where m = a constant (empirical)

$$k_0 = \frac{f_0 \bar{c}}{V}$$

$$s = \frac{V\tau}{\bar{c}} = \text{non-dimensional time}$$

f_0 = frequency at which peak occurs

\bar{c} = reference chord

V = free stream velocity

The coefficient "a" in equation (5-2) relates to equation (5-3) by

$$a = \frac{2\pi}{m} \frac{V}{\bar{c}}$$

Since m is a constant, it is noted that "a" in effect represents the ratio V_c/L previously discussed; V takes the place of V_c , and mc takes the place of L .

The power spectral function indicated by equation (5-3) is

$$\frac{G(k)}{\sigma^2} = \frac{m}{\pi} \left[\frac{1}{1 + m^2 (k_o + k)^2} + \frac{1}{1 + m^2 (k_o - k)^2} \right] \quad (5-4)$$

which contains the variable parameters m and k_o (see Reference 16, pages 86 and 87). It may also be expressed in non-dimensional form as

$$k_o \frac{G(k)}{\sigma^2} = \frac{\lambda}{\pi} \left[\frac{1}{1 + \lambda^2 (1 + \frac{k}{k_o})^2} + \frac{1}{1 + \lambda^2 (1 - \frac{k}{k_o})^2} \right] \quad (5-5)$$

where

$$k = \frac{fc}{V}$$

$$\lambda = mk_o$$

$$G(k) = \frac{V}{c} G(f)$$

and the ratio k/k_o is a plotting variable.

Various spectra indicated by equation (5-5) are shown in Figure 149.

5.2.3 Fitting Data to the Model - The characteristics of the mathematical model that can be directly related to similar characteristics of an experimental data plot include

- ° the location of the peak amplitude ($k = k_o$)
- ° the ratio of peak amplitude (at $k = k_o$) to the amplitude at zero frequency ($k = 0$).

The latter ratio is called η and can be calculated in terms of λ from equation (5-5). For the peak at $k = k_o$,

$$G(k_o) = \frac{\sigma^2 \lambda}{k_o \pi} \left(\frac{1}{1 + 4 \lambda^2} + 1 \right)$$

and for $k = 0$

$$G(0) = \frac{\sigma^2 \lambda}{k_o \pi} \left(\frac{2}{1 + \lambda^2} \right)$$

and

$$\eta = \frac{G(k_o)}{G(0)} = \frac{(1 + \lambda^2)(1 + 2\lambda^2)}{1 + 4\lambda^2}$$

Solving for λ yields

$$\lambda = \frac{1}{2} [4\eta - 3 + (16\eta^2 - 16\eta + 1)^{1/2}]^{1/2}, \eta > 0.933 \quad (5-6)$$

A plot of λ vs. η obtained from equation (5-6) is shown in Figure 150. Values of $\eta < 1.0$ have no physical significance in the mathematical model and are not included in the figure.

A method for simplifying and systemizing the procedure for fitting equation (5-5) to experimental data is described in the following procedure:

- (1) Determine f_o at the peak, then

$$k_o = f_o c/v$$

- (2) Find the ratio η of the peak (f_o) value to the $f = 0$ value.

- (3) Enter Figure 150 with this η and read out λ .

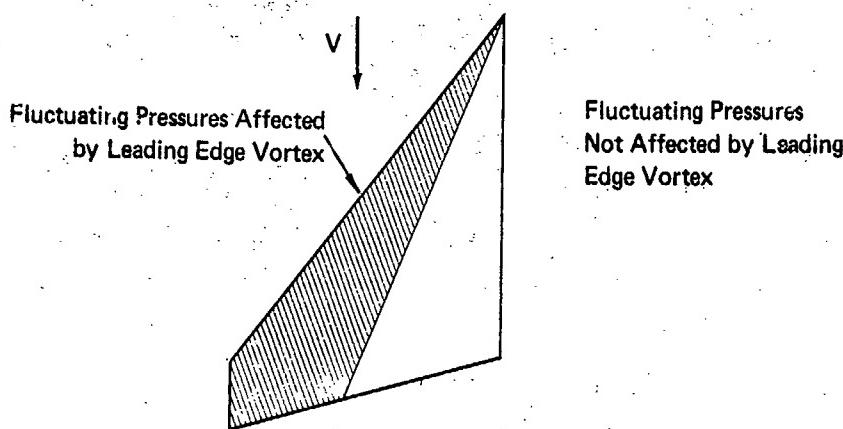
An example of how the spectrum so obtained fits a measured spectrum is shown in Figure 151, which was obtained for transducer 11 at Mach 0.7 and $\alpha_w = 12^\circ$ (see Figure 62). The constant values used in the mathematical model were $f_o = 700$ Hz, $c = 1.60$ feet, $v = 776$ ft/sec, $\sigma = 1.1$ psi, $\eta = 12.5$, and $\lambda = 4.85$.

Based on the results of Section 4, the existence of peaks in the power spectral density of the fluctuating pressures is dependent on the vortices existing over the wing. Figures 62, 65, 70, 74, 82, 87, 92, and 96 indicate on the basis of spectral content that there are three vortices of interest. These are associated with the inner wing leading edge, the tip, and the snag of the wing. The frequencies associated with these vortices and shown in the figures given above are plotted versus wing angle of attack, Mach number, and configuration in Figure 152. The plots versus angle of attack are for configurations 1 and 5 at Mach 0.9. They show that for all three vortices the frequency decreases as wing angle of attack increases over the range from 8° through 14° for configuration 1. The plots versus Mach number show that for configuration 1 the peak

frequencies decrease as Mach number increases over the range 0.7 through 0.9. For configuration 5, they show that the peak frequencies are less dependent upon Mach number over this range. As mentioned in Section 4.3.2, no pattern emerged in the spatial variation of the power spectral density plots for the Mach 1 test condition. No relationship between any spectral peaks and possible vortices over the wing was evident, thus no data are shown in Figure 152 for Mach 1. The trends evident from Mach 0.7 through Mach 0.9 are thought to continue for some increment in Mach number beyond 0.9, but the size of this increment is unknown. This lack of data at Mach 1.0 is not thought to be critical because low values of ΔC_{prms} are indicated in Figure 147. The plots versus configuration, which are essentially plots versus flap deflection, show that at Mach 0.7 and in the neighborhood of 12° wing angle of attack the frequencies are relatively independent of flap position. The snag vortex frequency is raised about fifty percent when the leading edge flaps are lowered 8° . Values of k_0 for particular flight conditions and flap deflections can be obtained by interpolating among graphs in Figure 152.

A wing other than that of the F-4 may or may not generate all three vortices discussed above. Most modern fighter wings will have a tip vortex and a leading edge vortex. They will probably not have what has been referred to above as a snag vortex unless they do in fact have a snag or similar leading edge discontinuity. Figures 62, 65, 70, 74, 82, 87, 92 and 96, and Figure 152 indicate that the frequencies associated with the leading edge and tip vortices on the F-4 wing are essentially the same. It is assumed that this relationship would hold true on other fighter wings. Thus, if a wing has a leading edge vortex and a tip vortex but no snag vortex, then for purposes of modeling, the effects of the tip vortex can be accounted for by the leading edge vortex; therefore, only the leading edge vortex need be considered.

5.2.4 Preliminary Design Data - In the preliminary design stage of a fighter aircraft, there are at least two ways to estimate the areas of the wing over which the fluctuating pressures are affected by vortices and which types of vortices they are. The quickest way is to use engineering judgment and consider the characteristics of the wing (e.g., does it have a snag) and the regions of the F-4 affected by vortex frequencies shown in Figures 62, 65, 70, 74, 82, 87, 92 and 96. For example, on a wing with a planform similar to that of the F-4 wing but having a smooth leading edge, the judgment for Mach 0.7 and $\alpha_w = 12^\circ$ might be as shown in the following sketch:



The second way to estimate the types of vortices present over a wing and the areas of the wing over which they affect the fluctuating pressures is to subject a model of the wing to a flow visualization test. As was indicated at the beginning of this section, a flow visualization test gives an indication of the direction and turbulence of the flow. Interpreting this in terms of the causes, whether vortices or other phenomena, is often difficult. It may or may not yield better results than engineering judgment alone.

5.2.5 Experimental Values of η - From the plots of η versus percent chord in Figures 97 through 104, a simplified model for the variation of η over the wing was developed and is shown in Figure 153. This model is similar to that for the rms pressure distribution over the wing except that the values of η at the corners of the wing planform are treated as variables and plotted versus wing angle of attack, Mach number, and configuration. The plots for configuration 1 show that $\eta = 1$ at the wing root for all α_w from 8° through 14° and all Mach numbers from 0.7 through 0.9. At the wing tip at Mach 0.9, η is higher at $\alpha_w = 12^\circ$ than at either 8° or 14° . At the tip at 12° wing angle of attack, η increases at the leading edge and decreases at the trailing edge as the Mach number increases from 0.7 through 0.9. As discussed in Section 5.2.3 in connection with k_o , data on spectral peaks at $M = 1.0$ are not presented because no pattern was evident. The trends shown for η in Figure 153 from Mach 0.7 to Mach 0.9 can be expected to continue for some increment beyond $M = 0.9$; but, again, the size of the increment is un-

known. The plots for configuration 5 in Figure 153(b) show that at the wing root and the tip leading edge, $\eta = 1$ for all α_w from 11° through 14° and all Mach numbers from 0.7 through 0.9. At the tip trailing edge at Mach 0.9, η is higher at $\alpha_w = 11^\circ$ than at 14° . At the tip trailing edge at $\alpha_w = 11^\circ$, η decreases as the Mach number increases from 0.7 through 0.9. Figure 153(c) shows the effect of model configuration on η at Mach 0.7 and α_w about 12° . At the root and leading edge of the tip, η is the same for configurations 1, 5, and 6. At the trailing edge of the tip η is the same for configurations 1 and 5 but lower for configuration 6. Values of η for particular flight conditions and flap deflections can be obtained by interpolating among graphs in Figure 153.

5.3 Spatial Correlation Effects

Conceptually, the cross-correlation between the buffet pressures at two separated points may be envisioned to embody a spatial decay effect and possibly some convection effect. On this basis, a model for the cross-correlation function may be written in the form

$$R^{12}(r, \tau) = \sigma_1 \sigma_2 e^{-\alpha|\Delta x|} e^{-\beta|\Delta y|} \rho(\tau - \tau') \quad (5-7)$$

where σ_1 and σ_2 denote the respective rms values at two points, Δx and Δy represent the x and y separation distances between the points, τ' relates to the time of convection of the pressures from one point to the other, and ρ denotes the normalized autocorrelation function. The following is another plausible form that combines the x and y dependency into a single spatial function r ,

$$R^{12}(r, \tau) = \sigma_1 \sigma_2 e^{-\delta|r|} \rho(\tau - \tau') \quad (5-8)$$

where r is simply the distance between the two points.

The cross spectrum indicated by equation (5-8) is

$$S^{12}(r, f) = \sigma_1 \sigma_2 e^{-\delta|r|} e^{-i2\pi f\tau'} \psi(r) \quad (5-9)$$

which indicates a magnitude

$$|S^{12}(r,f)| = \sigma_1 \sigma_2 e^{-\delta|r|} \psi(f) \quad (5-10)$$

and a phase angle θ between the Quad and Co power which is

$$\theta = 2\pi f \tau' \quad (5-11)$$

In Equations (5-9) and (5-10) ψ is the normalized power spectral density function. Note that if τ' is a constant then the phase versus frequency curve is a straight line passing through the origin with slope equal to $2\pi\tau'$. Note also that

$$\rho^{12}(r,\tau') \triangleq \frac{R^{12}(r,\tau')}{\sigma_1 \sigma_2} = e^{-\delta|r|} = \frac{|S^{12}(r,f)|}{\sigma_1 \sigma_2 \psi(f)} \triangleq \gamma^{12}(r,f) \quad (5-12)$$

where $\rho^{12}(r,\tau')$ is the cross correlation of the pressures at points 1 and 2 normalized by dividing by the product of the rms values of the pressures and $\gamma^{12}(r,f)$ is the magnitude of the cross power spectral density normalized by dividing by the square root of the product of the power spectral densities of the pressures.

The experimental results tended to fit the form indicated by equation (5-8). Attempts were therefore made to establish apparent convective effects by considering time delays τ' between various transducers. Theoretically, if an ordered convection field directed along a line between two transducers were involved, τ' would lead to a consistent convection velocity given by $V_c = r/\tau'$, where r is the distance between the two points under consideration. Studies using the r and τ' associated with many pairs of transducers proved to be unproductive in defining convection velocities. A more refined study, using data from sets of three transducers, gave promise of defining local convection velocity. However, this study was not completed due to the inconsistent nature of the flow field. This latter study assumed that disturbances propagate across the transducer set in a line, or front. The results indicated that the idea of an orderly consistent convection did not fit the data for the F-4 model wing. Apparently the various vortices that emanate from the leading edge mix in such a hetero-

geneous way to make the flow appear chaotic. Thus the best conclusion that can be drawn from the test results is that detailed consideration of convection cannot be made, and it is therefore neglected in this study. Essentially this amounts to setting $\tau' = 0$ in equations beginning with (5-8). Tests on other wings are needed to determine if similar results are found.

Results for spatial decay effects were found to be somewhat better, although still quite rough. In equation (5-12) the spatial decay factor represents essentially a cross-correlation coefficient between the two pressures, or

$$\rho^{12}(r, \tau') = \bar{\gamma}^{12}(r, f) = e^{-\delta|r|} \quad (5-13)$$

where δ is a spatial decay constant to be empirically established. In this study, the average value $\bar{\gamma}^{12}$ of the magnitude of the normalized cross power spectral density was used. Values of $\bar{\gamma}^{12}$ derived from several normalized cross power spectral density functions are shown in Figure 154 in terms of the separation distance r . The curve shown in this figure is an exponential fit of the data given by

$$\bar{\gamma}^{12} = e^{-0.25r} \quad (5-14)$$

(Although there is scatter in the plotted data of Figure 154, an exponential curve fit is the most tractable representation of the data, and it has been used successfully by previous investigators.) This expression can be converted to one of general use by expressing it in nondimensional form through use of the mean aerodynamic chord, thus

$$\bar{\gamma}^{12} = e^{-0.25 \bar{c} r/\bar{c}}$$

For the model $\bar{c} = 19.25$ inches, and thus in the form for general use $\bar{\gamma}^{12}$ is given by

$$\bar{\gamma}^{12} = e^{-4.8 r/\bar{c}} \quad (5-15)$$

Within the uncertainty in the value of the decay factor $\delta = \frac{4.8}{\bar{c}}$ as indicated by the scatter in the plotted points in Figure 154, α and β (see equation (5-7) for example) may also each be set equal to $\frac{4.8}{\bar{c}}$. Then an alternative expression is

$$\gamma^{12} = e^{-4.8|\Delta x|/\bar{c}} e^{-4.8|\Delta y|/\bar{c}} \quad (5-16)$$

Equations (5-15) and (5-16) represent different forms of the spatial decay factor that has been derived for general use from the F-4 tests. It is desirable to determine if tests on other wings yield a coefficient similar to the 4.8 value derived. In application to other wings, \bar{c} would be the value of the mean aerodynamic chord for the wing under consideration.

The above results for the cross correlation and cross power spectral density functions for the pressures at points 1 and 2 separated by a distance r may now be expressed in the terms of equations (5-3) and (5-5) as follows

$$R(t,s) = \sigma_1 \sigma_2 e^{-\delta r} e^{\frac{-2\pi s}{m}} \cos 2\pi k_o s \quad (5-17)$$

$$k_o \frac{G(r,k)}{\sigma_1 \sigma_2} = \frac{\lambda}{\pi} \left[\frac{1}{1 + \lambda^2 (1 + \frac{k}{k_o})^2} + \frac{1}{1 + \lambda^2 (1 - \frac{k}{k_o})^2} \right] e^{-\delta r} \quad (5-18)$$

where σ_1 and σ_2 refer to the respective rms values of pressure at the two points, $\delta = \frac{4.8}{\bar{c}}$, and the other parameters are as defined in Section 5.2.2.

5.4 Procedure for Applying Prediction Method

Following is a step by step procedure to be followed to predict the fluctuating pressures on a fighter airplane wing at a given point in the transonic speed, high angle of attack flight regime. The procedure is based on the prediction method described in this section.

5.4.1 Spectral Shape

STEP 1

V and \bar{c} are known.

STEP 2

Estimate the types and locations of the vortices. To do this, use:

- a) Engineering judgment considering the characteristics of the wing (is there a snag?) and the regions of the F-4 wing affected by vortex frequencies shown in Figures 62, 65, 70, 74, 82, 87, 92 and 96.
- b) Flow visualization tests combined with engineering judgement. If only leading edge and tip vortices are present, the tip vortex can be neglected. If a snag vortex overlaps another vortex, the effect of the other vortex should be neglected in the area of overlap.

STEP 3

Establish the nondimensional vortex frequency, k_o , from Figure 152. Assume k_o established by a vortex to be applicable over a chord line. If a vortex does not exist over part of the chord line, k_o will serve as a cutoff frequency in the model for the spectral shape to limit the frequency range over which most of the energy is distributed.

STEP 4

Establish n , the ratio of the peak to the low frequency level of the spectrum, from Figure 153.

STEP 5

With n , obtain the parameter λ from Figure 150.

STEP 6

With λ , determine the spectral shape of the $k_o \frac{G(k)}{\sigma^2}$ function from Figure 149.

STEP 7

With k_o , compute the nondimensional power spectral density as a function of the nondimensional frequency $k = \frac{k_o}{V}$:

$$k = k_o \left(\frac{k}{V} \right)$$

$$\frac{G(k)}{\sigma^2} = \frac{1}{k_o} \left(k_o \frac{G(k)}{\sigma^2} \right)$$

STEP 8

With \tilde{c} and V , calculate the normalized power spectral density $\frac{G(f)}{\sigma^2}$ as a function of the frequency f .

$$f = \frac{V}{c} k$$

$$\frac{G(f)}{\sigma^2} = \frac{c}{V} G(k)$$

5.4.2 Overall rms Level

STEP 1

Dynamic pressure q is known.

STEP 2

Establish $\Delta C_{p_{rms}}$ from Figure 147.

STEP 3

Compute σ as

$$\sigma = \Delta C_{p_{rms}} q.$$

SECTION 6

PREDICTION METHOD FOR BUFFET DYNAMIC RESPONSE

The structural dynamic response prediction technique chosen for this first generation buffet prediction method is based on work that is reported in References 10 and 21. That analysis, derived to estimate the acceleration response to buffet pressures of truncated conical shells, incorporates approximations that are considered consistent with the goals of this development. The problem formulation, mathematical modeling, and simplifying assumptions are discussed in this section, and equations of motion are presented. It is to be noted that essentially all of the development of the mathematical response equations presented in this section was done in the above mentioned References 10 and 21. Additional information is given in Reference 22.

6.1 Outline of Response Prediction Method

The steps involved in the response analysis are:

- (1) Divide the wing planform into a gridwork of surface areas (see Paragraph 6.2).
- (2) Define structural properties of the aircraft. The elastic vibration characteristics of the aircraft wing are specified in terms of uncoupled modes. The required characteristics are modeshapes $\phi_i(x,y)$, modal frequencies ω_i , generalized masses M_i , and modal damping coefficients ζ_i . These data, most conveniently defined for the case of zero flight speed, may be obtained either experimentally (for an existing airplane) or analytically.
- (3) Define the fluctuating pressures within each area element in terms of the pressure power spectra (specified as normalized power spectral densities, overall rms fluctuating pressure coefficients, freestream dynamic pressure, and spatial decay constant).
- (4) Determine generalized aerodynamic forces using pressure, area and modeshape definitions. The essentials of the mathematical treatment used in the response prediction method are presented below in Paragraph 6.3.
- (5) Compute response power spectra and rms values of response parameters at selected locations on the structure. Expressions for the response spectra are discussed in Paragraph 6.3.

6.2 Wing Area Sectioning

The wing planform is divided into a number of basic areas for the purpose of simplifying the computation of generalized aerodynamic forces. While the area sectioning may be done in several ways, the method selected for this study defines the boundaries of the areas with a series of constant percent chord lines intersecting with streamwise lines (See Figure 155). The basic areas, indicated by numbers at their centers, are also members of larger surface areas (designated as regions) that are indicated by numbers in circles. The regions are areas over which the spatial decay coefficients and the shapes of the power spectral densities of pressure, both discussed in Section 5, are assumed to be constant. The basic areas are sized so that cross correlation between these areas can be neglected. A decay value of $e^{-4.8 \frac{r}{\bar{c}}} \leq 0.3$ gives a value of r approximately $0.25\bar{c}$ so that basic areas with dimensions of about one-fourth the mean aerodynamic chord should fulfill this latter requirement. It should be noted that gross structural response, and not local response, is of most concern so that localized effects (such as correlation immediately across a basic area boundary) will not significantly affect overall wing response.

6.3 Overview of Mathematical Development

The aircraft structure has normal modes $\phi_i(x,y)$ corresponding to a set of normal coordinates $q_i(t)$. The modal response due to pressure excitation $p(x,y,t)$ is determined from the fundamental equation in the time domain,

$$\ddot{q}_i(t) + 2\zeta_i \omega_i \dot{q}_i(t) + \omega_i^2 q_i(t) = \frac{1}{M_i} \iint_{\text{wing planform}} \phi_i(x,y) p(x,y,t) dx dy \quad (6-1)$$

where

ω_i = frequency of mode ϕ_i

M_i = generalized mass of mode ϕ_i

ζ_i = damping ratio of mode ϕ_i

Once the modal responses $q_i(t)$ are determined, then the local displacement response $z_a(t)$ at any point "a" on the wing is determined by

$$z_a(t) = [\phi_{ai}] [q_i(t)] \quad (6-2)$$

which states that the total response at any point "a" is the sum of the products of modeshape values at "a" times the corresponding generalized coordinate values obtained from (6-1).

Although equations (6-1) and (6-2) are presented in the time domain, the random nature of the variables makes the solution of these equations not adaptable to deterministic techniques. Rather, the nature of the measured buffet pressures indicates that statistical methods of analysis are required. The well known procedures of power spectrum analysis have been used in References 10 and 21, and are followed here. The resulting equations, expressed in the frequency domain, are obtained by applying conventional Fourier transform techniques to the time functions. Therefore, the relationships that follow are presented in the form of power spectrum functions that are derived from the conventional time varying functions.

The following relationship may be considered as a frequency domain counterpart of (6-1) because it relates modal spectrum response to pressure spectrum forcing functions:

$$S_q^{ij}(\omega) = \frac{1}{Z_i(\omega)Z_j^*(\omega)} \sum_k \sum_l \int_{A_k} \int_{A_k'} S_p(x, y, x', y', \omega) \phi_i(x, y) \cdot \phi_j(x', y') dA_k dA'_l \quad (6-3)$$

where

$S_q^{ij}(\omega)$ = the response cross spectrum for the normal coordinates q_i and q_j

$S_p(x, y, x', y', \omega)$ = pressure cross spectrum between points x, y and x', y'

and the Z are frequency response functions for modes i and j ,

$$Z_i(\omega) = M_i \omega_i^2 [1 - (\frac{\omega}{\omega_i})^2 + i 2 \zeta_i (\frac{\omega}{\omega_i})] \quad (6-4)$$

$$Z_j^*(\omega) = M_j \omega_j^2 [1 - (\frac{\omega}{\omega_j})^2 - i 2 \zeta_j (\frac{\omega}{\omega_j})] \quad (6-5)$$

Wing areas are designated by A_k and A_l and the indices k and l both vary from 1 to the total number of basic areas. The frequency domain counterpart of equation (6-2) is expressed as

$$S_z^{ab}(\omega) = [\phi_{ai}] [S_q^{ij}(\omega)] [\phi_{bj}]^T \quad (6-6)$$

in which

ϕ_{ai} = the ith degree of freedom modeshape value at point "a"
and $S_z^{ab}(\omega)$ = displacement response cross spectrum between points a and b.

6.3.1 Modeshape Averaging - A simplification to the form of (6-3) is introduced by a modeshape averaging technique that is introduced in Reference 10. In this method, it is simply assumed that a modeshape displacement value is constant within any basic area A_k . The value of the modeshape used for any mode i within area A_k is taken as an average value

$$\bar{\phi}_{ik} = \frac{1}{A_k} \int_{A_k} \phi_i dA_k$$

Since the modeshape values within an area then become independent of x and y, equation (6-3) can be rewritten

$$S_q^{ij}(\omega) = \frac{1}{z_i(\omega) z_j^*(\omega)} \sum_k \sum_l \bar{\phi}_{ik} \bar{\phi}_{jl} \int_{A_l} \int_{A_k} S_p(x, y, x', y', \omega) dA_k dA'_l \quad (6-7)$$

With the following definition

$$S_p^{kl}(\omega) = \int_{A_l} \int_{A_k} S_p(x, y, x', y', \omega) dA_k dA'_l \quad (6-8)$$

equation (6-7) can be expressed in the form

$$S_q^{ij}(\omega) = \frac{1}{z_i(\omega) z_j^*(\omega)} [\bar{\phi}_{ik}] [S_p^{kl}(\omega)] [\bar{\phi}_{jl}]^T \quad (6-9)$$

6.3.2 Real Representation of Response Spectrum - Reviewing equations (6-6) and (6-9), which give the deflection response cross spectrum between points a and b, it should be recalled that the cross spectrum is in general a complex quantity. Therefore, the cross spectrum of any quantity, whether a measure or displacement, can be written in terms of a real and an imaginary part, viz.,

$$C^{12}(\omega) = C^{12}(\omega) - iQ^{12}(\omega) \quad (6-10)$$

The main interest here is the power spectrum of the response at a point, which is obtained by letting, for example, $b = a$ in the above equations. By definition a power spectrum is a real function; hence only the real part of equation (6-6) is considered in what follows. Since the only imaginary terms in equation (6-6) are contained within $[S_q^{ij}(\omega)]$, the real part of this equation for the special case of $b = a$ can be written as

$$C_z^{aa}(\omega) = [\phi_{ai}] [C_q^{ij}(\omega) \phi_{aj}]^T \quad (6-11)$$

Measured spectra are expressed only for positive frequencies, and are usually presented in terms of frequency in Hertz. Therefore it is expedient at this point to define the spectrums for positive frequencies, and for frequency in Hertz. Thus equation (6-11) becomes

$$C_z^{aa}(f) = [\phi_{ai}] [C_q^{ij}(f)] [\phi_{aj}]^T \quad (6-12)$$

Following the development in Reference 21, the real part of equation (6-9) can then be expressed in real terms, viz.,

$$\begin{aligned} C_q^{ij}(f) &= \frac{(1/M_i M_j \omega_i^2 \omega_j^2)}{H_1^2(f) + H_2^2(f)} [H_1(f) \sum_k \sum_l \bar{\phi}_{ik} \bar{\phi}_{jl} \\ &\quad \cdot \int_{A_k} \int_{A_k} C_p(x, y, x', y', f) dA_k dA_k \\ &\quad + H_2(f) \sum_k \sum_l \bar{\phi}_{ik} \bar{\phi}_{jl} \int_{A_k} \int_{A_k} Q_p(x, y, x', y', f) dA_k dA_k] \quad (6-13) \end{aligned}$$

where

$$H_1(f) = \left(1 - \left(\frac{f}{f_i}\right)^2\right) \left(1 - \left(\frac{f}{f_j}\right)^2\right) + 4 \zeta_i \zeta_j \frac{f^2}{f_i f_j} \quad (6-14)$$

$$H_2(f) = 2\zeta_j \frac{f}{f_j} \left(1 - \left(\frac{f}{f_i}\right)^2\right) - 2\zeta_i \frac{f}{f_i} \left(1 - \left(\frac{f}{f_j}\right)^2\right) \quad (6-15)$$

(Note: $H_2(f) = 0$ when $i = j$.)

Equation (6-13) is an expanded form of equation (6-3) making it more adaptable to the use of measured data.

6.3.3 Simplifying Assumption - It is now assumed that the cross correlation function (or normalized cross power spectral density magnitude) of the fluctuating pressures is negligibly small except when $l = k$. This is the case if the areas are chosen sufficiently large. The rationale used for the selection of area size based on decay data was presented in Paragraph 6.2. The cross correlation function between any two points lying within a basic area A_k is represented as the product of the autocorrelation function at the center of A_k and exponential decay functions of the form

$$D \approx e^{-\alpha|x-x'|} e^{-\beta|y-y'|} \quad (6-16)$$

The cross-correlation can then be written as

$$R_p(\mu, v, \tau) = R_o(\tau) e^{-\alpha\mu} e^{-\beta v} \quad (6-17)$$

where

$$\mu = |x-x'| \quad (6-18)$$

$$v = |y-y'| \quad (6-19)$$

and $R_o(\tau)$ is the autocorrelation function at the center of A_k .

The equation for the cross power spectrum given in equation (3-6) of Section 3.3 can be written as

$$\begin{aligned} S_p(\mu, v, f) &= \int_{-\infty}^{\infty} R_p(\mu, v, \tau) e^{-i2\pi f\tau} d\tau \\ &= \int_{-\infty}^{\infty} R_o(\tau) (e^{-\alpha\mu} e^{-\beta v}) (cos2\pi f\tau - i sin2\pi f\tau) d\tau \end{aligned} \quad (6-20)$$

The real and imaginary parts of this equation are the $C_p(x, y, x', y', f)$ and the $Q_p(x, y, x', y', f)$, respectively, of equation (6-13).

Substituting equation (6-17) into equation (6-20), integrating, and setting $l = k$ gives

$$\begin{aligned} C_p(x, y, x', y', f) &= \int_{-\infty}^{\infty} [R_o(\tau) e^{-\alpha\mu} e^{-\beta v}] \cos2\pi f\tau d\tau \\ &= C_p^{kk}(f) e^{-\alpha\mu} e^{-\beta v} \end{aligned} \quad (6-21)$$

$$\text{and } Q_p(x, y, x', y', f) = 0 \quad (6-22)$$

where $C_p^{kk}(f)$ is the power spectrum at the center of A_k . The function $Q_p(x, y, x', y', f)$ is zero because it comes from the integration of the product of an even function, $R_o(\tau)$, times an odd function, $\sin 2\pi f\tau$, over the range $(-\infty, \infty)$.

Using equation (6-21) in the first integral of equation (6-13) yields

$$\int_{A_k} \int_{A_k} C_p(x, y, x', y', f) dA_k dA_k = C_p^{kk}(f) \int_{A_k} \int_{A_k} e^{-\alpha\mu} e^{-\beta\nu} dA_k dA_k \quad (6-23)$$

The integral on the right side of this equation is called the decay correction factor for A_k , DCF_k .

$$DCF_k = \int_{A_k} \int_{A_k} e^{-\alpha\mu} e^{-\beta\nu} dA_k dA_k \quad (6-24)$$

To simplify the integration, A_k is assumed to be rectangular with chordwise dimension Δx and spanwise dimension Δy . Δy is the distance between the constant percent span lines which bound A_k . Δx is an average distance between the constant percent chord lines which bound A_k .

The resulting integration yields

$$DCF_k = \frac{1}{(\alpha\beta)^2} [e^{-(\alpha\Delta x)_k} + (\alpha\Delta x)_k^{-1} [e^{-(\beta\Delta y)_k} + (\beta\Delta y)_k^{-1}] \quad (6-25)$$

Equation (6-13) can now be written in the form

$$C_q^{ij}(f) = \frac{(1/M_1 M_1 \omega_i^2 \omega_j^2) H_1(f) [\bar{\phi}_{ik}] [C_{pd}^{kk}(f)] [\bar{\phi}_{jk}]^T}{H_1^2(f) + H_2^2(f)} \quad (6-26)$$

where

$$C_{pd}^{kk}(f) = C_p^{kk}(f) DCF_k \quad (6-27)$$

It is indicated in References 10 and 21 that a further simplification is made by neglecting the values of $C_q^{ij}(f)$ when $i \neq j$. Then equations (6-12) and (6-26) can be written

$$C_z^{aa}(f) = \sum_i \phi_{ai}^2 C_q^{ii}(f) \quad (6-28)$$

$$C_q^{ii}(f) = \frac{[\bar{\phi}_{ik}] [C_{pd}^{kk}(f)] [\bar{\phi}_{jk}]^T}{M_i^2 \omega_i^4 [(1 - (\frac{f}{f_i})^2)^2 + (2\zeta_i(\frac{f}{f_i}))^2]^2} \quad (6-29)$$

The computer program modified for computing the response spectrums provides the option of using or not using $C_q^{ij}(f)$ when $i \neq j$.

The acceleration response power spectra are found from equation (6-12) to be

$$C_z^{aa}(f) = [\phi_{ai}] [C_q^{jj}(f)] [\phi_{aj}]^T \quad (6-30)$$

where

$$C_q^{ij}(f) = (2\pi)^4 f^4 C_q^{ij}(f) \quad (6-31)$$

With the same simplifications used to obtain equation (6-28), equation (6-30) can be written as

$$C_z^{aa}(f) = \sum_i \phi_{ai}^2 C_q^{ii}(f) \quad (6-32)$$

where

$$C_q^{ii}(f) = (2\pi)^4 f^4 C_q^{ii}(f) \quad (6-33)$$

The mean square responses are given by the integrals of equations (6-28), (6-29), (6-32), and (6-33)

$$\sigma_{z_a}^2 = \int_0^\infty C_z^{aa}(f) df \quad (6-34)$$

$$\sigma_{q_i}^2 = \int_0^\infty C_q^{ii}(f) df \quad (6-35)$$

$$\sigma_z^2 = \int_0^\infty C_z^{aa}(f) df \quad (6-36)$$

$$\sigma_{\ddot{q}_i}^2 = \int_0^\infty C_{\ddot{q}}^{ii}(f) df \quad (6-37)$$

SECTION 7
PREDICTION OF AIRCRAFT RESPONSE AND COMPARISON WITH
MEASURED FLIGHT DATA

The method presented in Section 6 was used to predict the response of the F-4 aircraft to buffeting pressures at three flight conditions. The method presented in Section 5 was used to predict the fluctuating pressures which were used as input data in the response predictions. The predicted responses were compared with measured flight acceleration data to provide an indication of the validity of the buffeting pressure and response prediction methods and the results are presented in this Section.

7.1 Response Equations

Equations (6-28), (6-29), (6-32), and (6-33) were used to compute the response of the F-4 aircraft.

7.2 Wing Idealization

The F-4 wing was idealized as having a straight leading edge and being divided into 3 regions and 18 areas as shown in Figure 156. The power spectral density shapes in regions 1 and 2 are determined by the leading edge and snag vortices, respectively; and the shape in region 3 is determined by either the tip or snag vortex, depending on their relative dominance. The gridwork of areas is a compromise that provides reasonable definition of the structural vibration mode shapes and the overall rms fluctuating pressure distribution while limiting the maximum value of the normalized cross-correlation function for the pressures at the centers of adjacent areas to about 0.2 inboard and 0.6 outboard.

7.3 Structural Representation of F-4 Wing

Data for the first 10 symmetric and the first 10 antisymmetric normal modes of the F-4 wing with full wing fuel were used to represent the structure responding to the random excitation. The data are based on a finite element analysis program being developed for the F-4 wing in conjunction with the production F-4 effort, and they represent the best analytical model of the wing to date. The first four analytical and measured frequencies are shown in Table X and are in good agreement.

Table XI shows the natural frequencies and generalized masses for all 29 modes ordered as used in this study. Table XII presents the mode-shapes for these modes in a column format. The column numbers in Table XII correspond to the mode numbers in Table XI. Table XIII relates the

Table X
Comparison of Analytical and Measured F-4 Wing Vibration Frequencies, Hz

Wing Mode	Predominant Characteristic	Full Wing Fuel					
		Symmetric			Antisymmetric		
		F4H-1 Test	F-4E Test	F-4E Theory	F4H-1 Test	F-4E Test	F-4E Theory
1	1st Bending	8.05	8.3	8.4	10.5	10.0	10.4
2	2nd Bending	13.2	17.1	17.5	20.3	17.8	19.9
3	1st Torsion	25.6	29.8	29.9	28.2	30.0	30.5
4	3rd Bending	-	35.0	35.7	-	-	38.3

Table XI
Analytical F-4 Wing Vibration Frequencies
and Corresponding Generalized Masses

Mode No.	Symmetric or Antisymmetric	Natural Frequency (Hz)	Generalized Mass ($\frac{\text{Lb-Sec}^2}{\text{in}}$)
1	Symmetric	8.38	0.299
2		17.5	0.218
3		29.9	0.372
4		35.7	0.118
5		47.8	0.101
6		57.3	0.256
7		62.6	0.338
8		65.8	0.0888
9		79.6	0.186
10		94.0	0.168
11	Antisymmetric	10.4	0.218
12		19.9	0.319
13		30.5	0.202
14		38.3	0.134
15		48.7	0.110
16		57.8	0.282
17		64.1	0.343
18		66.0	0.0991
19		79.8	0.189
20		94.7	0.177

Table XII
Analytical F-4 Wing Vibration Modeshapes

1	2	3	4	5	6	7
-7.44700000-03	4.73000000-04	-1.83730000-02	1.70360000-02	4.85300000-03	-1.96560000-02	1.68950000-01
1.03800000-03	-2.49580000-02	1.82220000-02	4.59870000-02	-9.01580000-02	2.38363000-01	-6.14190000-02
1.38850000-02	-5.50600000-02	1.55140000-01	3.54650000-02	-1.50885000-01	-1.25050000-01	-1.74480000-01
4.21460000-02	-7.84800000-02	-2.31280000-01	1.16854000-01	1.91100000-02	-7.19900000-02	3.58846000-01
9.04760000-02	-1.47172000-01	3.37630000-02	8.55450000-02	-6.11310000-02	-1.44090000-02	-9.30620000-02
1.66753000-01	-2.48716000-01	7.09534000-01	-5.19000000-03	-1.40483000-01	-3.38722000-01	3.90279000-01
1.63392000-01	-1.74684000-01	-3.54801000-01	5.67440000-02	9.67960000-02	-1.76320000-01	-2.42964000-01
2.40476000-01	-2.08556000-01	5.05600000-02	-5.86680000-02	1.10184000-01	2.67400000-07	-1.54840000-01
3.29974000-01	-2.378500-0-01	7.59564000-01	-1.68228000-01	2.63964000-01	3.80674000-01	6.74222000-01
3.68190000-01	-4.28630000-02	-4.83C55000-01	-2.81769000-01	-1.37490000-01	-6.20320000-02	-1.97612000-01
4.19403000-01	-8.41070000-02	2.77100000-03	-2.80223000-01	7.10710000-02	2.85029000-01	8.03010000-02
5.1113520000-01	-3.68870000-02	7.32832000-01	-8.61330000-02	5.61752000-01	9.64119000-01	4.55722000-01
5.61000000-01	1.00000000-01	-4.73000000-01	-4.72000000-01	-2.93000000-01	9.60000000-01	1.25000000-01
6.46600000-01	2.60000000-01	1.20400000-01	-1.53200000-01	8.08000000-02	3.89400000-01	2.23400000-01
7.62753000-01	4.98844000-01	1.04451700-00	5.94657000-01	1.01054600-00	1.23757000-00	-9.05420000-02
8.11350000-01	6.43242000-01	-1.85816000-01	1.38200000-03	-3.72718000-01	-4.80876000-01	9.80120000-02
8.78820000-01	7.51614000-01	4.05733000-01	4.21124000-01	2.99699000-01	2.96343000-01	-9.91810000-02
9.66262000-01	9.17734000-01	1.00353400-00	9.19360000-01	1.01662600-00	1.10260400-00	-3.87656000-01
4.78209000-01	1.81570000-02	-4.26098000-01	-4.20674000-01	-1.58015000-01	1.18268000-01	-1.06710000-02
-1.20000000-02	1.10000000-02	8.00000000-03	-8.00000000-03	4.00000000-03	-6.00000000-03	-1.00000000-02
-1.50000000-02	1.30000000-02	6.00000000-03	-8.00000000-03	5.00000000-03	-6.00000000-03	-8.00000000-03
0.0	0.0	0.0	0.0	0.0	0.0	0.0
8	9	10	11	12	13	14
3.14300000-02	-4.86410000-02	-1.54889000-01	-5.62530000-02	6.56939000-02	-4.32800000-03	-1.18110000-02
-5.80235000-02	-5.73660000-02	-1.24192000-01	-4.63780000-02	2.43440000-02	4.20150000-02	7.53600000-03
2.10740000-01	-2.02495000-01	-6.29700000-02	-3.46300000-02	-4.39850000-02	1.32105000-01	-8.83000000-03
6.52280000-02	-2.87040000-02	4.80360000-02	-5.58500000-02	6.43200000-03	-1.28150000-01	1.29402000-01
3.42900000-03	-2.07600000-02	2.20970000-01	-8.97400000-03	-1.40198000-01	4.02770000-02	8.64190000-02
3.79800000-03	4.72120000-01	-1.14739000-01	6.80090000-02	-3.81622000-01	4.88875000-01	-7.76040000-02
-1.91600000-03	1.30040000-01	-2.11112000-01	2.76040000-02	-1.53908000-01	-2.61564000-01	1.41372000-01
-5.29920000-02	-1.58224000-01	-1.17320000-01	1.09592000-01	-2.84662000-01	-7.04400000-03	-2.50200000-02
-1.28522000-01	-5.24044000-01	-3.58200000-03	2.13884000-01	-4.44090000-01	4.69474000-01	-2.17824000-01
-1.42681000-01	-4.82563000-01	-2.77265000-01	2.07270000-01	-4.33400000-02	-4.28193000-01	-2.39677000-01
-7.27000000-02	-2.23132000-01	3.81000000-04	2.04868000-01	-2.08170000-01	-8.97030000-02	-2.71067000-01
1.59924000-01	-1.00759100-00	3.56208000-01	4.03000000-01	-2.38308000-01	4.74626000-01	-1.09794000-01
2.06000000-01	4.35000000-01	1.33000000-01	4.48000000-01	6.20000000-02	-4.52000000-01	-4.84000000-01
1.31400000-01	-2.70800000-01	2.98200000-01	5.57000000-01	1.55600000-01	5.18000000-02	-1.81200000-01
7.99618000-01	1.54952000-01	1.71350000-01	7.13301000-01	1.94536000-01	8.94900000-01	5.94304000-01
-3.59290000-01	-2.16456000-01	2.42010000-02	7.57610000-01	6.36746000-01	-9.15760000-02	-6.91360000-02
2.75435000-01	2.11188000-01	6.89460000-02	8.44820000-01	7.30752000-01	4.28933000-01	3.93358000-01
1.03240000-00	9.71515400-01	8.00680000-02	9.57906000-01	9.98408000-01	9.76714000-01	9.19376000-01
2.04769000-01	3.15556000-01	-1.40479000-01	3.53662000-01	-6.51750000-02	-4.18424000-01	-4.05270000-01
-1.00000000-02	2.00000000-02	1.99000000-02	0.0	0.0	0.0	0.0
-1.00000000-03	2.00000000-03	5.00000000-03	0.0	0.0	0.0	0.0
0.0	0.0	0.0	-1.00000000-03	0.0	0.0	-1.00000000-03
15	16	17	18	19	20	
2.52400000-02	-6.47520000-02	1.10169000-01	4.04061000-02	-4.23560000-02	-1.30094000-01	
-8.05110000-02	-2.63622000-01	1.44900000-02	-5.75010000-02	-4.92117000-02	-1.11122000-01	
-1.60194000-01	-1.03060000-01	-2.89395000-01	1.89301000-01	-2.30000000-01	-7.59700000-02	
4.45400000-03	-1.20278000-01	3.26678000-01	1.15876000-01	-4.51340000-02	-6.00400000-03	
-8.04020000-02	1.56400000-02	-6.84560000-02	-1.69200000-02	-2.43660000-02	2.43000000-01	
-1.36181000-01	-1.97142000-01	3.43059000-01	4.13990000-02	6.69942000-01	-1.40614000-01	
5.63680000-02	-1.37032000-01	-7.51616000-01	-3.58700000-02	1.39320000-01	-2.37964000-01	
1.12500000-01	3.71080000-02	-1.47046000-01	-8.07560000-02	-1.50290000-02	-2.35230000-02	
3.51400000-01	2.42136000-01	7.04700000-01	-1.17760000-02	-5.44513000-01	-1.31037000-01	
-1.34423000-01	-3.10920000-02	-6.58129000-01	1.20660000-01	4.96298000-01	-2.41941000-01	
1.20612000-01	2.52198000-01	5.36180000-02	8.42680000-02	-2.27164700-01	-1.20710000-02	
6.77176800-01	8.45553000-01	4.21083000-01	2.20509000-01	-1.04352700-01	2.36416000-01	
-2.48000000-01	8.30000000-02	6.30000000-02	2.17000000-01	4.10000000-01	1.65000000-01	
1.37800000-01	3.38800000-01	1.92400000-01	1.67600000-01	-2.87500000-01	2.15600000-01	
1.07628400-00	1.16849700-00	-1.40133000-01	8.14240000-01	1.16728000-01	1.42890000-01	
-4.06104000-01	-4.10264000-01	2.18216000-01	-3.65792000-01	-2.14184000-01	-2.22160000-02	
2.95520000-01	2.94311000-01	-1.82893000-01	7.19871000-01	2.07917000-01	7.66620000-02	
1.03419200-00	1.08862000-00	-7.16252000-01	1.04780200-00	-9.31930000-01	1.30100000-01	
-1.19792000-01	1.13439000-01	-8.54910000-02	7.13433000-01	3.79384000-01	-1.32006000-01	
0.0	0.0	0.0	0.0	0.0	0.0	
0.0	0.0	0.0	0.0	0.0	0.0	
0.0	0.0	-1.00000000-03	0.0	0.0	0.0	

Notes:

- Vertical Translations are Positive Up (Right Wing), Pitch Rotation is Positive Nose Up, and Roll Rotation is Positive Right Wing Tip Up.
- Values Shown for Vertical Translations of Points on the Wing Include Effects of Both Wing Elastic Deformations and Rigid Airplane Motions.
- The Columns Indicate Mode Number and the Rows Indicate Airplane Coordinate.
- See Table B-11 for the Natural Frequency and Generalized Mass of Each Mode.
- See Table B-IV for Row Identification.
- Exponential Notation is used, e.g., -7.4470-03 = -7.447 x 10⁻³.

Table XIII
Identification of Rows in
Modeshape Matrix (Table XII)

Row of Matrix	Airplane Coordinate
1	Vertical Translation of Center of Area 1
2	2
3	3
4	4
5	5
6	6
7	7
8	8
9	9
10	10
11	11
12	12
13	13
14	14
15	15
16	16
17	17
18	18
19	Vertical Translation of Flight Accelerometer
20	Rigid Airplane Vertical Translation
21	" " Pitch Rotation
22	" " Roll Rotation

rows of Table XII (i.e., the rows of the modeshape matrix) to airplane coordinates. The definition of the modeshapes at these coordinates (18 area centers and the flight accelerometer) was obtained by linear interpolation among the original 57 wing coordinates in the vibration solution, and the values shown were rounded to 3 significant figures in the response computations.

Structural damping coefficient (ζ_s) data, from Reference 23, are available for only the first two or three symmetric and antisymmetric wing vibration modes and are presented in Table XIV. Since the measured structural damping values increase with mode number through the third symmetric and second antisymmetric modes and since they cannot increase without limit, structural damping coefficients for the higher modes have been estimated as 0.1, which is approximately the largest value measured for the first three modes.

The total damping for an airplane in flight is due to both structural damping and aerodynamic damping. Aerodynamic damping coefficients (ζ_a) for the F-4 wing vibration modes used in this study were obtained from velocity versus damping flutter solutions, and values for the three dynamic pressures investigated herein are given in Table XIV. Also shown in Table XIV are the total modal damping ratios

$$\zeta = \frac{\zeta_s + \zeta_a}{\sqrt{2}}$$

Structural damping is larger than aerodynamic damping in all but the first one or two symmetric and antisymmetric modes. Response calculations were also made using the same value of ζ in all modes because there is considerable uncertainty in the damping values shown in Table XIV and there would be much more uncertainty in the preliminary design stage of a new airplane.

7.4 Flight Conditions

The response of the F-4 wing to buffeting pressures was predicted for the three flight conditions shown in Table XV. These flight conditions are ones for which measured acceleration power spectral density data were obtained at the flight accelerometer in the flight test program reported in Reference 2. For purposes of predicting the response, the first two flight conditions were considered to have the same Mach number (0.8) and angle of attack (10°). They are conditions of moderate buffet. The third is a condition of heavy buffet.

Table XIV
F-4 Wing Modal Damping Values

Mode No.	Frequency (Hz)		Structural Damping Coefficient, g_s (Full Wing Fuel) (1)	Aerodynamic Damping Coefficient, g_a			$\xi = \frac{g_s + g_a}{2}$		
	Measured (1)	Analytical		$q = 220$ psf	$q = 350$ psf	$q = 470$ psf	$q = 220$ psf	$q = 350$ psf	$q = 470$ psf
1	8.05	8.38	0.0172	0.194	0.251	0.306	0.106	0.134	0.162
2	19.2	17.5	0.04	0.063	0.081	0.097	0.052	0.061	0.069
3	25.6	29.9	0.084	0.031	0.040	0.047	0.058	0.062	0.066
4		35.7	0.1 (2)	0.052	0.065	0.075	0.076	0.083	0.088
5		47.8		0.041	0.051	0.058	0.071	0.076	0.079
6		57.3		0.023	0.027	0.031	0.062	0.064	0.066
7		62.6		0.034	0.044	0.049	0.067	0.072	0.075
8		65.8		0.015	0.019	0.020	0.058	0.060	0.060
9		79.6		0.023	0.029	0.033	0.062	0.065	0.067
10		94.0		0.060	0.074	0.085	0.080	0.087	0.093
11	10.5	10.4	0.030	0.154	0.206	0.236	0.092	0.118	0.133
12	20.2	19.9	0.108	0.049	0.062	0.070	0.079	0.085	0.089
13		30.5	0.1 (2)	0.036	0.045	0.051	0.068	0.073	0.076
14		38.3		0.051	0.063	0.071	0.076	0.082	0.086
15		48.7		0.046	0.056	0.065	0.073	0.078	0.083
16		57.8		0.023	0.028	0.037	0.062	0.064	0.069
17		64.1		0.036	0.045	0.050	0.068	0.073	0.075
18		66.0		0.010	0.012	0.013	0.055	0.056	0.057
19		79.8		0.020	0.024	0.028	0.060	0.062	0.064
20		94.7		0.053	0.066	0.076	0.077	0.083	0.088

(1) From Reference 23

(2) Estimated

7.5 Predicted Fluctuating Pressures

The procedures of Section 5.4 were used to predict the normalized power spectral density $\frac{G(f)}{\sigma^2}$ for each region and ΔC_{Prms} for each area. The boundaries of the leading edge, tip, and snag vortices were estimated based on Figures 62, 65, 70, and 74. The boundaries for flight conditions 1 and 2 are shown in Figure 157, and those for flight condition 3 are shown in Figure 158. The vortex types and corresponding values of k_o , n , and λ associated with each region are shown in Table XVI. The values of n and λ associated with a region are those evaluated at the center of the region since for the structural response computations the spectral shape of the fluctuating pressures is assumed constant for a region. The values of ΔC_{Prms} at the center of each area are listed in Table XVII. The values are the same for all three flight conditions. The mean aerodynamic chord of the F-4 wing is 192.5 inches. Hence, the streamwise and spanwise decay coefficients are

$$\alpha = \beta = \delta = \frac{48.125}{192.5} = 0.25 \text{ in}^{-1}$$

7.6 Results

7.6.1 Effect of Damping - The effect of the choice of damping ratio ζ on the response predictions is shown in Figure 159. All three curves are predictions of acceleration power spectral density at the flight accelerometer for flight condition 1. In each case, the damping ratio was the same for all 20 elastic wing modes. The values used were 0.02, 0.05, and 0.1. The curves are all higher than the corresponding measured data. Of the three curves shown, that for $\zeta = 0.05$ best matches the shape of the measured spectrum in that the ratios of peaks to adjacent valleys in the spectrums are similar. This is shown in Figure 161.

7.6.2 Variations in Measured Response Data - Measured acceleration power spectral density curves for the flight accelerometer at flight conditions 1 and 2 are shown in Figure 160. These flight conditions are essentially the same except they are at different altitudes and hence have different dynamic pressures. As discussed in Section 4.4.1, the overall rms level of the fluctuating pressures is generally assumed to be proportional to the freestream dynamic pressure, q . Other things being equal, the rms level of the response should also be proportional to q . One might thus expect the

Table XV
Flight Conditions for Which Responses of F-4 Wing
to Buffeting Pressures Were Predicted

Flight Condition	Aircraft Configuration	Mach No. M	Wing Angle of Attack (deg)	Altitude (ft)	Velocity (ft/sec)	Dynamic Pressure (psf)
1	1	0.82	9.5	25,000	830	350
2	1	0.79	10	35,000	770	220
3	1	0.92	10.5	25,500	930	470

Table XVI
Constants Defining Spectral Shapes

Flight Condition	Region	Vortex Type	k_0	η	λ
1 & 2	1	Leading Edge	2.9	1.4	1.1
	2	Snag	1.4	2.1	1.7
	3	Snag	1.4	2.6	1.9
3	1	Leading Edge	1.3	1.4	1.0 (1)
	2	Snag	0.8	2.1	1.6 (1)
	3	Snag	0.8	2.5	1.9

(1) Difference Between this Value of λ and the Corresponding Value for Flight Conditions 1 and 2 is due to Uncertainty in Graphical Interpolation from Figure 160.

Table XVII
 $\Delta C_{p_{rms}}$ at Centers of Areas for Flight Conditions 1, 2 and 3

<u>Area</u>	<u>$\Delta C_{p_{rms}}$</u>
1	0.052
2	0.056
3	0.060
4	0.056
5	0.069
6	0.081
7	0.060
8	0.079
9	0.098
10	0.062
11	0.086
12	0.11
13	0.064
14	0.093
15	0.12
16	0.066
17	0.098
18	0.13

two curves in Figure 160 to have the same shape, with the overall rms for flight condition 1 being higher than that for flight condition 2 by the ratio of the q's, i.e., by $350/220 = 1.6$. In fact, the curves are similar but not identical in shape, and they have the same overall rms level. While the reason for this is not clear, part of the difference between the actual and expected relationship between the two curves may be due to aero-elastic effects. Part may be due to the fact that the Mach number and angle of attack, while nominally 0.8 and 10° , respectively, for both q's are actually slightly different. Another possibility is that the rms fluctuating pressure coefficient is not independent of altitude.

7.6.3 Comparison of Predicted and Measured Response Data - Comparisons of predicted and measured acceleration response at the flight accelerometer for flight conditions 1, 2, and 3 are shown in Figures 161, 162, and 163, respectively. Predicted spectrums are shown for two different modal damping distributions. One distribution was obtained, as discussed previously, from the sum of the structural and aerodynamic damping in each mode and is tabulated in Table XIV. The other is a constant damping ratio of 0.05 used for all 20 modes. The value of 0.05 was chosen because it is in the range of values that have been found to be representative and the resulting ratios of peaks to adjacent valleys agree well with those for the measured data.

Two observations regarding the comparisons shown in Figures 161, 162, and 163 are (1) the shapes of the predicted response spectrums are in reasonable agreement with those of the measured response spectrums except over the middle frequency band while (2) the predicted responses are higher than the respective measured responses.

The differences between the predicted and measured spectral shapes in the 2 to 8, 8 to 12, 20 to 30, and 30 to 40 Hz frequency bands are now discussed in detail. In the 2 to 8 Hz band, the predicted spectrums decrease rapidly with decreasing frequency because no structural modes below 8.4 Hz were used in the response study. The measured spectrum for flight condition 2 also decreases rapidly with decreasing frequency below 8 Hz, but those for flight conditions 1 and 3 decrease slightly from 8 Hz and then remain essentially flat down to 2 Hz. Possible contributory causes of the latter behavior are the fuselage first torsion mode (which has significant wing and stabilator motion) at 6.3 Hz, rigid airplane short period and roll subsidence modes

between 0.3 and 0.8 Hz, low frequency bias in the data, and the smoothing effect of the 4 Hz bandwidth used in the spectral analysis.

In the 8 to 12 Hz band, the predicted spectrums, particularly those based on 0.05 damping ratio, have 2 peaks (due to symmetric and antisymmetric wing first bending modes) while the measured spectrums have only one. That only one peak exists in the measured spectrums can be explained by two facts. The first is that the 4 Hz analysis bandwidth used in computing the measured spectrums is considerably broader than the two predicted peaks. The second is that the total damping ratio in these two modes is considerably higher than the 0.05 value used in the constant damping ratio cases.

The measured spectrums contain a peak in the neighborhood of 24 to 26 Hz that is not contained in the predicted spectrums. It is not contained in the predicted spectrums because none of the analytical elastic wing modes used in the response calculations has a corresponding frequency between 20 and 29 Hz. However, ground vibration test data show that the fuselage second vertical bending mode has a frequency of 22 Hz and that it contains large stabilator motion and some motion at the wing location where the measured data shown here were obtained. Fluctuating pressures in the wing wake impinging on the stabilator could excite this mode. Allowing for some shift in frequency, this could cause the peaks at 24 to 26 Hz in the measured response spectrums. Ground vibration test data also show that the fuselage second torsion mode has a frequency of 26 Hz. This is closer to the peaks in the measured response spectrums; but, although this mode contains large stabilator motion, it has only negligible wing motion at the flight accelerometer wing location, where the measured data shown here were obtained.

The predicted acceleration response spectrums contain a broad hump composed of two peaks between 30 and 40 Hz. The symmetric and antisymmetric wing first torsion and wing third bending frequencies are in this band. The measured response spectrums shown here have only a valley between 30 and 40 Hz. However, environmental vibration data from another flight test (Reference 24) show that, during wind-up turns at about 5000 feet and about 23,000 feet and subsonic and transonic Mach numbers, there are strong peaks in the range of 30 to 40 Hz at about mid-chord by the wing fold and at the tip close to the leading edge. This indicates vibration modes in this frequency range have strong responses which would also be measured at the

wing flight accelerometer unless this location is close to node lines for these modes. If this location were close to these node lines on the airplane, then the accelerometer would measure little or no response in this frequency range and there would be a valley in the spectrums. However, ground vibration test data indicate this location is not on node lines for these modes in still air. It is possible these mode shapes change at air-speed; but at these relatively low dynamic pressures, it is doubtful that they change enough that the node lines all cross the measurement location. In short, the measured flight data of Reference 24 indicate strong wing response between 30 and 40 Hz, but no completely satisfactory explanation has yet been found for the absence of such response in the data from the Reference 2 flight test program presented here.

The predicted rms responses based on structural and aerodynamic damping are 4.6, 3.1, and 1.9 times the measured responses for flight conditions 1, 2, and 3, respectively. The predicted rms responses based on $\zeta = 0.05$ for all modes are roughly 20 percent higher than the corresponding rms responses based on structural and aerodynamic damping. Part of the reason that the predicted responses are higher than the measured responses is that the model for rms pressure coefficient shown in Figure 147 was deliberately selected to be somewhat conservative in that it is more representative of the high fluctuating pressure coefficient conditions. Another part of the reason may be that $\Delta C_{p_{rms}}$ in the tunnel, on which the model in Figure 147 is based, is higher than in flight. As shown in Figures 133 through 140, this is true at some flight conditions and some points on the wing. It was indicated in Section 4.4.1 that this may be due only to slight differences in the location of the stagnation vortex. There are insufficient flight data to be certain. If, however, $\Delta C_{p_{rms}}$ over the entire wing is higher in the tunnel than in flight, this would help explain the high predicted responses.

7.6.4 Summary of Comparison with Measured Response Data - In summary, the predicted response of the F-4 airplane in moderate and heavy buffet has been compared to measured data. There is reasonable agreement between the predicted and measured spectral shapes except for three or four frequency bands. Differences over these frequency bands are thought to be possibly due to data reduction and to differences between the aircraft in flight and its structural representation in this study. Although the predicted overall rms

level is higher than that measured, it is in quite reasonable agreement for the more severe buffet conditions. Some questions remain regarding the effects of altitude on the rms response and the effects of scaling from tunnel to flight on the rms pressure.

SECTION 8

CONCLUDING REMARKS

First generation methods for predicting buffeting dynamic pressures and the resulting structural dynamic response have been developed that are simple and usable. The fluctuating pressure prediction method provides a mathematical model for the overall rms levels and spectral shapes of the buffeting pressures. It is assumed that the entire upper wing surface is affected by fluctuating pressures, and curves are given relating the mathematical model parameters to flight conditions. The response computation technique was made appropriate to the uncertainties in the descriptions of the structure and the buffeting pressures. The assumptions reduce the amount of input data and computational time.

Validation of wind tunnel pressure measurements made on the model was accomplished by comparison with flight data. Although limited by the small number of flight transducers, these comparisons showed good agreement in the spectral shapes. In general, the model rms levels were somewhat higher. Aircraft response predictions are therefore expected to be somewhat conservative.

Comparison of predicted and measured dynamic response of the F-4 airplane in moderate and heavy buffet showed reasonable agreement in the spectral shapes and, for the more severe buffet condition, in the overall rms level. For the cases of moderate buffet, the predicted rms level was higher than that measured.

Several pertinent conclusions drawn from the test data include the following:

- o At high angles of attack the flow pattern over a highly swept wing with a leading edge snag is quite complex. The flow close to the upper surface is strongly affected by a vortex system consisting of leading edge, tip, and snag vortices causing abrupt changes in flow direction over the surface. The regions of high fluctuating pressures seem to be associated with these vortices, particularly the snag and tip vortices.
- o No discernible single "convection" mechanism for the transport of the fluctuating pressures was evident such as the downstream convection reported in studies of slender spacecraft launch vehicles. Disturbances seemed to emanate from multiple sources simultaneously and propagate in a complex manner.

- o The fluctuating pressure spectrums frequently exhibited peaks at frequencies believed to be associated with vortices. The frequency associated with the snag vortex was generally about half that of the leading edge and tip vortices. These frequencies, scaled to the flight vehicle, were at the higher end of the vehicle's primary structural resonances.
- o Maximum buffet intensities occurred at the high subsonic Mach numbers diminishing abruptly to small values at sonic and supersonic speeds.
- o Maximum rms wing root bending moments due to buffet were of the order of 7% of the corresponding steady bending moments.
- o Maximum fluctuating pressure coefficients were generally of the order of $\Delta C_{p_{rms}} = 0.2$.

The response prediction method presented in this report is based on techniques of observation, measurement, and analysis that are considered to provide a firm basis for development effort. It therefore provides a rational usable approach to the problem of assessing the nature of the fluctuating pressure distribution and the structural dynamic response of a highly swept fighter wing.

SECTION 9

RECOMMENDATIONS

This report presents a first generation method for predicting the dynamic response of an airplane wing to input buffet pressures. Simplifying assumptions have been made in regard to flow characteristics, mathematical modeling, and computational procedures. The simplifications employed were based upon existing technology, experience gained from earlier buffet research, and the realization that high levels of sophistication may not materially improve the predictions. The method developed here was used to predict the response of an F-4 wing to buffeting pressures, and Section 7 presents the results in comparison with flight data.

Additional refinement to the method should be based upon carefully conducted evaluation studies of the possible areas of refinement. Thorough study will help to insure that modifications do provide improvement and definite advantage over the existing method. Two possible levels of refinement to the prediction method presented herein are immediately available. The first consists of refining the existing mathematical model so that it can be readily extended to other aircraft. The second involves an increase in the complexity of the mathematical model based on a better understanding of the flow phenomena. These two levels of refinement are discussed below:

- (1) Extension to other aircraft of the present buffet loads prediction method could be enhanced by further wind tunnel tests to determine the effect of variations in wing geometry on such mathematical parameters as:
 - o Reduced frequency, k_0 , characteristic of the planform vortices
 - o Spectral amplification factor, n , corresponding to the characteristic reduced frequency
 - o Reduced spatial decay parameter, δ_cThe variations in wing geometry might include:
 - o Taper
 - o Sweep
 - o Camber
 - o Airfoil shape
- (2) If a comparison of measured data with results of the application of the prediction method as described in Item (1) indicate that more precise predictions are needed, then further research might

be pursued as follows:

- a. Define a systematic analytical/experimental attack on the problem, building successively on bases established in progressing from the simpler to the more complex problem parameters. It is suggested that an initial base of understanding might be developed for subsonic buffet prior to progressing to transonic buffet along with a progression from simple unswept planforms (without leading edge vortices) leading to the highly swept and delta planforms. Snag and other planform anomalies should be deferred to the later steps in the development to avoid obscuring basic geometry effects.
- b. Analytical sophistication should be the minimal necessary for adequate representation at each stage and increased only sufficiently to account for the next level of development.
- c. The experimental program should parallel the analytic development for logical evolution of the mathematical model.

Several specific topics discussed in this report might be included in the investigation described in (2) above or might merit further examination independent of the prediction method. They are:

- o Identification of suitable tunnels with low turbulence background
- o Steady state flow conditions over the wing (e.g., locations and sizes of vortices, separation bubbles, local convection directions, regions, separated flows) defined as functions of flow condition (free-stream flow condition and model orientation) either from analysis or experiment. Oil flow and tuft techniques need to be supplemented with additional investigations, such as:
 - * Survey of pitot-static profiles with height above the wing surface at a number of planform locations
 - * Survey of flow direction profiles with probe mounted tufts on and above the surface at the same planform locations used in the pitot-static surveys. Note whether tuft is stony or buffering.
- o Effect of local flow conditions (e.g., vortices) on spectral characteristics (i.e., predominant frequencies and overall levels) of fluctuating pressure. Insight might be gained by surveying steady and fluctuating pressures at the same flow conditions and planform locations used for the pitot-static and tuft surveys.

- Further examination of buffet characteristics between $M = 0.9$ and $M = 1.0$ where there is a sharp reduction in intensity.
- Scaling of rms pressure coefficient from model to full scale.
- Effect of altitude on structural dynamic response.
- Additional development of mathematical model for low frequency slope in pressure power spectral densities..
- Convection patterns on three-dimensional wings.
- Effect of using average mode approach in development of generalized forces.
- Effect on response prediction of neglecting correlation between areas.
- Effect of neglecting normal coordinate cross power spectral densities on response prediction.
- Provision for greater flexibility in the definition of regions.
- Optimization of the sizing of regions and basic areas.

The severity of the buffet dynamic loads problem should be evaluated on a broader basis than was possible with the existing data. The limited existing data from this and other recent programs suggest that rms wing root bending moments due to buffet are a small fraction of the static bending moment, i.e., 5-10% more or less. Similar data becoming available after this program should be collected and evaluated for a broader assessment of the problem severity. Toward this end, future flight and wind tunnel buffet programs should provide tape records of the bending moments for subsequent processing to separate the fluctuating bending moments from the static bending moments. Several different spanwise locations should be included to help identify the more critical areas. Collection of these data might also lead to a more direct technique for preliminary design prediction of buffet loads.

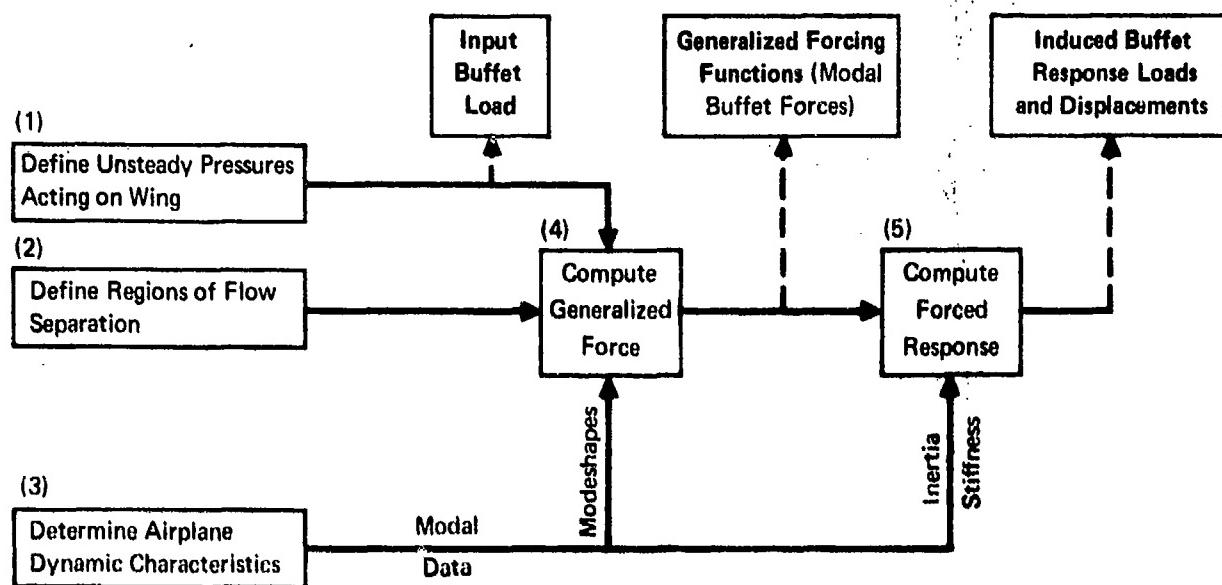


Figure 1 Buffet Loads Prediction Method

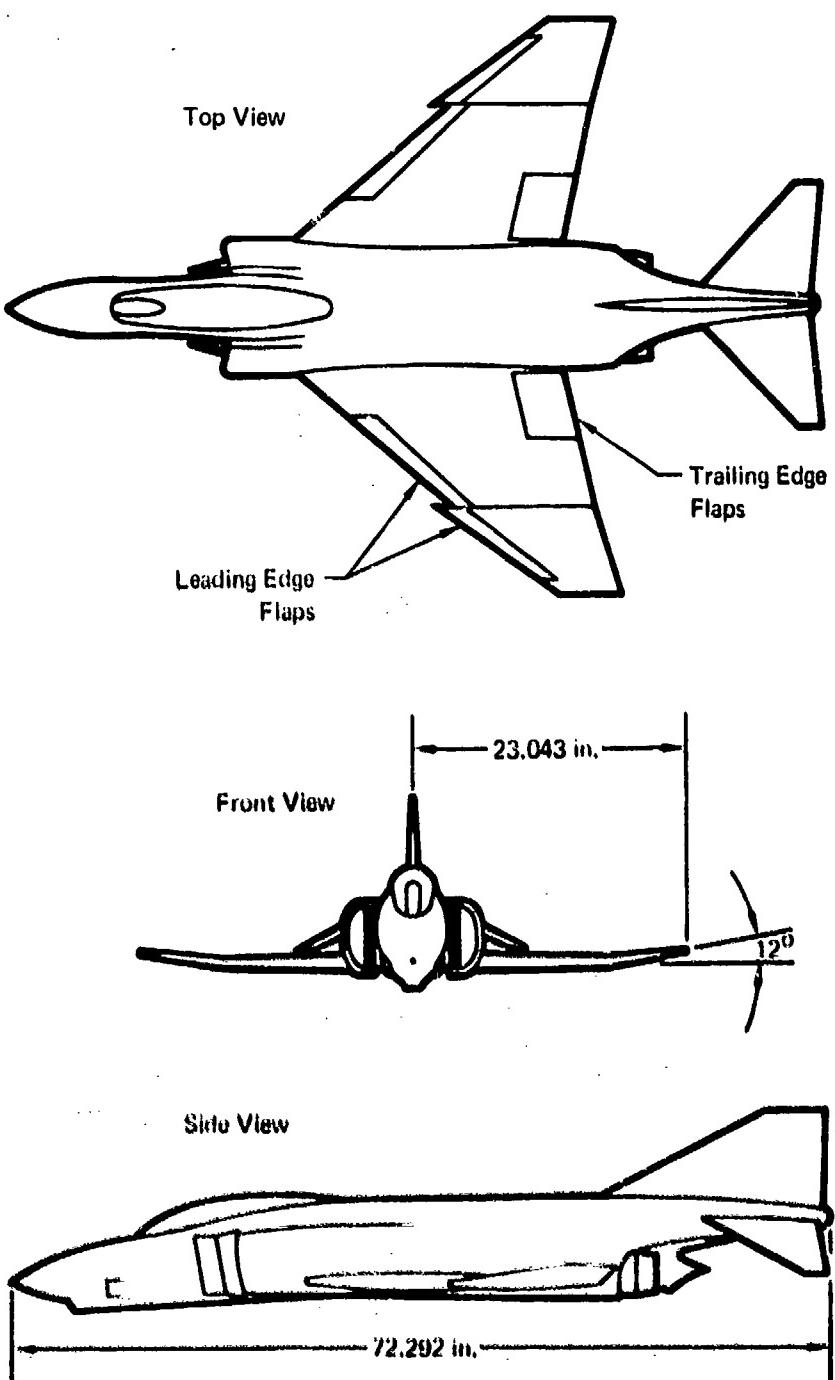


Figure 2 General Arrangement of F-4E 10% Model

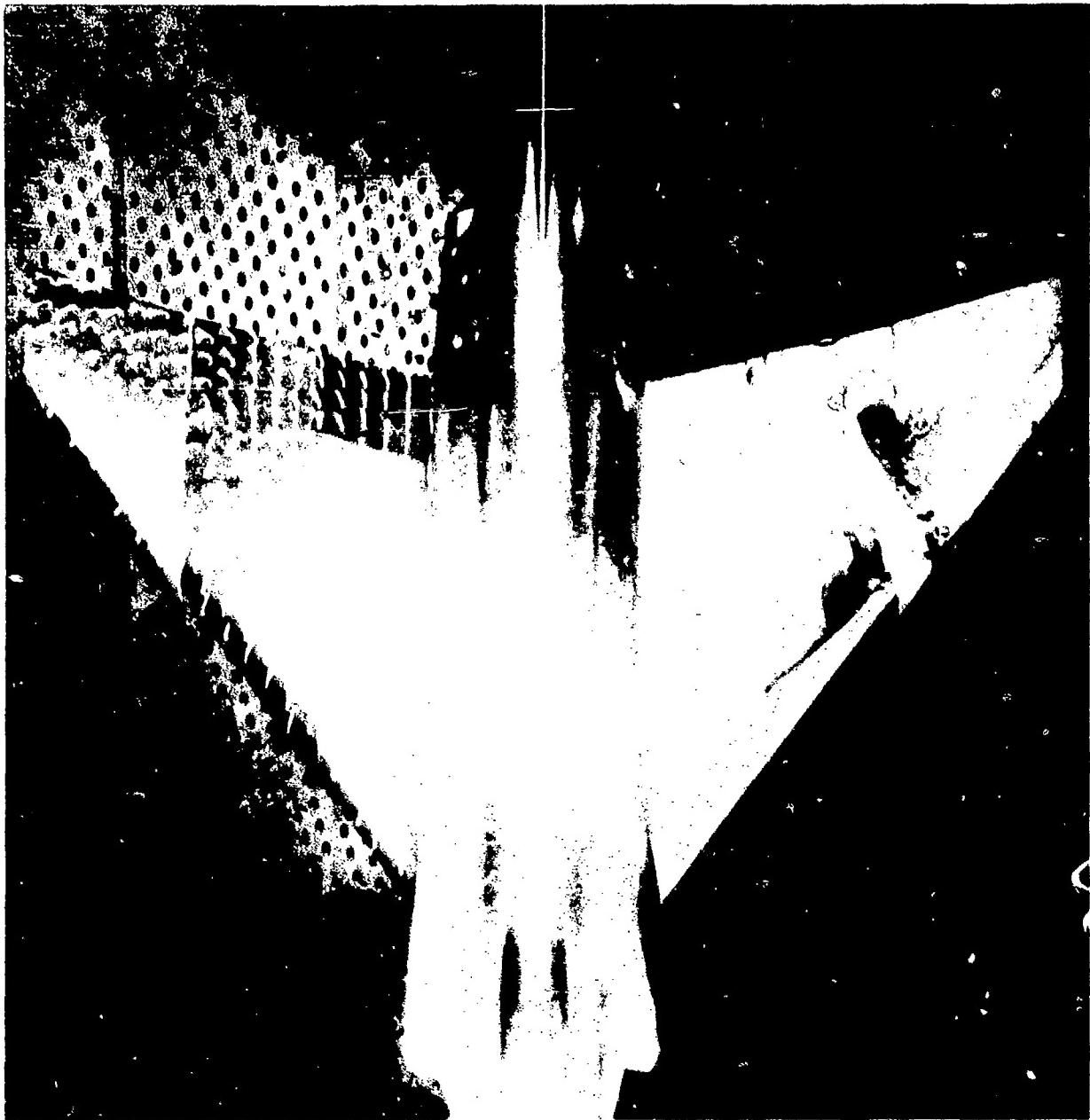


Figure 3 Tufts and Oil Flow on 10% F-4 Model

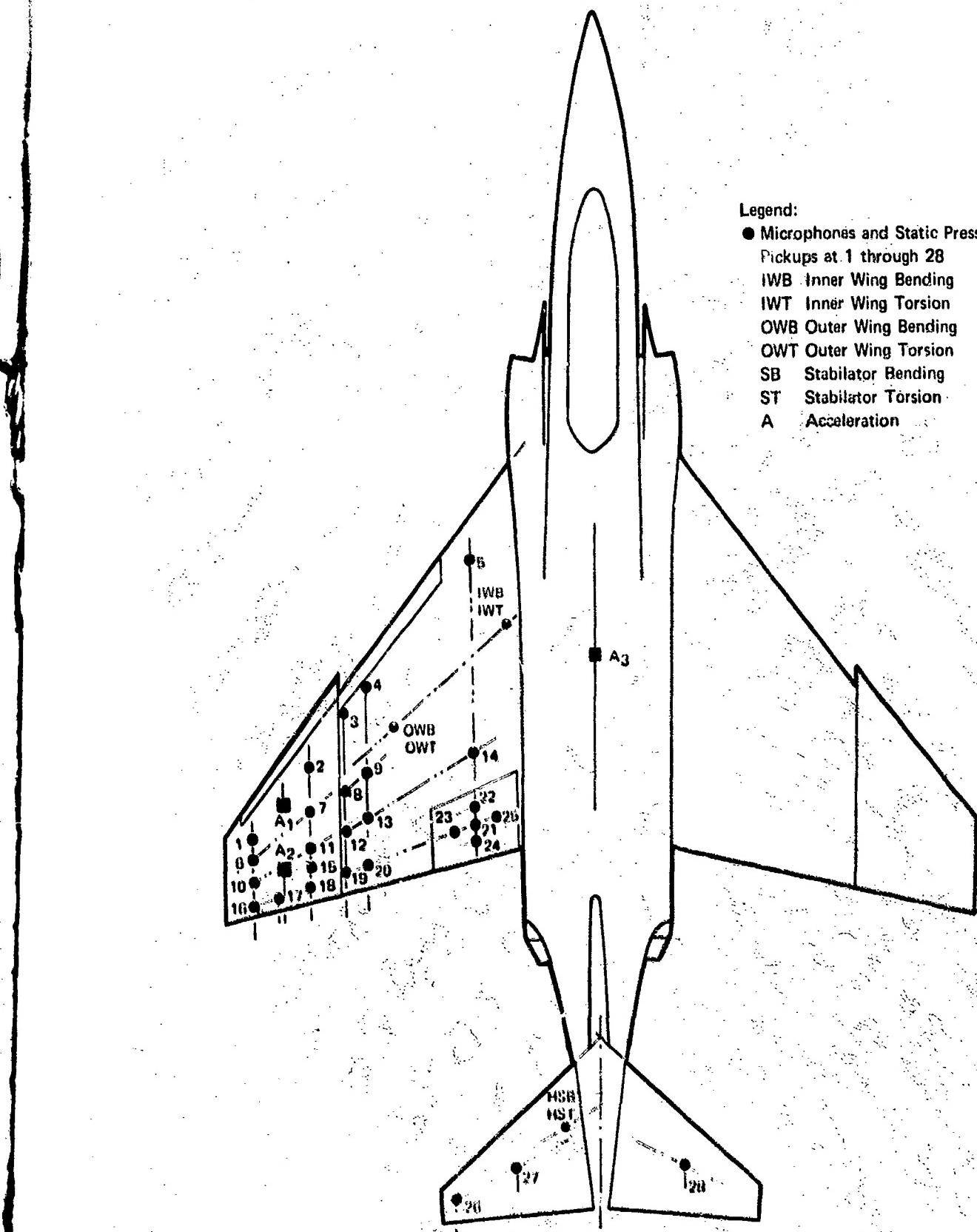


Figure 4 Model Instrumentation

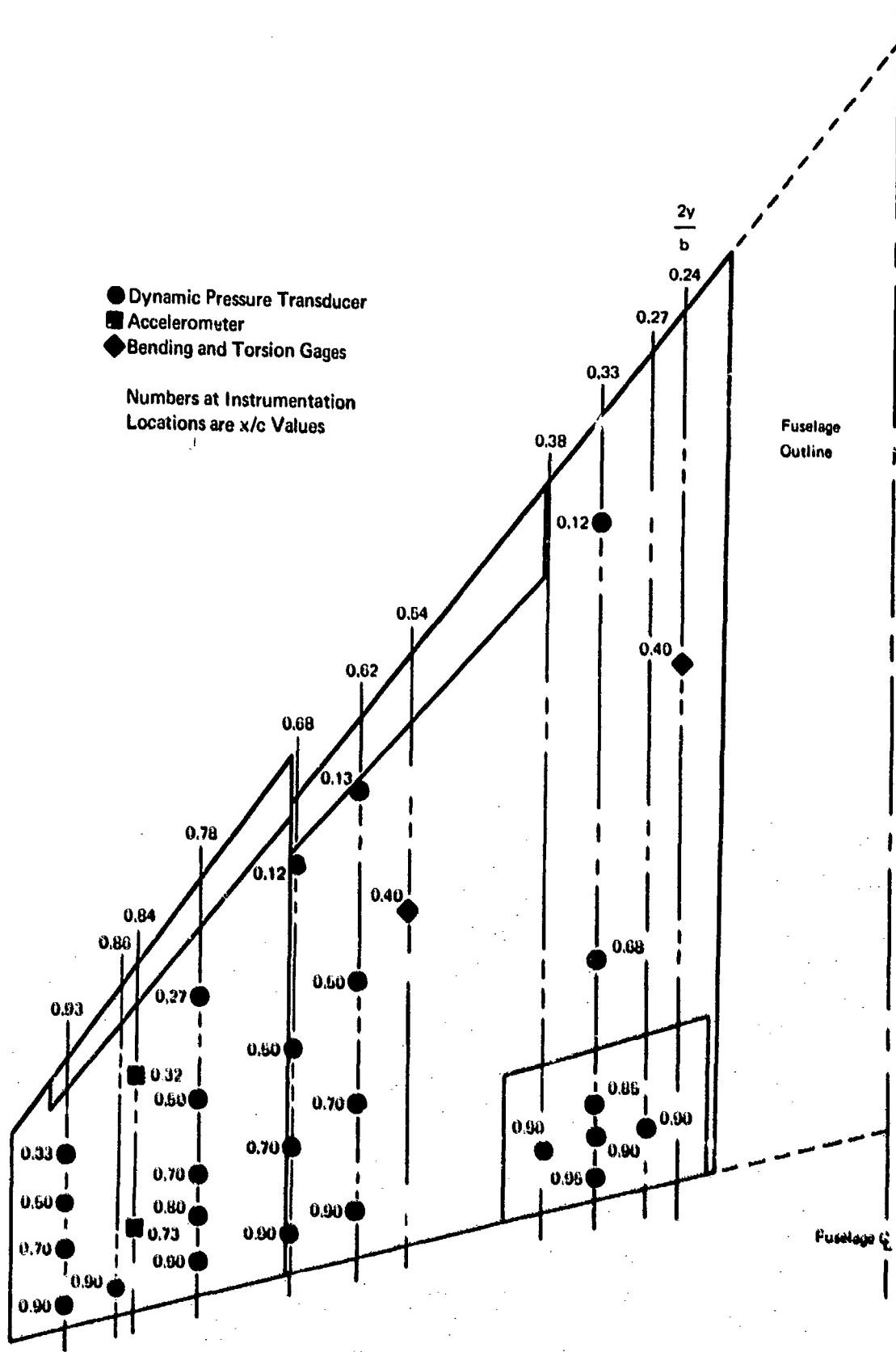


Figure 5 Wing Instrumentation Locations

Figure 6 Vibration Test Setup at MCAIR



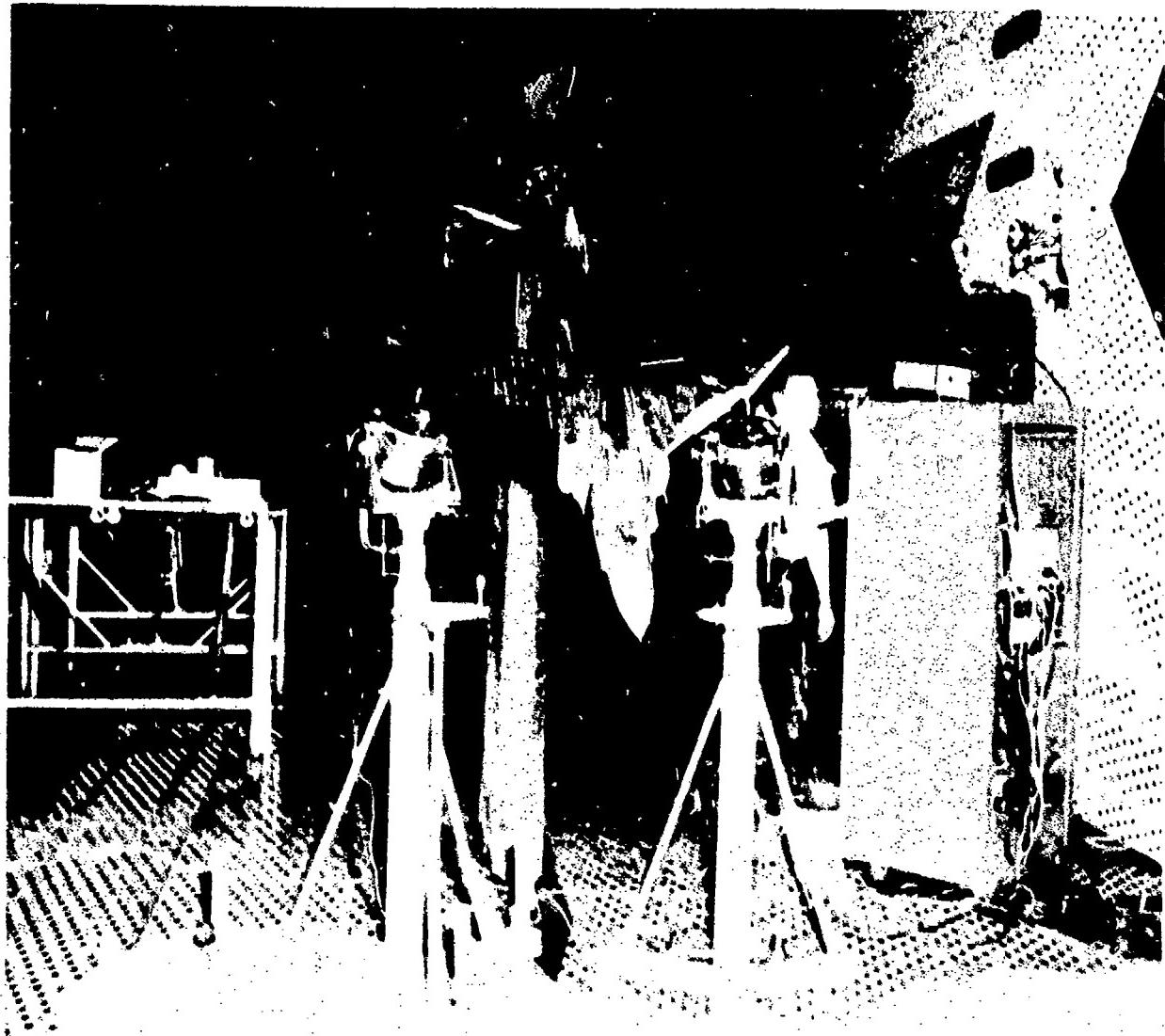


Figure 7 Vibration Test Setup at Wind Tunnel

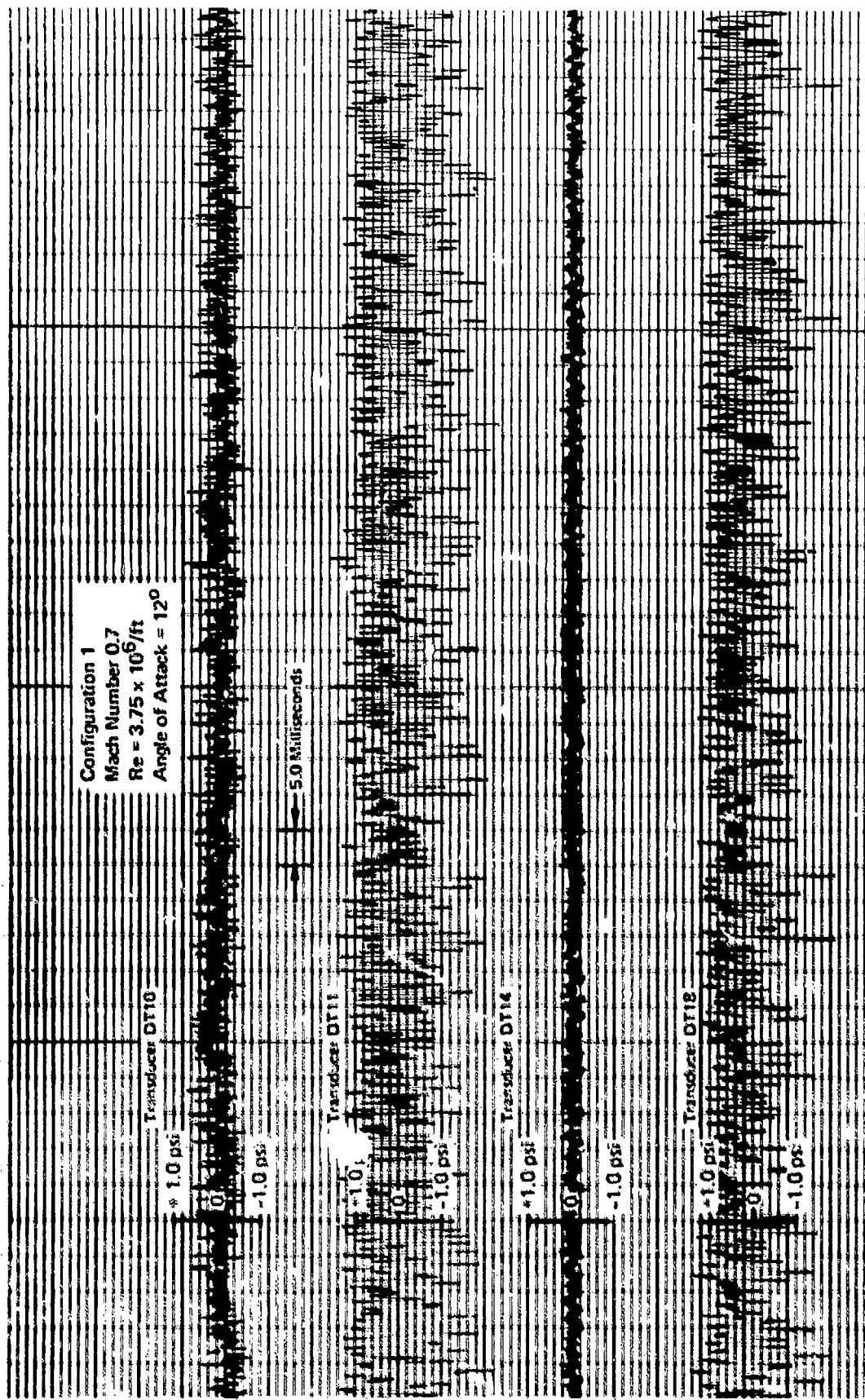


Figure 8 Fluctuating Pressure Oscilloscope Traces for Configuration 1, Mach 0.7, Wing Angle of Attack 12°

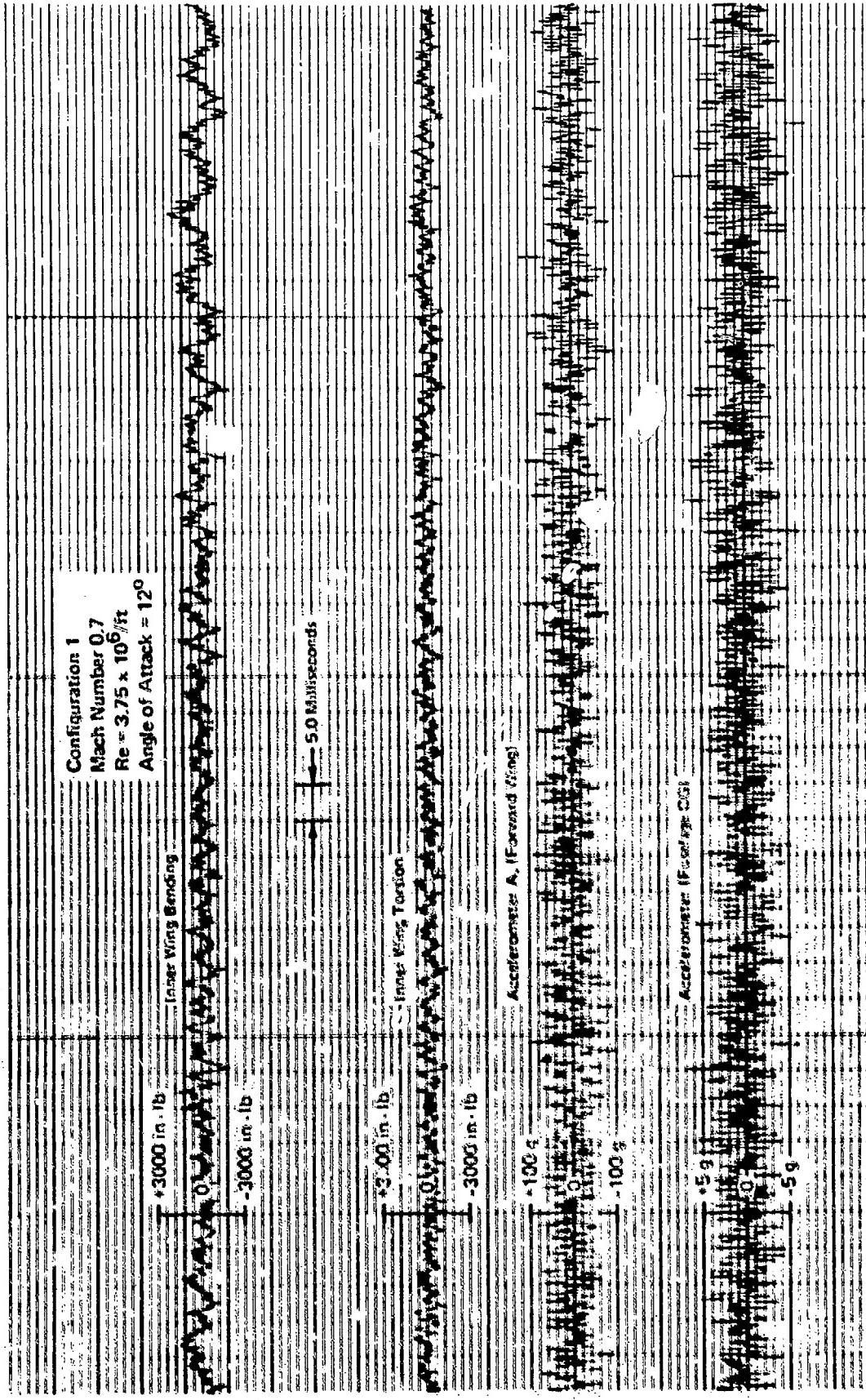


Figure 9 Bending, Torsion, and Acceleration Oscillograph Traces for Configuration 1, Mach 0.7, Wing Angle of Attack 12°

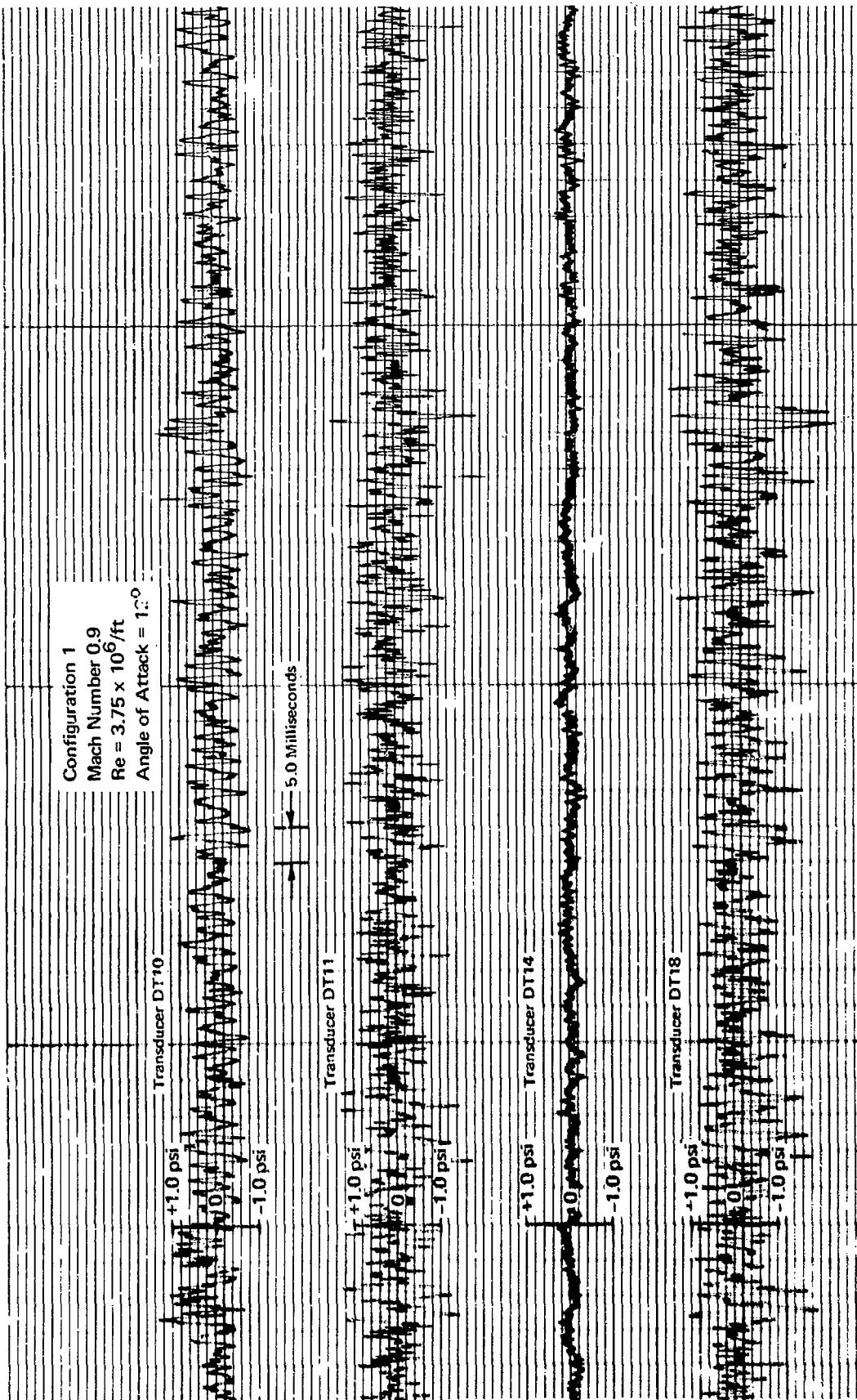


Figure 10 Fluctuating Pressure Oscillograph Traces for Configuration 1, Mach 0.9, Wing Angle of Attack 12°

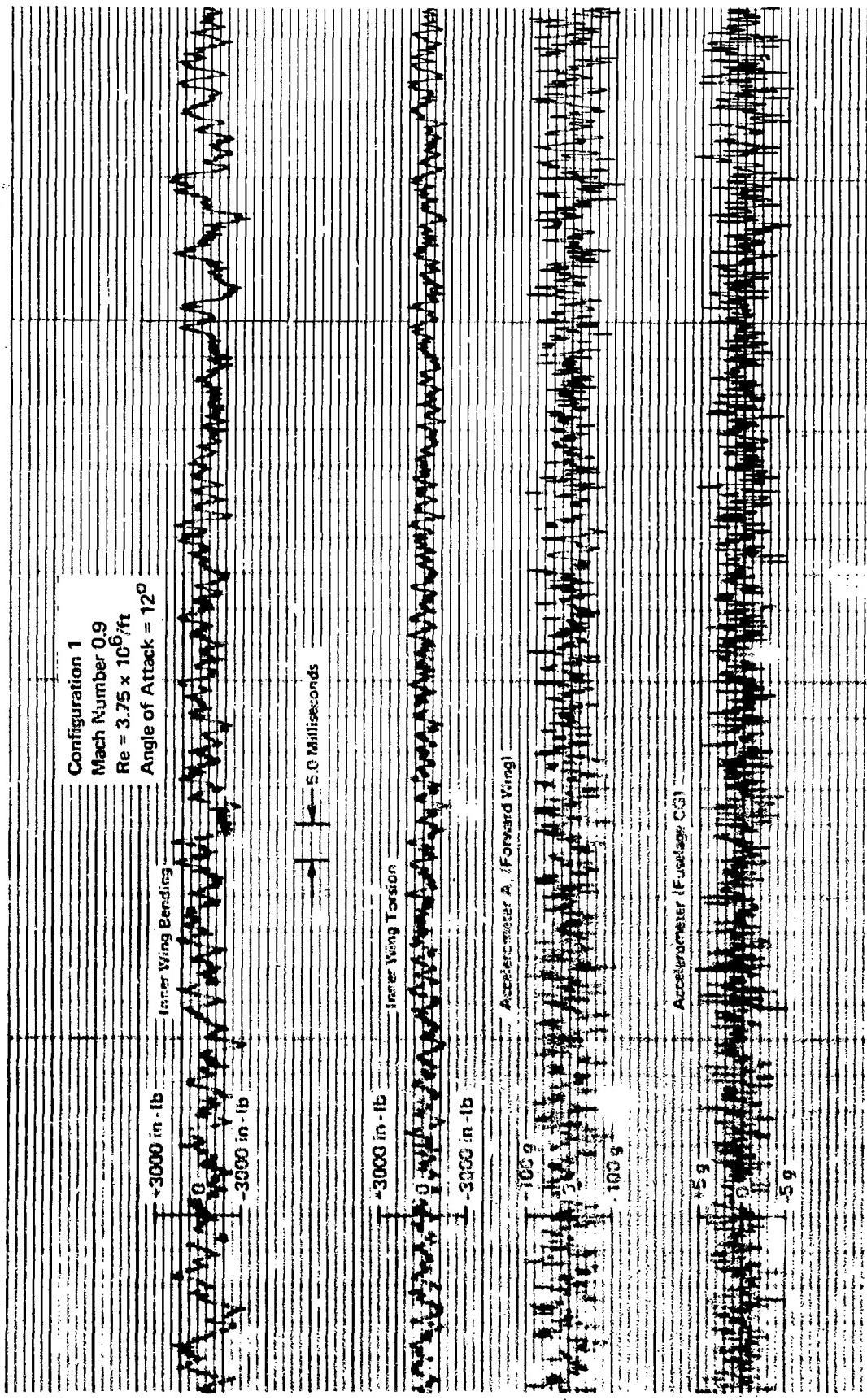


Figure 11 Bending, Tension, and Acceleration Oscillograph Traces for Configuration 1, Mach 0.9, Wing Angle of Attack 12°

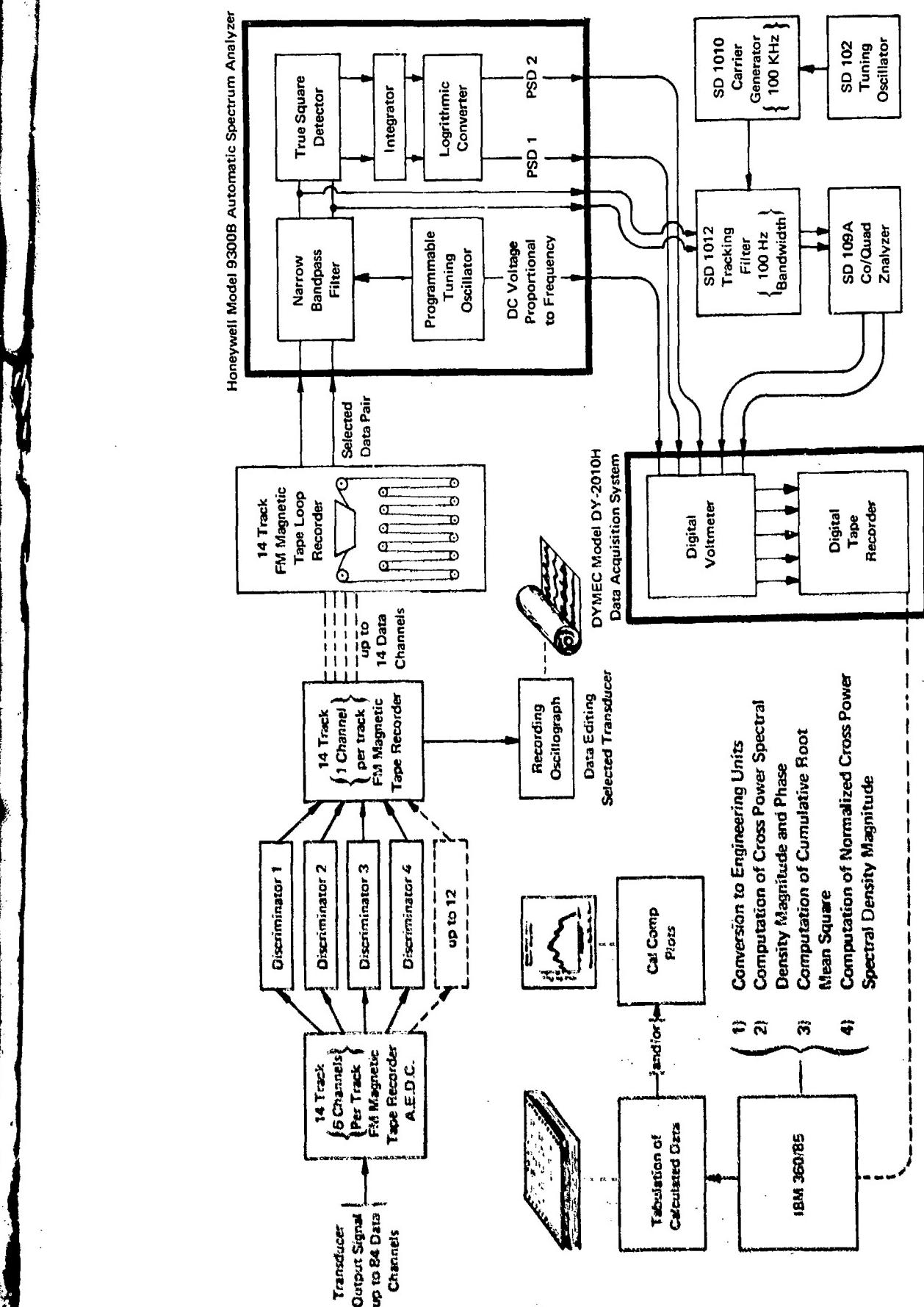


Figure 12 Flow Diagram of Spectral Data Reduction at MCAIR

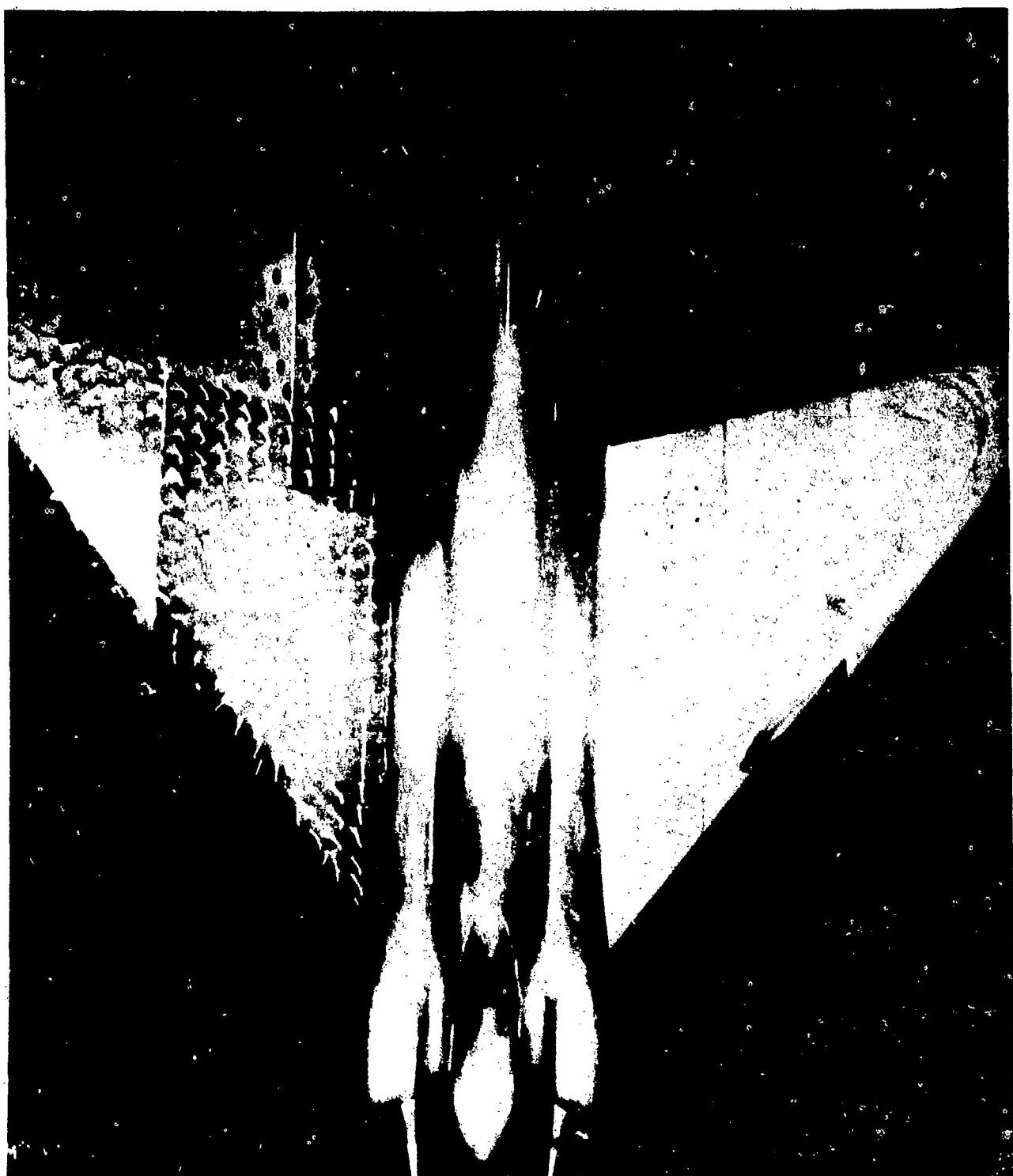


Figure 13 Tufts and Oil Flow (Photograph)

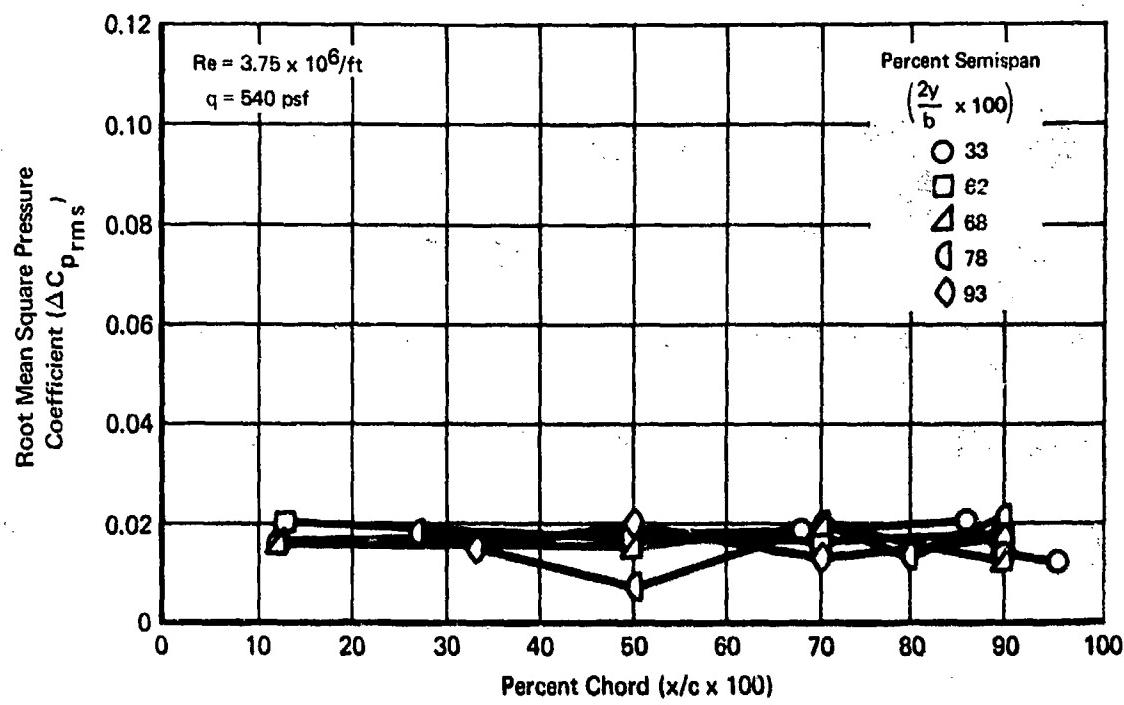


Figure 14 Root Mean Square Pressure Coefficient vs Percent Chord (Configuration 1,
Mach 0.7, Wing Angle of Attack -0.8°)

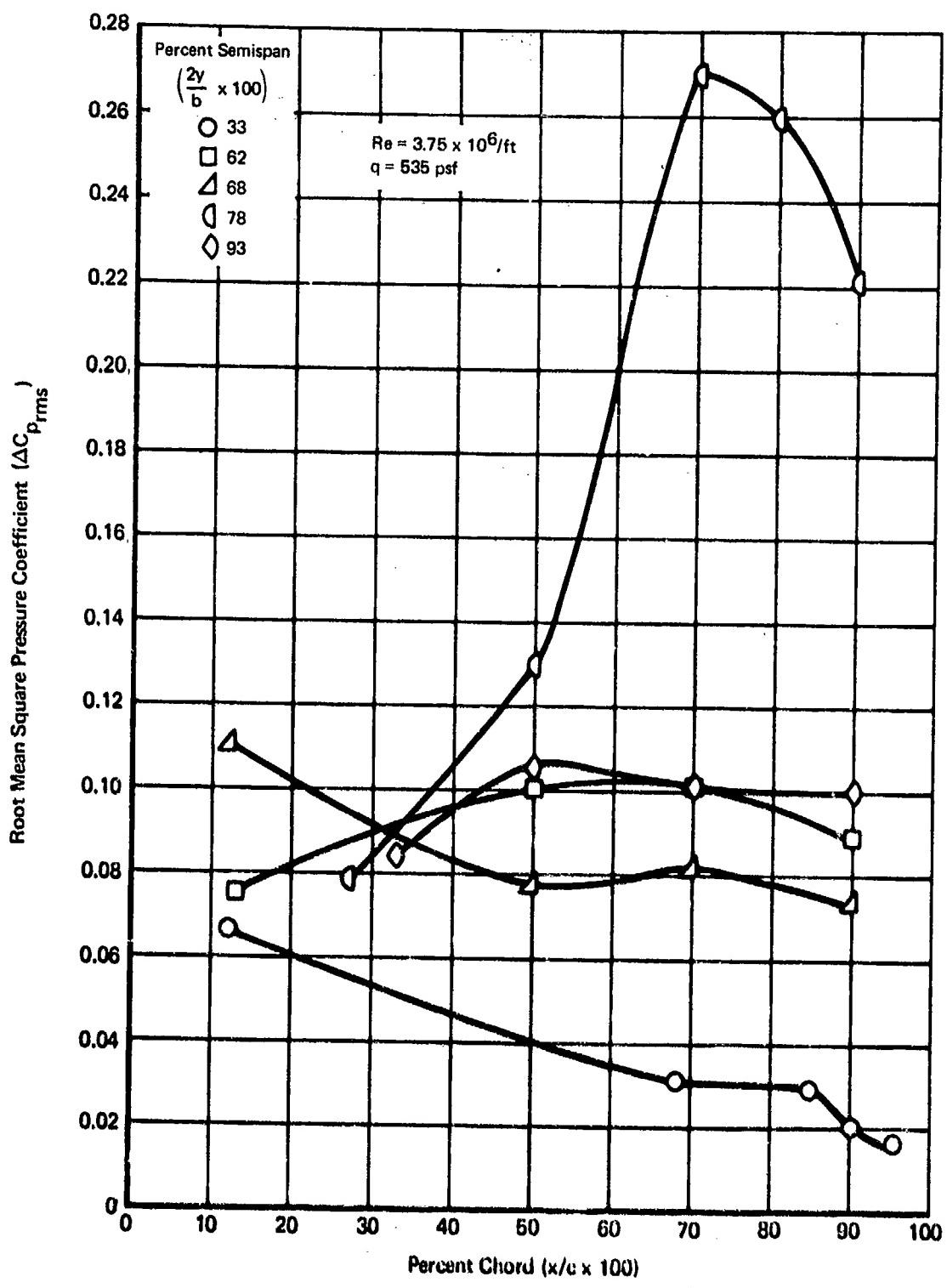


Figure 15 Root Mean Square Pressure Coefficient vs Percent Chord (Configuration 1,
Mach 0.7, Wing Angle of Attack 12°)

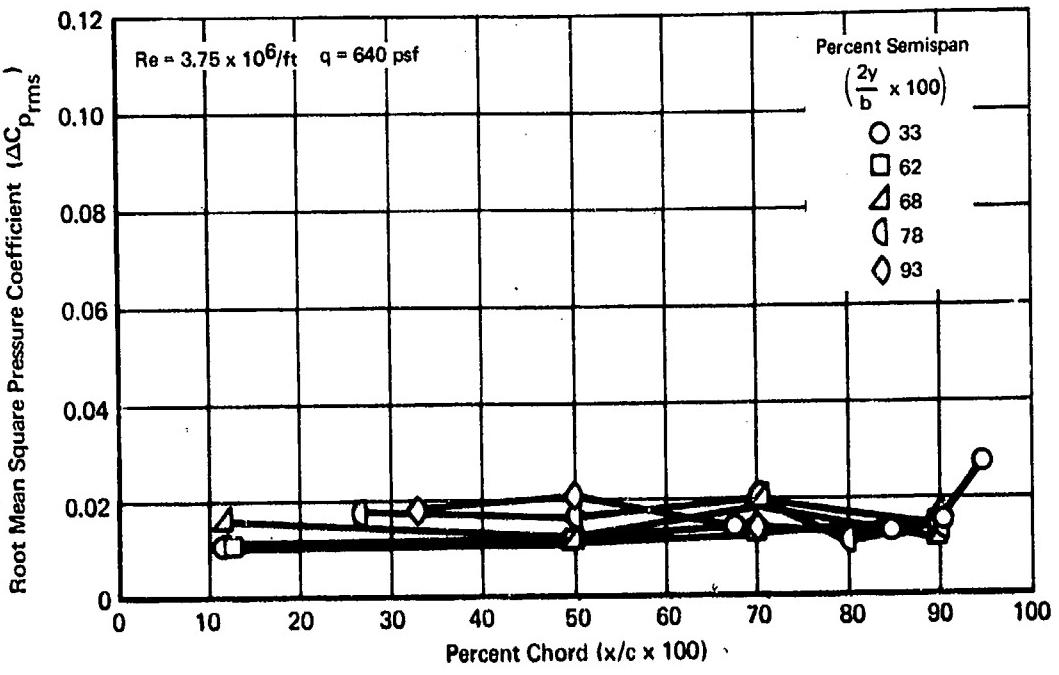


Figure 16 Root Mean Square Pressure Coefficient vs Percent Chord
(Configuration 1, Mach 0.9, Wing Angle of Attack -0.8°)

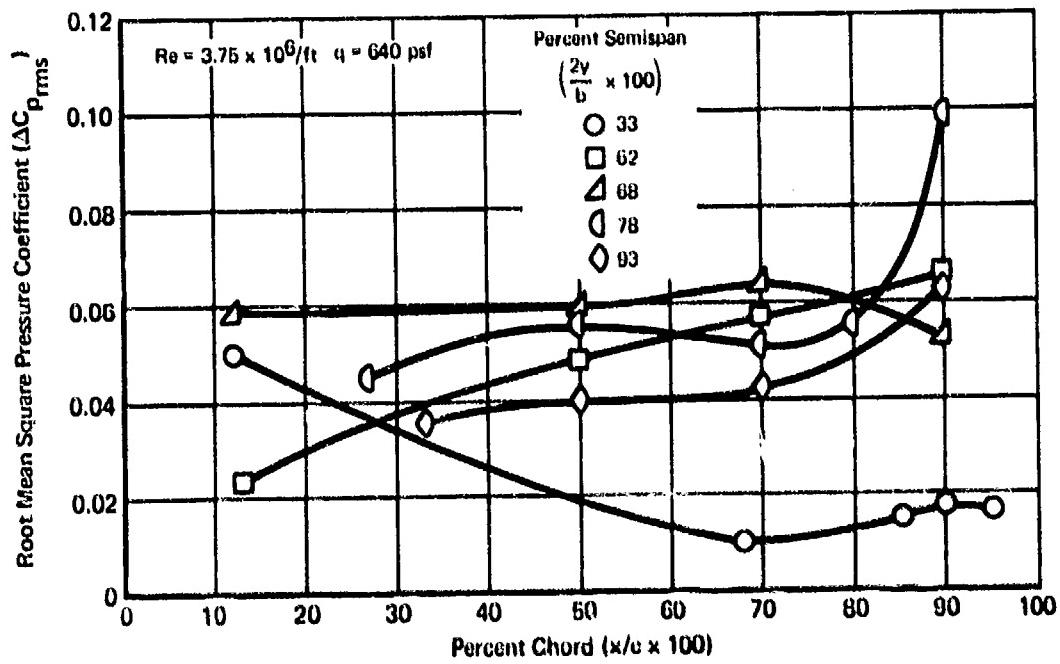


Figure 17 Root Mean Square Pressure Coefficient vs Percent Chord
(Configuration 1, Mach 0.9, Wing Angle of Attack 8°)

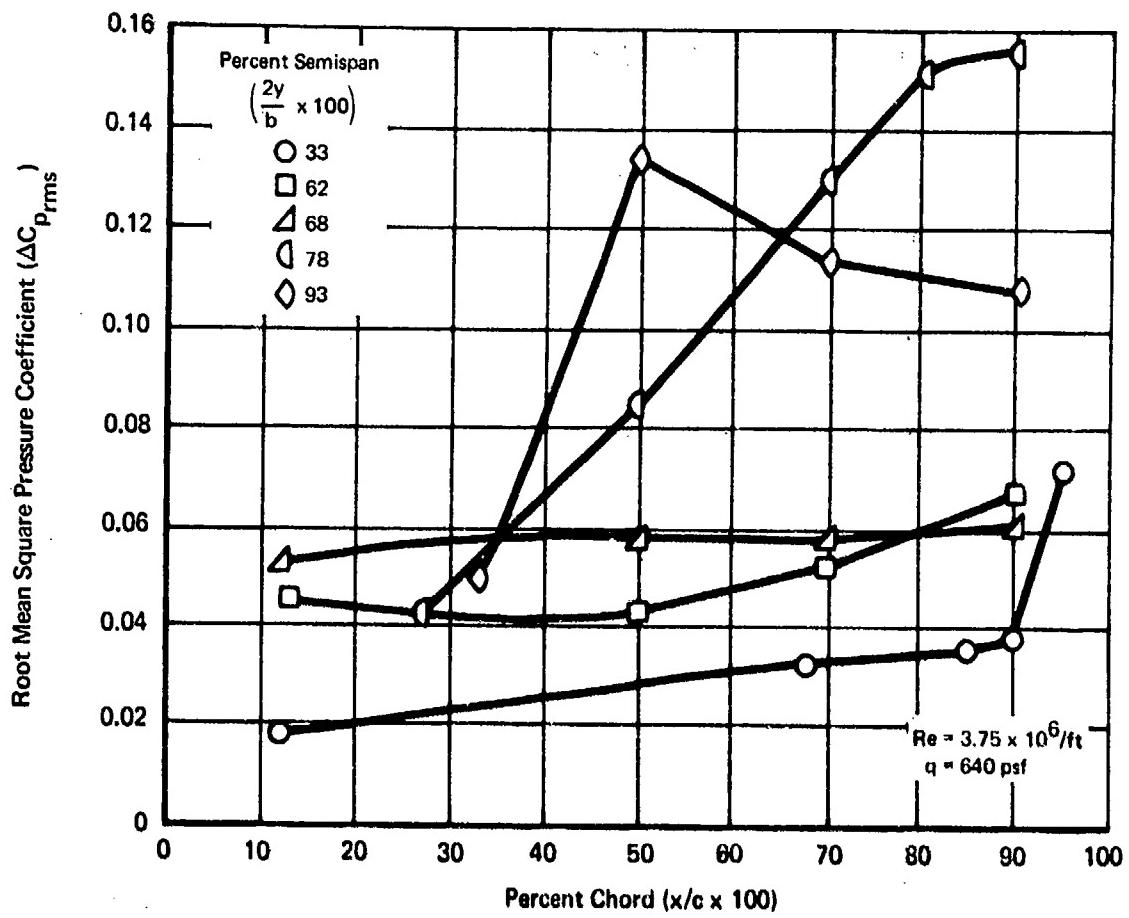


Figure 18 Root Mean Square Pressure Coefficient vs Percent Chord
 (Configuration 1, Mach 0.9, Wing Angle of Attack 12°)

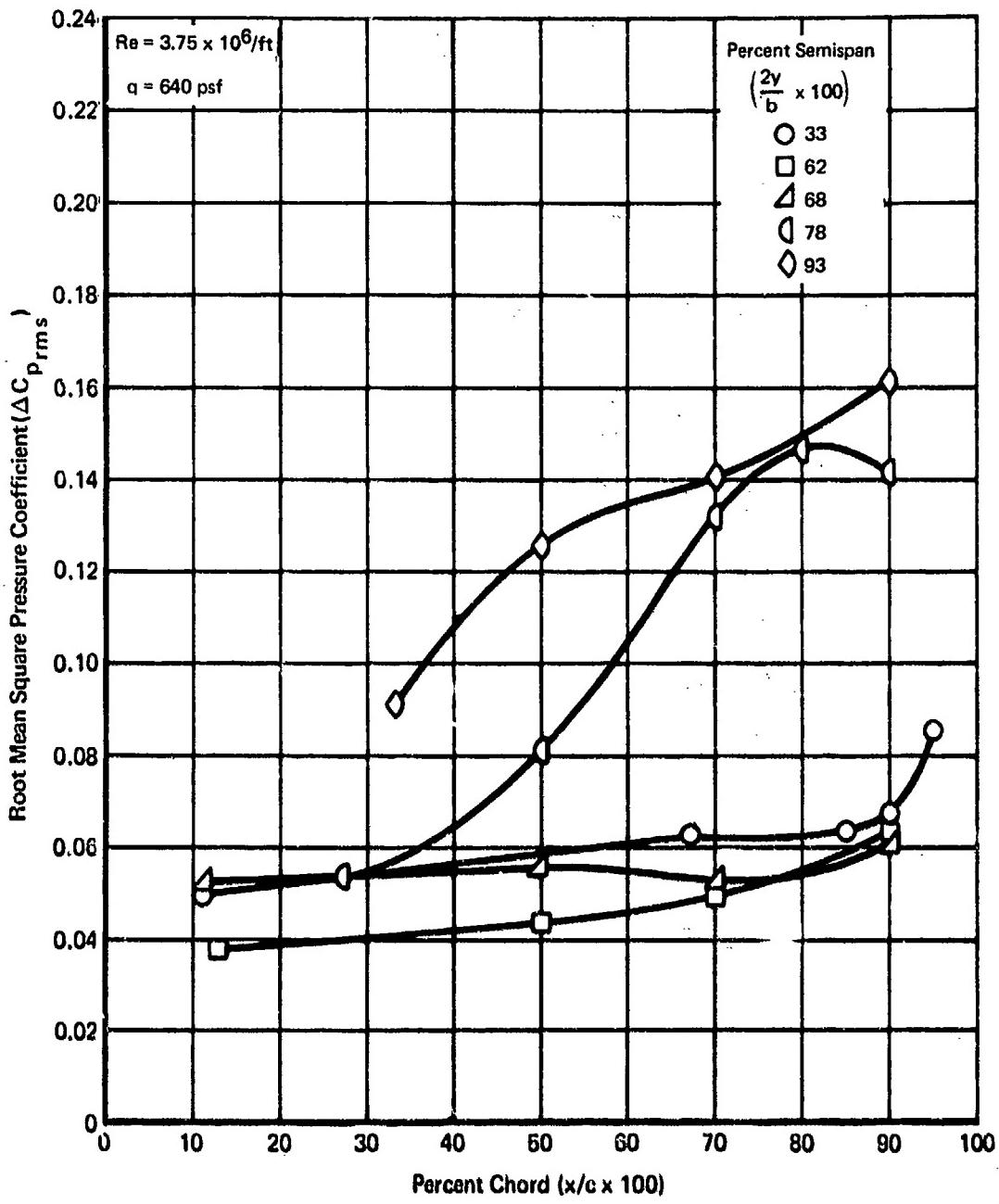


Figure 19 Root Mean Square Pressure Coefficient vs Percent Chord
(Configuration 1, Mach 0.9, Wing Angle of Attack 14°)

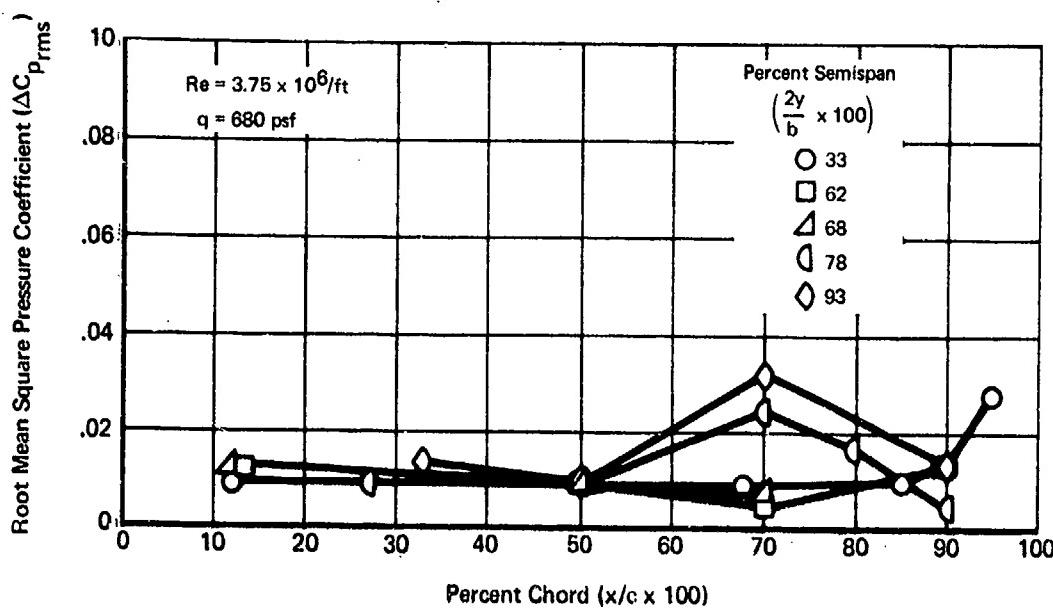


Figure 20 Root Mean Square Pressure Coefficient vs Percent Chord
(Configuration 1, Mach 1.0, Wing Angle of Attack 0°)

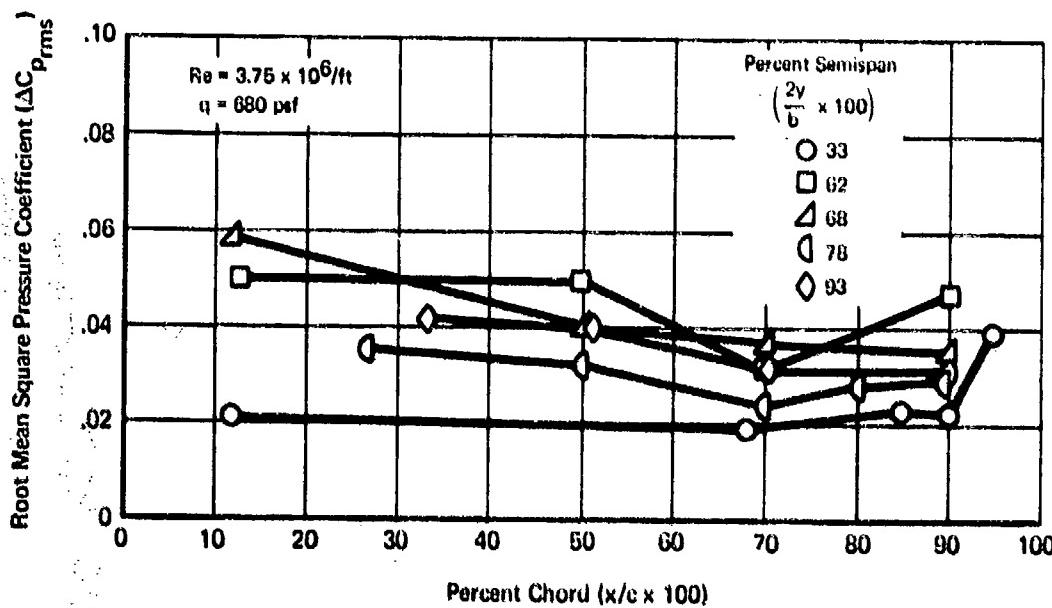


Figure 21 Root Mean Square Pressure Coefficient vs Percent Chord
(Configuration 1, Mach 1.0, Wing Angle of Attack 12°)

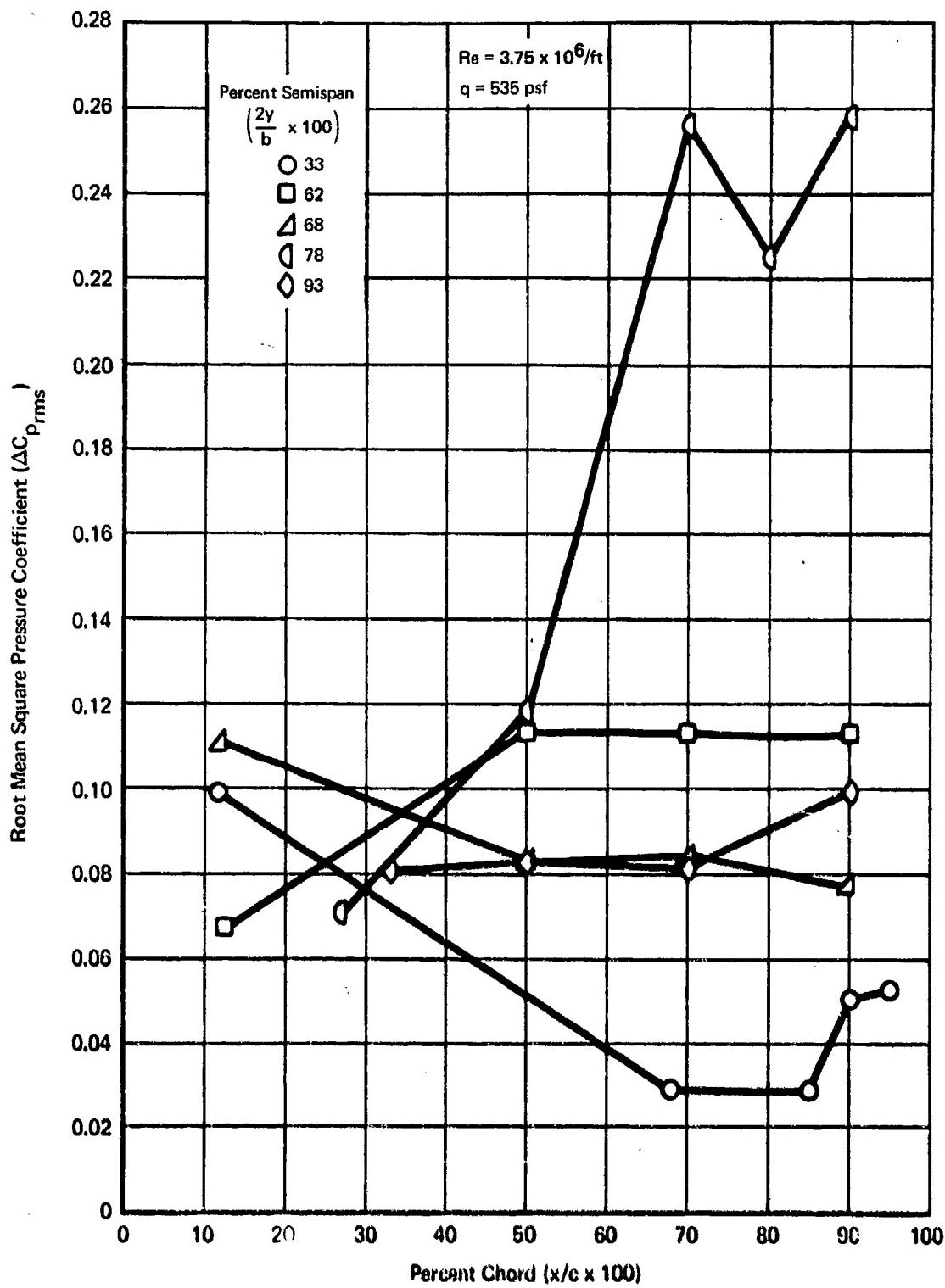


Figure 22 Root Mean Square Pressure Coefficient vs Percent Chord
(Configuration 5, Mach 0.7, Wing Angle of Attack 11°)

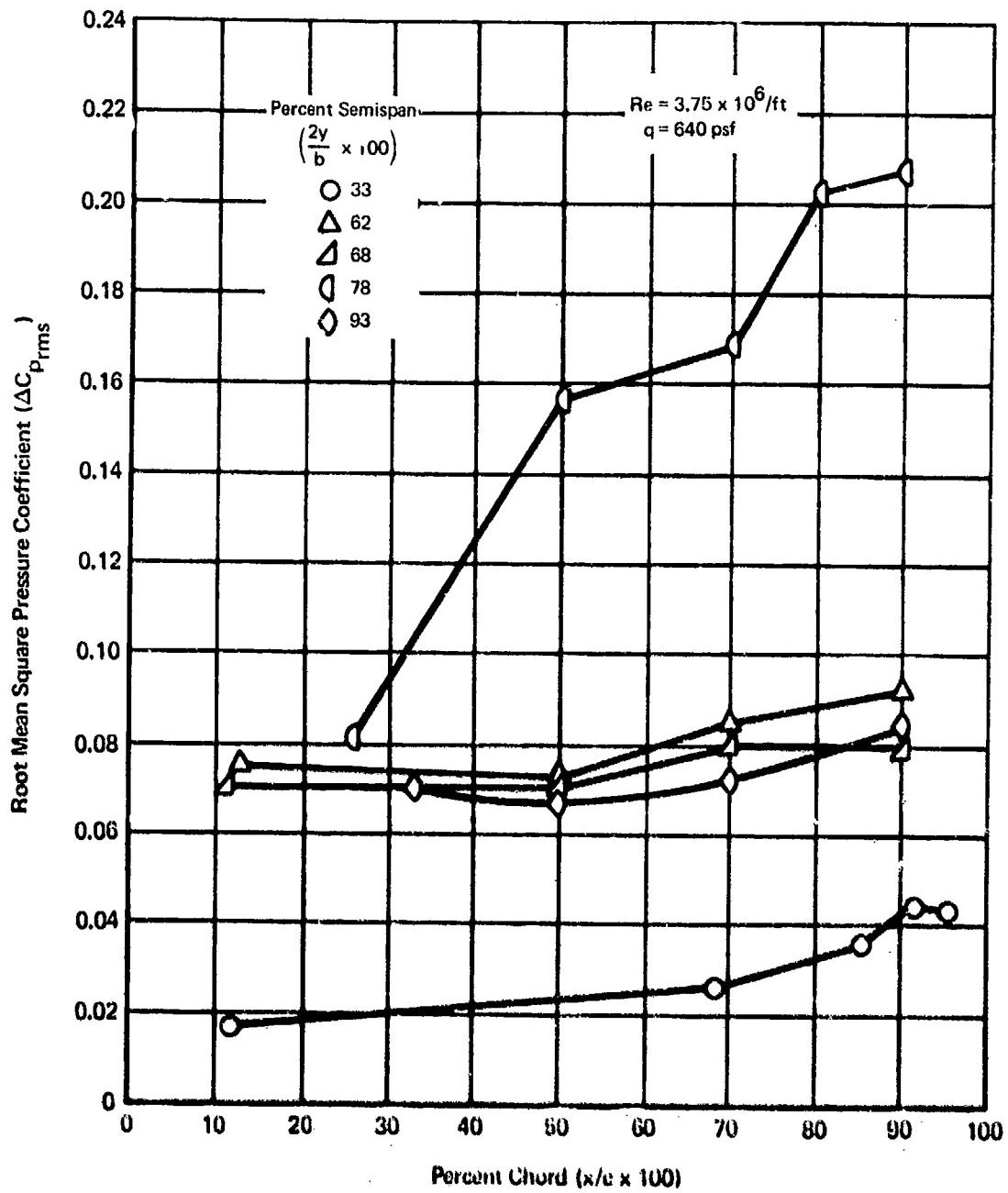
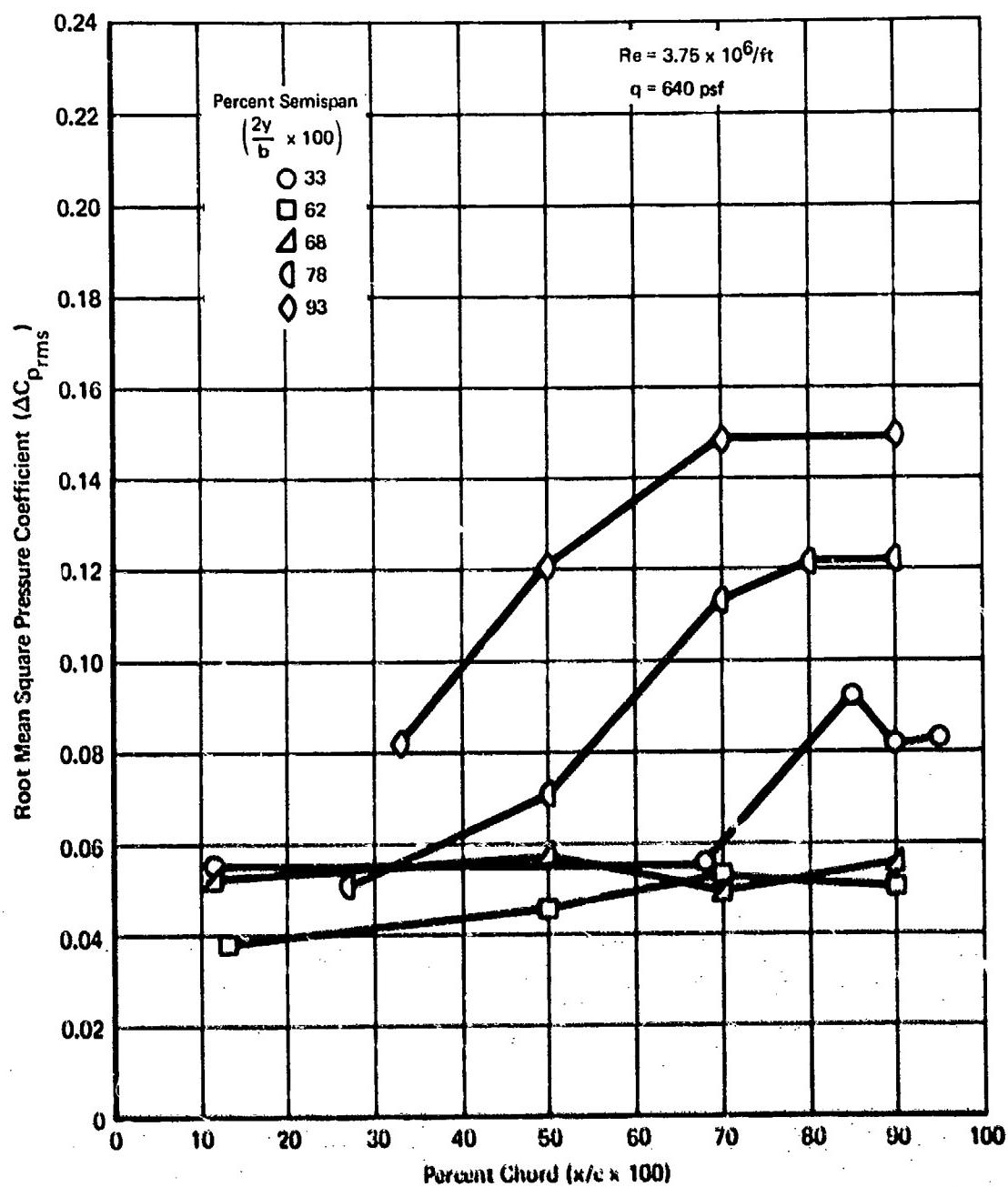


Figure 23 Root Mean Square Pressure Coefficient vs Percent Chord.
 (Configuration 5, Mach 0.9, Wing Angle of Attack 11°)



**Figure 24 Root Mean Square Pressure Coefficient vs Percent Chord
(Configuration 5, Mach 0.9, Wing Angle of Attack 14°)**

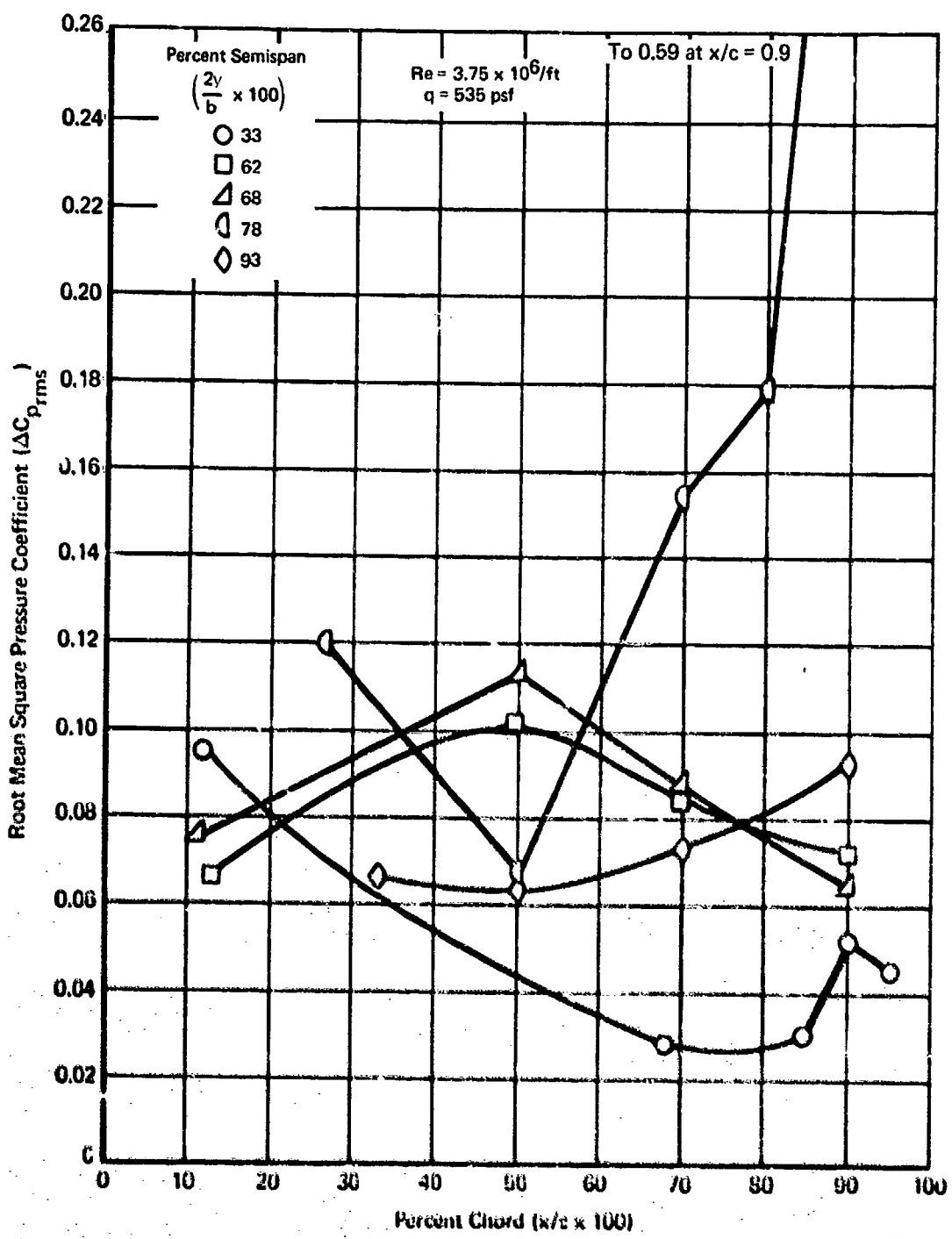


Figure 26 Root Mean Square Pressure Coefficient vs Percent Chord
 (Configuration 6, Mach 0.7, Wing Angle of Attack 11°)

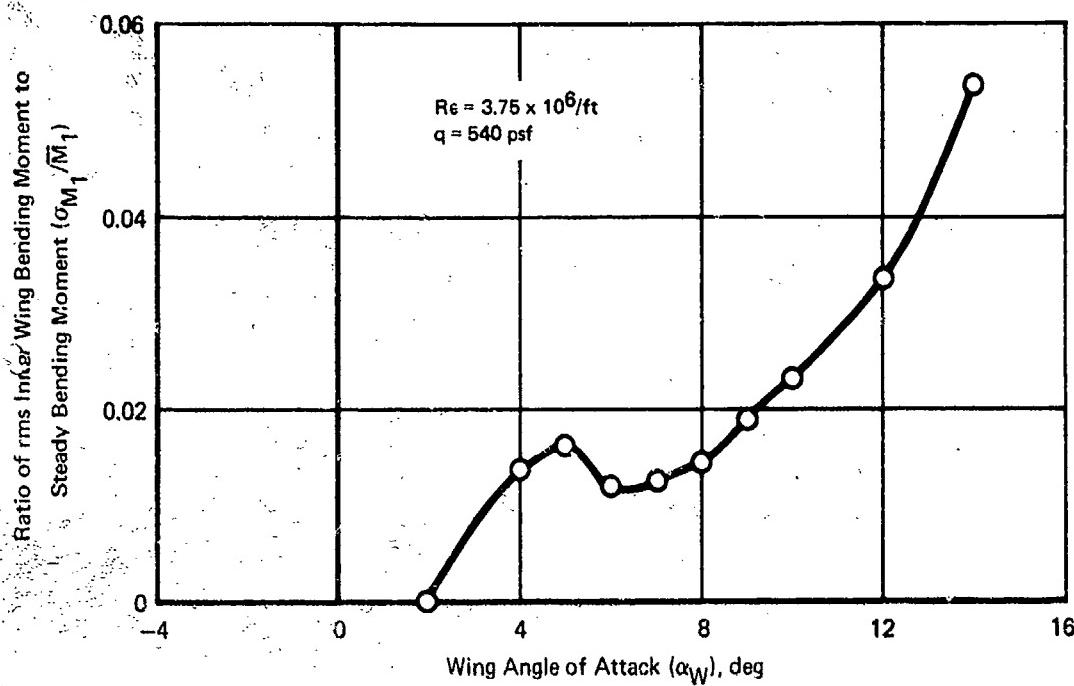


Figure 26 Ratio of rms Inner Wing Bending Moment to Steady Bending Moment,
Configuration 1, Mach 0.7

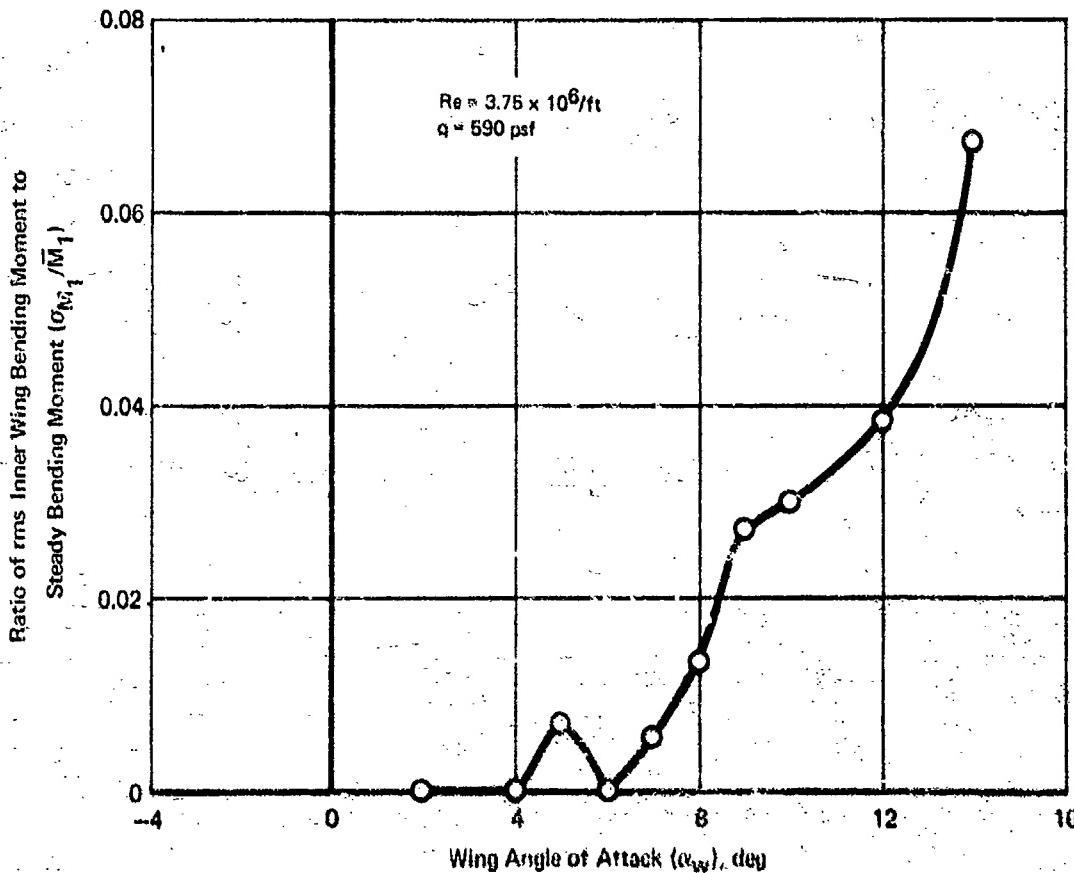


Figure 27 Ratio of rms Inner Wing Bending Moment to Steady Bending Moment,
Configuration 1, Mach 0.8

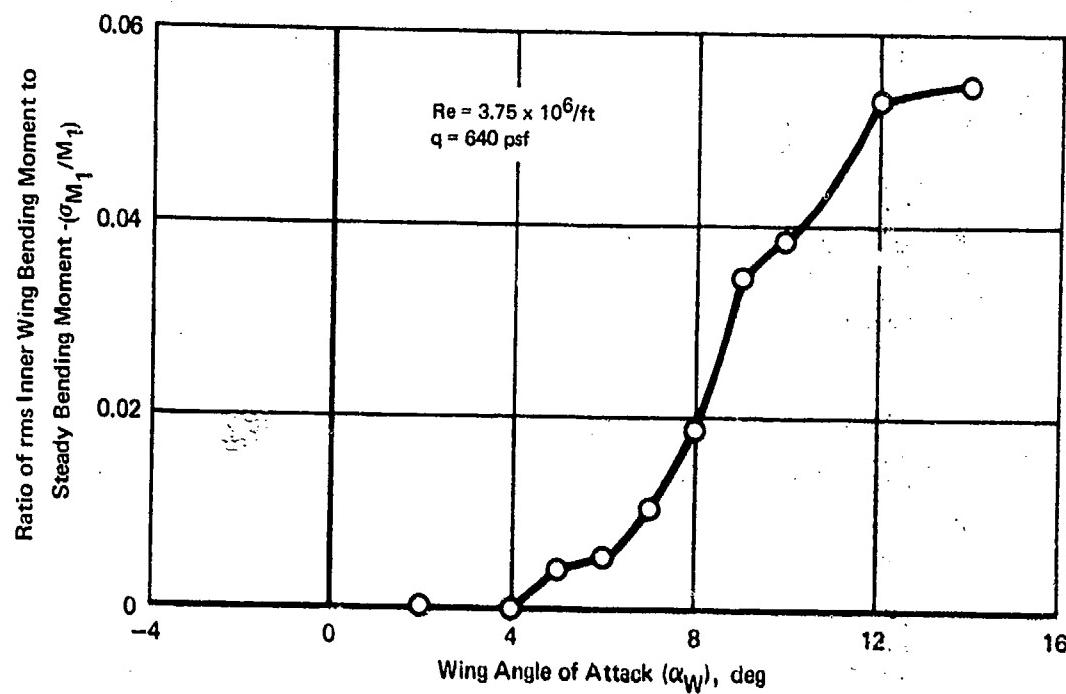


Figure 28. Ratio of rms Inner Wing Bending Moment to Steady Bending Moment
Configuration 1, Mach 0.9

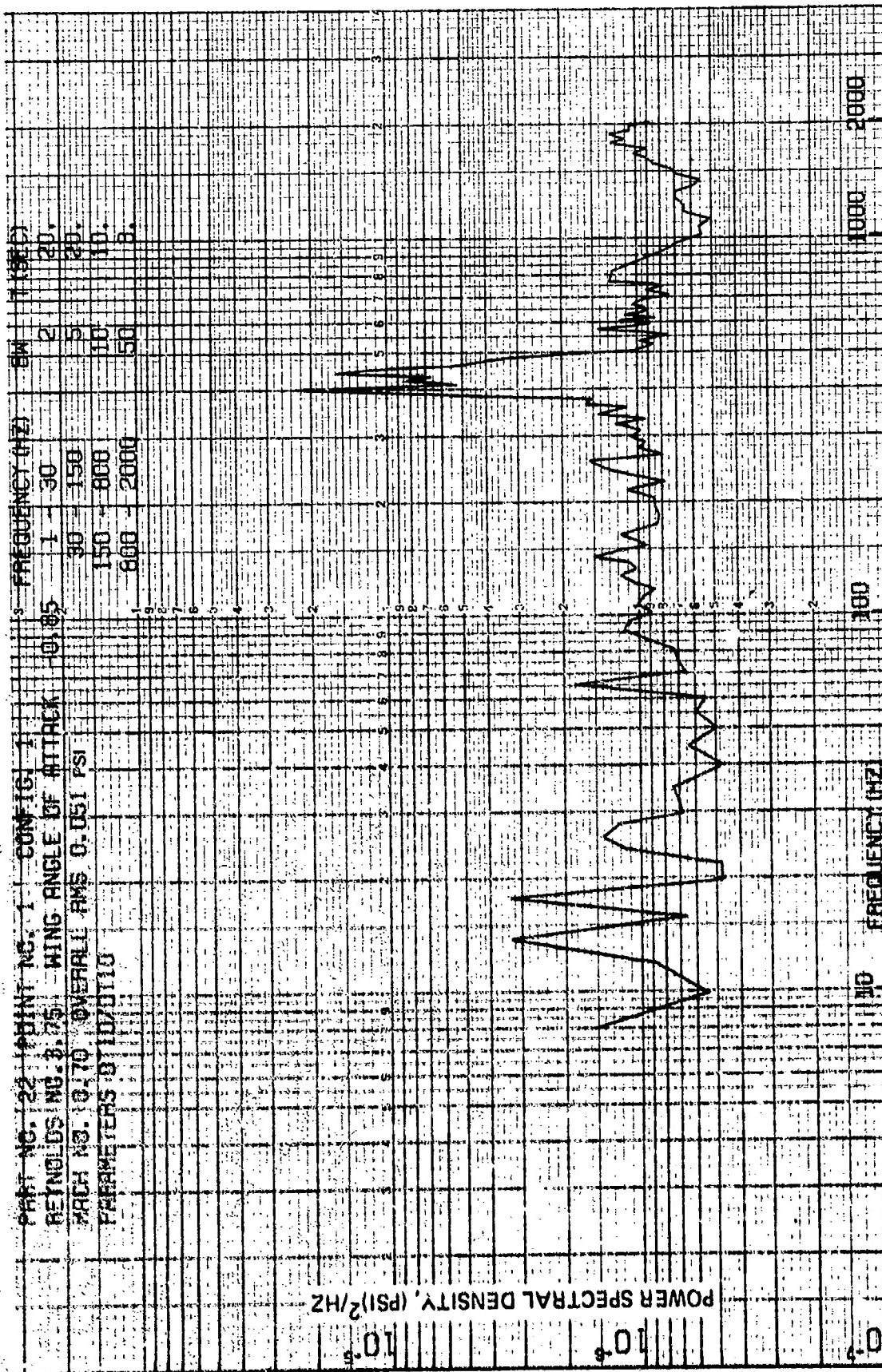


Figure 29 Fluctuating Pressure Power Spectral Density (Configuration 1, Mach 0.7, Wing Angle of Attack -1 Deg., Transducer 10)

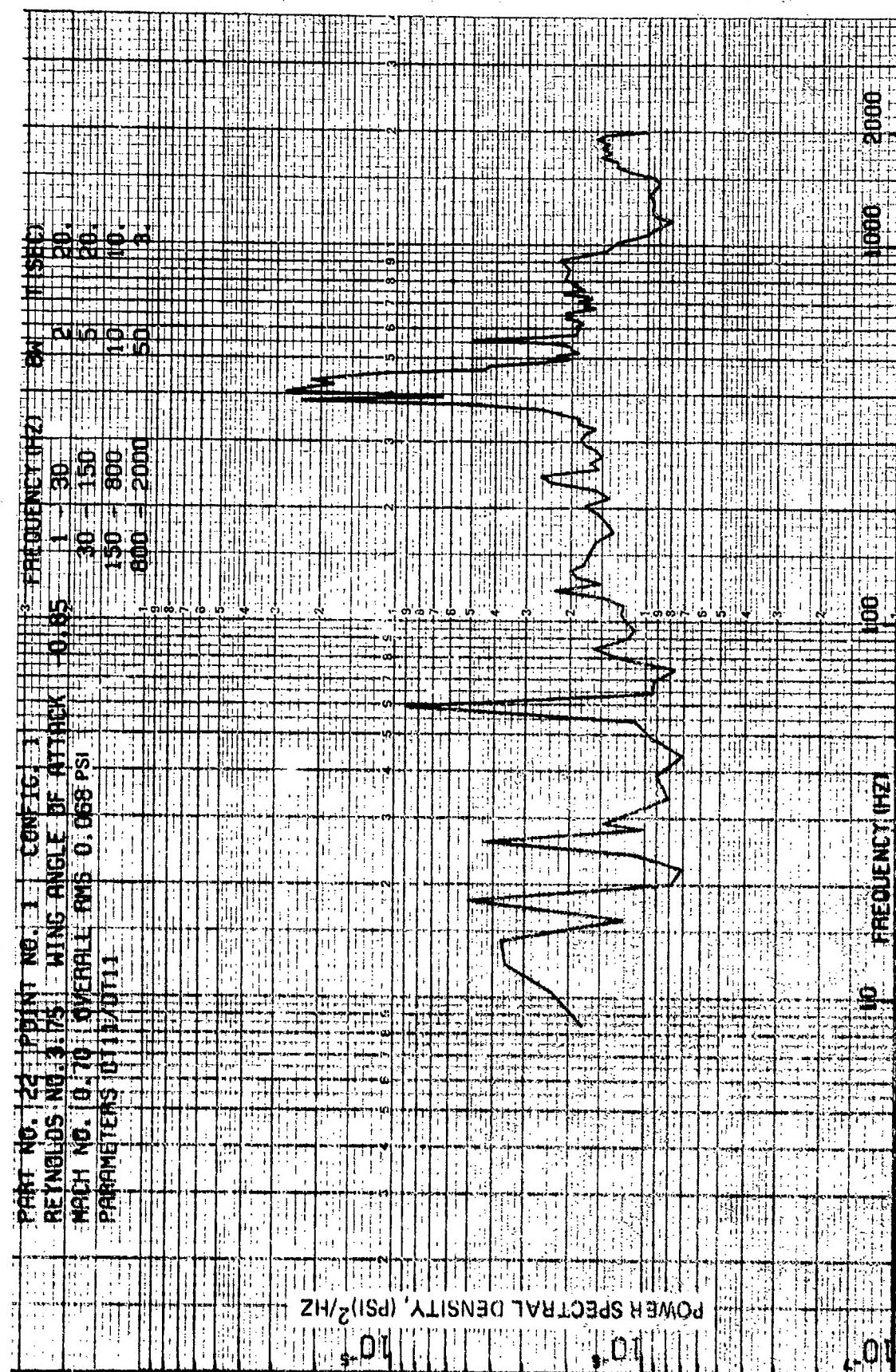


Figure 30 Fluctuating Pressure Spectral Density (Configuration 1, Mach 0.7,
Wing Angle of Attack - 1 Deg., Transducer 11)

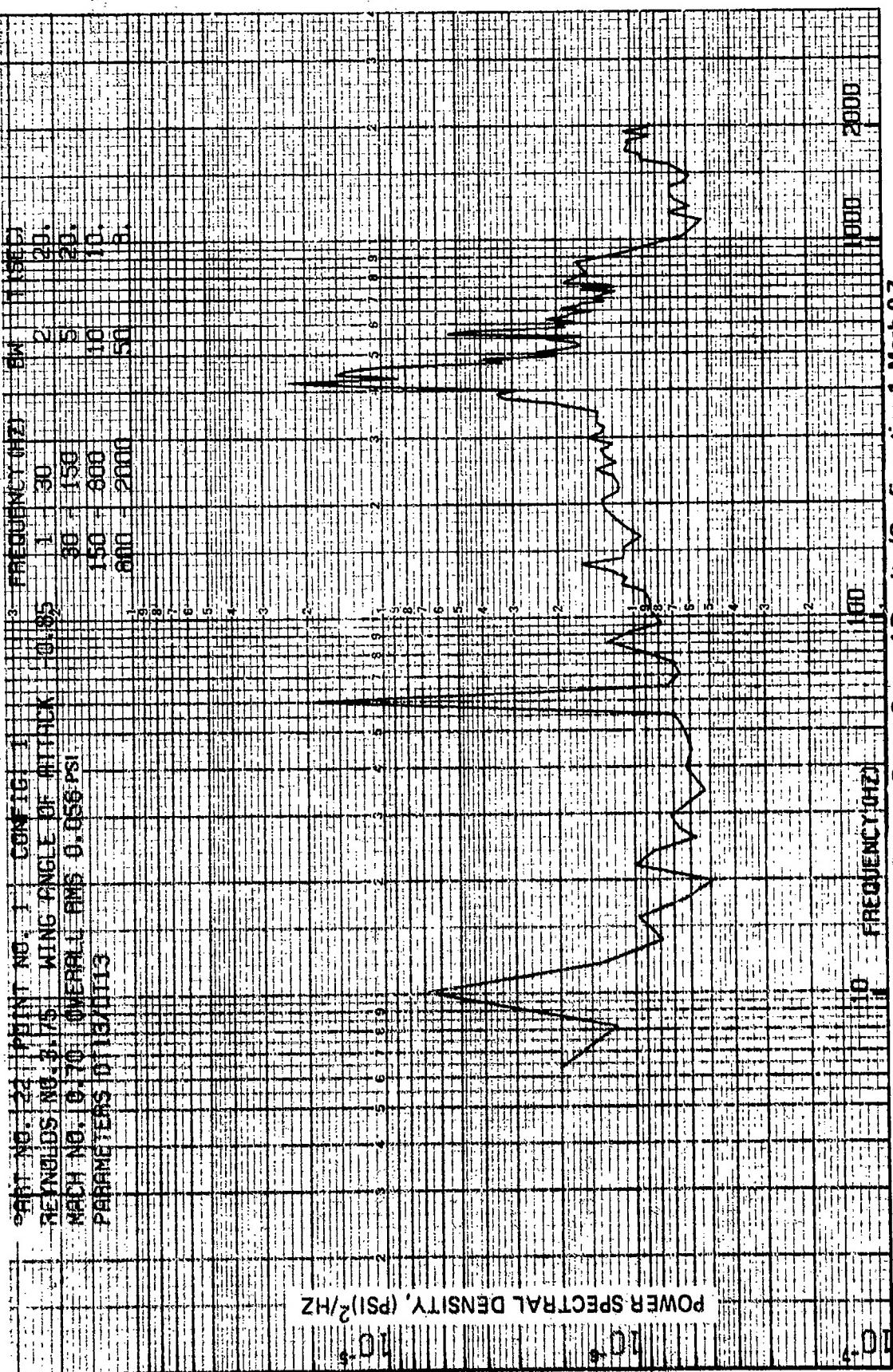
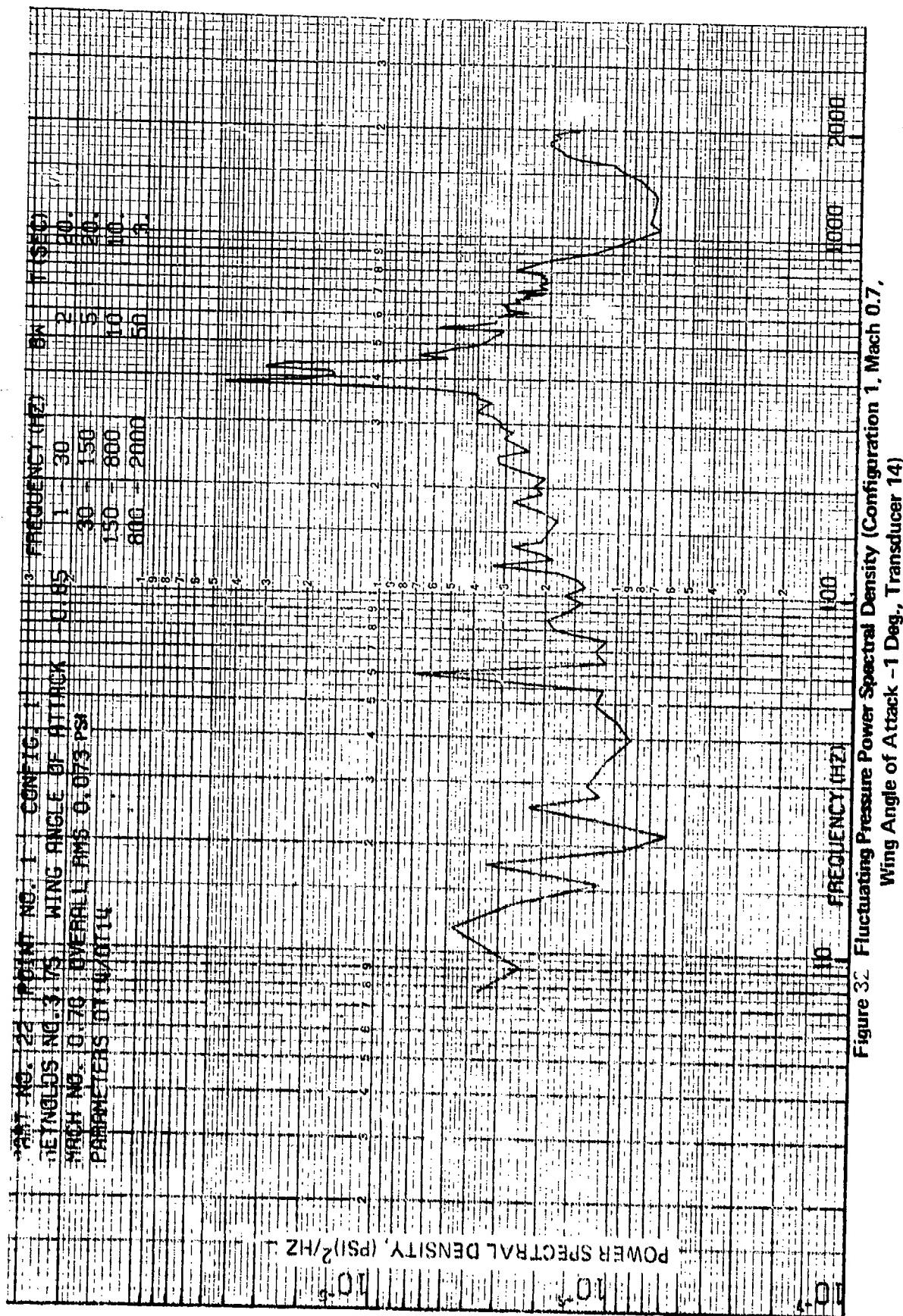


Figure 31 Fluctuating Pressure Power Spectral Density (Configuration 1, Mach 0.7,
Wing Angle of Attack - 1 Deg., Transducer 13)



507

Figure 3c Fluctuating Pressure Power Spectral Density (Configuration 1, Mach 0.7,
 Wing Angle of Attack -1 Deg., Transducer 14)

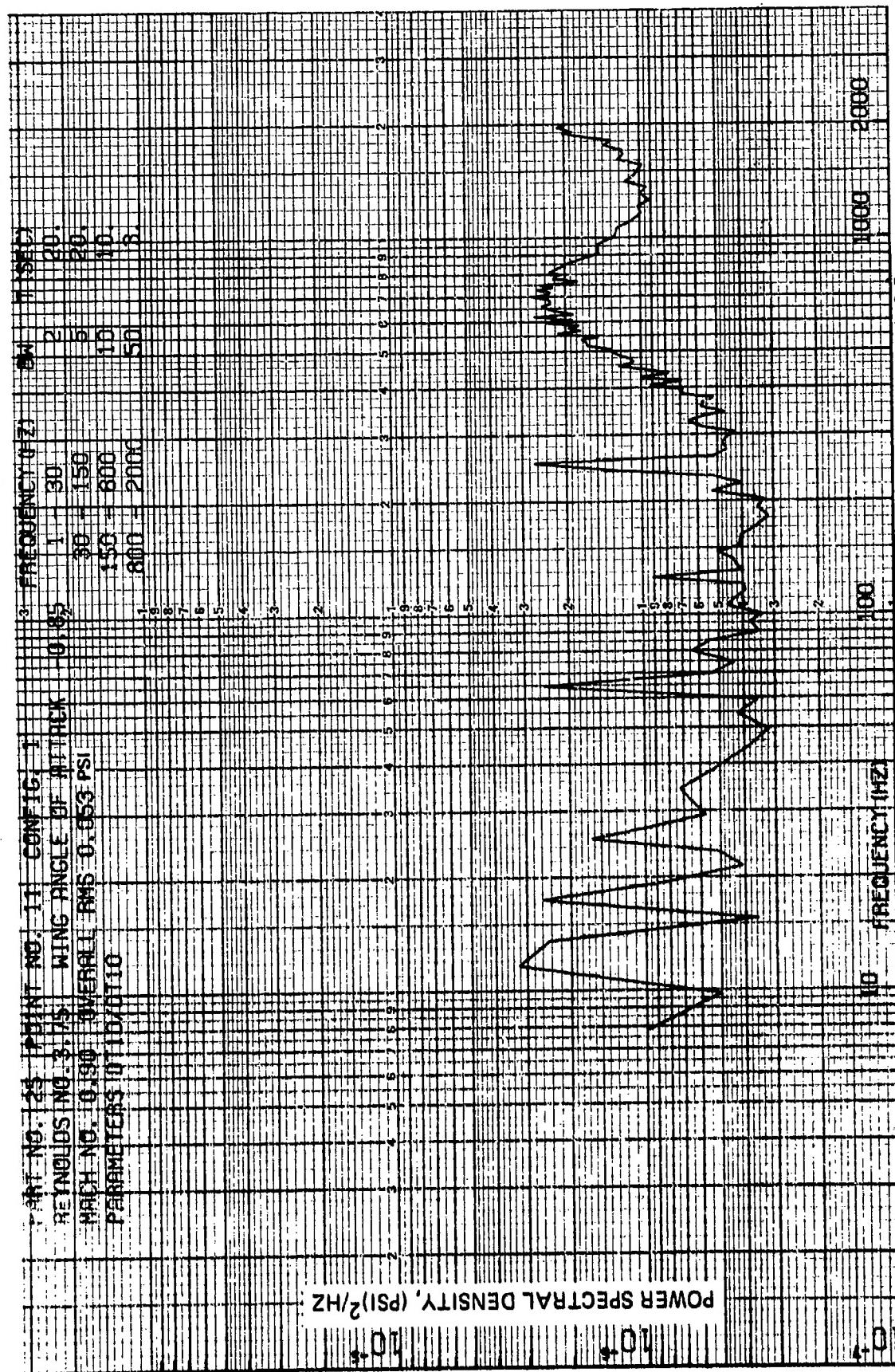


Figure 33 Fluctuating Pressure Power Spectral Density (Configuration 1, Mach 0.9, Wing Angle of Attack -1 Deg., Transducer 10)

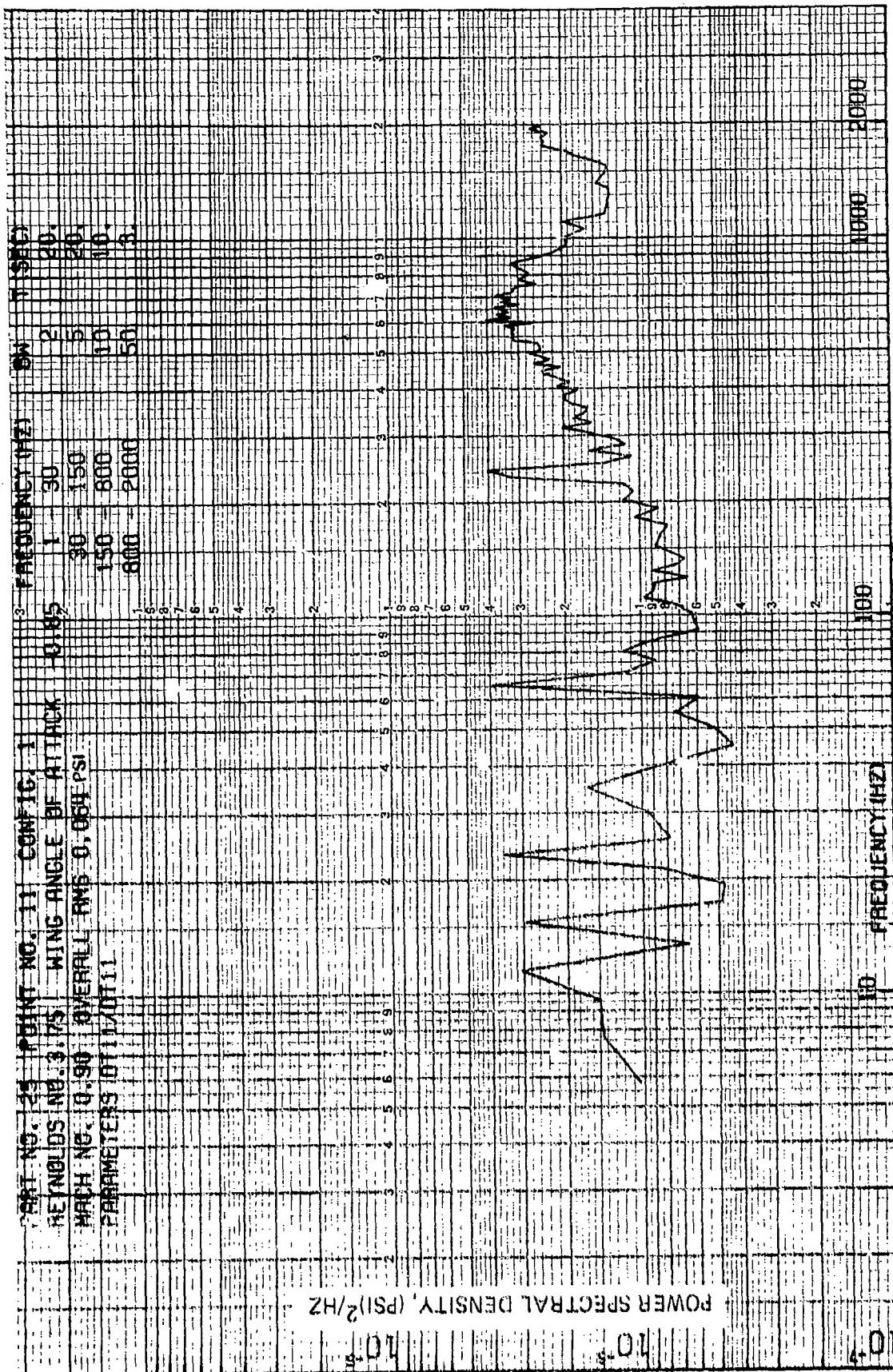


Figure 34 Fluctuating Pressure Power Spectral Density (Configuration 1, Mach 0.9, Wing Angle of Attack -1 Deg., Transducer 11)

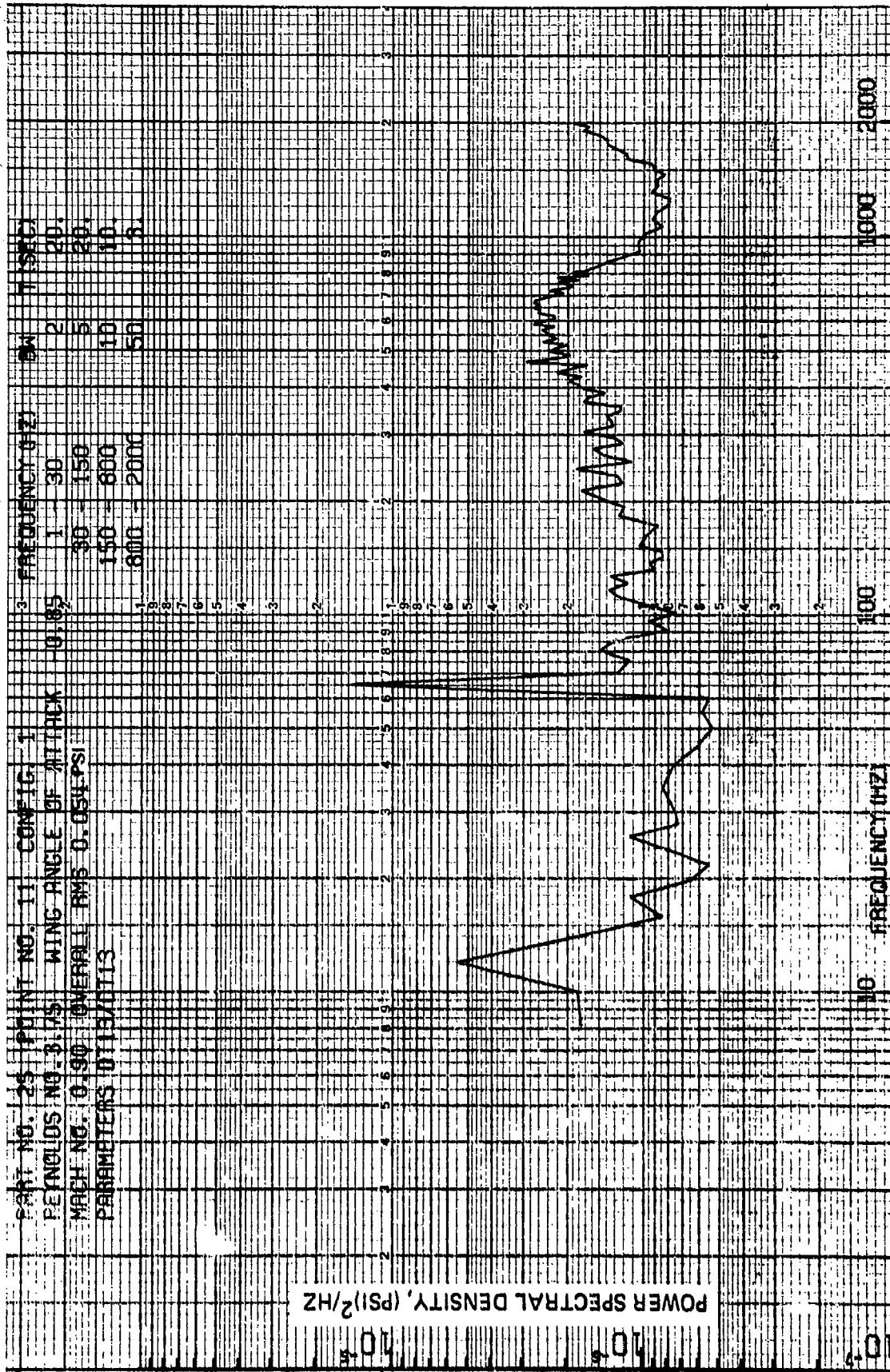


Figure 35 Fluctuating Pressure Power Spectral Density (Configuration 1, Mach 0.9, Wing Angle of Attack -1 Deg., Transducer 13)

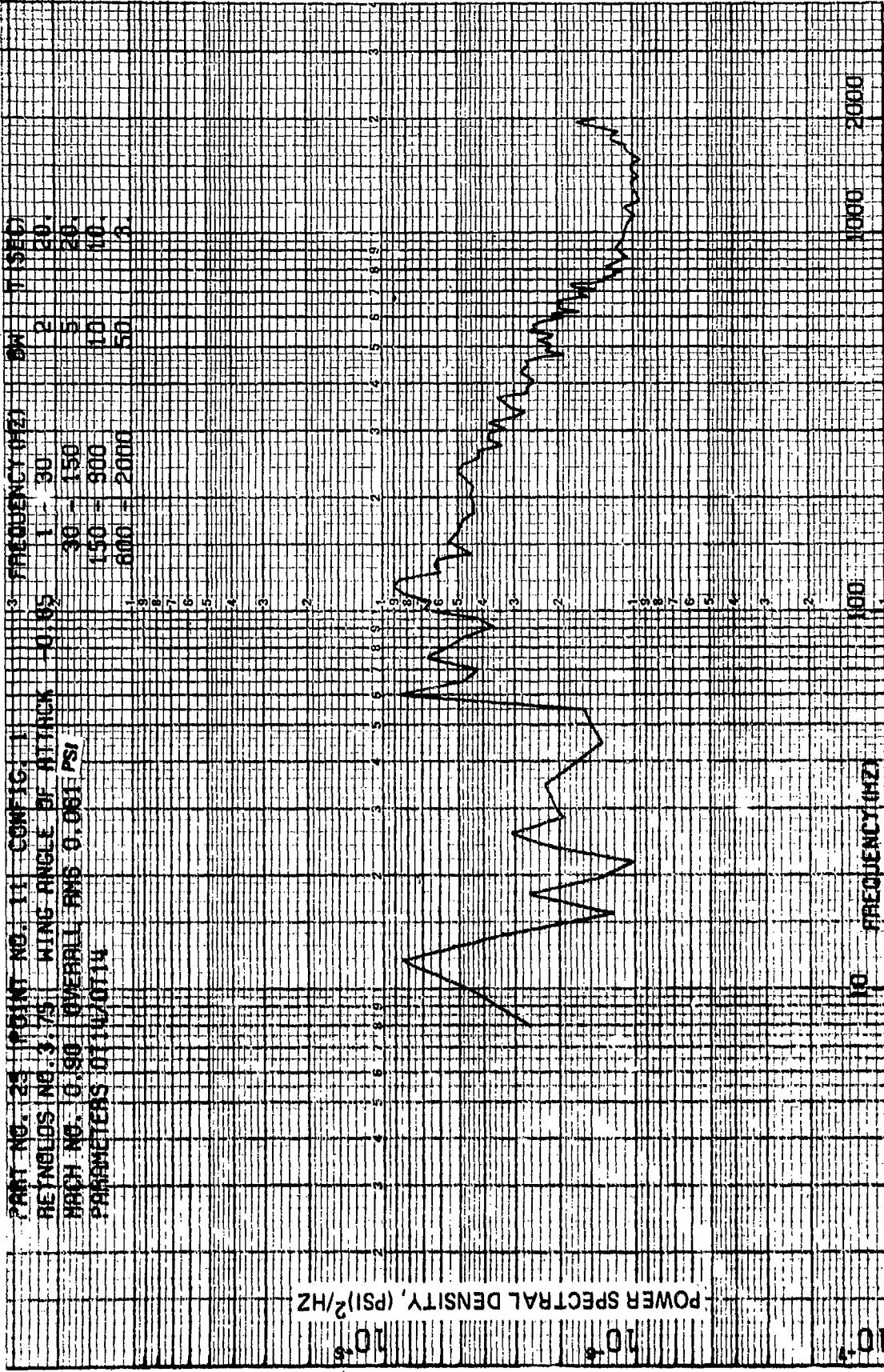


Figure 36 Fluctuating Pressure Power Spectral Density (Configuration 1, Mach 0.9,
Wing Angle of Attack -1 Deg., Transducer 14)

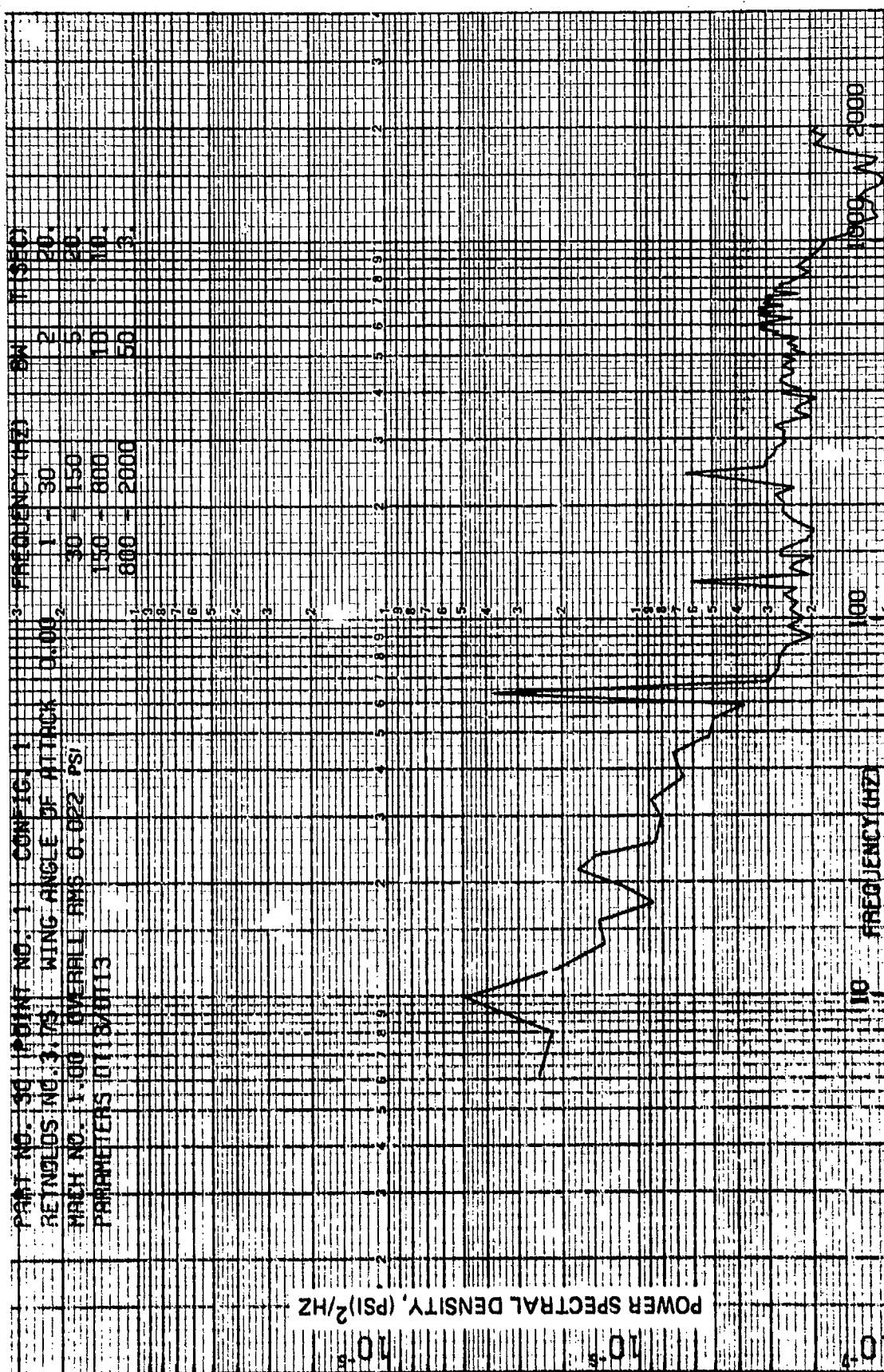


Figure 37 Fluctuating Pressure Power Spectral Density (Configuration 1, Mach 1.0,
Wing Angle of Attack 0 Deg., Transducer 13)

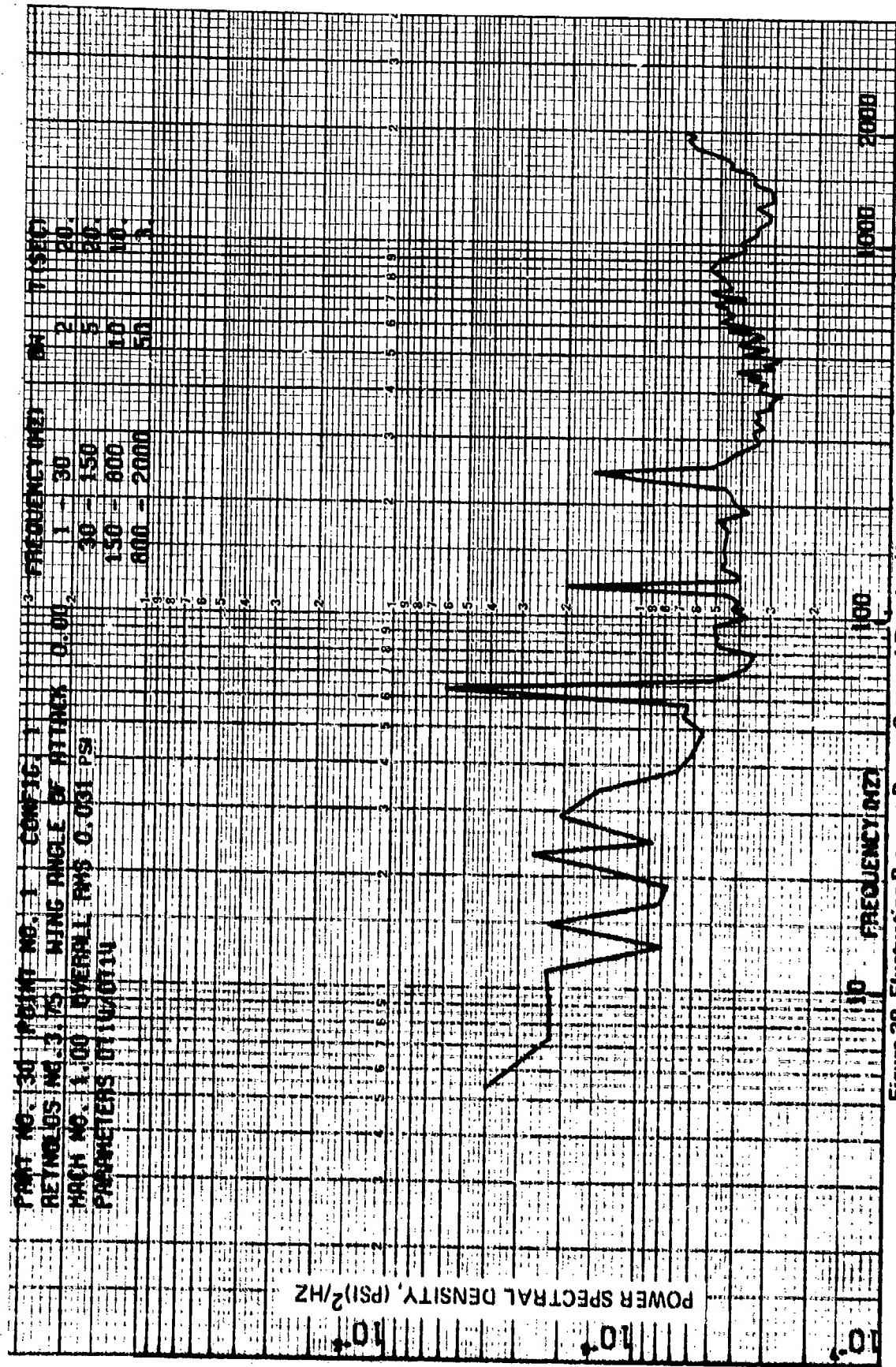


Figure 38 Fluctuating Pressure Spectral Density (Configuration 1, Mach 1.0, Wing Angle of Attack 0 Deg., Transducer 14)

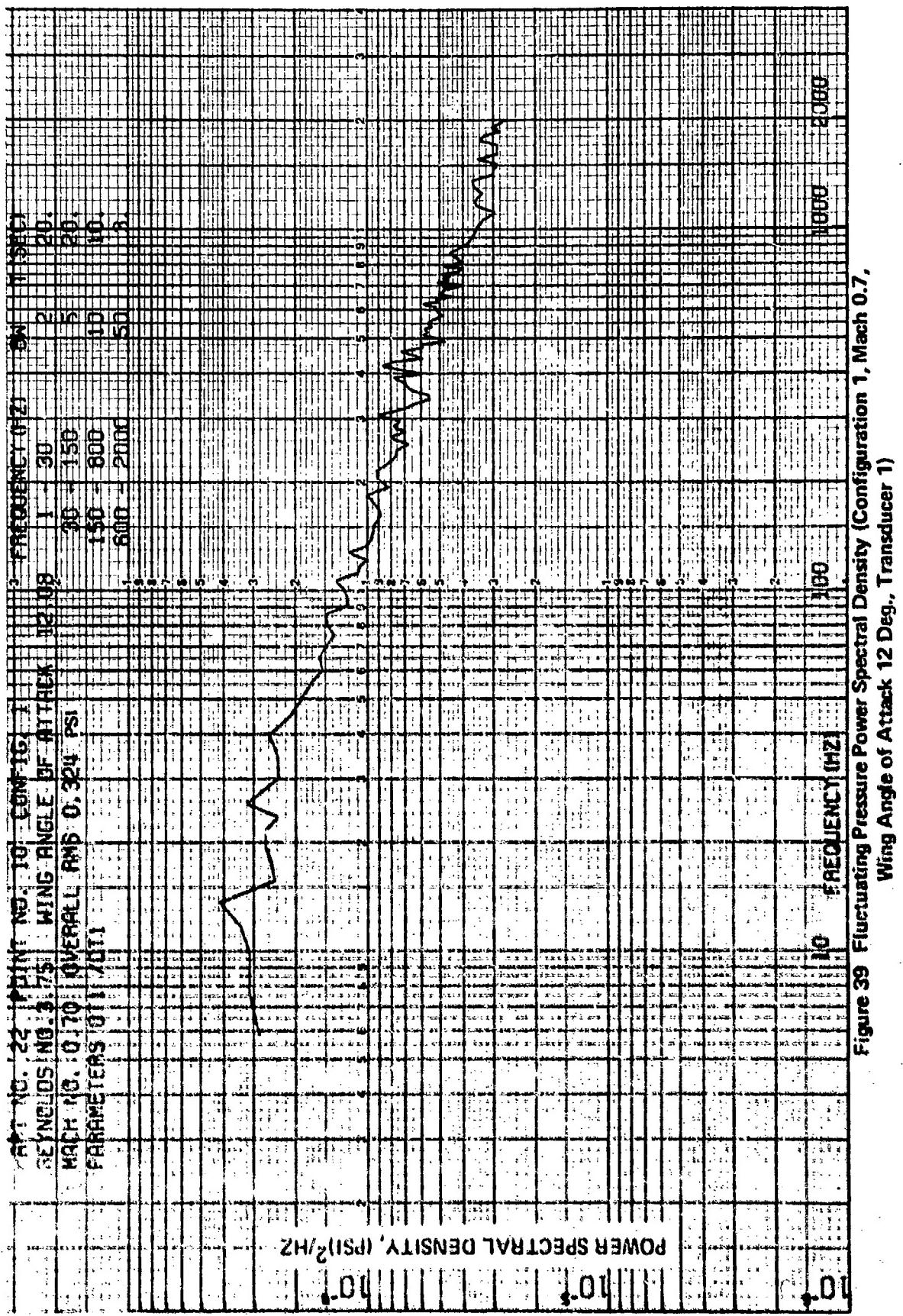


Figure 39 Fluctuating Pressure Power Spectral Density (Configuration 1, Mach 0.7,
Wing Angle of Attack 12 Deg., Transducer 1)

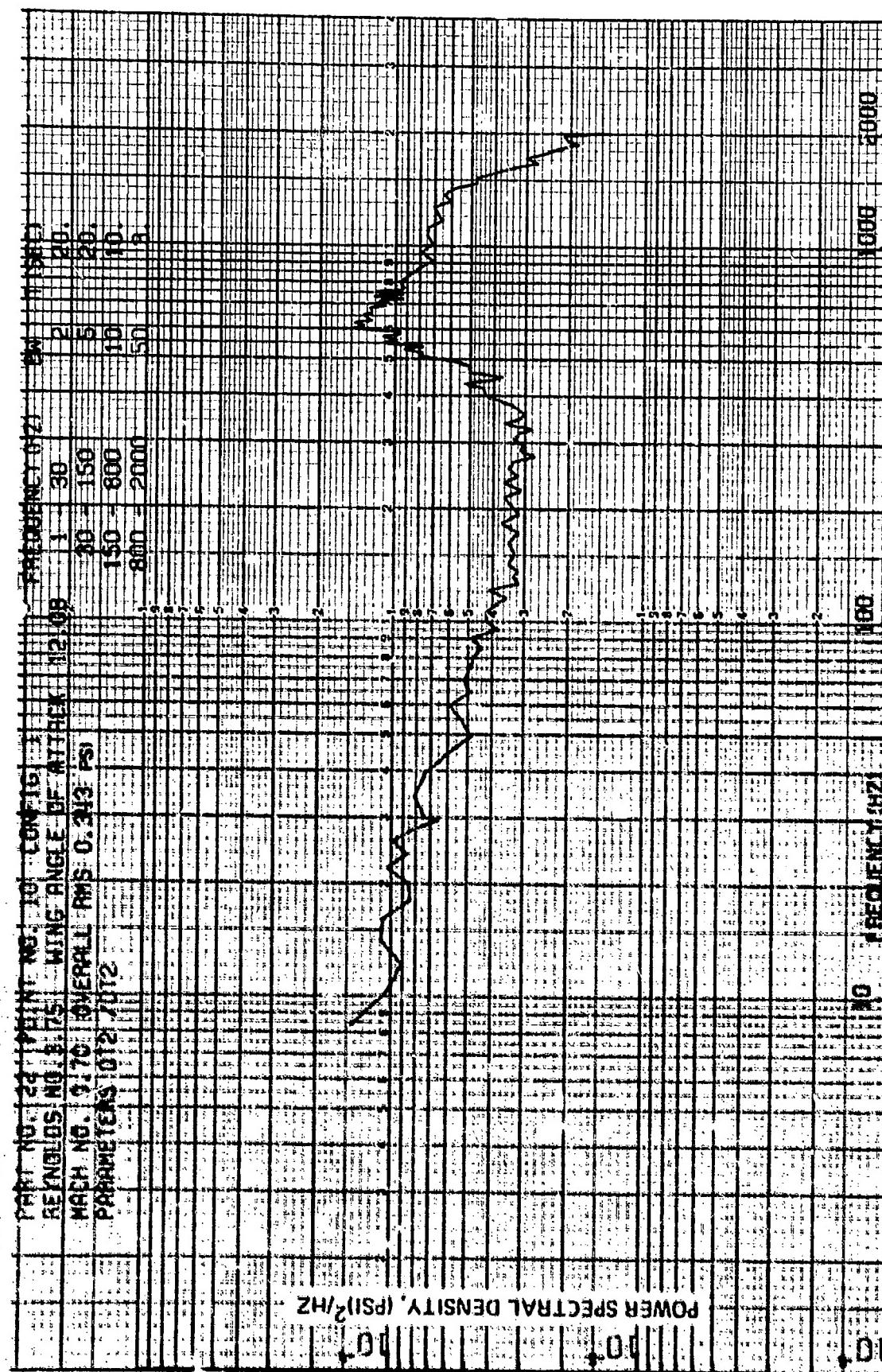


Figure 40 Fluctuation,3 Pressure Power Spectral Density (Configuration 1, Mach 0.7, Wing Angle of Attack 12 Deg., Transducer 2)

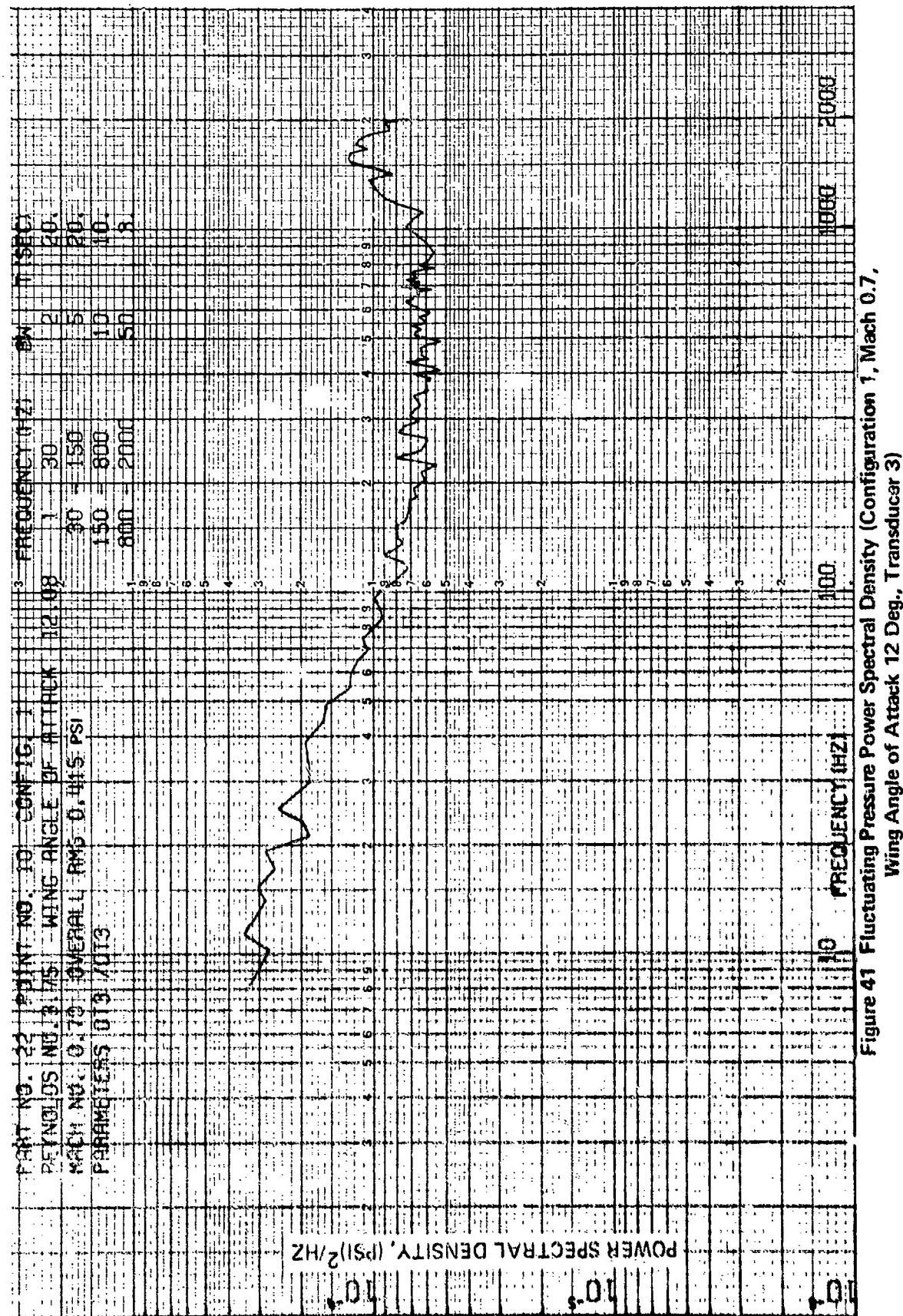


Figure 41 Fluctuating Pressure Power Spectral Density (Configuration 1, Mach 0.7,
 Wing Angle of Attack 12 Deg., Transducer 3)

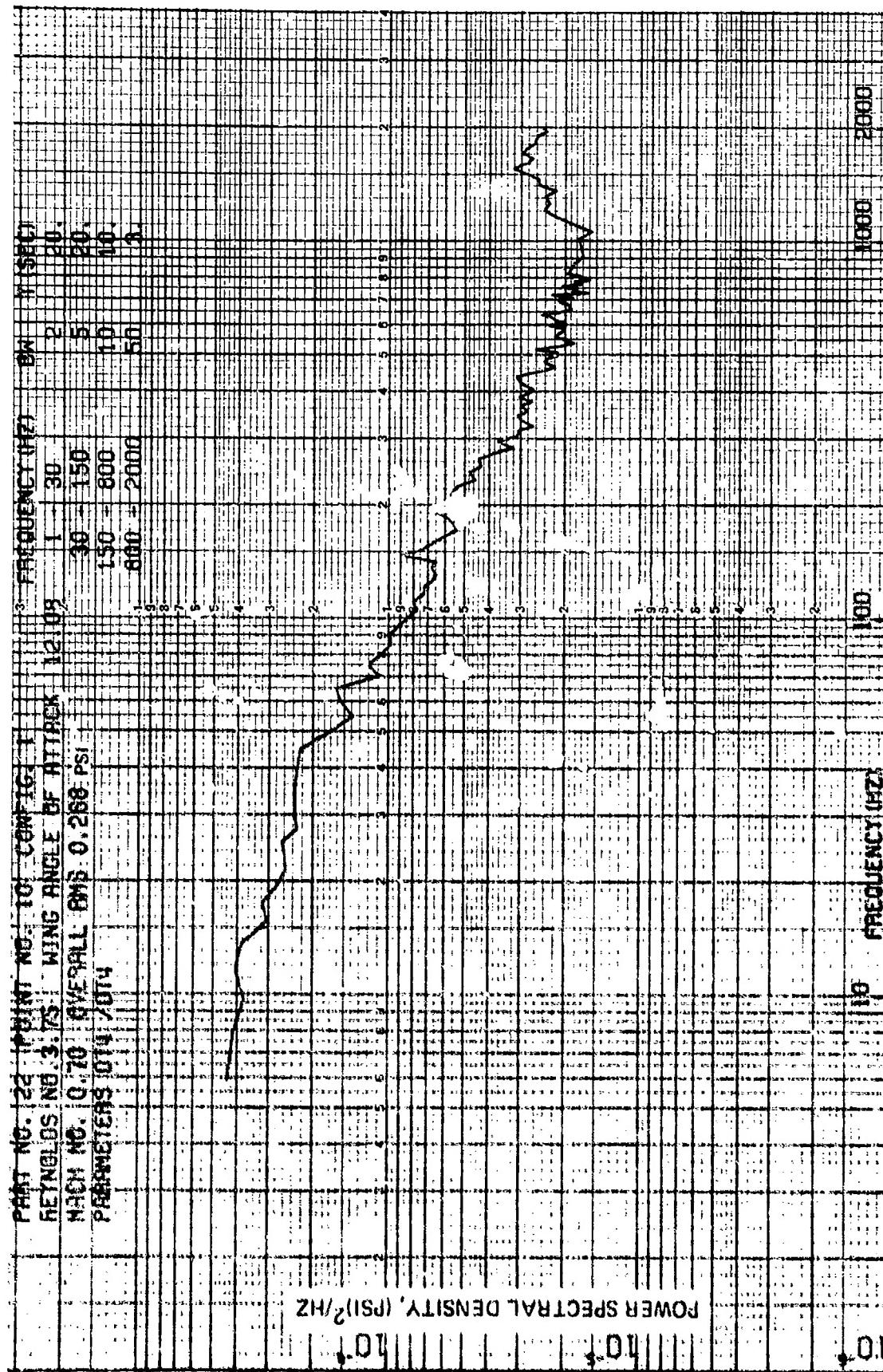


Figure 42 Fluctuating Pressure Power Spectral Density (Configuration 1, Mach 0.7,
Wing Angle of Attack 12 Deg., Transducer 4)

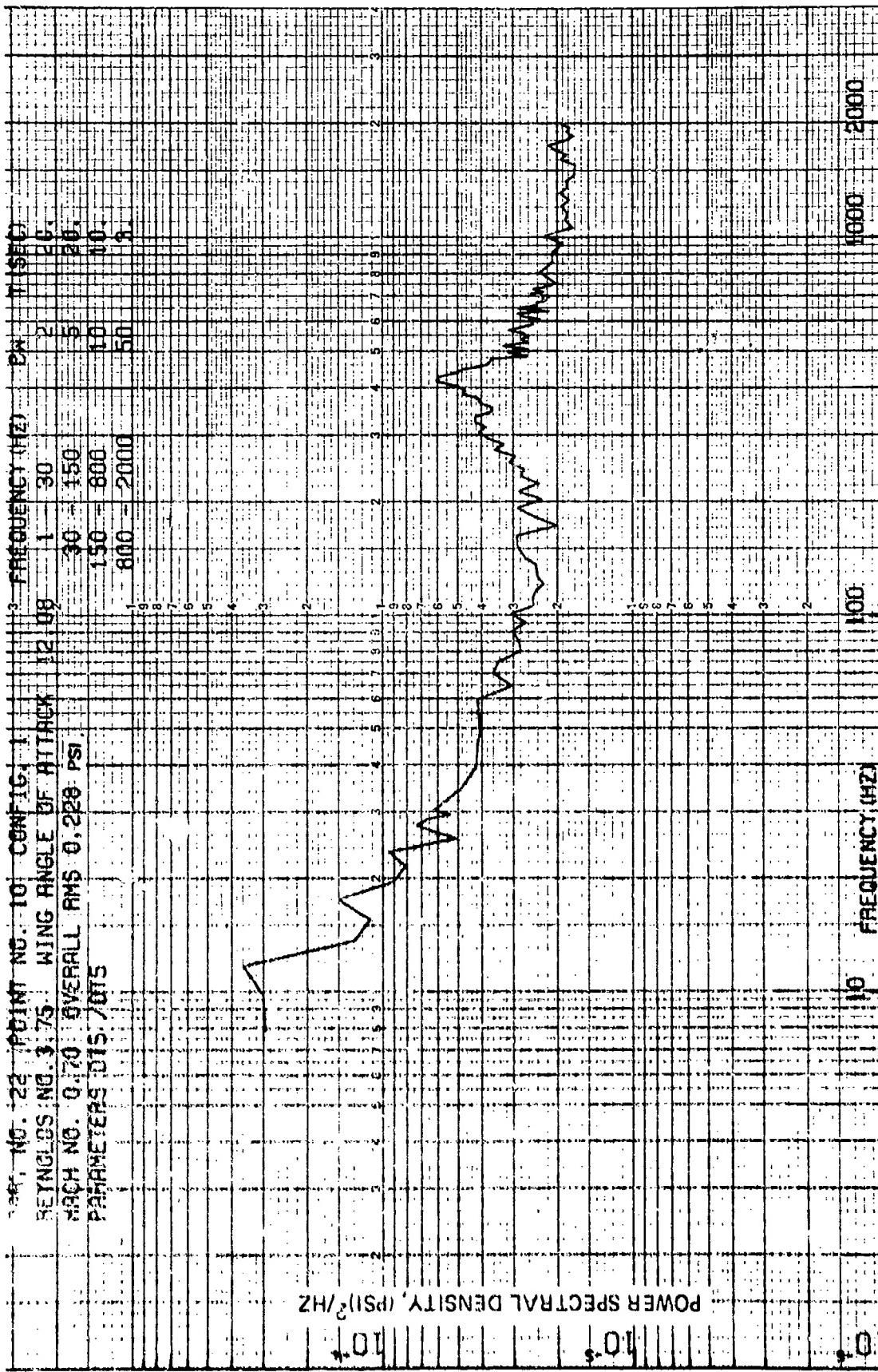


Figure 43 Fluctuating Pressure Power Spectral Density (Configuration 1, Mach 0.7,
 Wing Angle of Attack 12 Deg., Transducer 5)

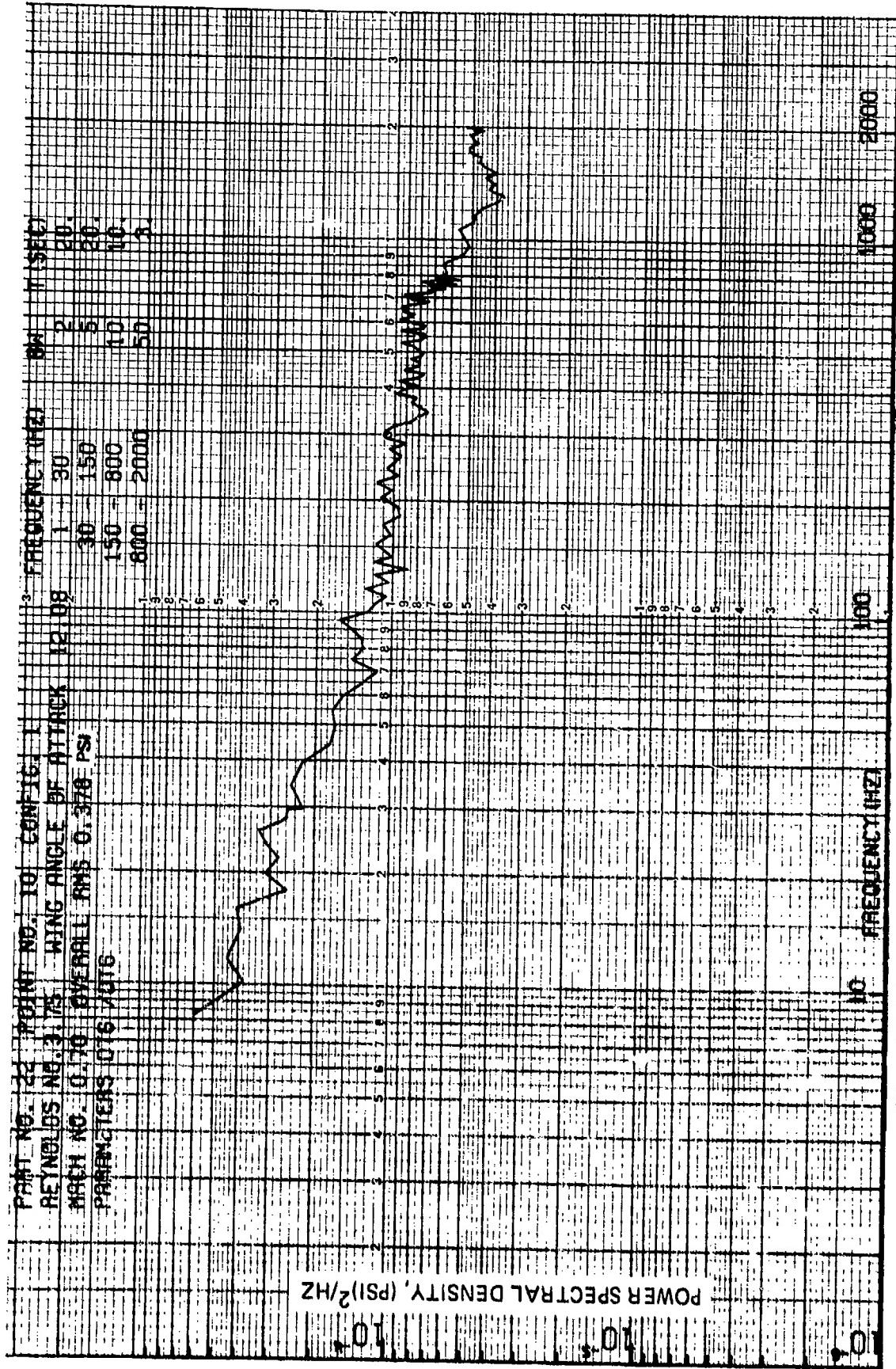


Figure 44 Fluctuating Pressure Power Spectral Density (Configuration 1, Mach 0.7,
 Wing Angle of Attack 12 Deg., Transducer 6)

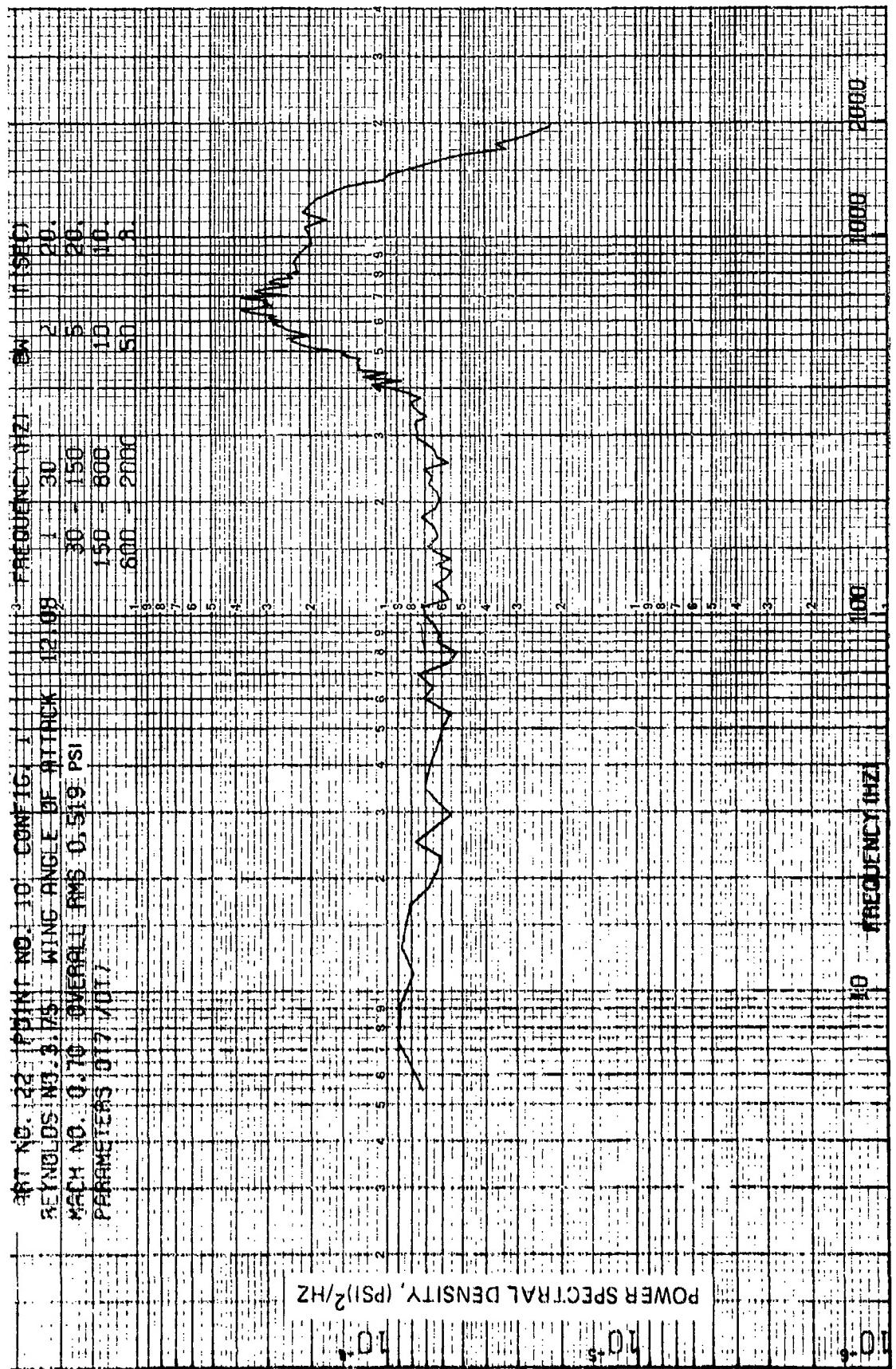


Figure 45 Fluctuating Pressure Power Spectral Density (Configuration 1, Mach 0.7,
 Wing Angle of Attack 12 Deg., Transducer 7)

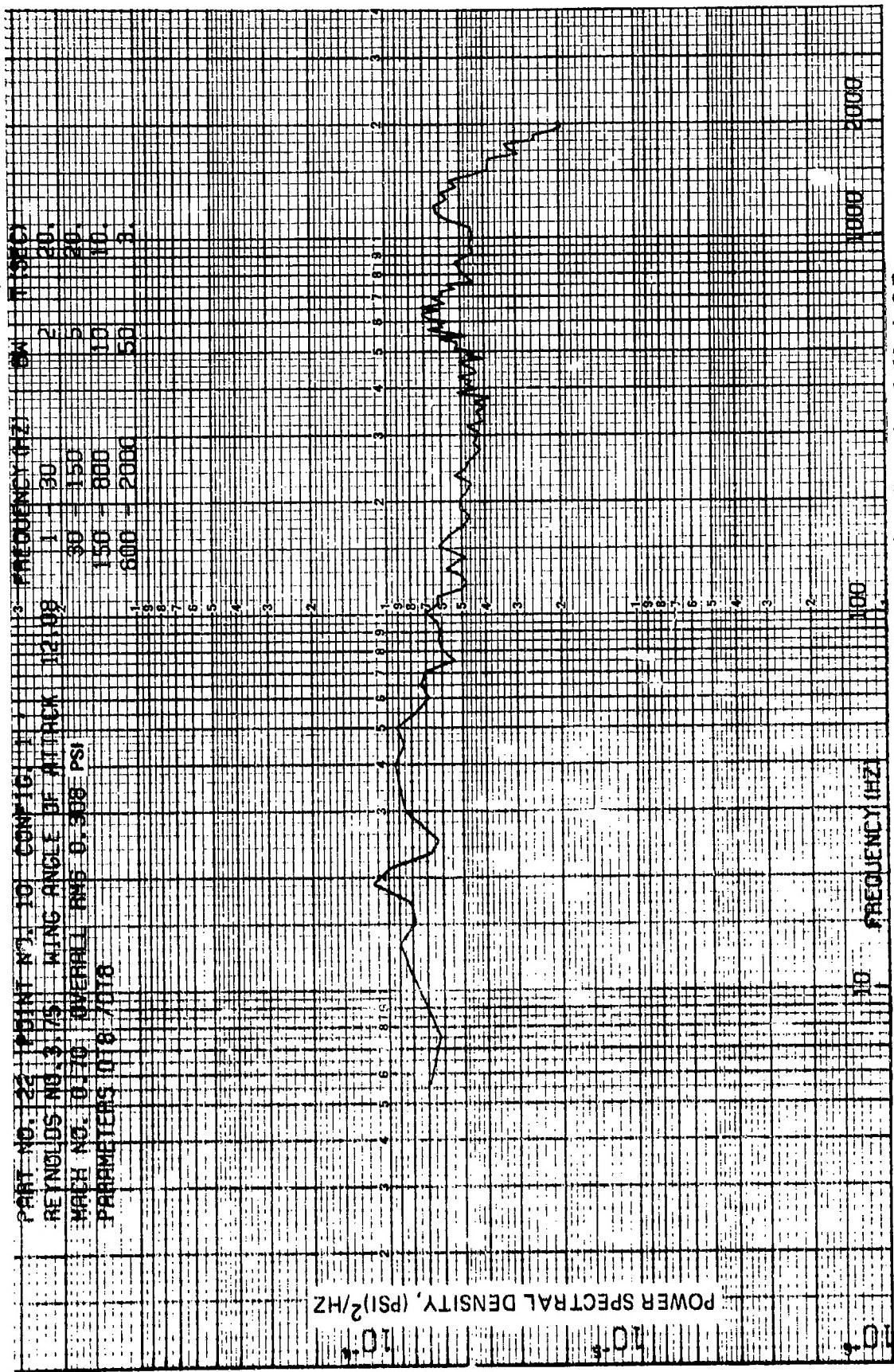


Figure 46 Fluctuating Pressure Power Spectral Density (Configuration 1, Mach 0.7, Wing Angle of Attack 12 Deg., Transducer 8)

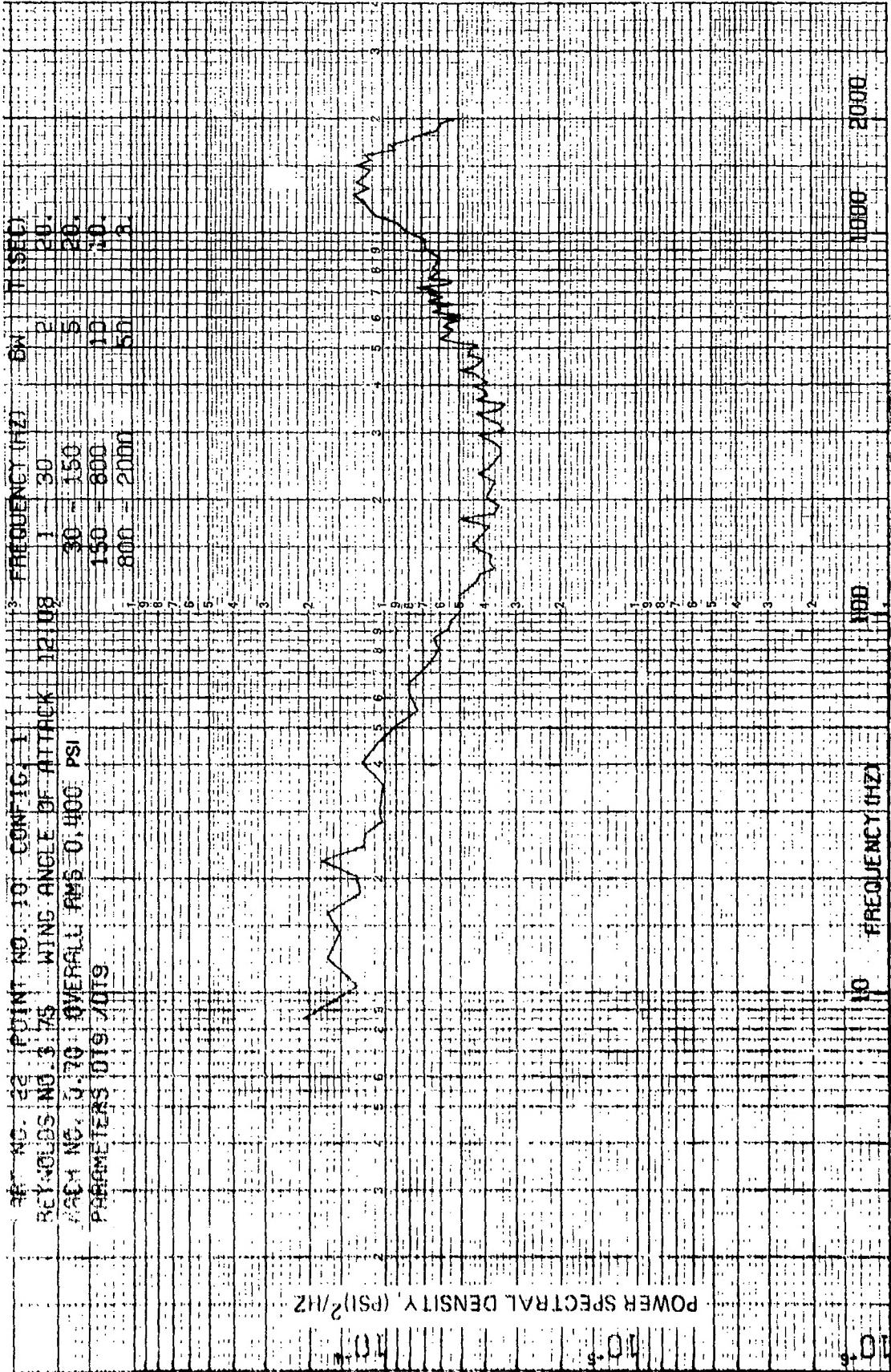


Figure 47 Fluctuating Pressure Power Spectral Density (Configuration 1, Mach 0.7,
 Wing Angle of Attack 12 Deg., Transducer 9)

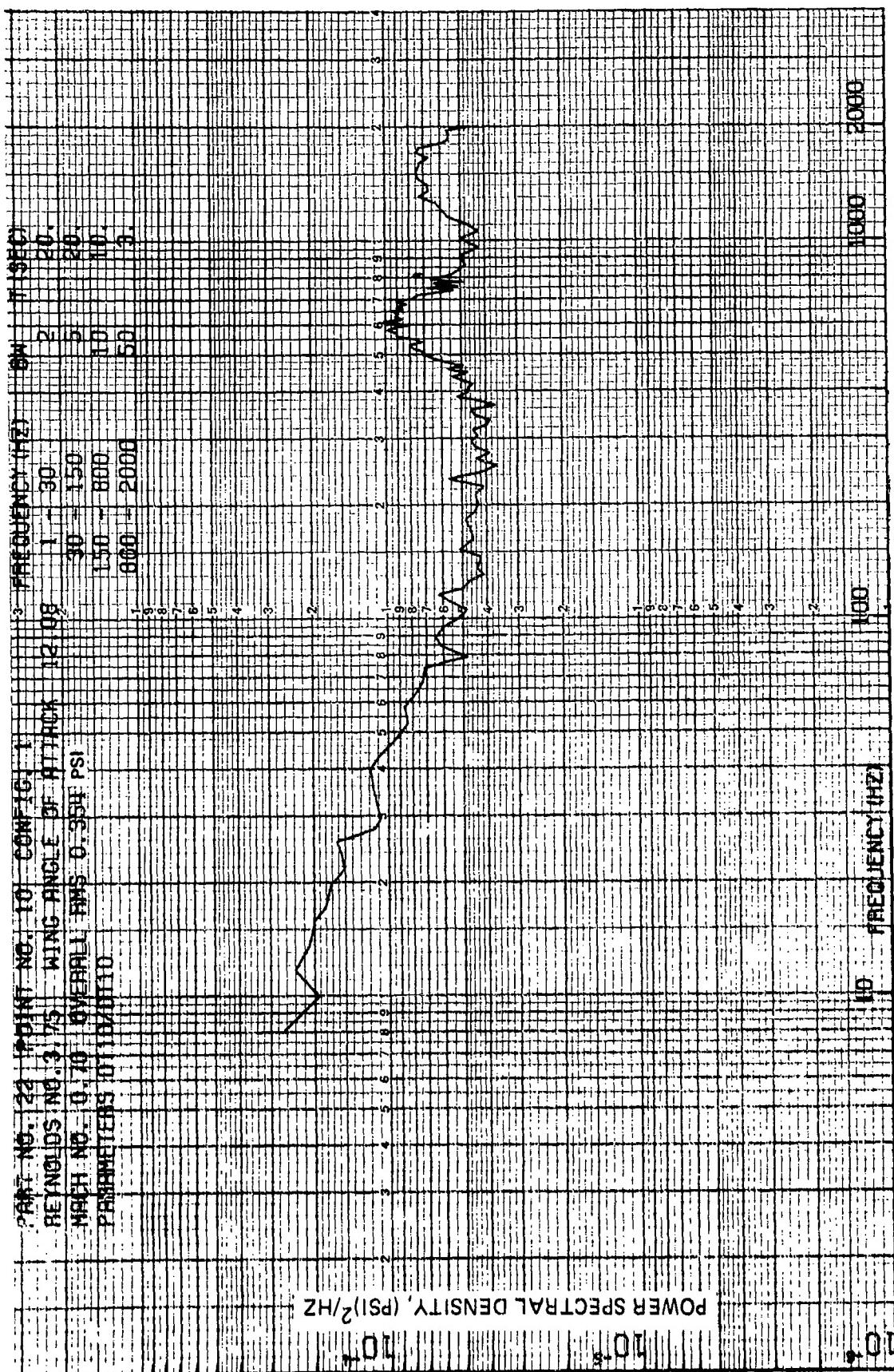


Figure 48 Fluctuating Pressure Power Spectral Density (Configuration 1, Mach 0.7,
 Wing Angle of Attack 12 Deg., Transducer 10)

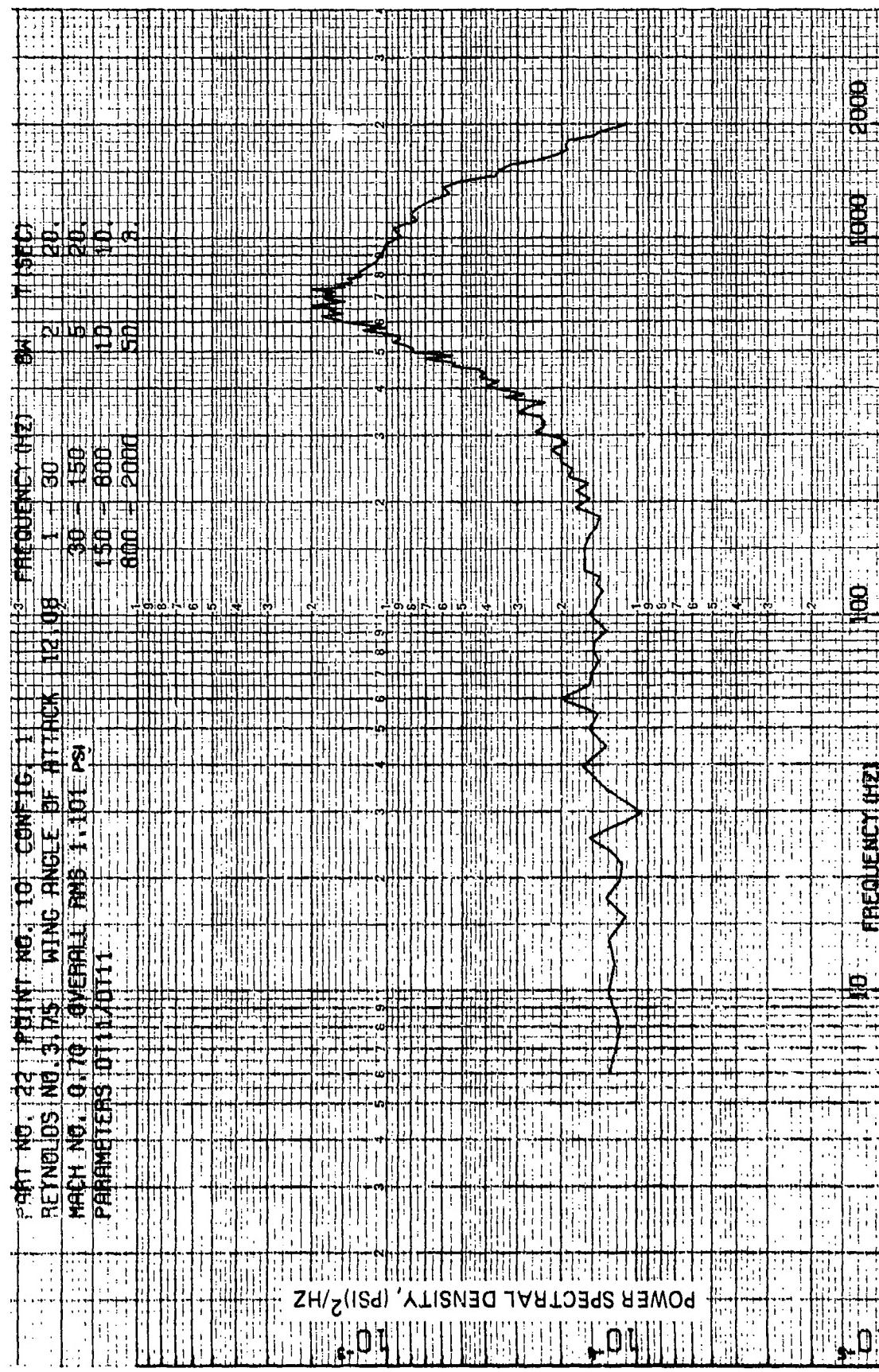


Figure 49 Fluctuating Pressure Power Spectral Density (Configuration 1, Mach 0.7,
Wing Angle of Attack 12 Deg., Transducer 11)

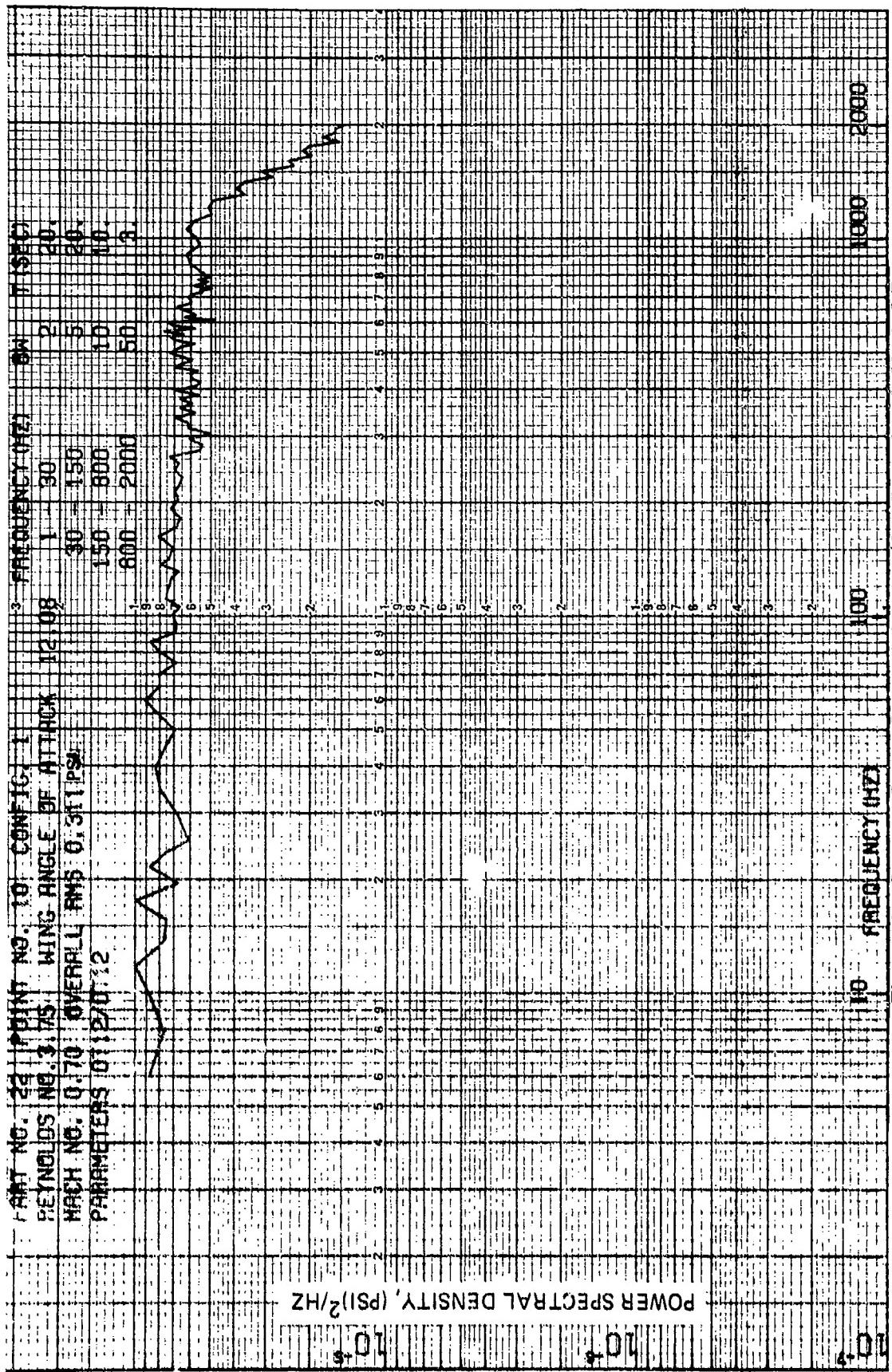


Figure 50 Fluctuating Pressure Power Spectral Density (Configuration 1, Mach 0.7, Wing Angle of Attack 12 Deg., Transducer 12)

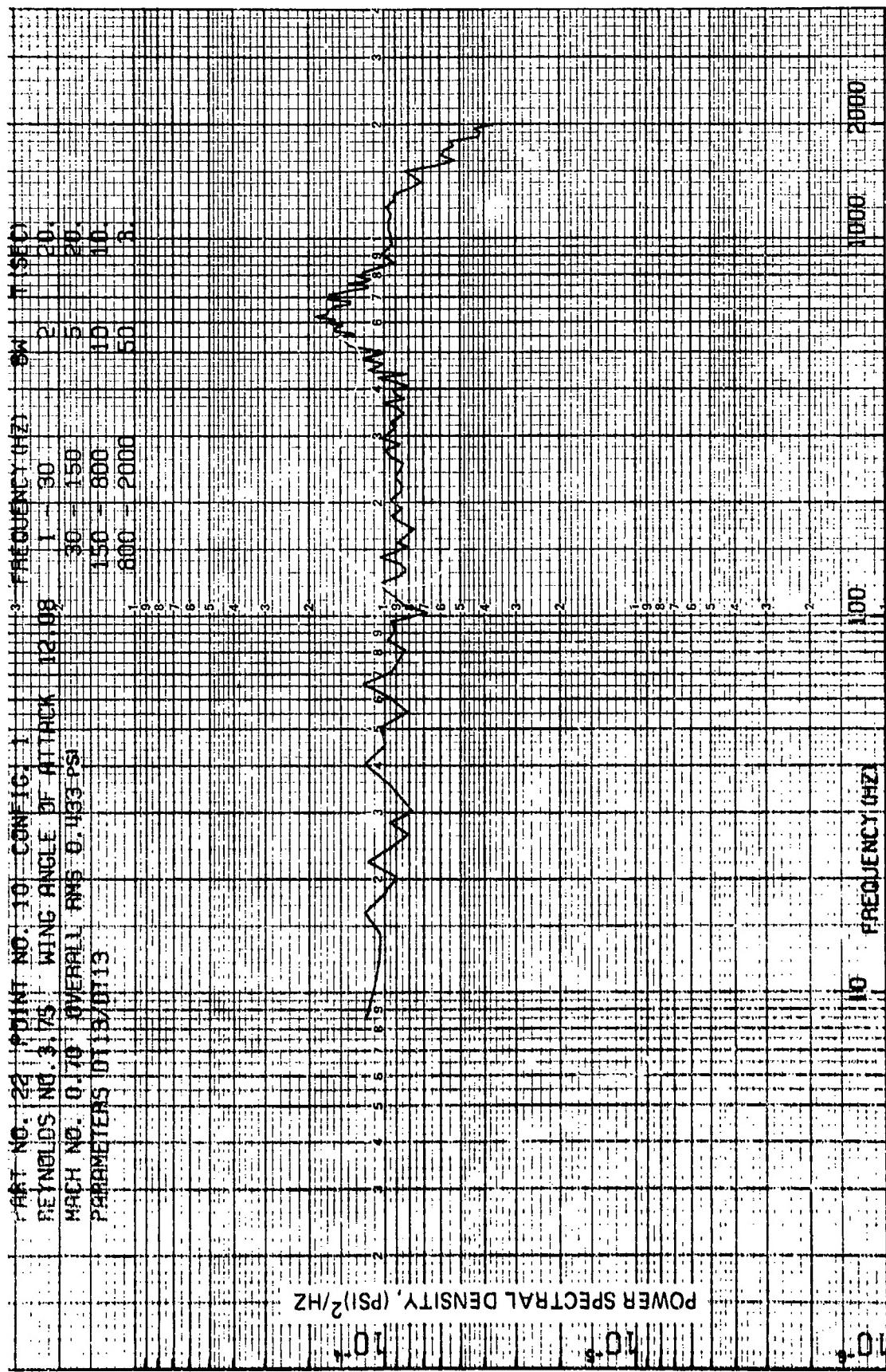


Figure 51 Fluctuating Pressure Power Spectral Density (Configuration 1, Mach 0.7, Wing Angle of Attack 12 Deg., Transducer 13)

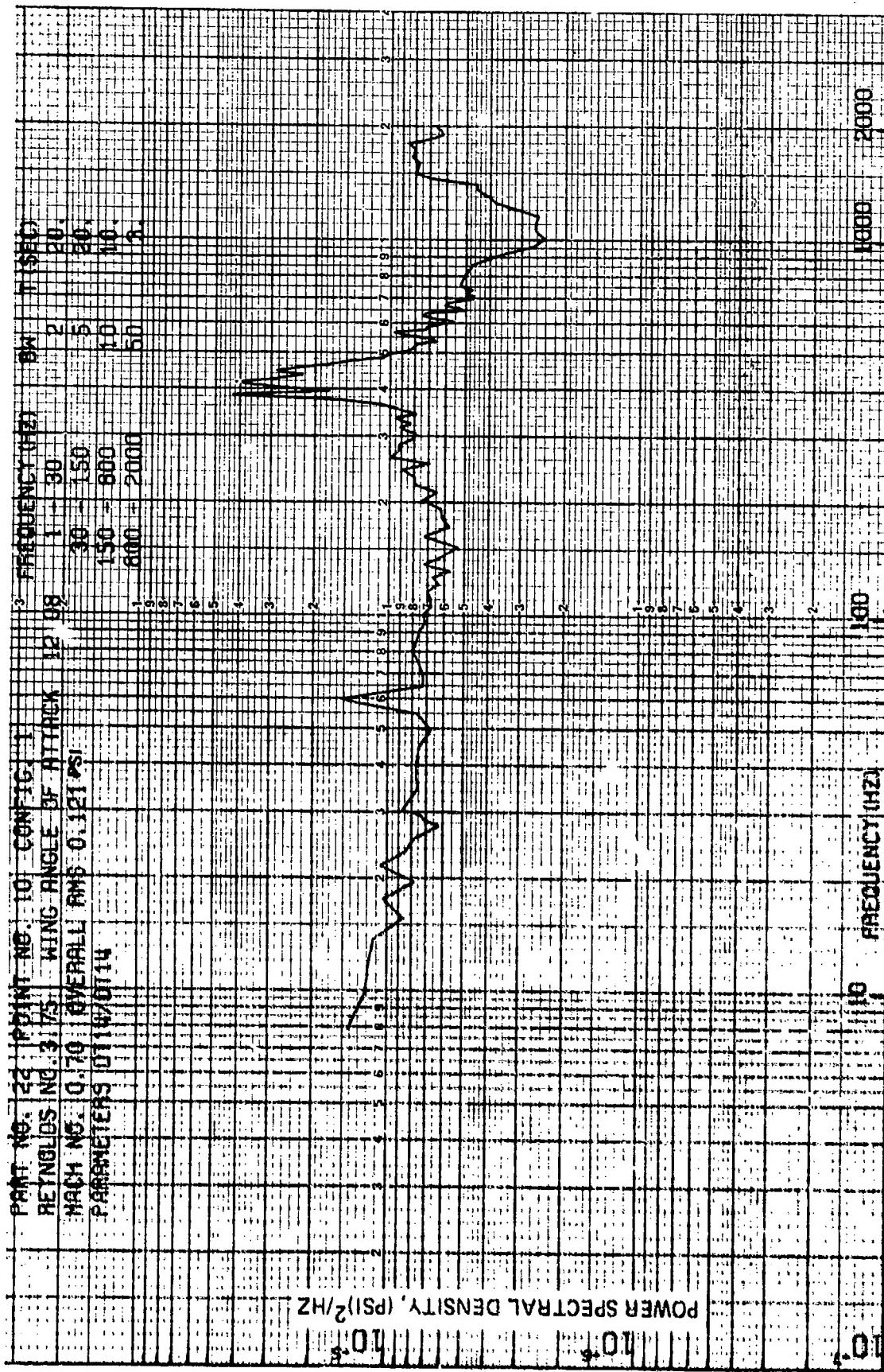


Figure 52 Fluctuating Pressure Power Spectral Density (Configuration 1, Mach 0.7,
 Wing Angle of Attack 12 Deg., Transducer 14)

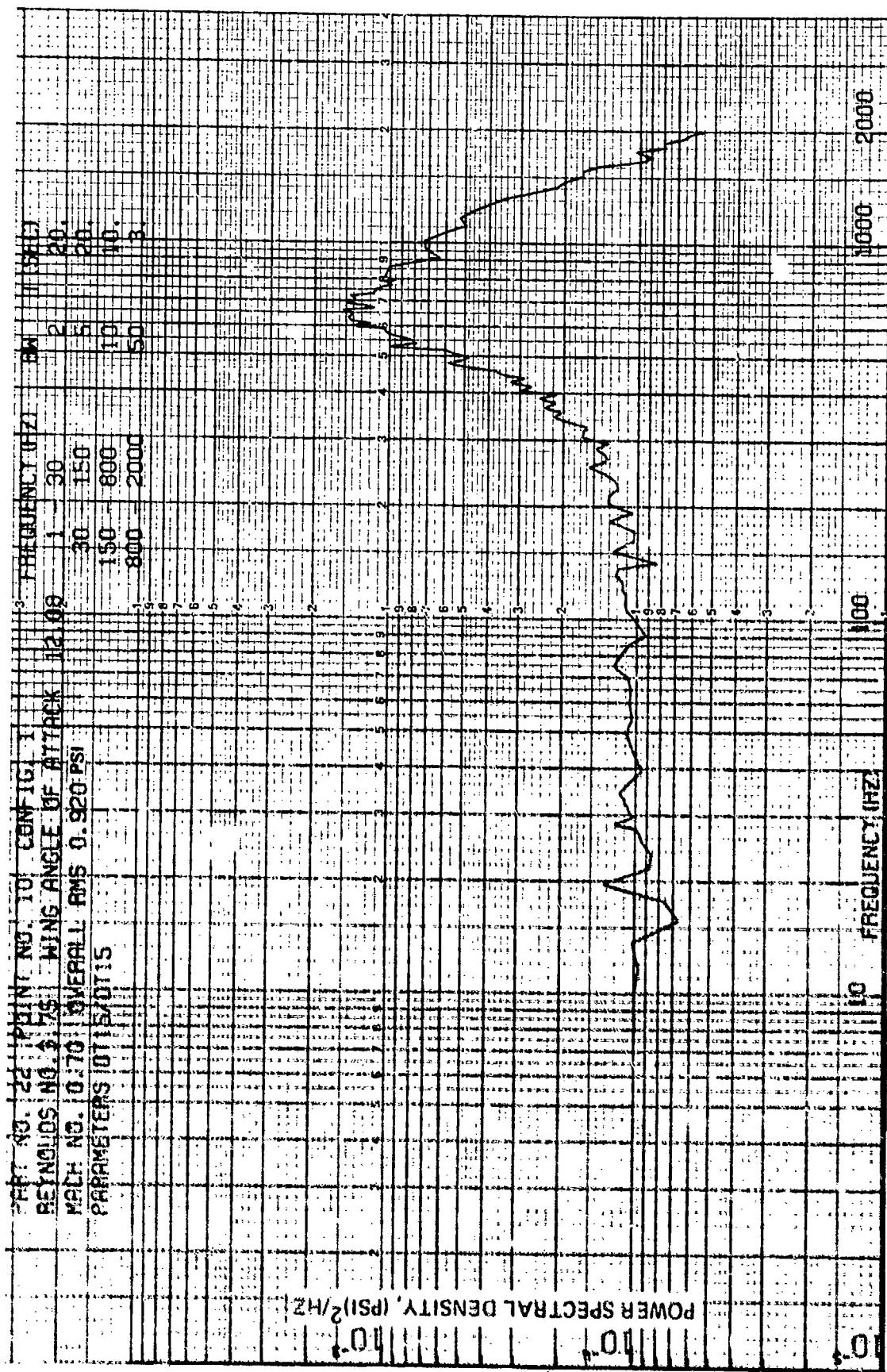


Figure 53 Fluctuating Pressure Power Spectral Density (Configuration 1, Mach 0.7)
 Wing Angle of Attack 12 Deg., Transducer 15

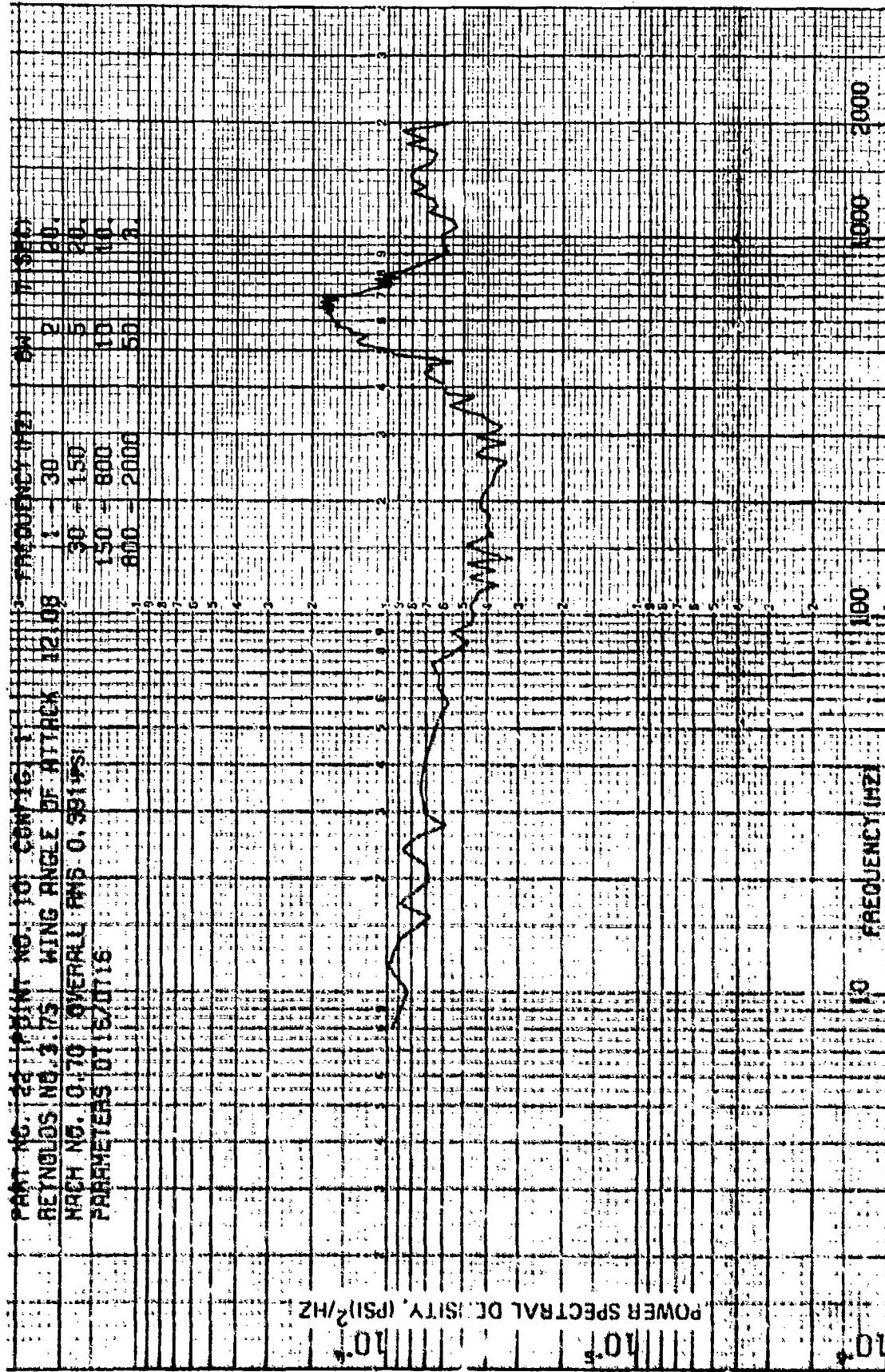


Figure 54 Fluctuating Pressure Power Spectral Density (Configuration 1, Mach 0.7, Wing Angle of Attack 12 Deg., Transducer 16)

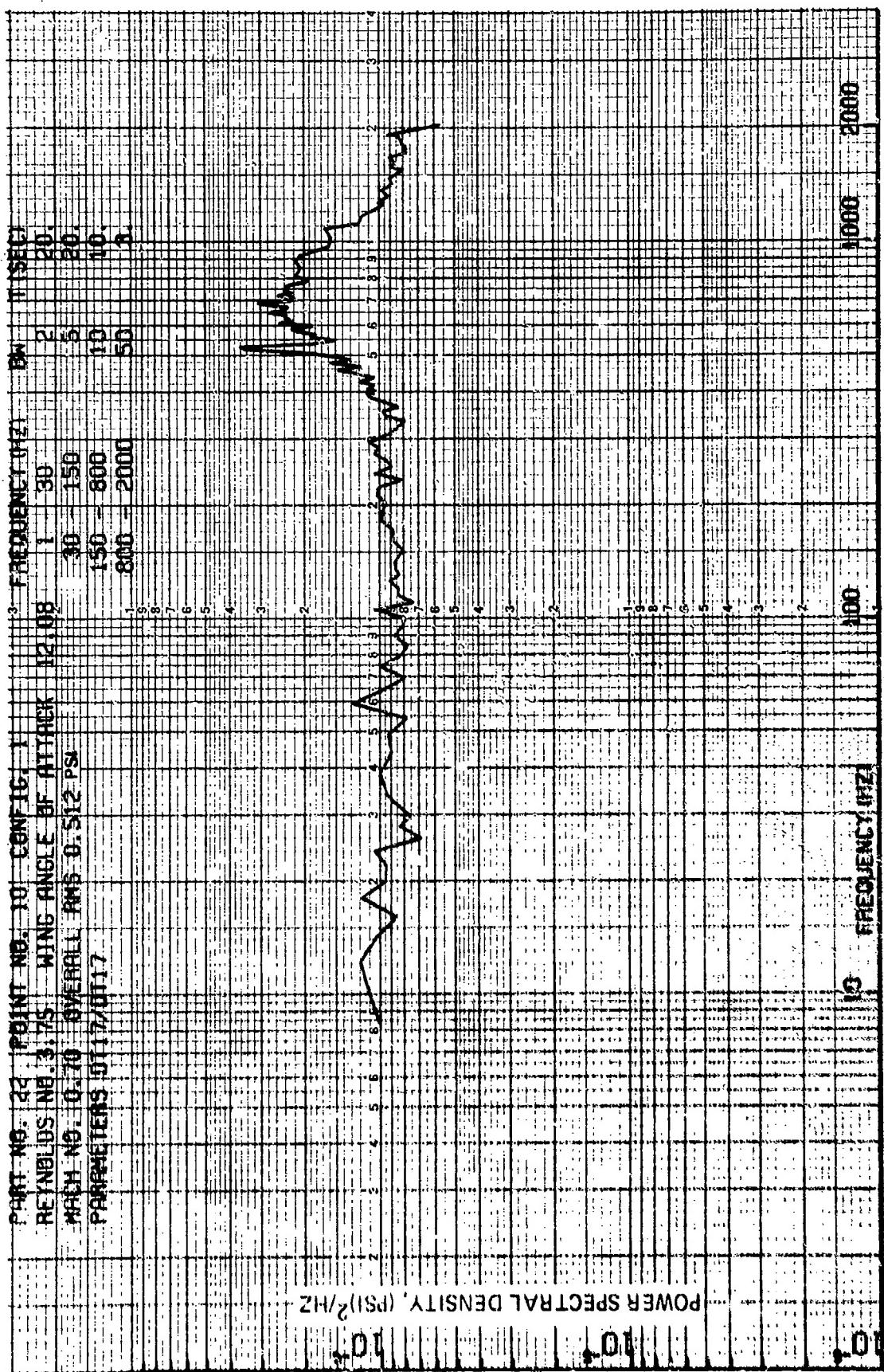


Figure 55 Fluctuating Pressure Power Spectral Density (Configuration 1, Mach 0.7, Wing Angle of Attack 12 Deg., Transducer 17)

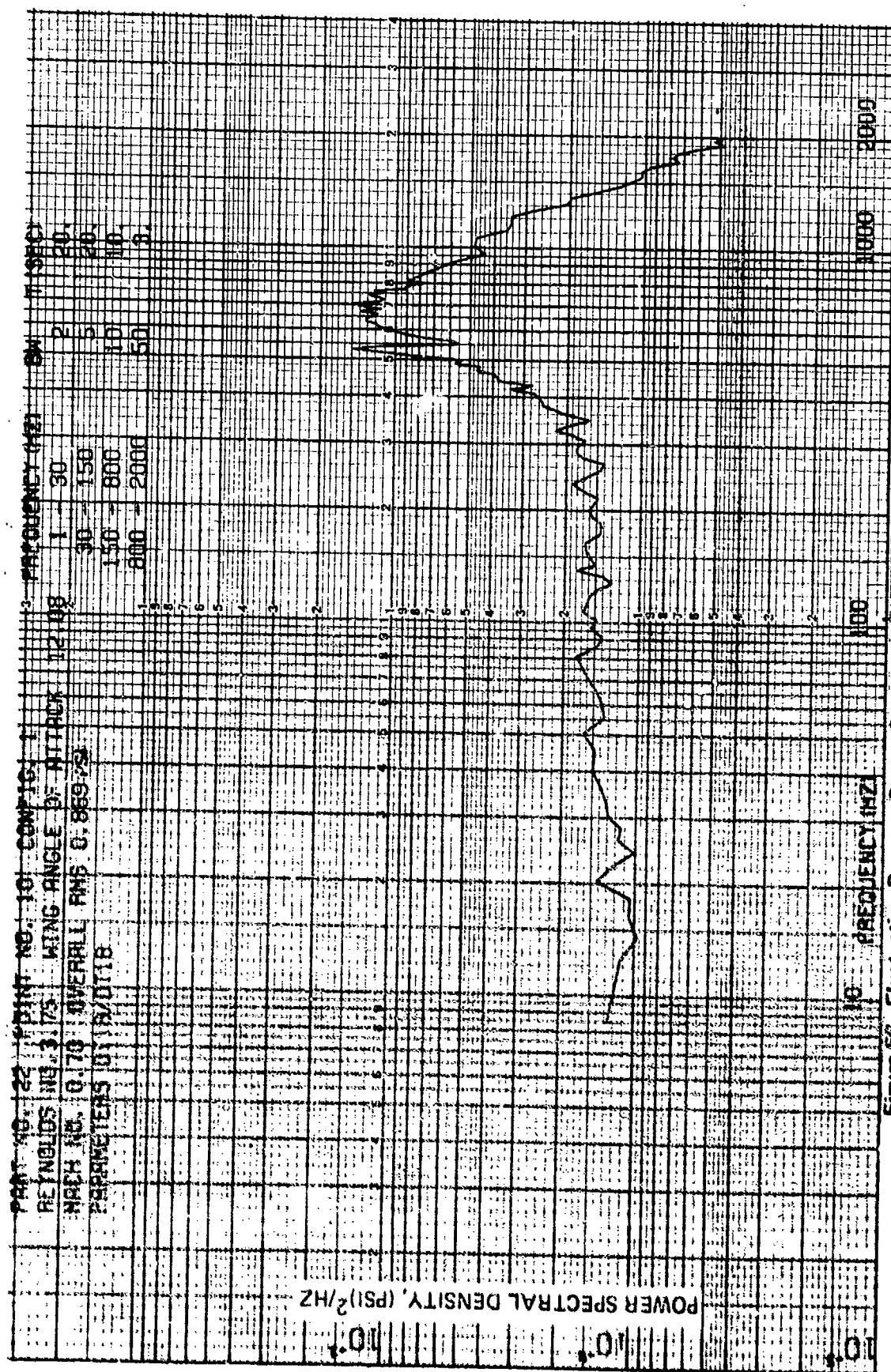


Figure 52 Fluctuating Pressure Power Spectral Density (Configuration 1, Mach 0.7,
 Wing Angle of Attack 12 Deg., Transducer 18)

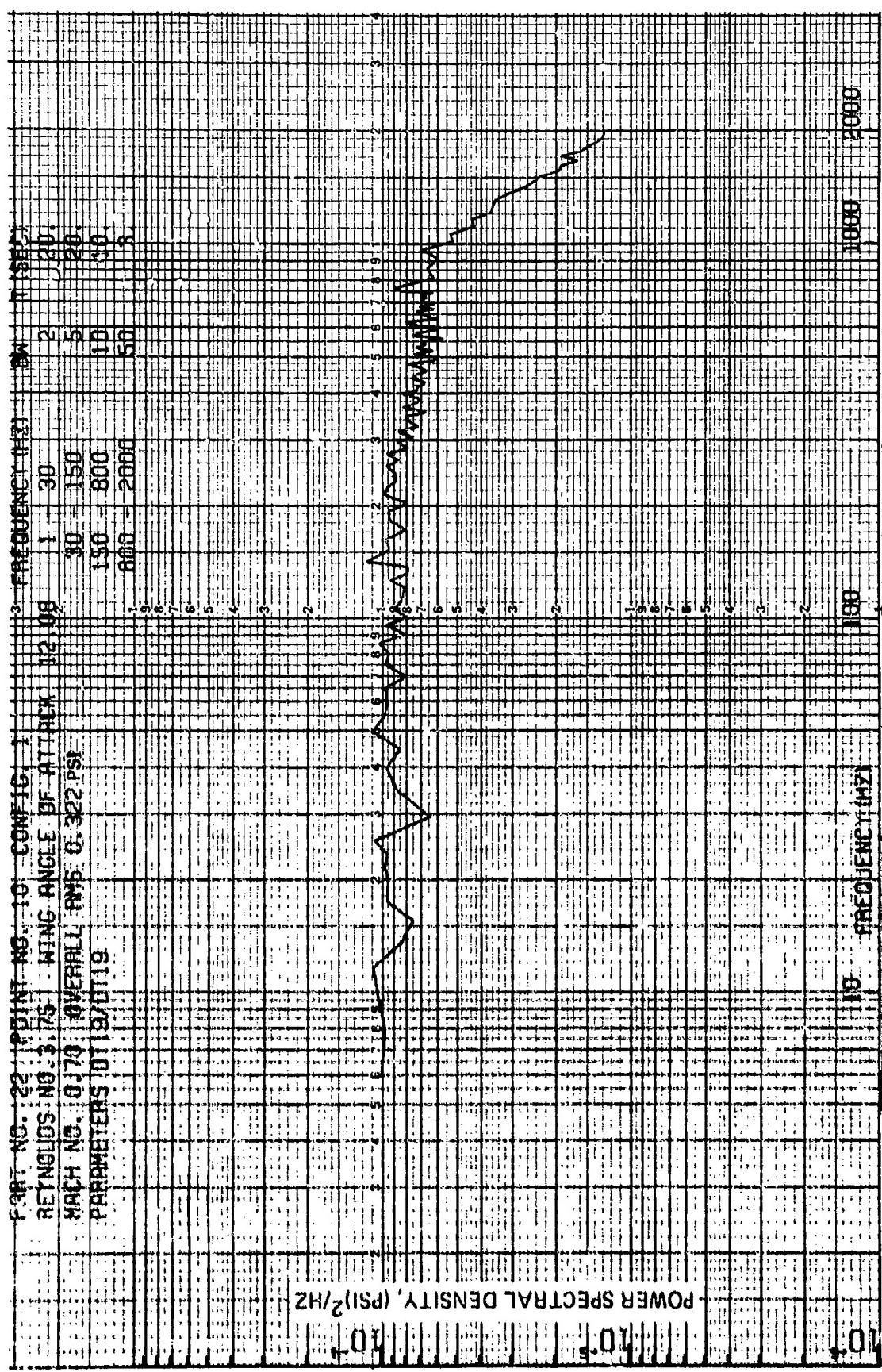


Figure 57 Fluctuating Pressure Power Spectral Density (Configuration 1, Mach 0.7),
Wing Angle of Attack 12 Deg., Transducer 19)

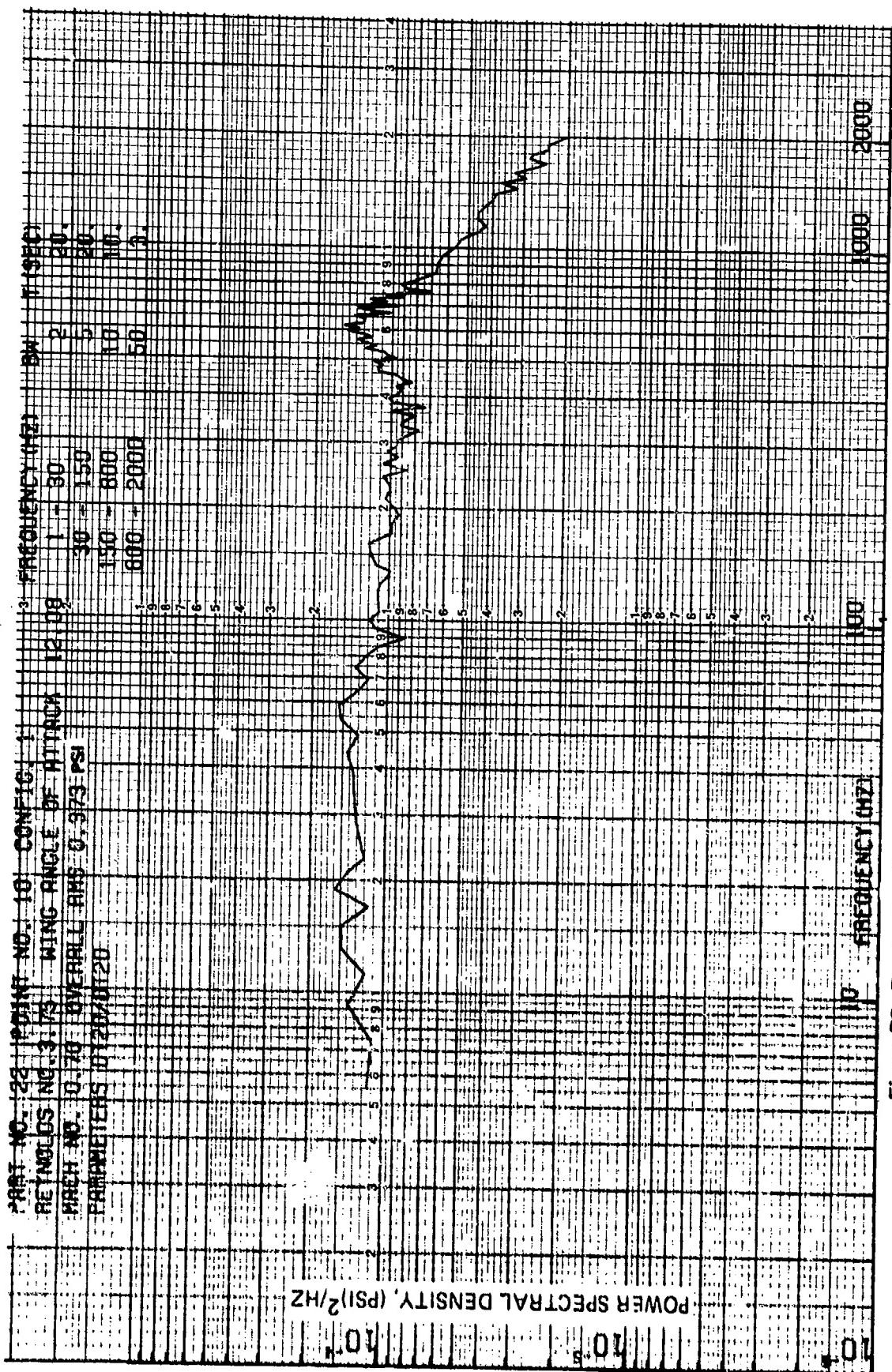


Figure 58 Fluctuating Pressure Power Spectral Density (Configuration 1, Mach 0.7,
 Wing Angle of Attack 12 Deg., Transducer 20)

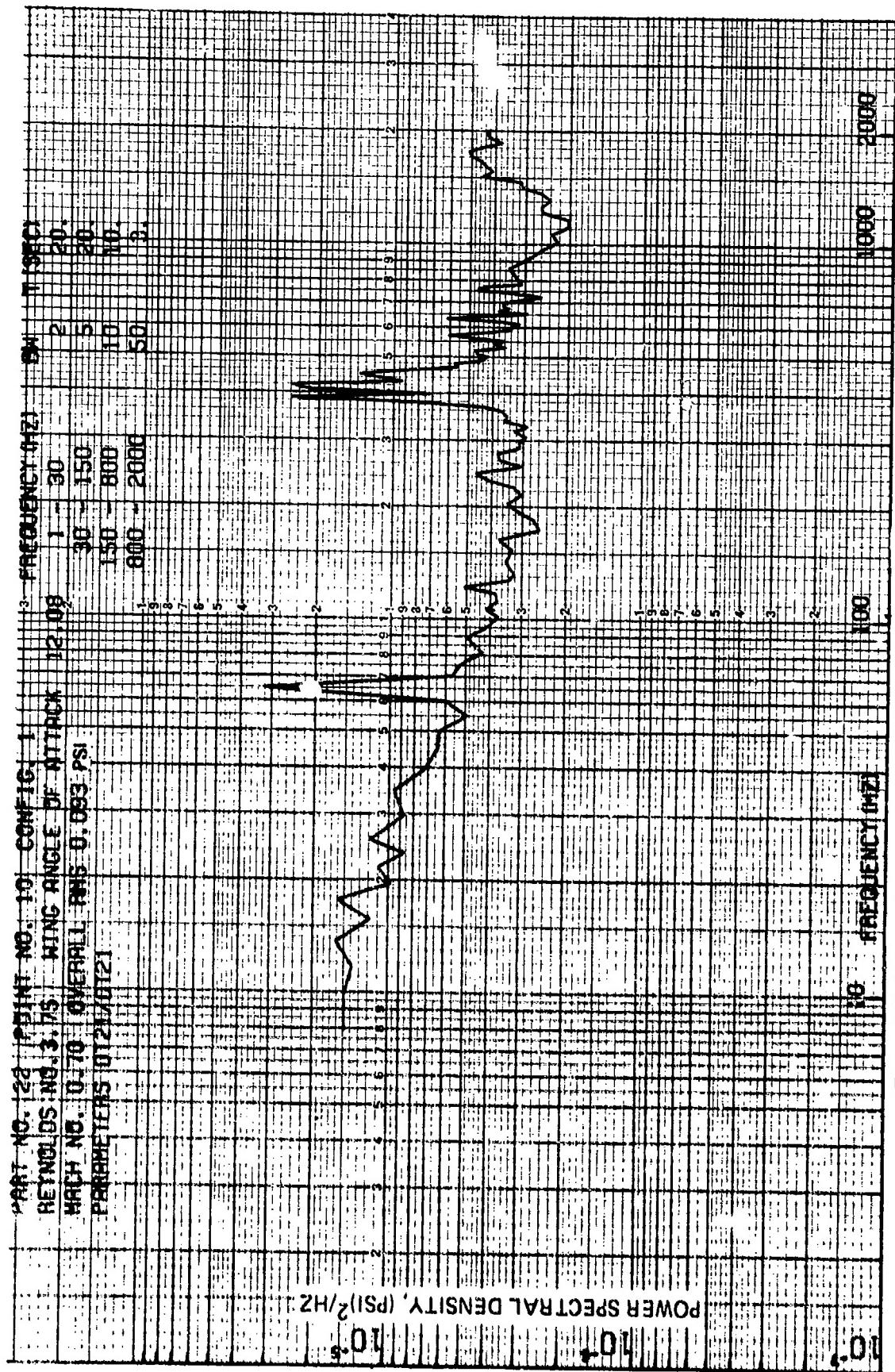


Figure 59 Fluctuating Pressure Power Spectral Density (Configuration 1, Mach 0.7,
 Wing Angle of Attack 12 Deg., Transducer 21)

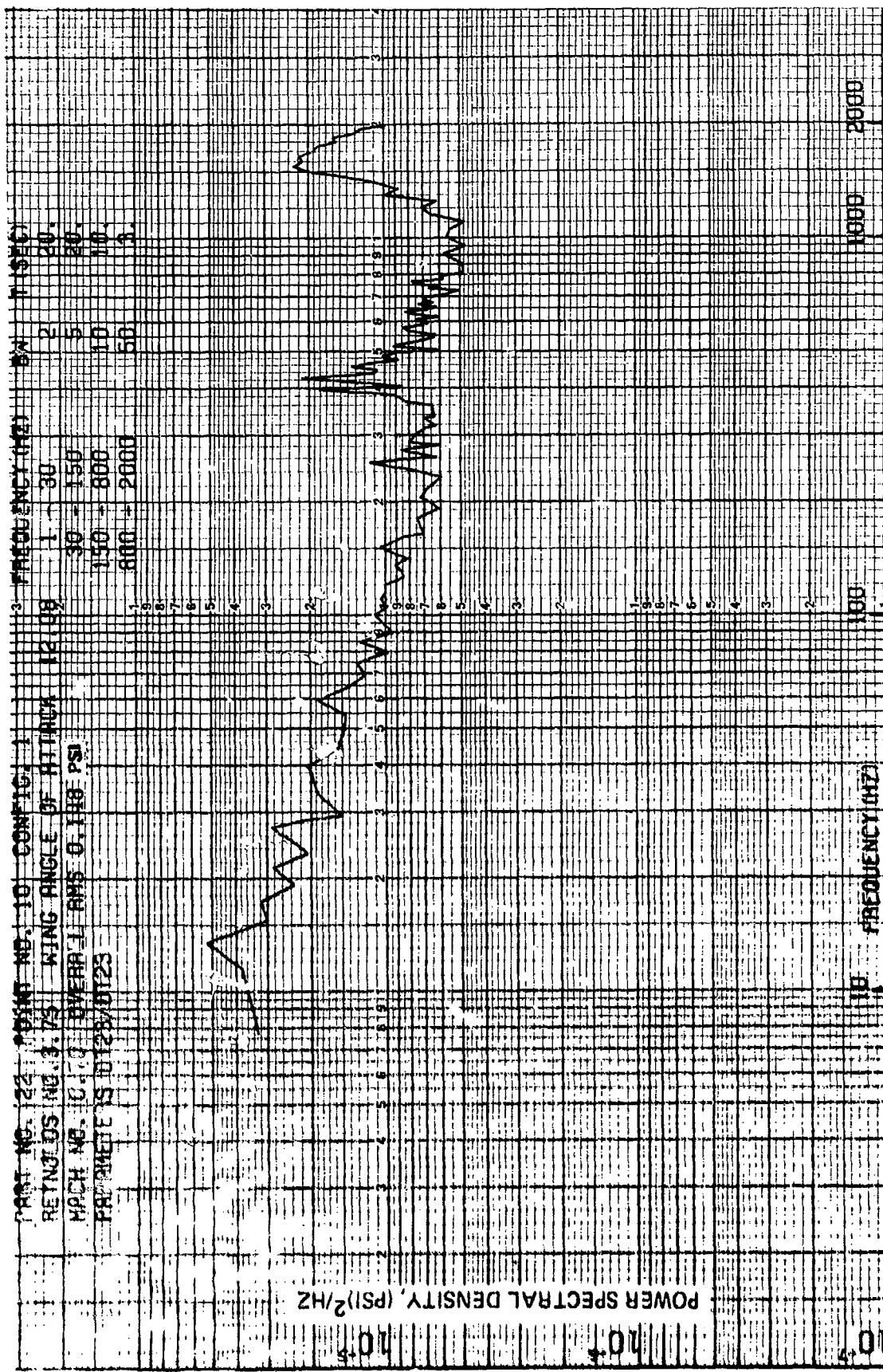


Figure 60 Fluctuating Pressure Power Spectral Density (Configuration 1, Mach 0.7, Wing Angle of Attack 12 Deg., Transducer 23)

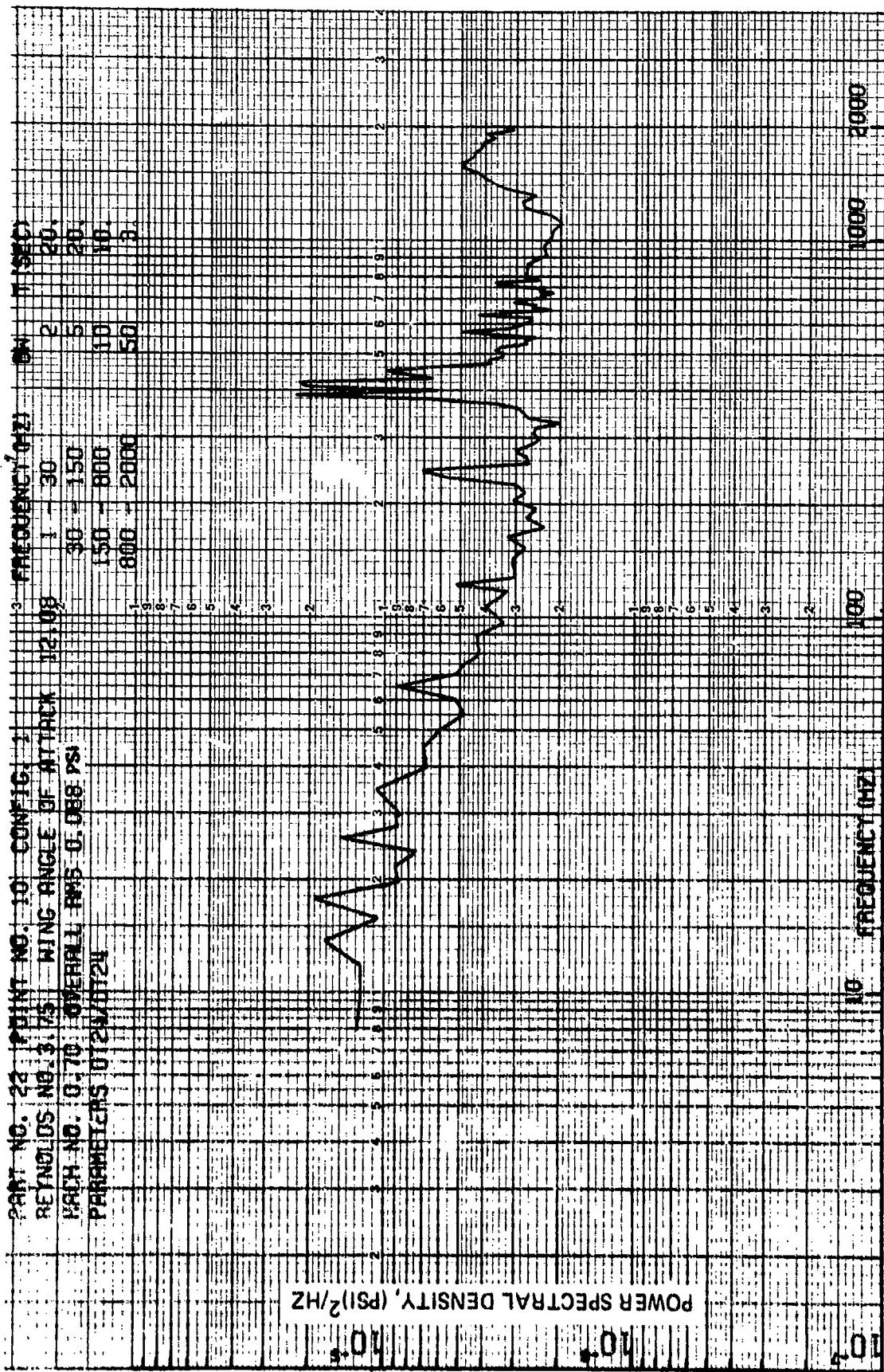


Figure 61 Fluctuating Pressure Power Spectral Density (Configuration 1, Mach 0.7, Wing Angle of Attack 12 Deg., Transducer 24)

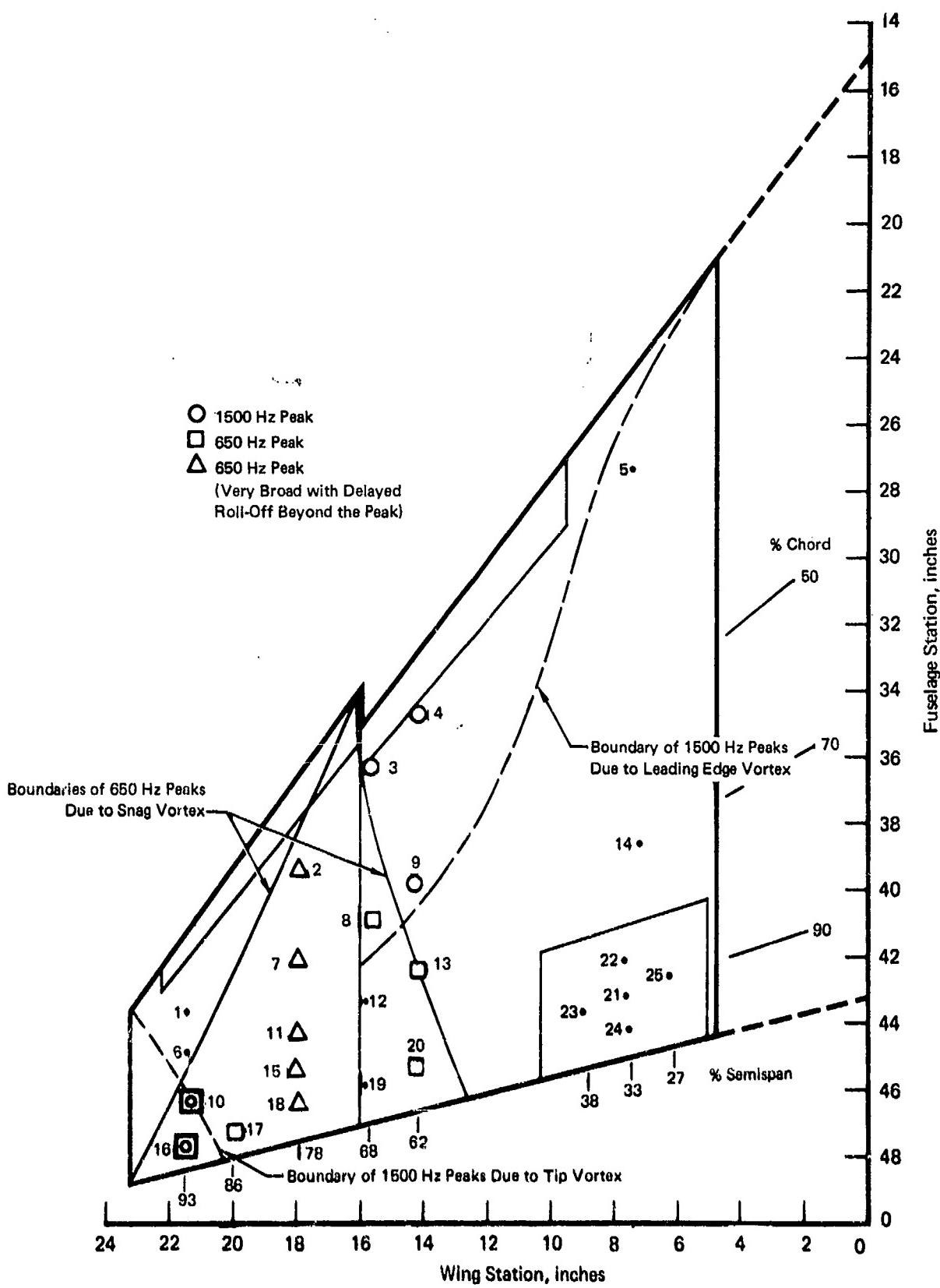


Figure 62 Wing Locations at which Peaks are Evident in Pressure Power Spectral Density Functions (Configuration 1, Mach 0.7, Wing Angle of Attack 12°)

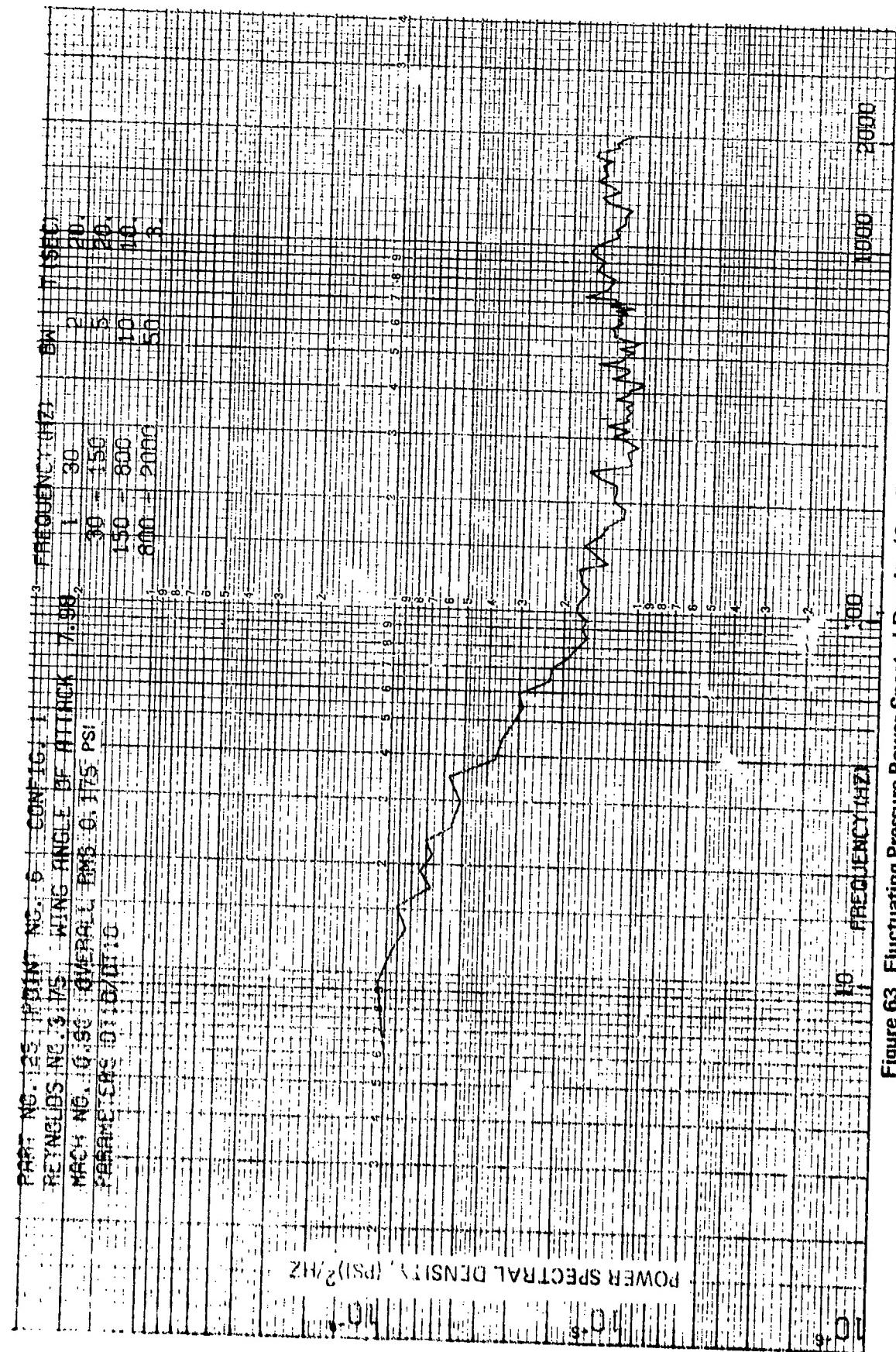


Figure 63 Fluctuating Pressure Power Spectral Density (Configuration 1, Mach 0.9, Wing Angle of Attack 8 Deg., Transducer 10)

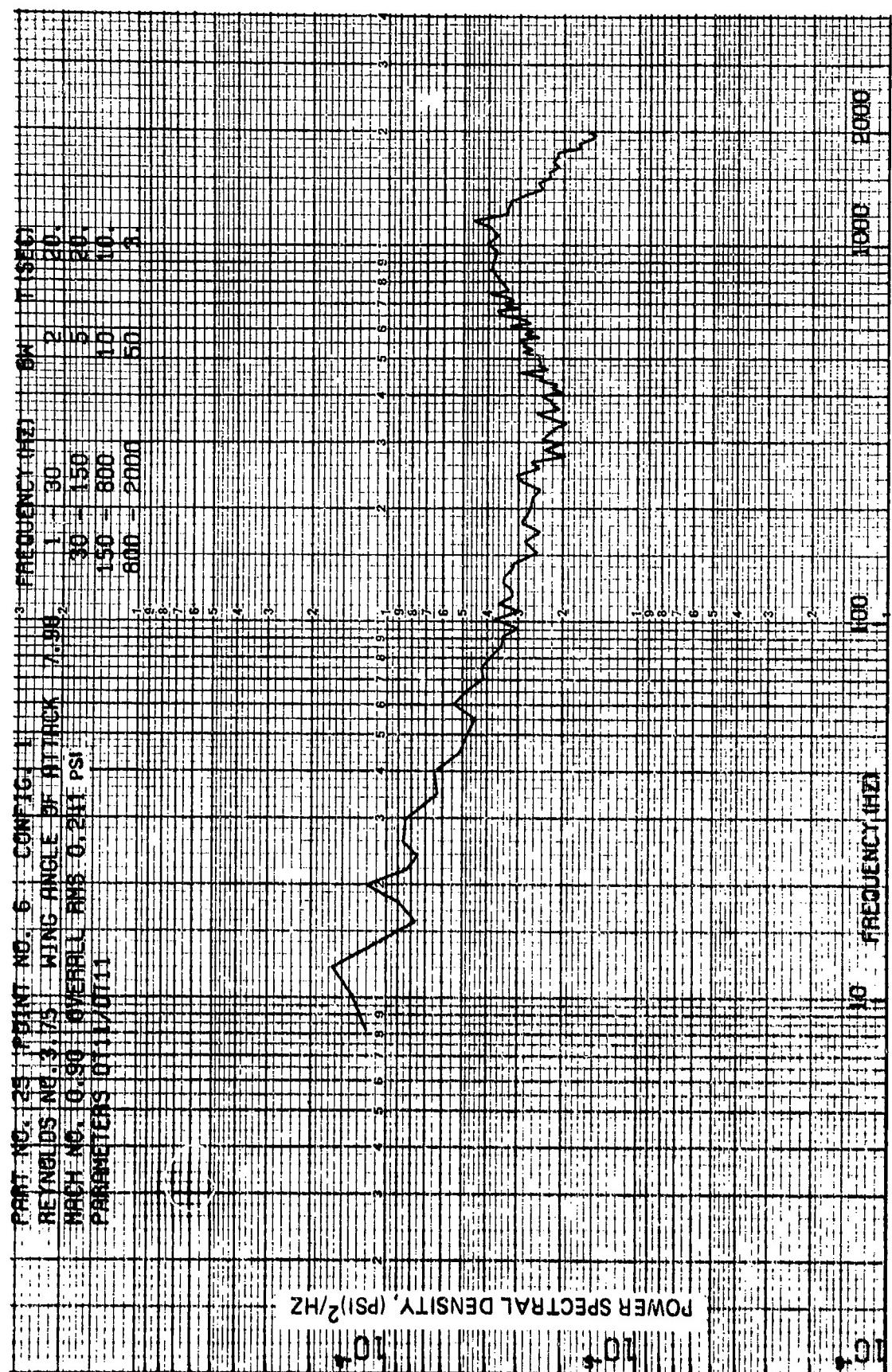


Figure 64 Fluctuating Pressure Power Spectral Density (Configuration 1, Mach 0.9, Wing Angle of Attack 8 Deg., Transducer 11)

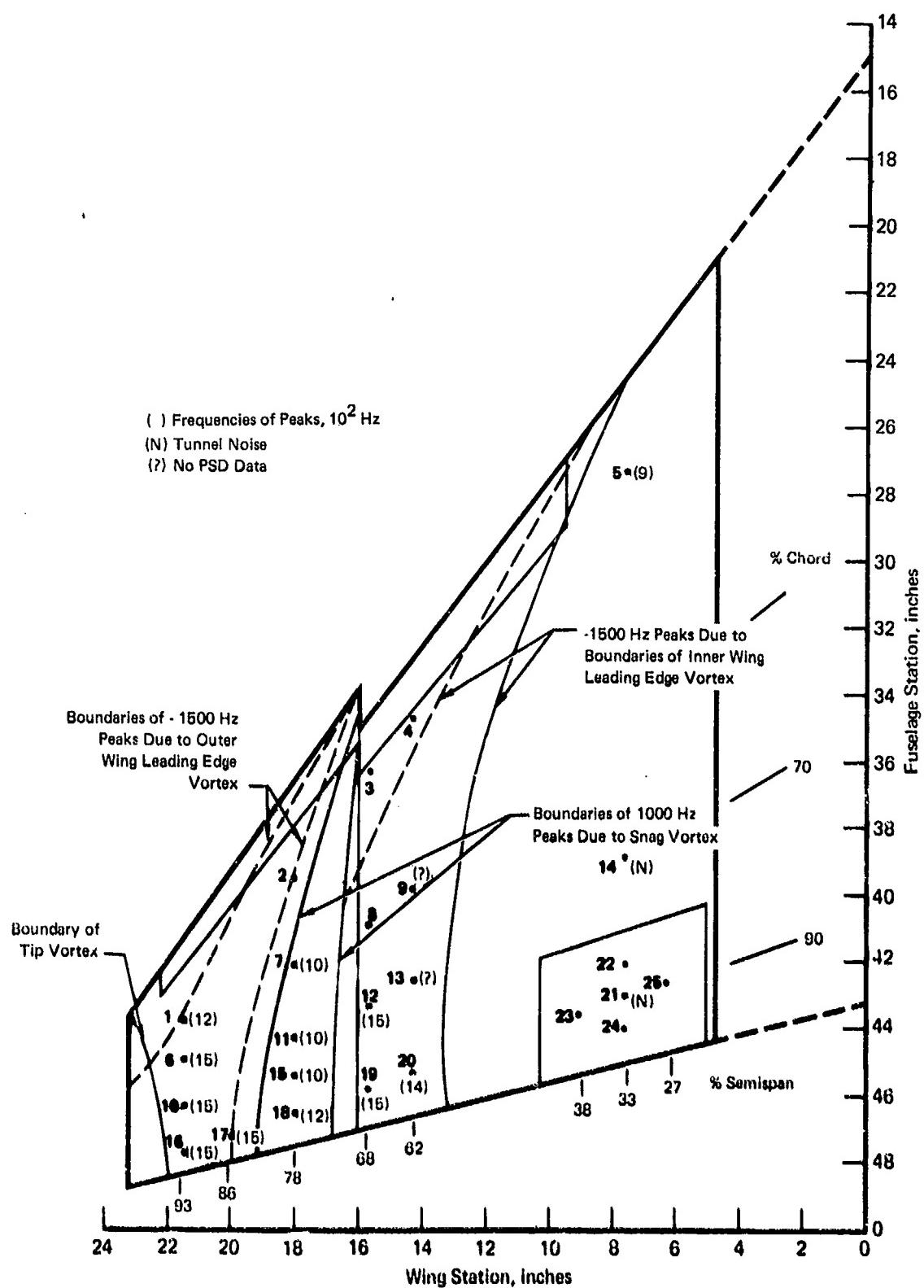


Figure 65 Wing Locations at which Peaks are Evident in Pressure Power Spectral Density Functions
(Configuration 1, Mach 0.9, Wing Angle of Attack 8°)

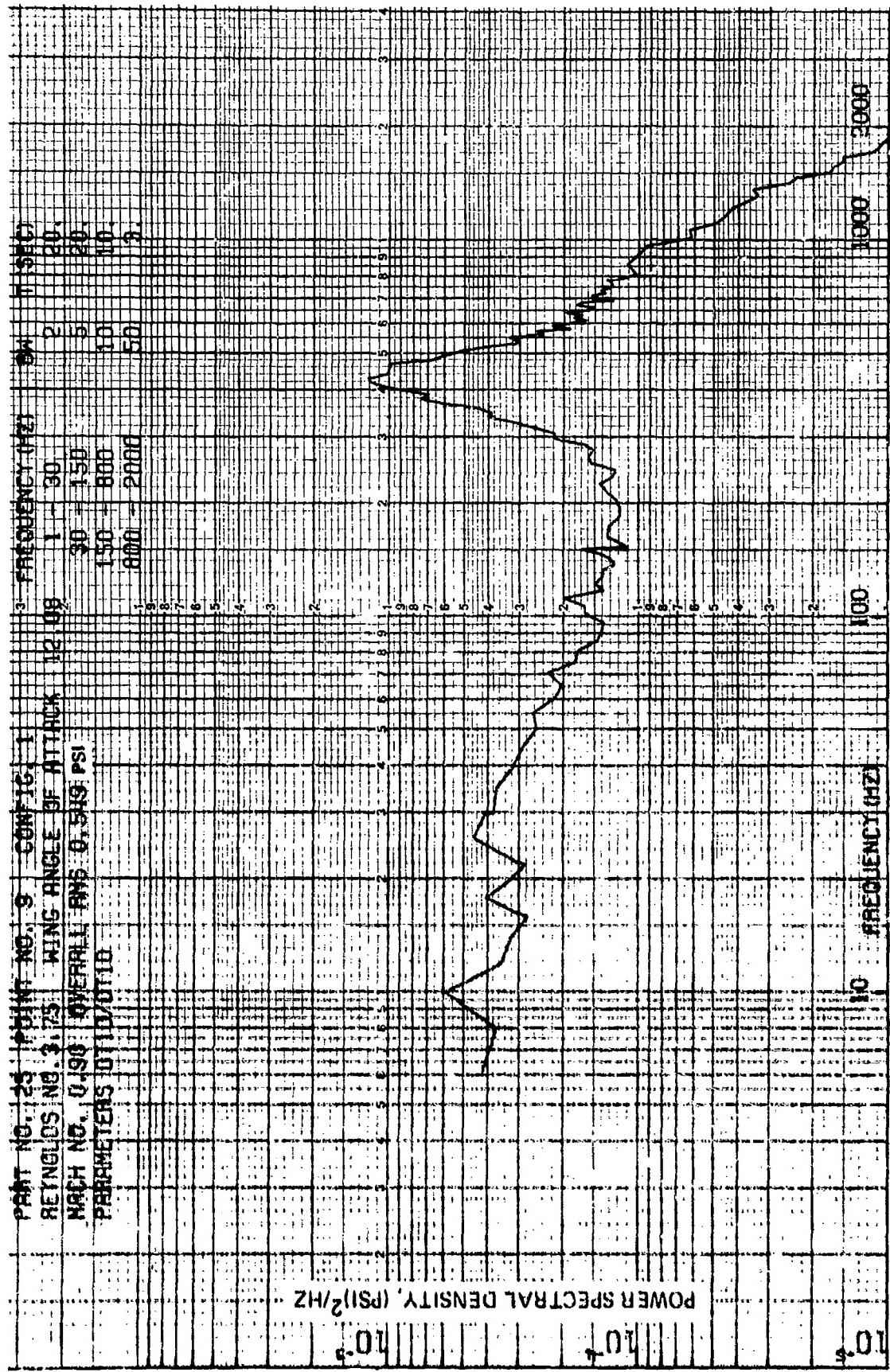
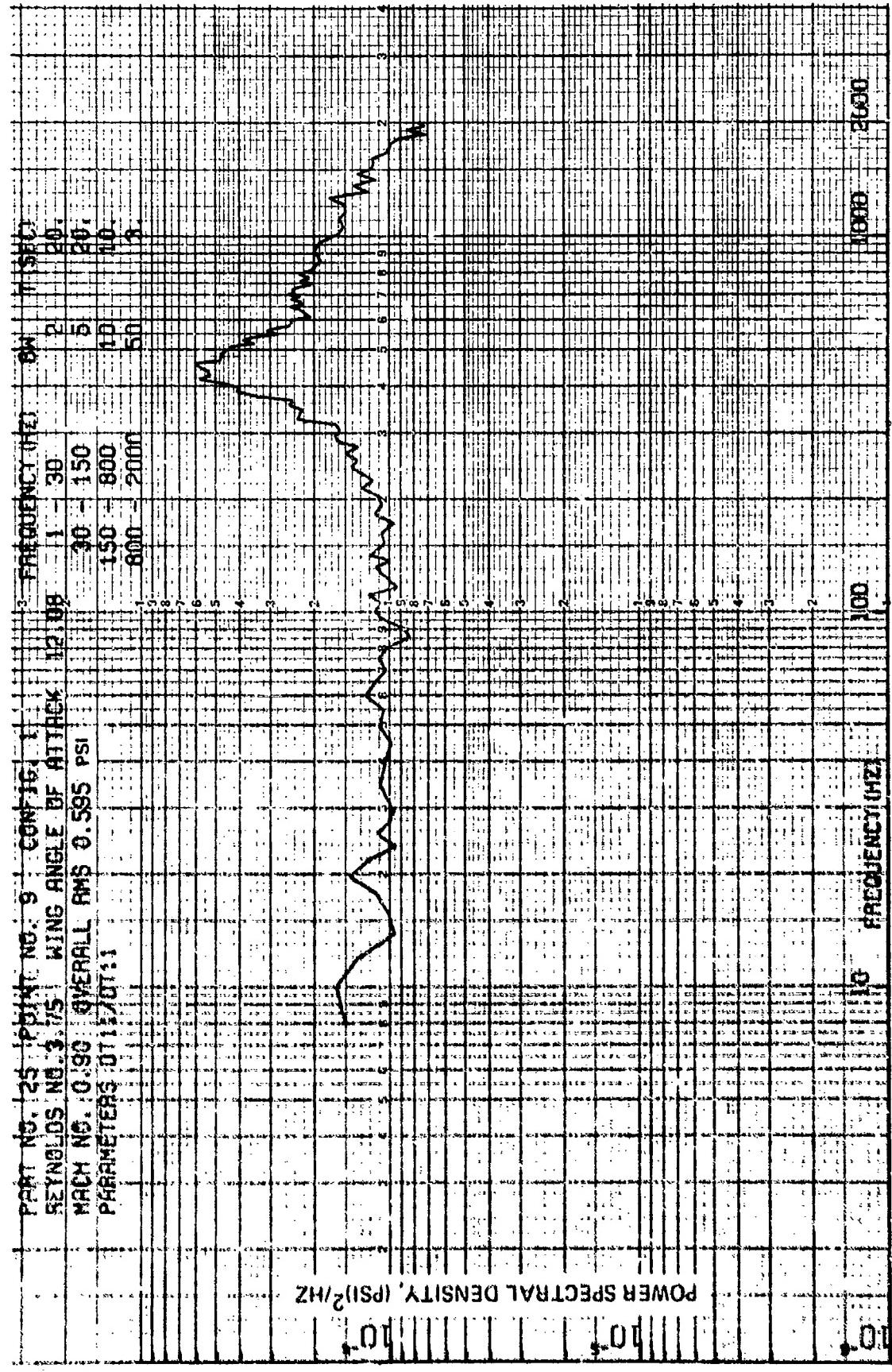


Figure 66 Fluctuating Pressure Power Spectral Density (Configuration 1, Mach 0.9,
Wing Angle of Attack 12 Deg., Transducer 10)



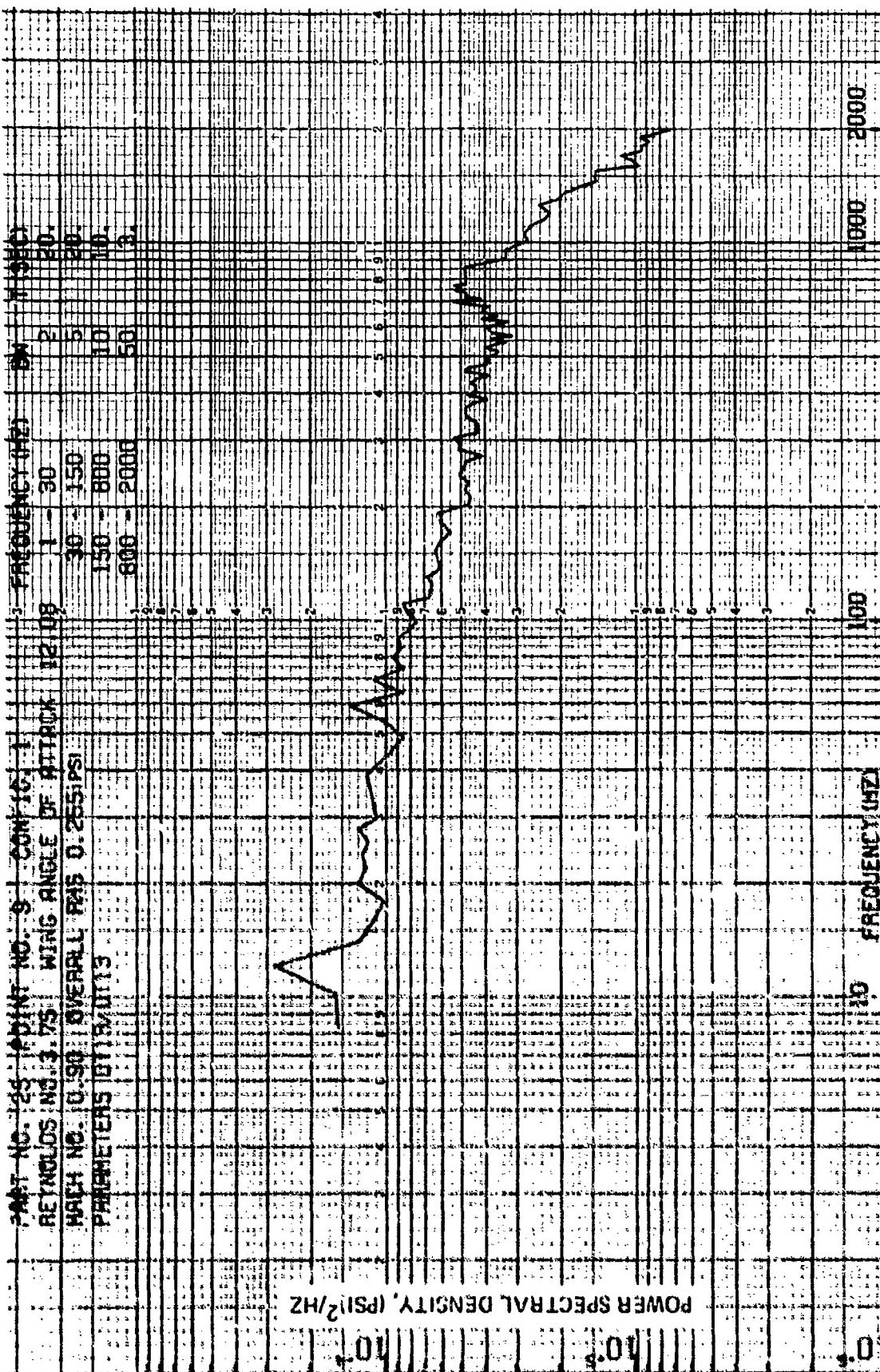


Figure 68 Fluctuating Pressure Power Spectral Density (Configuration 1, Mach 0.9,
 Wing Angle of Attack 12 Deg., Transducer 13)

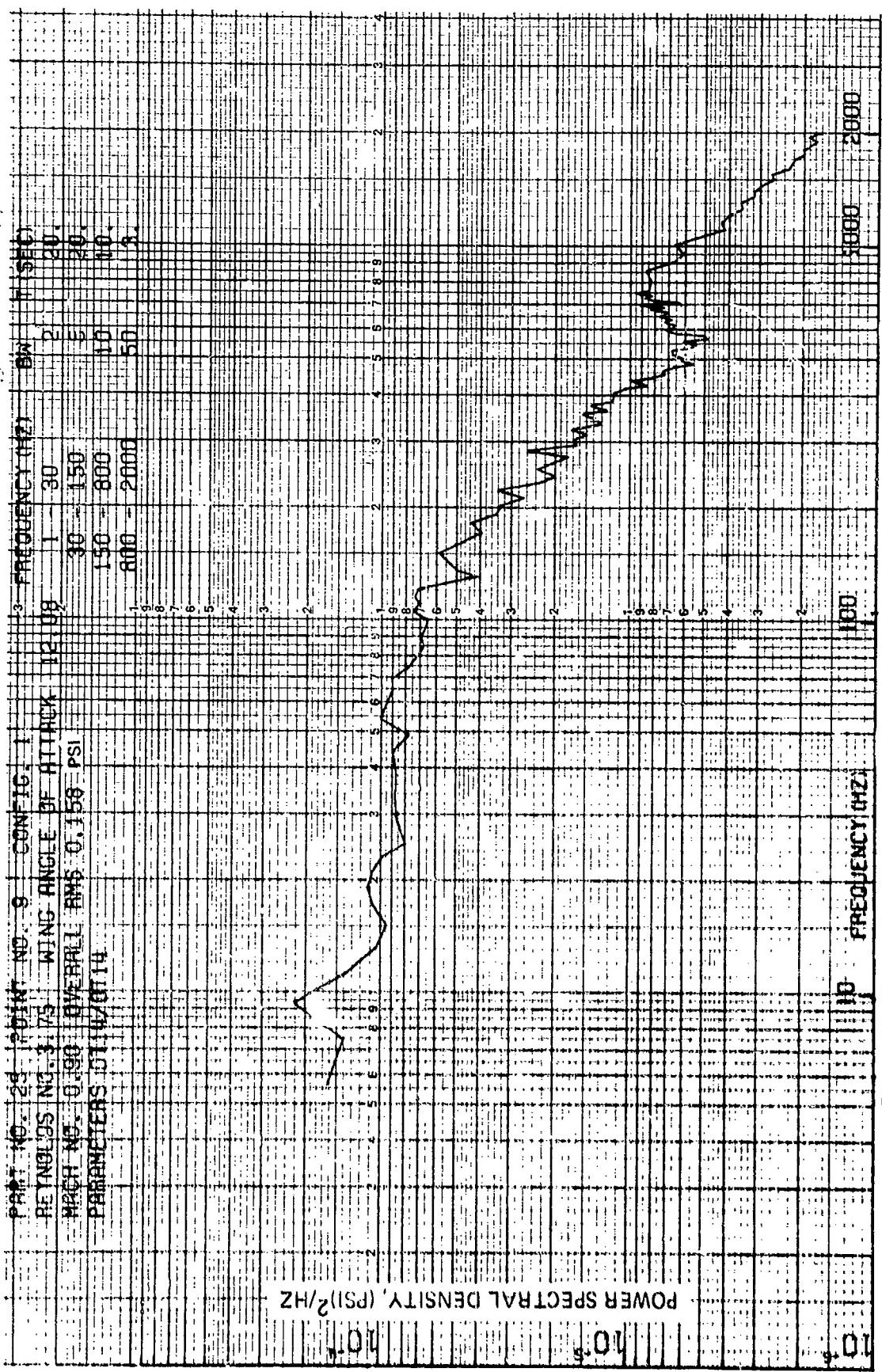


Figure 69 Fluctuating Pressure Power Spectral Density (Configuration 1, Mach 0.9, Wing Angle of Attack 12 Deg., Transducer 14)

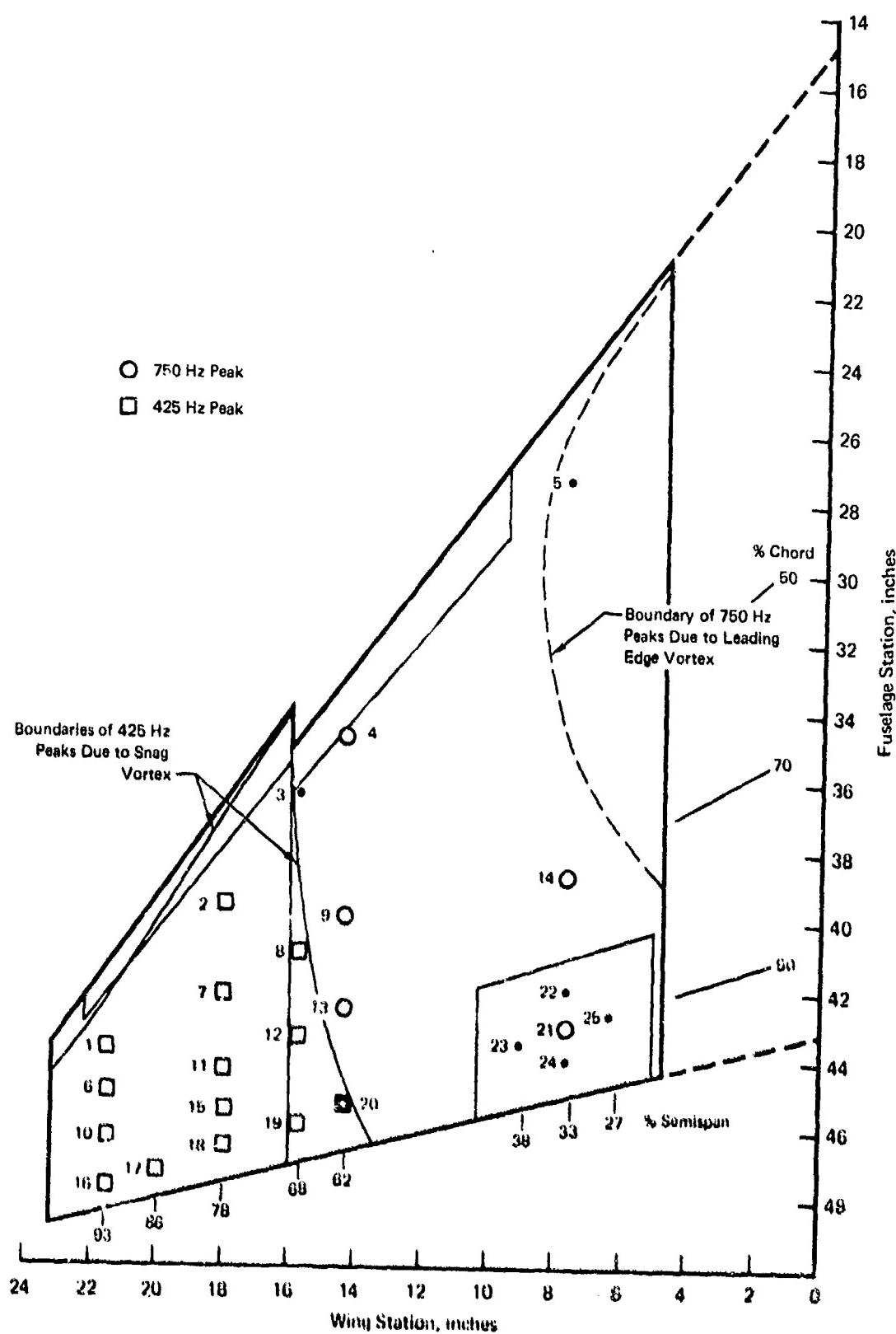


Figure 70 Wing Locations at which Peaks are Evident in Pressure Power Spectral Density Functions
(Configuration 1, Mach 0.9, Wing Angle of Attack 12°)

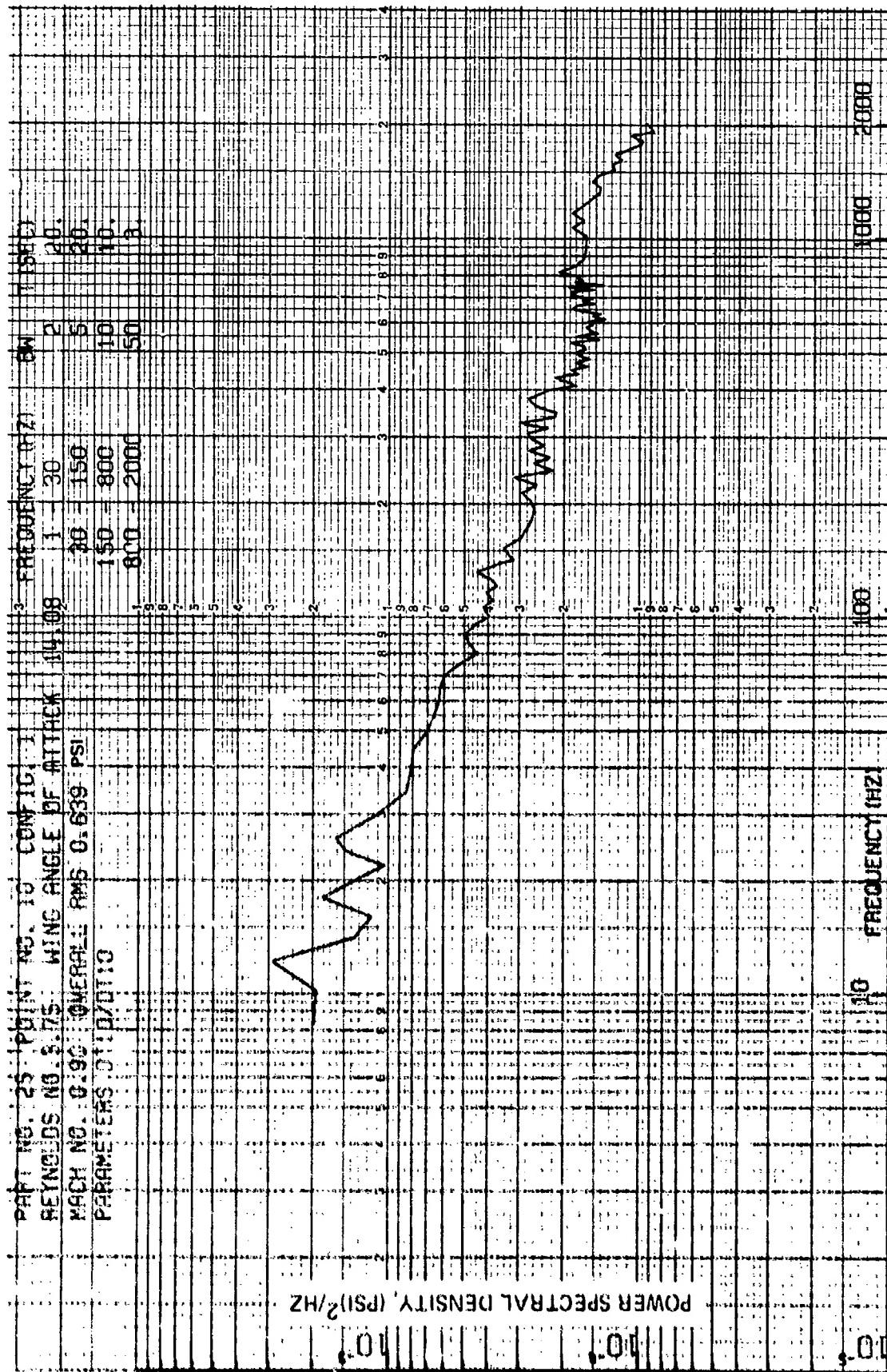


Figure 71 Fluctuating Pressure Power Spectral Density (Configuration 1, Mach 0.9,
 Wing Angle of Attack 14 Deg., Transducer 10)

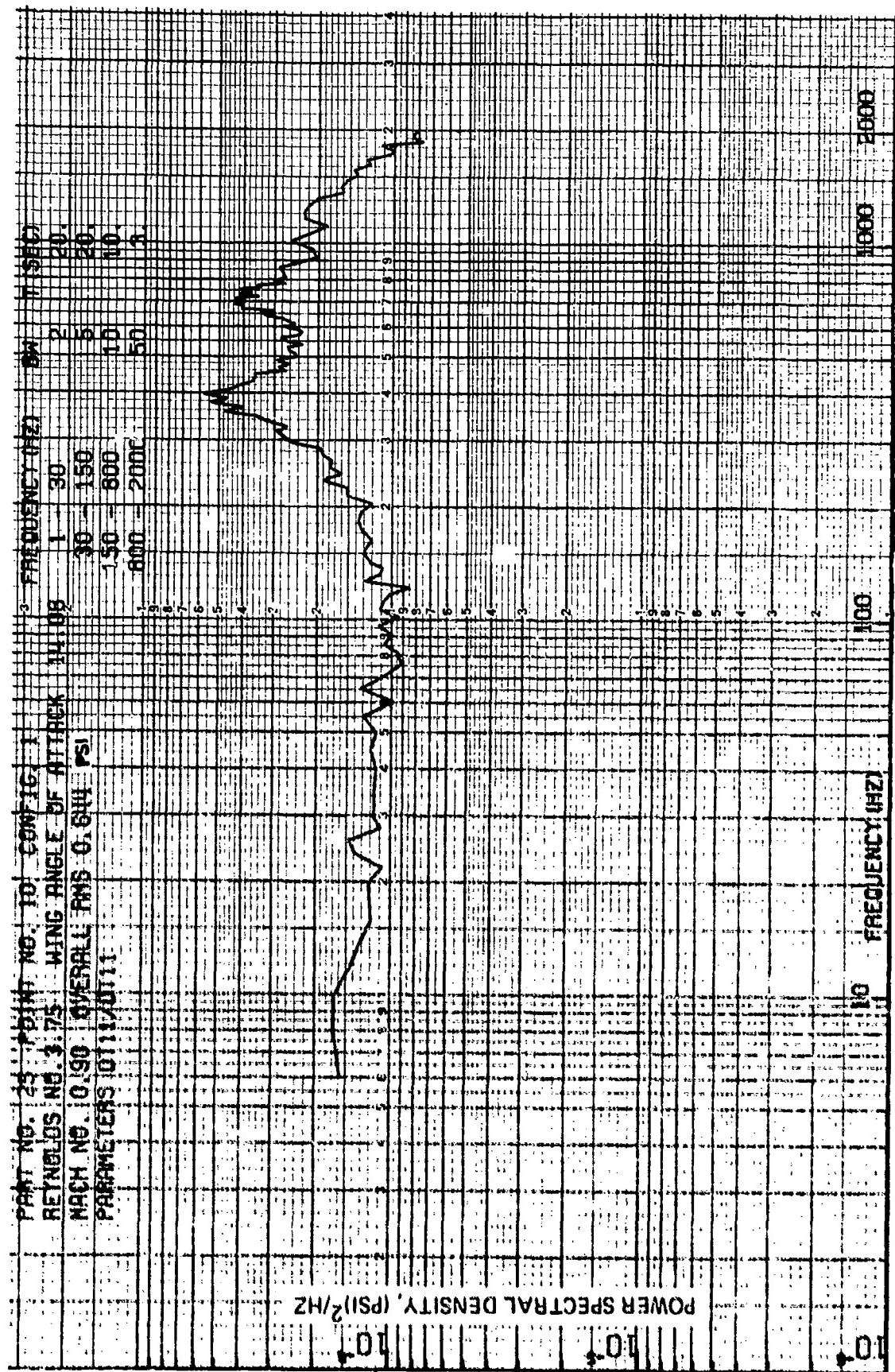


Figure 72 Fluctuating Pressure Power Spectral Density (Configuration 1, Mach 0.9,
 Wing Angle of Attack 14 Deg., Transducer 11)

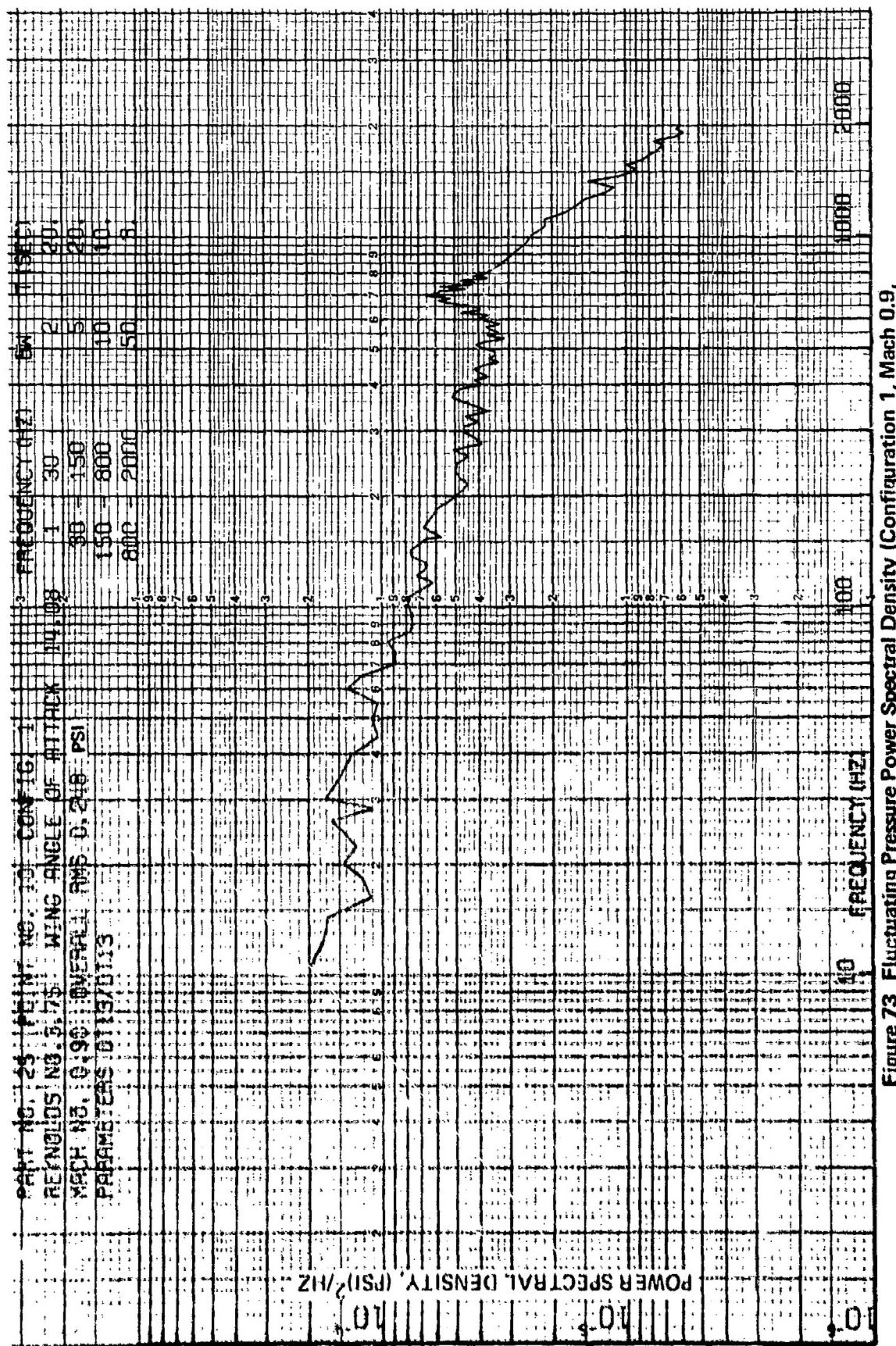


Figure 73 Fluctuating Pressure Power Spectral Density (Configuration 1, Mach 0.9, Wing Angle of Attack 14 Deg., Transducer 13)

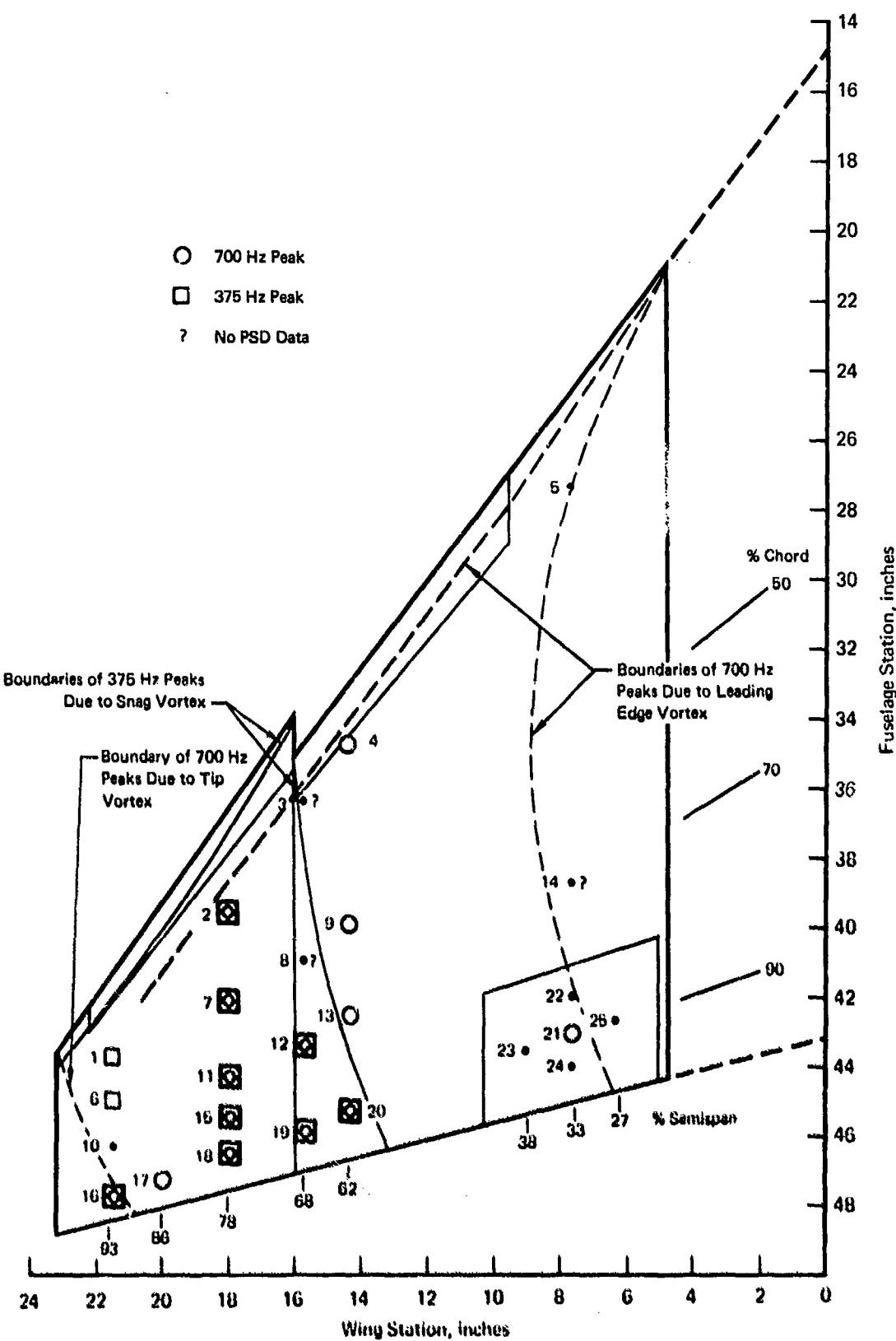


Figure 74 Wing Locations at which Peaks are Evident in Pressure Power Spectral Density Functions (Configuration 1, Mach 0.9, Wing Angle of Attack 14°)

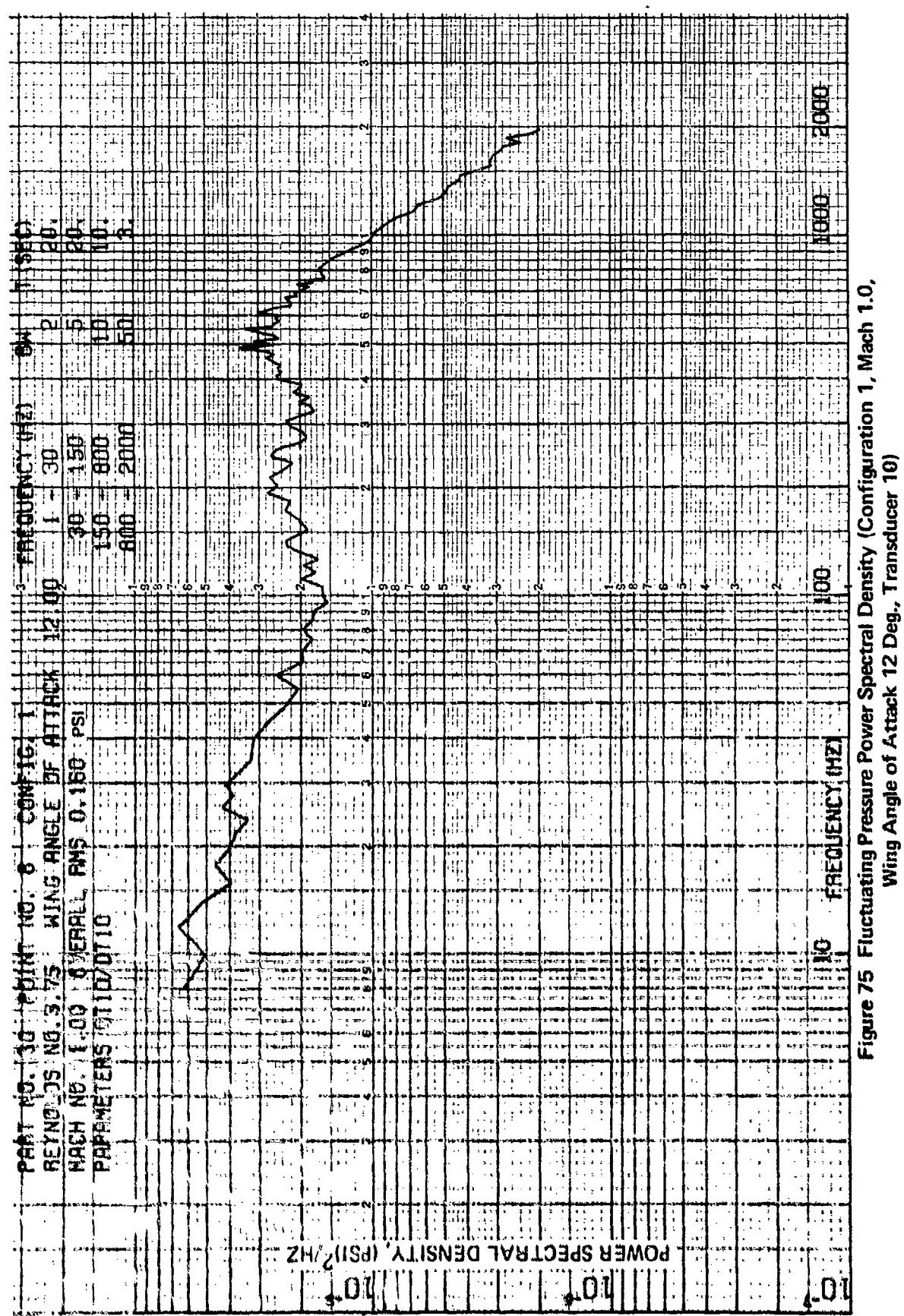


Figure 75 Fluctuating Pressure Power Spectral Density (Configuration 1, Mach 1.0,
 Wing Angle of Attack 12 Deg., Transducer 10)

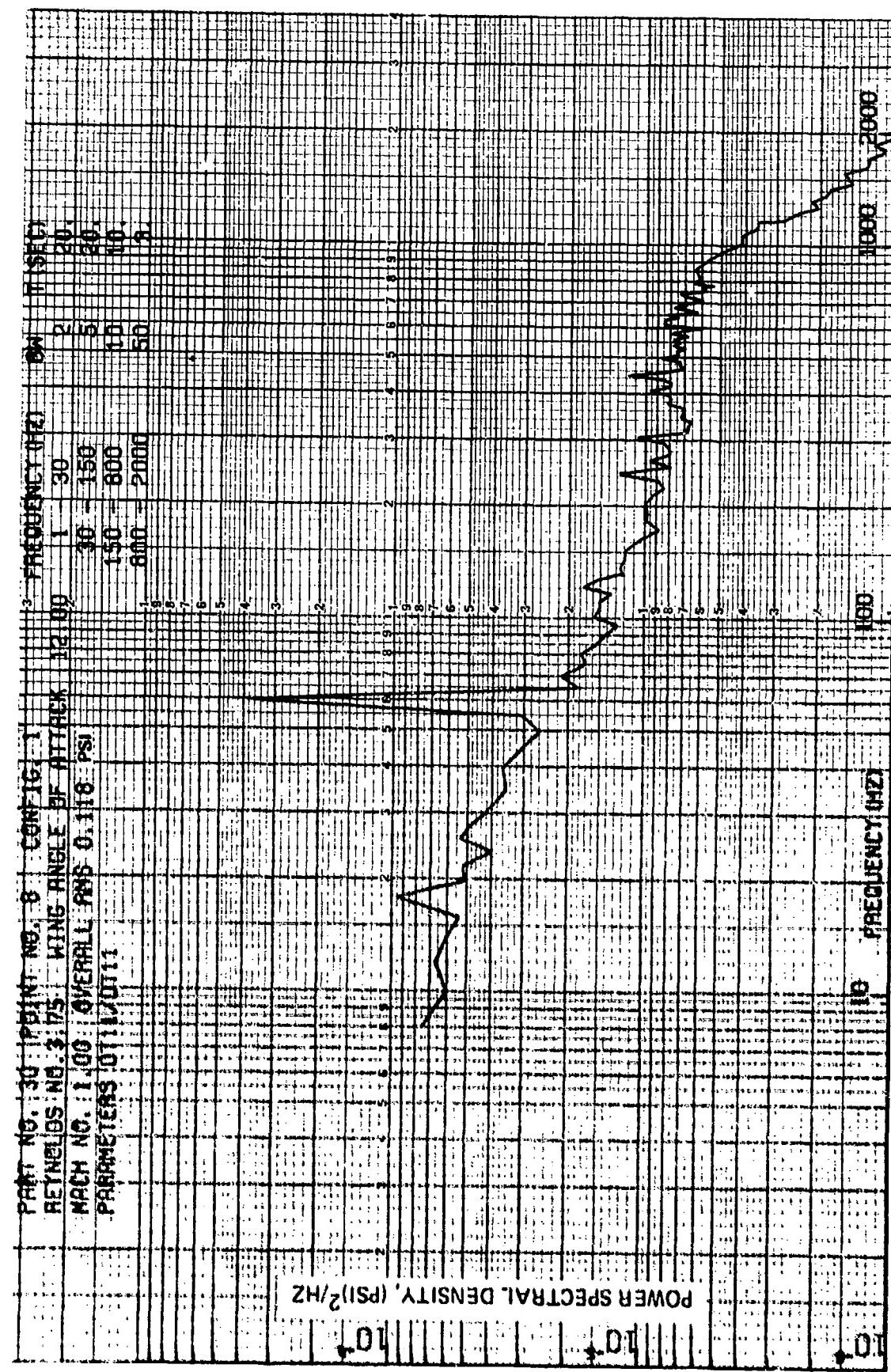


Figure 76 Fluctuating Pressure Power Spectral Density (Configuration 1, Mach 1.0,
 Wing Angle of Attack 12 Deg., Transducer 11)

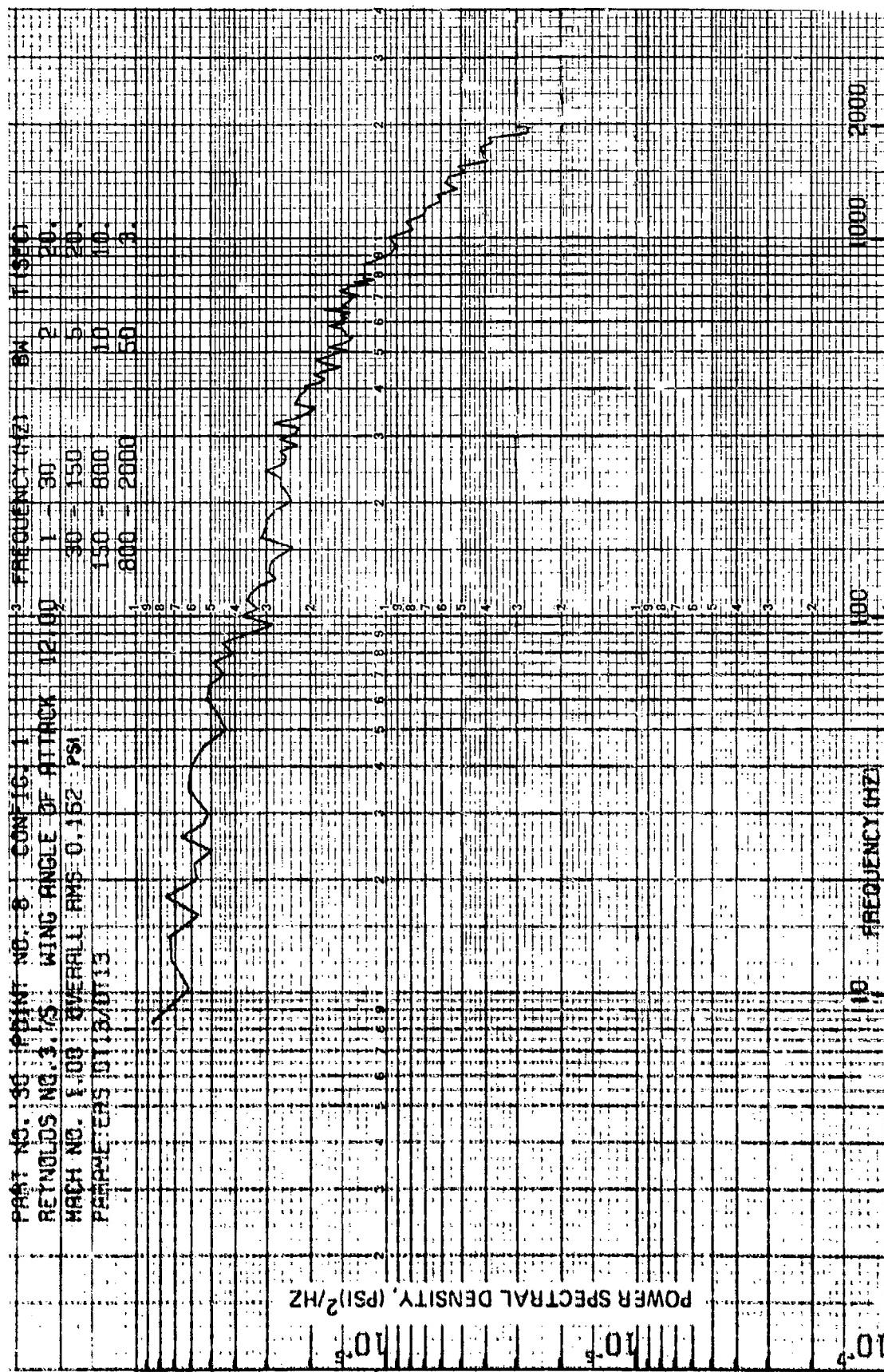


Figure 77 Fluctuating Pressure Power Spectral Density (Configuration 1, Mach 1.0,
 Wing Angle of Attack 12 Deg., Transducer 13)

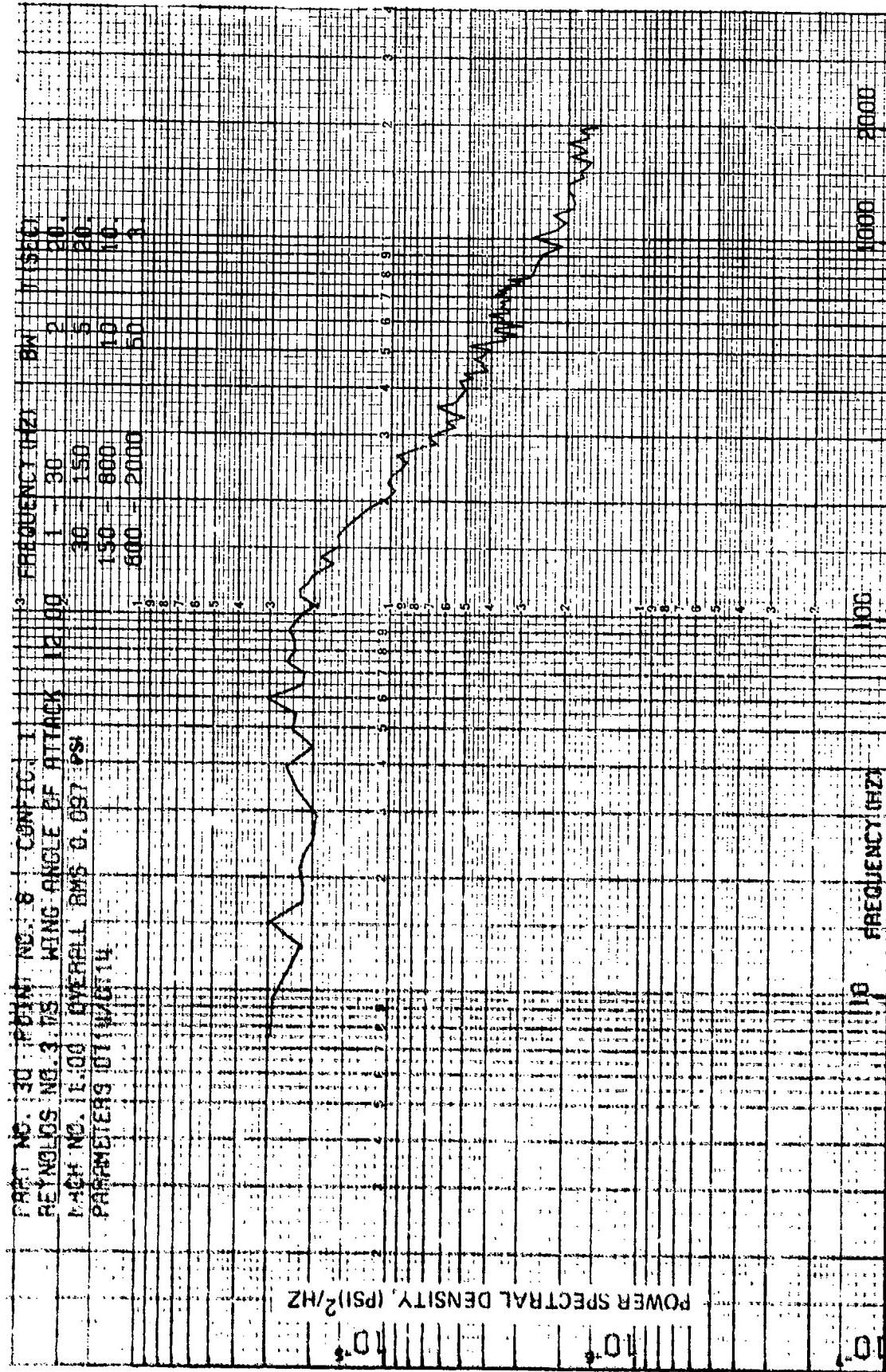


Figure 78 Fluctuating Pressure Power Spectral Density (Configuration 1, Mach 1.0,
 Wing Angle of Attack 12 Deg., Transducer 14)

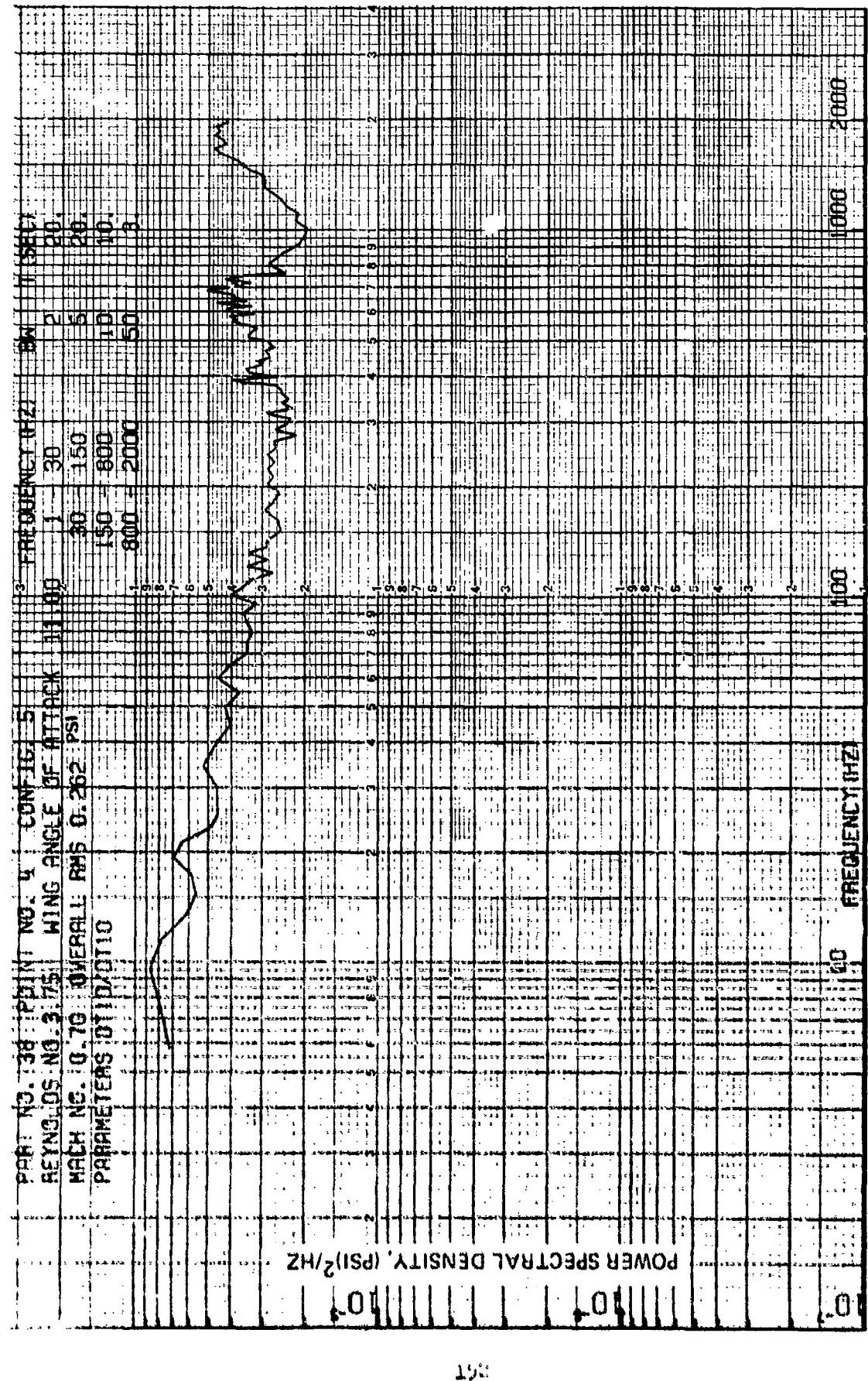


Figure 79 Fluctuating Pressure Power Spectral Density (Configuration 5, Mach 0.7,
Wing Angle of Attack 11 Deg., Transducer 10)

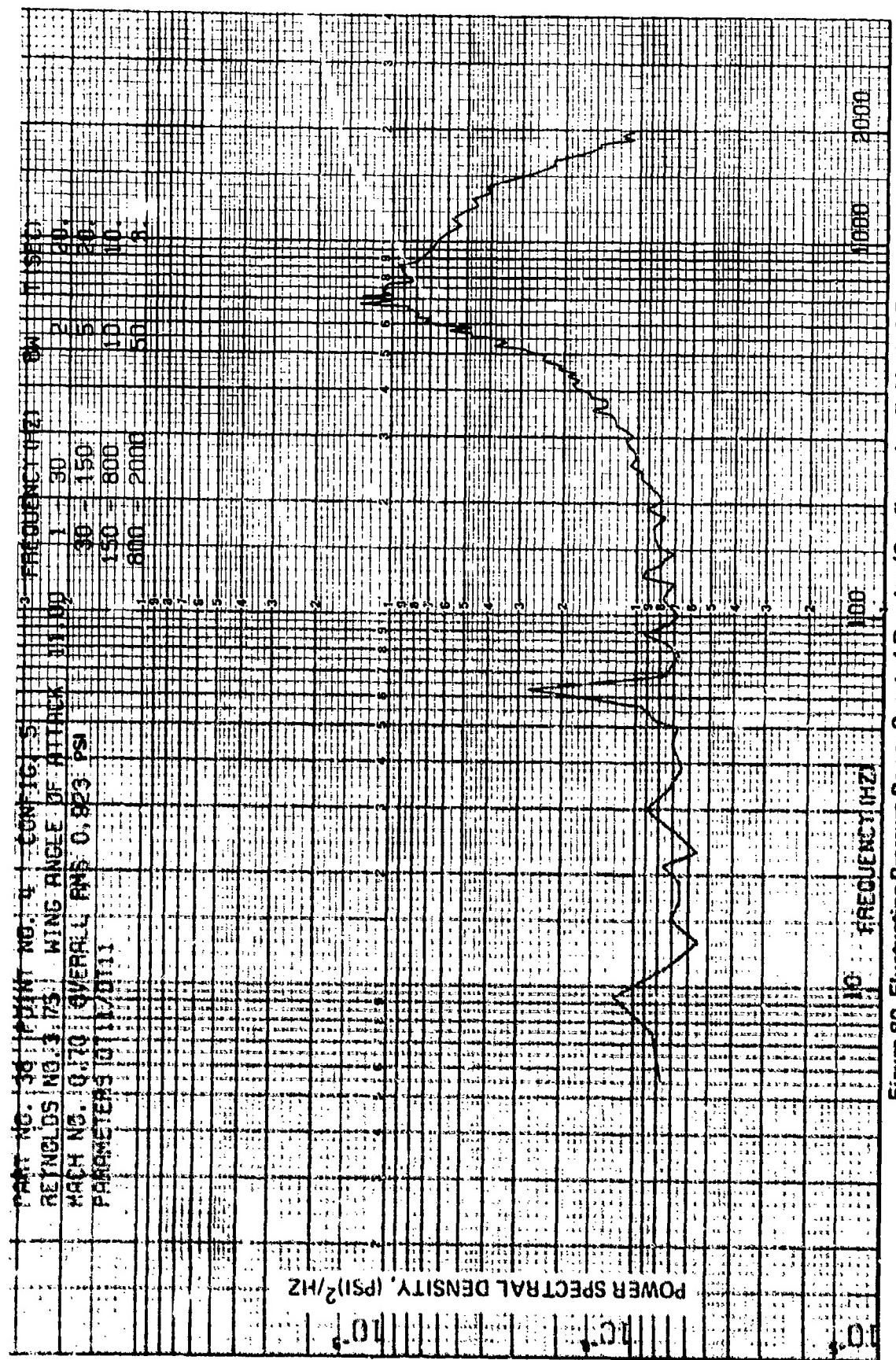


Figure 80 Fluctuating Pressure Power Spectral Density (Configuration 5, Mach 0.7, Wing Angle of Attack 11 Deg., Transducer 11)

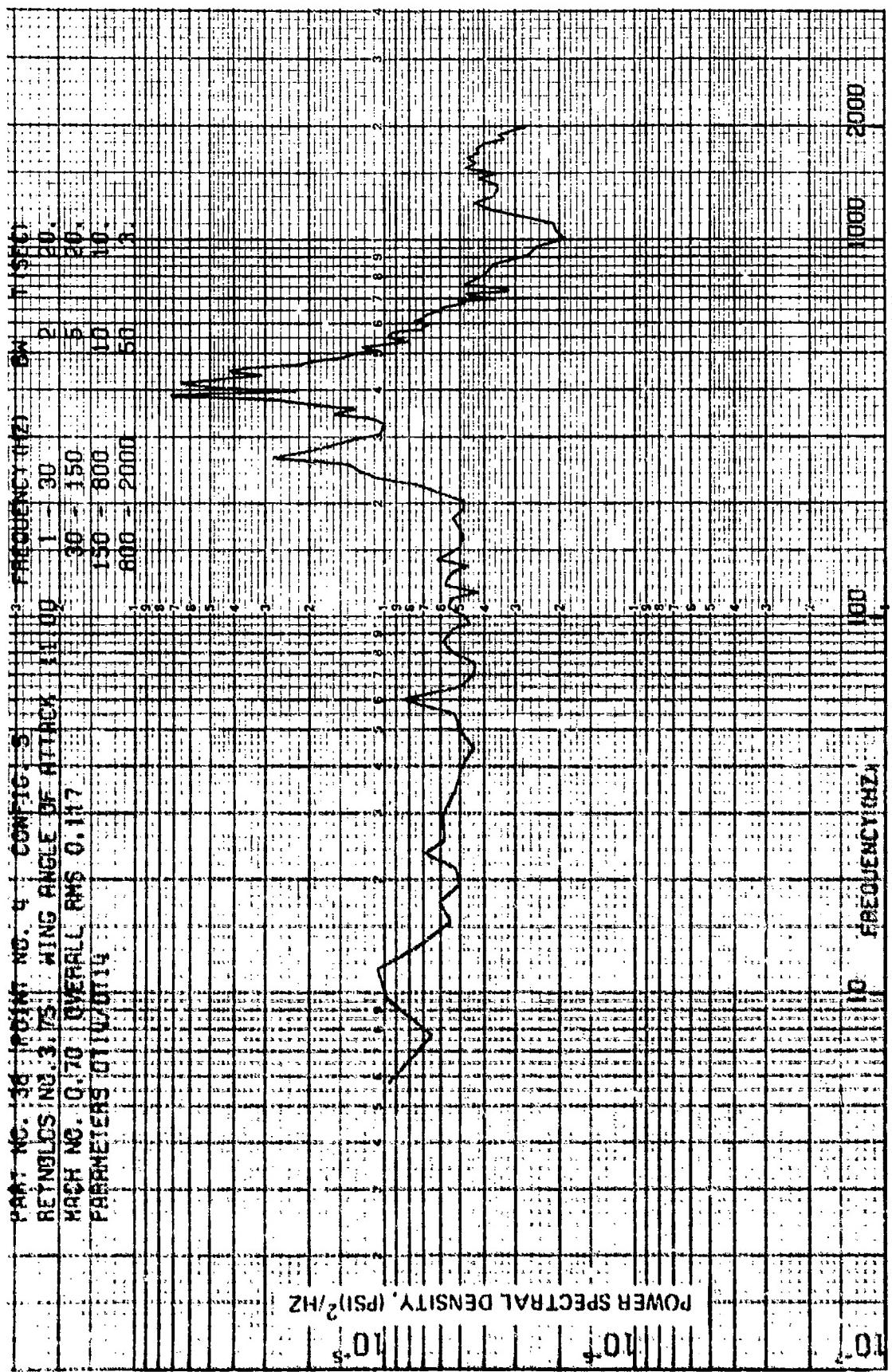


Figure 81 Fluctuating Pressure Power Spectral Density (Configuration 5, Mach 0.7,
Wing Angle of Attack 11 Deg., Transducer 14)

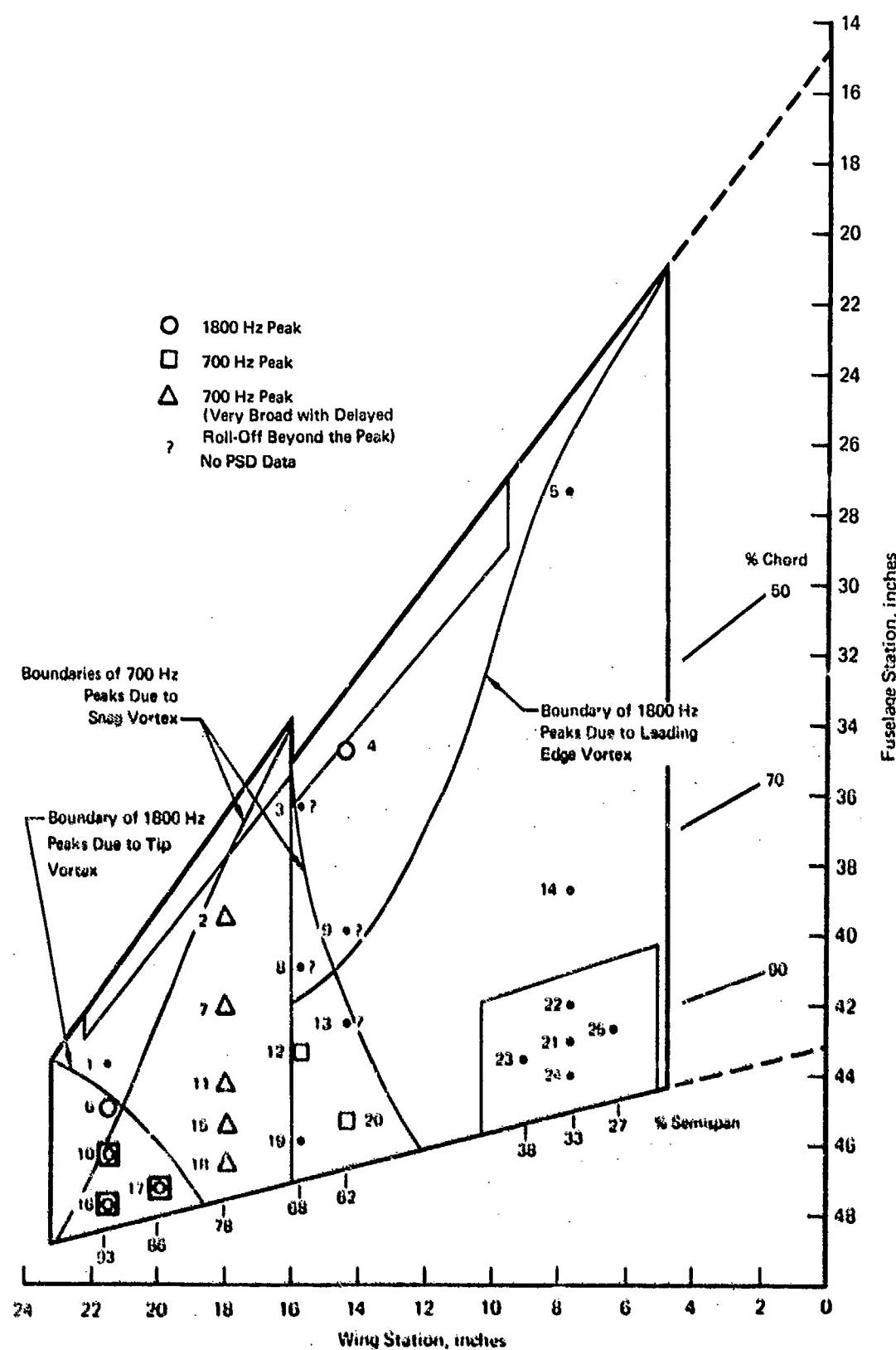


Figure 8c. Wing Locations at which Peaks are Evident in Pressure Power Spectral Density Functions (Configuration 5, Mach 0.7, Wing Angle of Attack 11°)

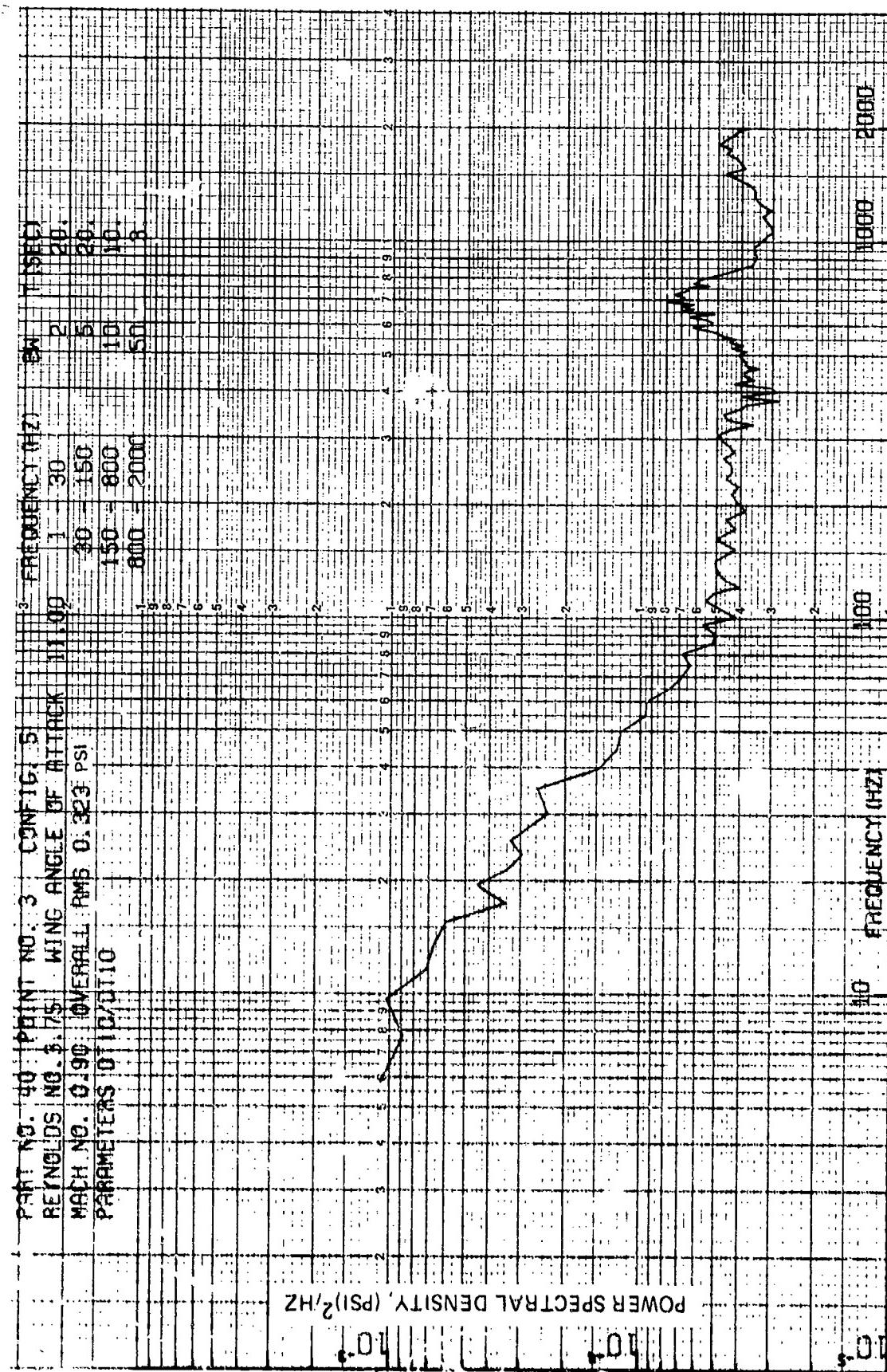


Figure 83 Fluctuating Pressure Power Spectral Density (Configuration 5, Mach 0.9, Wing Angle of Attack 11 Deg., Transducer 10)

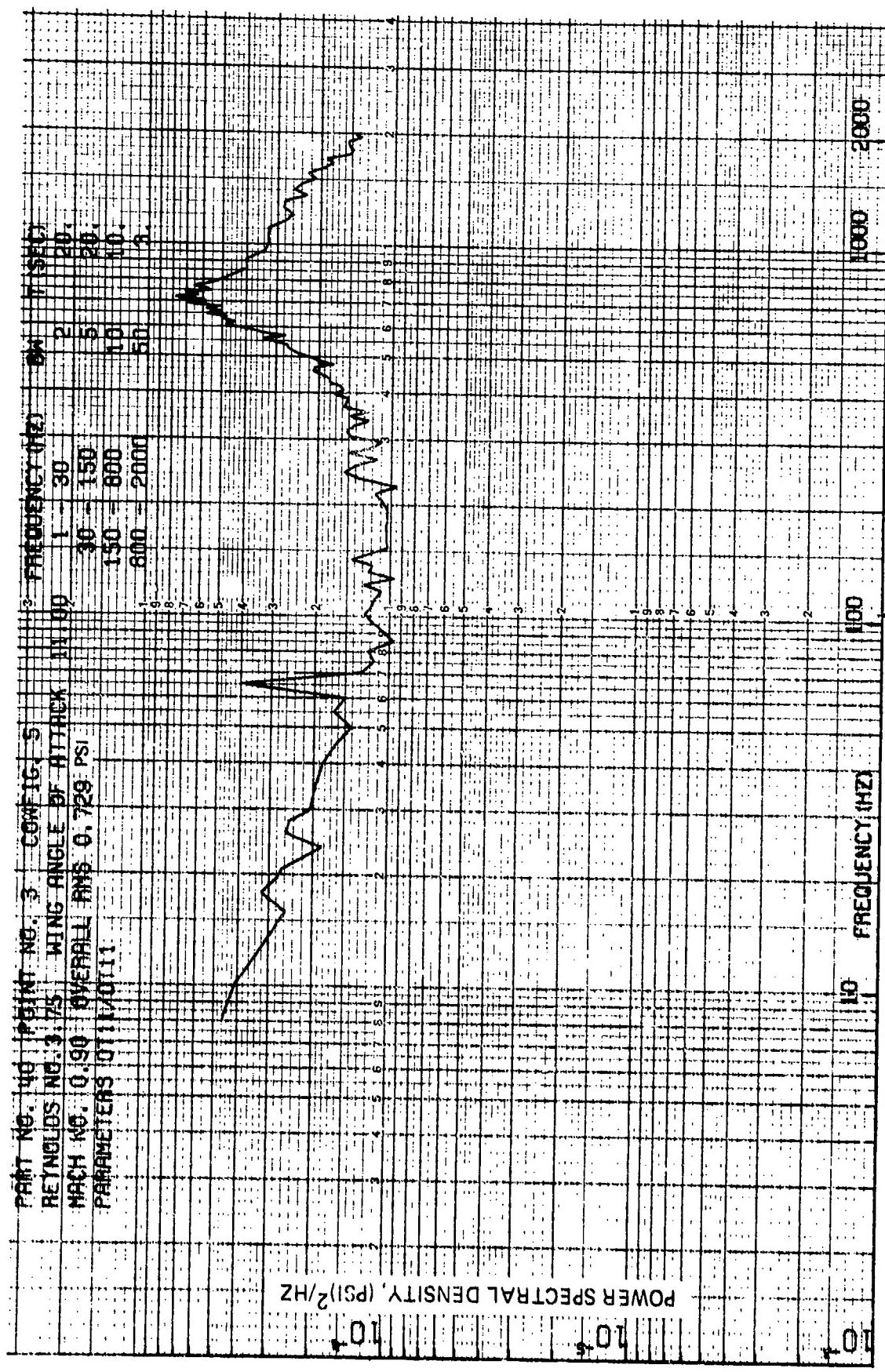


Figure 84 Fluctuating Pressure Power Spectral Density (Configuration 5, Mach 0.9,
 Wing Angle of Attack 11 Deg., Transducer 11)

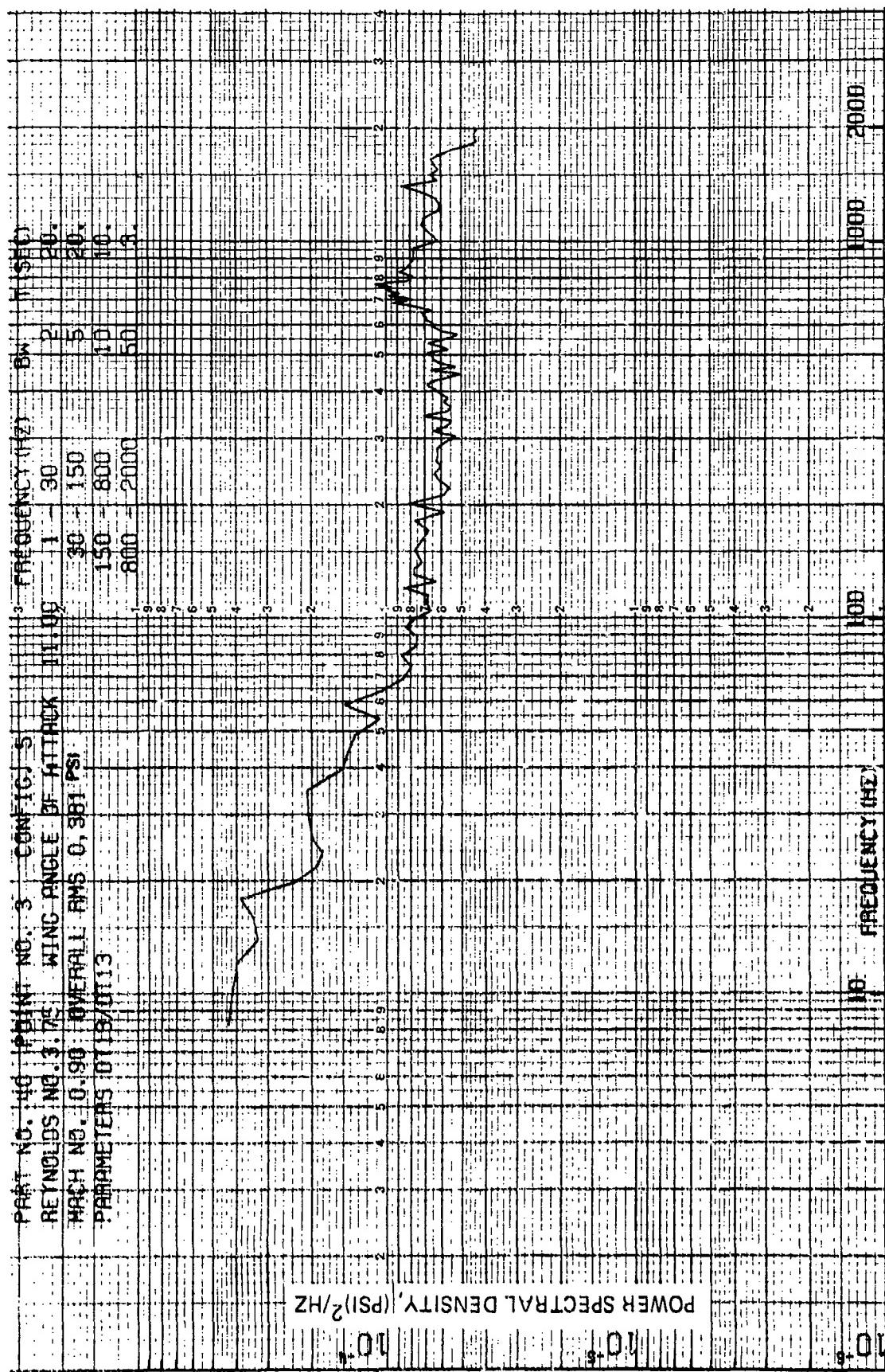


Figure 85 Fluctuating Pressure Power Spectral Density (Configuration 5, Mach 0.9,
 Wing Angle of Attack 11 Deg., Transducer 13)

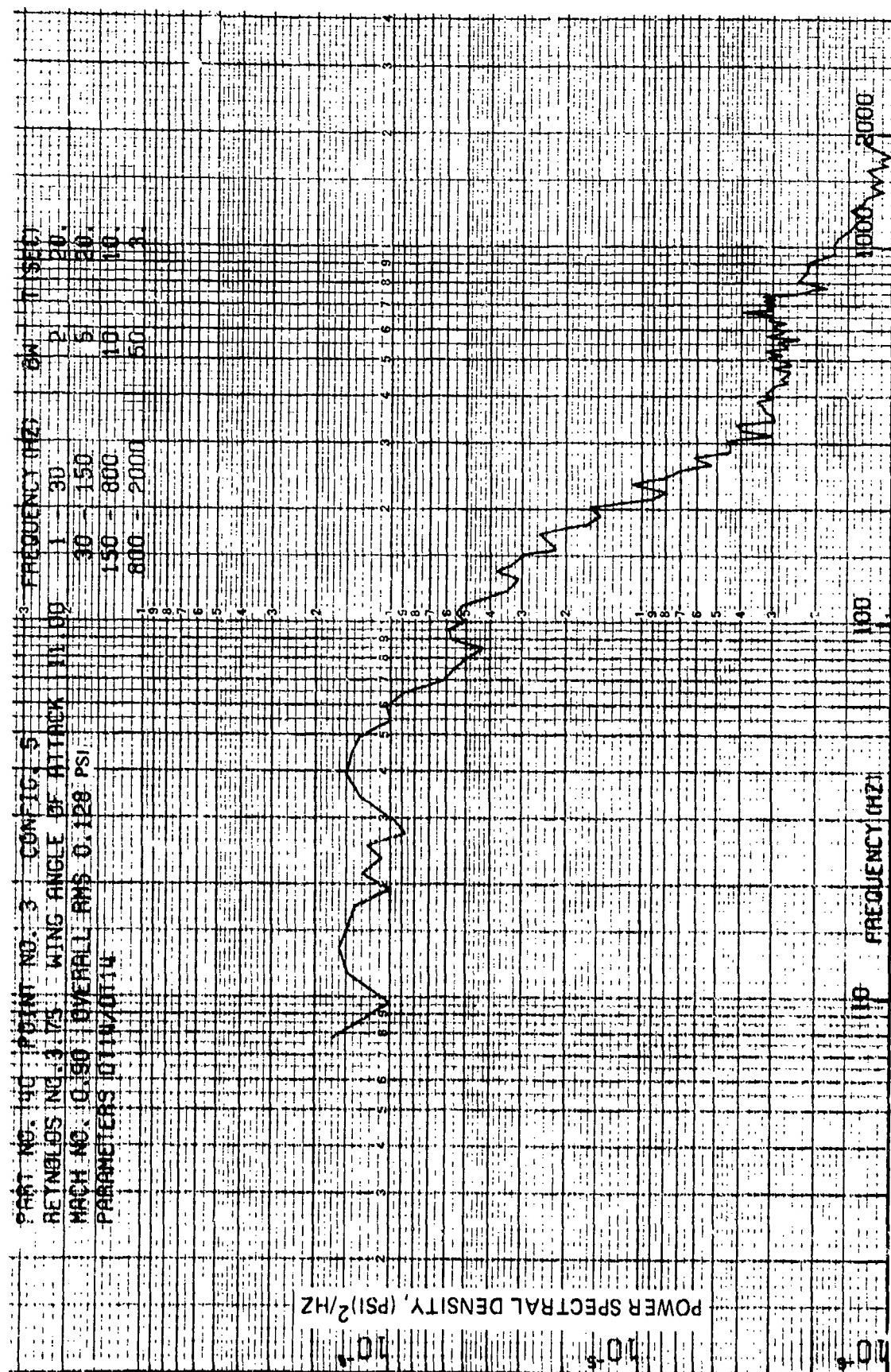


Figure 86 Fluctuating Pressure Power Spectral Density (Configuration 5, Mach 0.9,
 Wing Angle of Attack 11 Deg., Transducer 14)

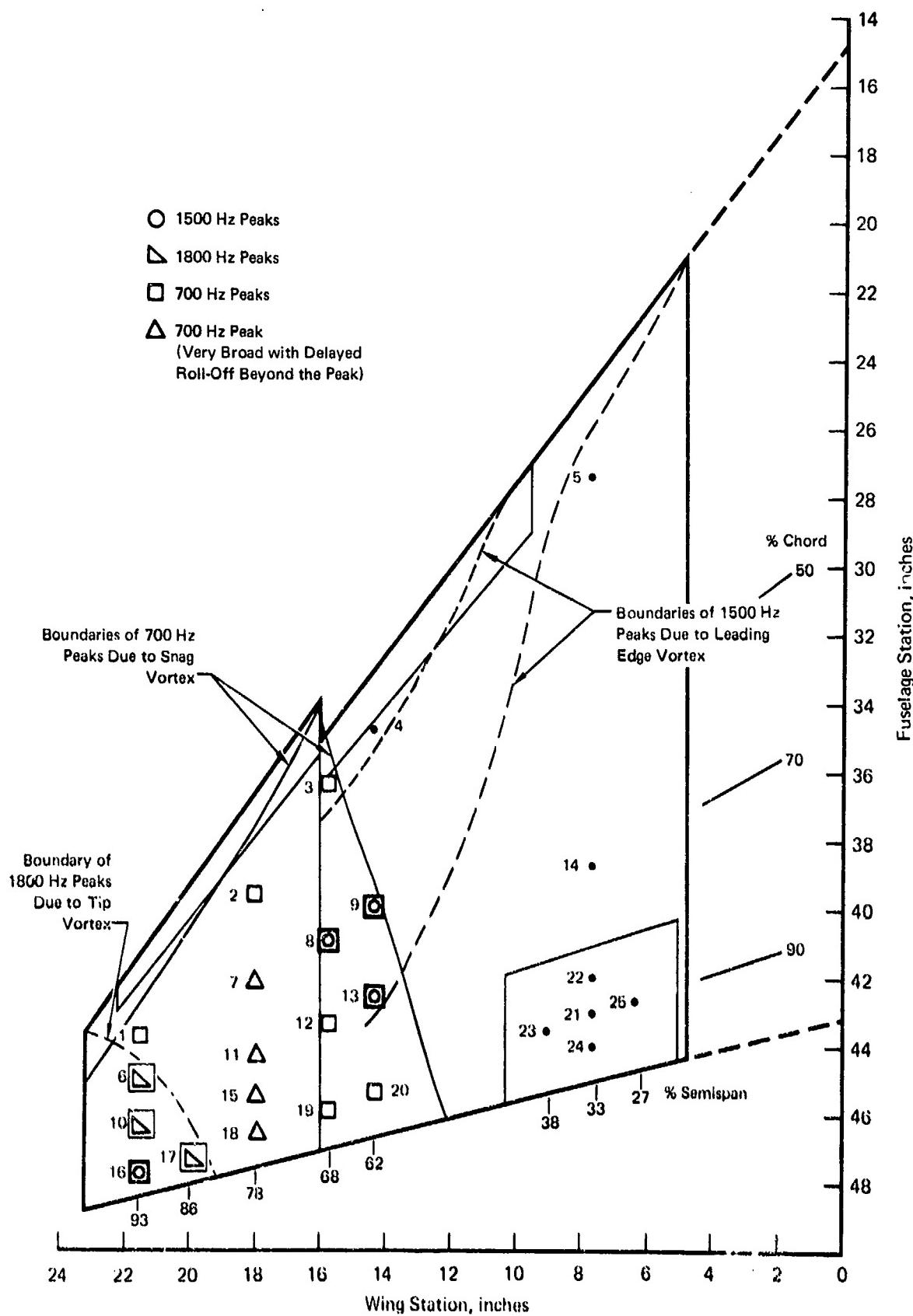


Figure 87 Wing Locations at which Peaks are Evident in Pressure Power Spectral Density Functions, (Configuration 5, Mach 0.9, Wing Angle of Attack 11°)

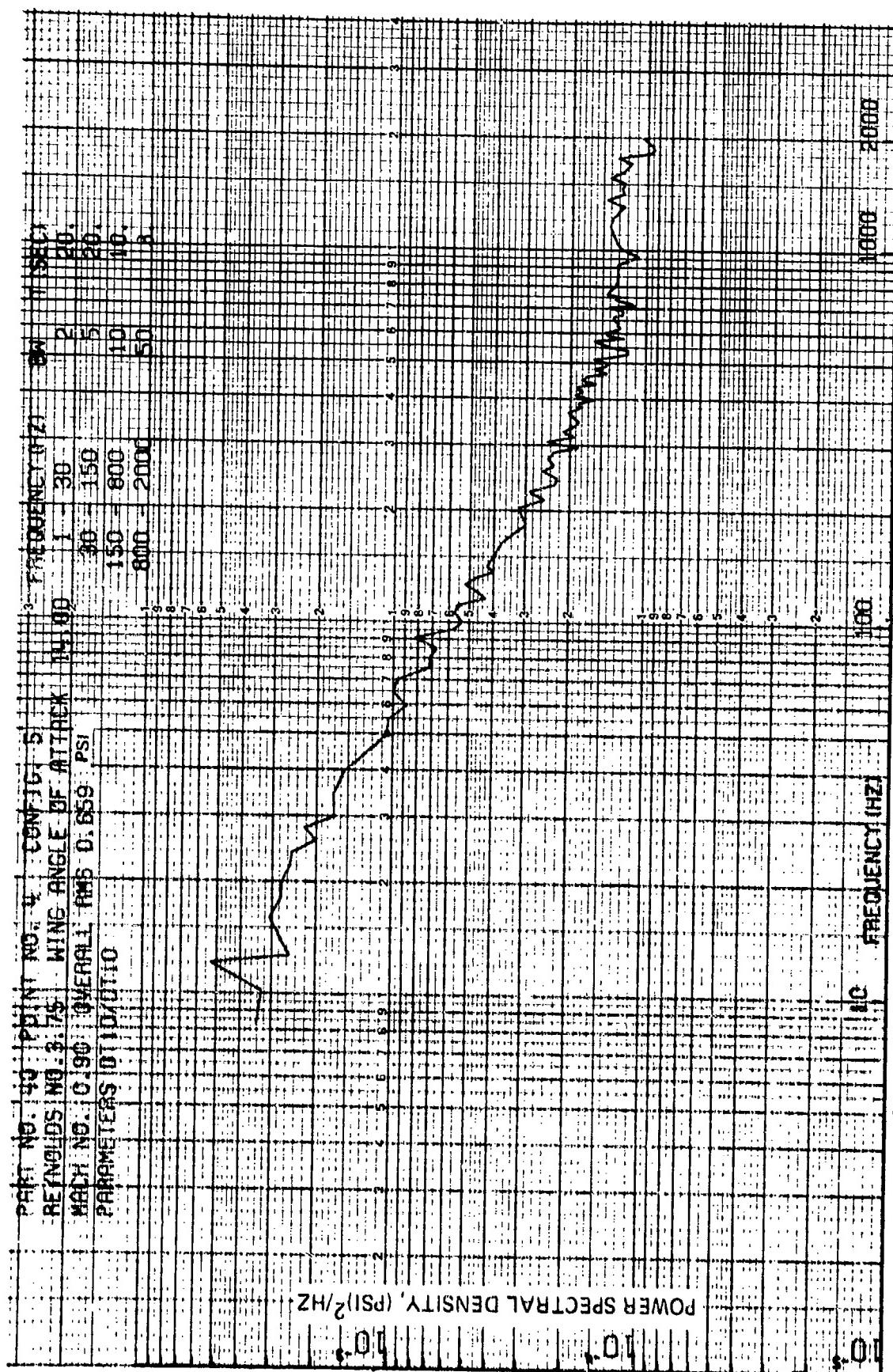


Figure 88 Fluctuating Pressure Power Spectral Density (Configuration 5, Mach 0.9,
 Wing Angle of Attack 14 Deg, Transducer 10)

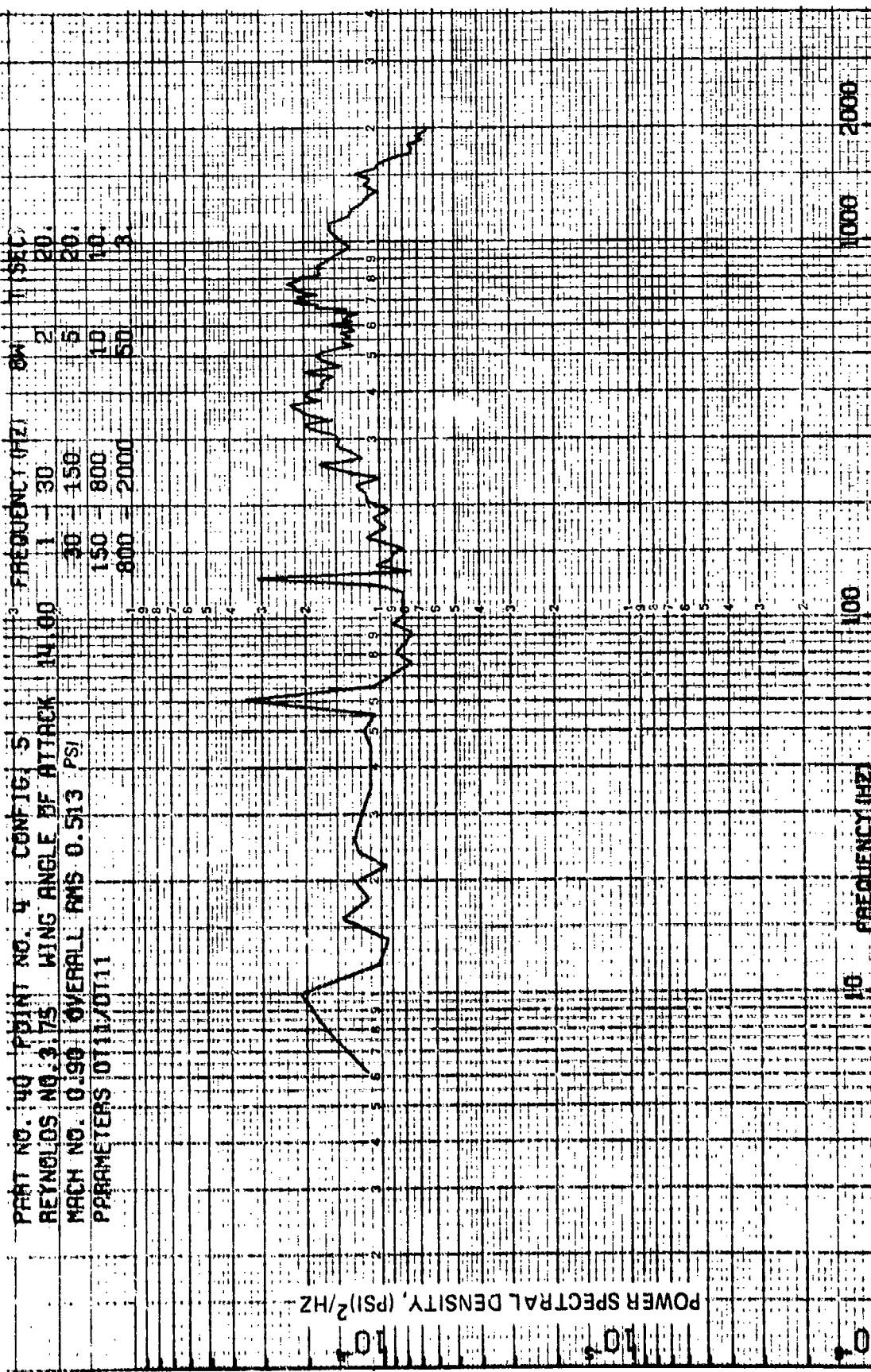


Figure 89 Fluctuating Pressure Power Spectral Density (Configuration 5, Mach 0.9,
Wing Angle of Attack 14 Deg., Transducer 11)

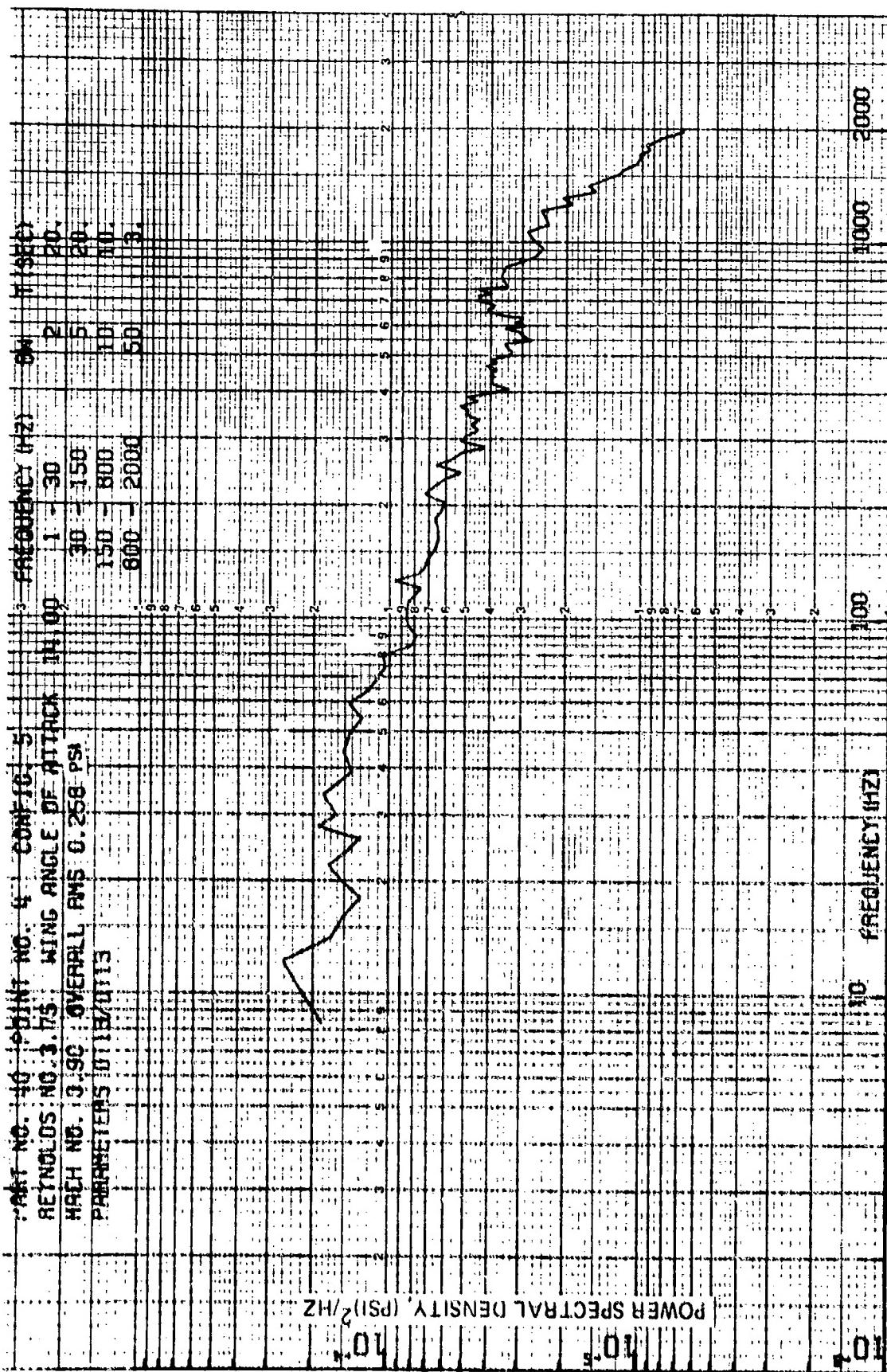


Figure 90 Fluctuating Pressure Power Spectral Density (Configuration 5, Mach 0.9,
 Wing Angle of Attack 14 Deg., Transducer 13)

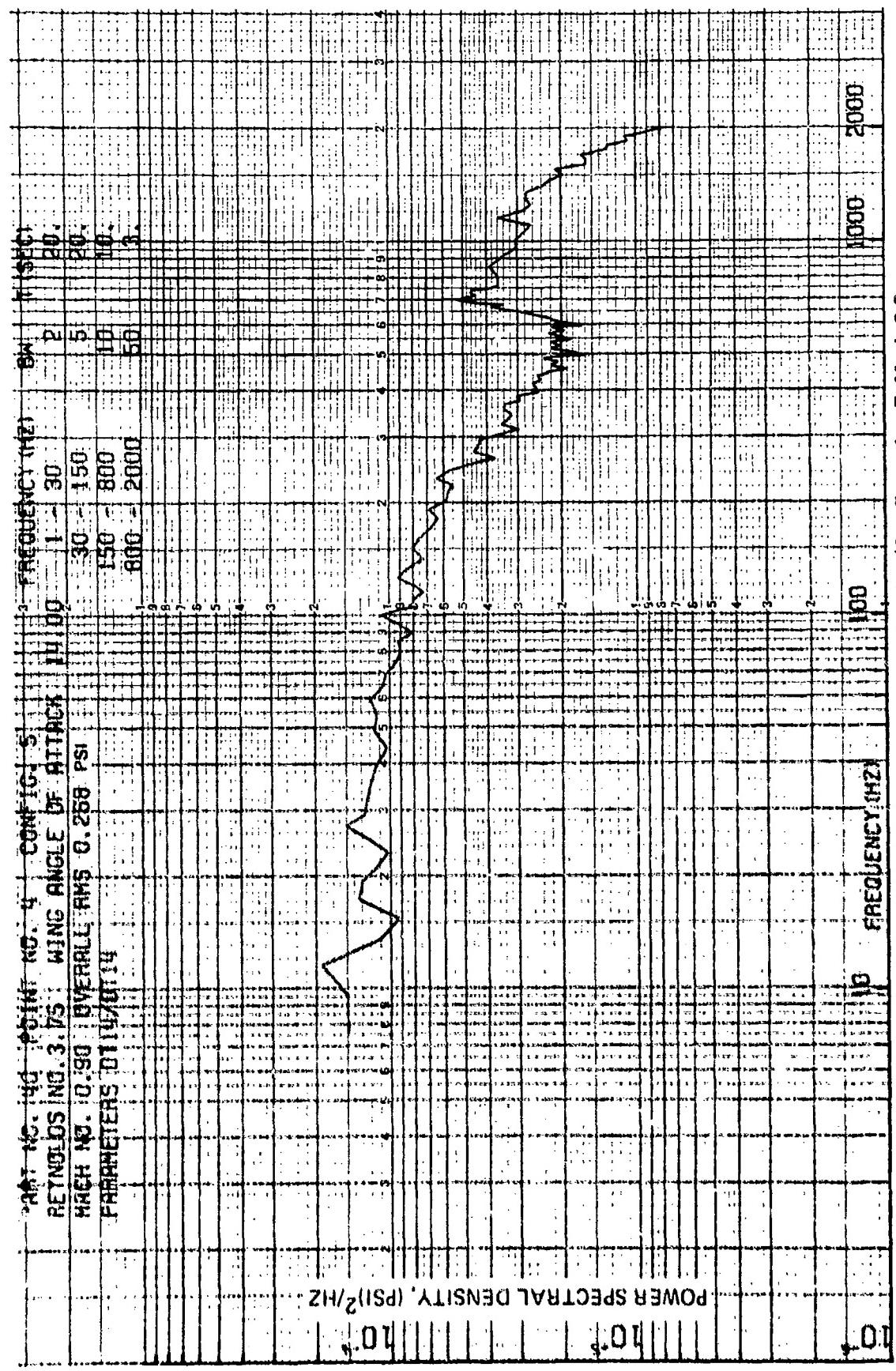


Figure 91 Fluctuating Pressure Power Spectral Density (Configuration 5, Mach 0.9,
 Wing Angle of Attack 14 Deg., Transducer 14)

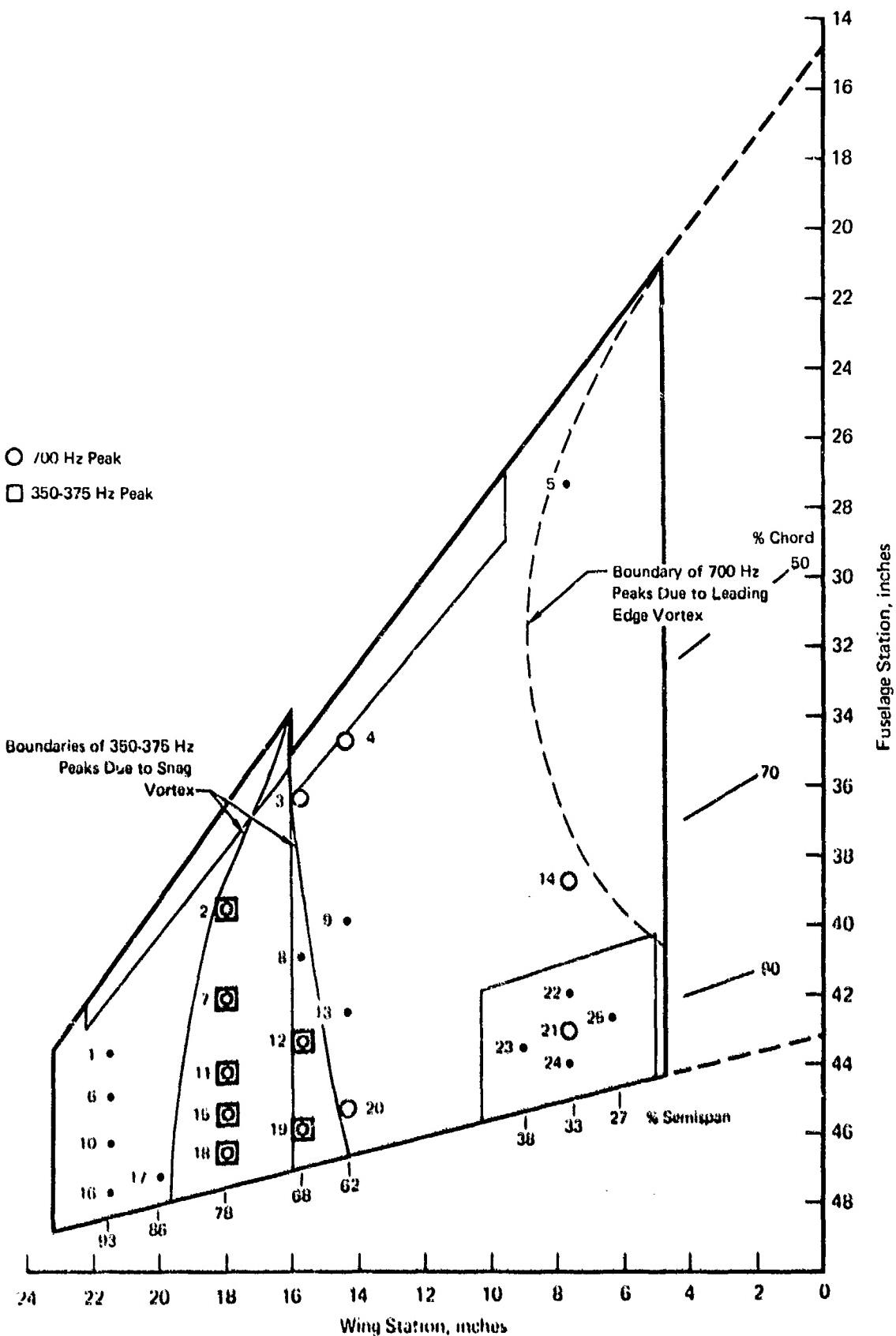


Figure 92 Wing Locations at which Peaks are Evident in Pressure Power Spectral Density Functions, (Configuration 6, Mach 0.9, Wing Angle of Attack 14°)

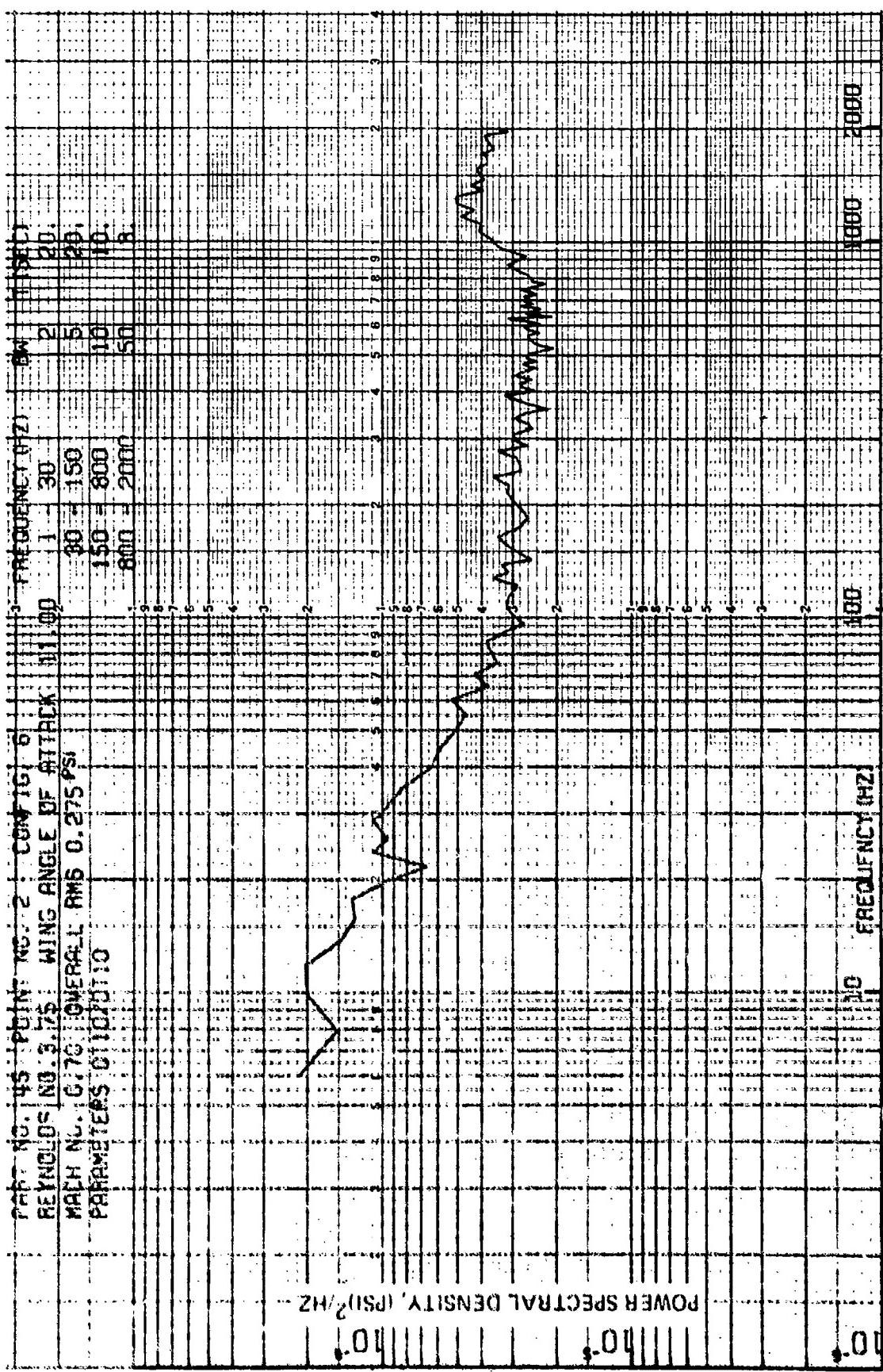


Figure 93 Fluctuating Pressure Power Spectral Density (Configuration 6, Mach 0.7,
Wing Angle of Attack 11 Deg., Transducer 10)

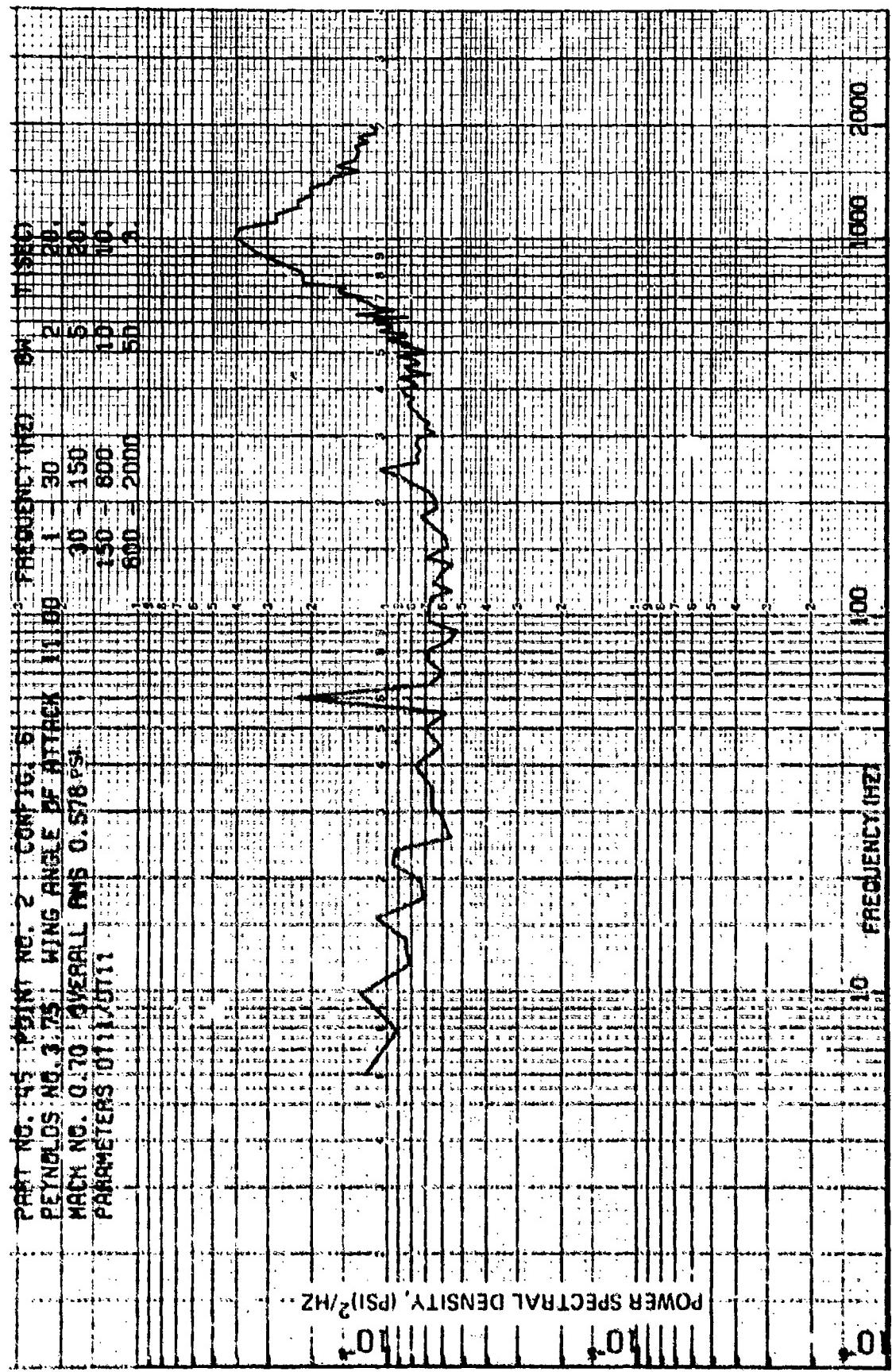


Figure 94 Fluctuating Pressure Power Spectral Density (Configuration 6, Mach 0.7,
 Wing Angle of Attack 11 Deg., Transducer 11)

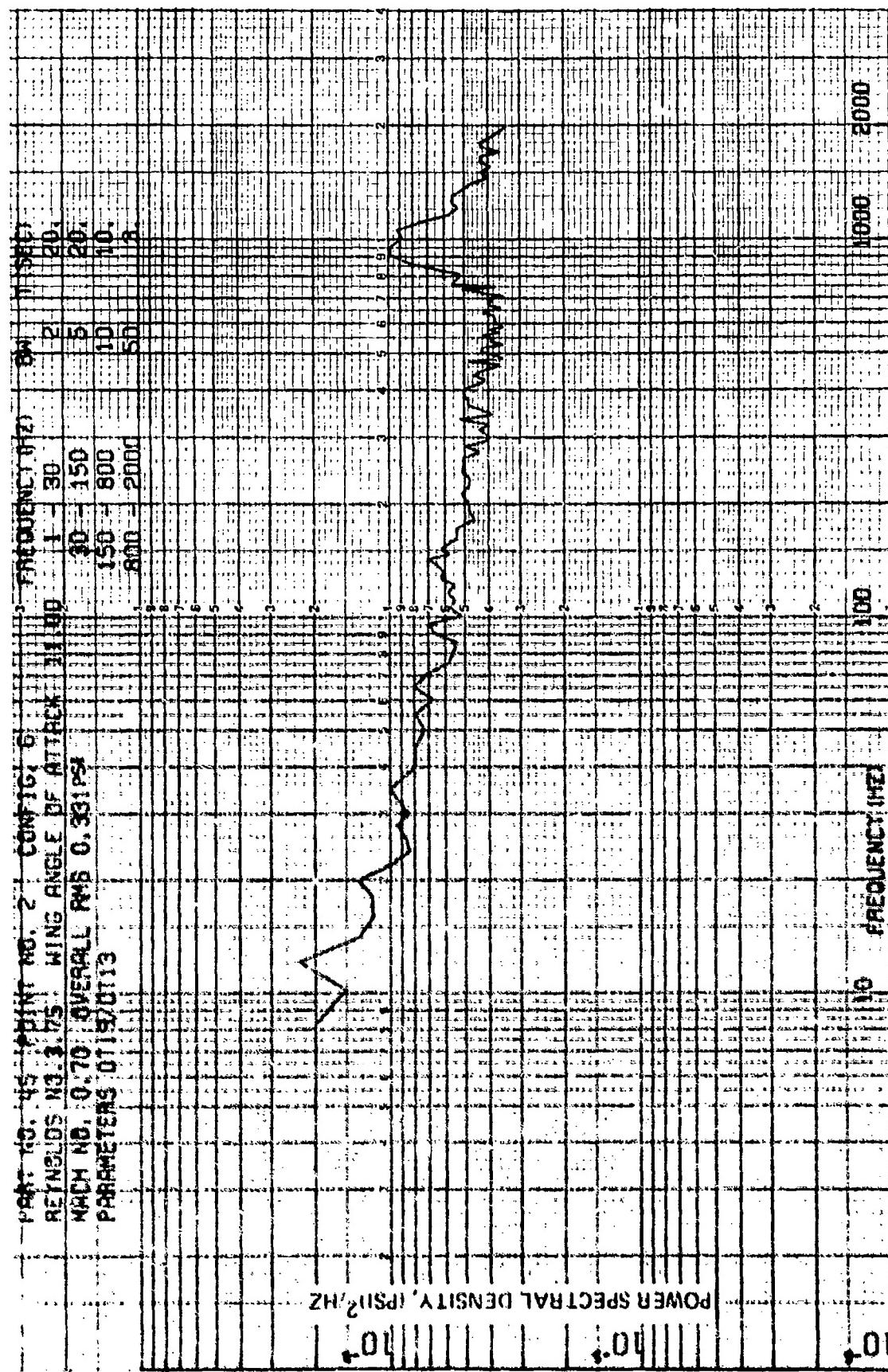


Figure 95 Fluctuating Pressure Power Spectral Density (Configuration 6, Mach 0.7, Wing Angle of Attack 11 Deg., Transducer 13)

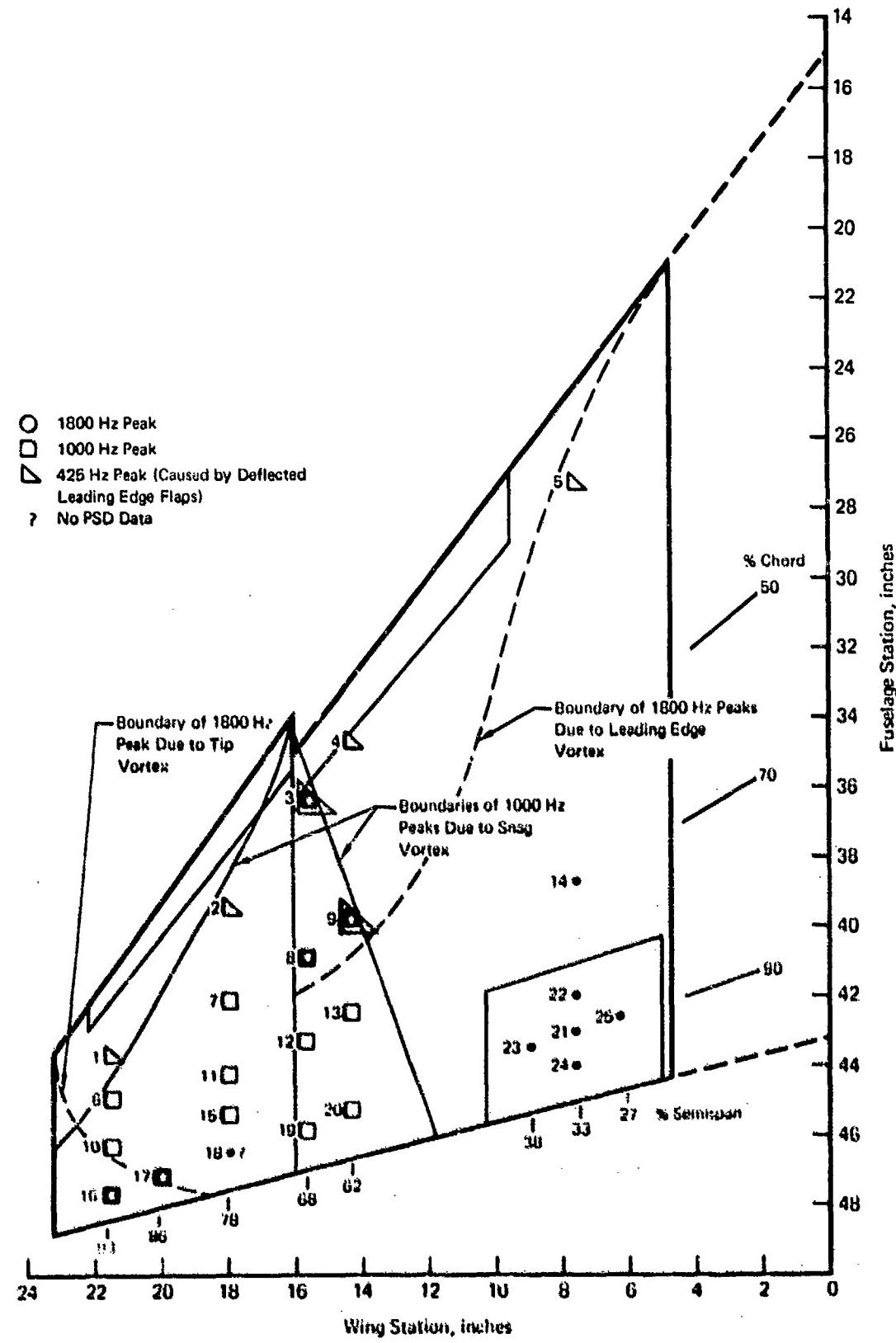


Figure 96 Wing Locations at which Peaks are Evident in Pressure Power Spectral Density Functions (Configuration 6, Mach 0.7, Wing Angle of Attack 11°)

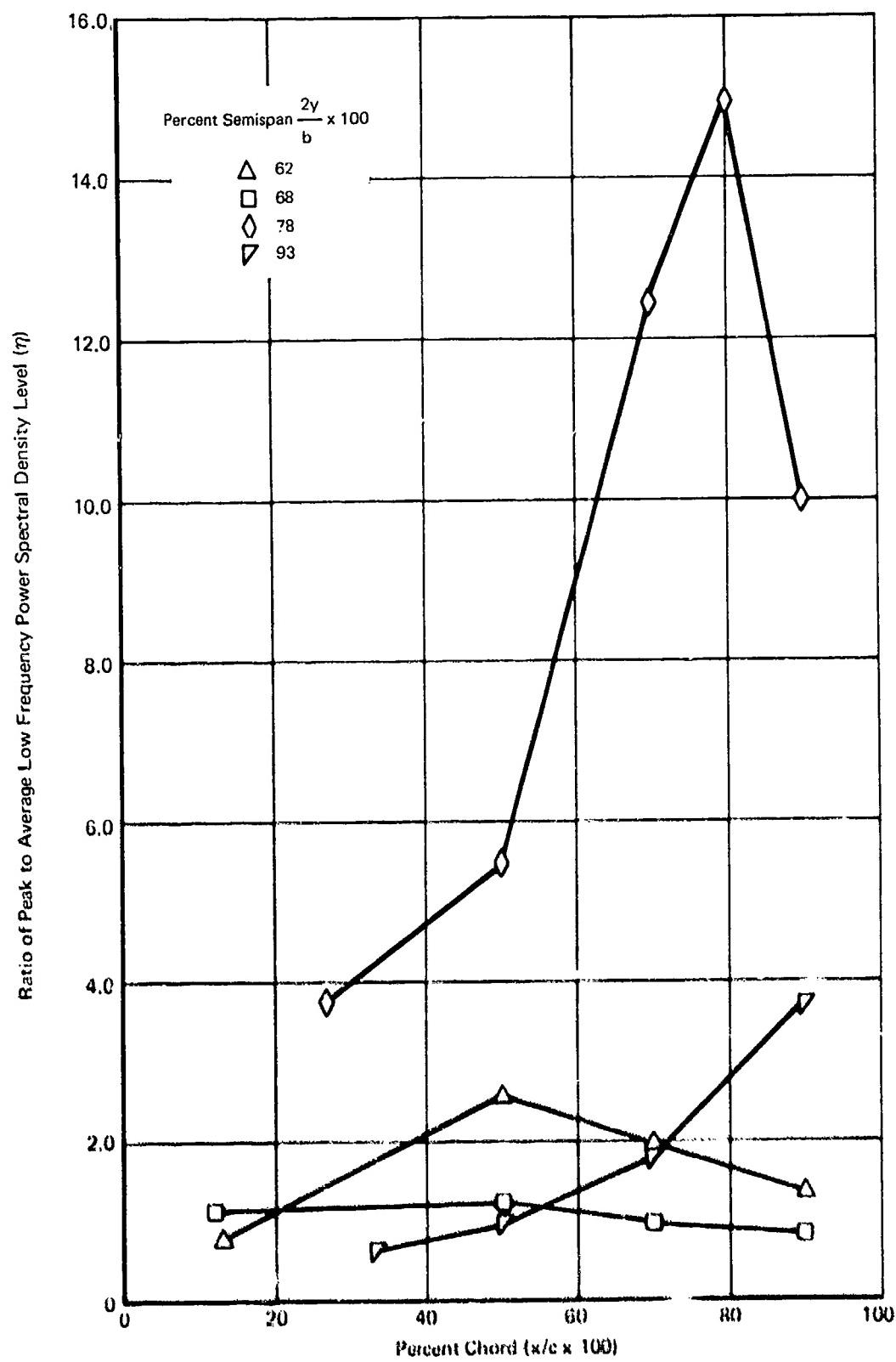


Figure 97 Ratio of Peak to Average Low Frequency Power Spectral Density Level vs Percent Chord
(Configuration 1, Mach 0.7, Wing Angle of Attack 12°)

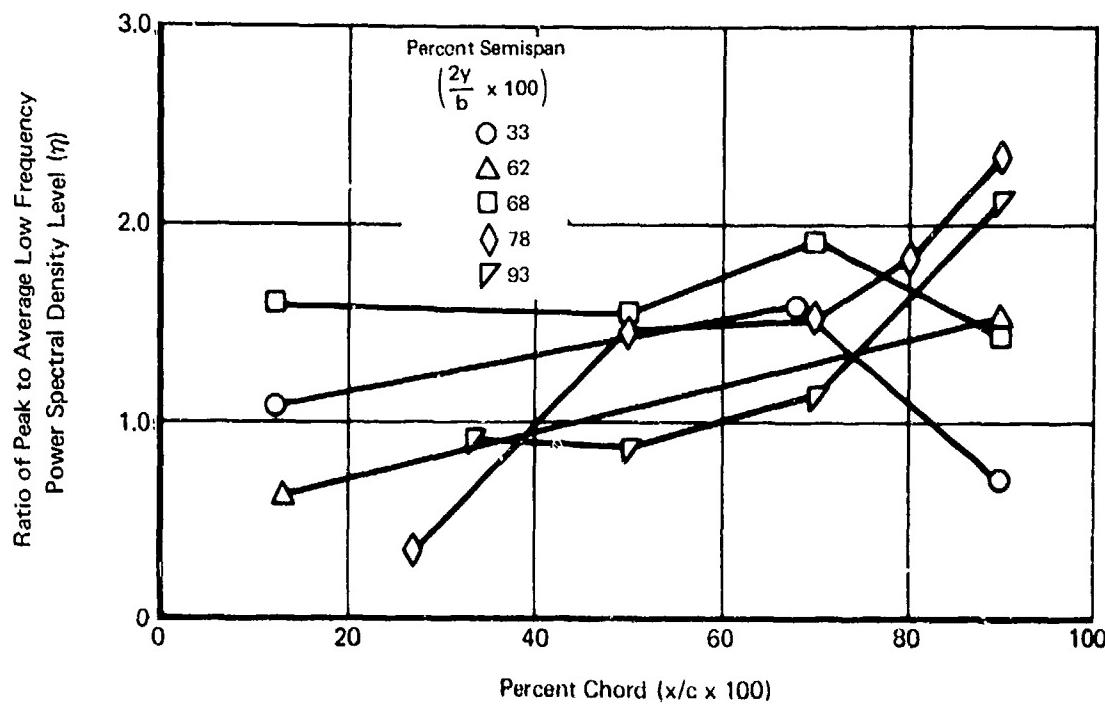


Figure 98 Ratio of Peak to Average Low Frequency Power Spectral Density Level vs Percent Chord
 (Configuration 1, Mach 0.9, Wing Angle of Attack 8°)

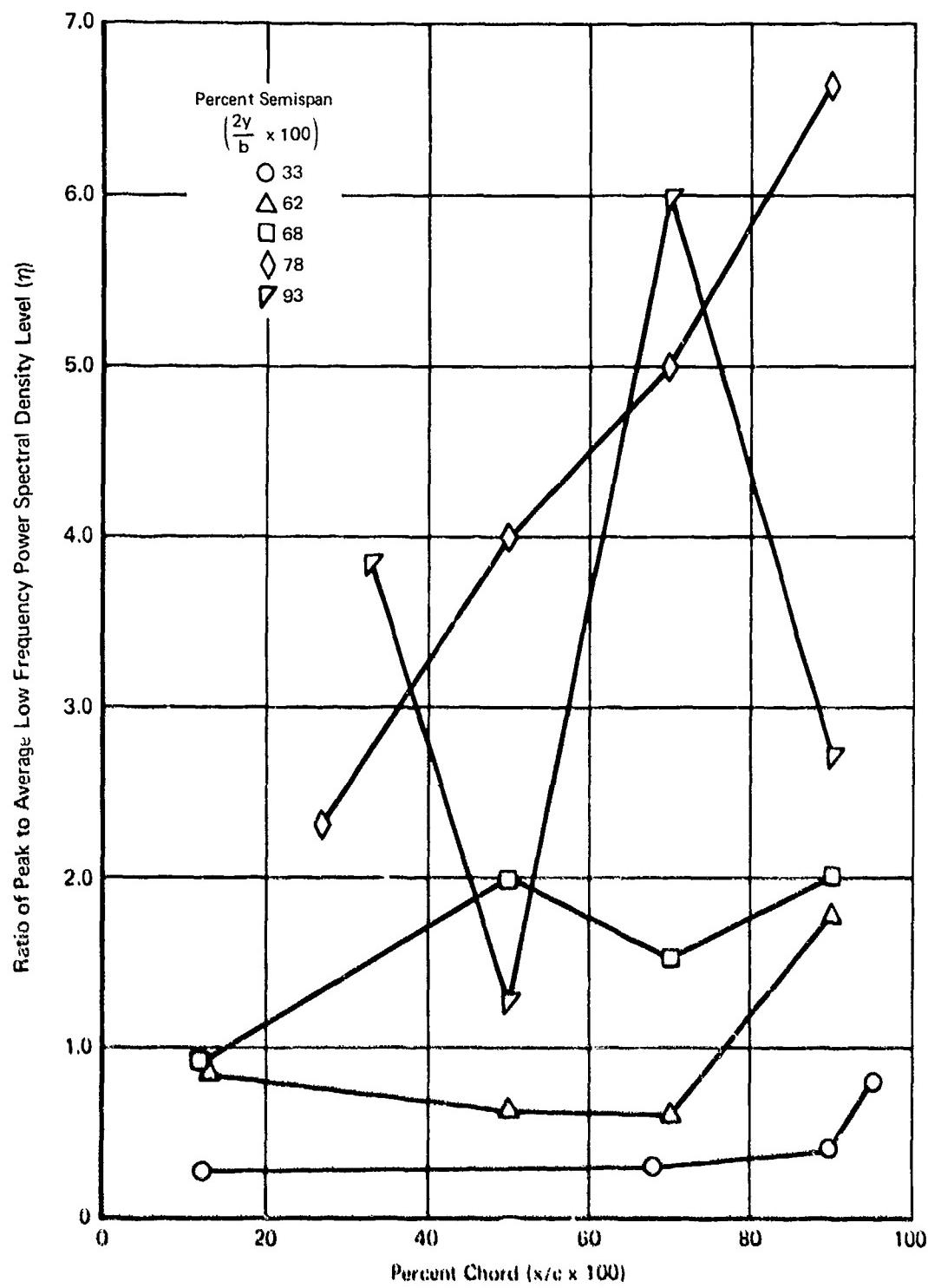


Figure 99 Ratio of Peak to Average Low Frequency Power Spectral Density Level vs Percent Chord
 (Configuration 1, Mach 0.9, Wing Angle of Attack 12°)

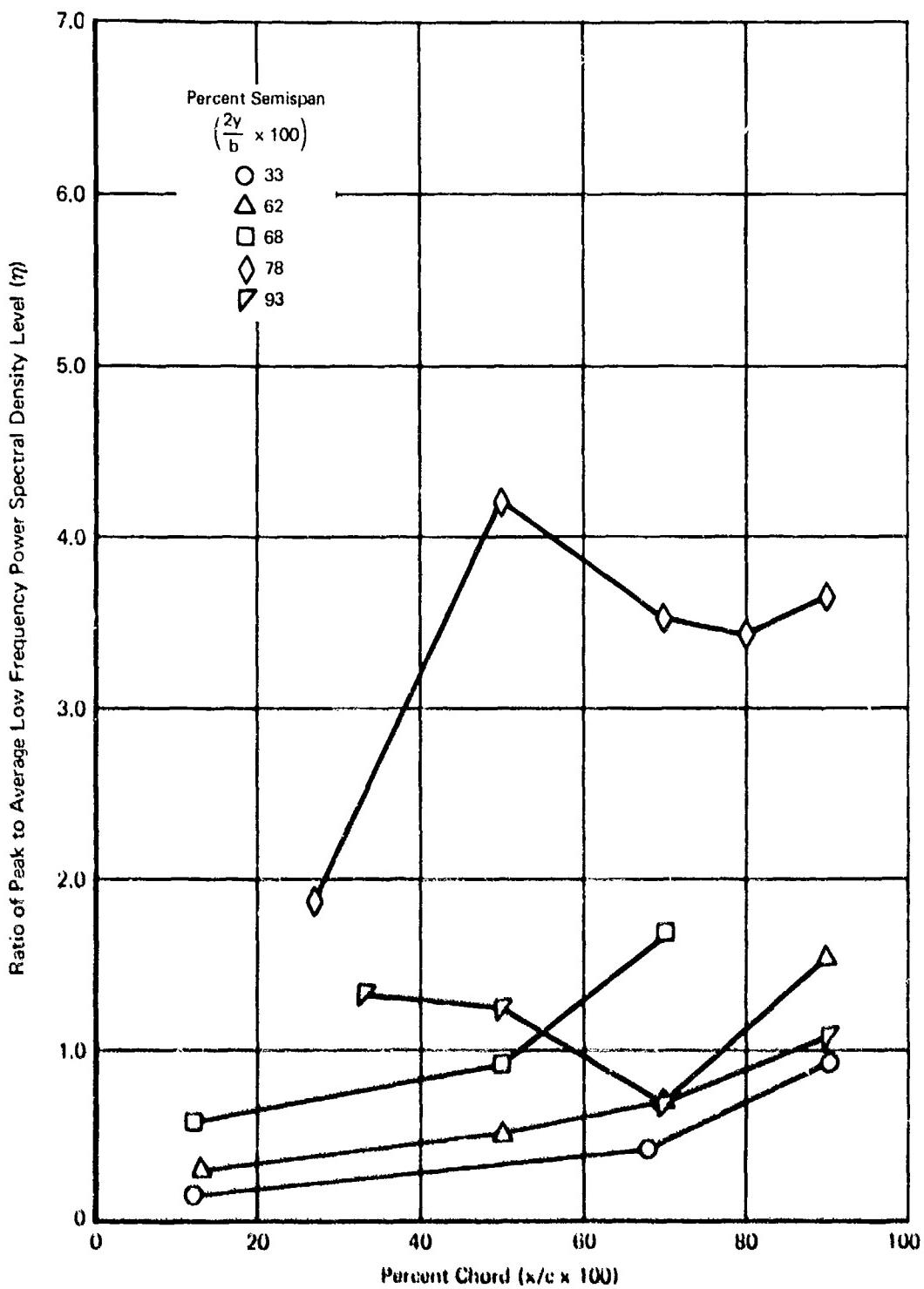


Figure 100 Ratio of Peak to Average Low Frequency Power Spectral Density Level vs Percent Chord
 (Configuration 1, Mach 0.9, Wing Angle of Attack 14°)

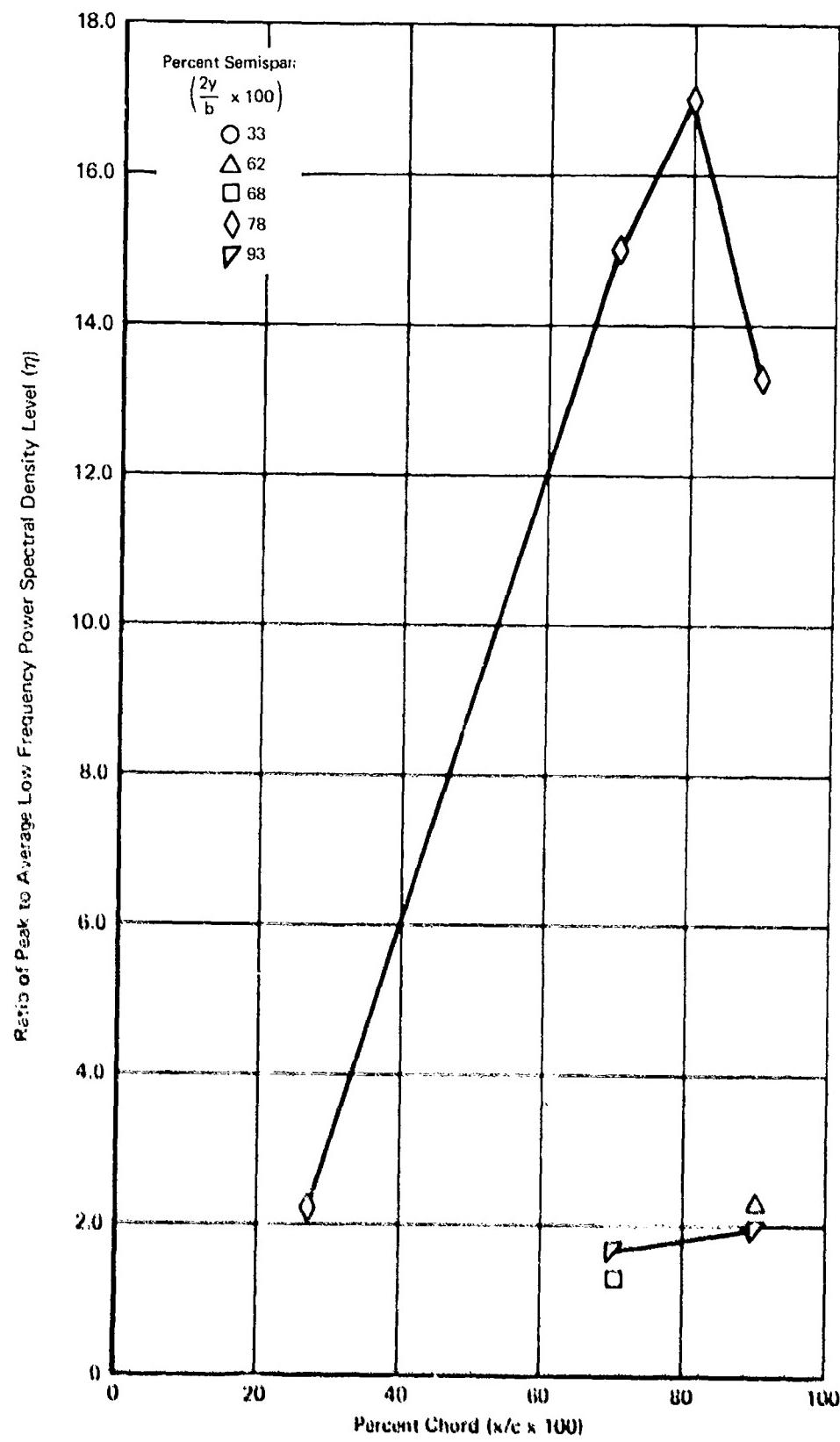


Figure 101 Ratio of Peak to Average Low Frequency Power Spectral Density Level vs Percent Chord
 (Configuration 5, Mach 0.7, Wing Angle of Attack 11°)

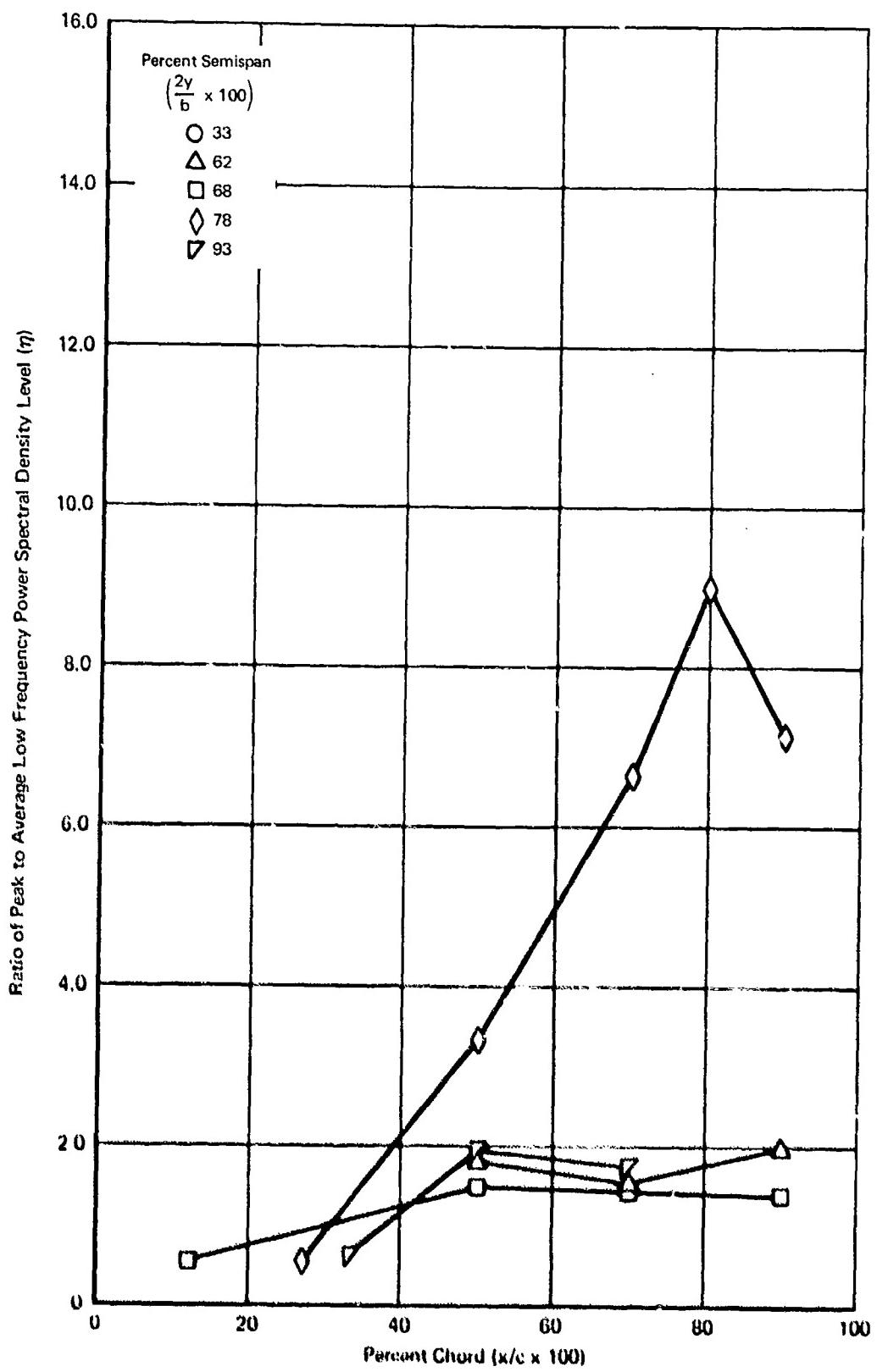
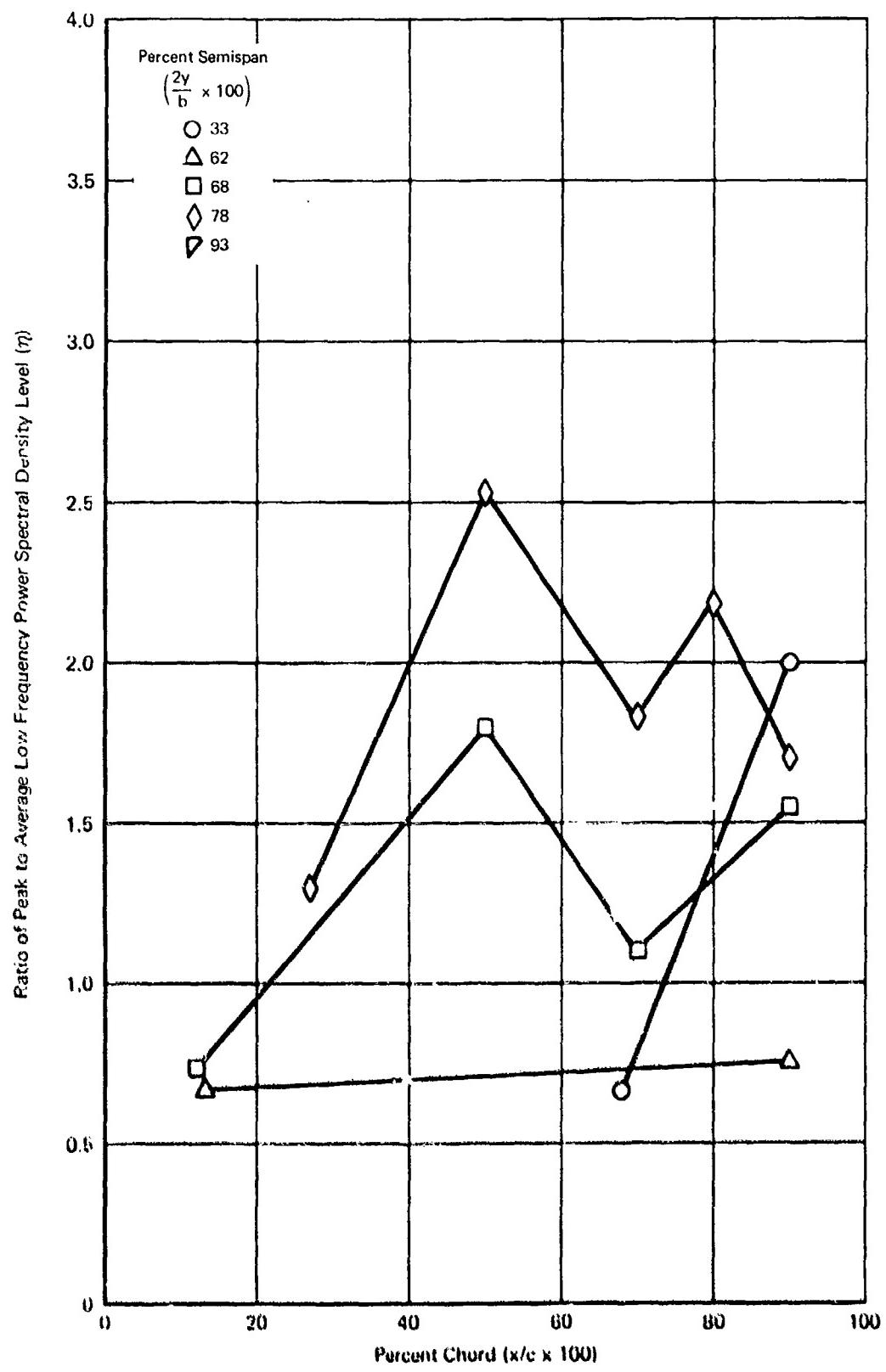


Figure 102 Ratio of Peak to Average Low Frequency Power Spectral Density Level vs Percent Chord
 (Configuration 5, Mach 0.9, Wing Angle of Attack 11°)



**Figure 103 Ratio of Peak to Average Low Frequency Power Spectral Density Level vs Percent Chord
(Configuration 5, Mach 0.9, Wing Angle of Attack 14°)**

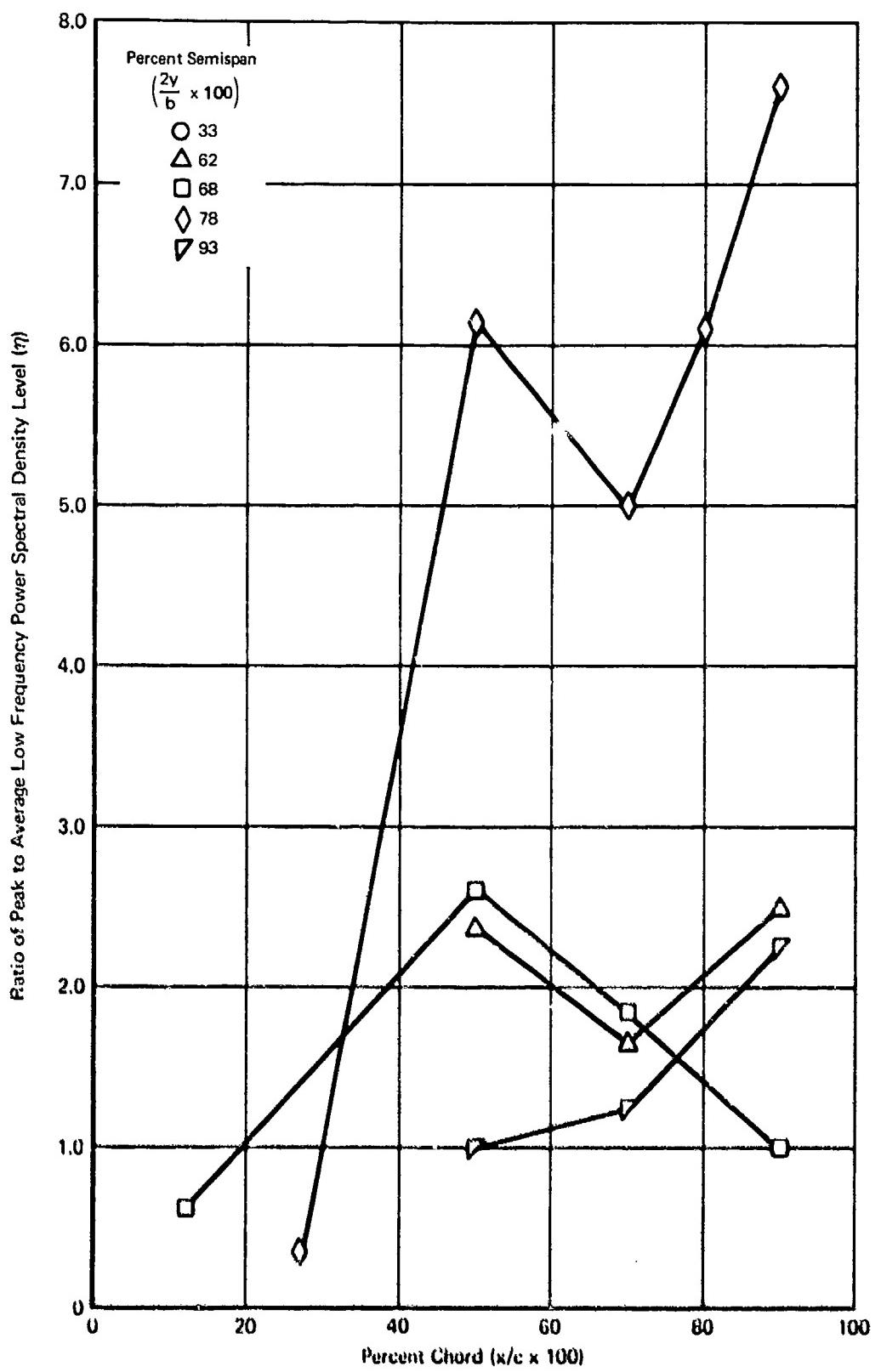


Figure 104 Ratio of Peak to Average Low Frequency Power Spectral Density Level vs Percent Chord
 (Configuration 6, Mach 0.7, Wing Angle of Attack 11°)

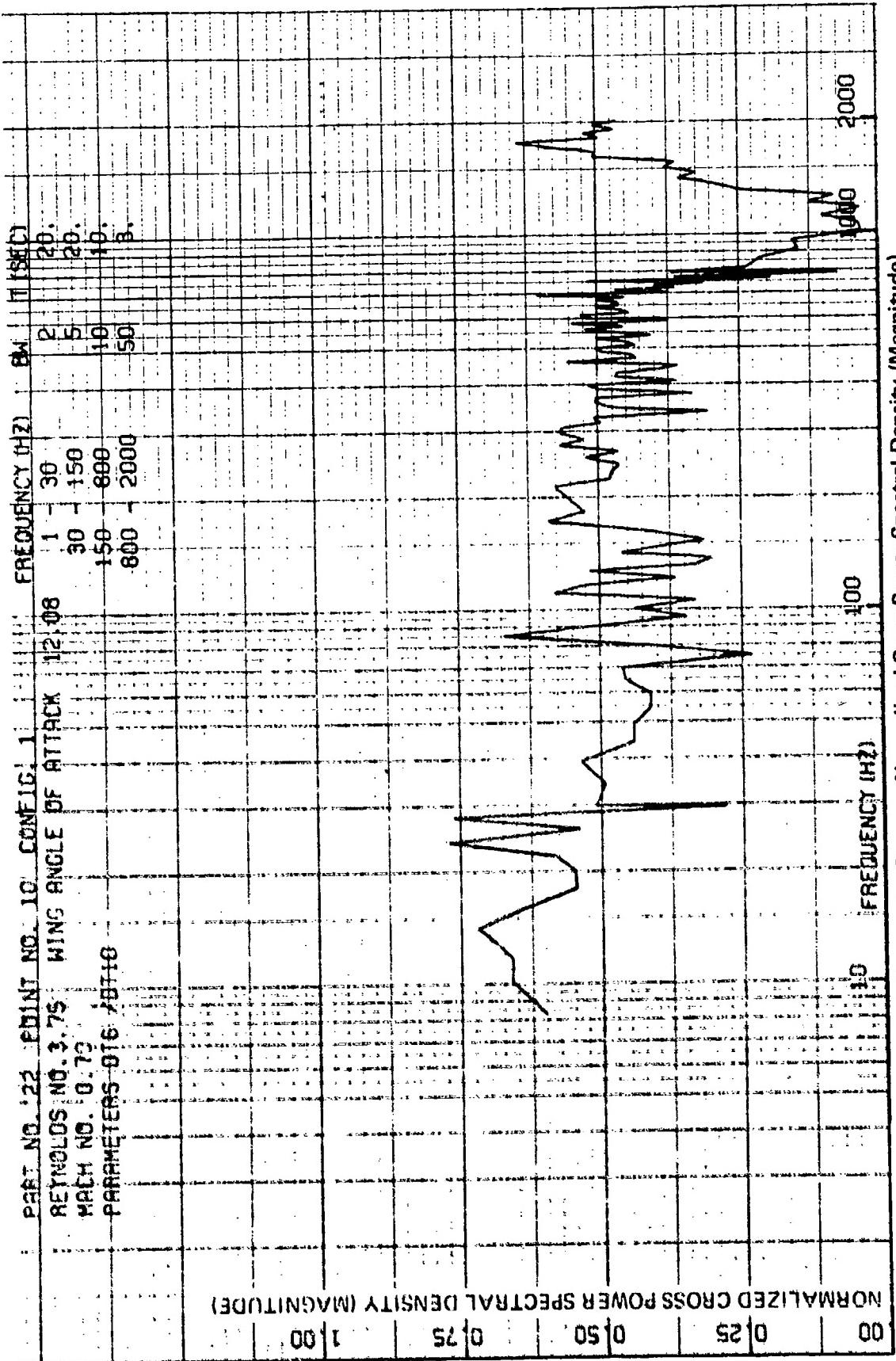


Figure 105 Fluctuating Pressure Normalized Cross Power Spectral Density (Magnitude)
(Configuration 1, Mach 0.7, Wing Angle of Attack 12 Deg., Transducers 6 and 10)

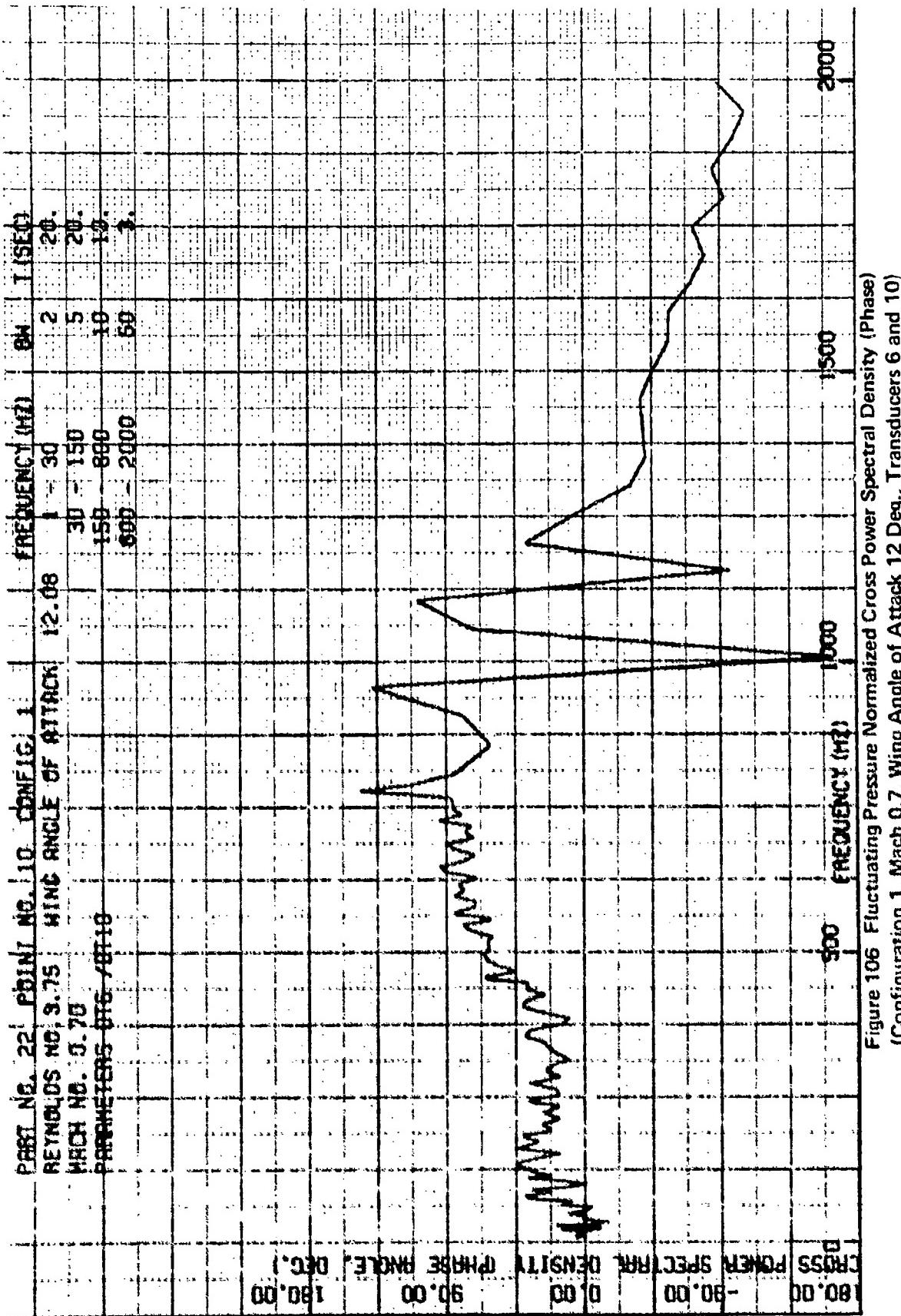


Figure 106 Fluctuating Pressure Normalized Cross Power Spectral Density (Phase) (Configuration 1, Mach 0.7, Wing Angle of Attack 12 Deg., Transducers 6 and 10)

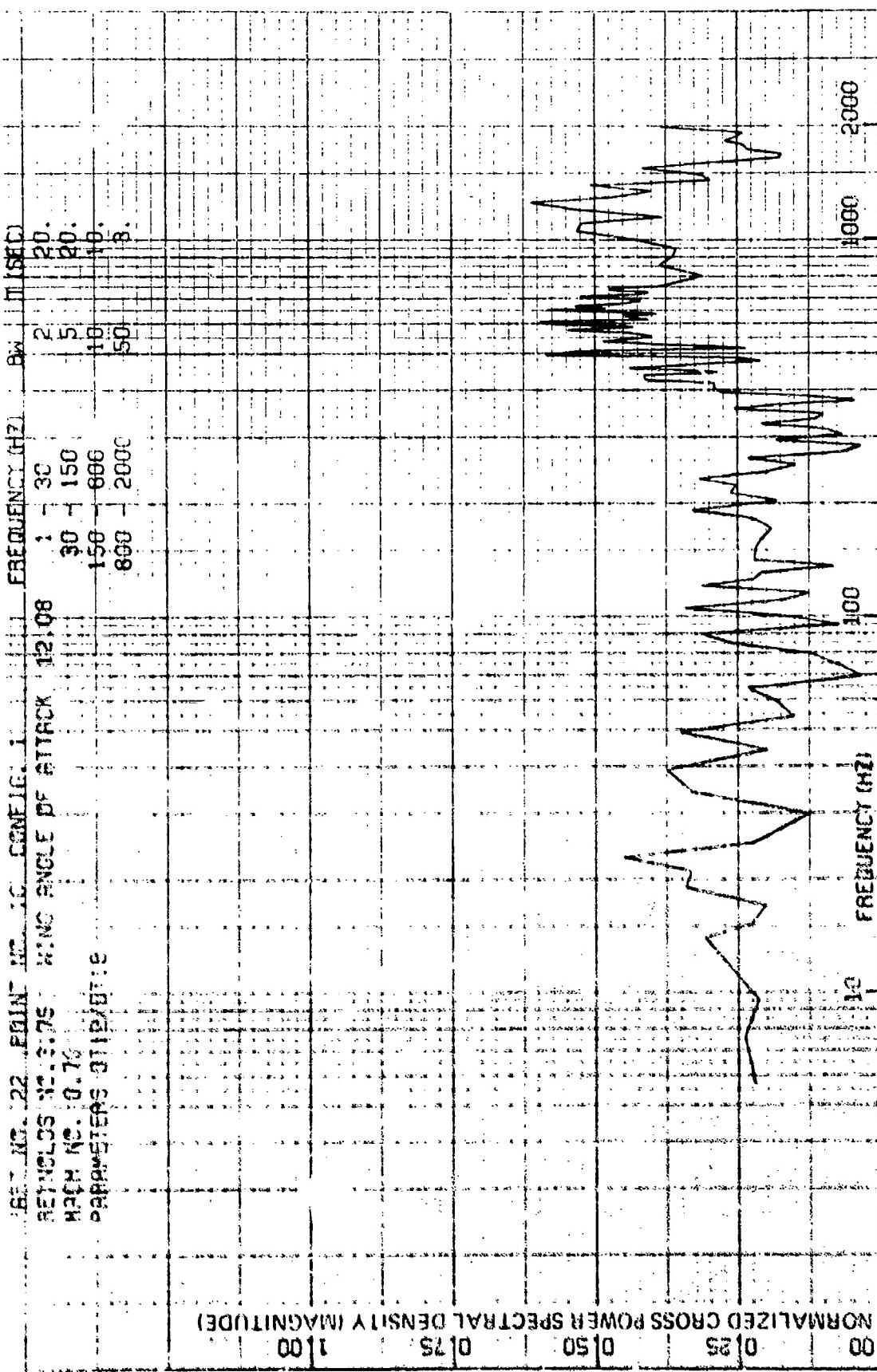


Figure 107 Fluctuating Pressure Normalized Cross Power Spectral Density (Magnitude)-
(Configuration 1, Mach 0.7, Wing Angle of Attack 12 Deg., Transducers 12 and 18)

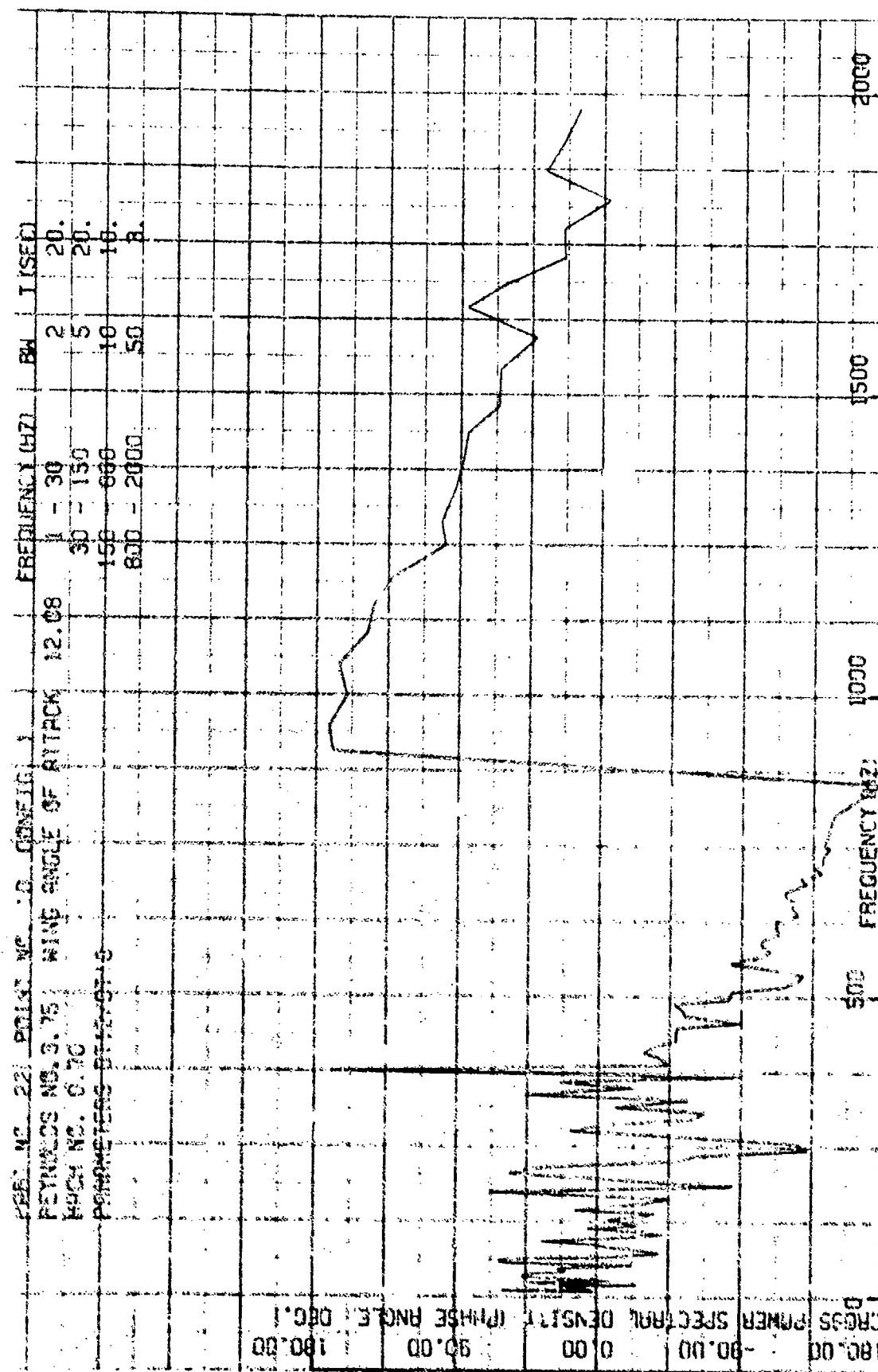


Figure 108 Fluctuating Pressure Normalized Cross Power Spectral Density (Phase)
(Configuration 1, Mach 0.7, Wing Angle of Attack 12 Deg., Transducers 12 and 18)

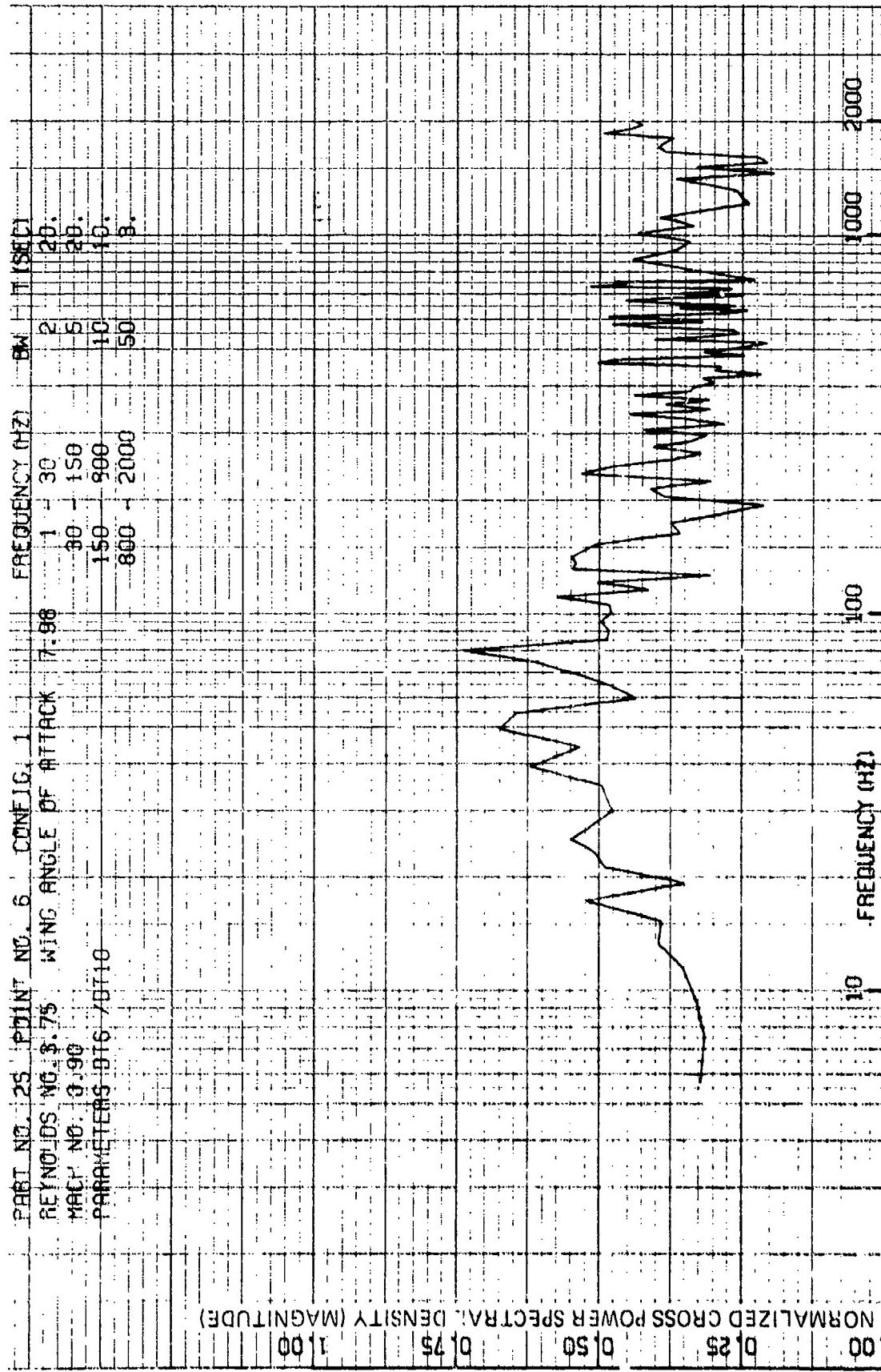


Figure 109 Fluctuating Pressure Normalized Cross Power Spectral Density (Magnitude)
 (Configuration 1, Mach 0.9, Wing Angle of Attack 8 Deg., Transducers 6 and 10)

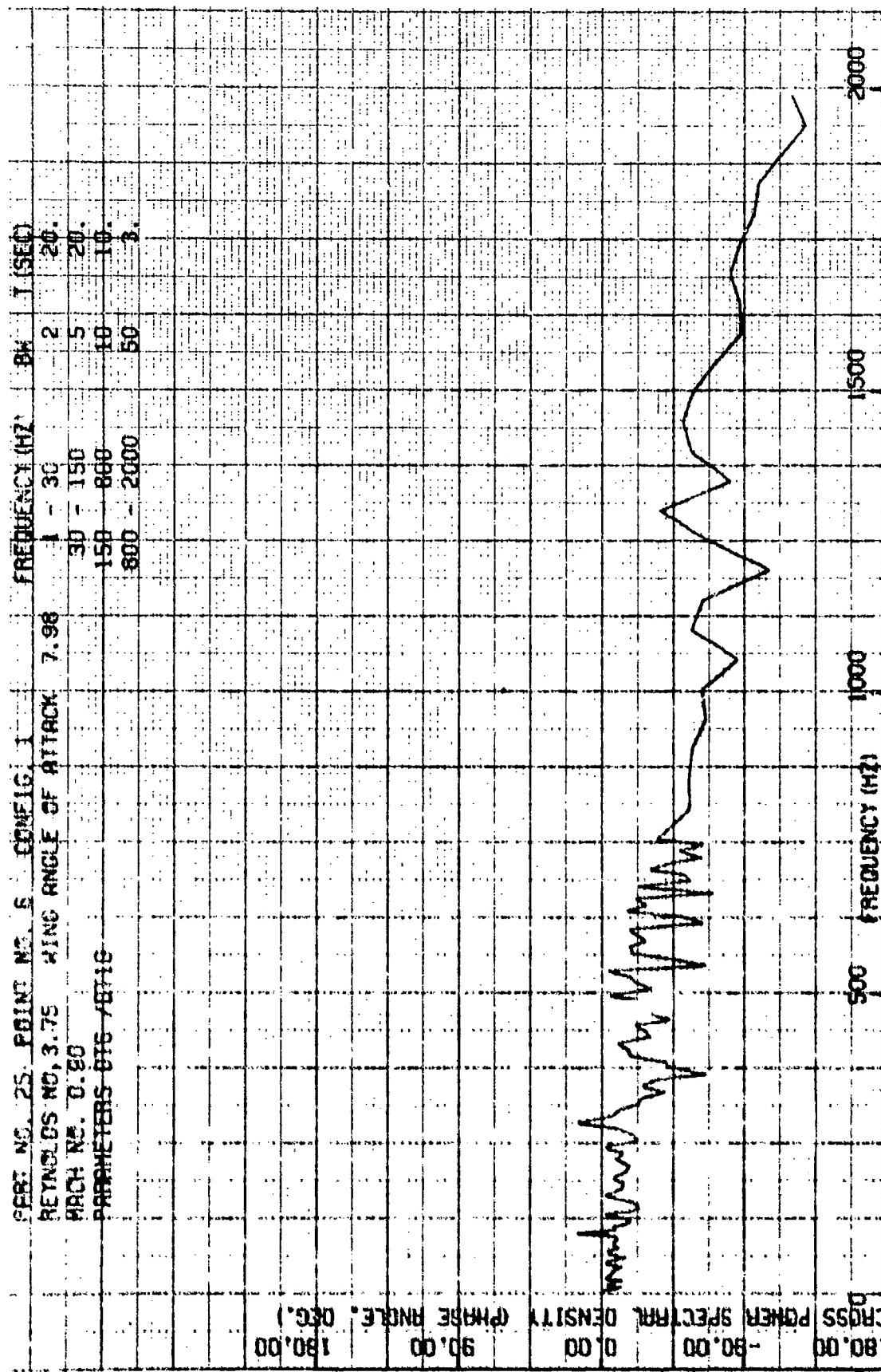


Figure 110 Fluctuating Pressure Normalized Cross Power Spectral Density (Phase)
 (Configuration 1, Mach 0.9, Wing Angle of Attack 8 Deg., Transducers 6 and 10)

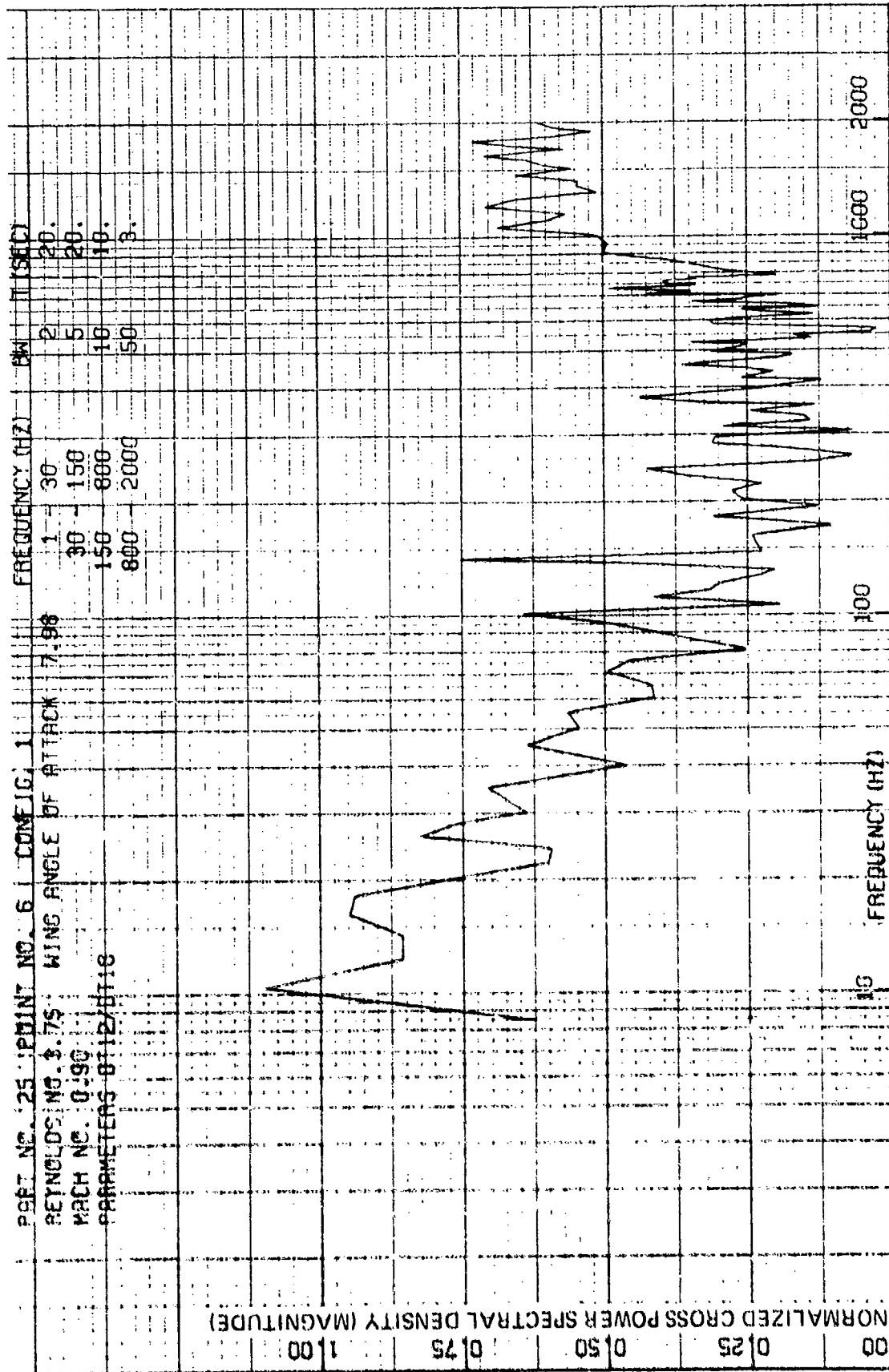


Figure 111 Fluctuating Pressure Normalized Cross Power Spectral Density (Magnitude),
 Configuration 1, Mach 0.9, Wing Angle of Attack 8 Deg., Transducers 12 and 18

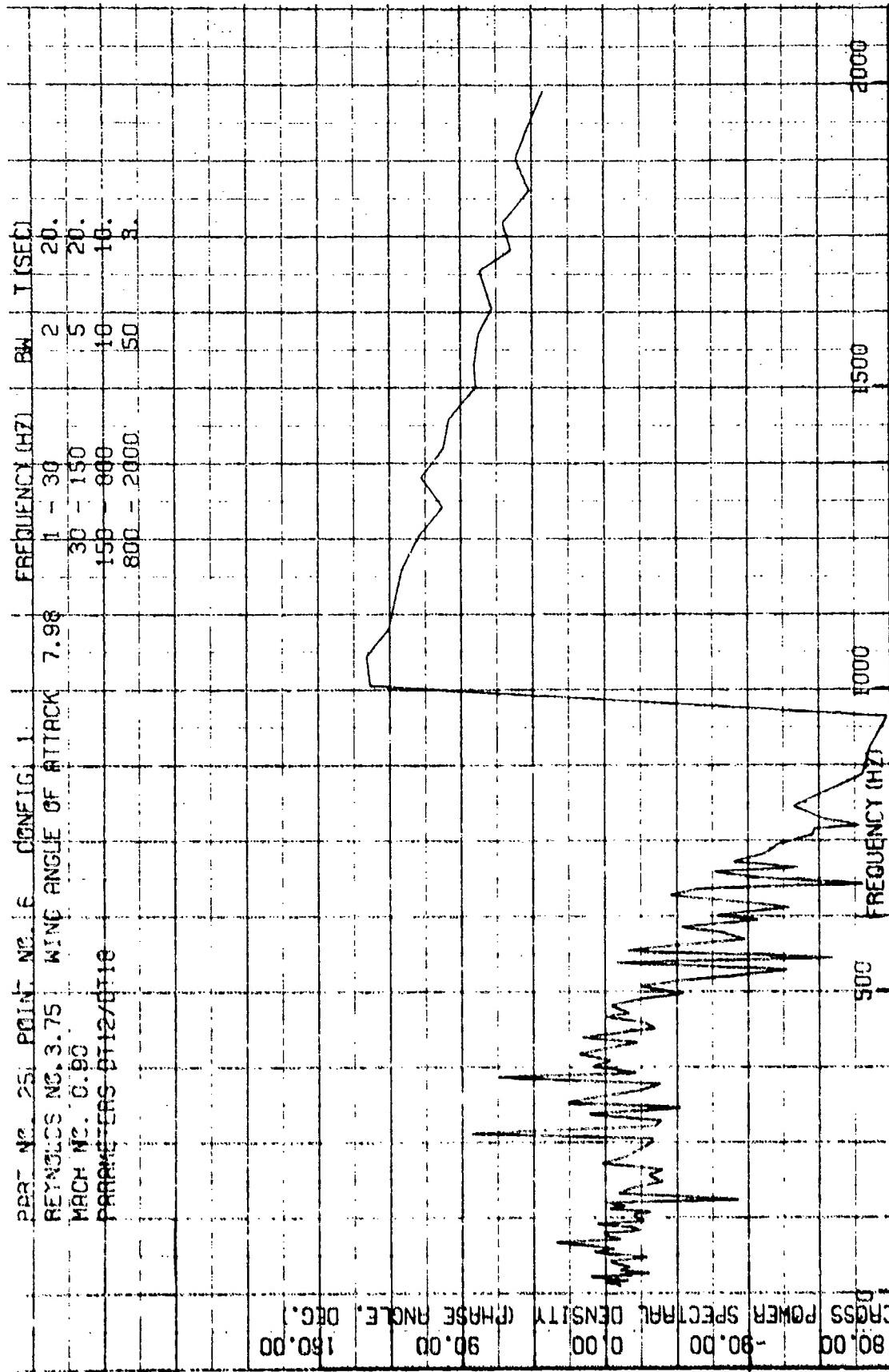


Figure 112 Fluctuating Pressure Normalized Cross Power Spectral Density (Phase)
 (Configuration 1, Mach 0.9, Wing Angle of Attack 8 Deg., Transducers 12 and 18)

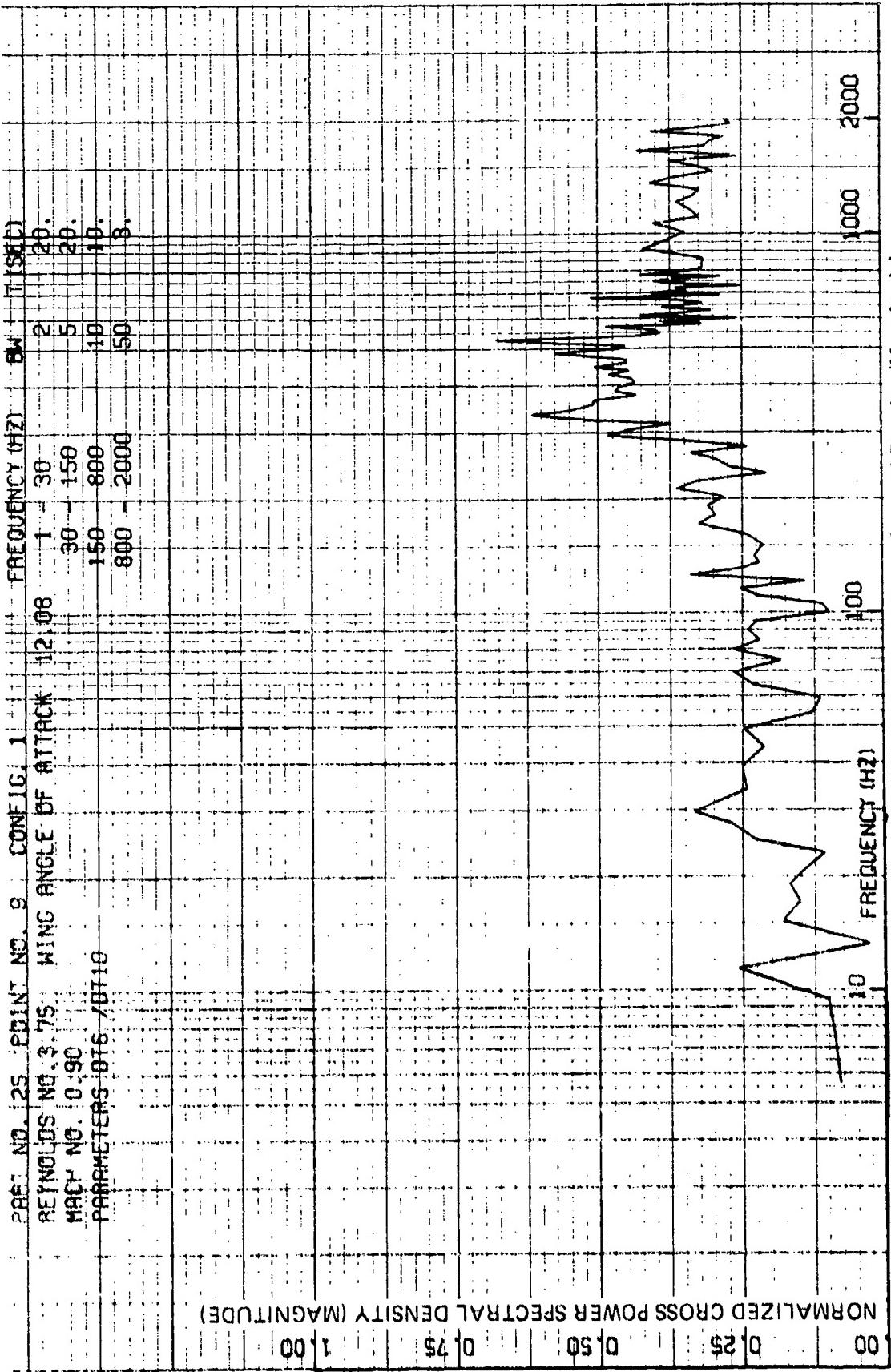


Figure 113 Fluctuating Pressure Normalized Cross Power Spectral Density (Magnitude)
 (Configuration 1, Mach 0.9, Wing Angle of Attack 12 Deg., Transducers 6 and 10)

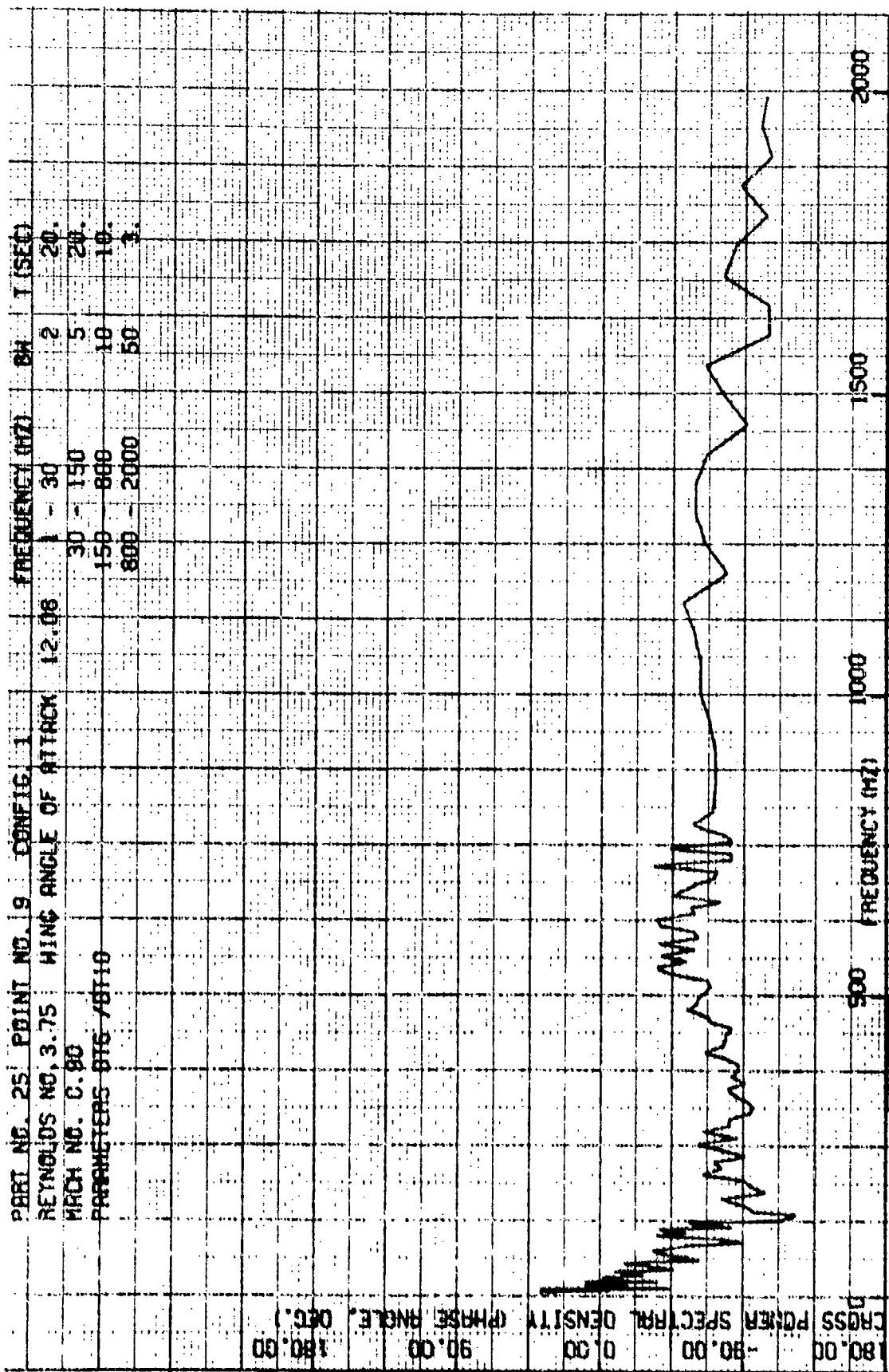


Figure 114 Fluctuating Pressure Normalized Cross Power Spectral Density (Phase)
 (Configuration 1, Mach 0.9, Wing Angle of Attack 12 Deg., Transducers 6 and 10)

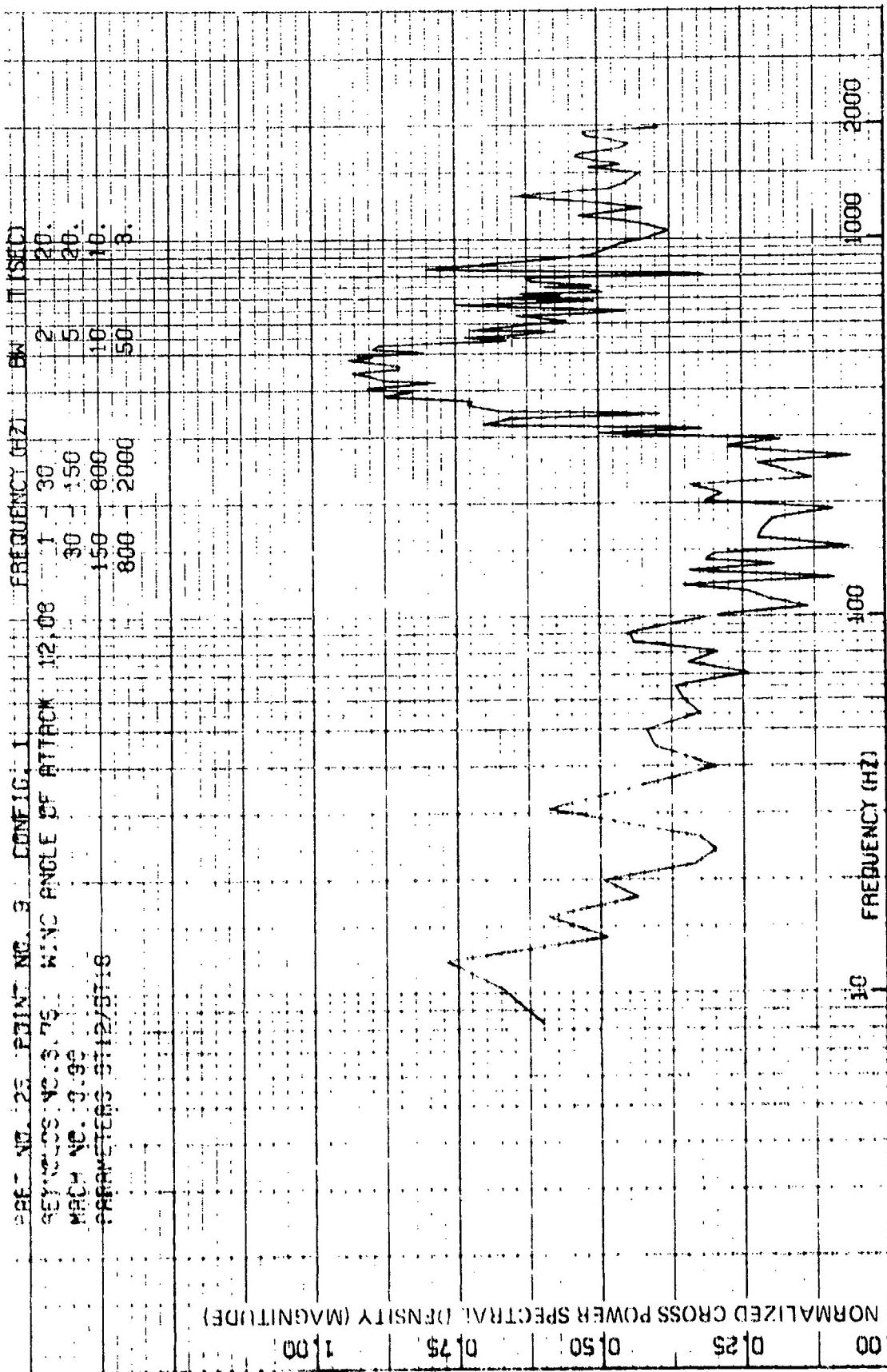


Figure 115 Fluctuating Pressure Normalized Cross Power Spectral Density (Magnitude)
 (Configuration 1, Mach 0.9, Wing Angle of Attack 12 Deg., Transducers 12 and 18)

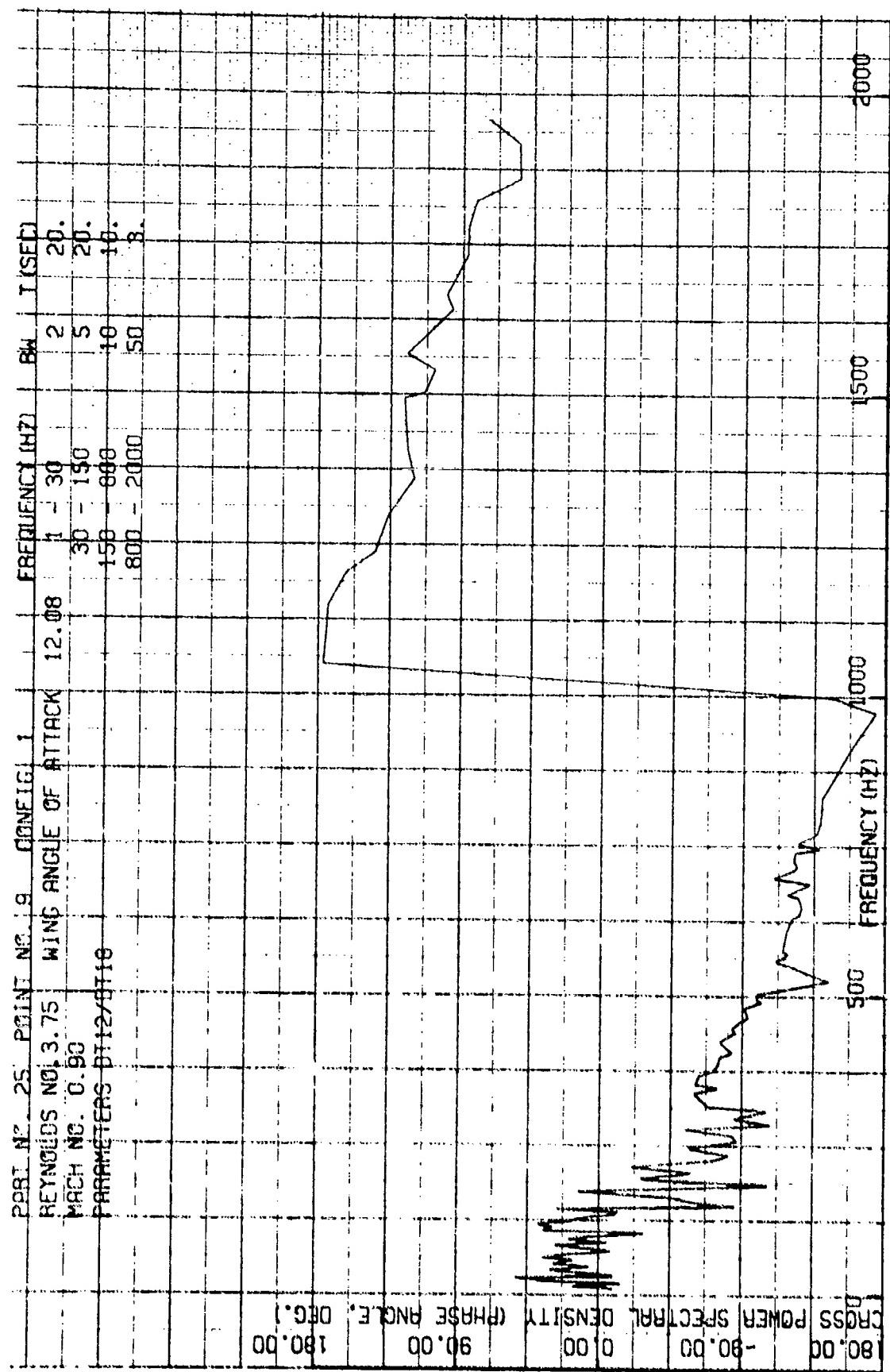


Figure 116 Fluctuating Pressure Normalized Cross Power Spectral Density (Phase)
 (Configuration 1, Mach 0.9, Wing Angle of Attack 12 Deg., Transducers 12 and 18)

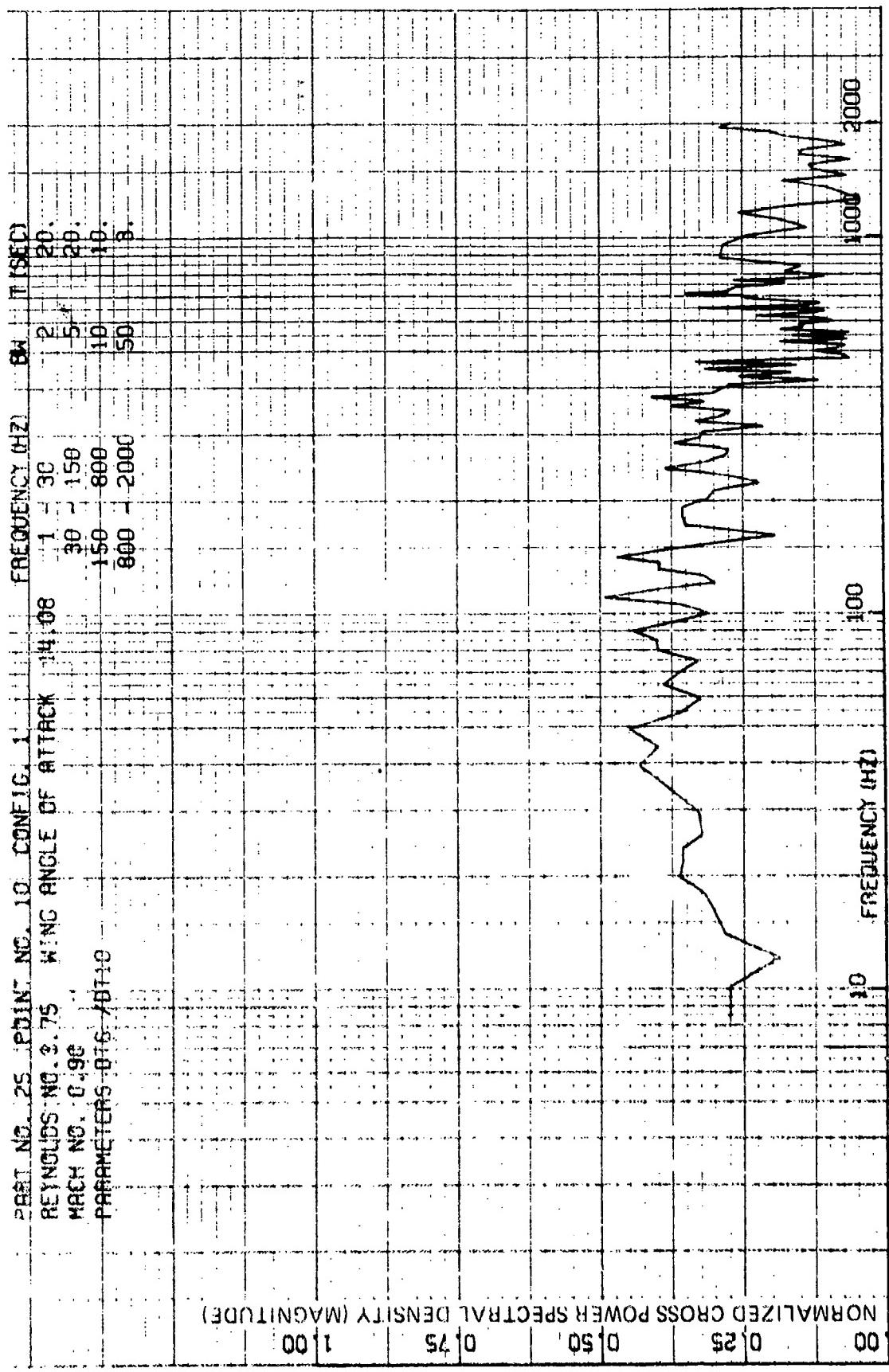


Figure 117 Fluctuating Pressure Normalized Cross Power Spectral Density (Magnitude)
 (Configuration 1, Mach 0.9, Wing Angle of Attack 14 Deg., Transducers 6 and 10)

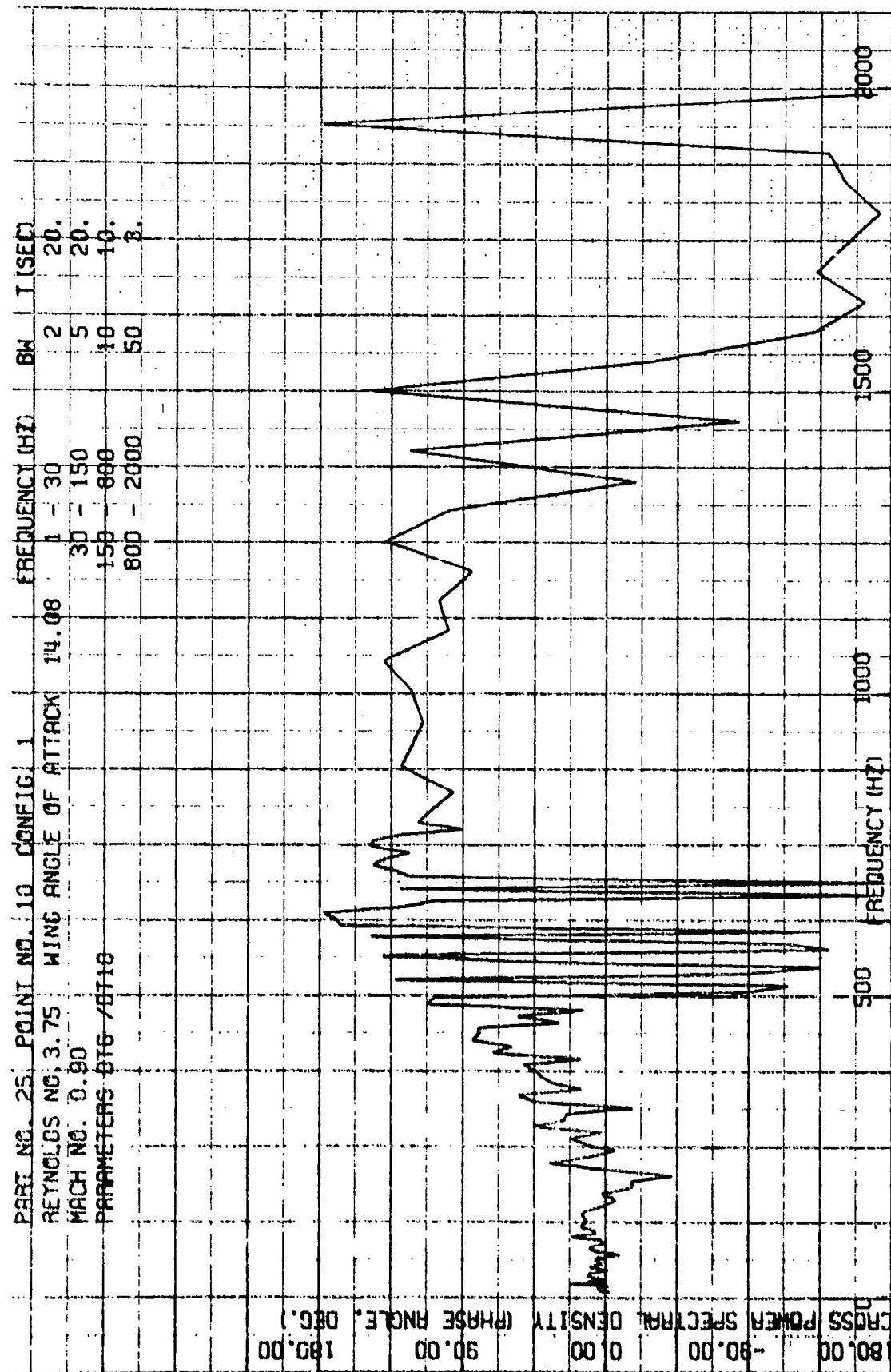


Figure 118 Fluctuating Pressure Normalized Cross Power Spectral Density (Phase)
(Configuration 1, Mach 0.9, Wing Angle of Attack 14 Deg., Transducers 6 and 10)

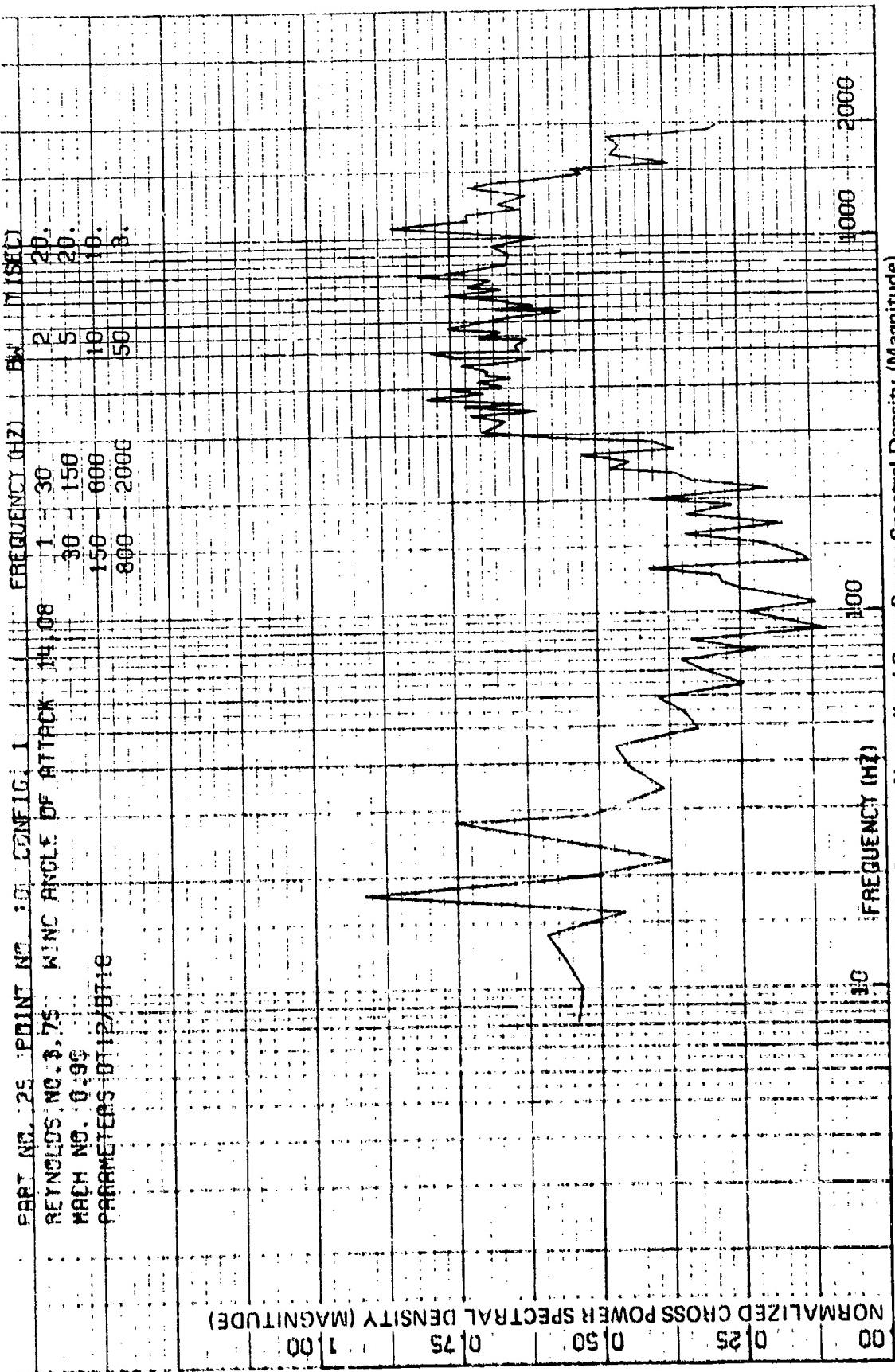


Figure 119 Fluctuating Pressure Normalized Cross Power Spectral Density (Magnitude)
 (Configuration 1, Mach 0.9, Wing Angle of Attack 14 Deg., Transducers 12 and 18)

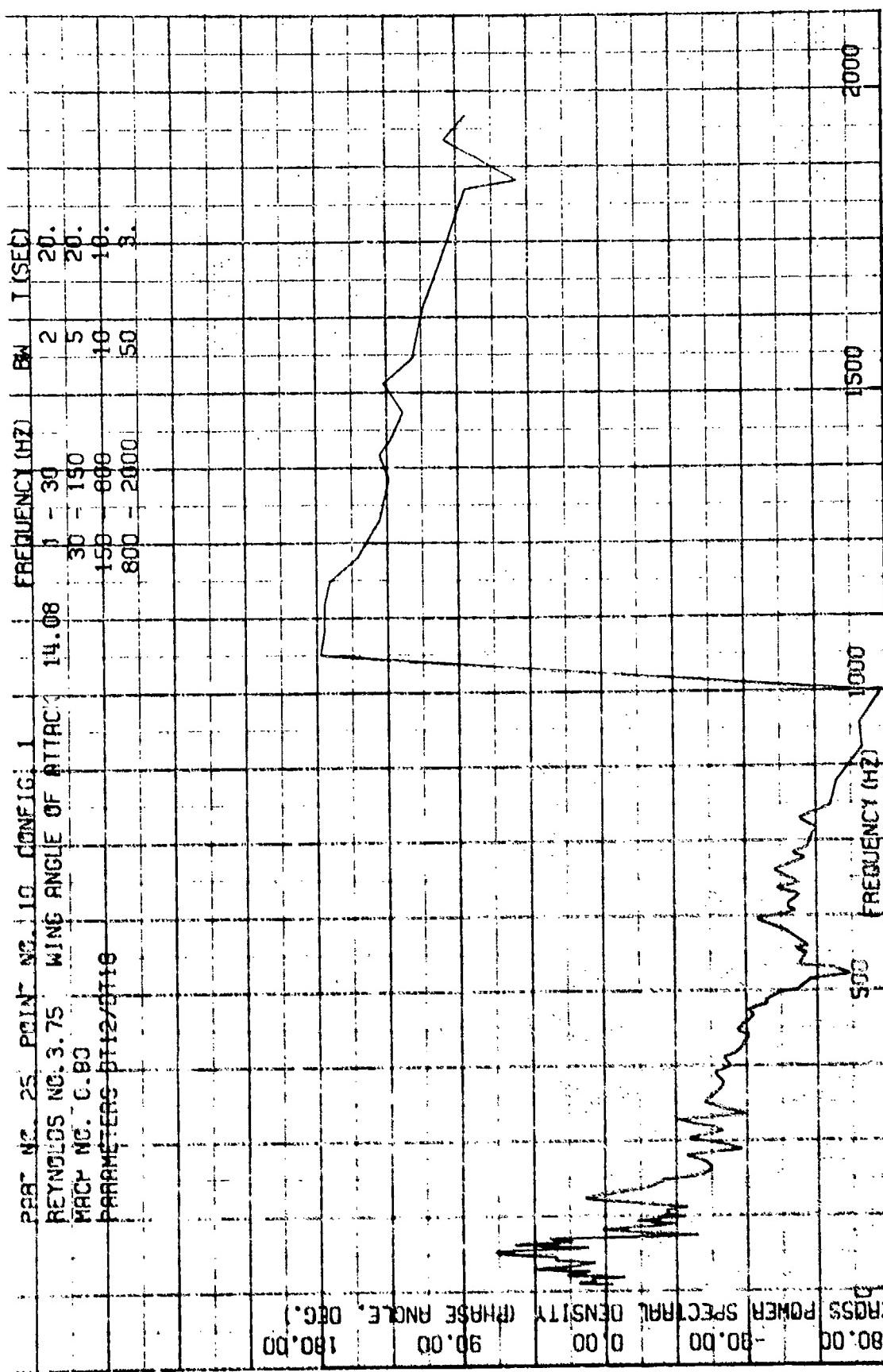


Figure 120 Fluctuating Pressure Normalized Cross Power Spectral Density (Phase)
(Configuration 1, Mach 0.9, Wing Angle of Attack 14 Deg., Transducers 12 and 18)

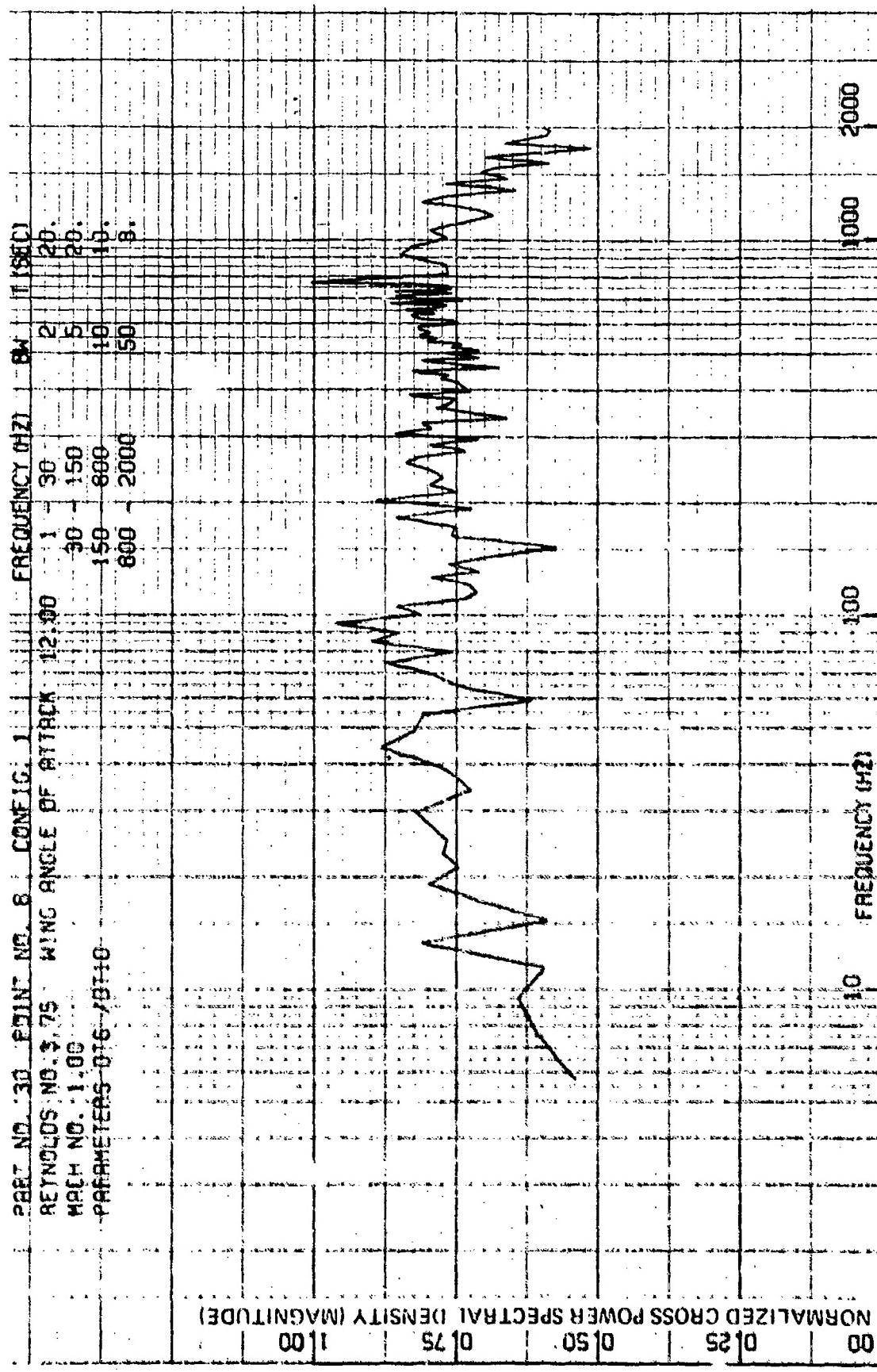


Figure 121 Fluctuating Pressure Normalized Cross Power Spectral Density (Magnitude)
 (Configuration 1, Mach 1.0, Wing Angle of Attack 12 Deg., Transducers 6 and 10)

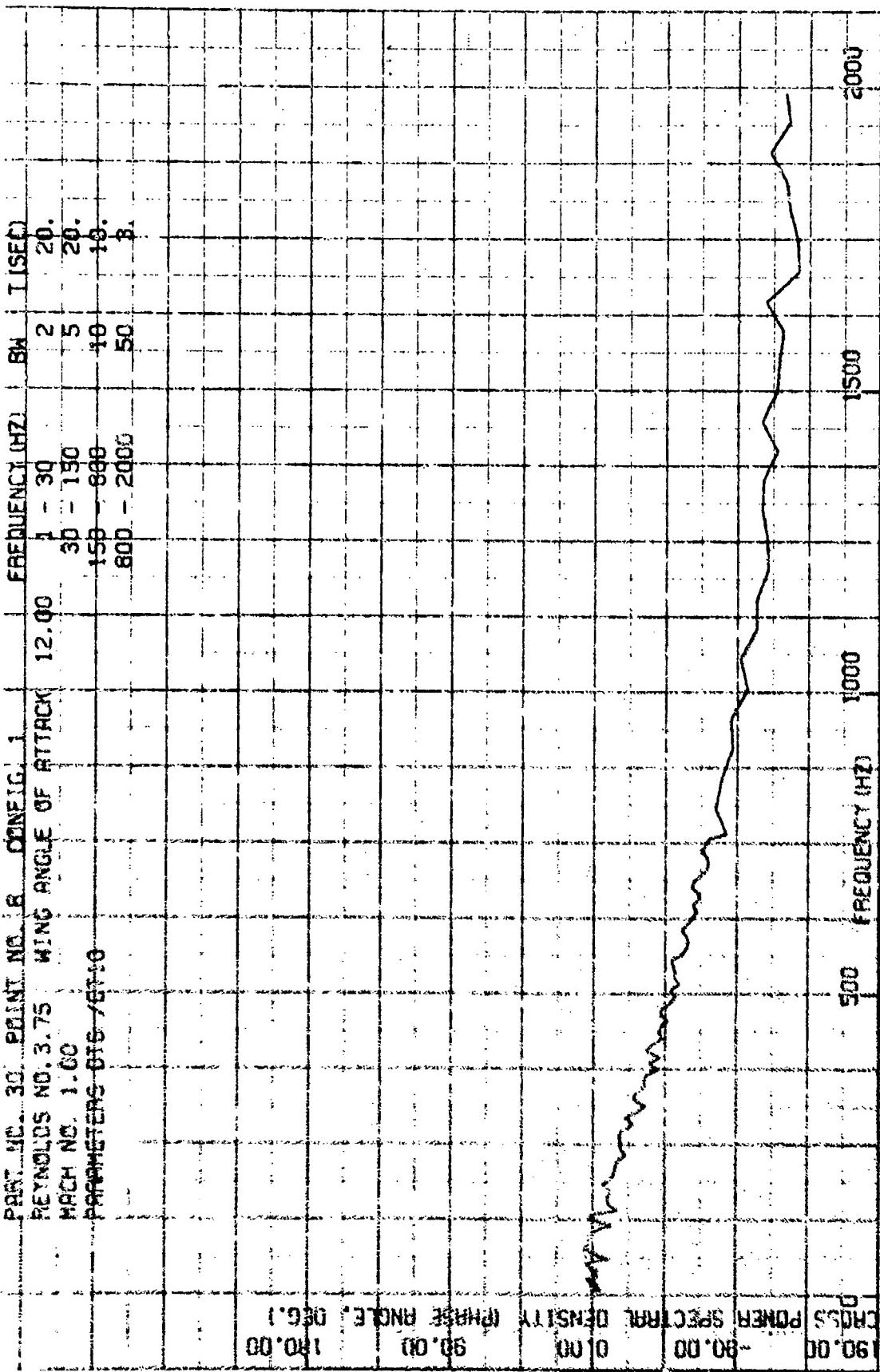


Figure 122 Fluctuating Pressure Normalized Cross Power Spectral Density (Phase)
 (Configuration 1, Mach 1.0, Wing Angle of Attack 12 Deg., Transducers 6 and 10)

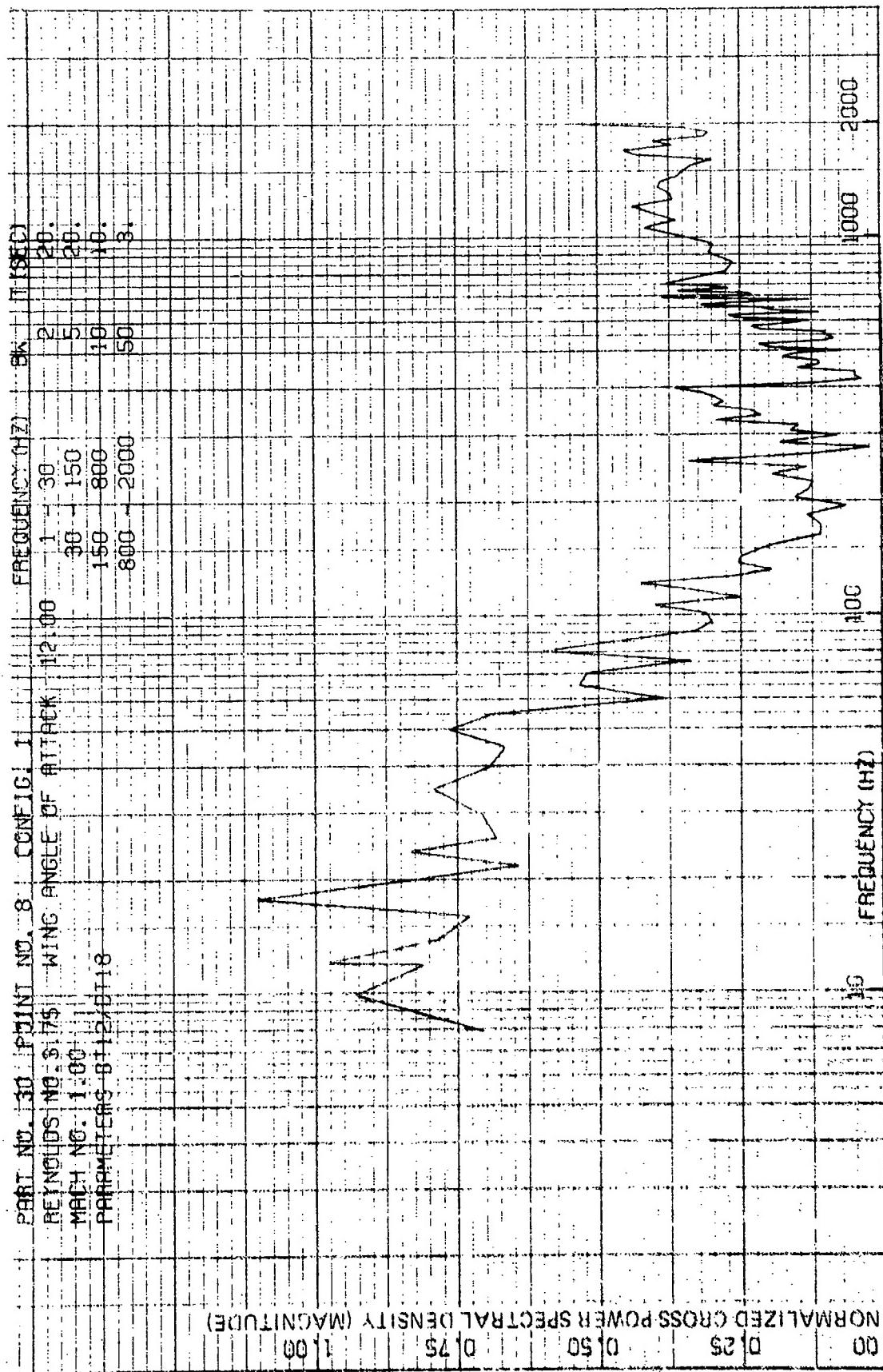


Figure 123 Fluctuating Pressure No normalized Cross Power Spectral Density (Magnitude)
 (Configuration 1, Mach 1.0, Wing Angle of Attack 12 Deg., Transducers 12 and 18)

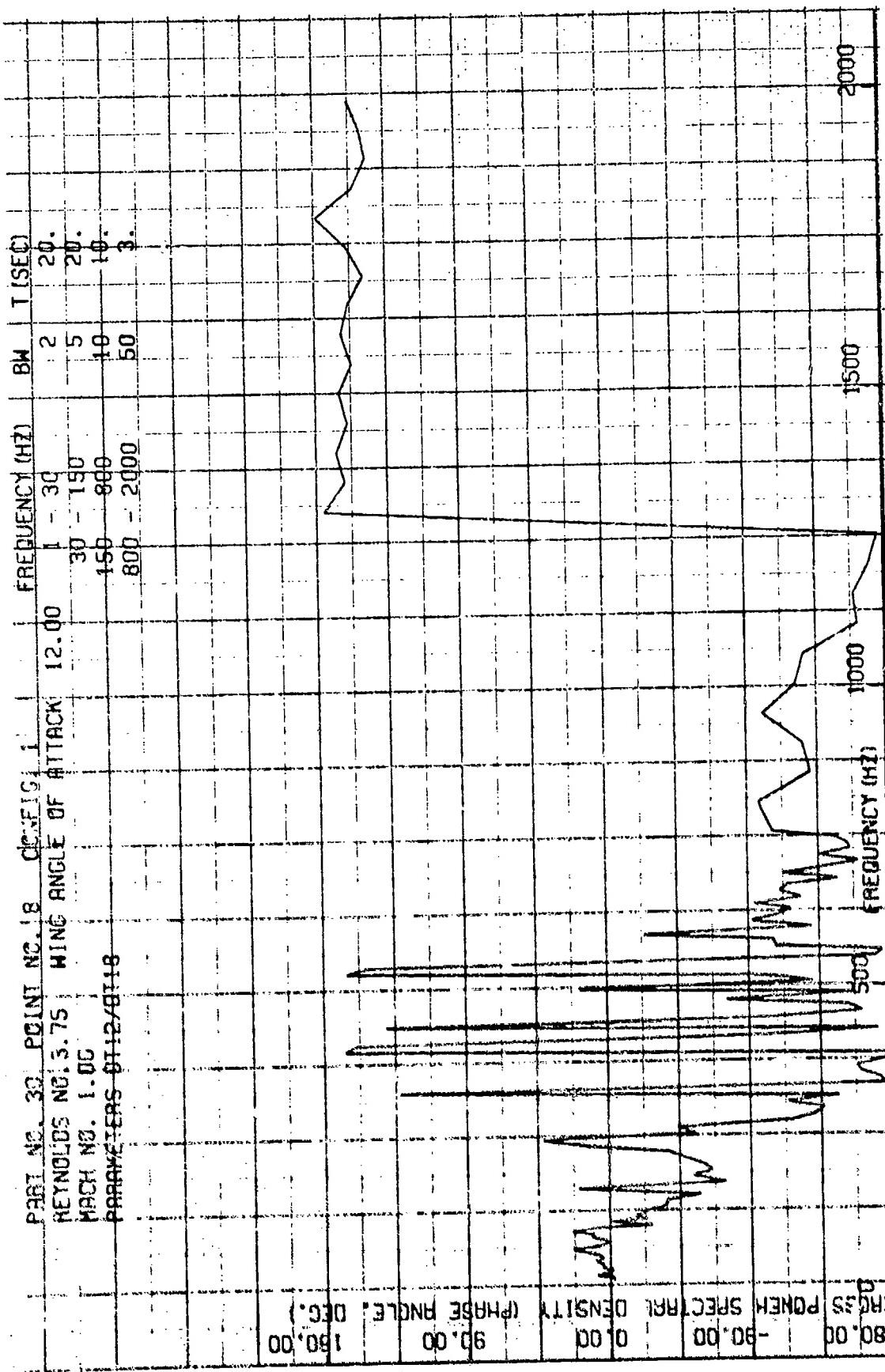


Figure 124 Fluctuating Pressure Normalized Cross Power Spectral Density (Phase)
 (Configuration 1, Mach 1.0, Wing Angle of Attack 12 Deg., Transducers 12 and 18)

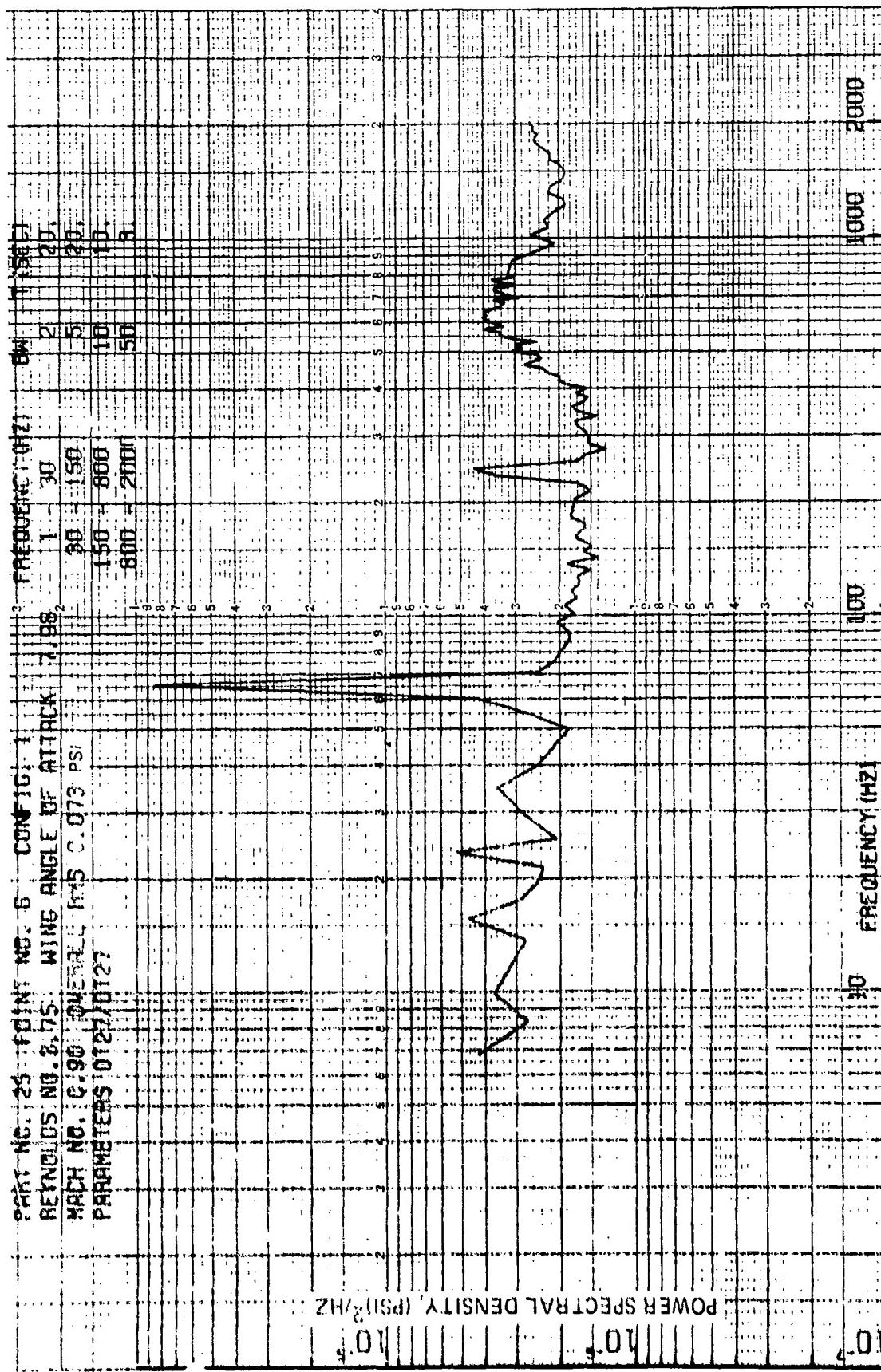


Figure 125 Fluctuating Pressure Power Spectral Density (Configuration 1, Mach 0.9, Wing Angle of Attack 8 Deg., Transducer 27)

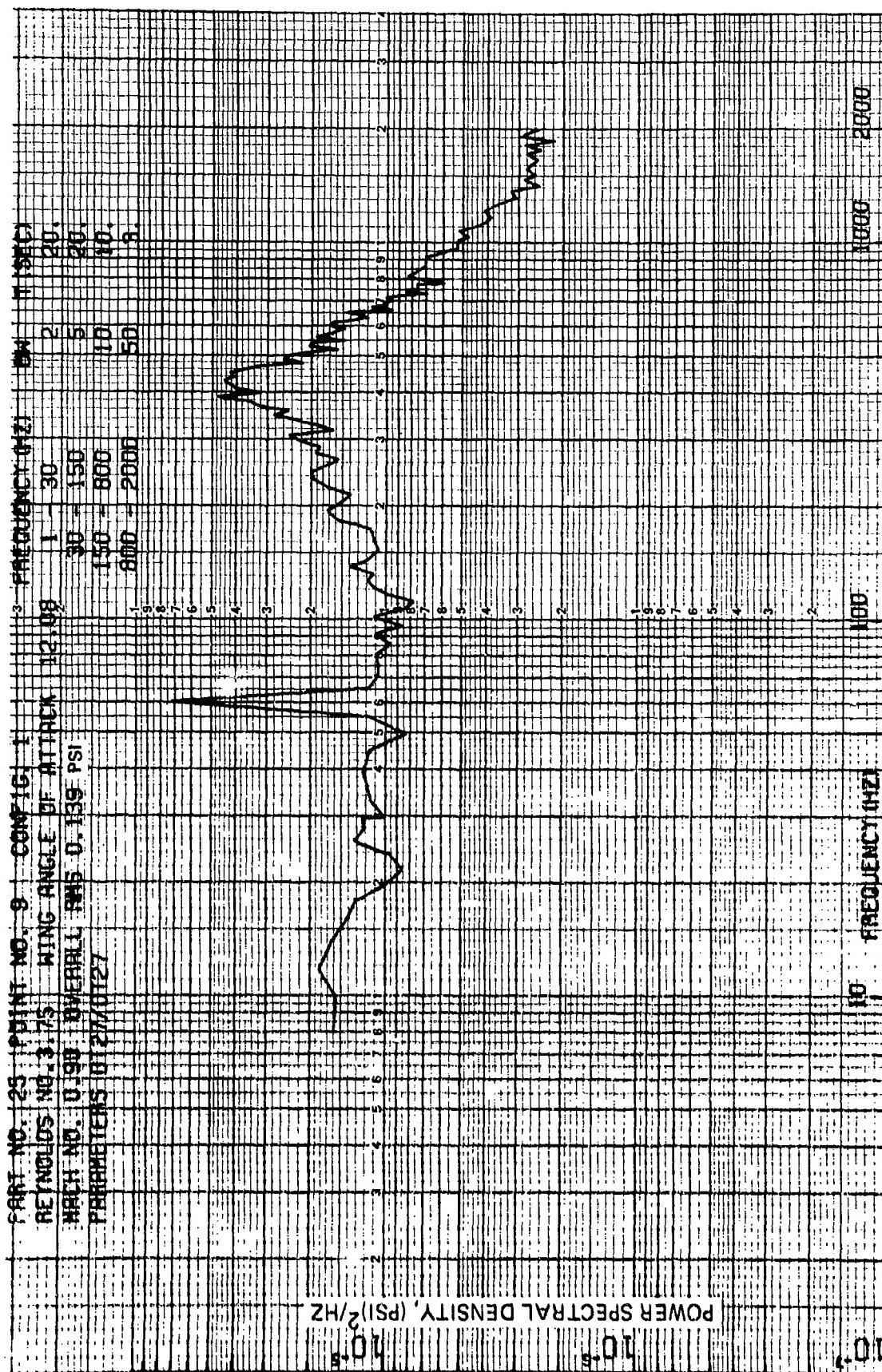


Figure 126 Fluctuating Pressure Power Spectral Density (Configuration 1, Mach 0.9, Wing Angle of Attack 12 Deg., Transducer 27)

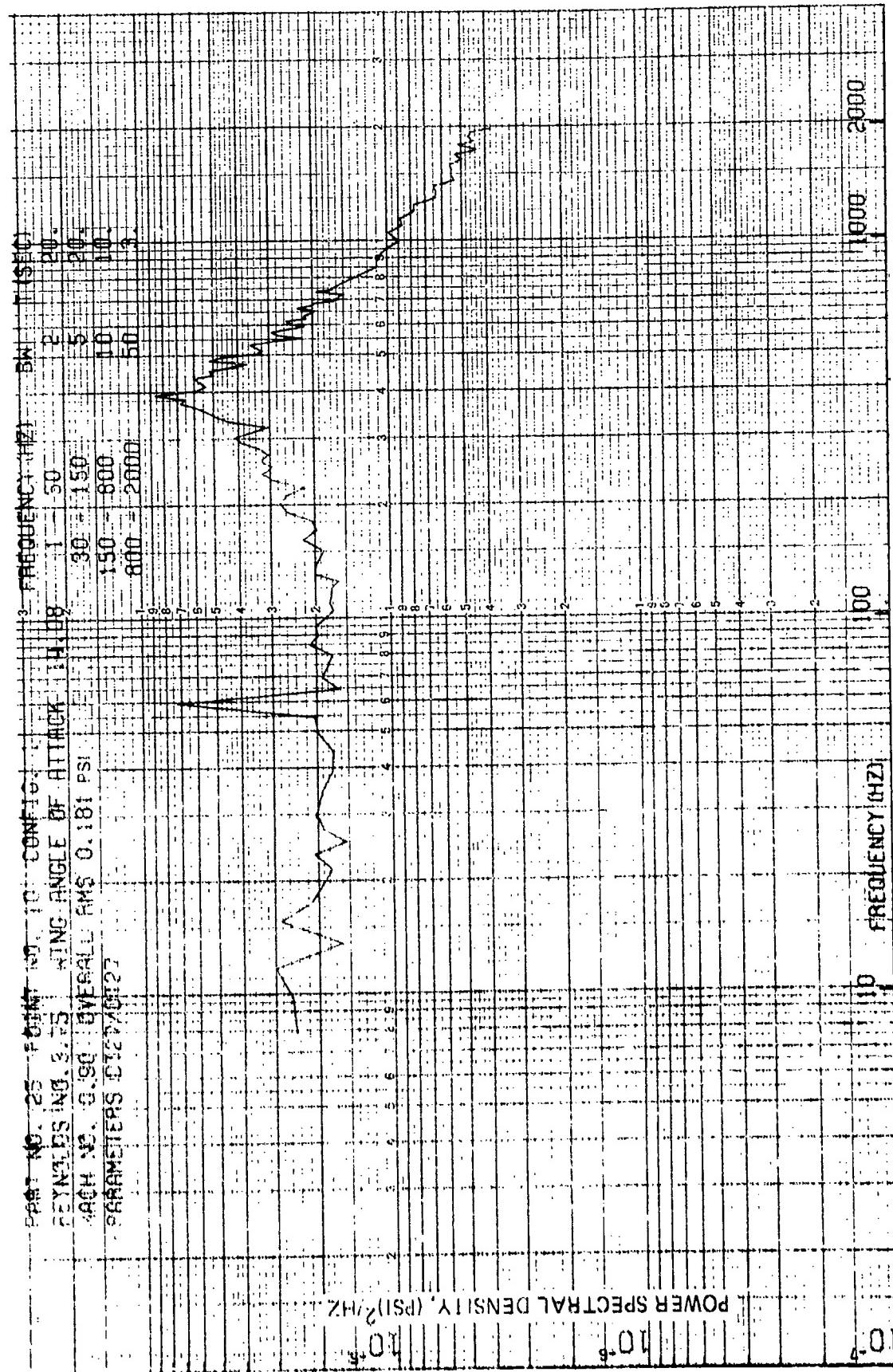


Figure 127 Fluctuating Pressure Power Spectral Density (Configuration 1, Mach 0.9, Wing Angle of Attack 14 Deg., Transducer 27)

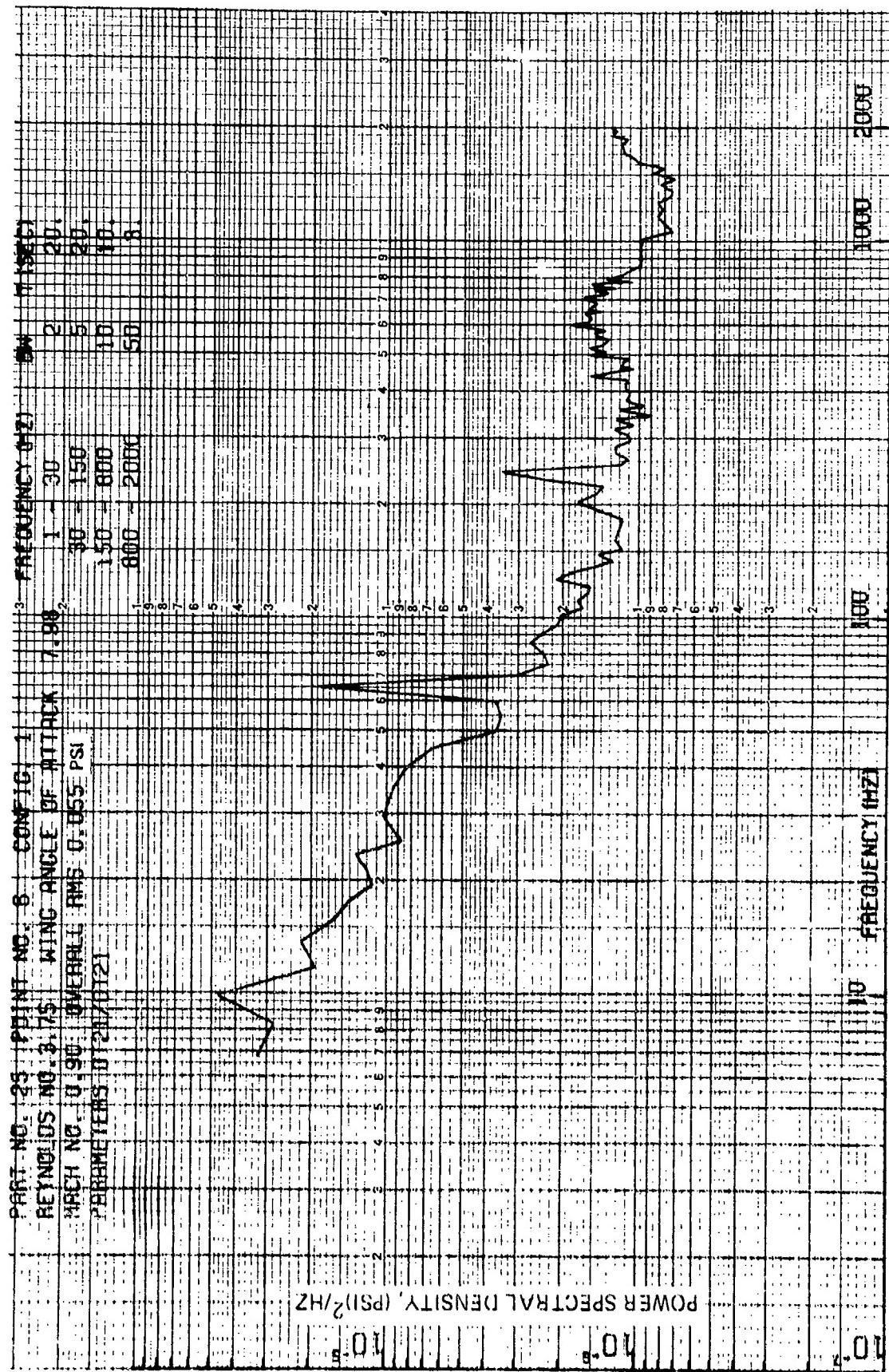


Figure 128 Fluctuating Pressure Power Spectral Density (Configuration 1, Mach 0.9,
Wing Angle of Attack 8 Deg., Transducer 21)

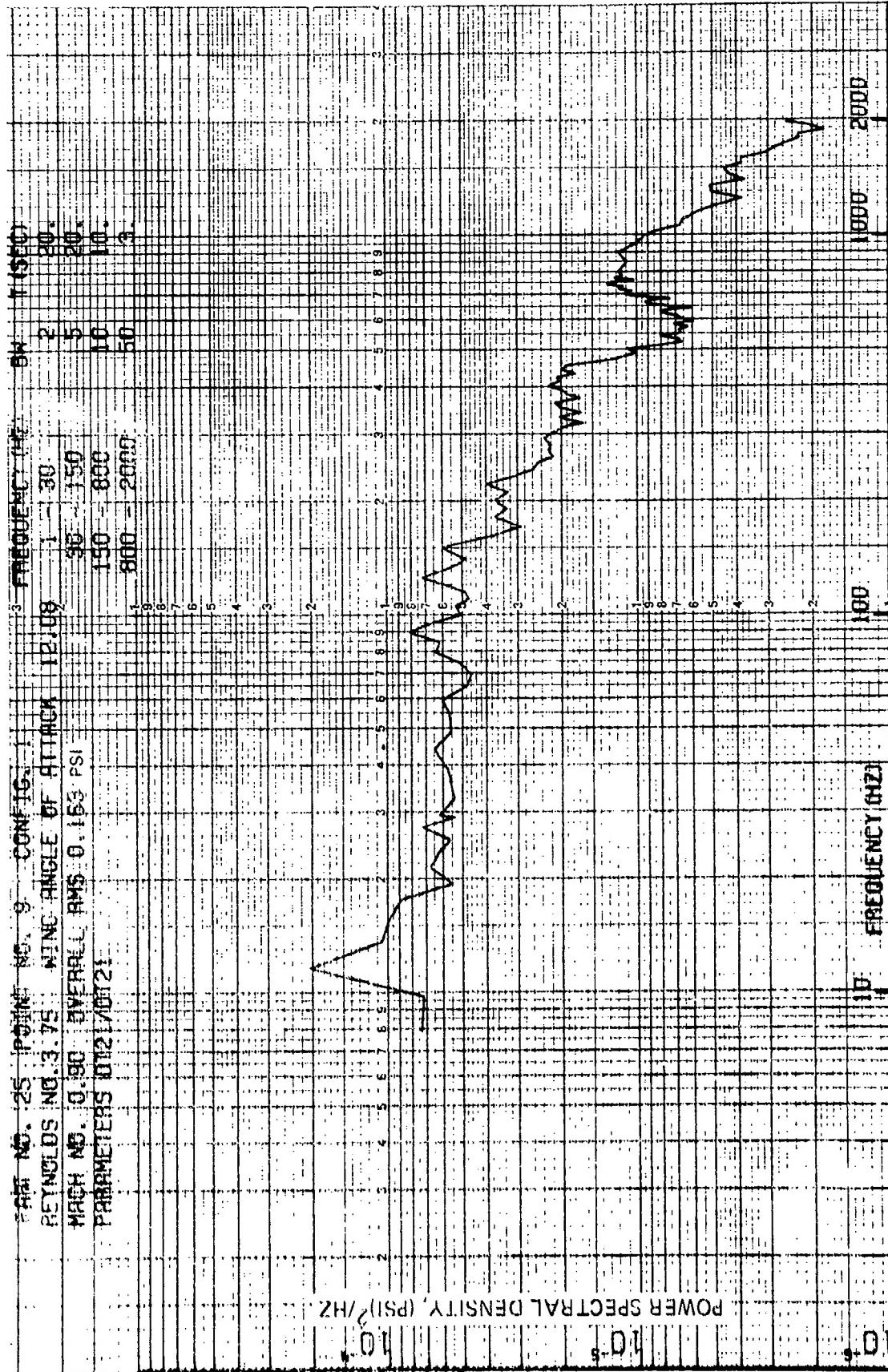


Figure 129 Fluctuating Pressure Power Spectral Density (Configuration 1, Mach 0.9, Wing Angle of Attack 12 Deg., Transducer 21)

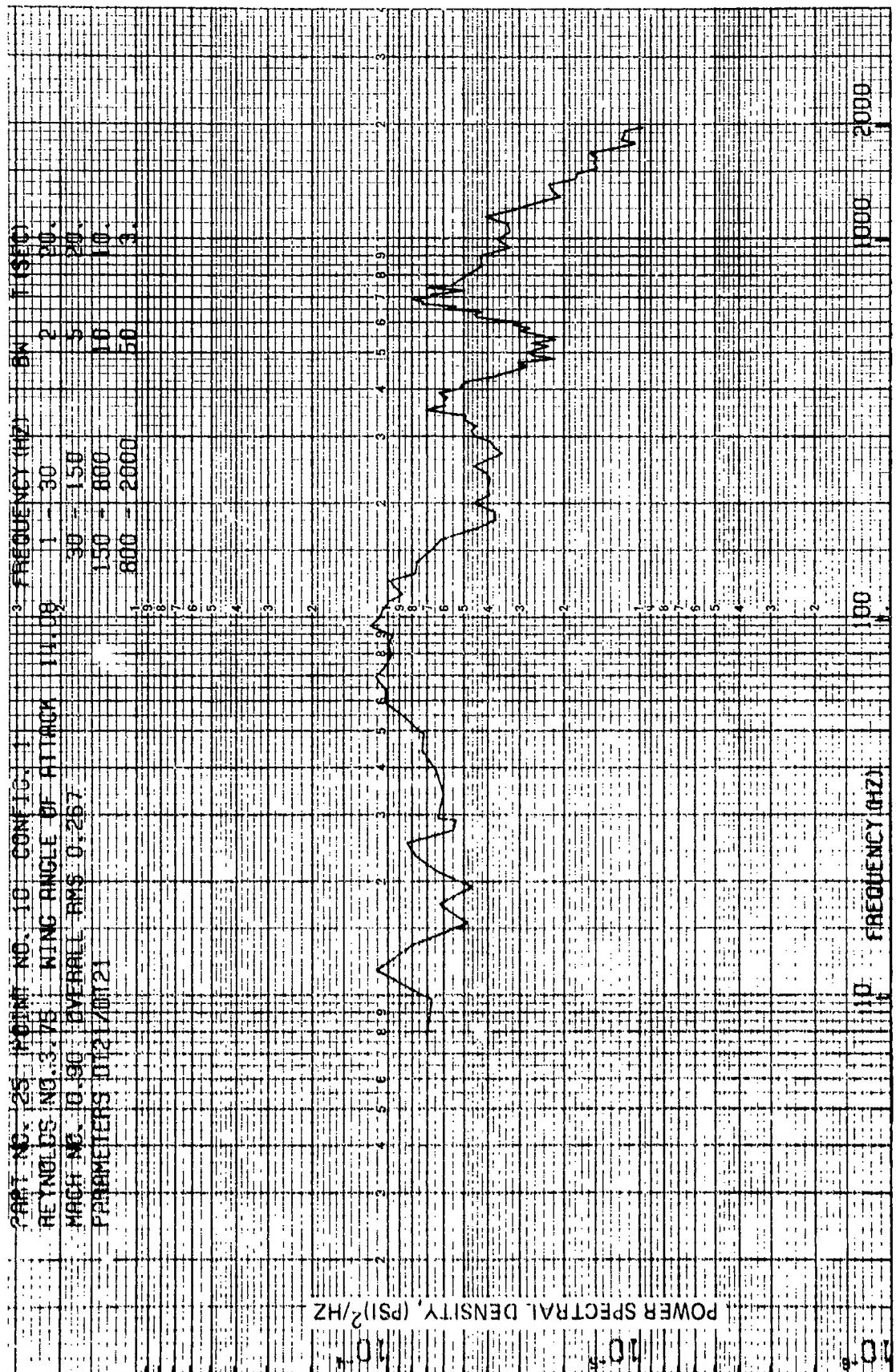


Figure 130 Fluctuating Pressure Power Spectral Density (Configuration 1, Mach 0.9, Wing Angle of Attack 14 Deg., Transducer 21)

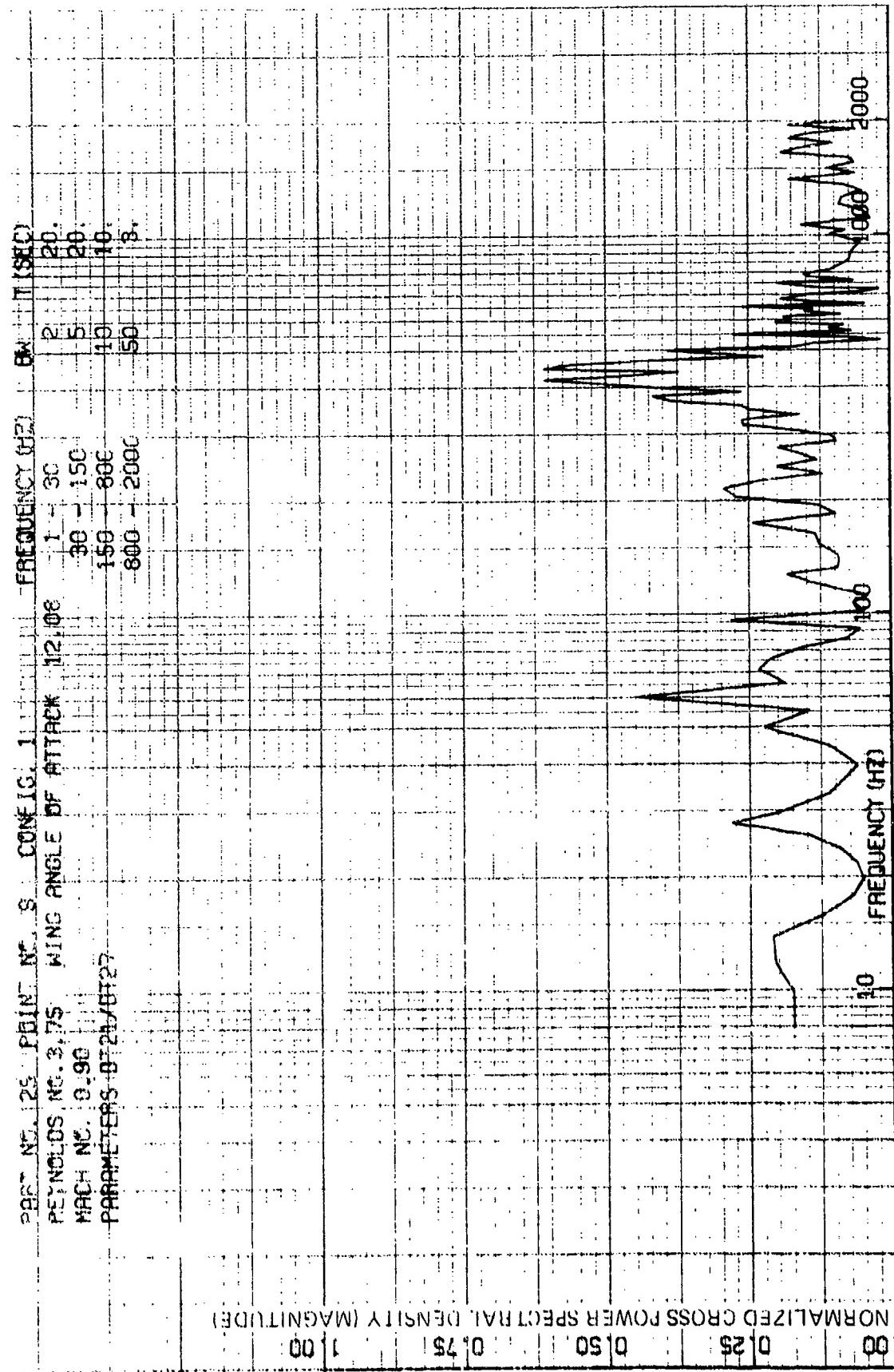


Figure 131 Fluctuating Pressure Normalized Cross Power Spectral Density (Magnitude)
 (Configuration 1, Mach 0.9, Wing Angle of Attack 12 Deg., Transducers 21 and 27)

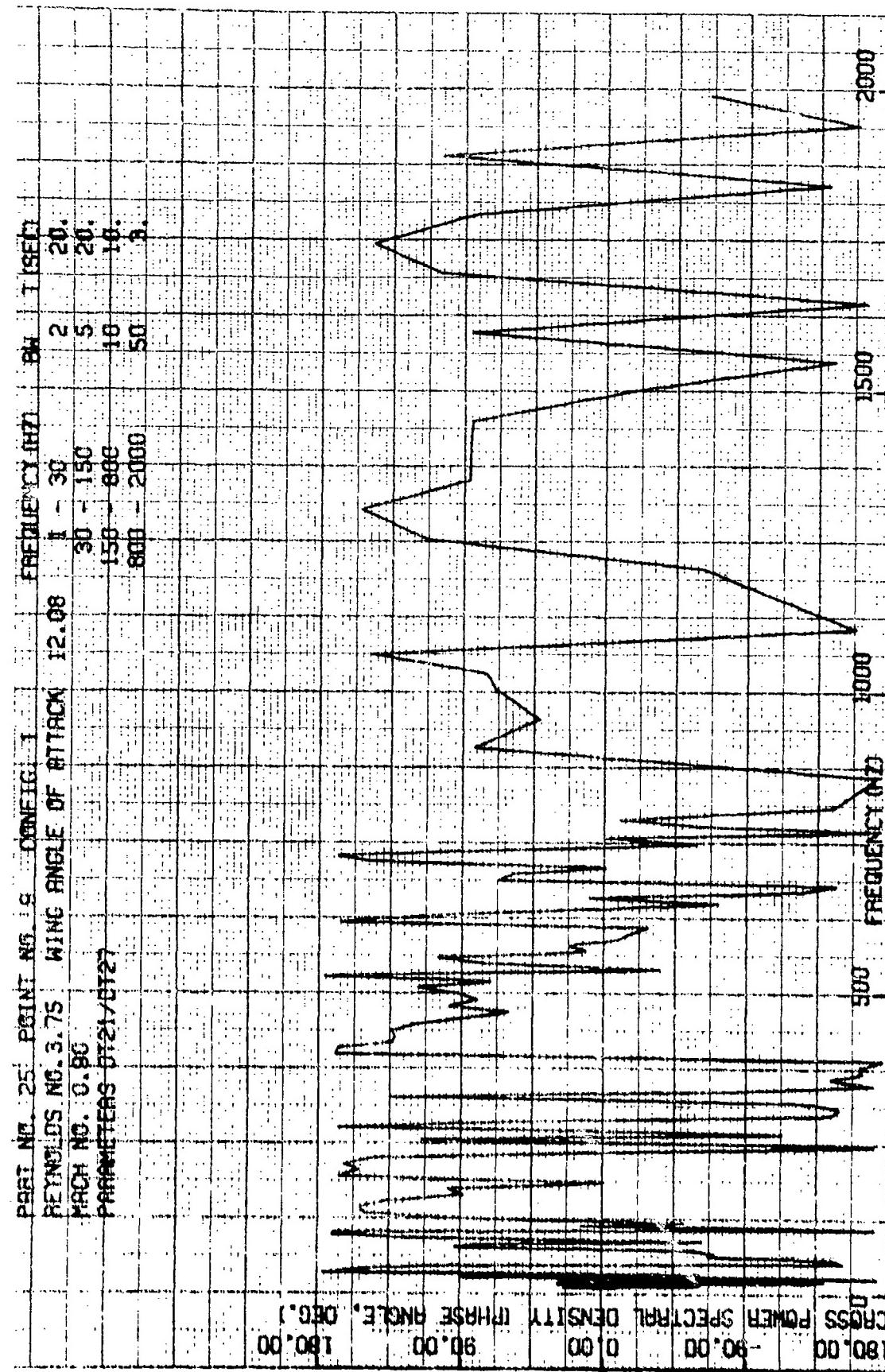


Figure 132 Fluctuating Pressure Normalized Cross Power Spectral Density (Phase)
 (Configuration 1, Mach 0.9, Wing Angle of Attack 12 Deg., Transducers 21 and 27)

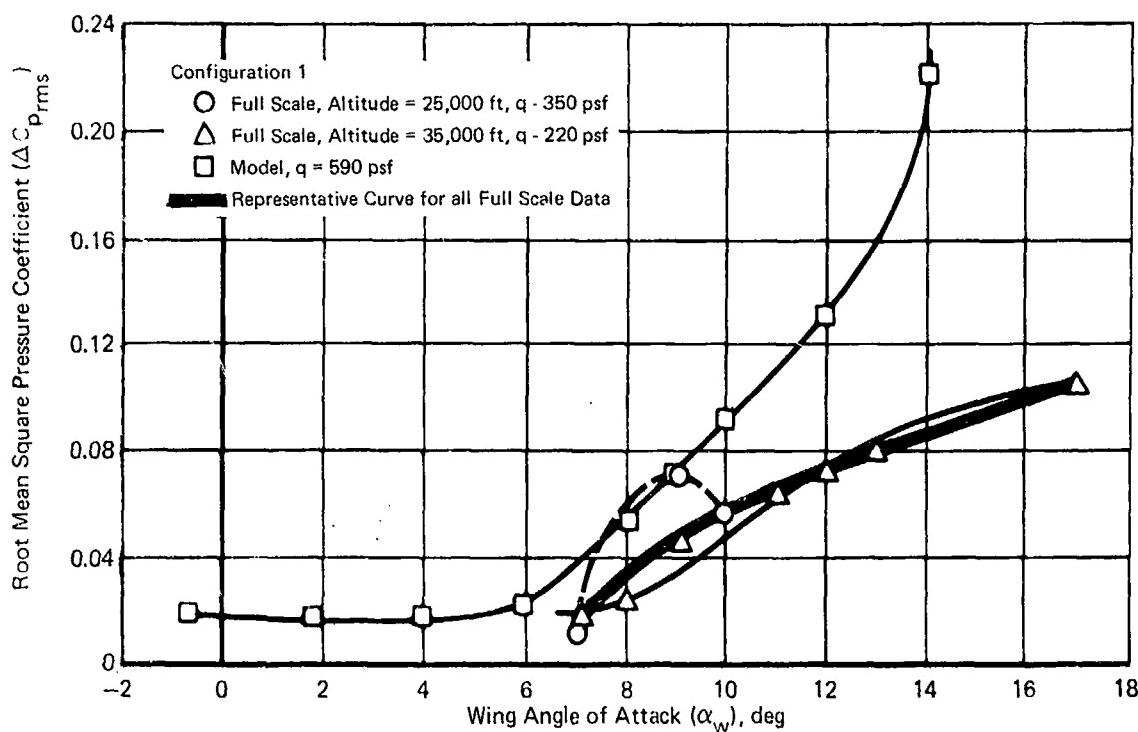


Figure 133 Comparison of Model and Full Scale rms Pressure Coefficient Variation with Angle of Attack at Mach 0.8, 90 Percent Chord, 86 Percent Semispan

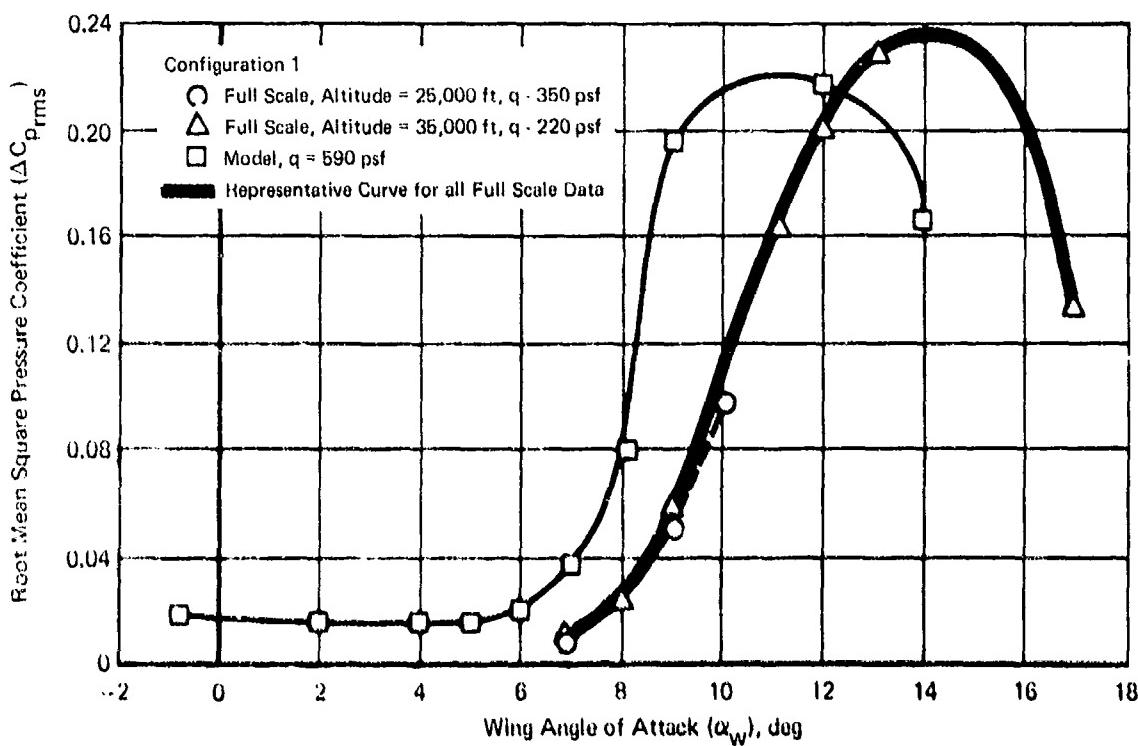


Figure 134 Comparison of Model and Full Scale rms Pressure Coefficient Variation with Angle of Attack at Mach 0.8, 90 Percent Chord, 78 Percent Semispan

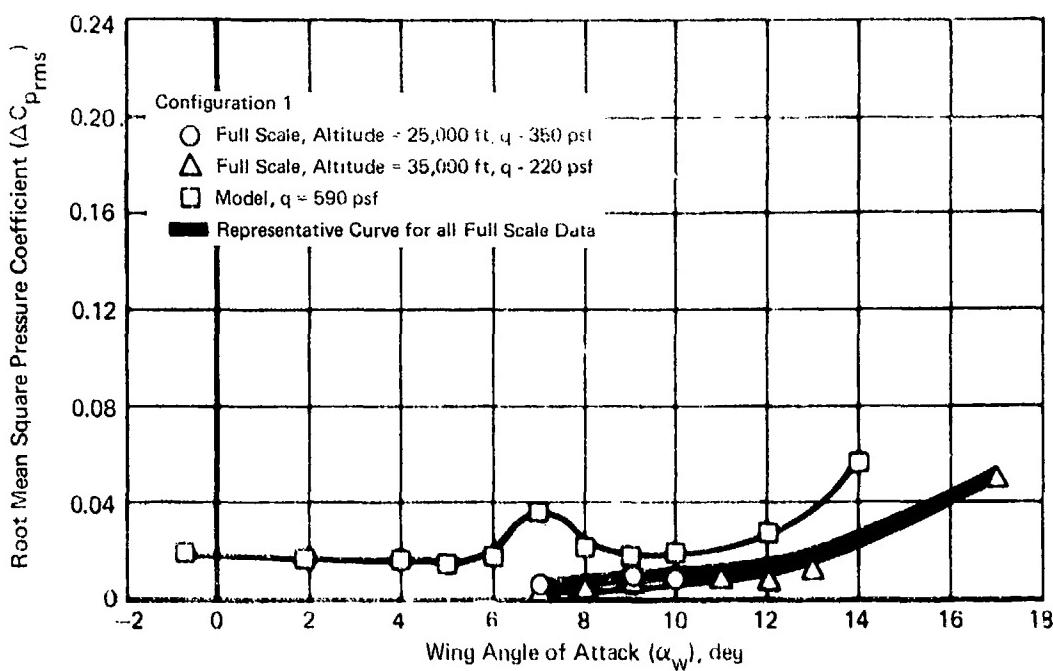


Figure 135 Comparison of Model and Full Scale rms Pressure Coefficient Variation with Angle of Attack at Mach 0.8, 90 Percent Chord, 33 Percent Semispan

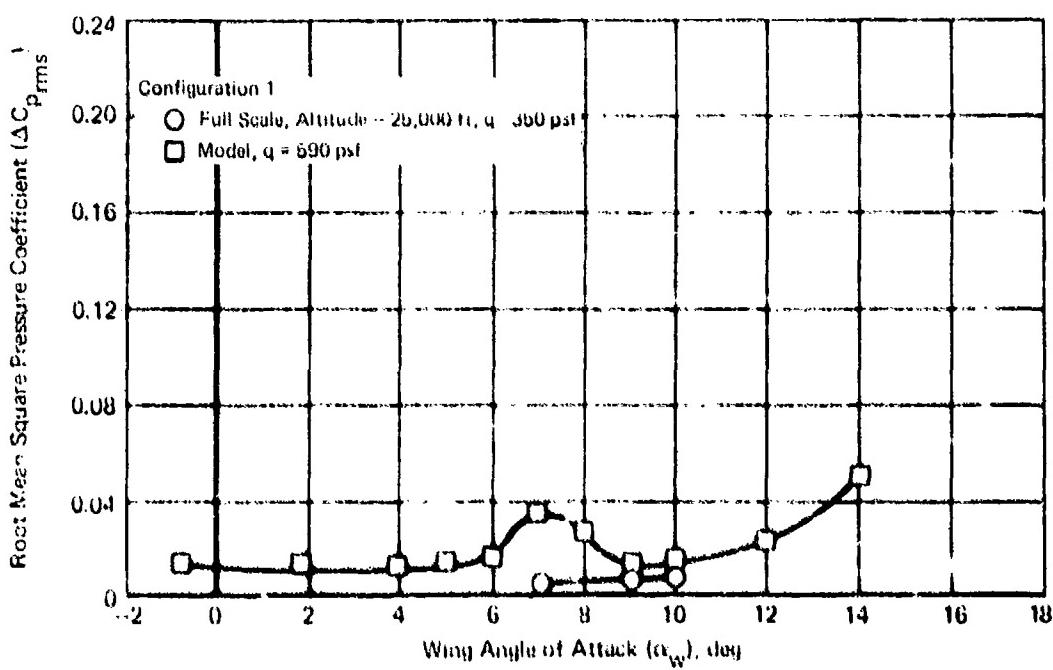


Figure 136 Comparison of Model and Full Scale rms Pressure Coefficient Variation with Angle of Attack at Mach 0.8, 95 Percent Chord, 33 Percent Semispan

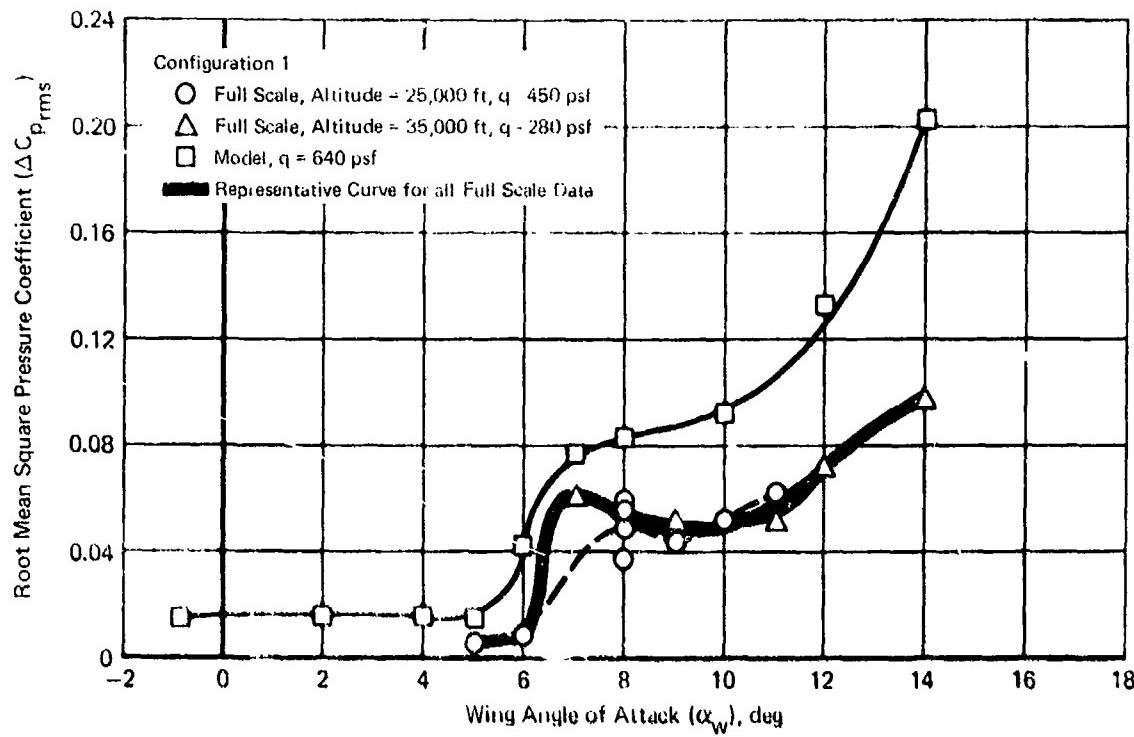


Figure 137 Comparison of Model and Full Scale rms Pressure Coefficient Variation with Angle of Attack at Mach 0.9, 90 Percent Chord, 86 Percent Semispan

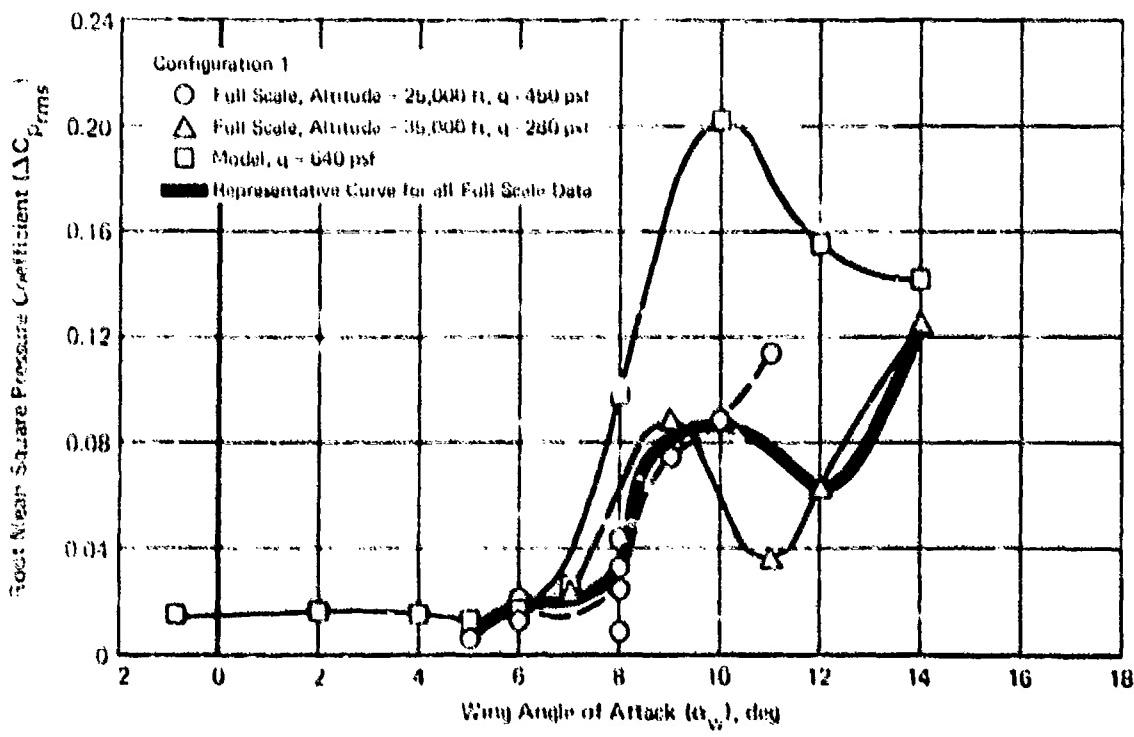


Figure 138 Comparison of Model and Full Scale rms Pressure Coefficient Variation with Angle of Attack at Mach 0.9, 90 Percent Chord, 78 Percent Semispan

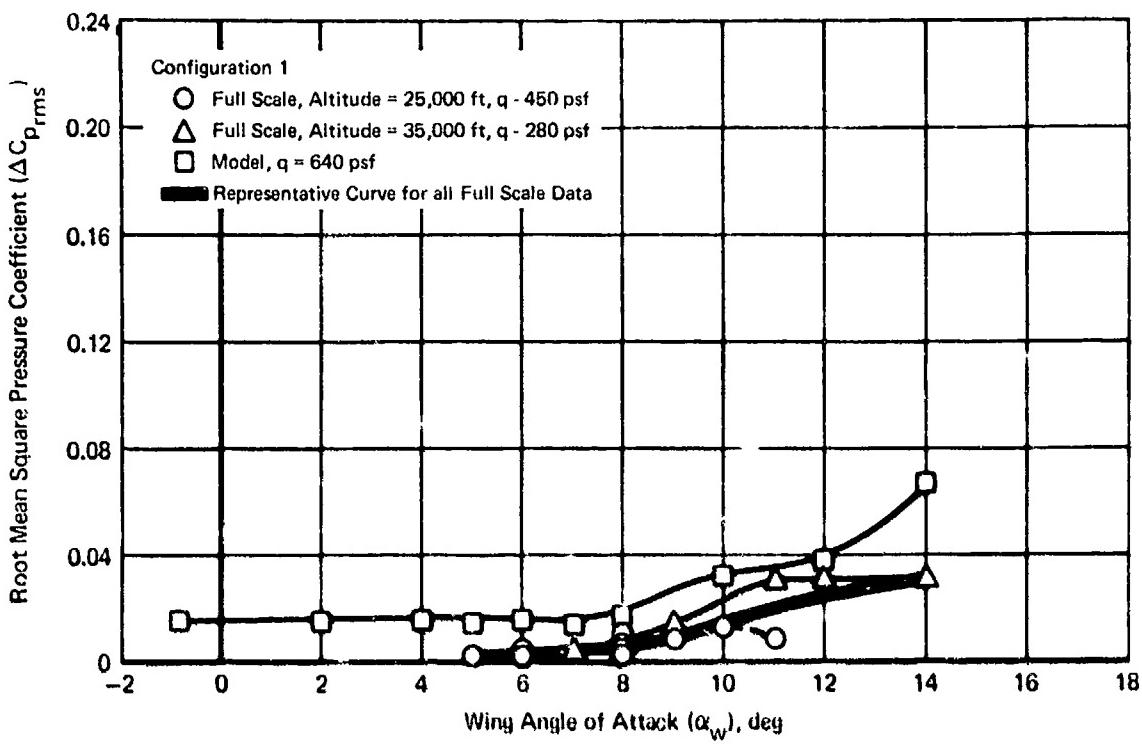


Figure 139 Comparison of Model and Full Scale rms Pressure Coefficient Variation with Angle of Attack at Mach 0.9, 90 Percent Chord, 33 Percent Semispan

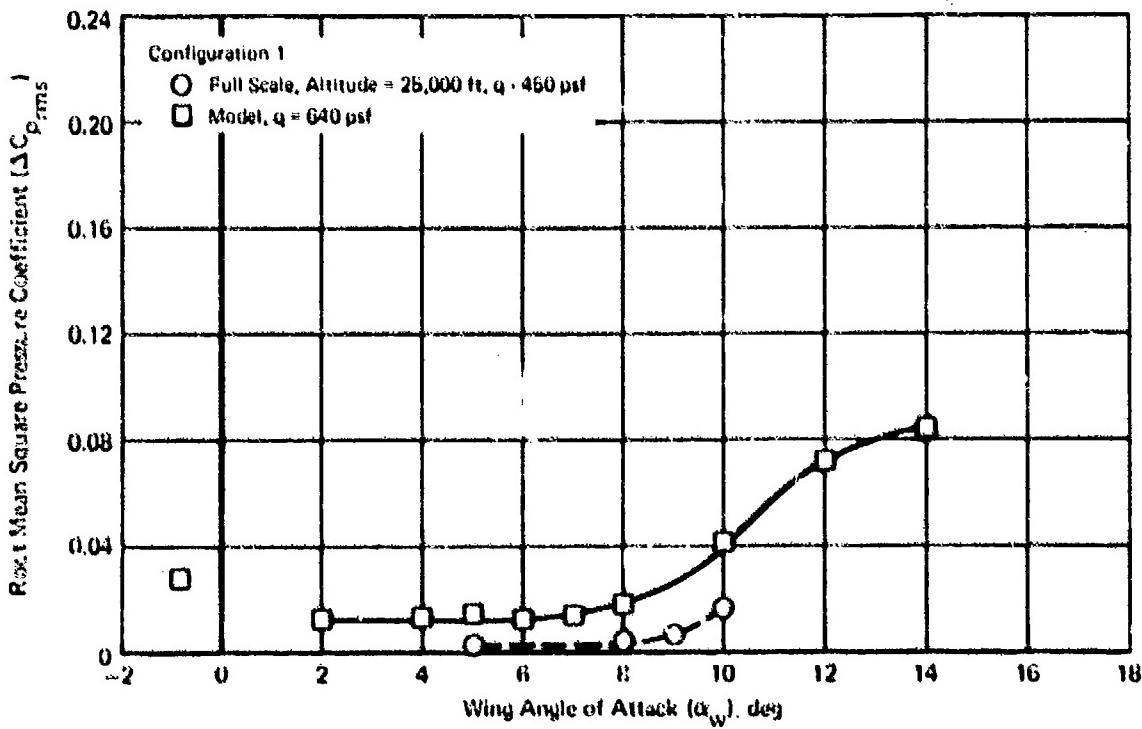


Figure 140 Comparison of Model and Full Scale rms Pressure Coefficient Variation with Angle of Attack at Mach 0.9, 95 Percent Chord, 33 Percent Semispan

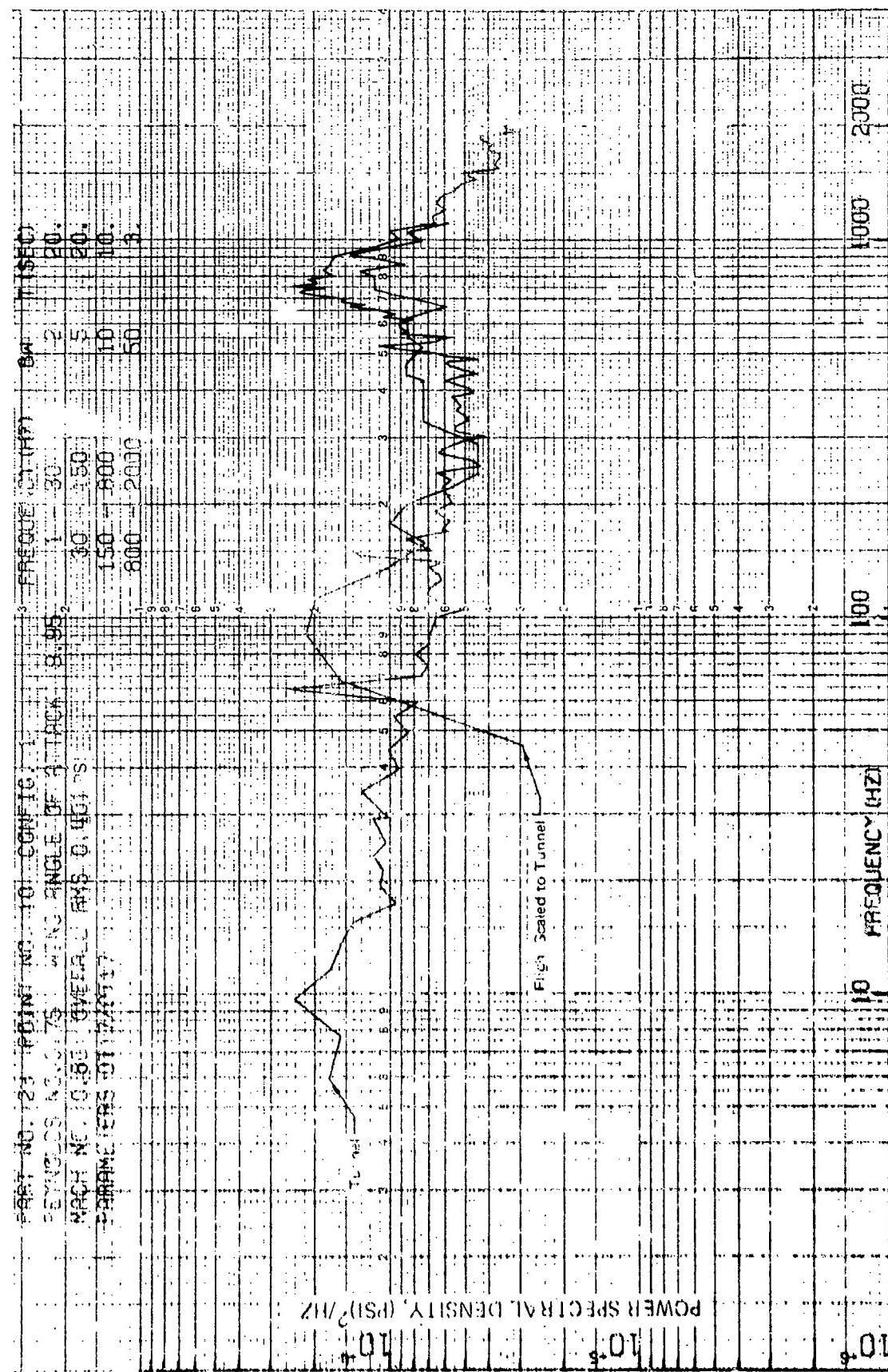


Figure 141 Comparison of Model and Full Scale Pressure Spectral Shape for Configuration 1
 (Mach 0.8, Wing Angle of Attack 12°, Transducer 17)

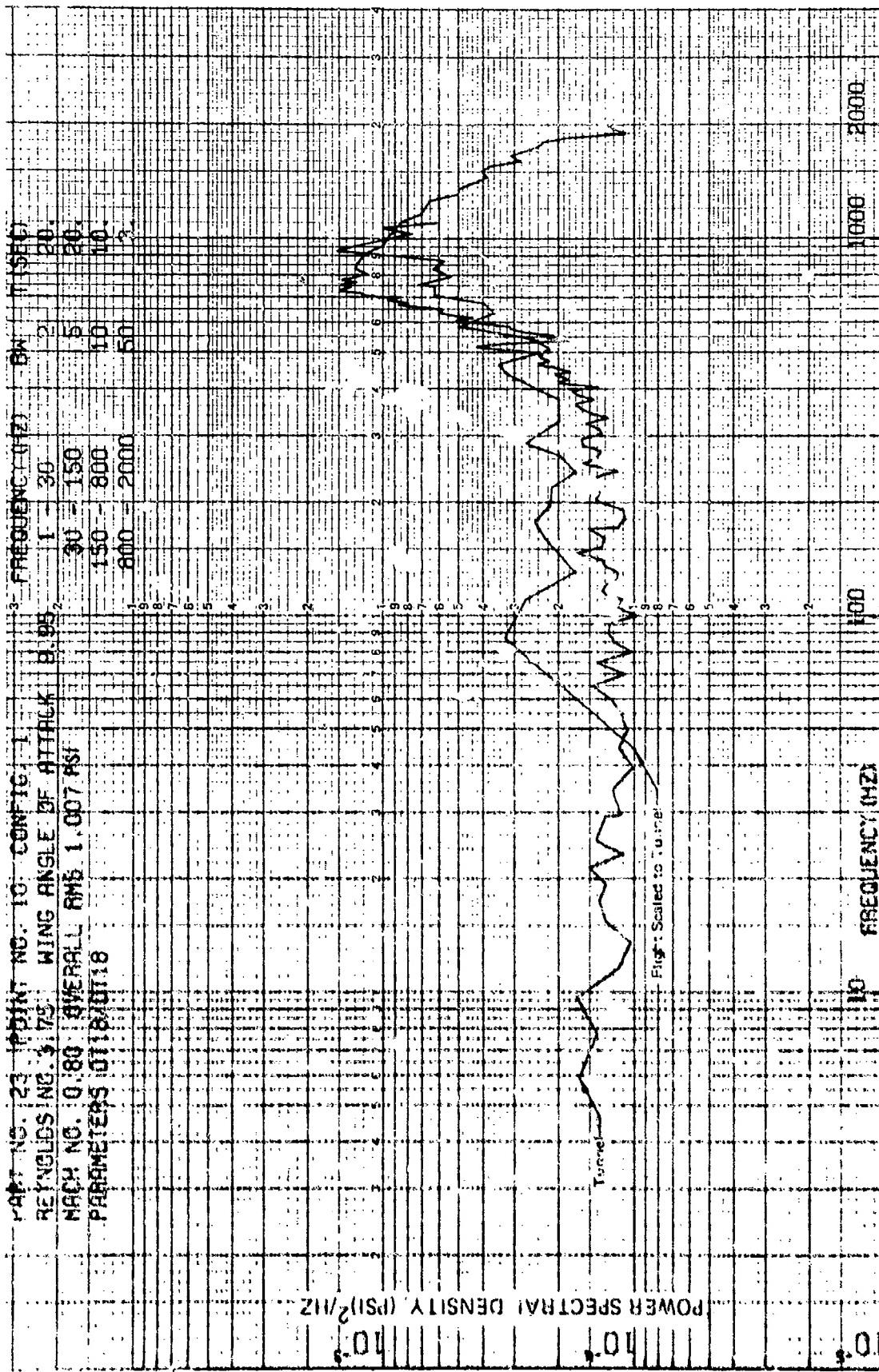


Figure 142 Comparison of Model and Full Scale Pressure Spectral Shape for Configuration 1
 (Mach 0.8, Wing Angle of Attack 12°, Transducer 18)

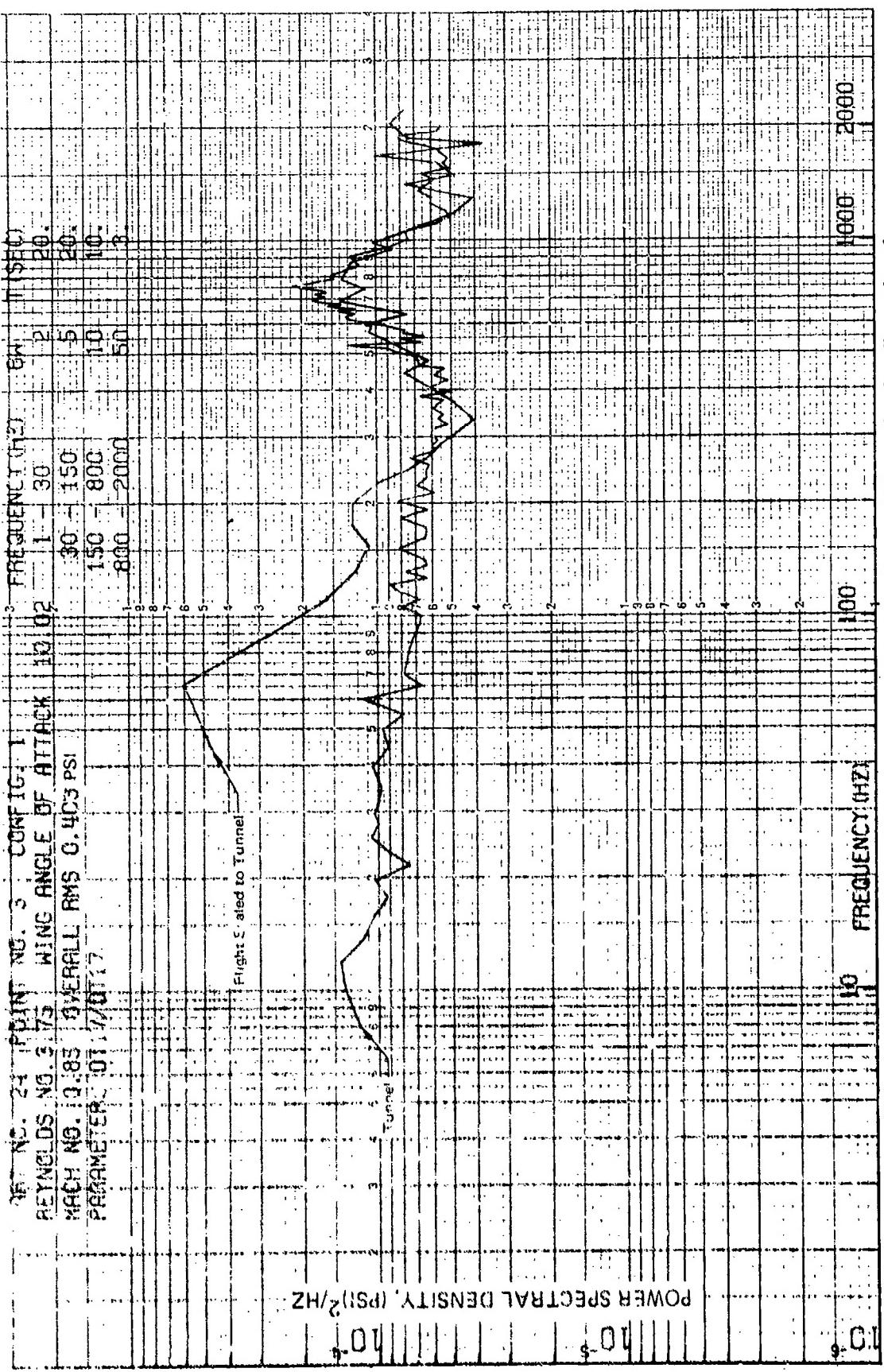


Figure 143 Comparison of Model and Full Scale Pressure Spectral Shape for Configuration 1
 (Mach 0.85, Wing Angle of Attack 10°, Transducer 17)

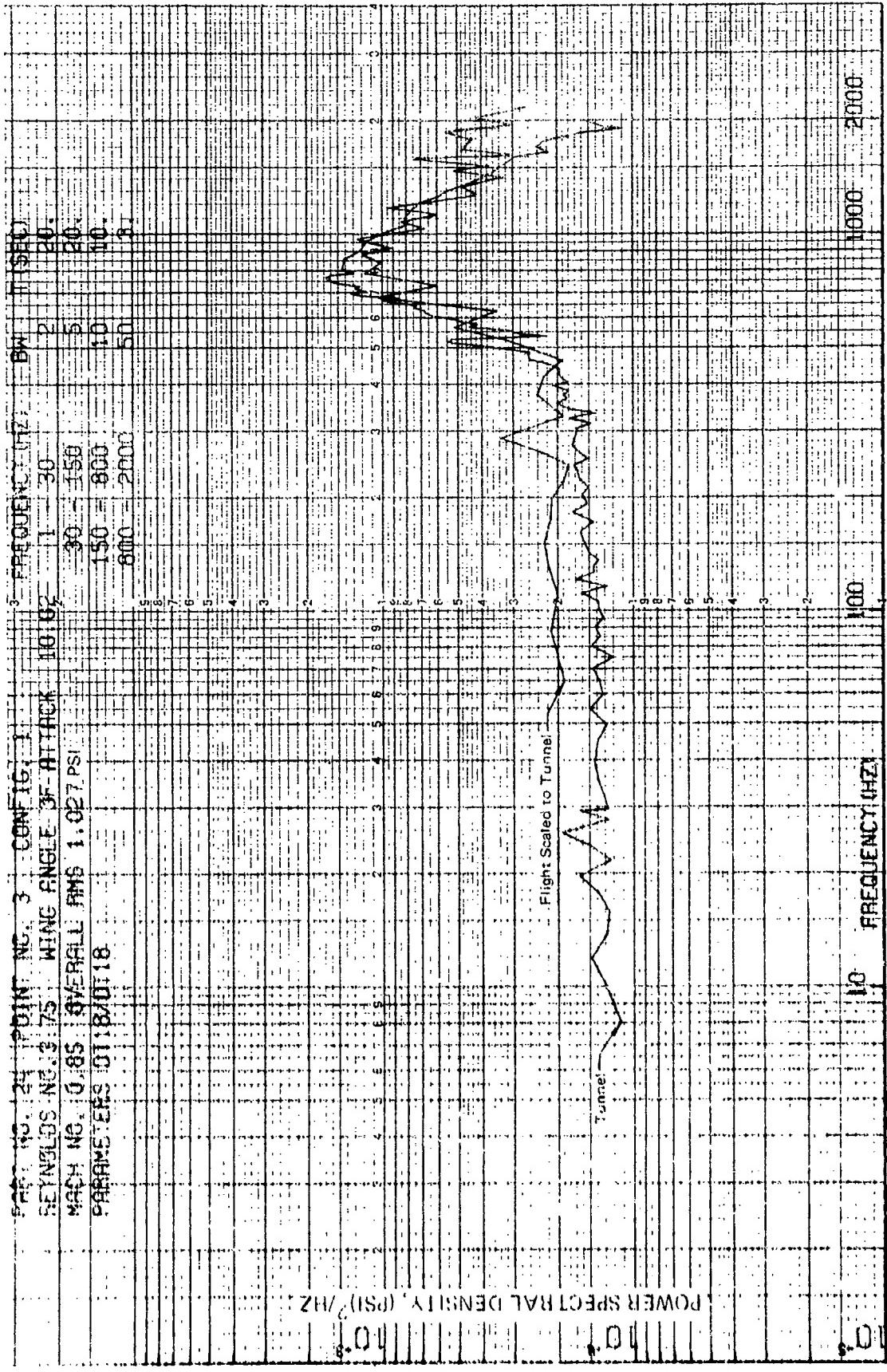


Figure 144 Comparison of Model and Full Scale Pressure Spectral Shape for Configuration 1
 (Mach 0.85, Wing Angle of Attack 10°, Transducer 18)

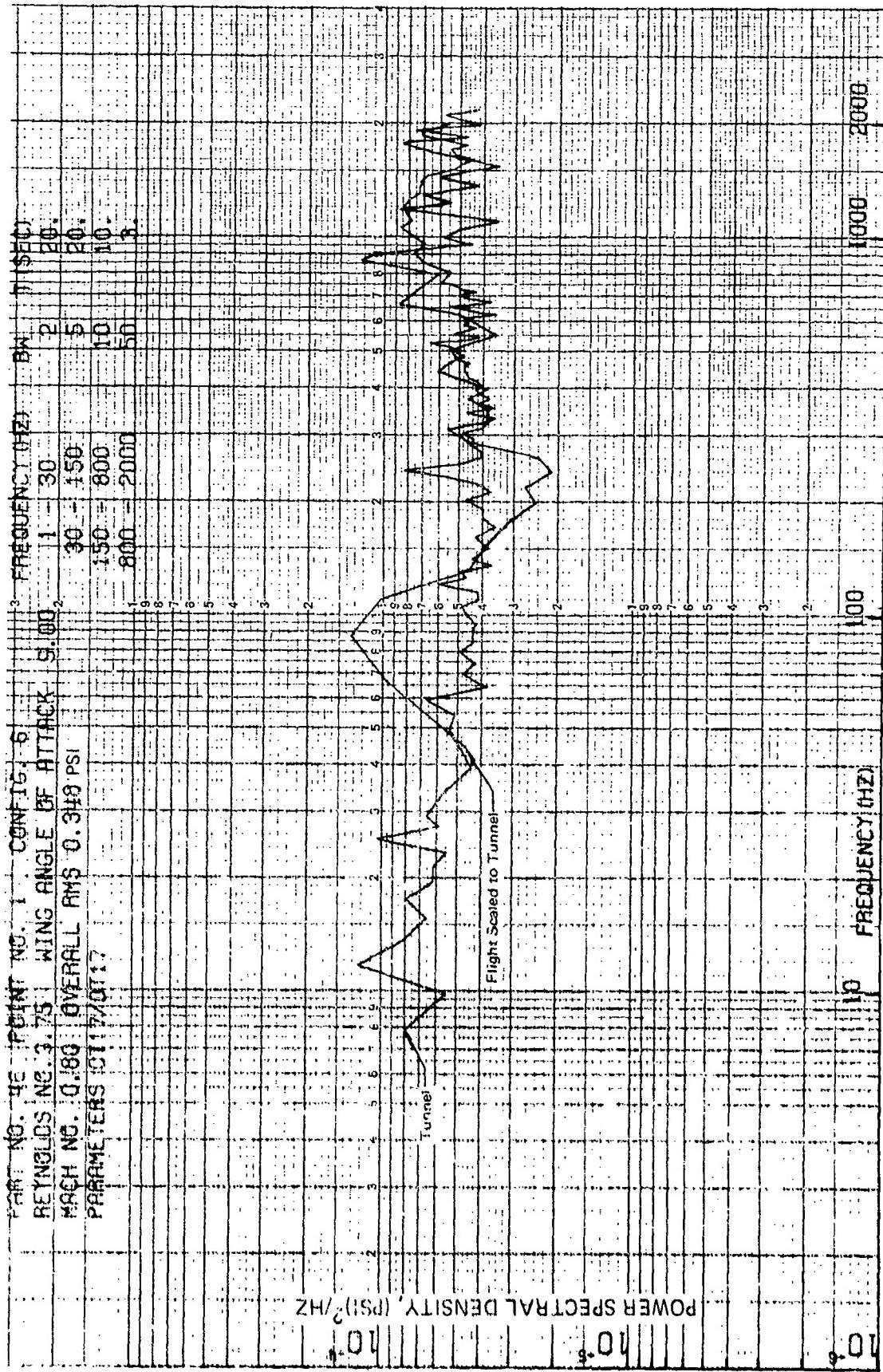


Figure 145 Comparison of Model and Full Scale Pressure Spectral Shape for Configuration 6
 (Mach 0.8, Wing Angle of Attack 9°, Transducer 17)

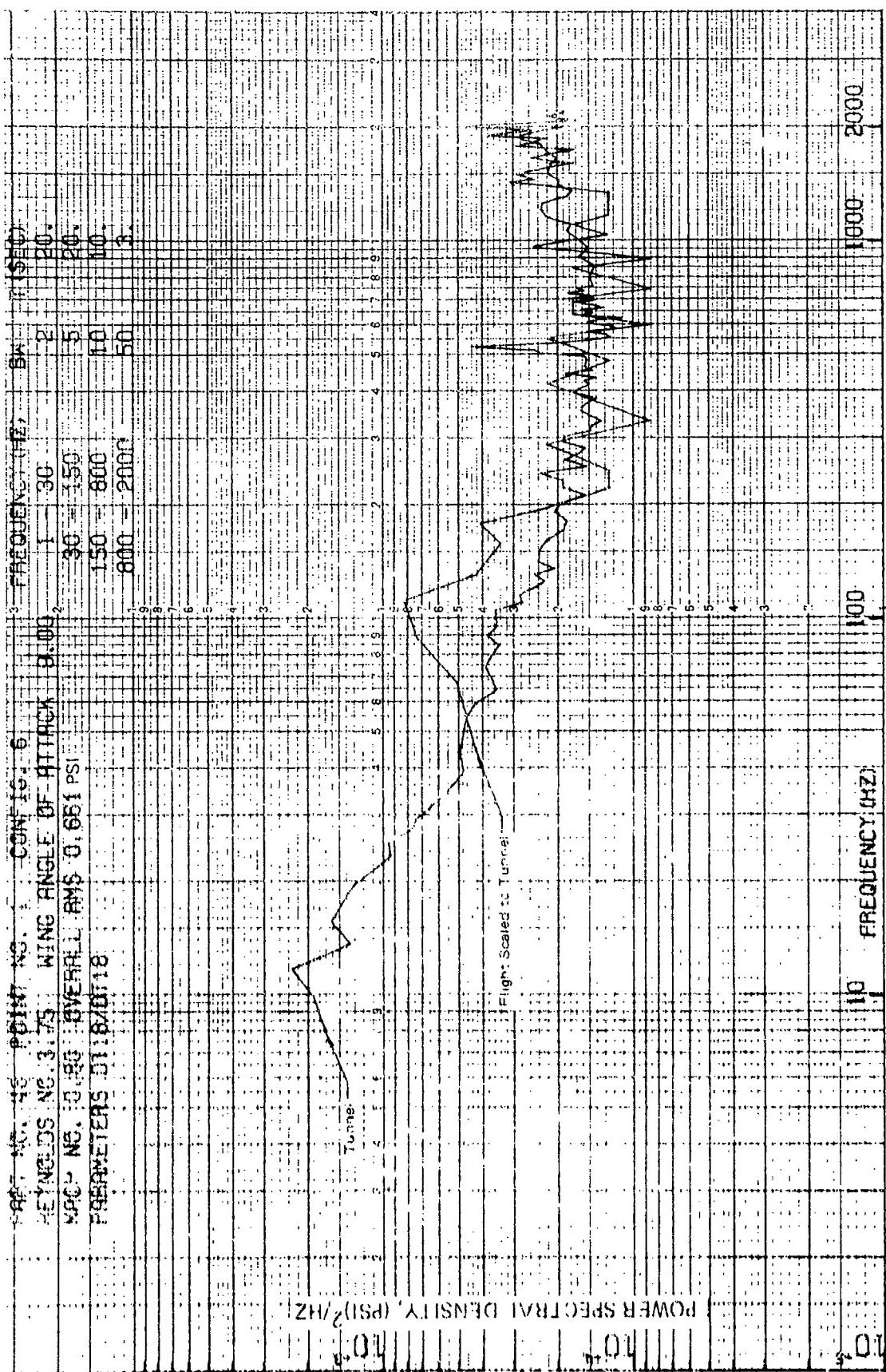


Figure 14b Comparison of Model and Full Scale Pressure Spectral Shape for Configuration 6
 (Mach 0.8, Wing Angle of Attack 9°, Transducer 18)

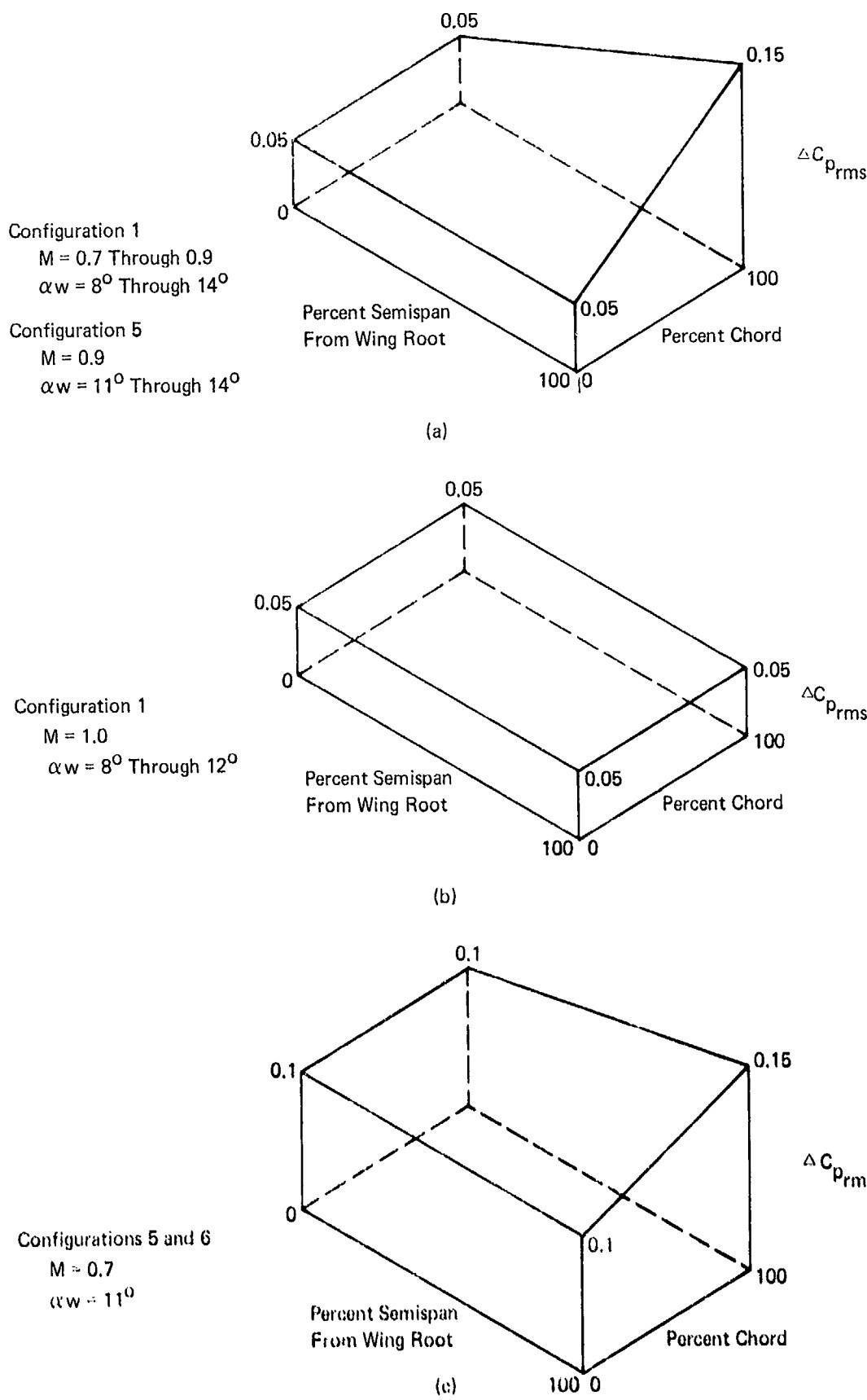


Figure 147 Model for rms Pressure Coefficient, $\Delta C_{p_{rms}}$

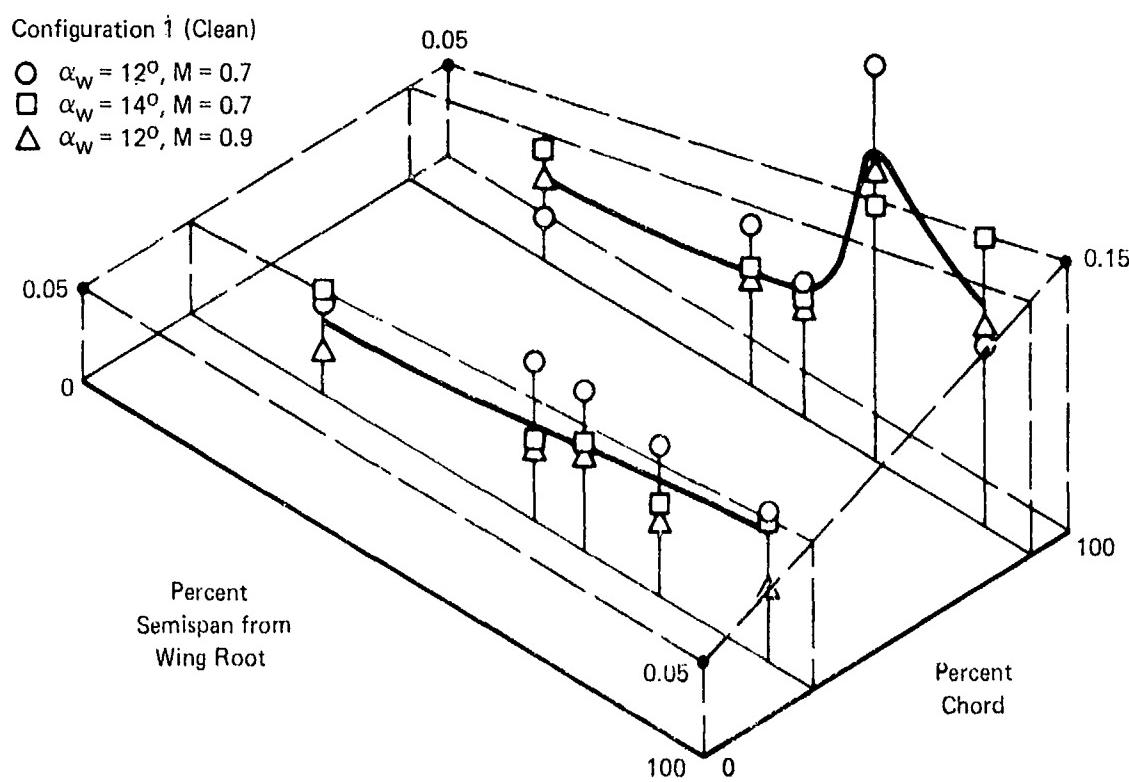


Figure 148 Comparison of Linear Model of rms Pressure Coefficient with Measured Data, Clean Wing.

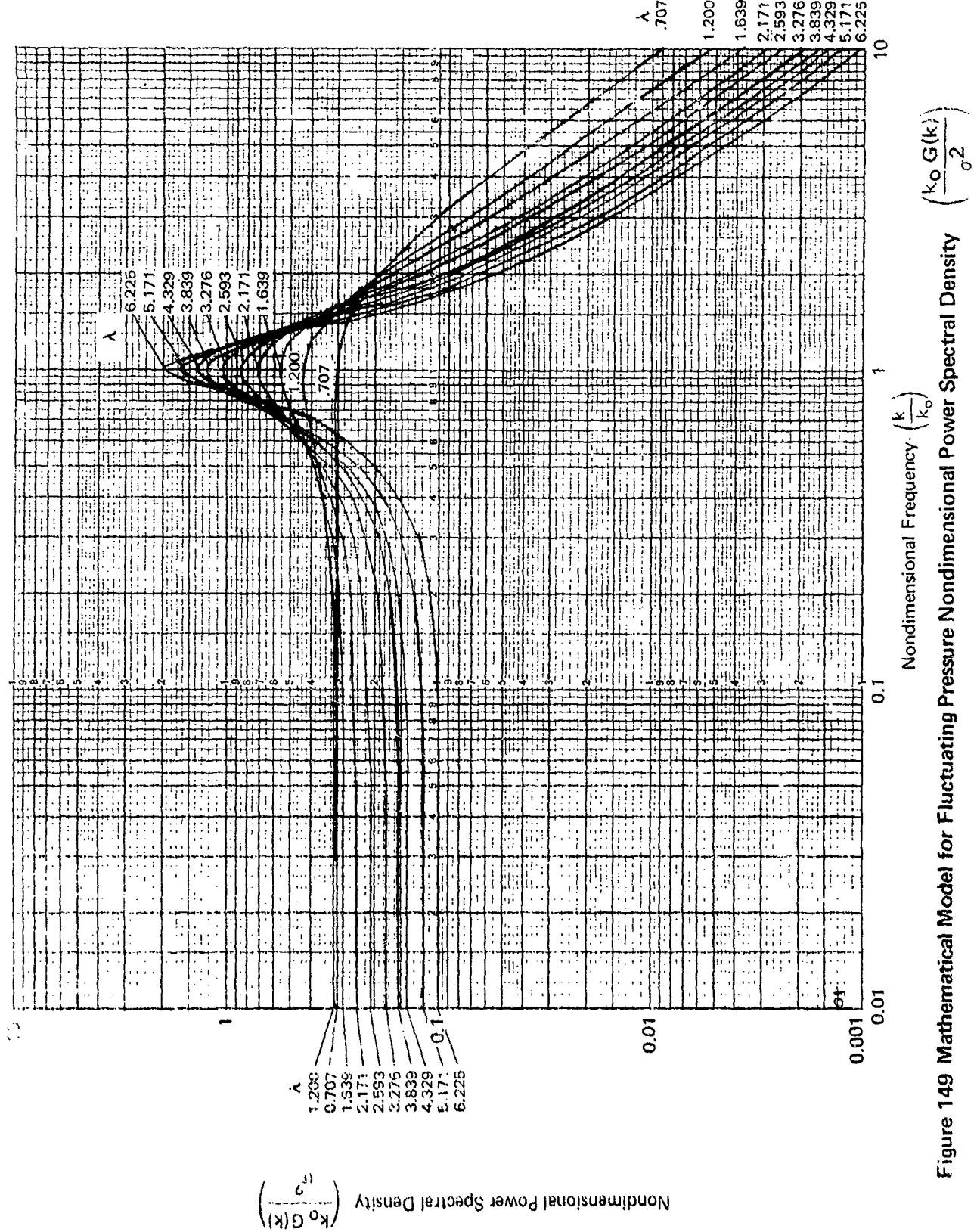


Figure 149 Mathematical Model for Fluctuating Pressure Nondimensional Power Spectral Density $\left(\frac{k_0 G(k)}{\sigma^2} \right)$

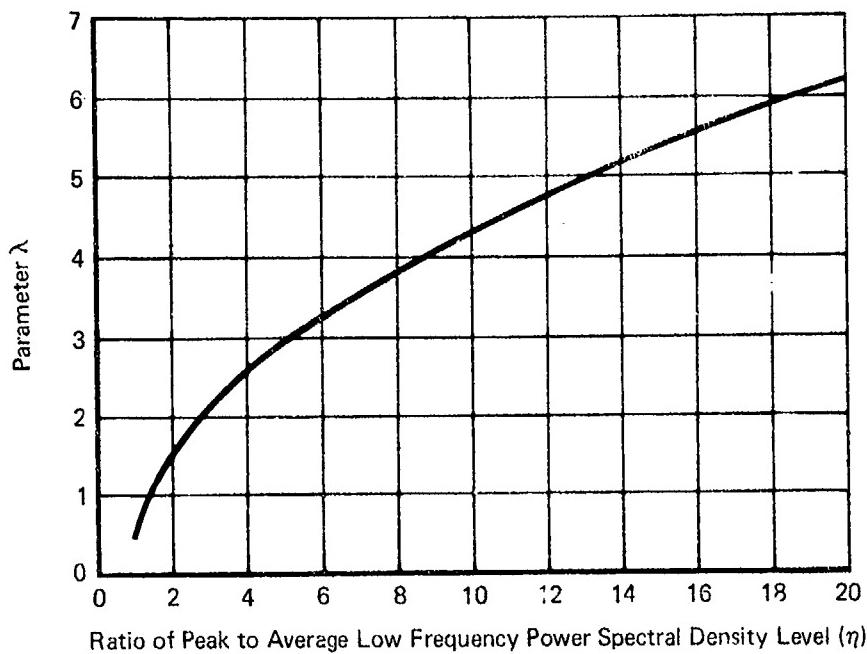


Figure 150 Buffet Pressure Prediction Parameter λ as a Function of Parameter η

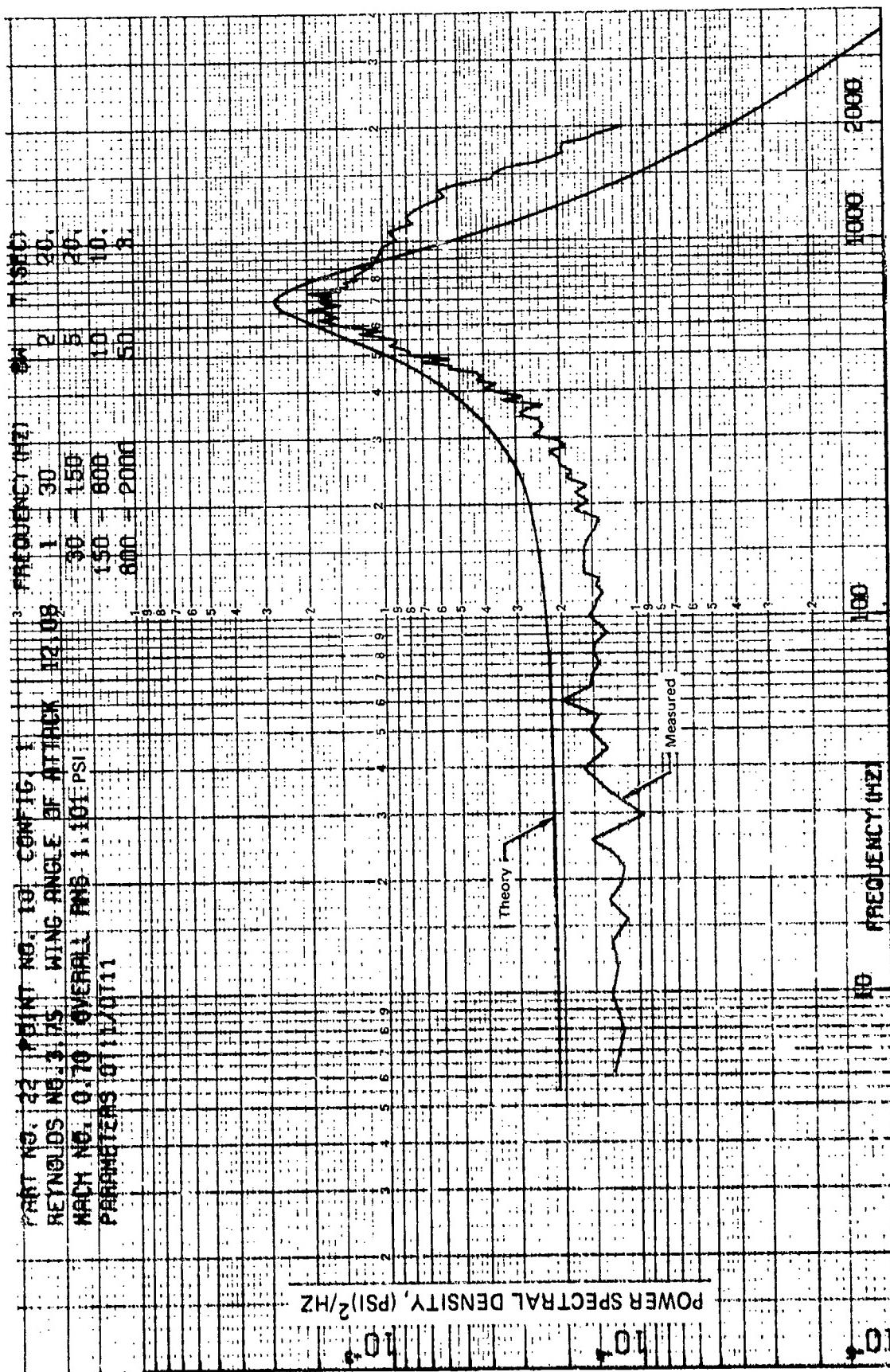
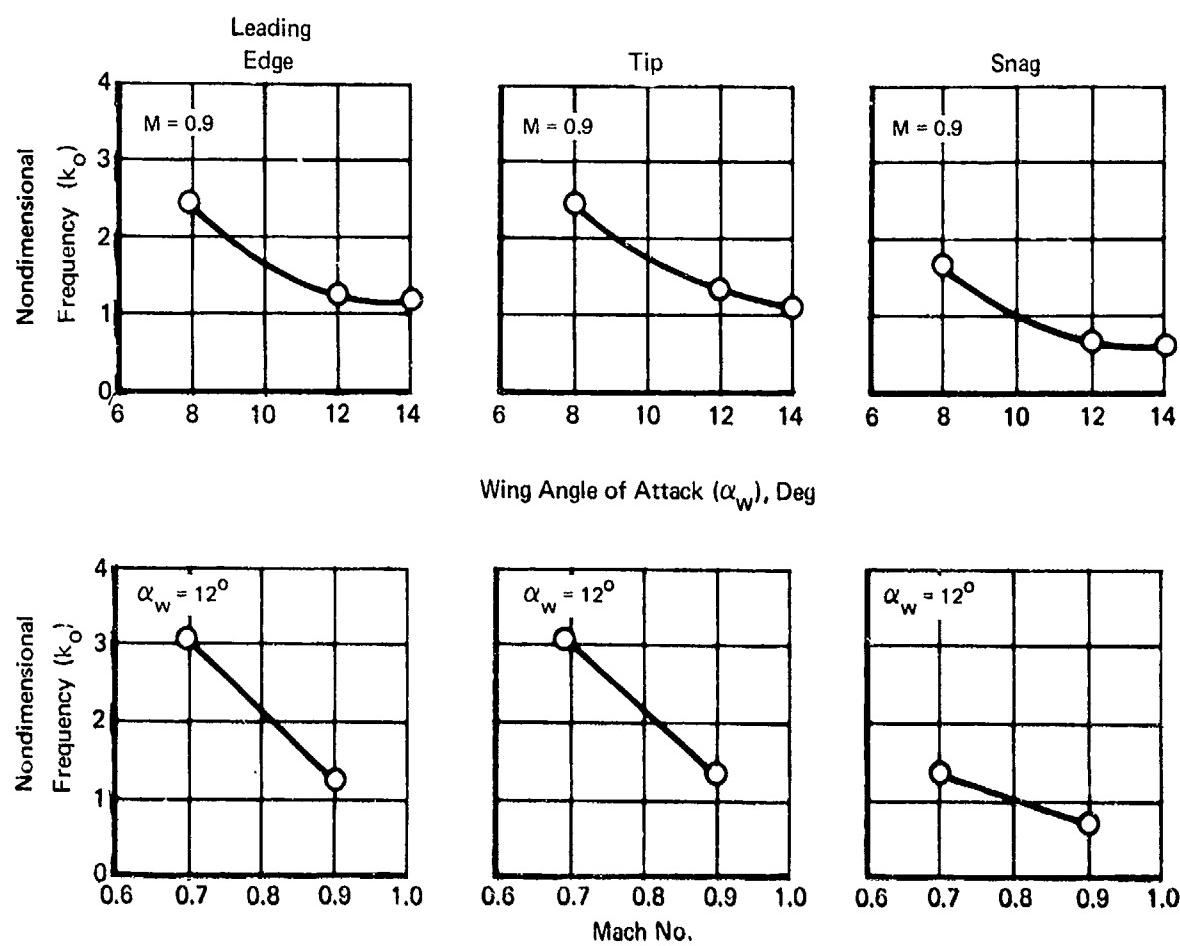
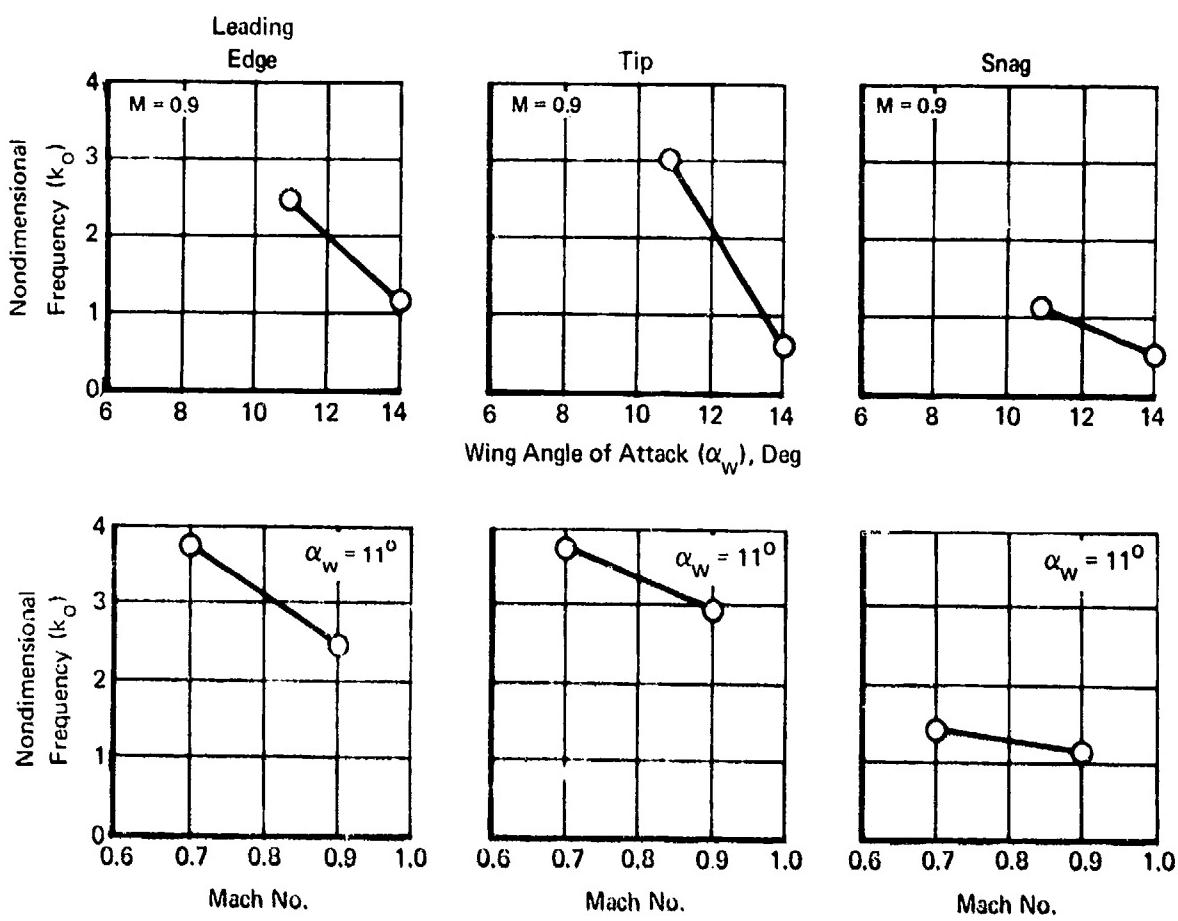


Figure 151 Comparison of Theoretical and Measured Power Spectral Density Spectra



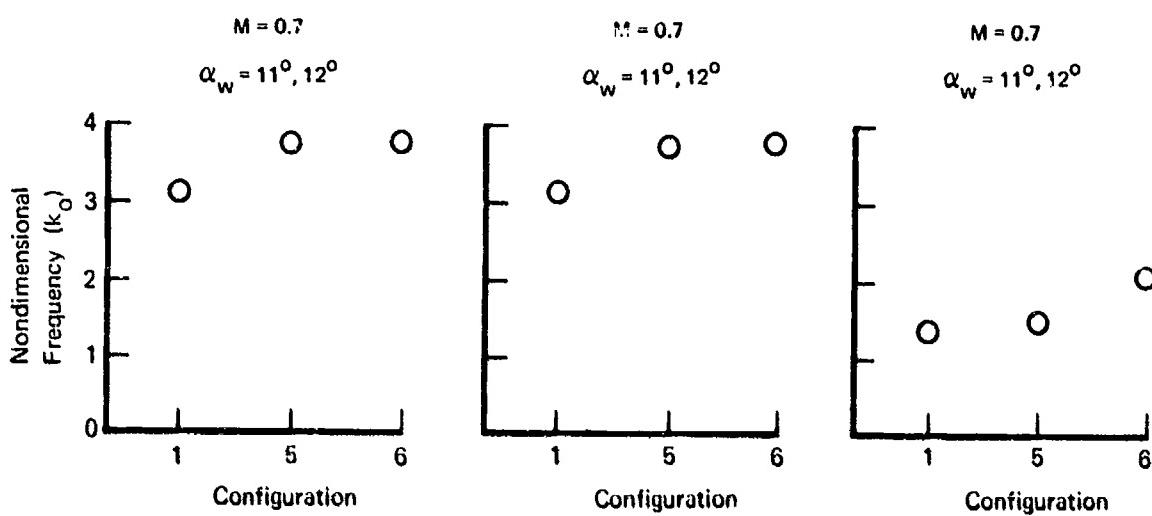
(a) Configuration 1

Figure 152 Nondimensional Frequencies Associated with Leading Edge, Tip,
and Snag Vortices



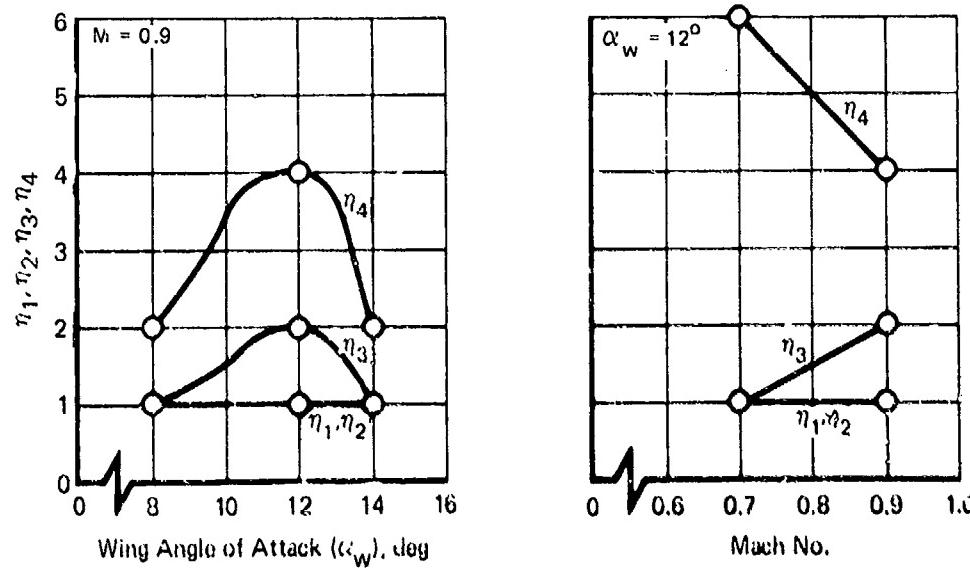
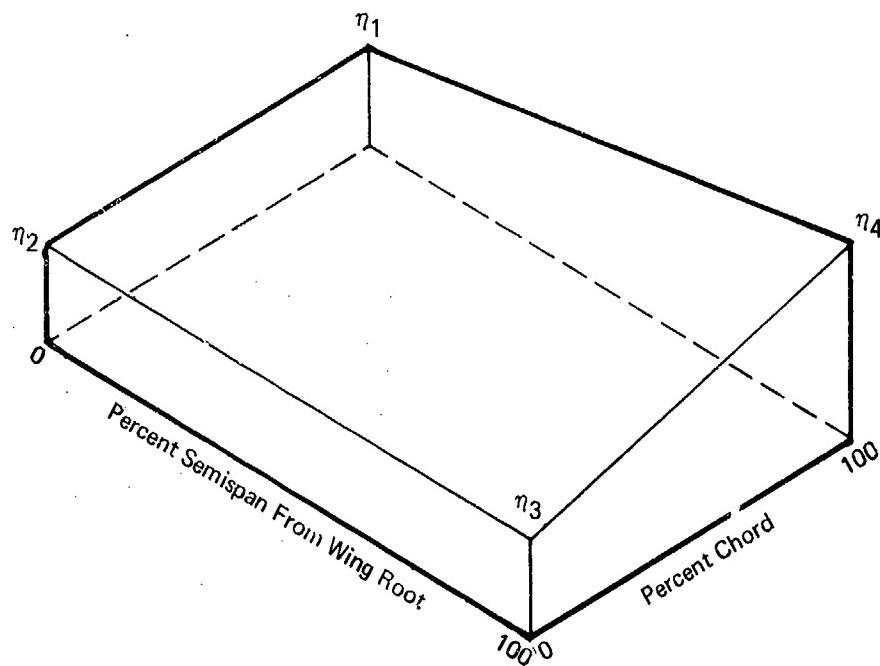
(b) Configuration 5

Figure 152 Nondimensional Frequencies Associated with Leading Edge Tip,
and Snag Vortices (Continued)



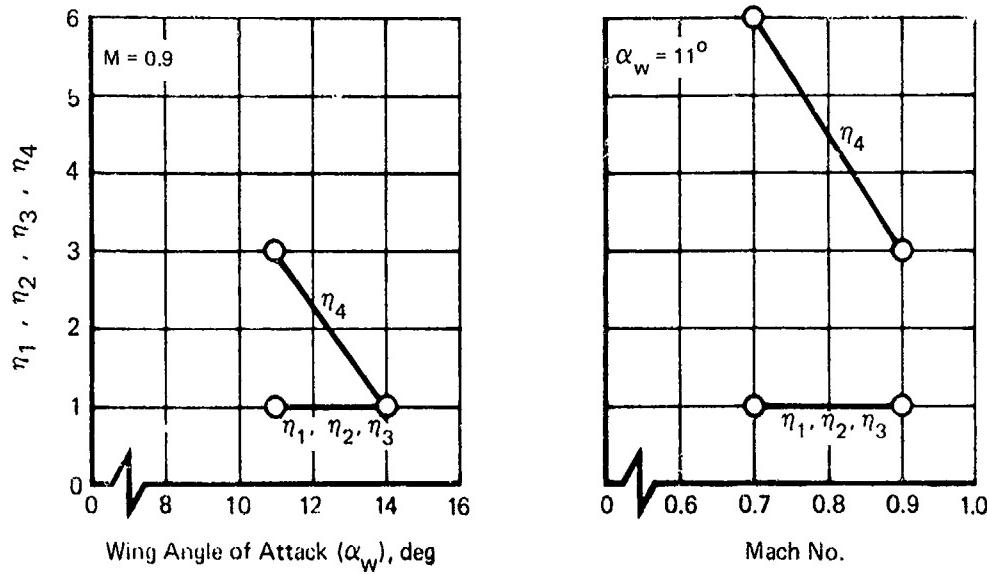
(c) Configurations 1, 5, 6

Figure 152 Nondimensional Frequencies Associated with Leading Edge, Tip, and Snay Vortices (Concluded)

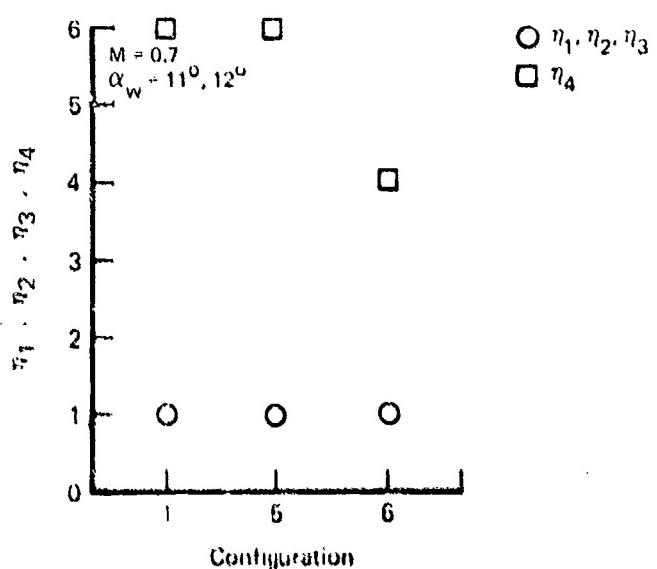


(a) Configuration 1

Figure 153 Model for Ratio of Peak to Average Low Frequency Power Spectral Density Level (η)



(b) Configuration 5



(c) Configurations 1, 5, 6

Figure 153 Model for Ratio of Peak to Average Low Frequency Power Spectral Density Level (η) (Continued)

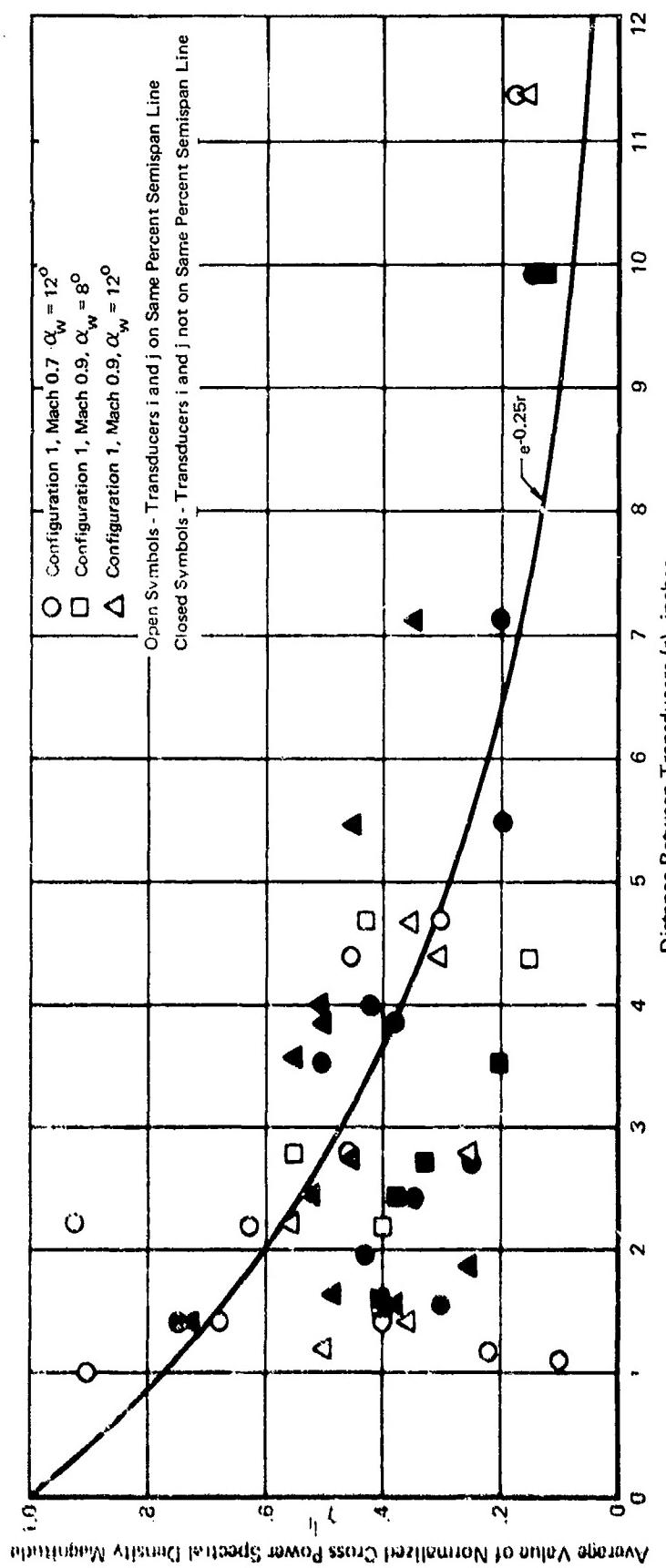
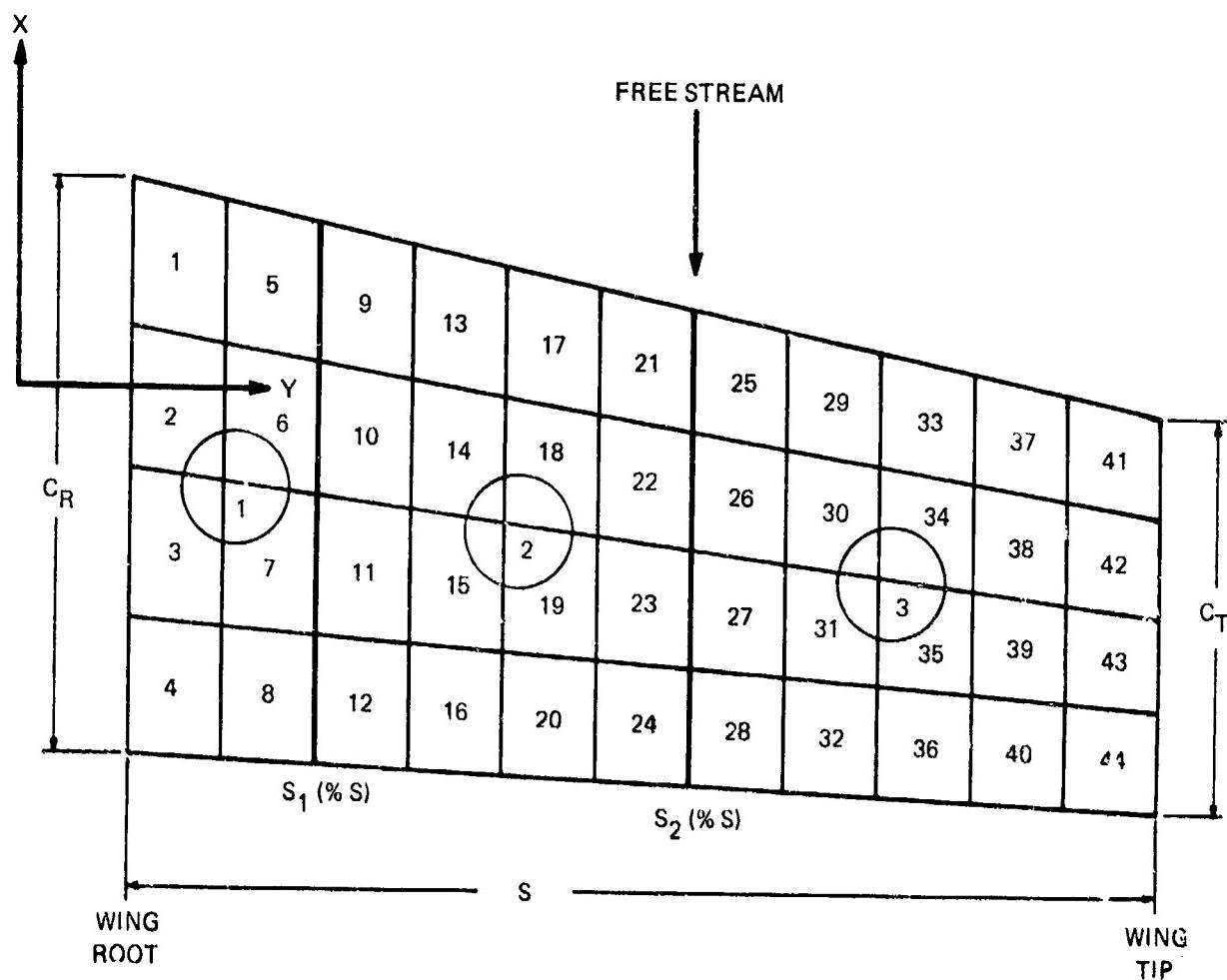


Figure 154 Spatial Decay of Pressure Normalized Cross Power Spectral Density



1 = AREA NUMBER



= REGION NUMBER

Figure 155 Example of Division of Wing Planform into Regions and Areas

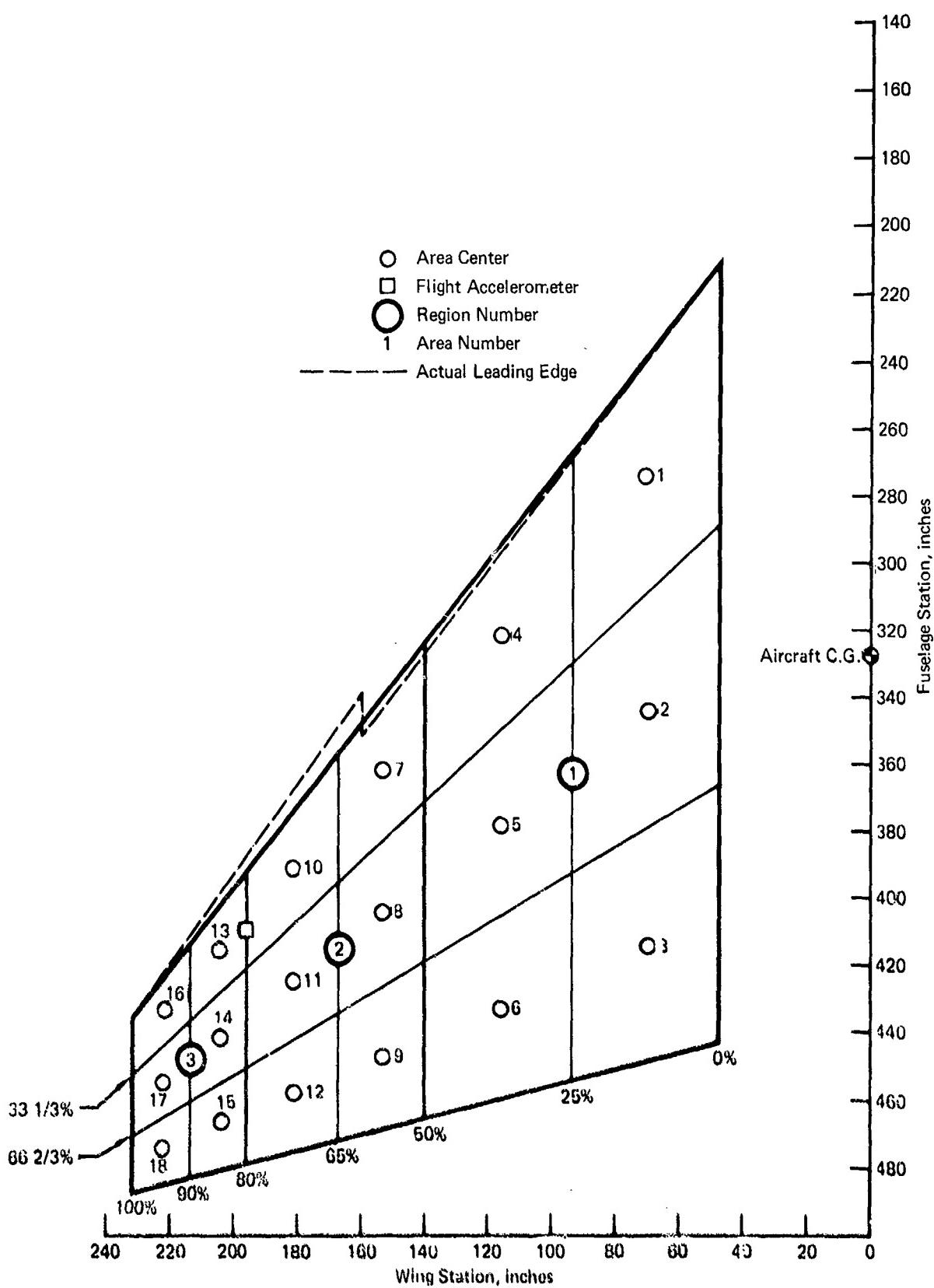


Figure 156 Idealization of F-4 Wing Planform for Prediction of Buffet Response

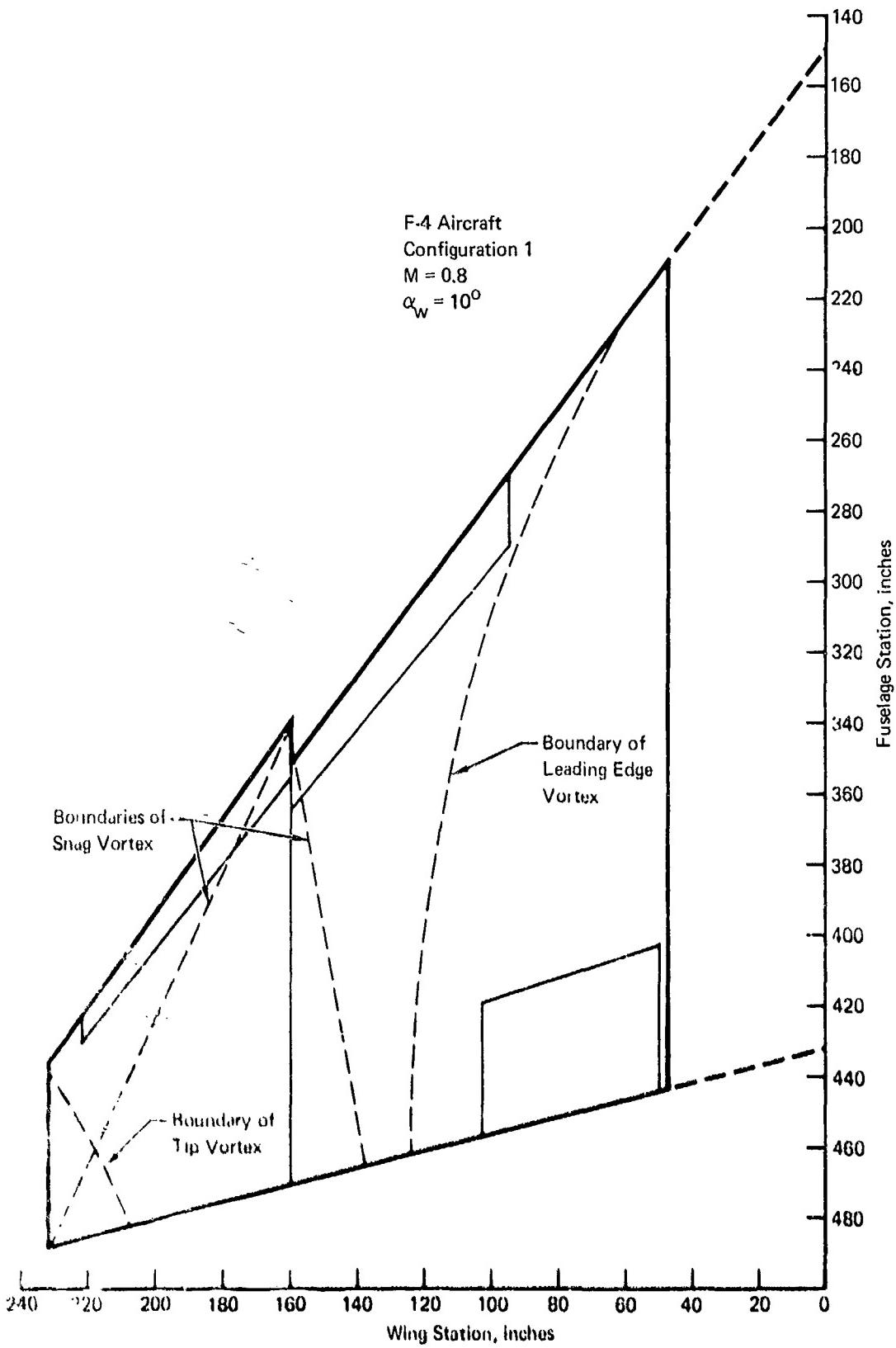


Figure 157 Estimated Locations of Vortices for Flight Conditions 1 and 2

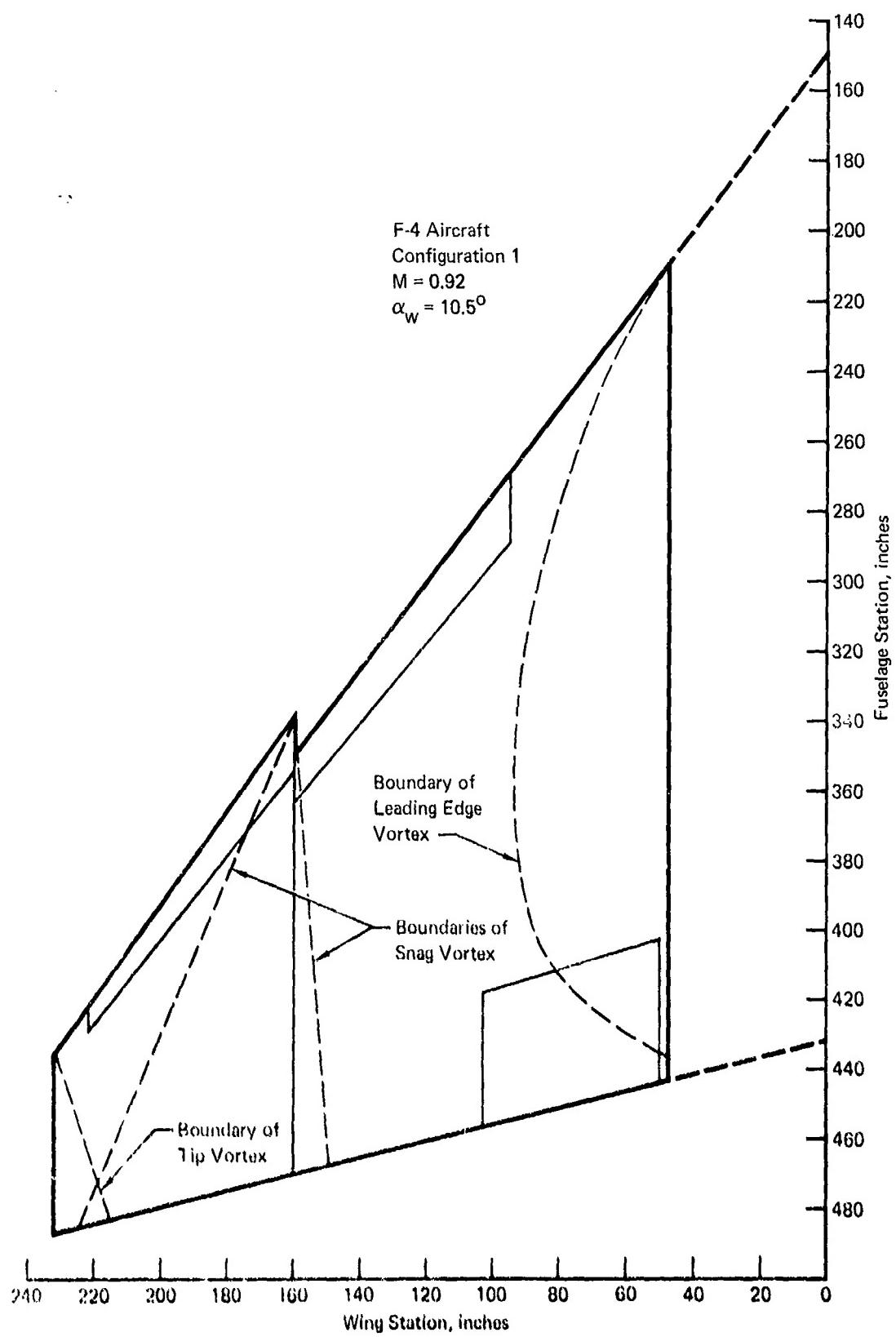


Figure 158 Estimated Locations of Vortices for Flight Condition 3

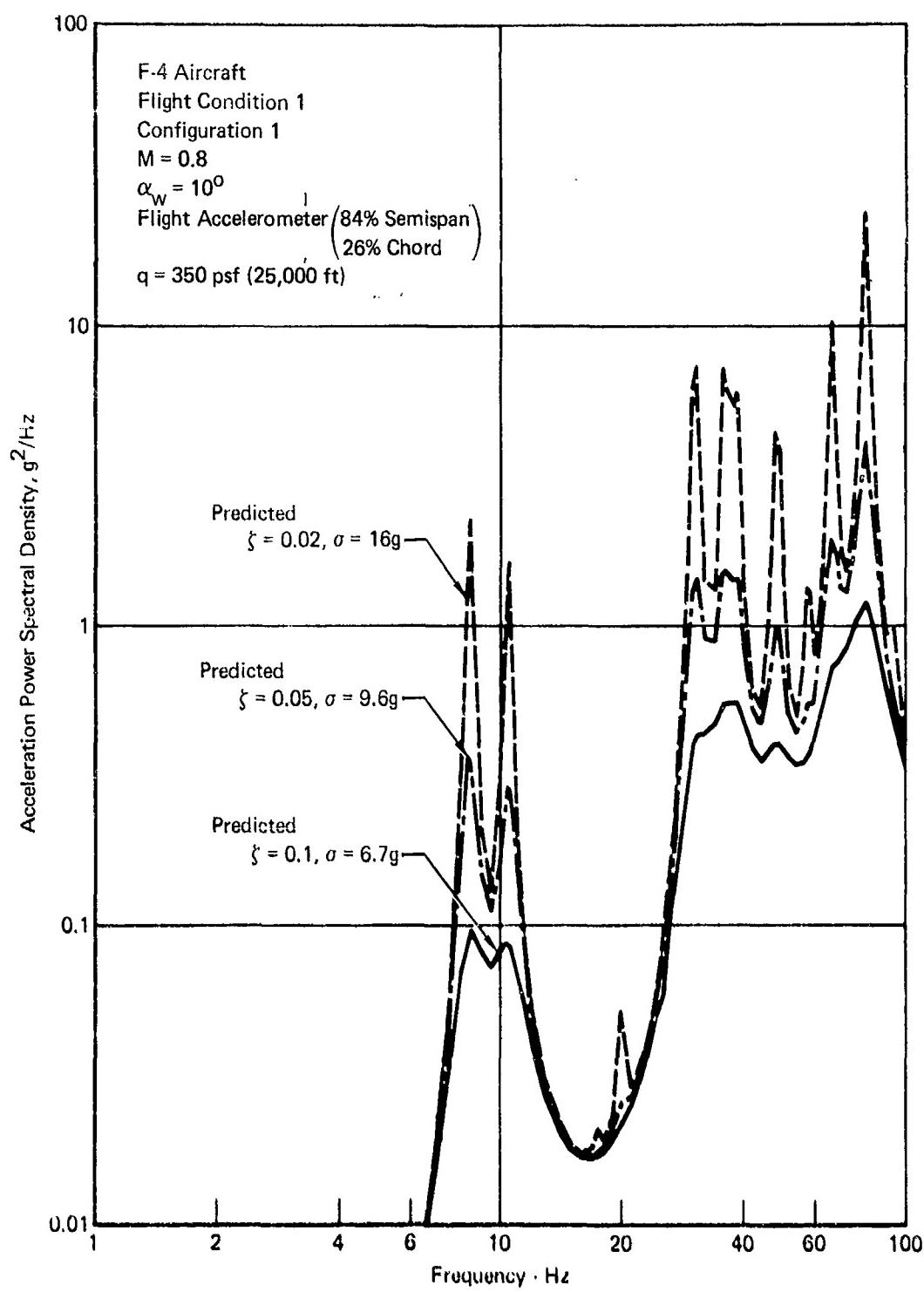


Figure 159 Effect of Damping Ratio on Predicted Acceleration Response

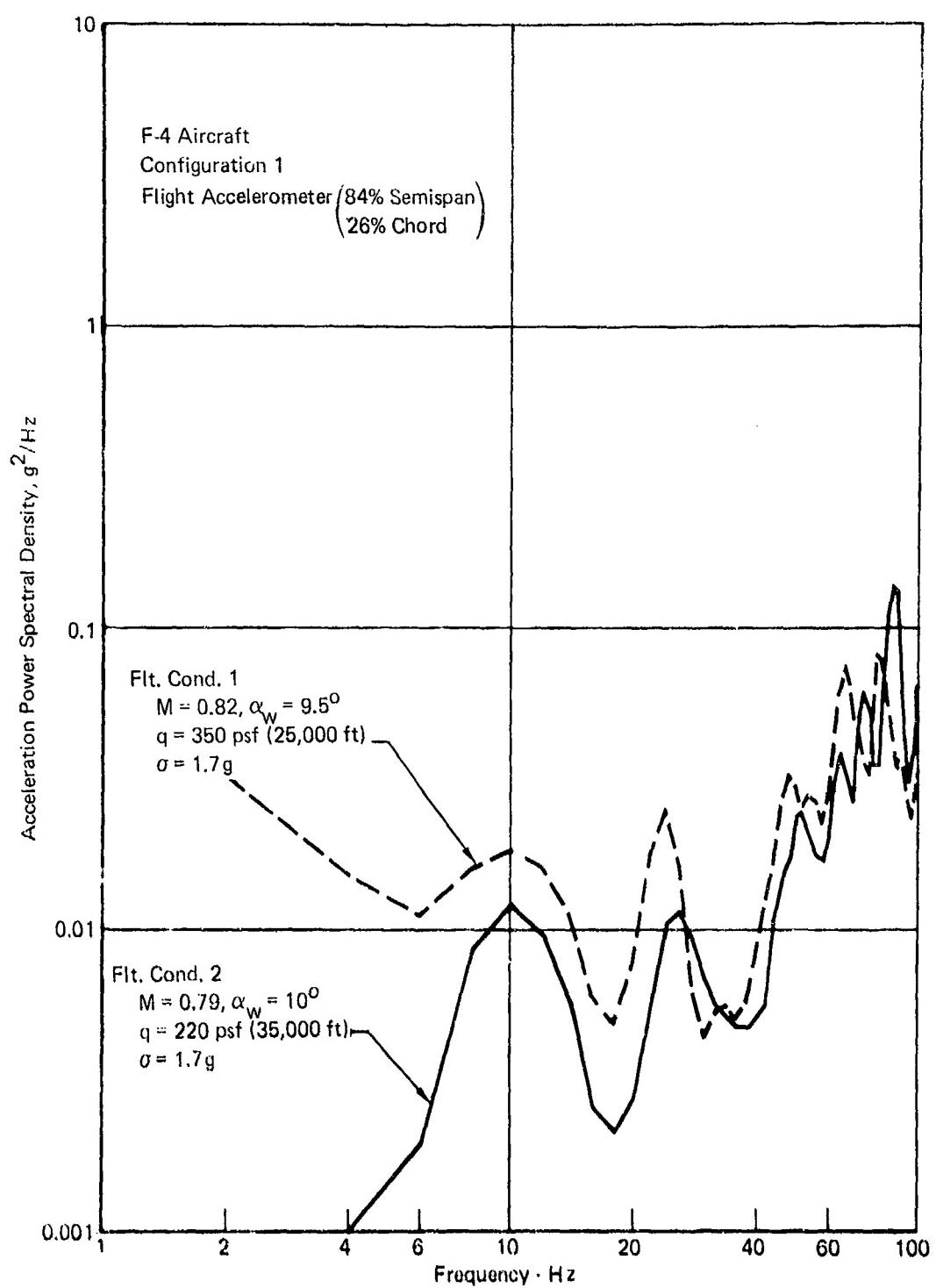


Figure 160 Comparison of Measured Acceleration Response at Two Dynamic Pressures

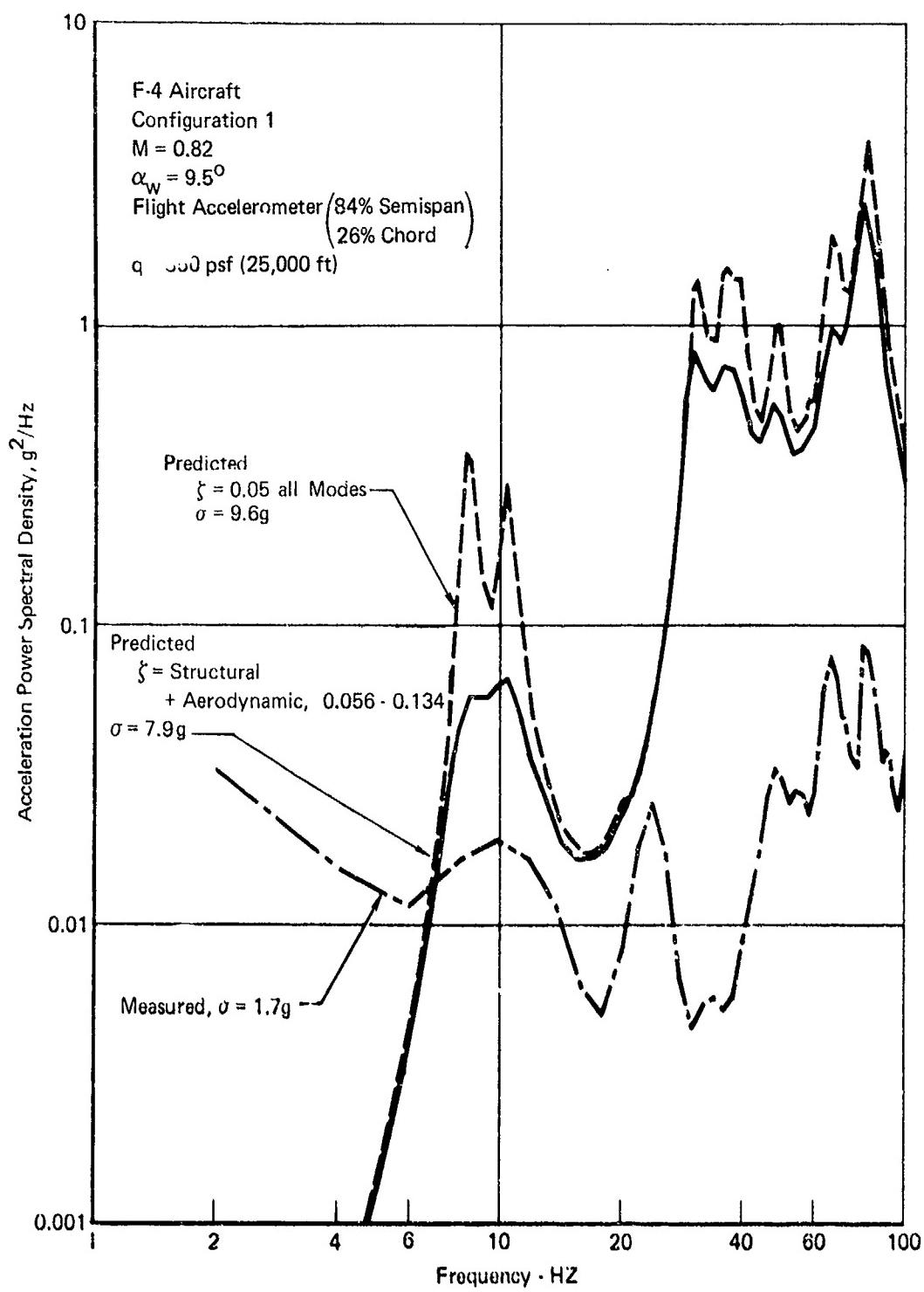


Figure 161 Comparison of Predicted and Measured Acceleration Response at Flight Condition 1

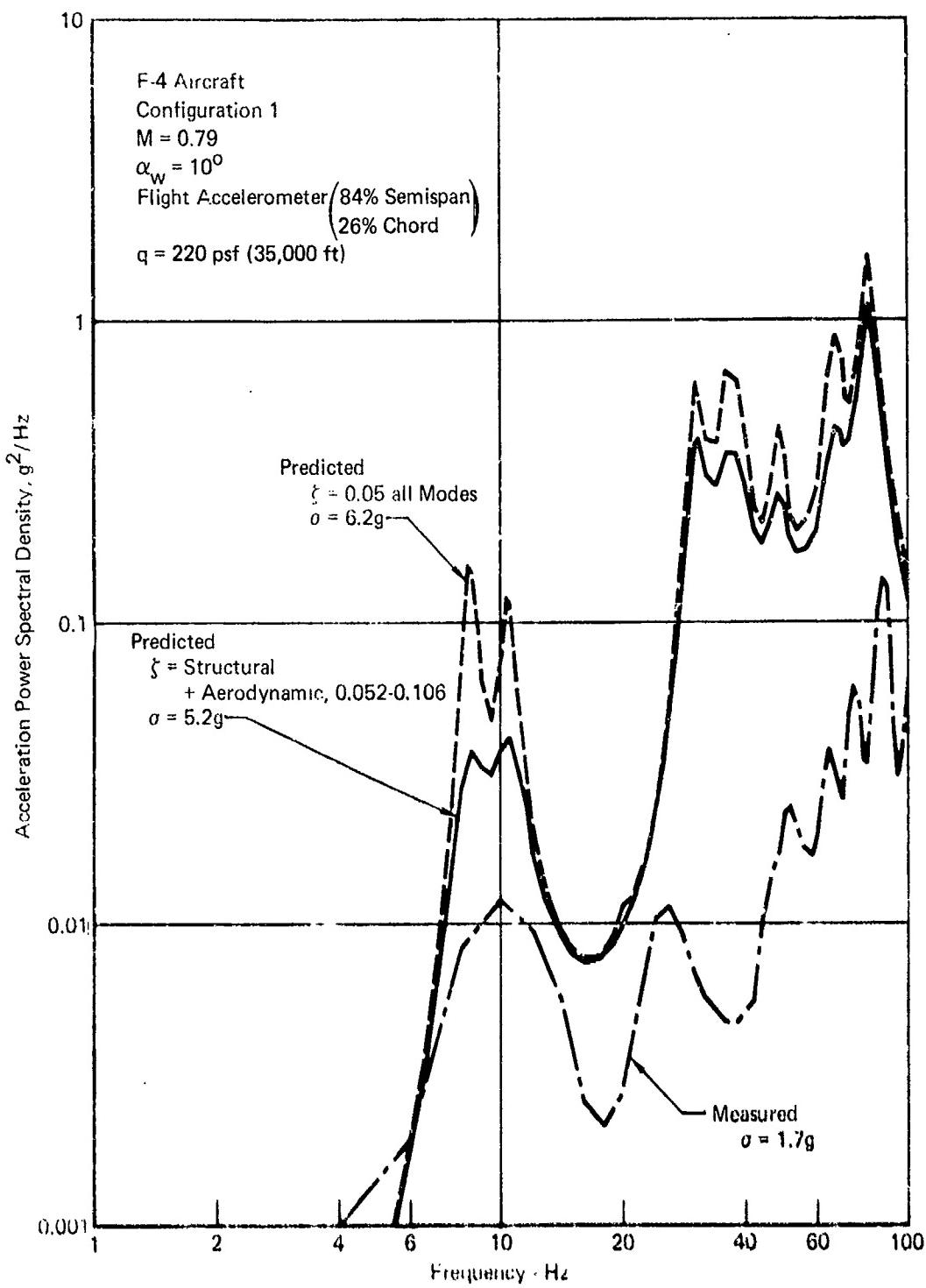


Figure 162 Comparison of Predicted and Measured Acceleration Response at Flight Condition 2

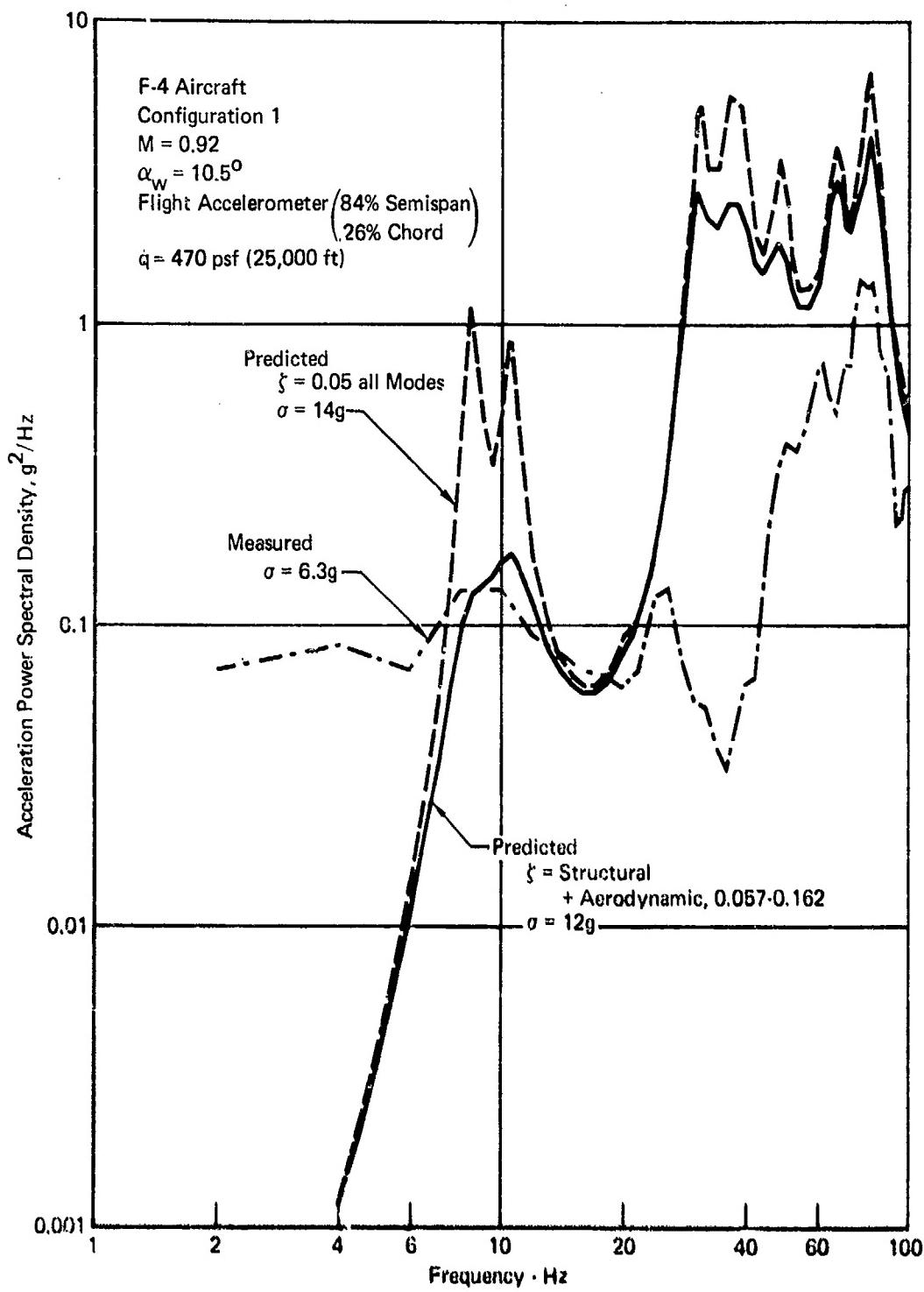


Figure 163 Comparison of Predicted and Measured Acceleration Response at Flight Condition 3

"PRECEDING PAGE BLANK-NOT FILMED."

APPENDIX A

FLOW ANALYSES

VISUALIZATION STUDIES

Methods of Analysis

Information available from the wind tunnel test for use in flow visualization studies included 16mm color movies and black and white still photos of the oil and tufts on the top surface of the wing.

Color movies of the wind tunnel tests were valuable tools in the analysis. The films were run at slow speeds and could be stopped for more detailed study of any given frame. From the flow visualization movies, flow charts were sketched and observations were recorded.

The tufts were classified by degree of oscillation and flow direction as follows:

- 1) STABLE - clearly definable flow direction, little or no oscillation - indicates undisturbed airflow.
- 2) MILD - clearly definable flow direction, base of tuft stable, end of tuft in a bounded oscillation.
- 3) MODERATE - definable flow direction; entire tuft oscillates in a bounded area.
- 4) RANDOM - indefinable flow direction; tuft oscillates with no definite pattern - indicates separated airflow.

The tuft flow directions were marked on scale drawings of the wings as were lines separating different flow directions.

The oil was analyzed in a similar manner. Sketches were made from the movies showing flow directions, pattern, and accumulations of the oil. Oil in flow directed aft and outboard was classified as attached. Areas where the oil collected were classified as separated regions. Areas where the oil has a forward flow direction were also classified as separated.

Still photos of selected conditions were used for comparative analysis. Flow patterns and general trends were correlated between oil and tufts. Criteria used in analyzing movies were also used for still photos. The degree of oscillation of the tufts was determined by the size of the blur of each tuft, and the flow direction. It appears that as the tufts oscillated, their back and forth motion against the surface of the wing polished the point and formed an arc-shaped area which reflected light into the cameras. At first glance, these light areas may be thought to be the tufts in oscillation. However, tufts in oscillation appear as a uniform blur, not as a spot with the tuft clearly visible.

In several cases, the tufts and the oil appeared to be indicative of different types of flow. Differences in the tuft and oil patterns may be due to different streamlines at and near the surface of the wing. The tufts are influenced by a layer as thick as the tufts, containing several streamlines. This gives the tufts three dimensions in which to react. The oil reacts only two dimensionally because it is affected only by the air on the surface of the wing. In some cases with leading edge separation, the oil flow flowed forward from the oil ports and did not reach the area aft of the oil ports. In such circumstances, the tufts were the better visual method of determining the type of airflow on the aft portion of the wing.

On the F-4 wing, there is a system of leading edge vortices which are responsible for many of the tuft and oil patterns. Their boundaries can be approximated by the changes of directions of the tufts, and by the circulatory behavior of the oil. The F-4 wing is like two wings in one, each with a leading edge vortex. See Figure A-1. The outer wing juts forward of the inner wing, creating a snag which generates another vortex aft along the fold line. Another vortex (the tip vortex) comes from beneath the wing and rolls over the wing tip. This complex system of vortices is a partial cause of leading edge separation, regions of oil circulation, different flow directions of the tufts, and the accumulation of oil in regions of low pressure.

Results

Variation of Flow Characteristics with Angle of Attack - These studies were run for Configuration 1 at Mach 0.9 and Reynolds Number of 1.25×10^6 /ft.

At $\alpha_w = 4^\circ$, see Figure A-2, the oil flows smoothly aft over the largest portion of the wing. There is some collection of the oil along the leading edge on the outboard panel, indicating separation which is probably caused by the leading edge vortices. The tufts on the area corresponding to the oil collection are directed outboard and are parallel to the leading edge. The tufts on the outboard panel are in mild to moderate oscillation. The tufts on the inner wing range from stable to mild oscillation.

At $\alpha_w = 8^\circ$ (Figure A-3), the oil over most of the wing flows outboard and aft, indicating smooth attached airflow. The leading edge vortices cause the oil to flow outboard along the leading edge and collect in the areas of separated flow. The abrupt changes in the flow directions of the

tufts are evidence of the leading edge vortices. Tufts on the outboard panel approach random motion, indicating separation. The only region of stable tufts lies next to the fuselage close to the leading edge, implying undisturbed airflow.

At $\alpha_w = 12^\circ$ (Figure A-4), the oil is swept outboard, parallel to the leading edge, until it hits the fold line and is deflected slightly aft. The tufts show the effect of the snag. The vortex generated by the snag deflects the innermost leading edge vortex and sweeps off the outboard panel (Figure A-1). The random motions of the tufts on the outer two thirds of the wing indicate that the airflow is detached.

At $\alpha_w = 16^\circ$ (Figure A-5), the oil collects on the inboard leading edge, along the wing flap, and along a line aft of the outboard leading edge flap, showing the vortices and indicating separation in the respective areas. Tufts in random motion indicate separation over a large percentage of the wing. Tufts along the leading edge show that the flow is directed inboard. This is caused by the vortices and the fact that at high angles of attack the pressure along the leading edge is lower inboard. On the tufted wing, the forward boundary of the leading edge vortex is indicated by the line of demarcation (Figure A-5) extending aft and outboard from the inboard leading edge. Inboard of the line, the tufts point outboard, but outboard of the line they are directed inboard.

At $\alpha_w = 20^\circ$ (Figure A-6), the oil shows that on the forward inboard portion of the wing the flow moves forward and inboard, aft, and then outboard. This motion is caused by the innermost leading edge vortex and the pressure distribution along the leading edge. The center of circulation can be approximated from the flow directions of the tufts. On the inboard leading edge a spinning tuft is found which corresponds with the area of circulating air. The tufts indicate separation over the entire wing. At this high angle of attack, the leading edge vortex is above the surface of the wing; however, the tufts are still affected and indicate the location of its forward boundary.

As the wing angle of attack (α_w) increases, the percentage of turbulent areas, indicated by the tufts, increases and the leading edge vortices move forward. Areas of separation are relatively stationary in their location, but increase in size and intensity as α_w gets larger.

Variation of Flow Characteristics with Mach Number - These studies were run for Configuration 1 at $\alpha_w = 12^\circ$ and Reynolds Number of $1.25 \times 10^6/\text{ft}$.

At $M = 0.7$ (Figure A-7), the oil on the inner wing moves aft and outboard, demonstrating smooth attached flow. The collection of oil along the leading edge indicates separation. The oil on the remainder of the outboard panel is swept off by the system of vortices. The random motions of the tufts on the outboard panel show this entire area is separated. The tufts on the remainder of the wing are in mild to moderate oscillation.

At $M = 0.9$ (Figure A-4), oil no longer collects on the leading edge. The tufts indicate that the area of separated flow has increased.

At $M = 1.0$ (Figure A-8), the oil begins to circulate in two areas: 1) on the inboard panel behind the leading edge flap, and 2) around the fold line, encompassing the entire outboard panel. These oil patterns are caused by a combination of the leading edge vortices, the snag vortex, separation, and the pressure distribution over the wing. The separated area shown by the tufts has decreased from that at $M = 0.9$, a small percentage. This trend seems to indicate a critical point between 0.9 and 1.0 ($0.9 \leq M_{CRIT} \leq 1.0$).

At $M = 1.2$ (Figure A-9), the oil present on the center of the wing collects on the leading edge, along a possible weak shock. The accumulation of oil on the wing tip is due to the leading edge vortices, including the snag vortex and the tip vortex. The oil on the outboard panel gathers along a shock line parallel to the trailing edge. Separation indicated by the tufts is limited to the periphery of the outer wing panel. The tufts in random motion at the trailing edge correspond with the area aft of the shock line in the oil. The boundaries of the leading edge vortices are definable by the changes in the flow directions of the tufts.

At a constant angle of attack, the area of separation increases as M increases to a point between 0.9 and 1.0, M_{CRIT} . Above M_{CRIT} , the area of separation decreases, at least up to $M = 1.2$.

Variation of Flow Characteristics with Reynolds Number - These studies were run for Configuration 1 at Mach 0.9.

At $\alpha_w = 8^\circ$, $Re = 1.25 \times 10^6/\text{ft}$. (Figure A-3), the leading edge vortices cause the oil to collect along the leading edge on the outboard panel, and just inboard of the snag. The tufts on the outboard panel are in moderate oscillation. The area of stable tufts is small and is inboard along the leading edge. This type of flow is typical for a highly swept wing at these conditions.

At $\alpha_w = 8^\circ$, $Re = 3.75 \times 10^6/\text{ft}$. (Figure A-10), there is no accumulation of oil on the inboard panel, and the oil on the outboard panel is closer to the snag. This might imply that as Re increases, the vortices appear to shift slightly inboard. The outboard panel is similar to that with the lower Reynolds number, but the stable area of tufts has increased. This stabilizing effect at the higher Re may be due to the thinning out of the viscous layer.

At $\alpha_w = 12^\circ$, a comparison of Figures A-4 and A-11 shows no noticeable Reynolds number effect in either the tufts or the oil. An examination of other photos has shown no noticeable Reynolds number effect for α_w from 1. to 11.

In summary, these studies suggest that increasing Reynolds number tends to increase the area of stable flow somewhat at the lower angles of attack near buffet onset but has no noticeable effect at angles of attack well beyond onset.

Best Available Copy

INSTRUMENTATION STUDIES

General

The instrumentation data used here to analyze the flow characteristics consisted of

- o Aerodynamic coefficient data, C_L
- o rms wing root bending moment, σ_M
- o Steady pressure coefficients from static pressure taps, C_p
- o rms pressure coefficients from high frequency pressure transducers, $\Delta C_{p\text{rms}}$

These studies probe into the flow characteristics at $M = 0.7$ and $M = 0.9$ and are divided generally into two categories: buffet onset and post-onset.

Buffet Onset

Measured lift coefficient, C_L , versus angle of attack is plotted in Figure A-12 for $M = 0.7$ and Figure A-13 for $M = 0.9$. Buffet onset, α_{BO} , is identified on these curves by the departure from linearity, i.e. $\alpha_{BO} = 9^\circ$ at $M = 0.7$ and $\alpha_{BO} = 7^\circ$ at $M = 0.9$. The exact point of departure from linearity may be subject to some uncertainty because the departure is not abrupt, as in Figure A-12. This is frequently the case, and the location of buffet onset--to a degree--depends on the analyst's interpretation of the curve connecting the test points.

Another indicator of buffet onset is the wing root rms bending moment. This data is presented in Figures A-14 and A-15 for $M = 0.7$ and 0.9 , respectively. Here, buffet onset is identified with a sudden, sharp rise in rms from a basically constant level below onset. This indicator presents a rather good identification of buffet onset, $\alpha_{BO} = 8^\circ$ at $M = 0.7$ and $\alpha_{BO} = 7^\circ$ at $M = 0.9$. It is less dependent on the analyst's interpretation than the onset identification based on C_L .

Static pressure (C_p) divergence is often used as an indicator of buffet onset. Such data is presented in Figures A-16 and A-17 for $M = 0.7$ and 0.9 respectively for the trailing edge (90% chord) static pressure taps. In Figure A-16, for $M = 0.7$, the first indication of flow separation is at $\alpha_w = 5^\circ$ where the tip trailing edge static pressure shows a sudden increase in C_p from its nominal value at the lower angles. At this angle of attack, $\alpha_w = 5^\circ$, the static pressures at the other trailing edge spanwise locations indicate that flow separation has not occurred at these locations. However, at $\alpha_w = 8^\circ$ all the other trailing edge static pressures

diverge simultaneously. From this information it is inferred that

- o A local area of flow separation initially occurs in the vicinity of the tip trailing edge at $\alpha_w = 5^\circ$
- o When α_w reaches 8° flow separation suddenly spreads to encompass the whole trailing edge.

For $M = 0.9$, Figure A-17 shows a similar pattern except that flow separation over the whole trailing edge now occurs at $\alpha_w = 6^\circ$ instead of 8° .

The validity in using static pressure divergence as an indicator of local flow separation (or at least local pressure fluctuations) is supported by the rms fluctuating pressure data, $\Delta C_{p,\text{rms}}$, shown in Figures A-18 and A-19 for $M = 0.7$ and 0.9 respectively. These show a rise in fluctuating pressure at the tip trailing edge at $\alpha_w = 5^\circ$ for $M = 0.7$ and $\alpha_w = 4^\circ$ for $M = 0.9$ reasonably corresponding to the static pressure divergences for the same location. They further show fluctuating pressure rises for the other trailing edge locations at about $\alpha_w = 7^\circ$ for $M = 0.7$ and $\alpha_w = 6^\circ$ for $M = 0.9$ again reasonably corresponding to the static pressure divergences for the same locations.

Buffet onset indications based on C_L and rms wing root bending moment are indicative of the gross flow picture over the wing while the static pressures, C_p , are indicative of local flow conditions existing near the static pressure taps. As a consequence, static pressure divergence is indicative of the initiation and growth of local areas of flow separation, while C_p and rms bending moment divergences are indicative of sufficient growth in local flow separation to be detectable on a gross scale. The latter is what is loosely defined as buffet onset. Even though a small area of local flow separation (tip trailing edge) is indicated at $\alpha_w = 5^\circ$ for both $M = 0.7$ and 0.9 , buffet onset is not considered to have occurred until α_w reaches 8° or 9° at $M = 0.7$ and 7° at $M = 0.9$.

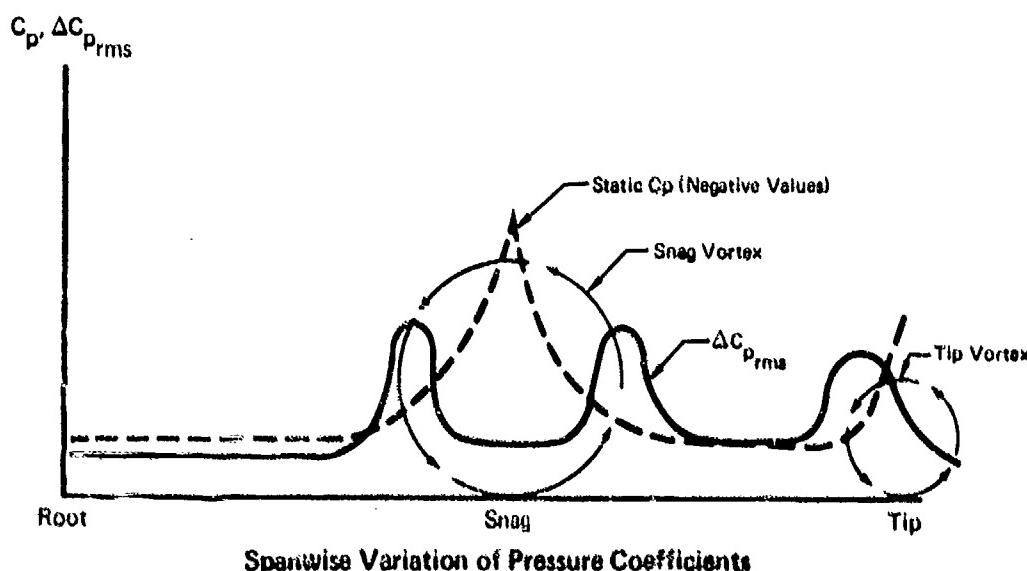
Post-onset

As mentioned elsewhere in this report, the F-4 wing with its high sweep, high taper and snag gives rise to complex flow patterns which are not treated at high angles of attack. These studies attempted to probe into the relationships between the vortex systems and regions of fluctuating pressure.

Best Available Copy

Static pressure data, C_p , is presented in Figures A-20 and A-21 for $M = 0.7$ and 0.9 respectively. These show spanwise C_p variations for 50%, 70%, and 90% chord locations. The pressure peaks (actually negative C_p peaks) are believed to be associated with vortices emanating from the tip and from the snag. The snag vortex is quite evident at the 50% and 70% chord locations while the tip vortex is most evident at the 90% and 70% chord locations. The tip vortex is never evident forward of 70% chord, while the snag vortex effect tends to move downstream and inboard at the higher angles of attack.

Rms fluctuating pressure data, $\Delta C_{p\text{rms}}$, is presented in Figures A-22 and A-23 for $M = 0.7$ and 0.9 respectively. Although not absolutely conclusive, if this data is compared to the corresponding static pressure data of Figures A-20 and A-21, there is a hint that the maximum fluctuating pressures seem to occur on either side of the vortex cores. This suggests a model of the flow pattern as sketched below.



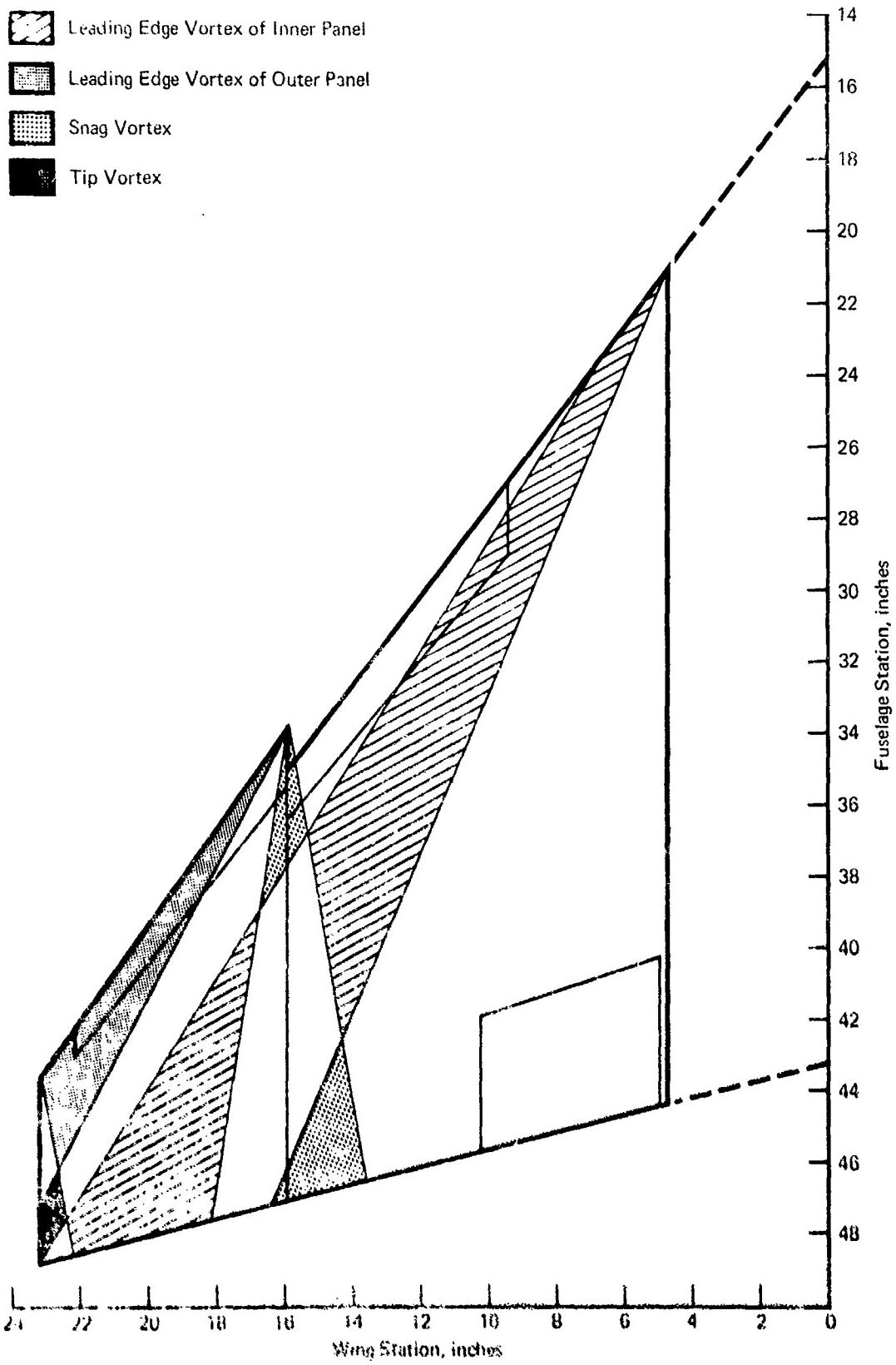


Figure A-1 Schematic of Four Plausible Vortex Patterns

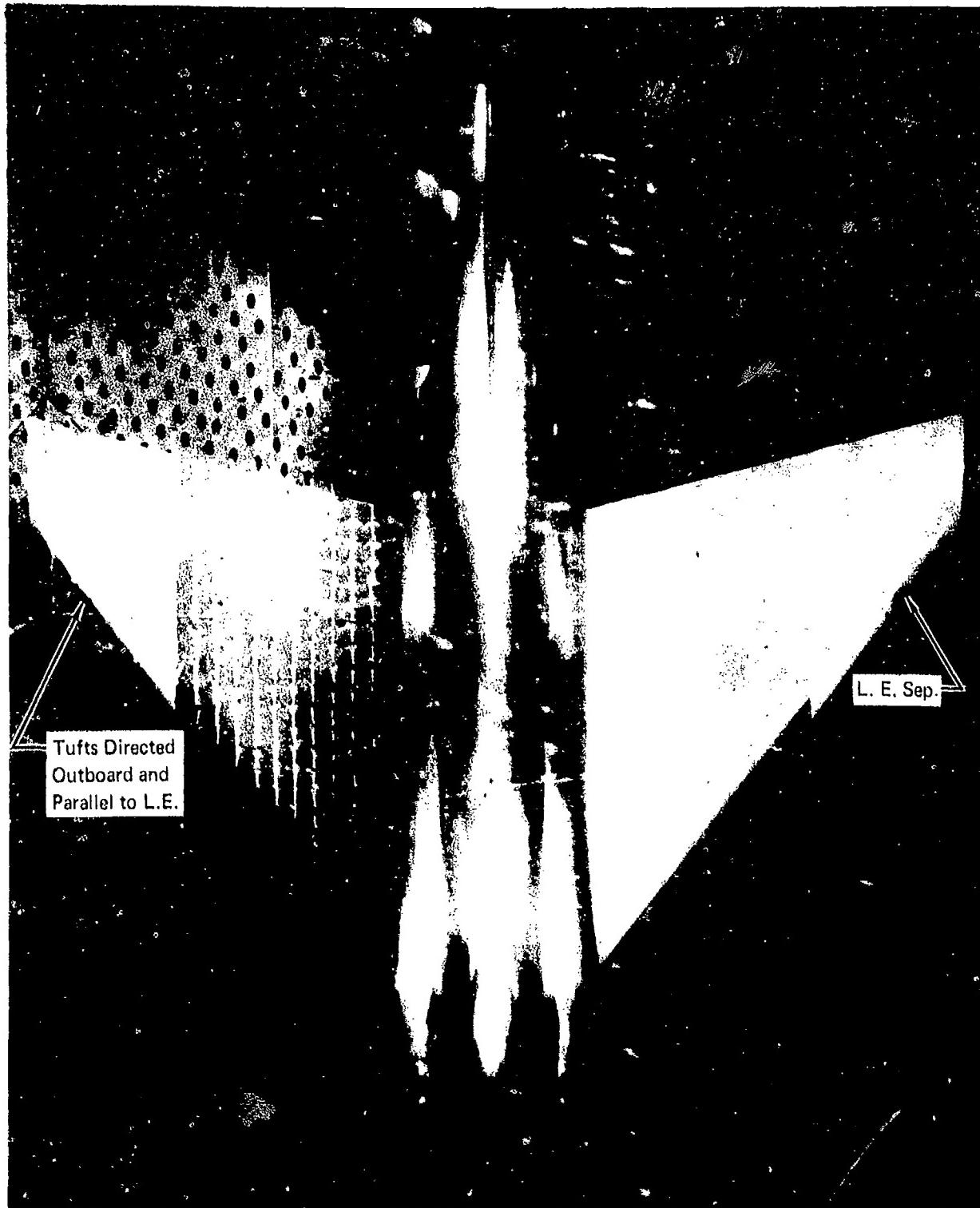


Figure A-2 Flow Visualization (Oil and Tufts)
Configuration 1, Mach 0.9, $Re = 1.25 \times 10^6/\text{ft}$, Wing Angle of Attack (α_w) = 4°

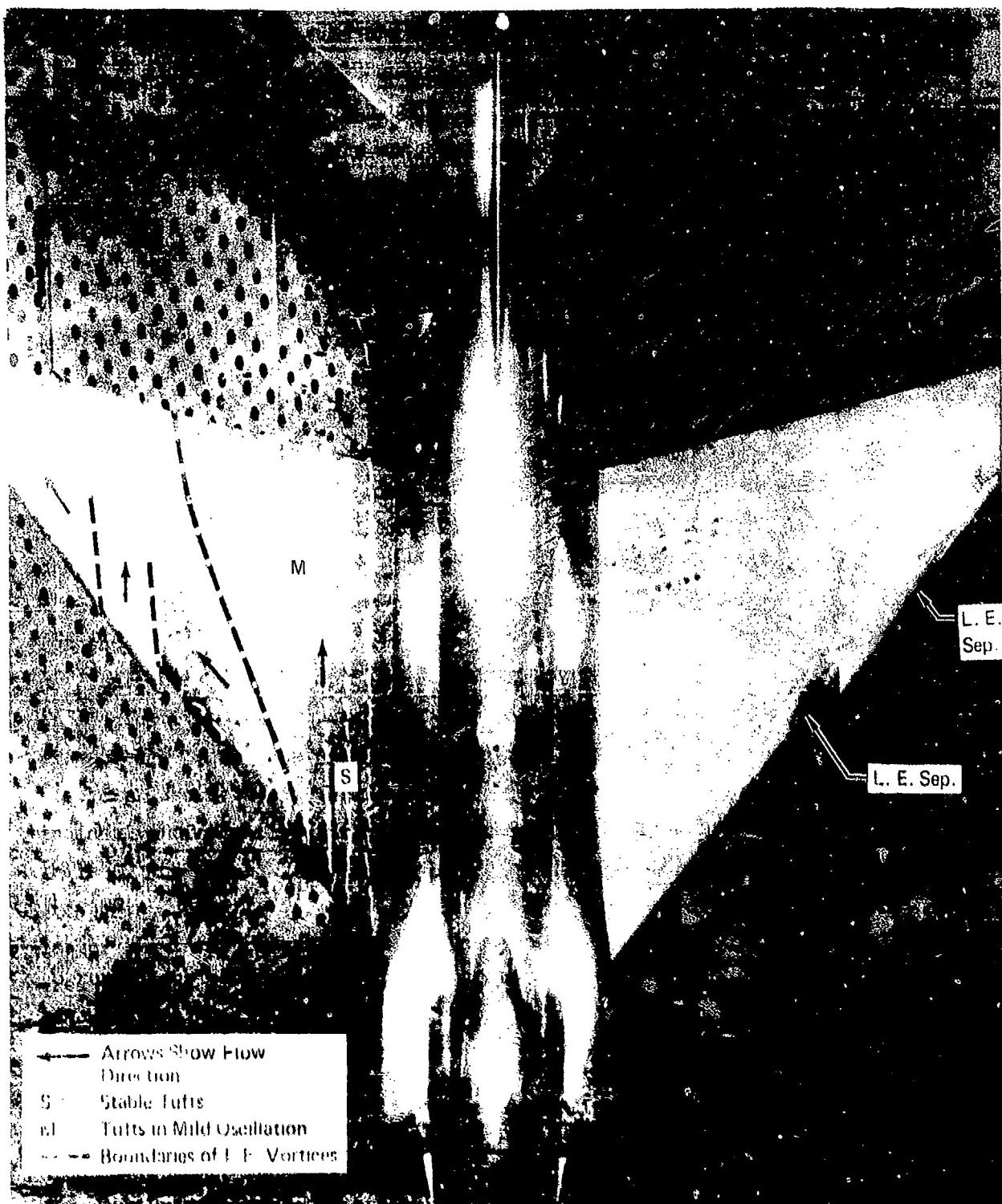


Figure A-3 Flow Visualization (Oil and Tufts)
Configuration 1, Mach 0.9, $Re = 1.25 \times 10^6/\text{ft}$, Wing Angle of Attack (α_w) = 8°

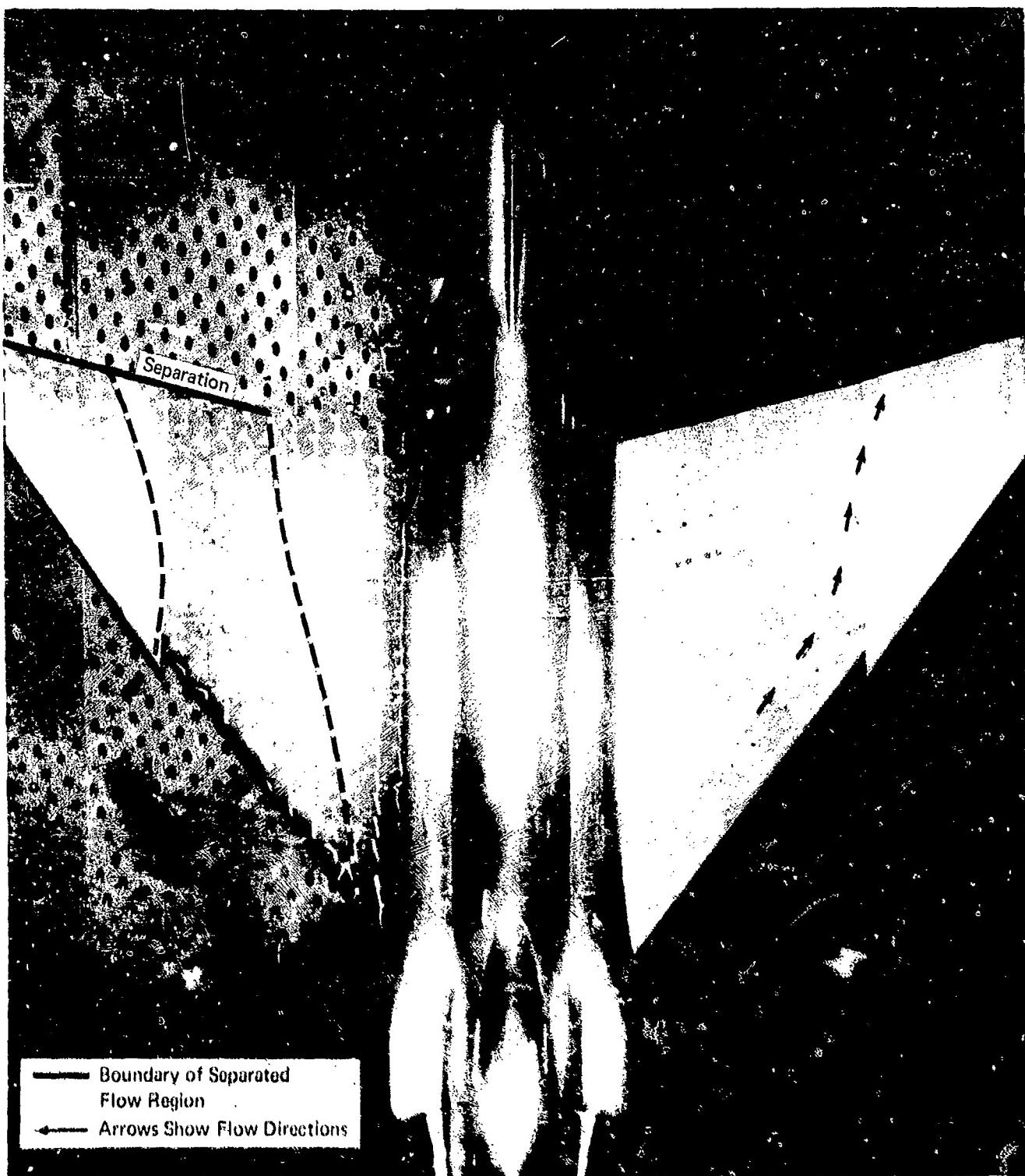


Figure A-4 Flow Visualization (Oil and Tufts)
Configuration 1, Mach 0.9, $Re = 1.25 \times 10^6/\text{ft}$, Wing Angle of Attack (α_W) = 12°

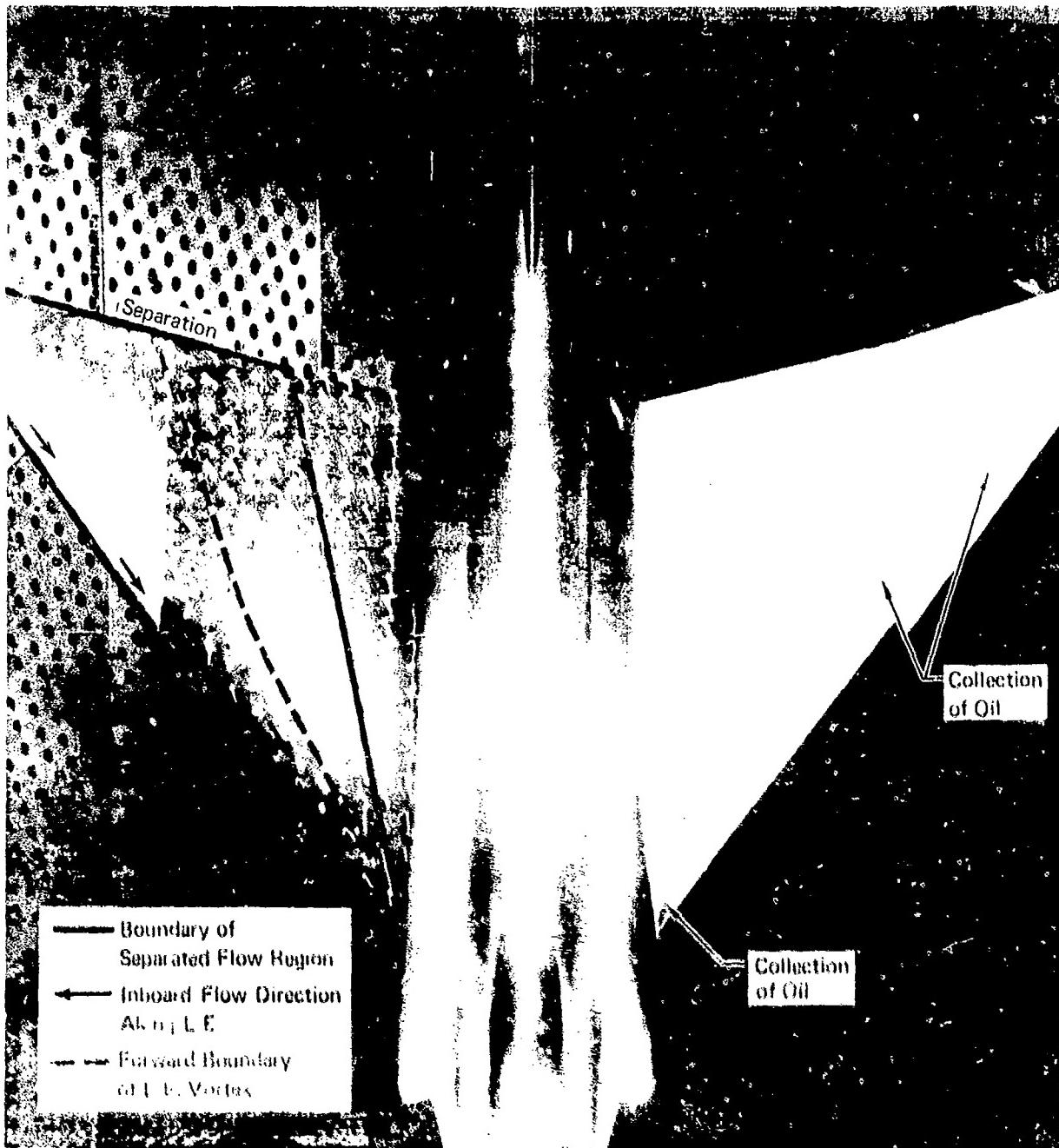


Figure A-5 Flow Visualization (Oil and Tufts)
Configuration 1, Mach 0.9, $Re = 1.25 \times 10^6/\text{ft}$, Wing Angle of Attack (α_w) = 16°

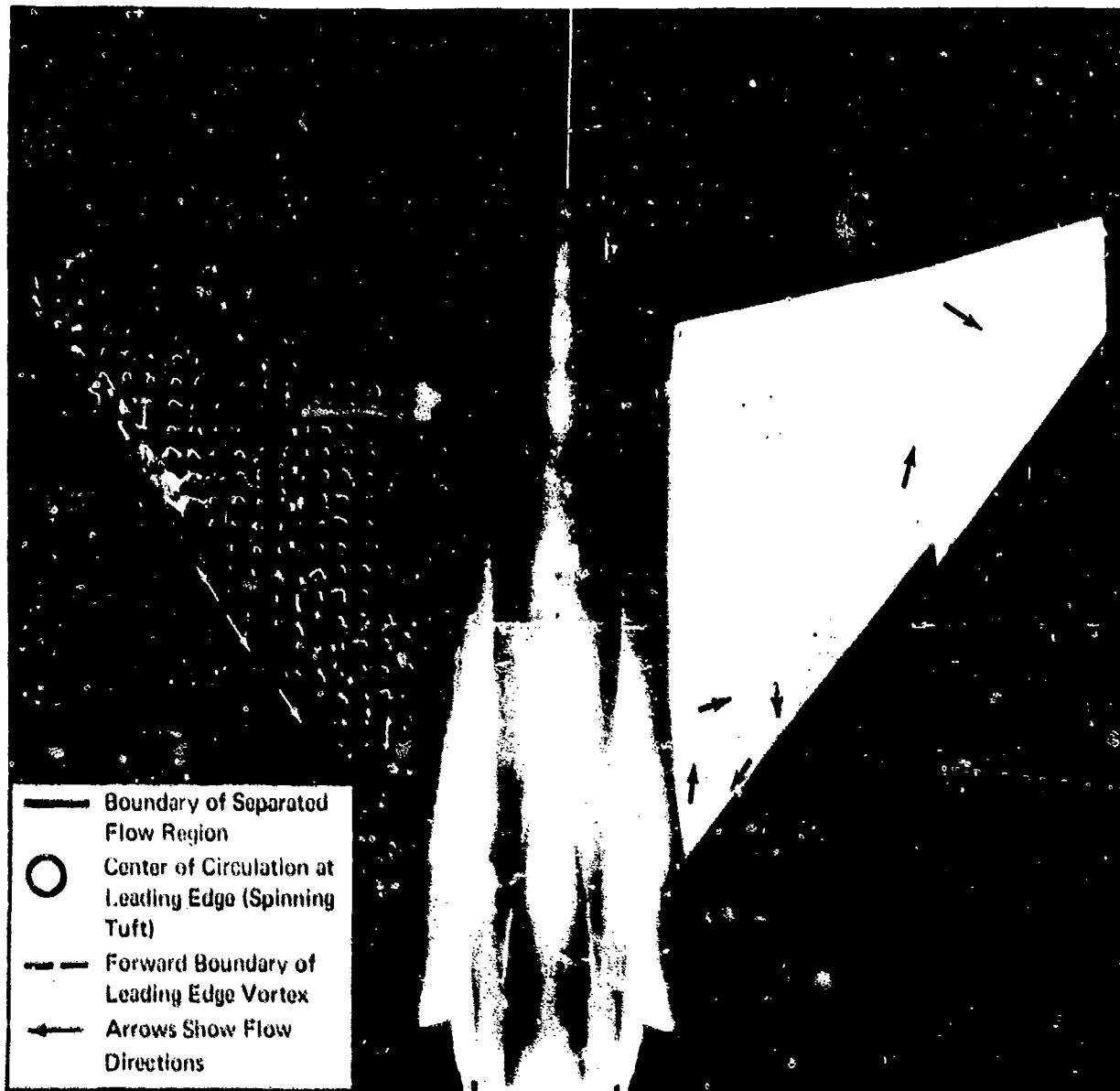


Figure A-6 Flow Visualization (Oil and Tufts)
Configuration 1, Mach 0.9, $Re = 1.25 \times 10^6/\text{ft}$, Wing Angle of Attack (α_w) = 20°

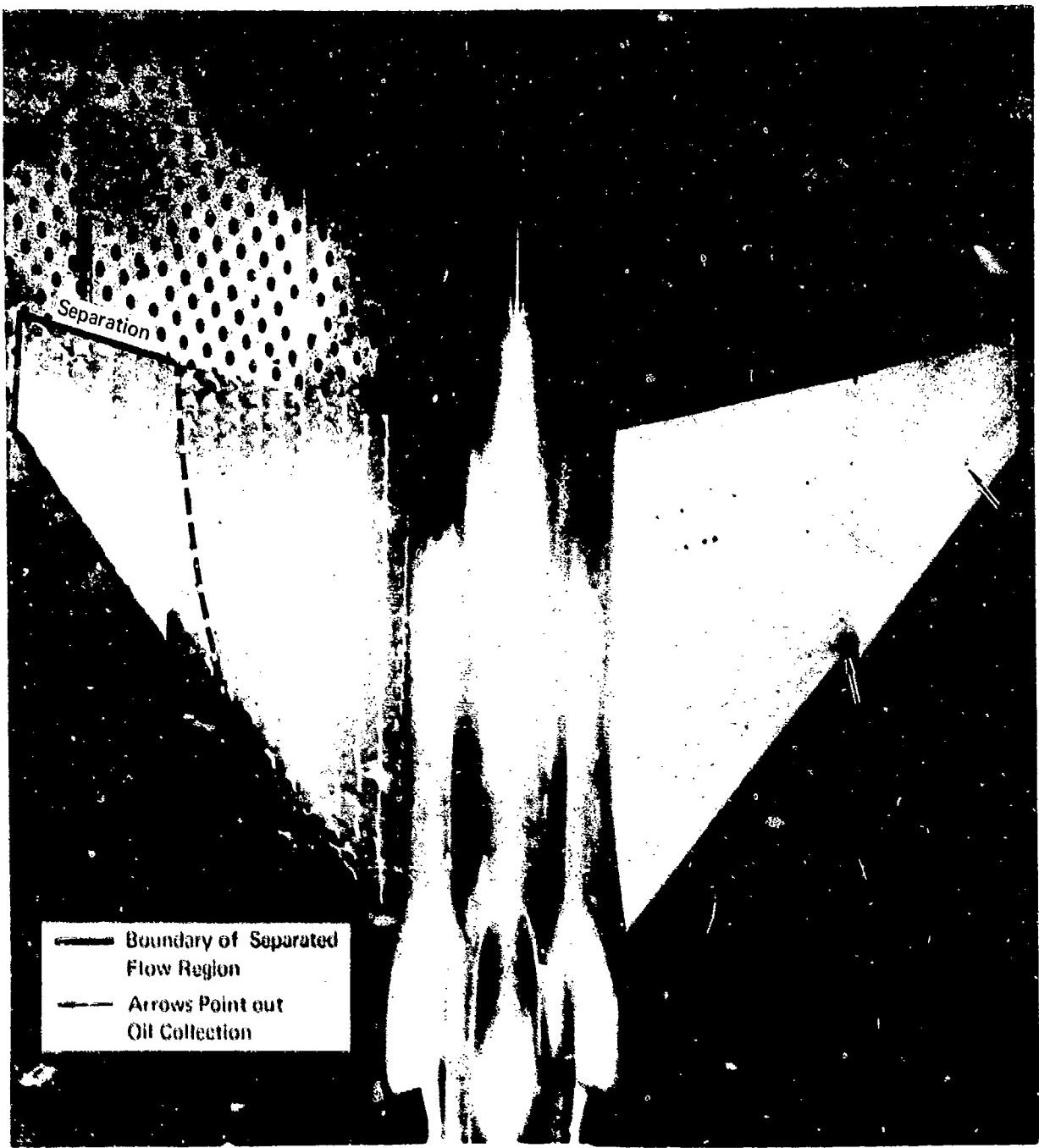


Figure A-7 Flow Visualization (Oil and Tufts)
Configuration 1, Mach 0.7, $Re = 1.25 \times 10^6/\text{ft}$, Wing Angle of Attack (α_w) = 12°

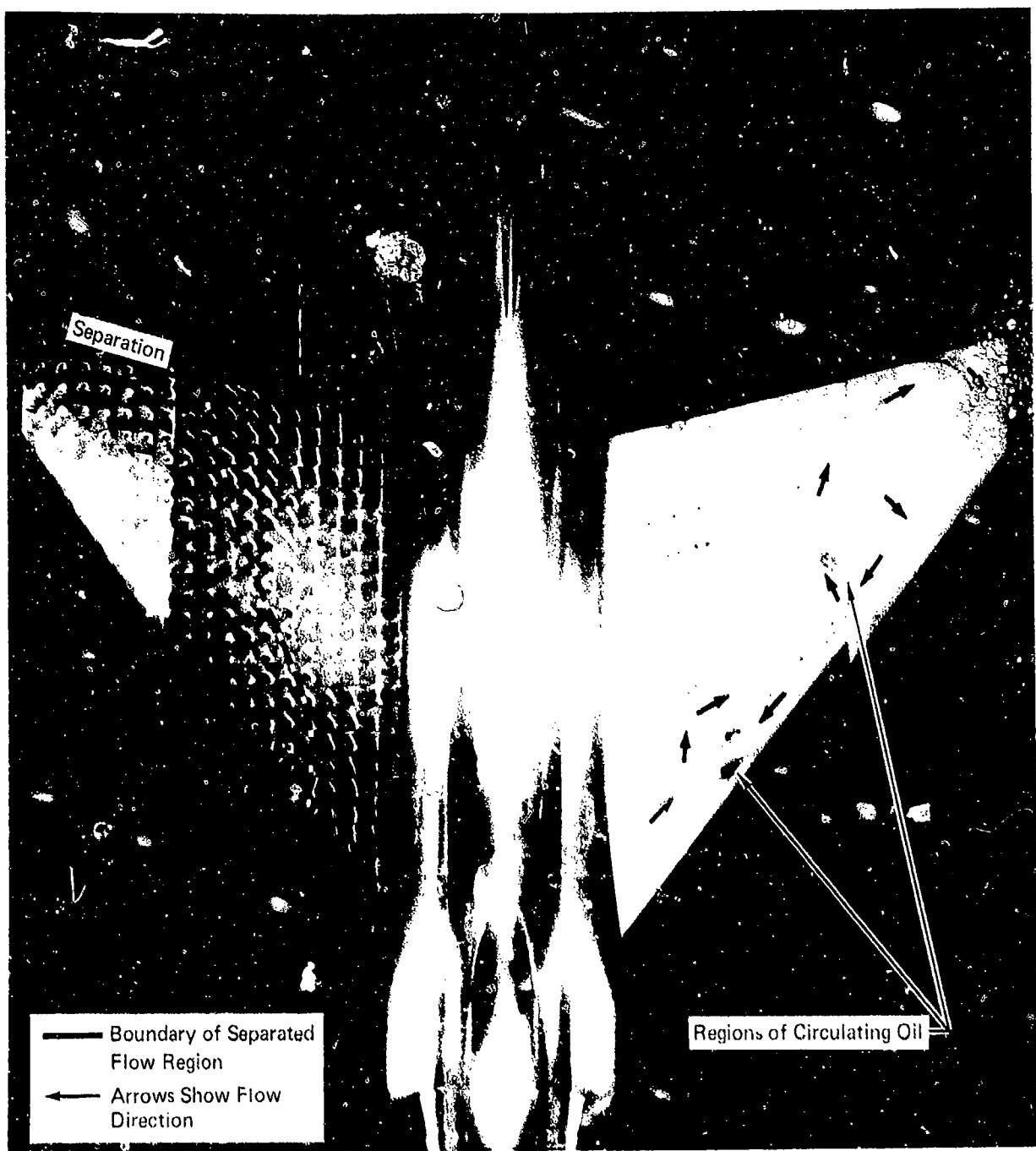


Figure A-8 Flow Visualization (Oil and Tufts)
Configuration 1, Mach 1.0, $Re \approx 1.25 \times 10^6/\text{ft}$, Wing Angle of Attack (α_W) = 12°

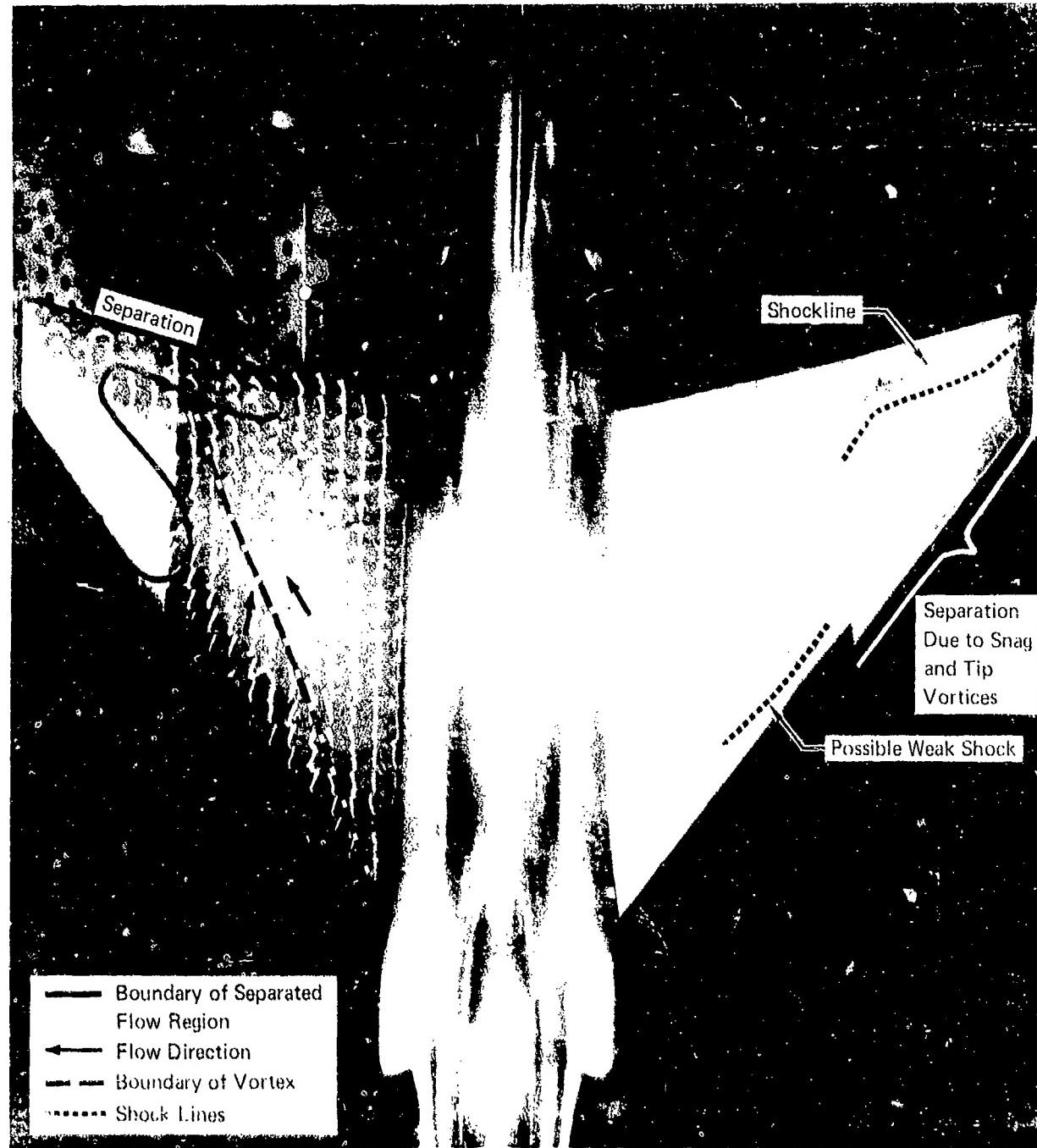
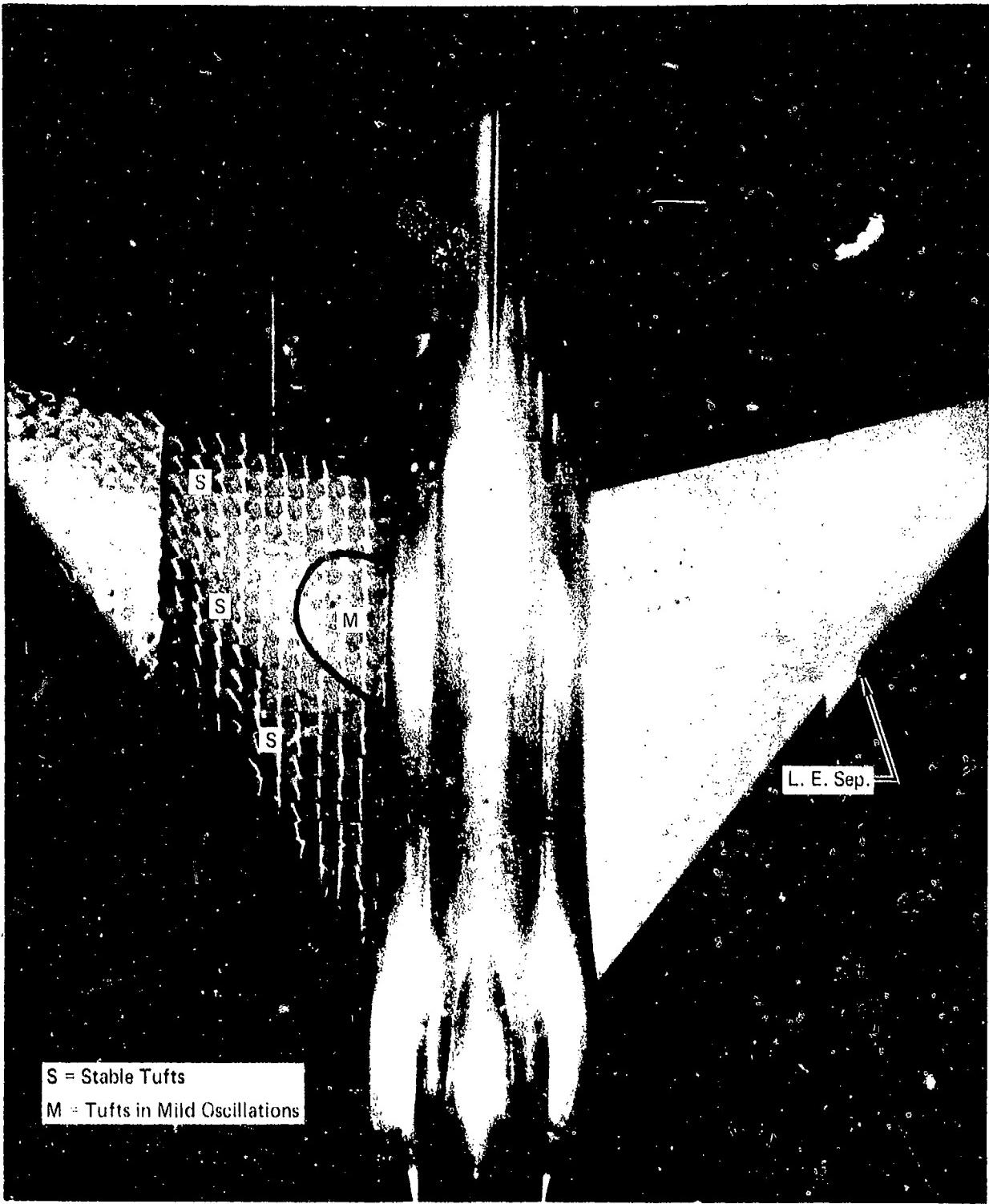


Figure A-9 Flow Visualization (Oil and Tufts)
Configuration 1, Mach 1.2, $Re = 1.25 \times 10^6/\text{ft}$, Wing Angle of Attack (α_W) = 12°



S = Stable Tufts

M = Tufts in Mild Oscillations

Figure A-10 Flow Visualization (Oil and Tufts)
Configuration 1, Mach 0.9, $Re = 3.75 \times 10^6/\text{ft}$, Wing Angle of Attack (α_w) = 8°

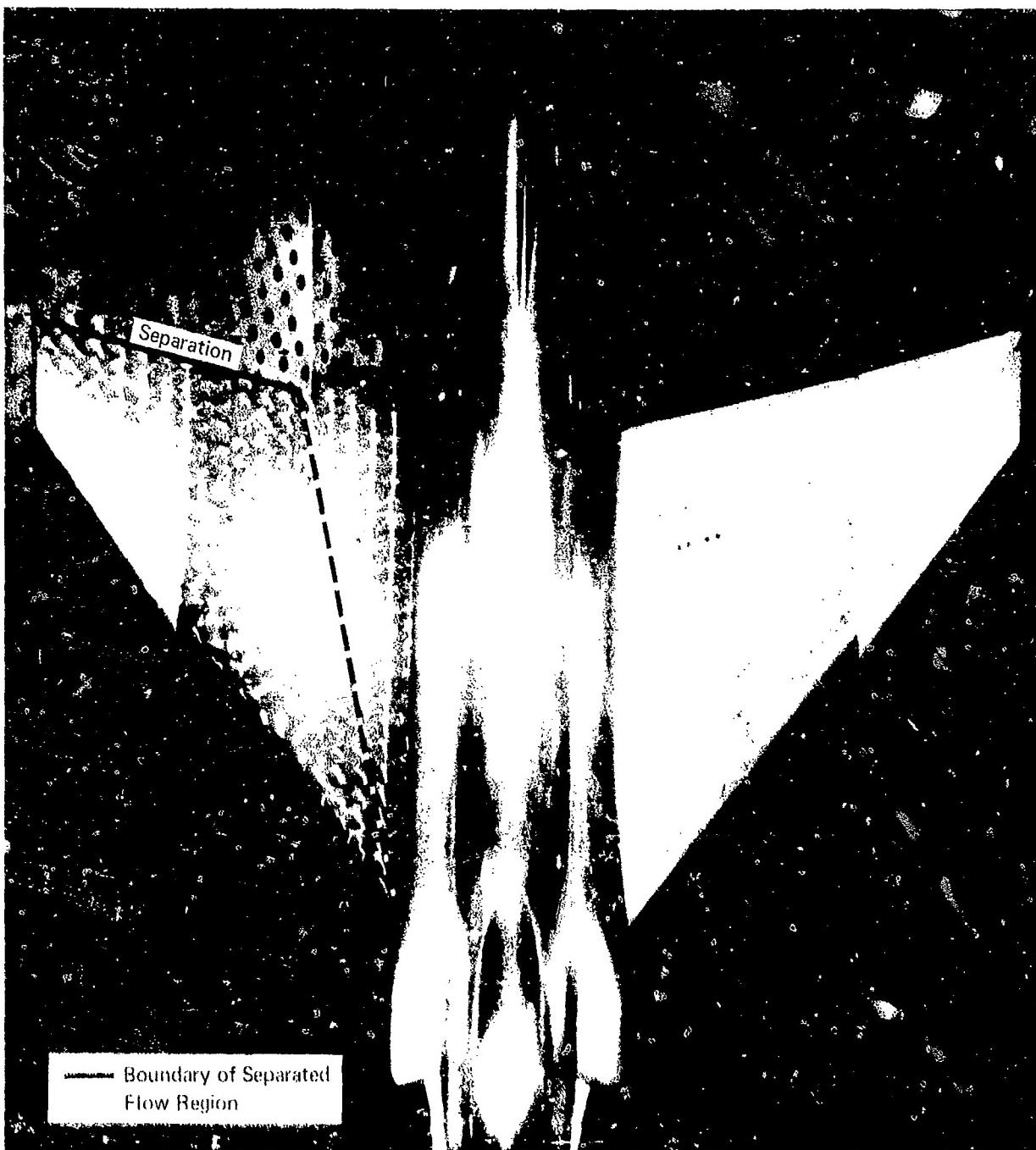


Figure A-11 Flow Visualization (Oil and Tufts)
Configuration 1, Mach 0.9, $Re = 3.75 \times 10^6/\text{ft}$, Wing Angle of Attack (α_W) = 12°

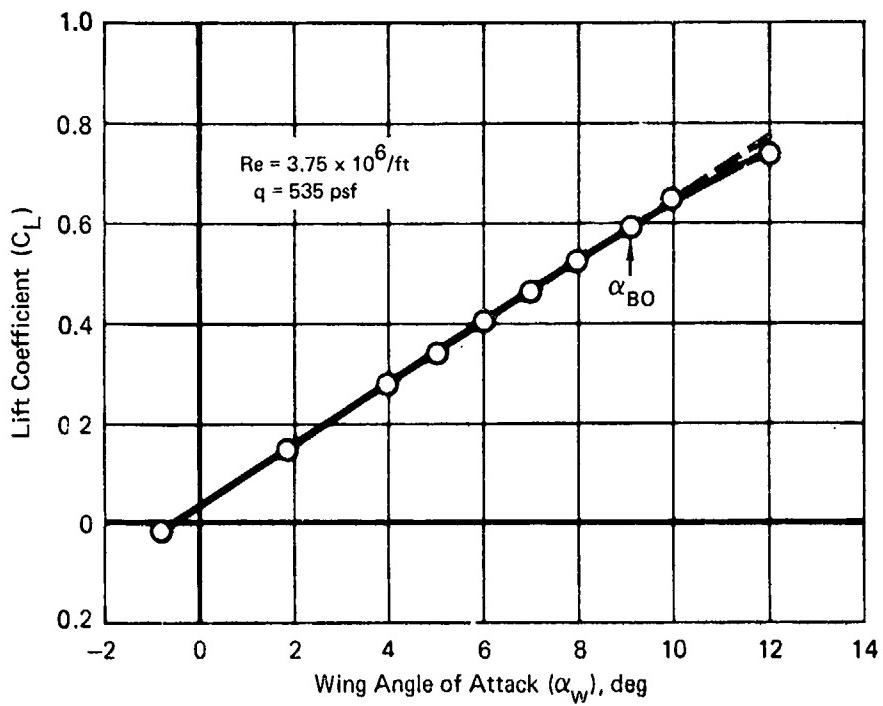


Figure A-12 Lift Coefficient vs Wing Angle of Attack for Configuration 1, Mach 0.7

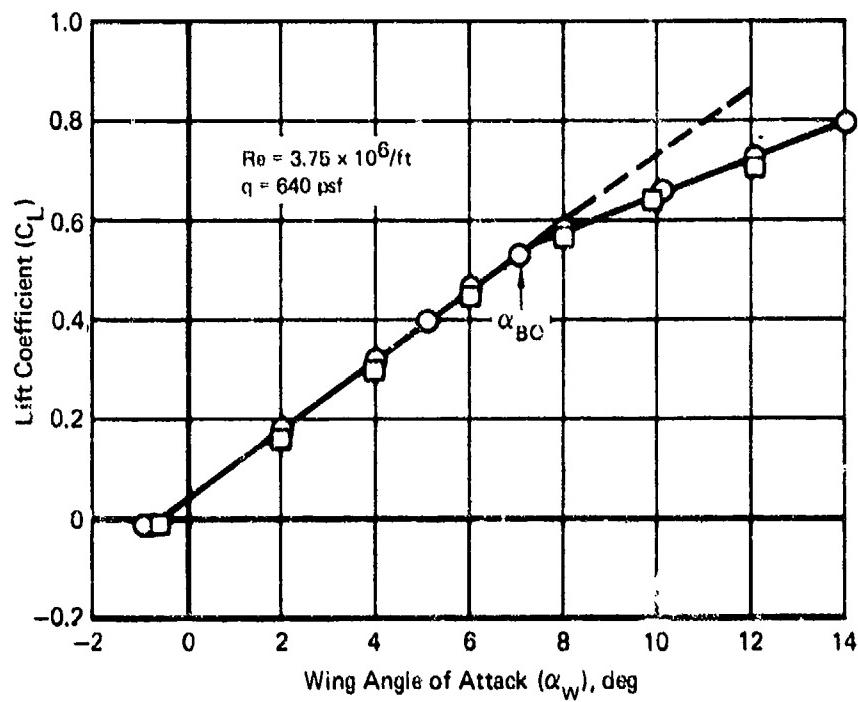


Figure A-13 Lift Coefficient vs Wing Angle of Attack for Configuration 1, Mach 0.9

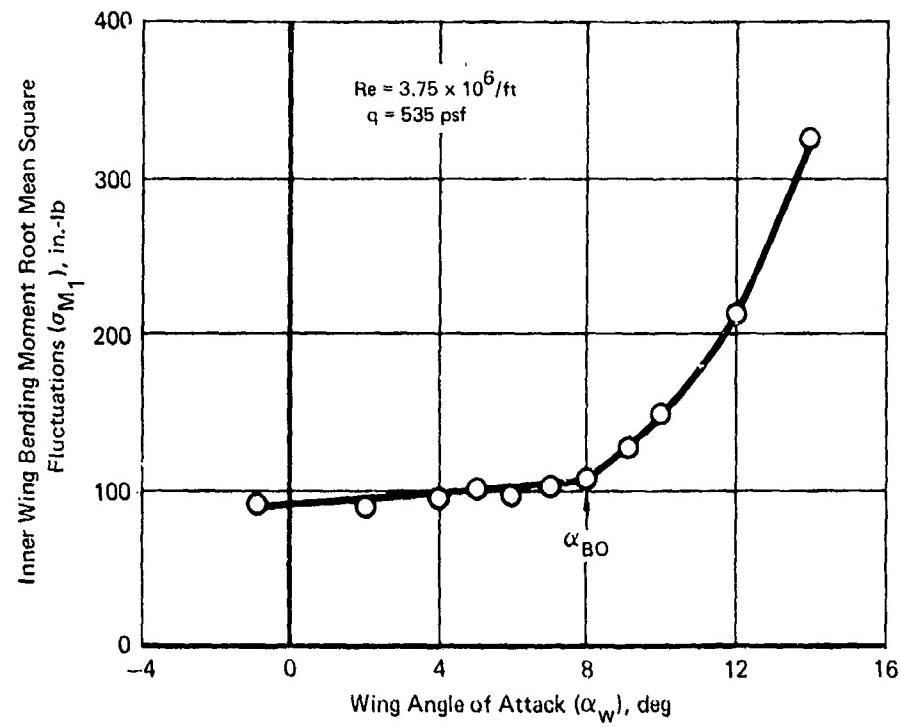


Figure A-14 rms Inner Wing Bending Moment vs Wing Angle of Attack for Configuration 1, Mach 0.7

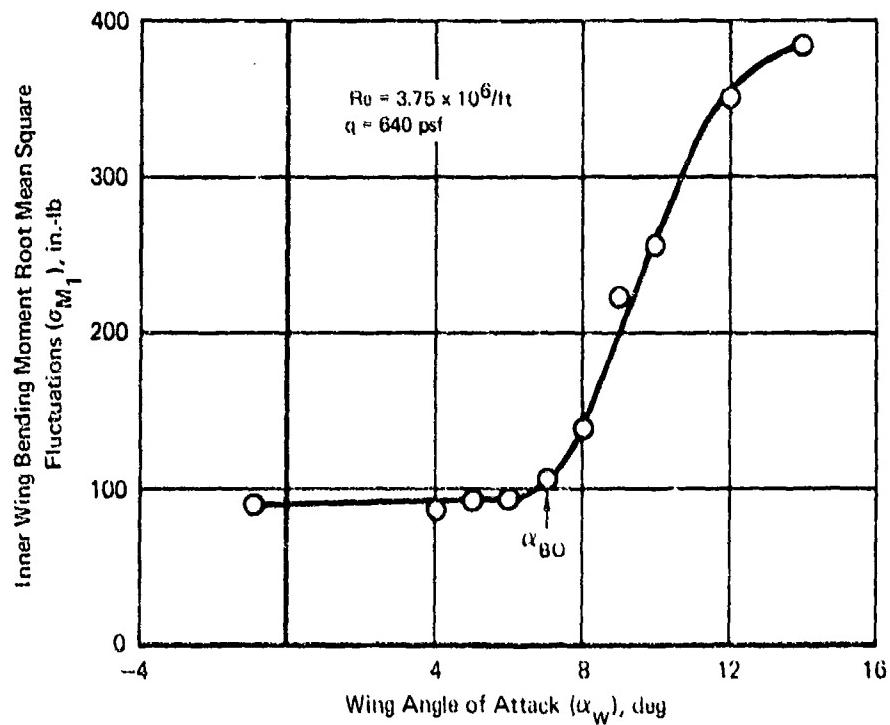


Figure A-15 rms Inner Wing Bending Moment vs Wing Angle of Attack for Configuration 1, Mach 0.9

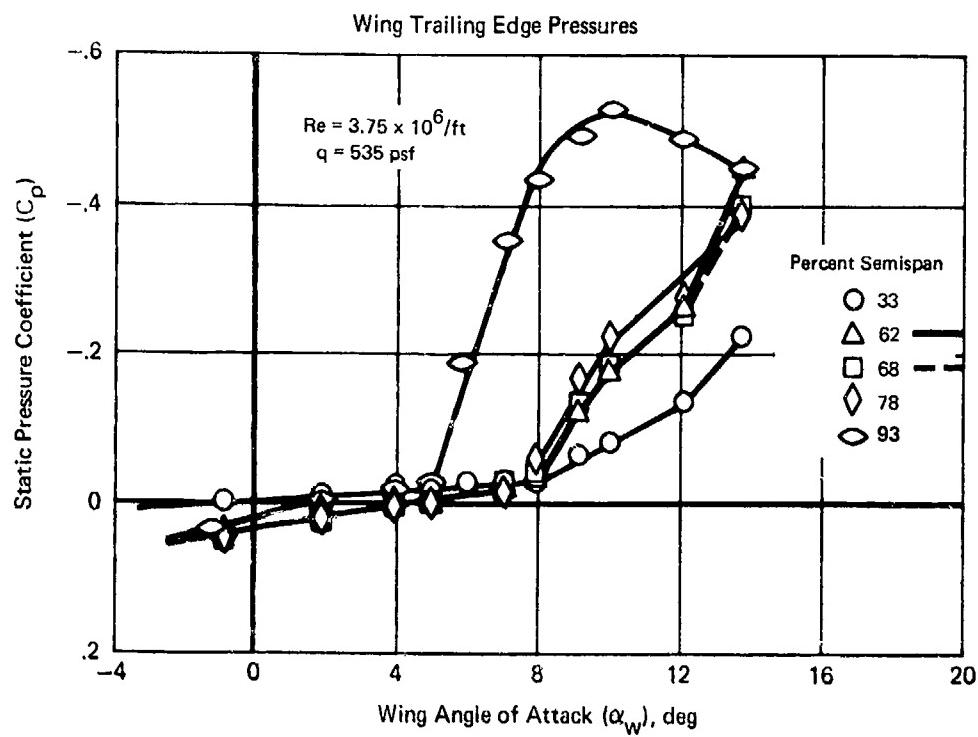


Figure A-16 Static Pressure Coefficient vs Wing Angle of Attack.
Configuration 1, Mach 0.7

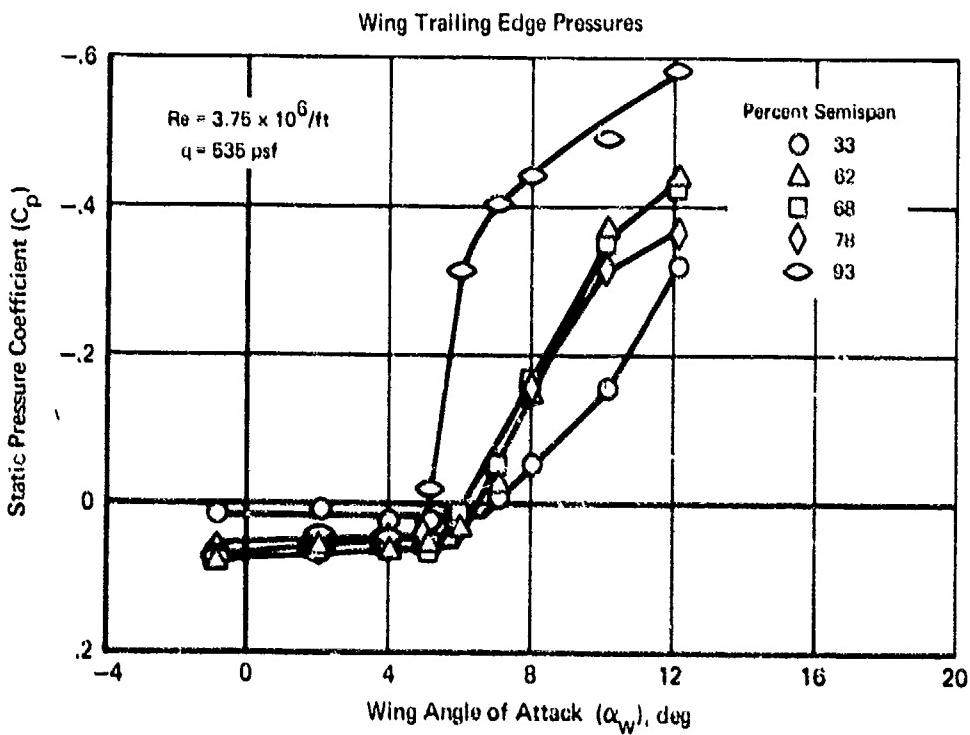


Figure A-17 Static Pressure Coefficient vs Wing Angle of Attack.
Configuration 1, Mach 0.9

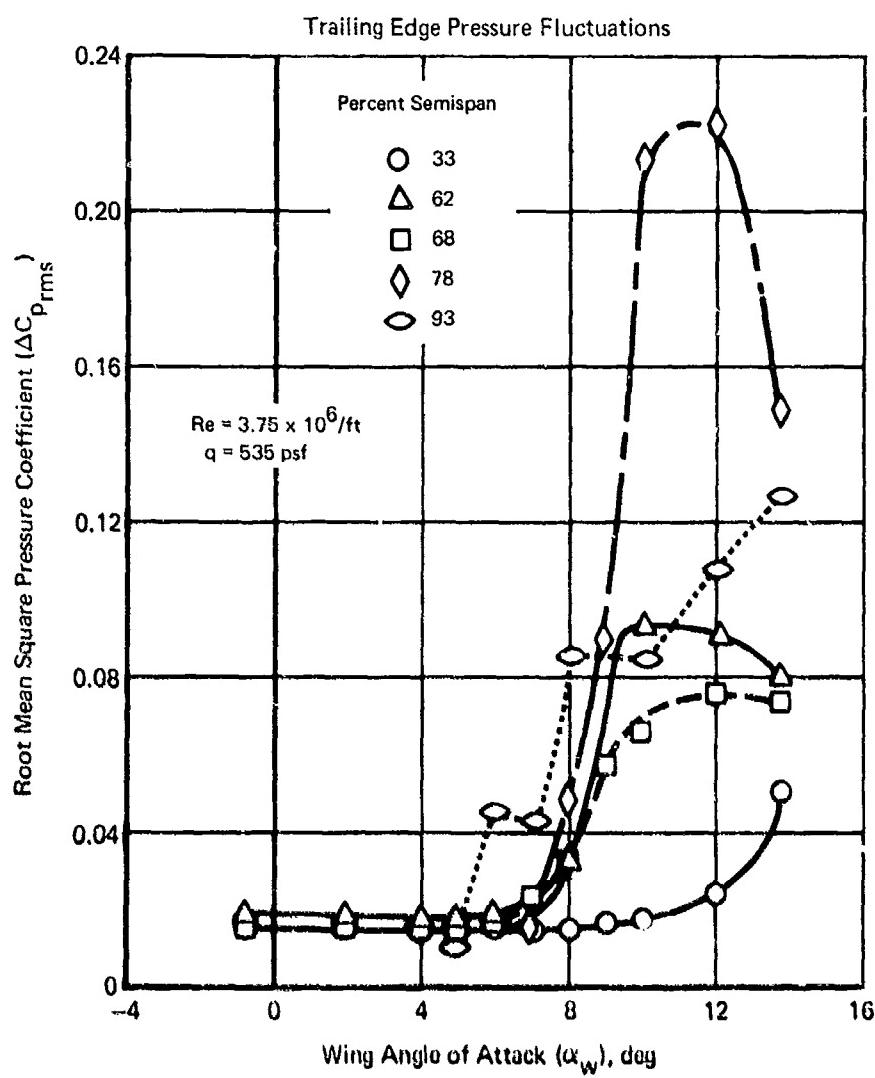


Figure A-18 Root Mean Square Pressure Coefficient vs Wing Angle of Attack.
 Configuration 1, Mach 0.7

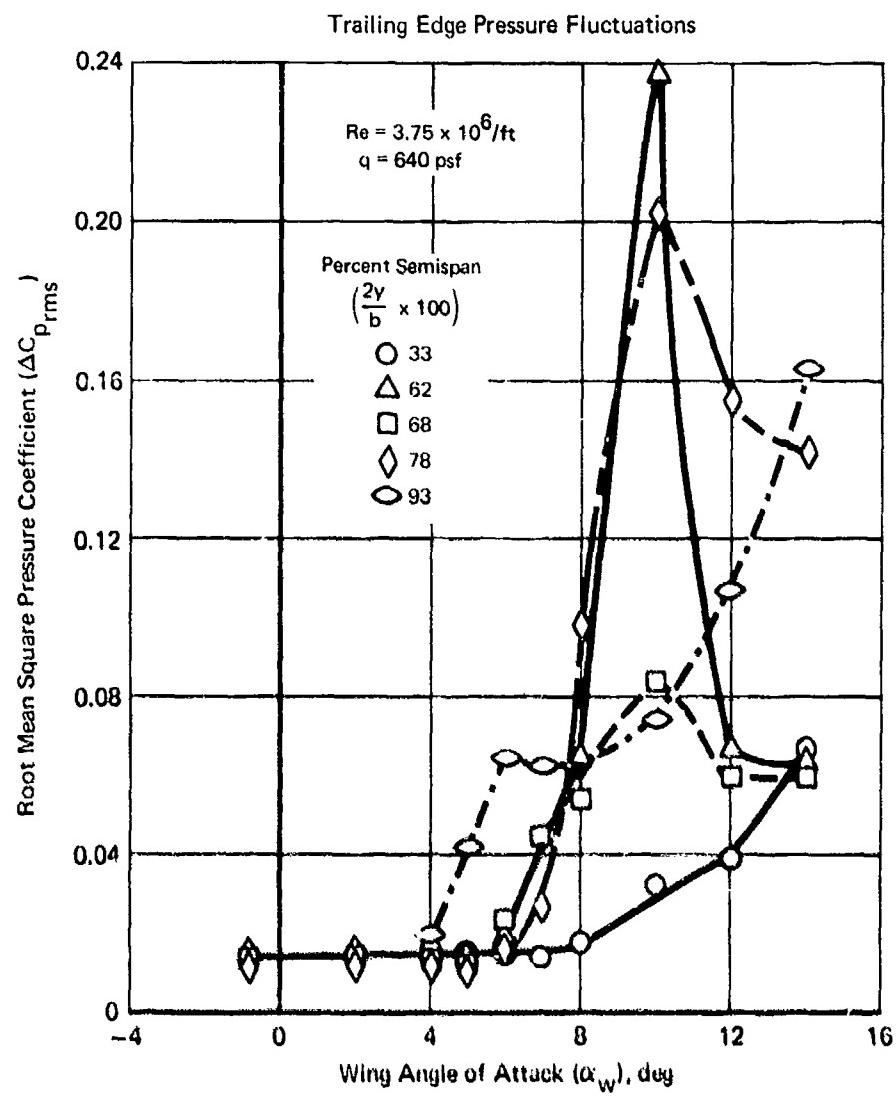


Figure A-19 Root Mean Square Pressure Coefficient vs Wing Angle of Attack
 Configuration 1, Mach 0.9

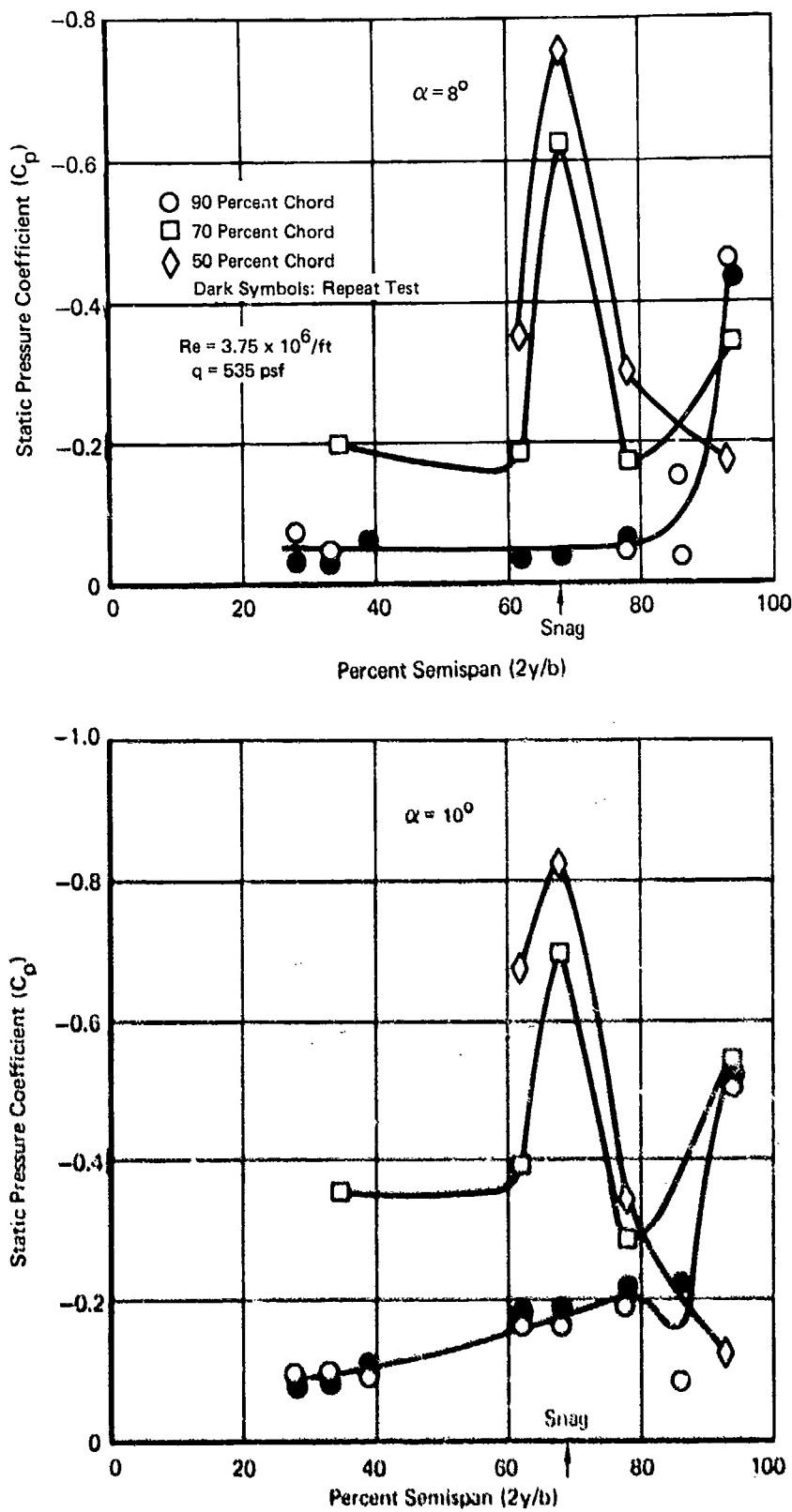


Figure A-20 Static Pressure Coefficient vs Percent Semispan
Configuration 1, Mach 0.7

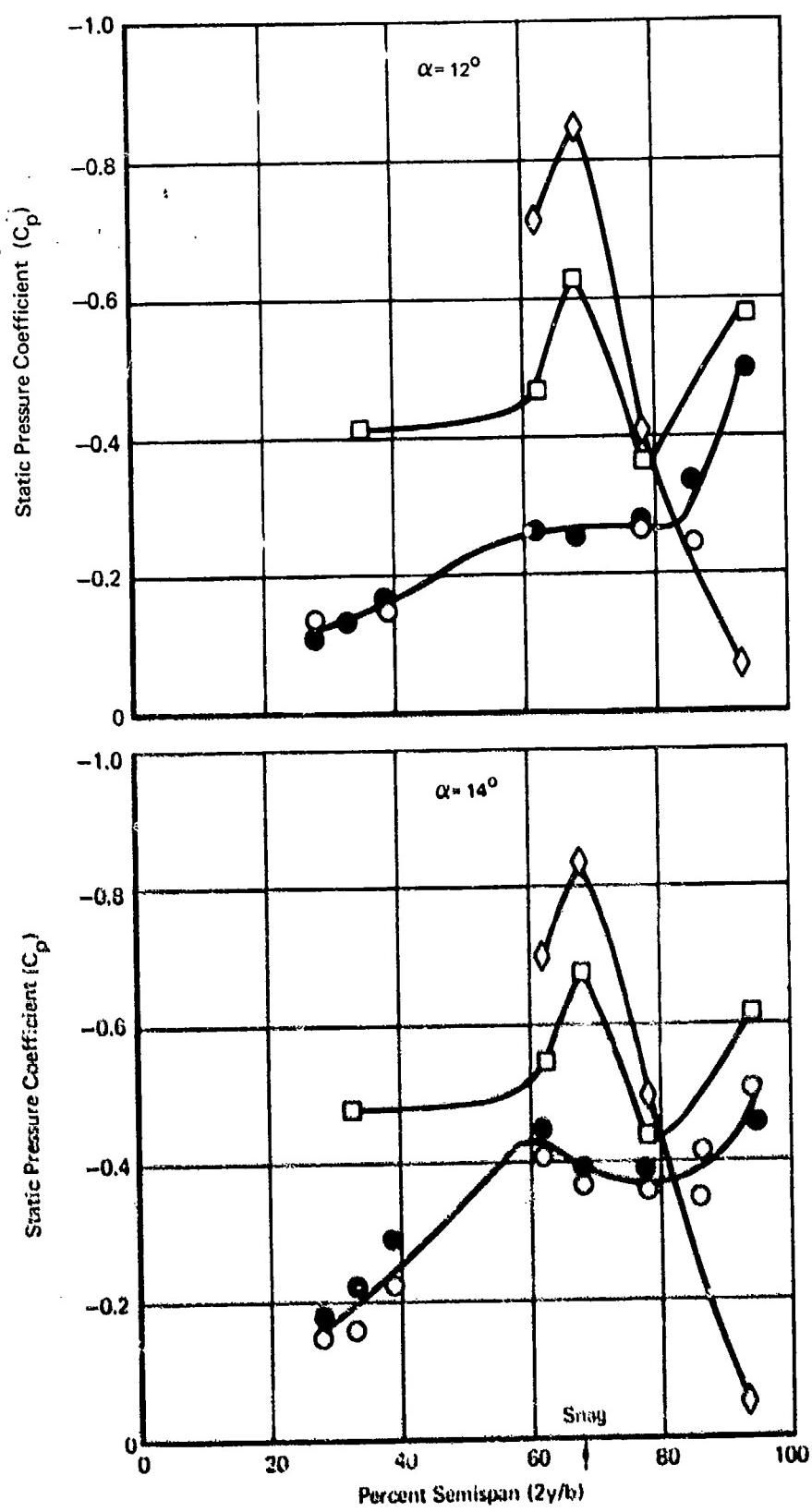


Figure A-20 Static Pressure Coefficient vs Percent Semispan.
Configuration 1, Mach 0.7 (Continued)

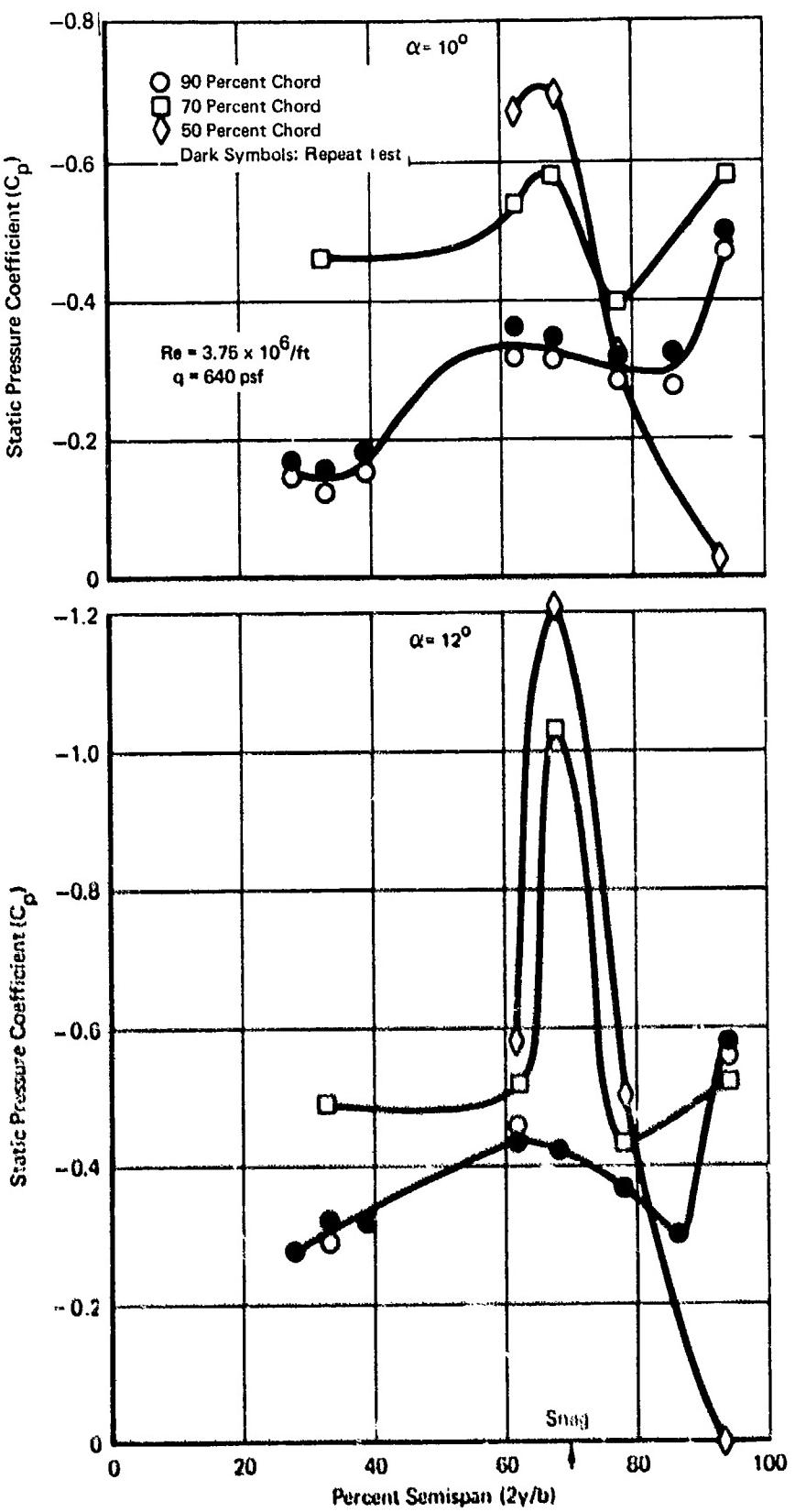


Figure A-21 Static Pressure Coefficient vs Percent Semispan Configuration 1, Mach 0.9.

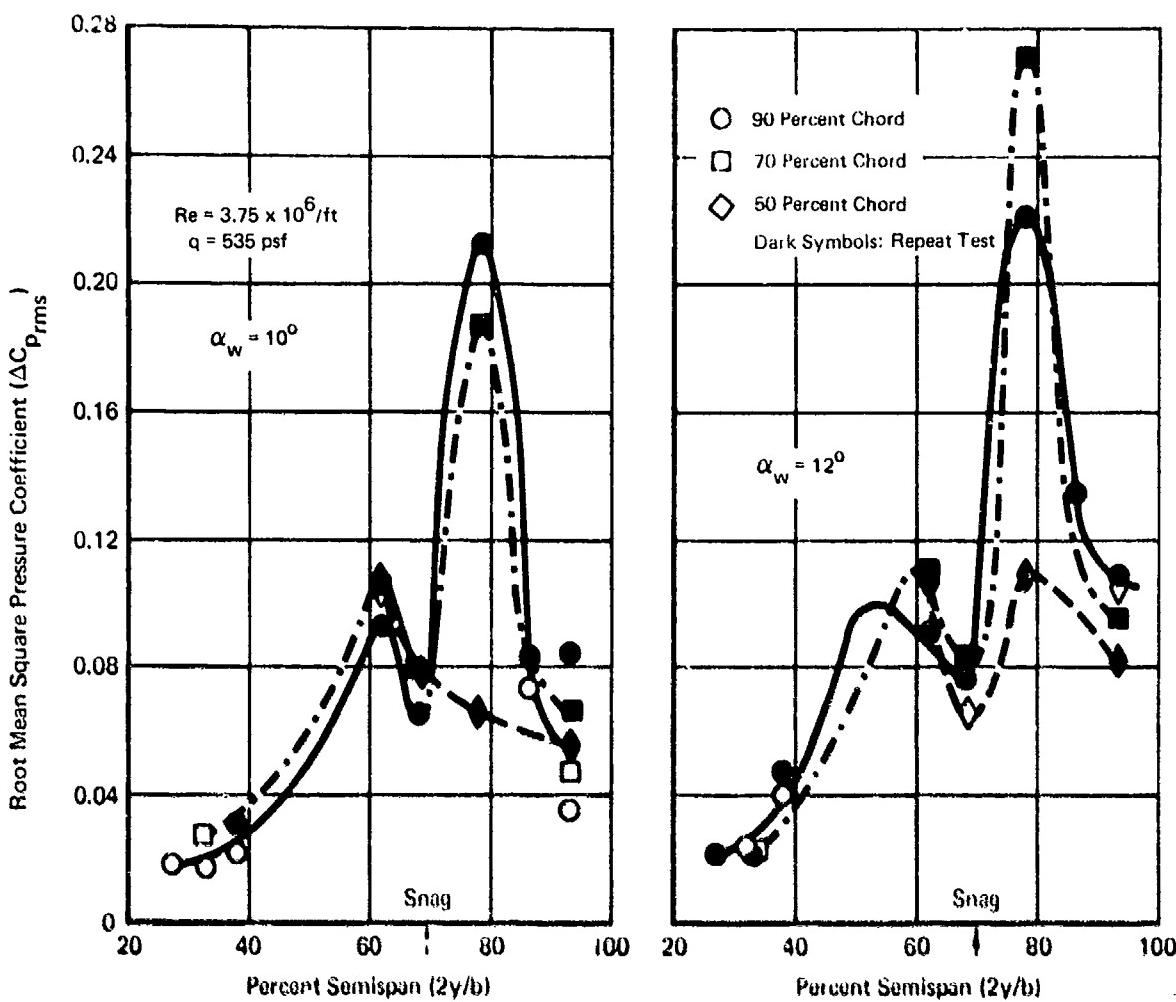
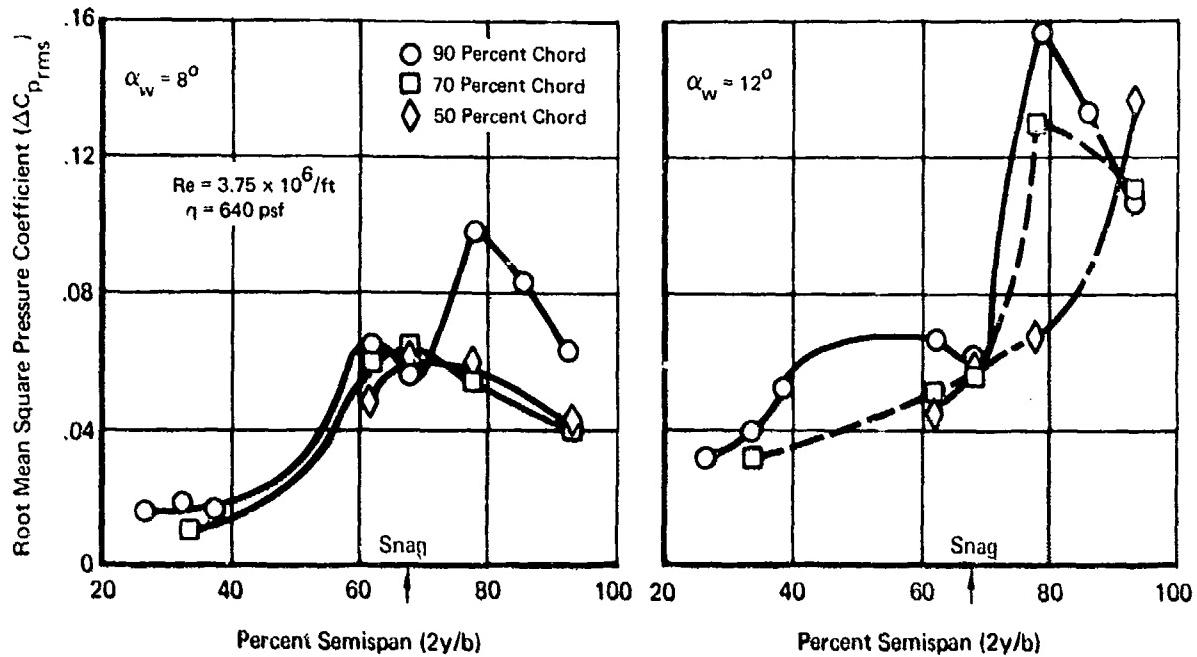


Figure A-22 Root Mean Square Pressure Coefficient vs Percent Semispan,
Configuration 1, Mach 0.7



**Figure A-23 Root Mean Square Pressure Coefficient vs Percent Semispan.
Configuration 1, Mach 0.9**

REFERENCES

1. Huston, W. B. and Skopinski, T. H., "Probability and Frequency Characteristics of Some Flight Buffet Loads", NASA Report NACA TN 3733, August 1956.
2. Cohen, Marshall, "Buffet Characteristics of the Model F-4 Airplane in the Transonic Flight Regime", Air Force Report AFFDL-TR-70-56, April 1970.
3. Titiriga, A. Jr., "F-5A Transonic Buffet Flight Test", AFFDL-TR-69-110, December 1969.
4. Cahill, J. F., and Stanewsky, E., "Wind Tunnel Tests of a Large-Chord, Swept-Panel Model to Investigate Shock-Induced Separation Phenomena", Air Force Report AFFDL-TR-69-78, October 1969.
5. Bies, David A., "A Review of Flight and Wind Tunnel Measurements of Boundary Layer Pressure Fluctuations and Induced Structural Response", NASA Report, CR-626, October 1966.
6. Black, T. J., "An Analytical Study of the Measured Wall Pressure Field Under Supersonic Turbulent Boundary Layers", NASA Report CR-888, April 1968.
7. Rose, R., and Nicholas, O. P., "Flight and Tunnel Measurements of Pressure Fluctuations on the Upper Surface of the Wing of a Venom Aircraft with a Sharpened Leading Edge", (British) Aeronautical Research Council. C.P. No. 1032, 1969.
8. Rainey, A. Gerald, "Progress on the Launch-Vehicle Buffeting Problem", Journal of Spacecraft and Rockets, Volume 2, Number 3, May-June 1965.
9. Houboolt, J.C. "Structural Response of Reentry Vehicles to Boundary Layer Noise", Aeronautical Research Associates of Princeton Inc., ARAP Report No. 65, March 1965.
10. Schweiker, J. W., and Davis, R. E., "Response of Complex Shells Structures to Aerodynamic Noise", National Aeronautics and Space Administration, NASA CR-450, April 1966.
11. Gregoire, J. E., "Wind Tunnel Flow Visualization Tests on the 10-Percent F-4E Model for Buffet Dynamic Loads", Series I (Volumes I, II, III), Air Force Report (To be published).
12. Black, J. A., "Force and Flow Visualization Tests on a 0.10-Scale Model of the F-4E Aircraft at Mach Numbers from 0.70 to 1.20", AEDC-TR-70-260, November 1970.

13. Gregoire, J. E., "Wind Tunnel Tests on the 10-Percent F-4E Model for Buffet Dynamic Loads," Series II, Air Force Test Report (To be published).
14. Stewart, A.A., "Vibration Tests of a Ten Percent Scale F-4E Buffet Loads Model", Air Force Test Report (To be published)
15. Arnold Engineering Development Center Test Facilities Handbook, (Eighth Edition) December 1969
16. Bendat, Julius S., and Piersol, Allan G., "Measurement and Analysis of Random Data", John Wiley and Sons, New York, 1966.
17. Lee, Y. W. "Statistical Theory of Communication", John Wiley and Sons, New York, 1964.
18. Coe, Charles F., "The Effect of Model Scale on Rigid-Body Unsteady Pressures Associated with Buffeting," Proceedings of Symposium on Aeroelastic and Dynamic Modeling Technology, USAF (RTD), TDR-63-4197, Part II, March 1964.
19. Garrick, I. E., and Rainey, A. Gerald, "Remarks on the State-of-the-Art of Buffet Loads Prediction", for Presentation to Structure and Materials Panel of AGARD, Paris, France, July 3-6, 1962.
20. Wilmarth, W. W., "Space-Time Correlations and Spectra of Wall Pressure in a Turbulent Boundary Layer." NASA Memo 3-17-59W, March 1959.
21. Davis, R. E., "Random Pressure Excitation of Shells and Statistical Dependence Effect of Normal Mode Response," NASA Final Report, NASA CR-311, September 1965.
22. Houbolt, J. C., "On the Response of Structures Having Multiple Random Inputs", presented before the meeting of the Wissenschaftliche Gesellschaft fur Luftfahrt E. V. (WGL), Essen, Germany, 9-12 April 1957.
23. Hamilton, W. W., and Peakar, R. E., "Model F4H-1 Airplane Ground Vibration Test Report", Report 6974, McDonnell Aircraft Company, St. Louis, 16 February 1960.
24. Davidson, P.H., "Final Report, Flight Test of Non-Operative TISEO to Evaluate Vibration and Acoustic Environment, Model F-4E", Report MDC A0081, McDonnell Aircraft Company, St. Louis, 15 October 1970.

UNCLASSIFIED

Security Classification

DOCUMENT CONTROL DATA - R & D

(Security classification of title, body of abstract and Indexing annotation must be entered when the overall report is classified)

1. ORIGINATING ACTIVITY (Corporate author) McDonnell Aircraft Company McDonnell Douglas Corporation St. Louis, Mo. 63166		2a. REPORT SECURITY CLASSIFICATION UNCLASSIFIED
		2b. GROUP
3. REPORT TITLE Buffet Dynamic Loads During Transonic Maneuvers		
4. DESCRIPTIVE NOTES (Type of report and inclusive dates) Final Report March 1970 - December 1971		
5. AUTHOR(S) (First name, middle initial, last name) R. E. Mullans C. E. Lemley		
6. REPORT DATE September 1972	7a. TOTAL NO. OF PAGES 268	7b. NO. OF REFS 24
8a. CONTRACT OR GRANT NO. F33615-70-C-1272	9a. ORIGINATOR'S REPORT NUMBER(S) AFFDL-TR-72-46	
b. PROJECT NO. 1370	c. OTHER REPORT NO(S) (Any other numbers that may be assigned this report)	
c. Task No. 137008 d.		
10. DISTRIBUTION STATEMENT Distribution limited to U.S. Government agencies only, test and evaluation; statement applied 12 June 1972. Other requests for this document must be referred to AF Flight Dynamics Laboratory, (FY), Wright-Patterson AFB, Ohio 45433		
11. SUPPLEMENTARY NOTES	12. SPONSORING MILITARY ACTIVITY Air Force Flight Dynamics Laboratory Air Force Systems Command WPAFB, Ohio 45433	
13. ABSTRACT <p>This report describes an empirical/theoretical study program to develop a first generation method for predicting the buffet dynamic loads and fighter aircraft responses that occur during transonic maneuvers. The prediction method applies to wing upper surface loads acting on the airplane and the induced aircraft dynamic responses. Wind tunnel tests of a 10% scale model of the YF-4E aircraft were used to enhance understanding of the buffet mechanism for lifting surfaces and to obtain data needed to deduce the surface load formulas. A first test phase (Series I) gave oil flow and tuft information regarding flow on the upper wing surfaces. A second test phase (Series II) was used to acquire both steady and fluctuating pressure and strain data as well as acceleration response. The fluctuating pressure data were converted to power and cross-power spectra and a mathematical model was formulated to describe the amplitude and the spatial and spectral distributions of the pressures on the wing. The mathematical pressure description was then used as the forcing function in a dynamic response computer program to assess the structural response. The method described in this report is intended for preliminary aircraft design computations of transonic aircraft buffet dynamic loads and responses. The salient feature is the mathematical description of the nature of buffeting flow over a lifting surface. This feature is generally applicable to prediction of aircraft structural dynamic responses. The general requirement for such calculations is contained in Military Specification MIL-A-8866A(USAF).</p>		

DD FORM 1 NOV 1973 1473

UNCLASSIFIED

Security Classification

Security Classification

14.	RDS	LII	ROLE	LINK B		LINK C	
		ROLE		WT	ROLE	WT	ROLE
	Buffet						
	Dynamic Loads						
	Responses						
	Separated Flow						
	Fluctuating Pressures						
	Transonic Maneuvering						